Capillary barriers on slopes subjected to rainfall: numerical modelling and development of simplified methods of analysis

Paverean Mudcharoen

Submitted in fulfilment of the requirement for the
Degree of Doctor of Philosophy

James Watt School of Engineering
College of Science and Engineering
University of Glasgow

March 2023

Abstract

Climate change is leading to increasing rainfall (particularly increasing frequency and severity of extreme rainfall events). As a consequence, problems of rainfall-induced slope instabilities are increasing and there is increasing need for methods of enhancing slope stability and preventing rainfall-induced instabilities. Capillary barrier systems (CBSs) are an attractive option for enhancing slope stability, because they use only naturally occurring geomaterials (sands and gravels) and therefore have low carbon footprint, as long as they can be locally sourced.

CBSs are soil cover systems, consisting of a finer layer of soil overlying a coarser layer of soil, that are intended to limit infiltration of water into the underlying soil. The function of a CBS is based on the contrast between the hydraulic properties (i.e. soil water retention curve and soil hydraulic conductivity curve) of the finer and coarser layers. The performance of a CBS on a slope depends upon both the water storage capacity of the CBS and the water transfer capacity down the slope. The aim of this PhD project was to use hydraulic and thermo-hydraulic numerical modelling to develop and validate simplified methods of analysis for sloping CBSs for enhancing slope stability that are suitable for use by practising geotechnical engineers in industry and that can account for the climate and meteorological conditions of an individual site.

The original research presented in the thesis can be divided into four major parts. The first part investigated horizontal CBSs subjected to continuous rainfall of constant intensity. This involved one-dimensional hydraulic FE numerical analyses and numerical validation of existing simplified methods (due to Stormont and Morris (1998) and Scarfone (2020)) for calculating water storage capacity at steady state of conventional horizontal CBSs and multi-layered horizontal CBSs respectively. This represented a more comprehensive numerical validation of these existing simplified methods than previously reported in the literature.

The second major component of original research investigated sloping CBSs subjected to continuous rainfall of constant intensity and involved two-dimensional hydraulic FE numerical analyses and development and numerical validation of a new simplified method for calculating water storage capacity and water transfer capacity (and hence diversion length). In all cases analysed, the

proposed new simplified method provided an excellent match to the results from the FE simulations, in contrast to an existing simplified method (proposed by Parent and Cabral (2006)), which assumed an unrealistic approximate final steady state suction profile (more appropriate for a horizontal CBS). The new simplified method was also successfully extended to multi-layered sloping CBSs.

The third part of the work used thermo-hydraulic FE analyses and hydraulic FE analyses to investigate the behaviour of sloping CBSs subjected to various simple patterns of intermittent rainfall of varying intensity. This led to improved understanding of the behaviour of sloping CBSs under more realistic rainfall conditions, including the effects of evaporation from the ground surface and hysteresis in the hydraulic behaviour of the CBS materials.

The final major original part of the research described in the thesis involved the development and successful numerical validation of a new simplified method of analysis for sloping CBSs subjected to extreme rainfall events. The new simplified method uses a method of slices to predict the variation with time of interface flow velocity (across the interface between finer and coarser layers) at any value of horizontal coordinate within the slope for any specified extreme rainfall event (i.e. any specified variation of rainfall intensity with time). This simplified method of analysis for extreme rainfall events could form a central part of a practical design methodology for sloping CBSs, suitable for use by practising engineers in industry.

Table of Contents

Acknowledgement

I would like to express my deepest gratitude to my supervisor Prof. Simon Wheeler, for his invaluable patience and amazing guidance. This endeavour would not have been possible without my supervisor, who generously provided brilliant technical knowledge and expertise. I am thankful for the extraordinary experience that he provided me to grow professionally. It has been an honour to learn from him.

Special thanks are due to Dr Riccardo Scarfone for providing the technical knowledge using the software CODE_BRIGHT and for continuous help and advice through the process of learning to use CODE_BRIGHT. I am also extremely grateful to Dr Thomas Shire, my former second supervisor, and Dr Zhiwei Gao, my second supervisor, for always being ready to help with any questions that I had.

I would like to acknowledge The Royal Thai Government, the Ministry of Transportation of Thailand, and Department of Highways for financial support.

Finally, I would like to provide special thanks to my husband Patara, my father, my sisters, and my family for their unconditional love, continuous support, and confidence. All this achievement I would like to dedicate to my mother. This one is for you, from me, your proud daughter. To my friends, thank you all for your support and for always making me feel like home.

Author's Declaration

I declare that the thesis has been composed by myself and that the work has not been submitted for any other degree or professional qualification. I confirm that the work submitted is my own except where explicitly stated otherwise in the text. My contribution to this work has been explicitly indicated below.

I acknowledge that this work was conducted under my supervisor Prof. Simon Wheeler. I specifically acknowledge that Prof. Wheeler identified the problem with the approximate suction profile assumed in the existing simplified method of analysis for sloping CBSs (see Section 5.1) and he developed the proposal for a new approximate suction profile (see Section 5.2). Prof. Wheeler also came up with the initial proposal for the simplified method of analysis of extreme rainfall events (see Section 7.1). I carried out all the numerical analysis and all the implementation of the various simplified methods.

Symbols/ Abbreviations

a	Soil constant for liquid film component of hydraulic conductivity
a_d, a_w	Values of a on main drying curve or main wetting curve
a^{Film}	Value of a in CODE_BRIGHT
A, B	Parameters in expression for liquid viscosity (CODE_BRIGHT)
A, B, C, D	Parameters in expression for gas viscosity (CODE_BRIGHT)
A_d	Dry albedo
A_d	Integration constant (defining scanning drying curve)
A_l	Surface albedo
A_w	Wet albedo
A_w	Integration constant (defining scanning wetting curve)
$\boldsymbol{b}$	Vector of body forces
c'	Cohesion of soil
$C(s)$	Correction factor (Fredlund and Xing 1994 SWRC model)
C_a	Specific heat of the atmospheric gas
C_{cloud}	Correction parameter for cloudiness
C^{Film}	Soil constant for liquid film component of hydraulic conductivity
C_r^{Film}	C^{Film} divided by saturated hydraulic conductivity k_s (CODE_BRIGHT)
C_s	Solid phase specific heat
d^{Film}	Exponential parameter component of hydraulic conductivity expression for liquid film (CODE_BRIGHT)
D	Empirical constant for diffusion coefficient
D	Particle diameter
D_g^w	Diffusion coefficient of vapour in gas phase

D_{10}, $D_{10,c}$, $D_{10,f}$	10% passing particle size of soil, coarser layer or finer layer
$D_{15,c}$	15% passing particle size of coarser layer
$D_{85,c}$	85% passing particle size of finer layer
e_T	Charge on an electron
e	Void ratio
e_g, e_l, e_s	Internal energy of gas, liquid, and solid phases
E	Evaporation rate
E_g^w, E_g^a, E_l^w, E_l^a	Advective energy fluxes
ES	Energy stored in soil layer
f^a	External supply of air
f^w	External supply of water
f^Q	An internal/external energy supply
$\mathbf{g}$	Gravitational acceleration
G_s	Energy flux leaving the layer at the lower boundary
h_g	Pneumatic head
h_l	Hydraulic head
h_v, h_{lv}, h_a	Free energy of vapour, liquid water or air
H	Henry's constant
H_c	Convective heat flux into the layer from the atmosphere
H_e	Latent heat of evaporation
H_s	Sensible heat flux into atmosphere
i	Rainfall intensity
$\boldsymbol{i}_c$	Energy flux due to conduction through porous medium
$\boldsymbol{i}_l^a$	Mass flux of dissolved air due to diffusion
$\boldsymbol{i}_g^w$	Mass flux of water due to diffusion of vapour
$\boldsymbol{i}_l^w$	Non-advective mass flux of water in liquid phase
$\mathbf{I}$	Identity matrix
I_{nf}	Rate of water intercepted by plant cover that does not infiltrate into the soil
$\boldsymbol{j}_a$	Total mass flux of air
$\boldsymbol{j}_e$	Total energy flux

$\boldsymbol{j}_s$	Total mass flux of solid
$\boldsymbol{j}_{sr}$	Surface runoff
$\boldsymbol{j}_{es}, \boldsymbol{j}_{eg}, \boldsymbol{j}_{el}$	Energy fluxes due to advection of solid, gas or liquid
$\boldsymbol{j}_g^a$	Mass flux of air in gas phase
$\boldsymbol{j}_l^a$	Mass flux of air in liquid phase
$\boldsymbol{j}_g^w$	Mass flux of water in gas phase
$\boldsymbol{j}_l^w$	Mass flux of water in liquid phase
$\boldsymbol{j}_g^0, \boldsymbol{j}_l^0, \boldsymbol{j}_e^0$	Prescribed gas or liquid flow rate or energy flux at the boundary
$\boldsymbol{j}_w$	Total mass flux of water at boundary
k_B	Boltzmann constant
k_{evap}	Numerical coefficient
k_g	Gas conductivity
k_{gr}	Relative conductivity of gas phase
k_l	Hydraulic conductivity
k_{lr}	Relative hydraulic conductivity
k_i	Intrinsic permeability
k_{rain}	Numerical coefficient
$k_s, k_{s,f}, k_{s,c}$	Saturated value of hydraulic conductivity of soil, of finer layer and coarser layer
k^{Bulk}	Bulk water component of hydraulic conductivity
k^{Film}	Liquid film component of hydraulic conductivity
k_{11}, k_{22} and k_{33}	Intrinsic permeability, 1st , 2nd and 3rd principal directions respectively
K	Von Karman's constant
L_D	Diversion length
L_{Da}, L_{Db}, and L_{Dc}	Final steady state diversion length corresponding to rainfall intensities i_a, i_b and i_c respectively
m	Soil constant for SWRC constitutive model (van Genuchten model)
m_d, m_w	van Genuchten soil constants for main drying curve or main wetting curve respectively
M_a, M_w	Molecular mass of air and water

n	Soil constant for SWRC constitutive model (van Genuchten model)
n_d, n_w	van Genuchten soil constants for main drying curve or main wetting curve respectively
p_a	Partial pressure of air in the gas phase
p_{at}	Atmospheric pressure
p_g	Pore gas pressure (as an absolute pressure)
p_{ga}	Atmospheric gas pressure
p_l	Pore liquid pressure (as an absolute pressure)
p_{l0}	Reference pressure
p_{vo}	Saturated vapour pressure in gaseous phase in contact with a planar gas-liquid interface
P	Precipitation rate
P_o	Soil constant for hydraulic constitutive model (van Genuchten model)
$P_{o,d}$, $P_{o,w}$	van Genuchten soil constants for main drying curve or main wetting curve respectively
$\bar{P}_o$	Value of P_o at a reference temperature of 20°C
$\boldsymbol{q}_g$	Advective flux of gas (volumetric flow rate of gas through unit cross-sectional area of soil)
q_h	Horizontal seepage velocity
q_i	Interface flow velocity per unit plan area
$\boldsymbol{q}_l$	Advective flux of liquid (volumetric flow rate of liquid through unit cross-sectional area of soil)
q_n	Seepage velocity normal to the interface
q_v	Vertical seepage velocity
Q	Complementary normal distribution function (Kosugi model)
Q_{max}	Water transfer capacity
Q_x	Water transfer across cross-section at horizontal coordinate x
r_1, r_2	Principal radii of curvature of liquid-gas interface
R	Universal gas constant (psychrometric law)
R_{ech}	Rate water recharged to underlying soil

R_h	Relative humidity within soil voids
R_{ha}	Atmospheric relative humidity
R_{ld}	Downward atmospheric long-wave radiation
R_{lu}	Upward long-wave radiation from soil surface
R_n	Net incoming radiation flux at soil surface
R_{off}	Surface run off
R_s	Global short-wave solar radiation
s	Matric suction
s_{AE}	Air entry value of suction
s_{AEX}	Air exclusion value of suction
$s_{AEX,f}$	Value of s_{AEX} for the finer layer
s_{BWC}	Bulk water continuity value of suction
$s_{BWC,c}$	Value of s_{BWC} for the coarser layer
s_c^* , s_f^*	Value of suction (for coarser layer or finer layer respectively) at which the hydraulic conductivity k_s is equal to the rainfall infiltration rate i
s_d , s_w	Values suction on the main drying curve and main wetting curve at the current value of S_l (hysteretic SWRC model)
s_{dry}	Suction value at oven-dryness
s_m	Soil constant for SWRC constitutive model (Kosugi model)
s_r	Suction value at which SWRC starts decreasing linearly in semi-logarithmic plot
s_0	Suction value at the last suction reversal point
s_1	Suction value at the bottom of lowest finer layer
s_2	Suction value at the top the first finer layer
s_3	Constant suction within intermediate coarser layer of multi-layered CBS
s_4	Suction value at top of finer layers in multi-layered CBS (except first finer layer)
S_g	Degree of gas saturation
S_l	Degree of liquid saturation

$S_{l,BWC}$	Value of degree of saturation at bulk water continuity point
$S_{l,BWD}$	Value of degree of saturation at bulk water discontinuity point
$S_{l,BWE}$	Value of degree of saturation at bulk water entry point
$S_{l,BWEX}$	Value of degree of saturation at bulk water exclusion point
S_l^C , S_l^B	Variables in expression for bulk water component of hydraulic conductivity
S_{le}	Effective degree of liquid saturation
S_{le0}	Effective degree of liquid saturation at last suction reversal point
$S_{le,d}$, $S_{le,w}$	Effective degree of liquid saturation on the scanning drying curve and scanning wetting curve respectively
$S_{le,Md}$, $S_{le,Mw}$	Effective degree of liquid saturation on the main drying curve and main wetting curve respectively
$S_{l,d}$, $S_{l,w}$	Degree of saturation on the scanning drying curve or scanning wetting curve
$S_{l,Md}$, $S_{l,Mw}$	Degree of saturation on main drying curve or main wetting curve
S_{lr}	Residual degree of saturation
$S_{lr,d}$, $S_{lr,w}$	Residual degree of saturation for the main drying curve and the main wetting curve
S_{ls}	Maximum degree of saturation
$S_{ls,d}$, $S_{ls,w}$	Maximum degree of saturation for the main drying curve and the main wetting curve
t	Time
t_c	Thickness of coarser layer
t_{CBS}	Total thickness of CBS
t_f	Thickness of finer layer
t_f^*	Critical thickness of finer layer
$t^k, t^{k+\varepsilon}, t^{k+\theta}$, t^{k+1}	time discretization
$t_{lag,1}$	Time-lag for breakthrough to commence after an increase of rainfall intensity

$t_{lag,2}$	Further time-lag for increase of interface flow rate after a further increase of rainfall intensity
$t_{lag,3}$	Time-lag before breakthrough ceases after a decrease of rainfall intensity
t_m	time at noon
t_s	time when autumn starts
T	Absolute soil temperature (in degree Kelvin)
T_a	Atmospheric temperature
u_a	Pore air pressure (relative to atmospheric)
u_w	Pore water pressure (relative to atmospheric)
$\boldsymbol{u}, \dot{\boldsymbol{u}}$	Solid displacement and solid displacement rate
v_a	atmospheric wind speed
WS	Water stored
$WS_{x,a}, WS_{x,b}, WS_{x,c}$	Steady state water stored at cross-section at x under rainfall intensities i_a, i_b and i_c respectively
WSC	Water storage capacity
WSC_a, WSC_b, WSC_c	Water storage capacities under rainfall intensities i_a, i_b and i_c respectively
x	Horizontal coordinate measured from the top of the slope
X_D	An empirical constant (Tokunaga, 2009) for C^{Film} estimation
z	Elevation relative to an arbitrary horizontal reference datum or relative to interface between finer layer and coarser layer
z_0	Roughness length
z_a	Screen height
Z	Ion charge
α	Constant factor for new simplified suction profile for sloping CBSs
α_f , α_c	Soil constant, for finer layer and coarser layer respectively
α_d	Drying value of contact angle at the receding edge
α_w	Wetting value of contact angle at front edge
α_T	Thermal expansion coefficient (liquid density)

β	Slope angle
β_g , β_l	Gas and liquid leakage coefficient for boundary conditions (numerical factor)
β_ρ	Parameter in expression for liquid density (CODE_BRIGHT)
γ_l , γ_g	Unit weight of liquid or gas
$\gamma_{l,n}$, $\gamma_{g,n}$, $\gamma_{e,n}$	Numerical liquid, gas or energy leakage coefficients
γ_w , γ_d	Soil constant for scanning wetting curves and scanning drying curves in hysteretic SWRC model
ε	Relative permittivity
ε_0	Permittivity of free space
ε_s	Emissivity of the ground surface
ε_a	Emissivity of the atmosphere
$\dot{\boldsymbol{\varepsilon}}$	Strain rate tensor
θ	Contact angle between liquid-gas interface and soil particle surface
θ_l^a	Mass of air per unit volume in liquid phase
θ_l^w	Mass of water per unit volume in liquid phase
θ_g^a	Mass of air per unit volume of gas
λ	Latitude
λ_{dry} , λ_{sat}	Thermal conductivity in dry or fully saturated conditions
λ_T	Thermal conductivity
λ_{solid}, λ_{gas} , λ_{liq}	Thermal conductivities of the solid phase, gas phase or liquid phase respectively
μ_g	Dynamic viscosity of gas
μ_l	Dynamic viscosity of liquid
μ_w	Dynamic viscosity of the permeating water
ξ	Soil constant (Fayer and Simmons (1995) SWRC)
ξ_d , ξ_w	Soil constant for the main drying curve and wetting curve respectively (hysteretic SWRC model)
ρ_a	Density of dry air
ρ_g	Density of gas
ρ_{ga}	Density of atmospheric gas

ρ_l	Density of liquid
ρ_{l0}	Reference density
ρ_s	Density of soil particles
ρ_v	Density of vapour (also known as absolute humidity)
ρ_{va}	Density of atmospheric vapour
ρ_{vo}	Density of saturated vapour
ρ_w	Density of permeating water
$\boldsymbol{\sigma}$	Total stress tensor
σ'	Effective stress
σ_R	Stefan-Boltzmann constant
σ_s	Surface tension
$\bar{\sigma}_s$	Value of σ_s at reference temperature of 20℃
σ_m	Soil constant for SWRC constitutive model (Kosugi model)
τ	Tortuosity parameter
τ_f	Shear strength
ϕ', ϕ'_f	Friction angle of soil and of finer layer
ϕ^b	Fredlund et al (1978)'s additional friction angle of unsaturated soil
Φ	Porosity
χ	Effective stress parameter in equation of Bishop (1959)
ψ	Stability factor
ω_l^a	Mass fraction of air in liquid phase (dissolved air mass fraction)
ω_g^w	Mass fraction of water in gas phase (vapour mass fraction)

AC	Air continuity point
AE	Air entry point
AEX	Air exclusion point
BWC	Bulk water continuity point
BWD	Bulk water discontinuity point
BWE	Bulk water entry point

BWEX	Bulk water exclusion point
CB	CODE_BRIGHT software
CBS	Capillary barrier systems
C.L	Coarser layer
CS	Coarse sand
E	Evaporation rate
FE	Finite element
FSGV	Capillary barrier system with finer layer made of fine sand and coarser layer made of gravelly sand
F.L	Finer layer
FS	Fine sand
full-H	Full hysteretic constitutive model
FoS	Factor of safety
GV	Gravelly sand
H	Hydraulic model
HELP	Hydrological Evaluation of Landfill Performance
ICL	Types of constitutive law in CODE_BRIGHT
ITYCL	Versions of that type of constitutive model in CODE_BRIGHT
LF	Liquid film
MD	Main drying curve
modM	modified Mualem SWRC constitutive model
modVG	modified van Genuchten SWRC constitutive model
MCBS	Multi-layered capillary barrier system
MS	Medium sand
MW	Main wetting curve
N	number of finer layers in multi-layered CBS
P	Precipitation rate (mass flow rate per unit plan area)
P1 to P10	Parameter numbers
P&C	Parent and Cabral (2006) simplified method
SHCC	Soil hydraulic conductivity curve
SS	Silty sand
SSGV	Capillary barrier system with finer layer made of silty sand and coarser layer made of gravelly sand
SWRC	Soil water retention curve

SWRC-VG	van Genuchten SWRC model
SWRC-modVG	Modified van Genuchten SWRC model
SWRC-hysteretic VG	Hysteretic van Genuchten SWRC model
SWRC-hysteretic modVG	Hysteretic modified van Genuchten SWRC model
TH	Thermo-hydraulic model
THMC	Thermo-hydro-mechanical-chemical model
US	Underlying soil
VG	van Genuchten SWRC constitutive model
VG-M	van Genuchten SWRC constitutive model and van Genuchten-Mualem SHCC constitutive model
WS	Water stored
WSC	Water storage capacity

Chapter 1 Introduction

1.1 Background

Capillary barrier systems (CBSs) generally consist of two layers with different soil particle sizes, a finer layer (F.L) overlying a coarser layer (C.L), placed over the ground to prevent percolation of water into the underlying soil. CBSs have been primarily used for landfill cover systems to prevent water infiltration into waste disposal (Mallants et al., 1999; Benson et al., 2007).

The function of a CBS is based on the contrast between the hydraulic properties (soil water retention curve (SWRC) and soil hydraulic conductivity curve (SHCC)) of the finer and coarser layers. In unsaturated conditions, at a given value of suction, the coarser layer is at much lower degree of saturation than the finer layer and, as consequence, the hydraulic conductivity of the coarser layer is lower than that of the finer layer (the reverse of the situation under saturated condition). This limits water percolation from the finer layer to the coarser layer, with the coarser layer acting as a low permeability barrier. Water is stored within the finer layer until the maximum storage capacity of the finer layer is reached, at which time water starts flowing down into the coarser layer (and then into the underlying soil). This breakthrough of water to the coarser layer corresponds to failure of the CBS.

The water storage capacity (WSC) of CBSs can be obtained by integrating the volumetric water content within the finer layer thickness at the time when breakthrough to the coarser layer commences. Stormont and Morris (1998) provided a simplified method for calculation of water storage capacity of horizontal CBSs subjected to continuous rainfall of constant intensity. This method uses the SWRC of the finer layer of the CBS and an approximate profile of suction in the finer layer (variation of suction s with height z) at the time of breakthrough. This approximate profile involves a hydrostatic suction profile $\frac{ds}{dz} = \gamma_l$ in the lower part of the finer layer (where γ_l is the unit weight of liquid water), and for the case of a thick finer layer, a constant value of suction s_f^* in the upper part of the finer layer (where s_f^* corresponds to the value of suction at which the hydraulic conductivity k_l of the material of the finer layer is equal to the rainfall infiltration

rate i). See Section 2.7.2 for fuller details, including the thickness of the lower part of the finer layer. For a thin finer layer, the approximate suction profile consists of the hydrostatic suction profile for the entire thickness of the finer layer. The explanation behind this simplified suction profile proposed by Stormont and Morris (1998) is set out fully in Section 2.7.2. Various authors subsequently provided limited experimental or numerical validation of this simplified method of calculating the water storage capacity of a horizontal CBS subjected to continuous rainfall of constant intensity. Scarfone et al. (2020a) performed advanced hydraulic numerical modelling of a limited number of cases and showed that the simplified method (employing the approximate suction profile) provided excellent matches to the suction profiles and water storage capacities observed in their numerical analyses. Scarfone (2020) also extended the simplified method to include multi-layered horizontal CBSs.

CBSs have also been proposed for slopes (Ross, 1990), to prevent rainfall percolation into underlying soils, thus keeping high suction within the underlying soil in order to retain slope stability. The effective performance of sloping CBSs depends upon both the water storage capacity (WSC) and the water transfer capacity down the slope (Ross, 1990; Steenhuis et al., 1991; Oldenburg and Pruess, 1993; Stormont, 1995). Water storage capacity and water transfer capacity are both dependent on the hydraulic properties of the two capillary barrier materials (soil water retention curve SWRC and soil hydraulic conductivity curve SHCC) and the geometry of the slope and CBS (i.e. length of slope, angle of slope, thickness of CBSs materials, and number of finer layers (multi-layered CBSs are possible)). Moreover, the performance of a CBS on a slope also depends upon meteorological conditions and soil-atmosphere interaction phenomena, which determine the variation of rainwater infiltration and evaporation (Stormont and Morris, 1998; Bussière et al., 2007; Zhan et al., 2013).

Several analytical or semi-analytical methods have been proposed to evaluate the water transfer capacity of a CBS on a slope subjected to continuous rainfall of constant intensity. Ross (1990) was the first author to study this problem. He obtained a complete analytical solution for a sloping CBS subjected to steady-state conditions (i.e. continuous rainfall of constant intensity), but he assumed a finer layer of infinite thickness and a rather unrealistic log-linear form for the

SHCC ($k_l = k_s \cdot exp^{-\alpha s}$, where k_s is the hydraulic conductivity under saturated conditions, at zero suction, s is the suction and α is a soil constant). The assumption of a finer layer of infinite thickness, while obviously unrealistic, did not completely invalidate the results, because all the water transfer occurs in the lowest part of the finer layer and beyond a certain thickness, further increases of thickness of the finer layer have no influence on the water transfer capacity (see Sections 2.8.2 and 5.5.2). Later, other authors developed revised analytical solutions for calculation of water transfer capacity, based on modifications to Ross's solution. For instance, Steenhuis et al. (1991) modified Ross's solution with a different assumption for the form of the SHCC and Stormont (1995) accounted for the effect of anisotropy in the hydraulic conductivity of the finer layer of the CBS. Parent and Cabral (2006) developed a revised semi-analytical method, by assuming an approximate suction profile at breakthrough which coincides with the approximate suction profile at breakthrough for a horizontal CBS provided by Stormont and Morris (1998). Unlike the analytical solution of Ross (1990), the semi-analytical method of Parent and Cabral (2006) does not assume a finer layer of infinite thickness and it can be used with any hydraulic conductivity constitutive model.

Various attempts have been made to validate these analytical or semi-analytical solutions for water transfer capacity of a sloping CBS by performing laboratory experimental tests, in-situ monitoring field tests or numerical modelling (Oldenburg and Pruess, 1993; Bussiere et al., 2003; Tami et al., 2004; Bussière et al., 2007; Aubertin et al., 2009; Li et al., 2013; Harnas et al., 2014; Liu et al., 2015). Generally, these authors found reasonable agreement between the predictions of water transfer capacity from a selected analytical or semi-analytical method and the corresponding results from experimental tests or numerical modelling. There were however some inconsistencies and often the comparison involved only a single case or a small number of cases, rather than a comprehensive parametric study.

All the existing analytical or semi-analytical proposals involve significant idealisations. Typically, they assume continuous rainfall of constant intensity. None of the proposed methods allow the full meteorological conditions of a site to be employed within a site-specific design of a CBS on a slope.

Multi-physics numerical modelling is capable of representing the long-term behaviour of a CBS on a slope subjected to realistic weather conditions (including long-term variations of rainfall and evaporation and extreme rainfall events). Scarfone (2020) showed that, for realistic simulations, the numerical modelling should include accurate representation of the hydraulic behaviour of the CBS materials, including hydraulic conductivity behaviour at very low values of degree of saturation (see Scarfone et al., 2020a) and retention hysteresis (see Scarfone et al., 2020b), and accurate representation of soil-atmosphere interactions. Unfortunately, however, this type of complex multi-physics numerical modelling is impractical as a standard design method for practising geotechnical engineers.

1.2 Project motivation and aim

Climate change is leading to increasing rainfall (particularly increasing frequency and severity of extreme rainfall events) in many parts of the world. As a consequence, problems of rainfall-induced slope instabilities are increasing and there is increasing need for methods of enhancing slope stability and preventing rainfall-induced instabilities, both for natural slopes and for earthwork slopes (embankments and cuttings). This need is likely to increase significantly in future decades. Methods of enhancing slope stability need to have low carbon footprint. CBSs are therefore attractive, because they use only naturally occurring geomaterials (sands and gravels), which can often be sourced locally, whereas many conventional methods of enhancing slope stability involve manufactured materials with high embedded carbon, such as concrete or geopolymers.

So far, however, CBSs have not been widely employed for enhancing slope stability and the few cases where they have been used tend to be in tropical regions. Reasons for the lack of use of CBSs on slopes include:

- lack of understanding or confidence within the wider geotechnical community of the principle of operation of a CBS (it is counter-intuitive to most geotechnical engineers that a coarse-grained material, such as gravel, can form an effective low permeability barrier);

- uncertainty about the effectiveness of CBSs on slopes under different climatic conditions;

- lack of a simple and reliable method for designing a CBS on a slope to ensure stability under the climatic and meteorological conditions of a specific site;

- concern that the volume of material required to form an effective CBS may be excessive if a significant area of slope requires stabilization;

- practical concerns about the long-term performance of CBSs on slopes, such as: surface durability of a sloping CBS and its susceptibility to surface erosion processes; or risks of fine-grained material washing into the CBS (either the finer layer or the coarser layer) and compromising the function of the CBS.

- lack of understanding and concerns within the geotechnical community on how best to incorporate the influence of vegetation and desiccation cracks on soil-atmosphere interactions at the surface of a CBS.

This thesis focuses mainly on the second and third issues within this list, but also includes contributions relevant to the remaining issues.

The aim of this PhD project was to develop and validate practical tools that could be used within a design process for sloping capillary barrier systems (CBSs) for enhancing slope stability. These tools need to be suitable for use by practising geotechnical engineers in industry and able to account for the climate and meteorological conditions of an individual site. These tools were likely to be in the form of simple calculation methods and should not involve use of complex multi-physics finite element modelling. Development of the simplified methods within this PhD project was to be performed by using improved understanding arising from appropriate finite element modelling undertaken as a major activity of the PhD. Validation of the simplified methods was to be performed by comparing against results from multi-physics numerical modelling incorporating realistic meteorological conditions (including evaporation and extreme rainfall events).

1.3 Objectives

1. To validate, by hydraulic numerical modelling, existing simplified methods for calculating the water storage capacity of horizontal conventional (Stormont and Morris, 1998) and multi-layered (Scarfone, 2020) CBSs under continuous rainfall of constant intensity. The numerical validation was to include more realistic modelling and a wider range of parametric conditions than achieved by previous authors.

2. To develop and then validate by hydraulic numerical modelling a simplified method for calculating the water storage capacity and water transfer capacity (and hence diversion length) of conventional or multi-layered CBSs covering a slope when subjected to continuous rainfall of constant intensity.

3. To investigate through thermo-hydraulic numerical modelling and hydraulic numerical modelling the behaviour of sloping CBSs when subjected to intermittent or varying intensity rainfall, including the effects of evaporation at the atmospheric boundary and hysteresis in the retention behaviour of the CBS materials.

4. To investigate through hydraulic or thermo-hydraulic numerical modelling the behaviour of sloping CBSs when subjected to realistic extreme rainfall events.

5. To develop a simplified method of analysis for CBSs on slopes subjected to extreme rainfall events, based on understanding achieved through previous numerical modelling. The simplified method would be validated by comparing against appropriate numerical simulations.

6. To consider how the simplified methods of analysis developed within the research could be incorporated within a practical design method for sloping CBSs, suitable for use by practising geotechnical engineers in industry, and to consider other practical aspects of the performance and design of CBSs on slopes.

All the numerical modelling performed within the project was hydraulic modelling or thermo-hydraulic modelling, rather than coupled hydro-mechanical or thermo-hydro-mechanical modelling i.e. mechanical behaviour of the soil was ignored, with all materials of a CBS considered as non-deforming. This was partly motivated by time constraints, given that the intention was to perform large numbers of numerical simulations (to form comprehensive parametric studies investigating multiple variables and scenarios) and that thermo-hydro-mechanical numerical modelling involving realistic rainfall patterns and soil-atmosphere interactions would have been very computationally demanding, with very long run-times for each numerical simulation.

Numerical analyses of rainfall-induced slope stability problems (with or without a CBS) can either be performed in a single stage by coupled hydro-mechanical or thermo-hydro-mechanical modelling or they can be performed in two stages by conducting hydraulic or thermo-hydraulic numerical modelling and then using the resulting distributions of pore pressures within separate stability analyses (e.g. within a limit analysis method). A crucial requirement if the two-stage approach is to be used (with coupling between mechanical and hydraulic behaviour ignored) is that any volumetric strains (arising from the mechanical behaviour) should be sufficiently small to have little impact on the hydraulic behaviour. If this requirement is not satisfied, the reliability of any hydraulic or thermo-hydraulic numerical modelling is not guaranteed.

In the work presented in this thesis, it was considered reasonable to assume that volume changes of the CBS materials would be small and would have little impact on the hydraulic behaviour, because both layers of a CBS are made of coarse-grained materials (even the finer layer is typically a fine sand or silty sand) and these coarse-grained materials generally show relatively small volumetric strains prior to failure. This is particularly likely to be the case for a CBS subjected to a critical extreme rainfall event, because the majority of the soil response (apart from any final initiation of failure) is likely to be in the elastic range, as a consequence of multiple previous cycles of wetting and drying during earlier rainfall events and intervening dry periods. Finally, it is also worth noting that coupled hydro-mechanical or thermo-hydro-mechanical numerical modelling using a relatively simple mechanical constitutive model for the coarse-grained materials

of a CBS (such as a linear elastic-perfectly plastic model with a Mohr-Coulomb yield criterion) would predict highly unrealistic volume changes, because of the use of a constant value of dilation angle, and the volume changes predicted with such a constitutive model might be even less realistic than the assumption of zero volume changes implicitly assumed in uncoupled hydraulic or thermo-hydraulic numerical modelling. Hence, coupled hydro-mechanical or thermo-hydro-mechanical numerical modelling would only have been justified in this project if a relatively sophisticated mechanical constitutive model (giving accurate predictions of soil volume changes) had been employed, and this was considered impractical because of the computational complexity and very long computational run times that would have been incurred.

1.4 Thesis structure

This thesis is arranged into nine chapters, including this chapter.

CHAPTER 2 provides the essential research background for this thesis, including the behaviour of unsaturated soils (highlighting soil retention behaviour and fluid transport behaviour), hydraulic constitutive modelling of unsaturated soils, soil-atmosphere interaction modelling and the behaviour and application of capillary barrier systems.

CHAPTER 3 presents the CODE_BRIGHT multi-physics finite element software used for the numerical modelling undertaken within this project, including implementation by Scarfone (2020) within CODE_BRIGHT of an advanced hydraulic constitutive model (Scarfone et al., 2020a) and an advanced hysteretic hydraulic constitutive model (Scarfone at al., 2020b).

CHAPTER 4 presents the results of numerical analyses validating the existing simplified methods (Stormont and Anderson (1998) and Scarfone (2020)) for calculating the water storage capacity of a horizontal conventional or multi-layered CBS subjected to continuous rainfall of constant intensity. This represents a fuller numerical validation than previously achieved, because the numerical modelling employed an advanced hydraulic constitutive model and multiple simulations were performed, representing a full parametric study covering all key variables.

CHAPTER 5 presents a new semi-analytical method for calculating the water storage capacity and water transfer capacity (and hence diversion length) of conventional or multi-layered sloping CBSs subjected to continuous rainfall of constant intensity, with this new method then validated by numerical modelling. Moreover, this chapter uses the numerical modelling to demonstrate further aspects of the behaviour of sloping CBSs subjected to continuous rainfall of constant intensity.

CHAPTER 6 presents numerical modelling of sloping CBSs subjected to simple patterns of intermittent or varying intensity rainfall, to provide important insights into how a sloping CBS behaves when the rainfall is not continuous and of constant intensity. The numerical modelling included both thermo-hydraulic modelling (with evaporation at the ground surface) and hydraulic modelling (without evaporation). The numerical modelling also included the effects of retention hysteresis in the CBS materials. Rainfall patterns investigated included single constant intensity rainfall events of limited duration, cyclic patterns of rainfall and realistic extreme rainfall events (including antecedent rainfall).

CHAPTER 7 presents the development and numerical validation of a new simplified method of analysis for sloping CBSs subjected to realistic extreme rainfall events.

CHAPTER 8 presents suggestions for the practical design of sloping CBSs, including how the simplified method of analysis for extreme rainfall events developed and validated in Chapter 7 could be incorporated within a practical design process.

CHAPTER 9 summaries the key conclusions of this thesis and recommendations for future work.

Chapter 2 Research background

In this chapter, the research background relevant to the project is analysed and critically reviewed in order to identify gaps in existing knowledge and provide information required for understanding the work presented in this thesis. The chapter consists of nine sections. The first six sections of these cover fundamental topics of relevance (pore pressures and suction in unsaturated soils, retention behaviour, flow processes in unsaturated soils, details of a specific advanced hydraulic constitutive model used throughout the project, shear strength of unsaturated soils, and soil-atmosphere interaction). The final three sections review existing knowledge on capillary barrier systems (horizontal capillary barrier systems, sloping capillary barrier systems and multi-layered capillary barrier systems).

2.1 Pore pressures and suction in unsaturated soils

Unsaturated soils contain three phases: (1) solid phase (i.e. soil grains), (2) liquid phase (typically water), (3) gas phase (typically air). Surface tension σ_s, expressed as force per unit length, occurs at the interface between liquid and gas phases (Fredlund, 2006), as shown in Figure 2-1. Surface tension is the result of unbalanced intermolecular forces exerted on water molecules located at the liquid-gas interface (Fredlund and Rahardjo, 1993).

If the liquid-gas interface is curved, the presence of surface tension means that, the pore-gas pressure p_g is not equal to the pore-liquid pressure p_l. The difference between pore-gas pressure and pore-liquid pressure is called the matric suction s:

$$s = p_g - p_l \tag{2-1}$$

Throughout this thesis, matric suction s is referred to simply as suction. Within this thesis, p_g and p_l are expressed as absolute pressures.

The value of suction s can be related to the principal radii of curvature of the liquid-gas interface by considering force equilibrium perpendicular to the interface for an infinitesimally small element of the interface, as shown in Figure 2-1:

$$p_l r_1 d\theta_1 r_2 d\theta_2 - p_g r_1 d\theta_1 r_2 d\theta_2 + 2\sigma_s r_1 d\theta_1 \sin\frac{d\theta_2}{2} + 2\sigma_s r_2 d\theta_2 \sin\frac{d\theta_1}{2} = 0 \quad \text{2-2}$$

$$s = p_g - p_l = \sigma_s \cdot \left(\frac{1}{r_1} + \frac{1}{r_2}\right) \quad \text{2-3}$$

where r_1 and r_2 are the principal radii of curvature of the interface (taken as positive if measured on the gas side of the interface). Equation 2-3 is known as the Young-Laplace equation (Young, 1805; and Laplace, 1806). Inspection of Equation 2-3 shows that the value of suction increases as the radii of curvature of the interface decrease. The value of surface tension σ_s is 0.07257 N/m for a water-air interface at 20°C (Kaye and Laby, 1926).

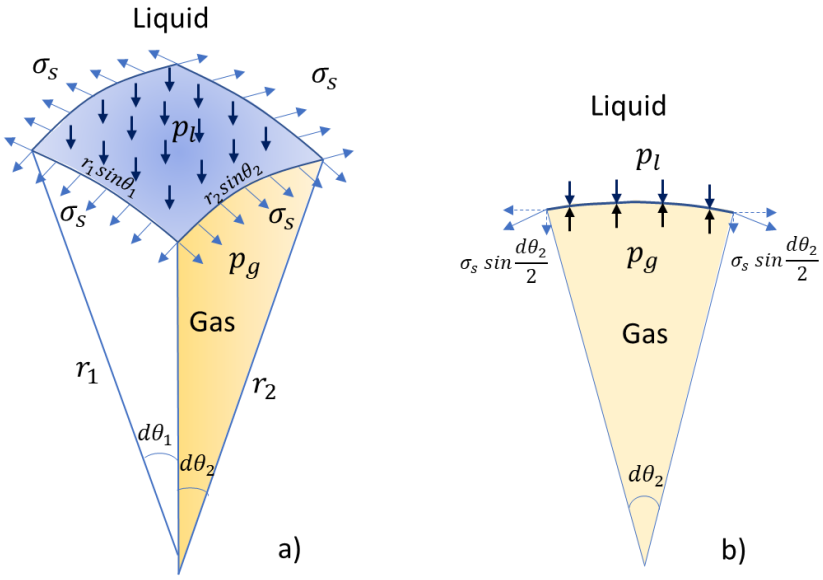

Figure 2-1 Liquid-gas interface

In unsaturated soils, where the liquid-gas interface comes into contact with a solid body (i.e. a soil particle), the contact angle θ is very small (approaching zero) when measured on the water side, provided that the soil particles are not hydrophobic (Brennen, 2014). This means that the liquid-gas interface is generally concave on the gas side, consequently, pore-gas pressure is higher than pore-liquid pressure ($p_g \geq p_l$). If the pore gas is air and this air is connected to the atmosphere at the ground surface, pore gas pressure is equal to atmospheric pressure ($p_g = p_{at}$) if there is no flow of air. Thus, pore-liquid pressure is generally negative relative to atmospheric pressure in an unsaturated soil ($p_l \leq p_{at}$).

When the radii of curvature of liquid-gas interfaces are very small, the value of s can exceed atmospheric pressure (see Equation 2-3). This means that the pore

liquid can be at a negative absolute pressure i.e. the pore liquid can be in a state of tension (Fredlund and Rahardjo, 1993). In coarse-grained unsaturated soils (sands and gravels) this occurs only at very low values of degree of saturation, whereas in fine-grained unsaturated soils (clays and silts) this occurs over a wide range of degree of saturation (see Section 2.2). Many authors have shown that the maximum negative value of pore water pressure within an unsaturated soil, as the soil approaches a dry condition, is approximately 1GPa (e.g. Campbell and Shiozawa, 1992).

Provided there is a state of local equilibrium between the liquid pore water and the water vapour in the pore gas phase, the matric suction s is related to the relative humidity R_h of the gas phase by the psychrometric Law (Fredlund and Rahardjo, 1993):

$$s = -\frac{RT\rho_l}{M_w}\ln R_h \qquad \textbf{2-4}$$

where R is the universal gas constant (8.314 J/(mol·K)), T is the absolute temperature (in degrees Kelvin), ρ_l is the liquid density and M_w is the molecular mass of water (0.01802 kg/mol). Relative humidity R_h is defined by:

$$R_h = \frac{\rho_v}{\rho_{vo}} \qquad \textbf{2-5}$$

where ρ_v is the vapour density (also known as the absolute humidity) and ρ_{vo} is the saturated vapour density. The value of ρ_{vo} depends on temperature T.

2.2 Retention behaviour

Retention behaviour describes the amount of liquid phase stored within the soil and how this varies with suction and with any other relevant aspects of soil state. Retention behaviour is one component of the hydraulic behaviour of an unsaturated soil, with fluid transport processes (see Section 2.3) forming the other component of this hydraulic behaviour.

In understanding the retention behaviour of an unsaturated soil, it is helpful to realise that liquid pore water is divided into three forms: bulk water, meniscus

water and liquid film water (Lebeau and Konrad, 2010), as shown in Figure 2-2. Bulk water is when water completely fills an individual void, whereas menicus water is when a water bridge occurs around an interparticle contact surrounded by air-filled voids. Liquid film water is a thin liquid film surrounding soil particles when pores are filled with air.

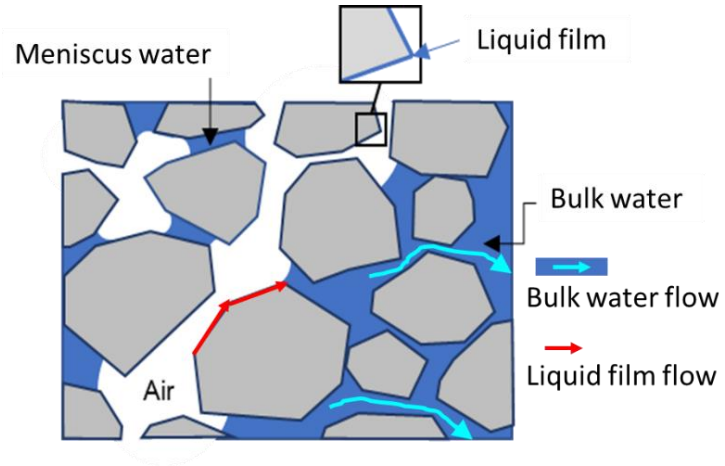

Figure 2-2 Liquid water forms within unsaturated soils (after Scarfone et al., 2020a)

2.2.1 Soil water retention curve

The soil water retention curve (SWRC), also known as the soil water characteristic curve, describes the relationship between matric suction s and the amount of liquid water stored within the soil, which can be expressed in terms of volumetric water content, gravimetric water content or degree of liquid saturation S_l. In this thesis, SWRC is expressed as the relationship between matric suction s and degree of liquid saturation S_l, as shown in Figure 2-3. The suction is typically presented on a logarithmic scale.

Inspection of Figure 2-3 shows that, for any given soil, as suction increases the degree of saturation falls. This represents retreat of the liquid-gas interfaces into smaller and smaller voids (with the larger voids gas-filled and the smaller voids liquid-filled) and a corresponding decrease in the radii of curvature of the interface (see Equation 2-3). For different soils, a finer-grained soil will require higher values of suction than a coarser-grained soil to produce the same values of degree of saturation (see Figure 2-3), because the smaller particles of a finer grained soil imply smaller void sizes and hence smaller values of radii of curvature of the liquid-gas interfaces at a given degree of saturation.

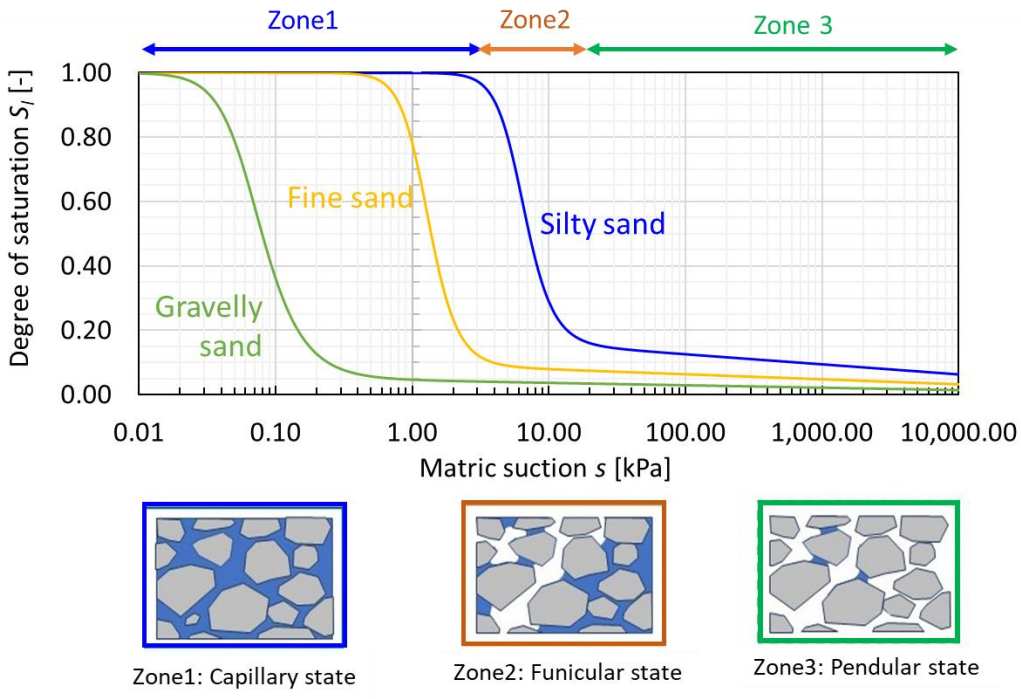

Figure 2-3 Soil water retention curve SWRC

Based on experimental results, Schubert et al. (1975) classified the distribution state of liquid in porous media into three states, namely: capillary state, funicular state and pendular state (Figure 2-3). Looking at the solid blue line (silty sand) in Figure 2-3, capillary state (zone 1), at the lowest values of s, represents a saturated condition ($S_l = 1$), when all pores are filled with bulk water, there is no gas phase and there is no meniscus water or liquid film water. Funicular state (zone 2), at intermediate values of s, represents an unsaturated condition at high or intermediate values of S_l, where there are pores filled with bulk water and other pores filled air, but these air-filled voids also include meniscus water (at interparticle contacts around the air-filled voids) and liquid film water (a thin water layer covering the surface of the solid particles around air-filled voids). Lastly, pendular state (zone 3), at the highest values of s, represents unsaturated conditions at low values of degree of saturation, where all the voids are air-filled, no bulk water is present, and the only liquid water is in the forms of menicus water and liquid film water.

For a given soil, the SWRC is not unique, because it depends upon two factors. Firstly, the SWRC depends upon whether the soil is following a wetting process or a drying process and the previous history of wetting and drying (Haines, 1930). This phenomenon is known as retention hysteresis (see Section 2.2.2). Secondly, the SWRC is affected by any change of void ratio of the soil (compression) because

a change of void ratio implies changes in the dimensions of individual voids and hence changes in the radii of curvature of the liquid-gas interfaces corresponding to a given degree of saturation (Wheeler et al., 2003; and Gallipoli, 2012). In this thesis, however, the soils will be treated as non-deformable and therefore no review of the effect of changes of void ratio on SWRC is included.

2.2.2 Water retention hysteresis

Geotechnical and Soil Science researchers found the SWRC for a given soil is not unique: different curves are followed during drying and wetting paths, an effect known as water retention hysteresis (see Figure 2-4).

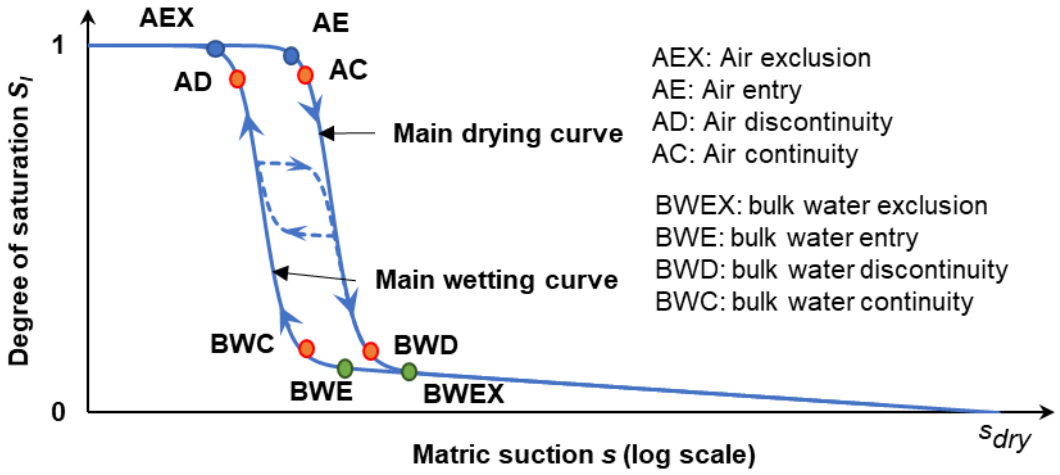

Figure 2-4 Soil water retention curves (SWRC) for main drying process and main wetting process (after Scarfone et al., 2020a)

Figure 2-4 shows hysteresis in the suction and degree of saturation relationship for a typical coarse-grained unsaturated porous material. The main drying curve represents a drying process which starts from full saturation (initial point at $S_l = 1$ and $s = 0$), then dries to very high value of suction to almost dry state. Conversely, the main wetting curve represents a wetting process which starts at a very high value of suction, corresponding to an almost dry state (initial point at $S_l \approx 0$). Some researchers (e.g. Likos et al., 2014) differentiate between a "primary drying curve" (initial point at $S_l = 1$, $s = 0$) and a "main drying curve" (initial point at $s = 0$ and at a value of S_l corresponding to the final state reached at the end of a previous main wetting curve). In many experimental results presented in the literature, the main drying curve is different to the primary drying curve (e.g. Klausner, 2012), because of the influence of air trapping during wetting. Scarfone and Wheeler (2022) showed, however, that if a wetting

retention test is performed sufficiently slowly to ensure full equalization of internal pore liquid and pore gas pressures with those applied externally at all points in the test (this requires sufficient time for dissipation of excess pore gas pressures by diffusion of dissolved air once air trapping occurs), then the end point of a main wetting test (at $s = 0$) must correspond to a saturated condition ($S_l = 1$). Hence, there is no need to distinguish between a main drying curve and a primary drying curve and the former term is used throughout this thesis.

If drying starts from an intermediate point (rather than from $S_l = 1$) or wetting starts from an intermediate point (rather than $S_l \approx 0$), the SWRC will follow a different curve, as indicated by the dashed lines in Figure 2-4. These are known as scanning curves (Hanks et al., 1969). During a particular drying or wetting process, the particular scanning curve followed will depend upon the starting values of S_l and s, which depend in turn on the precise history of wetting and drying followed previously by the soil. The full water retention behaviour therefore consists of a main wetting curve, a main drying curve, an infinite number of possible scanning wetting curves and an infinite number of possible scanning drying curves.

Scarfone (2020) and Scarfone et al. (2020b) describes key transition points on the main drying curve and the main wetting curve (see Figure 2-4). For a main drying process, as a soil is gradually drying from fully saturated state $(S_l = 1)$, air progressively enters into individual voids, with air typically entering the largest voids first. The suction value corresponding to the point where air enters the first voids, and where S_l first drops below 1, is called the air-entry value (s_{AE}). Until this air entry point (AE in Figure 2-4), the soil is in a saturated condition and a capillary state (zone 1 in Figure 2-3). As suction increases above s_{AE}, and more voids become air filled, the volume of bulk water decreases, and the degree of saturation S_l falls, but the number of meniscus water bridges increases, and the surface area of soil particles covered by liquid film water also increases. When sufficient numbers of voids are air-filled, the air-filled voids form continuous pathways through soil. This is known as the air continuity point (AC in Figure 2-4), corresponding to the gas phase first forming continuous paths within the porous medium. As the main drying process continues, the number of voids filled with bulk water gradually decreases until these water-filled voids no longer form continuous pathways through the soil. This point is called the bulk water

discontinuity point (BWD in Figure 2-4). On further drying, a point is reached at which the last voids empty of bulk water and become air-filled. This is known as the bulk water exclusion point (BWEX in Figure 2-4). Beyond this point, the only liquid water present is in the forms of menicus water and liquid film water. The water distribution from air entry point (AE) until bulk water exclusion point (BWEX) is the funicular state (zone 2 in Figure 2-3), whereas from BWEX onwards it is the pendular state (zone 3 in Figure 2-3). From point BWEX onwards, a large increase in suction corresponds to only a very small decrease of degree of saturation. This decrease of degree of saturation within the pendular state is because individual menicus water bridges reduce in size as suction increases and the thickness of liquid films reduces as suction increase (see Section 2.4.2). Ultimately, soil is completely dried at a suction value s_{dry} of approximately 1 GPa (Richards, 1965; Campbell and Shiozawa, 1992). This value of s_{dry} is independent of soil type (with the possible exception of some clays, because of their complex surface electro-chemistry), because it corresponds to the value of suction at which liquid water films on the surface of soil particles break down, because the thickness of the films reduces to a value only several times larger than the dimensions of water molecules (see Section 2.3.3).

Scarfone (2020) and Scarfone et al. (2020b) used similar concepts to define key transition points on the main wetting curve (see Figure 2-4). From pendular state (all voids air-filled, with the only liquid water in the forms of menicus water and liquid film water) at high suction and low degree of saturation, bulk water starts filling individual voids, with the smallest voids generally filling first and filling of the first voids known as the bulk water-entry point (BWE in Figure 2-4). This point represents a transition from the pendular state to the funicular state. BWE point can be identified as the change in the slope or the transition point (Akin and Likos, 2017) of the main wetting SWRC. As wetting continues from this bulk water entry point, more voids fill with bulk water, until a continuous liquid path is created through water-filled voids at the bulk water continuity point (BWC in Figure 2-4). Subsequently, the gas phase become discontinuous at the air discontinuity point (AD in Figure 2-4). Finally, the air exclusion point (AEX in Figure 2-4) represents filling of the last voids with bulk water, so beyond this point there is no longer any gas phase, and the soil is in saturated condition in the capillary state.

The main physical reason for hydraulic hysteresis is the difference in the location of the gas-liquid interface within an individual void at the points controlling entry of air to that void (during drying) or entry of water to that void (during wetting). This is illustrated in Figure 2-5. The small sketch in the upper right of Figure 2-5 (labelled A) shows air about to enter a specific void during a drying process, with this corresponding to the point labelled A on the main drying SWRC. The critical situation during this drying process is when the gas-liquid interface is at the narrow entry point to the void and hence the suction corresponding to this entry of air into the void is related (through the Young-Laplace expression of Equation 2-3) to the radius of this narrow entry throat. In contrast, during a wetting path, such as point B on the main wetting SWRC in Figure 2-5, entry of water into the same void is governed by a situation where meniscus water bridges around different particle contacts surrounding the voids are about to coalesce (see the small sketch labelled B in the lower right of Figure 2-5). Hence, the suction corresponding to entry of water into the void during a wetting process is related (through the Young-Laplace equation) to the radius of the void. As the radius of the void is larger than the radius of the entry throat, the suction required for water to enter a void during wetting is less than the suction required for air to enter the same void during drying (compare point A on the main drying SWRC and point B on the main wetting SWRC in Figure 2-5). This effect is sometimes known as the “ink bottle effect” (Haines, 1930).

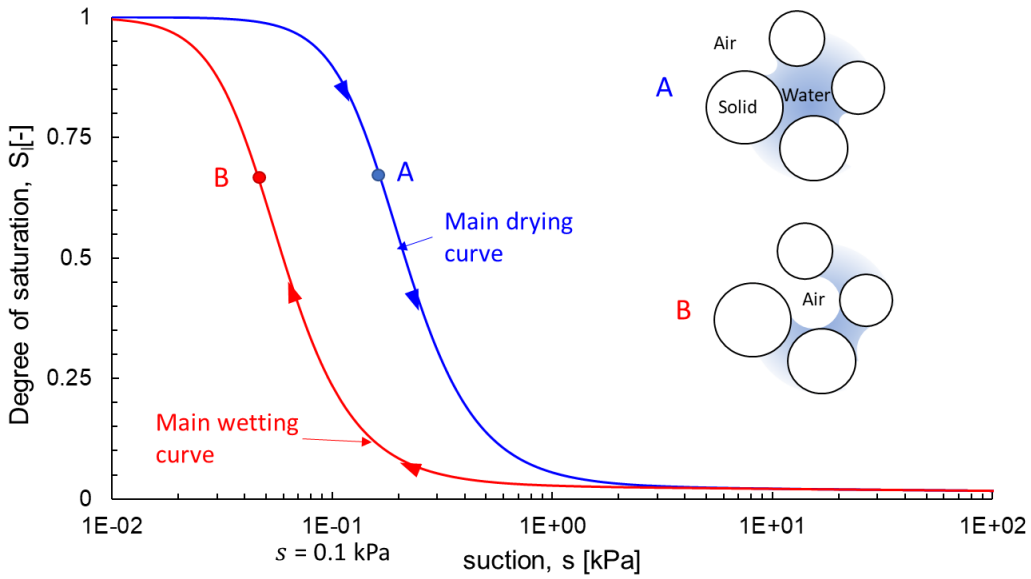

Figure 2-5 Main physical explanation for water retention hysteresis (“ink bottle effect”)

A second reason for hysteresis in the water retention behaviour is 'contact angle hysteresis' (Laroussi and De Backer, 1979; Lu and Likos, 2004). At interfaces between solid, gas and liquid, the solid-liquid contact angle is larger during a wetting process (when a wetting front is advancing) than during a drying process (when a wetting front is retreating). Figure 2-6 shows the concept of contact angle hysteresis for a drop of water on an inclined solid surface. As the drop geometry reaches steady-state under gravity forces, it is found that the wetting value of contact angle α_w at the front edge is larger than the drying value of contact angle α_d at the receding edge (Laroussi and De Backer, 1979).

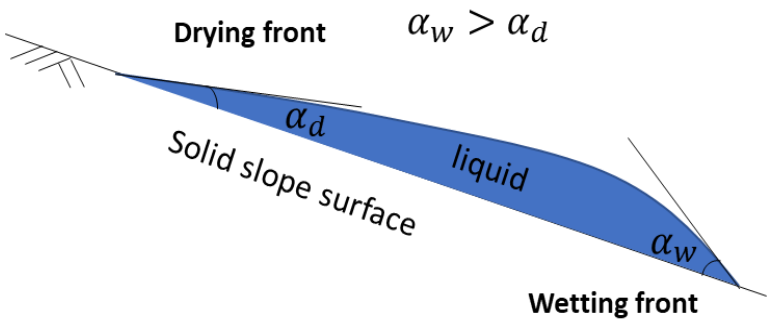

Figure 2-6 Wetting and drying contact angles for a water droplet (after Lu and Likos, 2004)

Water retention hysteresis will typically have important impacts for unsaturated soil problems involving reversals of wetting and drying. For instance, Zhang et al. (2009) presented results of numerical modelling of capillary barrier systems (CBS) with either a hysteretic SWRC model or a non-hysteretic SWRC model, which showed that incorporation of hysteresis resulted in higher water storage of the CBS, higher evaporation rate at the ground surface once rainfall infiltration stopped and lower percolation into the coarser soil layer of the CBS. Muneta et al. (2005) similarly demonstrated the effects of retention hysteresis on the suction distribution profiles and water storage capacities of CBSs.

2.2.3 Constitutive modelling of SWRC without hysteresis

This section reviews the most commonly used basic SWRC equations that do not account explicitly for retention hysteresis. These equations either can be used to predict a single unique SWRC or they can be used to predict a main wetting curve or a main drying curve as part of a full hysteretic retention model. Extension to constitutive modelling of SWRC with hysteresis is reviewed in Section 2.2.4

Three of the most widely used conventional SWRC models are those proposed by Brooks and Corey (1964), van Genuchten (1980) and Kosugi (1996). These three conventional models all assume that, as suction s varies, the degree of saturation S_l varies between a maximum value S_{ls} at s = 0 and a minimum value S_{lr} (the residual degree of saturation) at s tends to infinity (Figure 2-7), where S_{ls} and S_{lr} are constants. The degree of saturation S_l at any intermediate value of s is then given by:

$$S_l = S_{lr} + S_{le} \cdot (S_{ls} - S_{lr}) \qquad \textbf{2-6}$$

where S_{le} is the effective degree of saturation, which varies with s and which has a value between 0 and 1. Brooks and Corey (1964), van Genuchten (1980) and Kosugi (1996) proposed three different expressions for the variation of S_{le} with s.

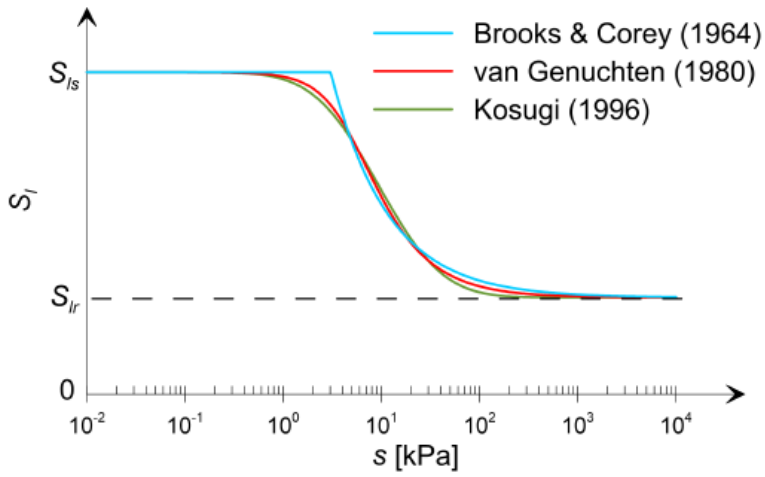

Figure 2-7 Conventional SWRC models (from Scarfone, 2020)

According to Brooks and Corey (1964), the variation of effective degree of saturation S_{le} with suction s is given by:

$$S_{le} = \begin{cases} 1 & \text{if } s < s_{AE/AEX} \\ \left(\frac{s_{AE/AEX}}{s}\right)^n & \text{if } s > s_{AE/AEX} \end{cases} \qquad \textbf{2-7}$$

where s_{AE} is the air entry value of suction (used if prediction of a main drying SWRC is required), s_{AEX} is the air exclusion value of suction (used instead of s_{AE} if prediction of a main wetting SWRC is required) and n is a soil constant. Inspection of Equation 2-7 (in combination with Equation 2-6) shows that the Brooks and Corey (1964) expression predicts a constant value of degree of saturation $S_l = S_{ls}$ for suction values from zero to the air entry value or air exclusion value, with S_l

then reducing with increasing suction above s_{AE} or s_{AEX} according to a simple inverse power law and asymptotically approaching the residual value of degree of saturation S_{lr} as suction tends to infinity.

The van Genuchten (1980) model can be expressed as:

$$S_{le} = \left[\frac{1}{1+\left(\frac{s}{P_0}\right)^n}\right]^m \quad \text{2-8}$$

where P_0, n and m are soil constants. van Genuchten (1980) also suggests that the two soil constants m and n can be related by:

$$m = 1 - \frac{1}{n} \quad \text{2-9}$$

The Kosugi (1996) model can be expressed as:

$$S_{le} = Q\left(\frac{\ln\left(\frac{s}{s_m}\right)}{\sigma_m}\right) \quad \text{2-10}$$

where Q is the complementary normal distribution function and s_m and σ_m are soil constants.

Figure 2-7 shows an example of a comparison (presented by Scarfone (2020)) of the Brooks and Corey (1964), van Genuchten (1980) and Kosugi (1996) models, with the values of the various soil constants in the three models selected to give the best possible matching.

Conventional constitutive SWRC models, such as those shown in Figure 2-7, provide reasonable matches to experimental SWRCs at high and medium degree of saturation, but struggle at low degree of saturation (high suction), because they all suggest that degree saturation asymptotically approaches a limiting non-zero value S_{lr} (the residual degree of saturation) as suction tends to infinity, whereas experiment results show that S_l continues to gradually decrease with increasing suction and the soil reaches a dry condition $(S_l = 0)$ at a finite value of suction s_{dry} of approximately 1 GPa (Richards, 1965; Campbell and Shiozawa, 1992). This continuing reduction of S_l in the high suction range is associated with the pendular

state (see Figure 2-3) and it is attributable to the reduction of size of meniscus water bridge and the reduction of thickness of liquid water films as suction increase. s_{dry} corresponds to the point where it is no longer possible to form meniscus water bridges or liquid water films, because their thickness has reduced to a value approaching the dimensions of water molecules. Various new SWRC equations or modifications to existing SWRC equations have been proposed to address this issue.

Fredlund and Xing (1994) proposed a new SWRC expression incorporating a correction factor $C(s)$ which is function of s that forces S_l to slowly decrease until it reaches zero at s = 1 GPa. The Fredlund and Xing (1994) SWRC model can be expressed as:

$$S_l = C(s) \cdot \frac{S_{ls}}{\left[\ln\left[e + \left(\frac{s}{P_0}\right)^n\right]\right]^m} \quad \textbf{2-11}$$

where P_0,n and m are soil constants and $C(s)$ is given by:

$$C(s) = \frac{\ln\left(1 + \frac{s}{s_r}\right)}{\ln\left[1 + (s_{dry}/s_r\right]} \quad \textbf{2-12}$$

where s_r is an additional soil constant giving the suction at which the SWRC starts linearly decreasing in a semi-logarithmic plot and s_{dry}= 1GPa.

Fayer and Simmons (1995) proposed a method for modifying conventional SWRC expressions to force S_l to gradually reduce to zero at a suction s_{dry}= 1GPa. Fayer and Simmons (1995) applied this approach to the model of Brooks and Corey (1964). Zhang (2011) and Khlosi et al. (2006) subsequently applied the same approach to the conventional models of van Genuchten (1980) and Kosugi (1996) respectively. In this approach developed by Fayer and Simmons (1995), S_l is still given by Equation 2-6, but in this equation S_{lr} is no longer a constant but is instead a function of suction given by:

$$S_{lr} = \xi \ln\left(\frac{S_{dry}}{s}\right) \quad \textbf{2-13}$$

where ξ is a soil constant and s_{dry}= 1GPa. Combining Equations 2-6, 2-13 and 2-7, the modified Brooks and Corey model is then given by:

$$S_l = \begin{cases} S_{ls} & \text{if } s < s_{AE/AEX} \\ \xi \ln\left(\frac{s_{dry}}{s}\right) + \left(\frac{s_{AE/AEX}}{s}\right)^n \cdot \left[S_{ls} - \xi \ln\left(\frac{s_{dry}}{s}\right)\right] & \text{if } s > s_{AE/AEX} \end{cases} \quad \textbf{2-14}$$

Similarly, combining Equations 2-6, 2-13 and 2-8, the modified version of the van Genuchten model is given by:

$$S_l = \xi \ln\left(\frac{s_{dry}}{s}\right) + \left[\frac{1}{1 + \left(\frac{s}{P_0}\right)^n}\right]^m \cdot \left[S_{ls} - \xi \ln\left(\frac{s_{dry}}{s}\right)\right] \quad \textbf{2-15}$$

Finally, combining Equations 2-6, 2-13 and 2-9, the modified version of the Kosugi model is:

$$S_l = \xi \ln\left(\frac{s_{dry}}{s}\right) + Q\left(\frac{\ln\left(\frac{s}{s_m}\right)}{\sigma_m}\right) \cdot \left[S_{ls} - \xi \ln\left(\frac{s_{dry}}{s}\right)\right] \quad \textbf{2-16}$$

Campbell and Shiozawa (1992) and Rossi and Nimmo (1994) proposed alternative methods for adjusting conventional SWRC expressions to force S_l to gradually reduce to zero at a suction s_{dry} = 1 GPa.

Peters (2014) proposed an empirical SWRC model by dividing the degree of saturation into two components: capillary liquid (i.e. bulk water and meniscus water) and absorptive liquid (i.e. liquid film water). However, the mathematical expression of Peters (2014) is rather complex, and the model has a discontinuity of gradient at the connection point between the capillary and absorptive ranges, which might cause numerical instability during computational modelling.

2.2.4 Constitutive modelling of SWRC with hysteresis

Numerous researchers have improved the description of SWRCs by incorporating the influence of retention hysteresis (e.g. Everett, 1955; and Gallipoli, 2012). Pham et al. (2005) reviewed hysteretic models for soil water retention behaviour by comparison of selected models against experimental datasets collected from

the literature. According to this review, hysteretic water retention models can be classified into two categories: i) domain models and ii) empirical models.

Domain models are also referred to as physical models, because they are based on the physical principal of associating groups of voids (domains) with two different suction values, one associated with drying of the voids and the other associated with wetting of voids. Different domain models make different assumptions relating to the sequence in which domains wet and dry and whether domains act independently of each other or are affected by adjacent domains because of phenomena such as pore blockage. This results in different relationships linking the forms of scanning drying curves and scanning wetting curves to the shapes of the main drying curve and main wetting curve.

Néel (1942,1943) and Everett (1955) presented some of the earliest development of domain models, with subsequent proposals for domain models including Poulovassilis (1962), Philip (1964), Topp (1971), Mualem (1974), Mualem (1977) and Mualem (1984). Domain models have been widely used in soil science, hydrogeology and other fields involving transport in porous media, but they have not proved popular in geotechnical engineering. This is because domain models do not provide good matches to the experimental SWRCs of some types of soils (Pham et al., 2005). Domain models have not been used in the research reported here and hence they are not reviewed further in this section. Pham et al. (2005) and Scarfone (2020) provide more information on domain-based hysteretic water retention models.

Within geotechnical engineering, empirical hysteretic SWRC models are more widely used than domain-based physical hysteretic SWRC models. These empirical hysteretic SWRC models simply involve empirical expressions for the forms of scanning drying curves and scanning wetting curves and how these are related to the shapes of the main drying curve and main wetting curve, with no underlying physical basis for the proposed relationships between the different curves.

The simplest empirical hysteresis SWRC model involve proposed shapes for the scanning curves that are independent of the shapes of the main drying curve and main wetting curve. For example, Hanks et al. (1969) proposed a model with all scanning curves as parallel straight lines in a water retention plot (with suction on

a linear scale), with the location of each individual scanning curve defined by the requirement to pass through the last point of suction reversal. Subsequently, Wheeler et al. (2003), Khalili et al. (2008) and Nuth and Laloui (2008) proposed models with all scanning curves as parallel straight lines in a semi-logarithmic water retention plot (i.e. typically in the S_l: $\ln s$ plane). These simple empirical hysteretic SWRC models predict rather unrealistic forms for scanning curves and numerical problems may arise because they predict discontinuities of gradient where a scanning drying curve joins the main drying curve or where a scanning wetting curve joins the main wetting curve. A further problem arises at very high and very low values of degree of saturation, where the gradient of the scanning curves can exceed the gradients of the main drying and main wetting curves.

The majority of empirical hysteretic SWRC models assume that the shapes of all drying scanning curves are related in some way to the shape of the main drying curve and the shapes of all scanning wetting curves are similarly related to the shape of main wetting curve. These types of empirical hysteretic SWRC models can be divided into three main groups, as described in the following paragraphs.

The first group of these models include Scott et al. (1983) and Kool and Parker (1987). They are sometimes known as scaling-down models. In this type of hysteretic SWRC model, each scanning curve is defined by an appropriate fixed scaling-down of the vertical dimensions of the corresponding main curve, defined in terms of either degree of saturation S_l or, more typically, equivalent degree of saturation S_{le}, as used in Equation 2-6. For example, the values of S_{le} on a scanning drying curve would all be a constant scaled-down ratio of the corresponding values of S_{le} on the main drying curve. The scaled-down ratio for an individual scanning drying curve would be based on the requirement to pass through last point of suction reversal. Similarly, the values of (1-S_{le}) on a scanning wetting curve would all be a constant scaled-down ratio of the corresponding values of (1-S_{le}) on the main wetting curve, i.e. the ratio of the distance AC to the distance BC would be constant along the entire scanning wetting curve shown in Figure 2-8a. Hence, the equations for the value of effective degree of saturation on a scanning drying curve $S_{le,d}$ or on a scanning wetting curve $S_{le,w}$ at a particular value of suction s are:

$$S_{le,d} = a_d S_{le,Md}(s) \quad \text{2-17}$$

$$\left(1 - S_{le,w}\right) = a_w \left(1 - S_{le,Mw}(s)\right) \quad \text{2-18}$$

where $S_{le,Md}(s)$ is the value of equivalent degree of saturation on the main drying curve at the same suction s, a_d is a constant for an individual scanning drying curve, $S_{le,Mw}(s)$ is the value of equivalent degree of saturation on the main wetting curve at the same suction s and a_w is a constant for an individual scanning wetting curve. The value of a_d or a_w is fixed by the requirement for the scanning curve to commence from the last point of suction reversal.

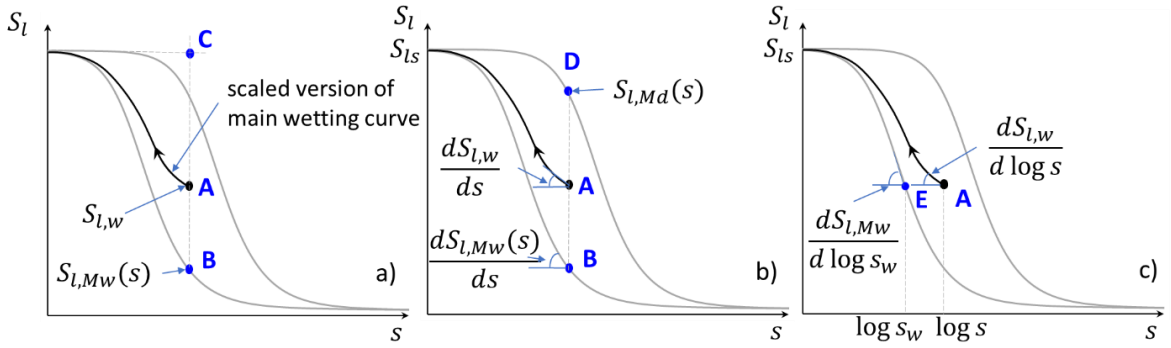

Figure 2-8 Different types of empirical hysteretic SWRC models a) scaling-down models, b) slope models and c) bounding surface-based models (after Scarfone, 2020)

A problem with these scaling-down model is that, for certain shapes of main drying curve or main wetting curve, predicted scanning drying curves can sometimes lie below the main wetting curve and predicted scanning wetting curves can sometimes lie above the main drying curve. Parker and Lenhard (1987) presented a modified version of a scaling-down hysteretic SWRC model to avoid this issue.

The next group of empirical hysteretic SWRC models (e.g. Jaynes, 1984) are sometimes referred to as slope models. In these models, the slope of a scanning curve at a particular value of suction is related to the slope of the corresponding main curve at the same value of suction but scaled by a ratio which depends on the location of the scanning curve relative to the main wetting and drying curves (all measured vertically in the retention plot, at the current value of suction). This is illustrated in Figure 2-8b, where the gradient of a scanning wetting curve at A is given by the gradient of the main wetting curve at point B multiplied by a scaling ratio which depends on the relative size of the distance AD and BD. For the case of the model of Jaynes (1984), the scaling ratio is simply AD/BD. This can be written as:

$$\frac{dS_{l,w}}{ds} = \frac{\left[S_{l,Md}(s) - S_{l,w}\right]}{\left[S_{l,Md}(s) - S_{l,Mw}(s)\right]} \frac{dS_{l,Mw}(s)}{ds} \quad \text{2-19}$$

where $\frac{dS_{l,w}}{ds}$ is the gradient of the scanning wetting curve at a value of suction s, $S_{l,Md}(s)$, $S_{l,Mw}(s)$ and $S_{l,w}$ are the values of S_l on the main drying curve, the main wetting curve and the scanning wetting curve respectively, all measured at the current value of suction s, and $\frac{dS_{l,Mw}(s)}{ds}$ is the slope of the main wetting curve at this same value of s. If suction reversal occurs on the main drying curve, the slope of the wetting scanning curve at the point where it departs from the main drying curve will be zero and the slope of the scanning wetting curve then tends to the slope of the main wetting curve as the scanning wetting curve approaches the main wetting curve. The same concepts apply to drying scanning curves, with the equation for the slope $\frac{dS_{l,d}}{ds}$ of a scanning drying curve given by:

$$\frac{dS_{l,d}}{ds} = \frac{\left[S_{l,d} - S_{l,MW}(s)\right]}{\left[S_{l,Md}(s) - S_{l,Mw}(s)\right]} \frac{dS_{l,Md}(s)}{ds} \quad \text{2-20}$$

where $\frac{dS_{l,d}}{ds}$ is the gradient of the scanning wetting curve, $S_{l,d}$ is the value of S_l on the scanning drying curve, and $\frac{dS_{l,Md}(s)}{ds}$ is the slope of the main drying curve, all measured at this same value of s.

The last group of empirical hysteretic SWRC models are often referred to as bounding surface models, because of their conceptual similarity to bounding surface plasticity mechanical constitutive models. Examples include Li (2005), Liu and Muraleetharan (2006), Raveendiraraj (2009), Zhou et al. (2012) and Gallipoli et al. (2015). In these models, the gradient of a scanning curve is related to the gradient of the corresponding main curve at a point on this main curve where an elastic line from the point on the scanning curve intersects the main curve, but with the gradient of the scanning curve scaled by a ratio which depends upon the distance between the point on the scanning curve and the point where the elastic line from the point on the scanning curve intersects the main curve. If elastic changes of degree of saturation are ignored (which is often done in this approach), the elastic line is replaced by a horizontal line in the retention plot. This means that the slope of the scanning curve at a particular value of degree of saturation

S_l is related to the slope of the corresponding main curve at the same value of S_l. For example, in Figure 2-8c, the slope of the scanning wetting curve at A is related to the slope of main wetting curve at E, but with a scaling factor that depends upon the distance AE.

In many of these bounding surface hysteretic SWRC models, the relationship between the slope of the scanning curve and the slope of the corresponding main curve is expressed in terms of the slope measured in a semi-logarithmic plot (i.e. with suction on a logarithm scale). For example, in the model of Zhou et al. (2012) the slope of a wetting scanning curve in the semi-logarithmic plot $\frac{dS_{l,w}}{dlogs}$ is a scaled ratio of the slope the main wetting curve in the same plot $\frac{dS_{l,Mw}}{dlogs}$, measured at the same value of degree of saturation value S_l:

$$\frac{dS_{l,w}}{dlogs} = \left(\frac{s_w}{s}\right)^{\gamma_w} \cdot \frac{dS_{l,Mw}}{dlogs_w} \qquad \textbf{2-21}$$

In Equation 2-21, s_w is the image value of suction on the main wetting curve, which is the suction value corresponding to a point on the main wetting curve at the same degree of saturation as a point on the scanning wetting curve at suction s (see Figure 2-8). The scaling factor in Equation 2-21 involves the ratio $\frac{s_w}{s}$ but also an exponent γ_w which is a soil constant (with a positive value). The value γ_w controls the gradients of the scanning wetting curves and how sharply they converge with the main wetting curve. As the value of γ_w tends to infinity, the scanning wetting curves tend to horizontal straight lines until they reach the main wetting curve. A similar expression is used for scanning drying curves:

$$\frac{dS_{l,d}}{dlogs} = \left(\frac{s}{s_d}\right)^{\gamma_d} \cdot \frac{dS_{l,Md}}{dlogs_d} \qquad \textbf{2-22}$$

where s_d is the value of suction on the main drying curve at the same value of S_l as a point on the scanning drying curve at suction s and γ_d is a further soil constant.

Raveendiraraj (2009), Gallipoli (2012) and Gallipoli et al. (2015) proposed bounding surface hysteretic water retention models involving relationships very similar to Equations 2-21 and 2-22, but they also included dependency of the

retention behaviour on changes of void ratio (i.e. retention behaviour was affected by soil compression). Gallipoli et al. (2015) also showed that, with the main wetting curve and main drying curve represented by conventional van Genuchten (1980) expressions and scanning wetting and drying curves then represented by Equations 2-21 and 2-22, it was possible to derive closed form expressions for the shapes of scanning curves.

Bounding surface empirical hysteretic SWRC models have proved popular in geotechnical engineering because they have sufficient flexibility to provide reasonable matching to experimentally observed scanning curves but, if the main wetting curve and main drying curve have already been defined, only two additional soil constants (γ_w and γ_d) are required to define all scanning wetting curves and all scanning drying curves.

2.3 Water transport in unsaturated soils

2.3.1 Fluid transport processes

Liquid water flow in unsaturated soils occurs within continuous liquid paths formed by the bulk water and by thin liquid films connected by meniscus water bridges (see in Figure 2-2). The advective flux of liquid $\boldsymbol{q}_l$ (volumetric flow rate of liquid through unit cross-sectional area of soil) is governed by Darcy's law as follows:

$$\boldsymbol{q}_l = -k_l \cdot \nabla h_l \qquad \textbf{2-23}$$

where k_l is the hydraulic conductivity (with units such as m/s), ∇h_l is the hydraulic gradient and h_l is the hydraulic head, defined as:

$$h_l = z + \frac{p_l}{\gamma_l} \qquad \textbf{2-24}$$

where z is elevation relative to an arbitrary horizontal reference datum, p_l is pore liquid pressure and γ_l is the unit weight of the liquid ($\gamma_l = \rho_l \mathrm{g}$, where ρ_l is the liquid density and g is gravitational acceleration).

Similarly, the advective flux of gas $\boldsymbol{q}_g$ (volumetric flow rate of gas through unit cross-sectional area of soil) is governed by Darcy's law which can be expressed as:

$$\boldsymbol{q}_g = -k_g \cdot \nabla h_g \quad \text{2-25}$$

where k_g is the gas conductivity, ∇h_g is the pneumatic gradient and h_g is the pneumatic head, defined as:

$$h_g = z + \frac{p_g}{\gamma_g} \quad \text{2-26}$$

where γ_g is the unit weight of the gas and p_g is the pore gas pressure.

In addition to flow of liquid, water transport in unsaturated soils can occur through movement of water vapour. Vapour transport is the sum of two components: advection (vapour carried along by any movement of the gas phase) and diffusion (vapour moving relative to the gas phase as a consequence of any gradient in vapour concentration). The mass flux of water (mass flow rate through unit cross-sectional area of soil) due to advection of vapour is given by the gas volumetric flow rate $\boldsymbol{q}_g$ (from Equation 2-25) multiplied by the vapour density ρ_v.

The mass flux of water due to diffusion of vapour $\boldsymbol{i}_g^w$ is given (De Vries, 1958) by Fick's Law as:

$$\boldsymbol{i}_g^w = -\left(\tau \Phi \rho_g S_g D_g^w \mathbf{I}\right) \nabla \omega_g^w \quad \text{2-27}$$

where τ is a tortuosity parameter, Φ is porosity, ρ_g is gas density, S_g is degree of gas saturation ($S_g = 1 - S_l$), $\mathbf{I}$ is the identity matrix, ω_g^w is the mass fraction of water in the gas phase and D_g^w is the diffusion coefficient of vapour in the gas phase (units such as m^2/s). The mass fraction of water in gas phase is given by:

$$\omega_g^w = \frac{\rho_v}{\rho_a + \rho_v} = \frac{\rho_v}{\rho_g} \quad \text{2-28}$$

where ρ_v, ρ_a and ρ_g are the densities of water vapour, dry air and gas phase respectively. Olivella et al. (1996) suggest the following empirical expression for the diffusion coefficient for water vapour in air:

$$D_g^w = \mathrm{D}\left(\frac{(T)^n}{p_g}\right) \quad \text{2-29}$$

where p_g is the absolute gas pressure (in units of Pa), T is the absolute temperature and D and n are empirical constants. Olivella et al. (1996) suggest D = 5.9x10^{-6} m^{2}s^{-1}K^{-n}Pa and n = 2.3. They also suggest that it will normally be sufficient to assume a constant value of τ_0 for the tortuosity τ in the Equation 2-27.

With the vapour density being a function of relative humidity R_h and saturated vapour density ρ_{v0} (see Equation 2-5), R_h being a function of suction s and temperature T (psychrometric law of Equation 2-4) and ρ_{v0} being a function of T, this means that a gradient of ρ_v exists if there is either a gradient of suction s or a gradient of temperature T within the soil. Hence, diffusion of water vapour occurs if there is either a gradient of suction or a gradient of temperature. For low values of suction, such as occur within relatively coarse-grained soils, such as those within capillary barrier systems, the value of relative humidity R_h is always very close to unity, irrespective of any variation of s or T (see Equation 2-4), and in these situations any gradient of density of vapour ρ_v is almost entirely due to variation of density of saturated vapour ρ_{v0} caused by temperature variation. Hence, in unsaturated soils at low values of suction, significant diffusion of water vapour occurs only when there is gradient of temperature within the soil.

If transport of air needs to be considered, as well as transport of water, account must be taken of any movement of dissolved air (within the liquid phase) as well as movement of gaseous air. The mass flux of gaseous air is given by multiplying the volumetric flux of gas $\boldsymbol{q}_g$ (from Equation 2-25) by the dry air density ρ_a. Provided there is a state of local equilibrium between the gaseous air and the air dissolved in the pore liquid phase, the concentration of dissolved air is governed by Henry's Law (Henry, 1832). The mass flux of dissolved air includes an advective component (dissolved air carried along by any movement of the liquid phase) and a diffusion component (dissolved air moving relative to the liquid phase because of a gradient in dissolved air concentration).

2.3.2 Soil hydraulic conductivity curve

For an unsaturated soil, the value of hydraulic conductivity k_l appearing in Darcy's Law (Equation 2-23), which governs the flow of liquid water through the soil, decreases dramatically (by many orders of magnitude) as the degree of saturation

S_l reduces and this is represented by the soil hydraulic conductivity curve (SHCC), which is a plot of k_l against S_l or against suction s. The SHCC is almost without hysteresis if plotted as k_l against S_l (see Fredlund and Rahardjo, 1993), but it will show hysteresis in the funicular range if it is presented as k_l plotted against s (see Figure 2-9).

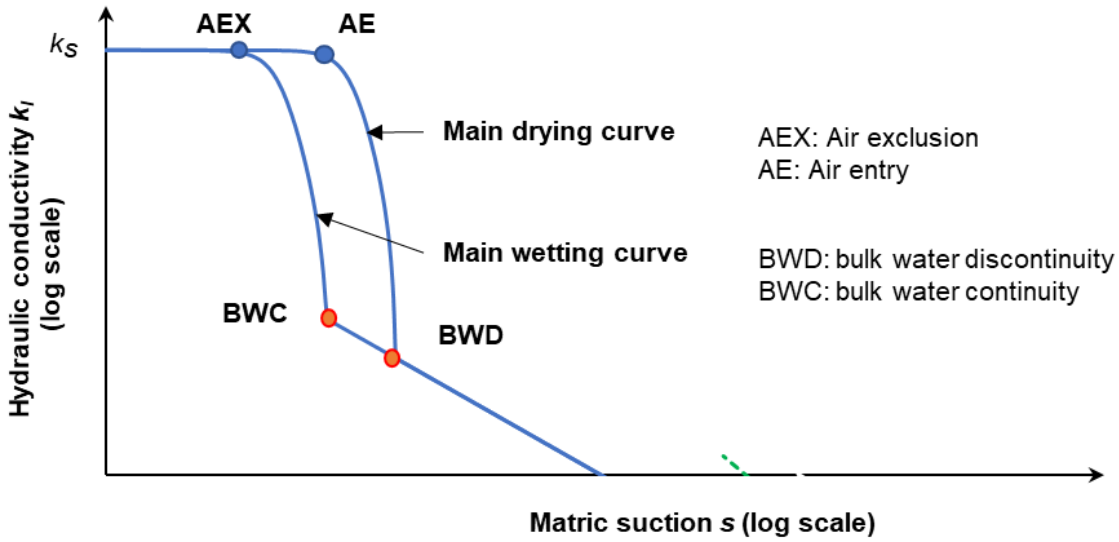

Figure 2-9 Soil hydraulic conductivity curve (SHCC) for main drying process and main wetting process (after Scarfone et al., 2020a)

The value of k_l for a soil in an unsaturated condition can be expressed in term of the saturated hydraulic conductivity k_s (the hydraulic conductivity of the same soil when in a saturated condition):

$$k_l = k_{lr} k_s \qquad \textbf{2-30}$$

where k_{lr} is the relative hydraulic conductivity. Hence, the SHCC is defined by the value of k_s and the variation of k_{lr} with degree of saturation or suction.

The saturated value of hydraulic conductivity k_s is given (Krynine, 1948) by:

$$k_s = \frac{k_i \rho_w \mathrm{g}}{\mu_w} \qquad \textbf{2-31}$$

where k_i is the intrinsic permeability (a property of the soil, with units of m^2) and ρ_w and μ_w are the density and dynamic viscosity of the permeating water. Equation 2-31 shows that the saturated hydraulic conductivity of a soil depends upon the soil (through k_i) and on the properties of the permeating fluid (through

ρ_w and μ_w). The value of k_i (and hence k_s) depends upon the size and connectivity of the voids within the soil. The value of k_s for a coarse-grained soil, such as sand, will be many orders of magnitude greater than the value of k_s for a fine-grained soil, such as clay. For a given saturated soil, the value of k_i (and hence k_s) will vary with soil porosity Φ (i.e. varying during soil compression), with any reduction of Φ producing a decrease of k_s. However, any variation of k_s with porosity is often ignored, particularly during unsaturated hydraulic modelling, when variation of k_l caused by variation of degree of saturation or suction completely dominates any much smaller variation of k_l resulting from changes of k_s produced by variation of porosity.

At high and moderate values of degree of saturation S_l, corresponding to the funicular state (see Figure 2-3), the unsaturated hydraulic conductivity k_l is dominated by the flow of liquid water through interconnected bulk water. In contrast, at low value of S_l, corresponding to the pendular state, the value of k_l is associated with flow in the liquid films.

2.3.3 Constitutive modelling of soil hydraulic conductivity curve

Direct measurement of the soil hydraulic conductivity curve (SHCC), the variation of k_l with either degree of saturation S_l or suction s, is technically challenging and time-consuming and therefore costly. This is particularly true at low values of degree of saturation, where liquid water flow occurs only by film flow and values of k_l are extremely low. It is therefore typically only the value of saturated hydraulic conductivity k_s that is directly measured and the variation of k_l with suction is then predicted with a constitutive expression for the relative hydraulic conductivity k_{lr} that is linked to the retention properties of the soil (i.e. determined from the SWRC, which has been measured experimentally and fitted to a suitable SWRC constitutive model). This linking of the SHCC to the SWRC is considered physically reasonable, because both SWRC and SHCC are controlled by the pore size distribution of the soil. This is, however, only true when movement of liquid water is dominated by flow of bulk water. At low values of degree of saturation, when movement of liquid water occurs only by film flow, it is unlikely that the SHCC can be derived from the SWRC, and a different approach for predicting the variation of k_l with suction is required in this range.

The most widely-used SHCC models relate the variation of relative hydraulic conductivity k_{lr} to the SWRC, and hence they implicitly ignore the contribution of liquid film flow (which becomes important at low values of S_l). These conventional SHCC models are based on a statistical approach from Burdine (1953) and Mualem (1976), which assumes that the unsaturated hydraulic conductivity depends on the pore-size distribution and that soil pores can be modelled as a bundle of cylindrical tubes with each individual tube either filled or empty of water and with liquid water flow occurring only in the former. However, these models are likely to be inappropriate at low degree of saturation where few if any pores are entirely filled with water and these do not form continuous liquid paths.

According to the Burdine (1953) model:

$$k_{lr} = {S_{le}}^2 \frac{\int_{S_{lr}}^{S_l} \frac{dS_l}{s^2}}{\int_{S_{lr}}^{S_{ls}} \frac{dS_l}{s^2}} = {S_{le}}^2 \frac{\int_0^{S_{le}} \frac{dS_{le}}{s^2}}{\int_0^1 \frac{dS_{le}}{s^2}} \quad \textbf{2-32}$$

where S_{le} is the effective degree of saturation and S_{lr} is a (constant) residual degree of saturation (see Equation 2-6). Brooks and Corey (1964) combined their SWRC expression of Equation 2-7 with the Burdine (1953) expression of Equation 2-32 to give the following expression defining k_{lr} and hence the SHCC:

$$k_{lr} = {S_{le}}^{3+\frac{2}{n}} \quad \textbf{2-33}$$

where n is the constant appearing in the Brooks and Corey (1964) SWRC expression.

Mualem (1976) developed an alternative statistical model of the cylindrical tube analogy of soil pores, different to that proposed by Burdine (1953), resulting in the following alternative expression for k_{lr}:

$$k_{lr} = {S_{le}}^{0.5} \left[\frac{\int_{S_{lr}}^{S_l} \frac{dS_l}{s}}{\int_{S_{lr}}^{S_{ls}} \frac{dS_l}{s}} \right]^2 = {S_{le}}^{0.5} \left[\frac{\int_0^{S_l} \frac{dS_{le}}{s}}{\int_0^1 \frac{dS_{le}}{s}} \right]^2 \quad \textbf{2-34}$$

van Genuchten (1980) combined his SWRC expression of Equation 2-8 with the Mualem (1976) expression of Equation 2-34 to give the following expression for k_{lr}:

$$k_{lr} = \sqrt{S_{le}}\left(1 - \left(1 - S_{le}^{\frac{1}{m}}\right)^{m}\right)^{2} \quad \textbf{2-35}$$

where m is the constant appearing in the van Genuchten (1980) SWRC expression. The combination of the SWRC expression of Equation 2-8 and the SHCC expression of Equation 2-35 is the well-known van Genuchten-Mualem hydraulic constitutive model for unsaturated soils.

As an alternative to the van Genuchten-Mualem expression of Equation 2-35, Kosugi (1996) combined his SWRC expression of Equation 2-10 with the Mualem (1976) expression of Equation 2-34 to give the following expression for k_{lr}:

$$k_{lr} = \sqrt{S_{le}}\{Q[(Q^{-1} \cdot S_{le}) + \sigma_m]\}^2 \quad \textbf{2-36}$$

where Q and σ_m are parameters occurring in the Kosugi (1996) SWRC expression.

Conventional SHCC models, such as those described by Equations 2-33, 2-35 and 2-36, are inappropriate at low degree of saturation, where few pores are entirely filled with bulk water and these do not form continuous liquid paths. Rossi and Nimmo (1994) and Fayer and Simmons (1995) tried to solve this obstacle by simply replacing the effective degree of saturation with the actual degree of saturation in the Mualem SHCC model. However, this was not entirely successful (Scarfone, 2020).

In recent decades, several authors have attempted to derive analytical expression for the contribution of liquid film flow to the hydraulic conductivity of unsaturated soils. Tuller and Or (2001) analysed the case of flow within liquid films on the surface of soil particles, connected by meniscus water bridges at particle contacts. Their model is however mathematically very complex and involves parameters that are difficult to measure experimentally (i.e., pore geometry and specific surface area).

Peters and Durner (2008) proposed an expression for k_l as the sum of a contribution from bulk water flow (which dominates at high values of degree of saturation) and a contribution from film flow (which dominates at low values of degree of saturation). Unfortunately, however, it is difficult to calibrate the empirical parameters involved in the expression for the film flow contribution.

Tokunaga (2009) presented a detailed theoretical analysis of film flow in an idealised soil consisting of identical smooth spherical particles containing no bulk water (i.e. in the pendular range). Tokunaga (2009) showed that, for this idealised case and for the range of suctions of interest in gravels, sands and silts, the value of hydraulic conductivity is given by:

$$k^{Film} = \frac{4\pi^2 \rho_l g(1-\Phi)}{\mu_l D}\left(\frac{\varepsilon\varepsilon_0}{2}\right)^{1.5}\left(\frac{k_B T}{Z e_T}\right)^3\left(\frac{2\sigma_s}{D}+s\right)^{-1.5} \quad \textbf{2-37}$$

where D is the particle diameter, Φ is the porosity, ρ_l is liquid density, μ_l is liquid viscosity, σ_s is the surface tension at liquid-gas interface, Z is the ion charge, T is the absolute temperature, ε, k_B and e_T are physical constants (ε is the relative permittivity (78.54), ε_0 is the permittivity of free space ($8.85\text{x}10^{-12}\text{C}^2\text{J}^{-1}\text{m}^{-1}$), k_B is the Boltzmann constant ($1.381\text{x}10^{-23}$ JK^{-1}), and e_T is the charge on an electron ($1.602\text{x}10^{-19}\text{C}$)). The derivation of Equation 2-37 was based on Langmuir's model for the thickness of the liquid film. Not only is Equation 2-37 mathematically complex, it was also found to give values of k^{Film} that were significantly different to experimental measurements, because of the idealisations involved in the theoretical derivation (e.g. identical smooth spherical soil particles). Very importantly, however, Equation 2-37 shows how key variables affect the value of k^{Film}. For example, inspection of Equation 2-37 shows that k^{Film} varies with $(\frac{2\sigma_s}{D}+s)$ raised to a power -1.5, because of how the thickness of liquid films reduces with increasing suction s. In addition, inspection of Equation 2-37 shows that k^{Film} is proportional to $(1-\Phi)/D$, because particle size D and soil porosity Φ influence the area and connectivity of water films within unit volume of soil. These insights arising from Equation 2-37 were vital in the development of the advanced hydraulic constitutive model described in Section 2.4.

Subsequently, several researchers attempted to develop expressions for the hydraulic conductivity of unsaturated soils accounting for the contribution of film

flow with expressions based on modifications of the Tokunaga (2009) model of Equation 2-37. Examples include Lebeau and Konrad (2010), Zhang (2011) and Peters (2013). None of these, however, have seen significant application within geotechnical engineering, because they all involve physical or empirical factors that are difficult to determine experimentally.

2.4 An advanced hydraulic constitutive model for unsaturated soils.

Scarfone (2020) and Scarfone et al. (2020a, 2020b) developed an advanced hydraulic constitutive model (SWRC and SHCC) that was used throughout the numerical modelling of CBSs described in Chapters 4 to 7 of this thesis. Particular features of the advanced hydraulic constitutive model are that it provides realistic modelling of SWRC and SHCC at low values of degree of saturation (including the contribution of film flow to hydraulic conductivity) and it includes the effects of retention hysteresis on both SWRC and SHCC. Scarfone et al. (2020a) showed that realistic constitutive modelling at low degree of saturation (including the contribution of film flow) is important for accurate numerical modelling of the phenomenon of breakthrough in CBSs. Also, Scarfone et al. (2020b) demonstrated that water retention hysteresis is important when a CBS is subjected to real meteorological conditions, involving intermittent rainfall and hence reversals of wetting and drying of the materials of the CBS.

2.4.1 Soil water retention curve (SWRC)

In the advanced hydraulic constitutive model, the main drying SWRC and main wetting SWRC are each modelled by the modified van Genuchten expression proposed by Fayer and Simmons (1995), presented earlier in Section 2.2.3 (see Equation 2-15) and given again here as Equation 2-38:

$$S_l = \xi \ln\left(\frac{s_{dry}}{s}\right) + \left[\frac{1}{1+\left(\frac{s}{P_0}\right)^n}\right]^m \cdot \left[S_{ls} - \xi \ln\left(\frac{s_{dry}}{s}\right)\right] \qquad \text{2-38}$$

The form of SWRC predicted by Equation 2-38, referred to as the “modVG” expression throughout this thesis, is illustrated in Figure 2-10a, together with the

corresponding conventional van Genuchten ("VG") SWRC expression. The notable feature of the modVG expression is that, at low values of S_l, the value of S_l decreases approximately linearly with the logarithm of s, to reach zero at a suction s_{dry} (typically taken as 1 GPa). The soil constant ξ controls the gradient of this approximately linear section of the SWRC.

Scarfone et al. (2020a) validated the modVG SWRC expression by comparing with experimental data for various soils and demonstrating that the expression was a good match to the experimental results over the full range of S_l.

For the modelling of water retention hysteresis (i.e. the prediction of scanning SWRCs), Scarfone (2020) and Scarfone et al. (2020b) used a bounding surface approach based on the proposals of Zhou et al. (2012) and Gallipoli et al. (2015), described earlier in Section 2.2.4. According to Equations 2-21 and 2-22 in Section 2.2.4, the gradient of scanning drying curves $\left(\frac{dS_l}{d\log s}\right)_d$ and the gradient of scanning wetting curves $\left(\frac{dS_l}{d\log s}\right)_w$ are related respectively to the gradient of the main drying curve $\left(\frac{dS_l}{d\log s_d}\right)_{Md}$ or the gradient main wetting curve $\left(\frac{dS_l}{d\log s_w}\right)_{Mw}$, all taken at the same value of degree of saturation S_l. Scarfone (2020) and Scarfone et al. (2020b) suggested a slightly revised form of this approach, where degree of saturation S_l in Equations 2-21 and 2-22 has been replaced by the effective degree of saturation S_{le}:

$$\left(\frac{dS_{le}}{d\log s}\right)_d = \left(\frac{s}{s_d}\right)^{\gamma_d}\left(\frac{dS_{le}}{d\log s_d}\right)_{Md} \quad \textbf{2-39}$$

$$\left(\frac{dS_{le}}{d\log s}\right)_w = \left(\frac{s_w}{s}\right)^{\gamma_w}\left(\frac{dS_{le}}{d\log s_w}\right)_{Mw} \quad \textbf{2-40}$$

where γ_d and γ_w are soil constants and s_d and s_w are the values of suction on the main drying curve or main wetting curve at the same value of S_{le} as the point under consideration on a scanning curve (see Figure 2-11). The purpose in changing Equations 2-21 and 2-22 to Equations 2-39 and 2-40 (i.e. replacing S_l by S_{le}) was to ensure that closed form solutions could be derived for the shape of individual scanning curves even when the relatively complex modVG expression was used for the main drying and main wetting SWRCs. Scarfone et al. (2020b) also argued that

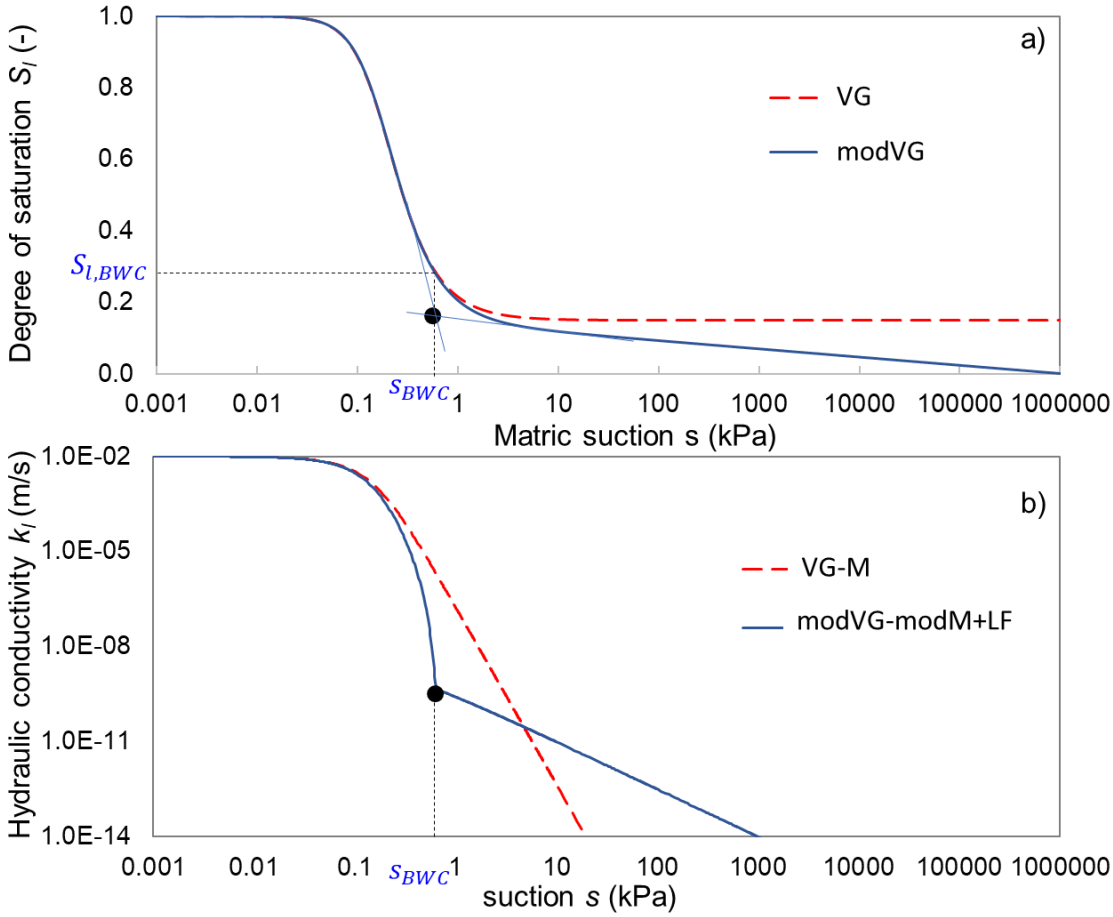

Figure 2-10 a) SWRC, comparison between the modified van Genuchten (modVG) and van Genuchten (VG) models; b) SHCC, comparison between the modified van Genuchten – modified Mualem + liquid film (modVG-modM+LF) model and the van Genuchten-Mualem (VG-M) model

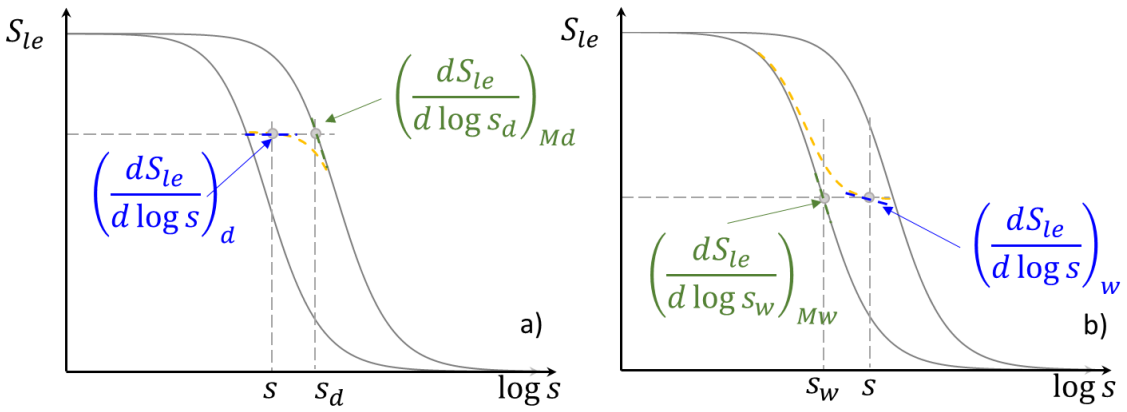

Figure 2-11 Modelling of scanning water retention curves a) drying scanning curve and b) wetting scanning curve (after Scarfone, 2020)

Equations 2-39 and 2-40 were more physically reasonable than Equations 2-21 and 2-22. With the main drying curve and main wetting curve defined by the modVG expression, the value of effective degree of saturation S_{le} on a drying curve (main or scanning), in Equation 2-39, can be related to the corresponding degree of saturation S_l by:

$$S_{le} = \frac{S_l - \xi_d \ln\left(\frac{S_{dry}}{s}\right)}{S_{ls,d} - \xi_d \ln\left(\frac{S_{dry}}{s}\right)} \text{ for drying} \quad \textbf{2-41}$$

where $S_{ls,d}$ and ξ_d are the values of the relevant soil constants for the main drying curve. Similarly, the value of S_{le} on a wetting curve (main or scanning), in Equation 2-40, can be related to the corresponding degree of saturation S_l by:

$$S_{le} = \frac{S_l - \xi_w \ln\left(\frac{S_{dry}}{s}\right)}{S_{ls,w} - \xi_w \ln\left(\frac{S_{dry}}{s}\right)} \text{ for wetting} \quad \textbf{2-42}$$

where $S_{ls,w}$ and ξ_w are the values of the relevant soil constants for the main wetting curve.

In Equations 2-39 and 2-40, s_d and s_w are the inverse functions of the main drying curve and main wetting curve respectively, when these main curves are expressed as relationships between S_{le} and s. With the main drying and wetting SWRCs represented by the VG or modVG expressions, this results in the following expressions for s_d and s_w:

$$s_d = P_{0,d} \cdot \left(S_{le}^{-\frac{1}{m_d}} - 1\right)^{\frac{1}{n_d}} \quad \textbf{2-43}$$

$$s_w = P_{0,w} \cdot \left(S_{le}^{-\frac{1}{m_w}} - 1\right)^{\frac{1}{n_w}} \quad \textbf{2-44}$$

where $P_{0,d}$, m_d and n_d are the values of the van Genuchten soil constants P_0, m and n for the main drying curve and $P_{0,w}$, m_w and n_w are the corresponding values for the main wetting curve. Scarfone (2020) and Scarfone et al. (2020b) then showed that combination of Equations 2-43 or 2-44 with Equations 2-39 or 2-40 leads to the following closed form expressions for the variation of S_{le} along a scanning drying curve or a scanning wetting curve:

$$S_{le,d} = \left\{1 + \left[\frac{1}{P_{0,d}}(s^{\gamma_d} - A_d)^{1/\gamma_d}\right]^{n_d}\right\}^{-m_d} \quad \textbf{2-45}$$

$$S_{le,w} = \left\{1 + \left[\frac{1}{P_{0,w}}(s^{-\gamma_w} - A_w)^{-1/\gamma_w}\right]^{n_w}\right\}^{-m_w} \quad \text{2-46}$$

The integration constants A_d and A_w in Equations 2-45 and 2-46 can be calculated from the requirement that the scanning curve must pass through the last point of suction reversal:

$$A_d = s_0^{\gamma_d} - \left[P_{0,d} \cdot \left(S_{le0}{}^{-\frac{1}{m_d}} - 1\right)^{\frac{1}{n_d}}\right]^{\gamma_d} \quad \text{2-47}$$

$$A_w = s_0^{-\gamma_w} - \left[P_{0,w} \cdot \left(S_{le0}{}^{-\frac{1}{m_w}} - 1\right)^{\frac{1}{n_w}}\right]^{-\gamma_w} \quad \text{2-48}$$

where S_{le0} and s_0 are the effective degree of saturation and suction respectively at the reversal point. The value of S_{le0} can be determined from the value of S_l at the reversal point by Equation 2-41 or Equation 2-42.

Finally, with the main drying and main wetting SWRCs represented by the modVG expression, the closed form expressions for the variation of S_l along a scanning drying curve or a scanning wetting curve are given by Scarfone (2020) and Scarfone et al. (2020b) as:

$$S_{l,d} = \xi_d \ln\left(\frac{S_{dry}}{s}\right) + S_{le,d} \cdot \left(S_{ls,d} - \xi_d \ln\left(\frac{S_{dry}}{s}\right)\right) \quad \text{2-49}$$

$$S_{l,w} = \xi_w \ln\left(\frac{S_{dry}}{s}\right) + S_{le,w} \cdot \left(S_{ls,w} - \xi_w \ln\left(\frac{S_{dry}}{s}\right)\right) \quad \text{2-50}$$

where $S_{le,d}$ or $S_{le,w}$ is predicted from Equations 2-45 or 2-46 with the constant of integration A_d or A_w calculated from Equations 2-47 or 2-48.

Scarfone (2020) and Scarfone et al. (2020b) showed that this advanced hysteretic SWRC model, with main drying and wetting SWRCs represented by the modVG expression of Equation 2-38 and scanning SWRCs represented by Equations 2-45 to 2-50, can provide a good match to experimental SWRC data covering the full range of S_l and including reversals of drying and wetting. This advanced hysteretic SWRC model, referred to as “hysteretic modVG” was used throughout the work presented in this thesis.

The values of soil constants required in the "hysteretic modVG" SWRC model are s_{dry} and then $P_{0,d}$, m_d, n_d, $S_{ls,d}$ and ξ_d for the main drying curve, $P_{0,w}$, m_w, n_w, $S_{ls,w}$ and ξ_w for the main wetting curve and γ_d and γ_w for the scanning curves. It is normal, however, to assume $s_{dry} = 1$GPa as a default value, n values related to corresponding m values by Equation 2-9 and $S_{ls,d} = S_{ls,w} = 1$ on the assumption that main drying curve and main wetting curve must tend to a saturated condition as suction tends to zero (see Section 2.2.2). In addition, it will normally be acceptable to assume $m_d = m_w = m$ and $\xi_d = \xi_w = \xi$ (see Section 3.2.4). This means that the required values of soil constants are reduced to $P_{0,d}$, $P_{0,w}$, m, ξ, γ_d and γ_w. The values of these parameters can be determined by best-fitting to experimental results from a water retention test that includes the main drying curve, the main wetting curve, at least one scanning drying curve and at least one scanning wetting curve. The value of ξ would be determined by fitting the pendular range of the main drying and main wetting curves (i.e. at very low values of S_l), the values of $P_{0,d}$, $P_{0,w}$ and m would then be determined by fitting the capillary and funicular ranges of the main drying and main wetting curves (i.e. excluding very low values of S_l) and finally the values of γ_d and γ_w would be determined by fitting the scanning drying curves and scanning wetting curves respectively.

2.4.2 Soil hydraulic conductivity curve (SHCC)

Scarfone (2020) and Scarfone et al (2020a, 2020b) present an advanced SHCC model, for use with the modVG SWRC model or the hysteretic modVG SWRC model. In this SHCC model, the hydraulic conductivity k_l consist of two terms: a bulk water component of hydraulic conductivity k^{Bulk} and a liquid film component of hydraulic conductivity k^{Film}:

$$k_l = k^{Bulk} + k^{Film} \qquad \textbf{2-51}$$

The bulk water component k^{Bulk} is determined from the SWRC using a modified version of the Mualem (1976) approach described in Section 2.3.3 and the liquid film component k^{Film} is given by a new expression, based on the work of Tokunaga (2009) described in Section 2.3.3. Hence, the combined SWRC-SHCC hydraulic constitutive model is referred to as "modVG-modM+LF" (modified van Genuchten

– modified Mualem + liquid film) if hysteresis is ignored or "hysteretic modVG-modM+LF" if hysteresis is included.

The expression for the bulk water component of hydraulic conductivity k^{Bulk} involves the saturated hydraulic conductivity k_s and a modified version of the van Genuchten – Mualem expression for relative hydraulic conductivity k_{lr} given in Equation 2-35:

$$k^{Bulk} = k_s\sqrt{S_l^C}\left(1-\left(1-(S_l^B)^{1/m}\right)^m\right)^2 \quad \textbf{2-52}$$

Comparison of Equation 2-52 with Equation 2-35 shows that, in the modified Mualem (modM) approach of Equation 2-52, the effective degree of saturation S_{le} appearing twice in Equation 2-35 has been replaced by two slightly different variables S_l^C and S_l^B. The expressions for S_l^C and S_l^B are as follows:

For drying:

$$S_l^C = \frac{S_l - S_{l,BWD}}{1 - S_{l,BWD}};\ S_l^B = \frac{S_l - S_{l,BWEX}}{1 - S_{l,BWEX}} \quad \textbf{2-53}$$

For wetting:

$$S_l^C = \frac{S_l - S_{l,BWC}}{1 - S_{l,BWC}};\ S_l^B = \frac{S_l - S_{l,BWE}}{1 - S_{l,BWE}} \quad \textbf{2-54}$$

where $S_{l,BWD}$, $S_{l,BWC}$, $S_{l,BWEX}$ and $S_{l,BWE}$ are the values of degree of saturation at the bulk water discontinuity, bulk water continuity, bulk water exclusion and bulk water entry points respectively (see Section 2.2.2 and Figure 2-4). The values of $S_{l,BWD}$ and $S_{l,BWEX}$ in Equation 2-53 are determined from the main drying curve, but Equation 2-53 is then applied during any drying processes, irrespective of whether on the main drying curve or on a scanning drying curve. Similarly, the values of $S_{l,BWC}$ and $S_{l,BWE}$ in Equation 2-54 are determined from the main wetting curve, but Equation 2-54 is then applied to any wetting processes, whether on the main wetting curve or a scanning wetting curve. Scarfone (2020) and Scarfone et al. (2020a) provide physical explanations for the definitions of S_l^C and S_l^B given in

Equations 2-53 and 2-54 and for the use of these in the expression for k^{Bulk} of Equation 2-52.

The important difference between the modM expression for k^{Bulk} of Equation 2-52 and the conventional VG-M expression for k_l given by combining Equation 2-35 with the VG SWRC expression is that the modM expression predicts that k^{Bulk} is zero at the bulk water discontinuity point during drying or at the bulk water continuity point during wetting, whereas the conventional VG-M expression predicts that k_l only asymptotically approaches zero as suction tends to infinity. The modM prediction of k^{Bulk} going to zero at the bulk water discontinuity or continuity point is, of course, physically realistic, because flow of bulk water can occur only when there are continuous liquid paths within the bulk water.

The values of $S_{l,BWD}$, $S_{l,BWC}$, $S_{l,BWEX}$ and $S_{l,BWE}$ are difficult to determine experimentally. Scarfone (2020) and Scarfone et al. (2020a) therefore recommended to assume $S_{l,BWD}$= $S_{l,BWEX}$ and $S_{l,BWC}$= $S_{l,BWE}$ and then to determine each of these values from a graphical construction applied to the relevant main SWRC, as illustrated in Figure 2-10a. Note that assuming $S_{l,BWD}$=$S_{l,BWEX}$ and $S_{l,BWC}$= $S_{l,BWE}$ means that S_l^C= S_l^B during wetting and drying processes. According to Scarfone (2020) and Scarfone et al. (2020a), these assumptions and use of this graphical procedure will tend to underestimate the values of $S_{l,BWD}$ and $S_{l,BWC}$ and overestimate the values of $S_{l,BWEX}$ and $S_{l,BWE}$ and these errors will tend to compensate each other when Equation 2-52 is used to calculate the value of k^{Bulk}.

After examination of the theoretical expression derived by Tokunaga (2009) (see Equation 2-37), Scarfone (2020) and Scarfone et al. (2020a) proposed the following expression for the liquid film component of hydraulic conductivity k^{Film}:

$$k^{Film} = C^{Film} \cdot (a + s)^{-1.5} \qquad \textbf{2-55}$$

where C^{Film} and a are soil constants and s is suction. The soil constant a is a dummy parameter. It is required in Equation 2-55 to ensure that k^{Film} does not tend to infinity as s tends to zero. The precise value selected for a is unimportant, provided that it is large enough to ensure that the predicted value of k^{Film} is negligible compared to k^{Bulk} in most of the funicular range and small enough that

a is negligible compared to the value of s in the pendular range. The latter requirement means that Equation 2-55 predicts a linear variation of k_l (with a gradient of -1.5) in a log-log plot against suction in the range where liquid flow occurs only as film flow, as reported by, for example, Peters (2013). Scarfone (2020) and Scarfone et al. (2020a) suggested that a value of a between $S_{l,BWD}/100$ and $S_{l,BWD}/10$ for drying and between $S_{l,BWC}/100$ and $S_{l,BWC}/10$ for wetting would fulfil these requirements.

The value of the soil constant C^{Film} in Equation 2-55 can be determined experimentally, if experimental measurements of k_l are available at very low values of degree of saturation, where liquid flow is entirely within liquid films. However, experimental data of this type are rarely available. In this case, Scarfone (2020) and Scarfone et al. (2020a) suggested, after inspection of the theoretical expression of Tokunaga (2009) of Equation 2-37, the following expression for estimating the value of C^{Film}:

$$C^{Film} = X_D \frac{(1-\Phi)}{D_{10}} \qquad \textbf{2-56}$$

where D_{10} represent the particle size corresponding to 10% passing in a sieve analysis, Φ is soil porosity and X_D is an empirical constant. The value of Φ used in Equation 2-56 should be a representative constant value of porosity for the soil, even in hydro-mechanical numerical modelling where the porosity may vary slightly. After comparison with experimental data for a number of soils, Scarfone (2020) and Scarfone et al. (2020a) suggested $X_D = 2.35\text{x}10^{-9}$ mm.ms^{-1}.kPa$^{1.5}$ as a standard default value. Note that these units for X_D are appropriate if the value of D_{10} in Equation 2-56 is expressed in mm and the values of k^{Film} and $(a+s)$ in Equation 2-55 are expressed in m/s and kPa respectively.

Figure 2-10b shows a comparison between the SHCC predictions of the new hydraulic constitutive model (modVG-modM+LF) and the conventional hydraulic constitutive model (VG-M). The new model predicts much lower values of hydraulic conductivity k_l than conventional model for value of suction around $s_{BWD/BWC}$, because the new model correctly predicts that k^{Bulk} goes to zero at $s_{BWD/BWC}$. Conversely, however, the new model predicts significantly higher

values of k_l than the conventional model at high value of s, because it predicts an appropriate variation of k^{Film} with s.

Scarfone et al. (2020a) demonstrated, by comparison with various sets of the experimental measurement of k_l from the literature, that the new modVG-modM+LF hydraulic constitutive model accurately represents the hydraulic conductivity variation of unsaturated soils over the full range of degree of saturation. Inspection of Figure 2-10b indicates that the conventional VG-M SHCC expression may therefore overestimate the value of k_l by several orders of magnitude at suction values around $s_{BWD/BWC}$ and it may underestimate values of k_l by several orders of magnitude at higher values of suction. Scarfone et al. (2020a) also demonstrated that liquid film flow can have a significant influence on the variation of suction in the coarser layer of a CBS and hence that it is important to include this film flow in numerical modelling of CBSs.

The values of soil constants required for the modM+LF SHCC model (additional to those already required for the SWRC model) are k_s, $S_{l,BWD}$, $S_{l,BWEX}$, $S_{l,BWC}$, $S_{l,BWE}$, C^{Film} and a. In practice, it is typically only the value of saturated hydraulic conductivity k_s that will require an additional laboratory test, because, as described above, it will usually be acceptable to assume $S_{l,BWD} = S_{l,BWEX}$ and $S_{l,BWC} = S_{l,BWE}$, with these values determined from the main drying SWRC and main wetting SWRC respectively using the type of graphical construction illustrated in Figure 2-10a, C^{Film} can be determined from Equation 2-56 (using the default value of X_D in combination with the value of soil porosity Φ and the value of D_{10} from the particle size distribution) and the precise value of the dummy parameter a is unimportant, as long as it satisfies the requirements set out earlier.

2.5 Shear strength of unsaturated soils

Mechanical FE modelling has not been performed in the work presented in this thesis, as discussed in Section 1.3. Thermo-hydraulic numerical modelling (with the soil considered as non-deforming) was performed in this thesis and by Scarfone (2020). Values of suction s and degree of saturation S_l from the thermo-hydraulic FE modelling could then be used to consider the impact on soil shear strength and hence on slope stability through separate stability analyses, as performed by

Scarfone (2020). Hence, shear strength is the only aspect of mechanical behaviour of unsaturated soils of relevance to this project.

Bishop (1959) proposed that the effective stress in unsaturated soil can be defined by:

$$\sigma' = (\sigma - u_a) + \chi \cdot (u_a - u_w) \quad \textbf{2-57}$$

where σ is total stress, u_a is pore air pressure (where $u_a = p_g - p_{at}$), u_w is pore water pressure (where $u_w = p_l - p_{at}$), and χ is the effective stress parameter, which is a function of degree of saturation, with $\chi = 1$ when $(S_l = 1)$, and $\chi = 0$ when $(S_l = 0)$. The first term on the right-hand side of Equation 2-57 $(\sigma - u_a)$ represents the net normal stress. The second term $\chi \cdot (u_a - u_w)$ represents the contribution of suction $(u_a - u_w)$ to the effective stress. Subsequent research (e.g. Jennings and Burland, 1962) showed that a single Bishop's effective stress is unable to represent all aspects of the mechanical behaviour of unsaturated soils. In particular, use of a single effective stress is unable to represent properly the yielding behaviour of unsaturated soils including , for example, the occurrence of collapse compression on wetting (Alonso et al., 1990). Thus, many researchers proposed the use of two independent stress state variables to represent the full mechanical behaviour of unsaturated soils. These two independent stress state variables are most commonly selected as net stress $(\sigma - u_a)$ and suction $s = (u_a - u_w)$(Alonso et al., 1990) but other combinations of two stress variables have also been proposed. These alternative combinations often include a first stress variable similar to Bishop's proposal of Equation 2-57 with suction or some function of suction as a second stress variable (e.g. Wheeler et al., 2003).

Fredlund et al. (1978) proposed a linear form of shear strength variation for unsaturated soil using the two independent stress variables of net stress and suction:

$$\tau_f = c' + [(\sigma - u_a) \cdot \tan \phi' + (u_a - u_w) \cdot \tan \phi^b] \quad \textbf{2-58}$$

where τ_f is the shear strength, c' and ϕ' are the conventional cohesion and friction angle of the soil (applicable under saturated or dry conditions) and ϕ^b is an additional friction angle indicating the rate of increase of shear strength with

suction. The term involving $\tan\phi^b$ predicts a linear relationship between shear strength and suction. However, Escario and Saez (1986) and subsequent authors demonstrated that the relationship between shear strength τ_f and $(u_a - u_w)$ is non-linear and a constant value of ϕ^b is therefore not appropriate.

Subsequently, authors such as Gallipoli et al. (2003) showed that the shear strength τ_f (but not all aspects of mechanical behaviour) of unsaturated soils could be uniquely related to a single stress variable of the type proposed by Bishop (1959) (see Equation 2-57) and with $\chi = S_l$. This results the following expression for shear strength τ_f for a cohesionless unsaturated soil:

$$\tau_f = \big((\sigma - u_a) + S_l s\big)\tan\phi' \qquad \textbf{2-59}$$

Equation 2-59 predicts a non-linear increase of shear strength with suction, because S_l is not constant, but reduces with increasing s, according to the SWRC. Inspection of Equation 2-59 indicates that suction s enhances the shear strength of an unsaturated soil, through the contribution of the component $S_l s \cdot \tan\phi'$. Wetting of the soil will generally lead to reduction of the product $S_l s$ (the reduction of s tending to outweigh any increase of S_l) and hence to weakening of the soil.

2.6 Soil-atmosphere interaction

Many researchers have studied soil-atmosphere interactions and their influence on soil behaviour (e.g. Blight, 1997; Khire et al., 2000; Lu and Likos, 2004; Gens, 2010; Dong et al., 2015; Tsiampousi et al., 2017; Cheng et al., 2019). The depth of the near surface unsaturated zone is highly sensitive to soil-atmosphere interaction, such as precipitation, evaporation and evapotranspiration, see Figure 2-12 (Lu and Likos, 2004).

Figure 2-12 shows that the unsaturated zone can be conceptually divided into two zones: a seasonally unsteady-state zone and a steady-state zone. Time dependent atmospheric conditions and soil-atmosphere interactions including precipitation, evaporation, atmospheric relative humidity, atmospheric temperature, and wind speed cause soil suction near the ground surface to fluctuate. The depth of the active zone depends strongly on the local geological and climate conditions.

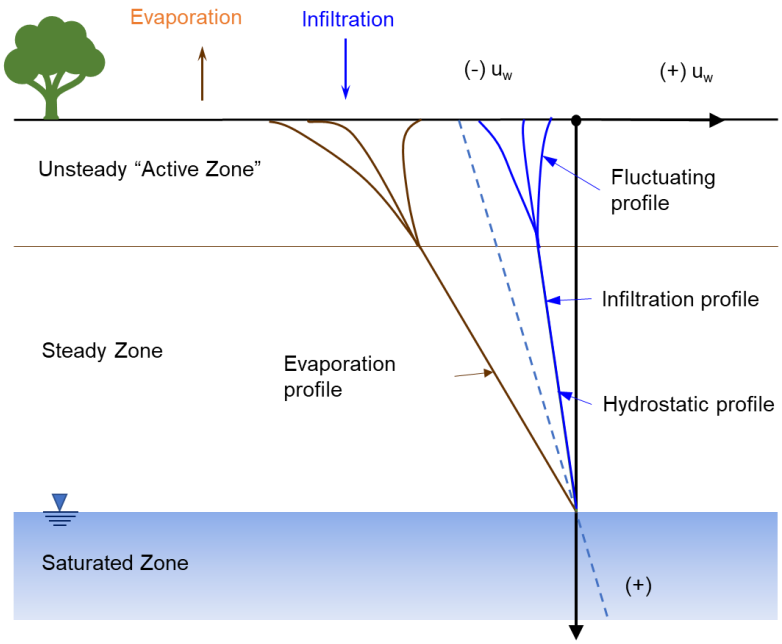

Figure 2-12 Conceptual suction profiles in unsaturated soil under various surface flux boundary conditions (after Lu and Likos, 2004)

Below the active zone, the soil suction profile in the steady zone is controlled by factors including soil type, net surface water influx, vegetation, and presence of an underground water table.

Thus, it is necessary to considering soil-atmosphere interaction in order to evaluate thermo-hydraulic behaviour of unsaturated soils including the behaviour of capillary barrier systems.

2.6.1 Water balance and energy balance

Several forms of mass and energy transfer occur between the soil surface and the atmosphere. Figure 2-13 shows the key phenomena of soil-atmosphere interaction (Brutsaert, 1982). Soil-atmosphere interaction refers to all the phenomena of water mass exchanges (e.g. precipitation P and evaporation E) and energy exchanges (e.g. radiation flux R_n, latent heat of evaporation flux and sensible heat flux H_s) between soil and atmosphere.

For hydraulic numerical modelling of a surface layer of soil, such as the hydraulic numerical modelling of CBSs presented in Chapters 4 to 7 of this thesis, water mass exchanges at the soil-atmosphere interface, such as rainwater infiltration and evaporation, are clearly important. Energy exchanges at the soil-atmosphere

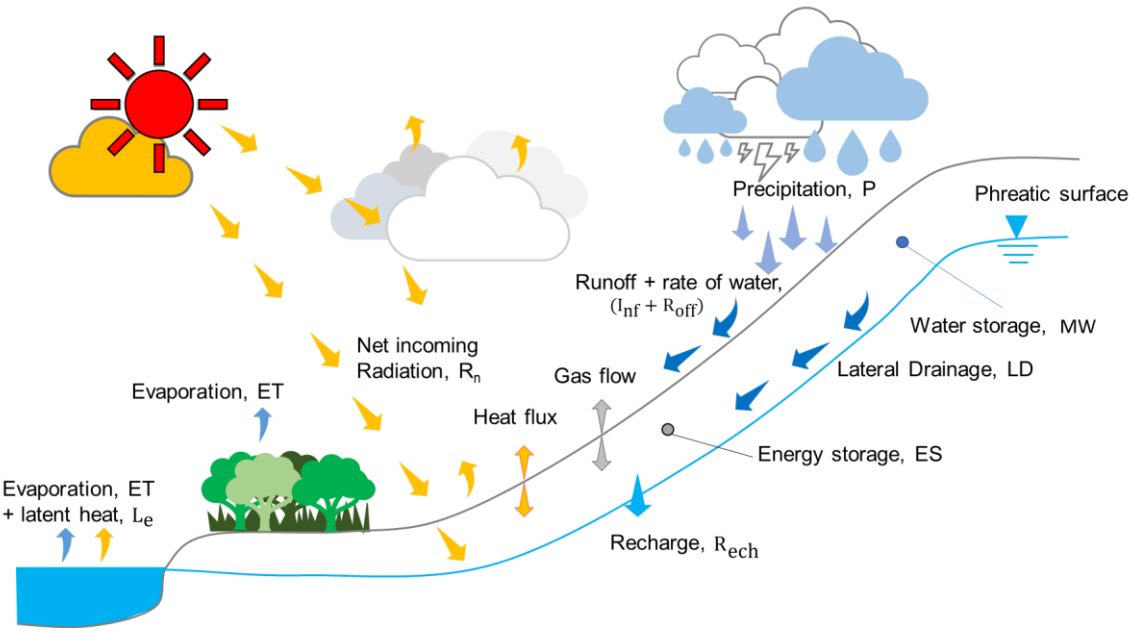

Figure 2-13 Soil-atmosphere interaction components and water mass flow phenomena in a surface layer of soil (after Scarfone, 2020).

interface are also important, because these influence the temperature distribution within the soil, which affects both the mass flux of water within the soil due to vapour diffusion (see Section 2.3.1) and the rate of water evaporation at the soil-atmosphere interface (because this is influenced by the temperature of the soil at the ground surface).

The conservation of water mass in a surface layer of soil (see Figure 2-13) can be expressed (Blight, 1997) as:

$$P - \left(I_{nf} + R_{off}\right) = E + R_{ech} + MW \qquad \textbf{2-60}$$

where P is precipitation, I_{nf} is the rate of water intercepted by plant cover that does not infiltrate in the soil, R_{off} is the surface run-off rate, E is evapo-transpiration rate (i.e. evaporation and transpiration of plants), R_{ech} is the rate of water recharged to the underlying soil (all expressed as mass flow rates per unit plan area) and MW is the rate of increase of water storage (the mass of water stored in the reference layer per unit plan area). $\left(P - \left(I_{nf} + R_{off}\right)\right)/\rho_l$ represents the volumetric rainfall infiltration rate i at the ground surface.

The expression for conservation of energy can be expressed (Brutsaert, 1982) as:

$$R_n - H_e - H_s - G_s + H_c = ES \quad \text{2-61}$$

where R_n is the net incoming radiation flux at the soil surface, H_e is the latent heat of evaporation, H_s is the sensible heat flux into atmosphere, G_s is the energy flux leaving the layer at the lower boundary, and H_c is the convective heat flux into the layer from the atmosphere (all expressed per unit plan area), and ES is the rate of increase of energy stored in the layer (per unit area).

2.6.2 Evaporation

Evaporation into the atmosphere is the result of complex soil-atmosphere interaction phenomena. A simplified analytical solution for the evaporation rate E, presented by Brutsaert (1982), is based on various simplifying assumptions, including: uniform density of moist air in the atmosphere; incompressibility of the moist air; constant viscosity of the moist air; no variation of atmospheric parameters (i.e., temperature, humidity, and wind speed) in the horizontal direction ; and a simplified description (based on dimensional analysis) of the turbulence in the lowest part of atmospheric boundary layer. This simplified analytical solution is known as an aerodynamic diffusion relation:

$$E = \frac{K^2 v_a \psi}{\left(\ln \frac{z_a}{z_0}\right)^2} (\rho_v - \rho_{va}) \quad \text{2-62}$$

where ρ_{va} and ρ_v are the vapour density in the atmosphere and in the gas in the soil voids at the ground surface respectively, K is von Karman's constant (K = 0.4), ψ is a stability factor, v_a is atmospheric wind speed, z_0 is roughness length, and z_a is the screen height at which v_a and ρ_{va} are measured. ρ_{va} depends upon the temperature and relative humidity of the atmosphere (T_a and R_{ha}), whereas ρ_v depends upon the temperature of the soil at the ground surface T_s and the relative humidity of the gas with soil voids at the ground surface R_{hs}.

Similar to the evaporation rate, the sensible heat flux H_s can be obtained by an aerodynamic diffusion relation (Brutsaert, 1982):

$$H_s = \frac{K^2 v_a \psi}{\left(\ln \frac{z_0}{z_a}\right)^2} \rho_{ga} C_a (T_s - T_a) \quad \text{2-63}$$

where ρ_{ga} is atmospheric gas density and C_a is the specific heat of the atmospheric gas.

2.6.3 Radiation

The net incoming radiation flux at the soil surface R_n has can be expressed as the combination of various terms (Brutsaert, 1982) as:

$$R_n = R_s(1 - A_l) + \varepsilon_s R_{ld} - R_{lu} \quad \text{2-64}$$

where R_s is global short-wave solar radiation, A_l is the surface albedo, R_{ld} is the downward atmospheric long-wave radiation, ε_s is the emissivity of the ground surface (which depends on the surface properties), and R_{lu} is the upward long-wave radiation from the soil surface.

R_{ld} and R_{lu} are given by:

$$R_{ld} = C_{cloud}\varepsilon_a\sigma_R T_a^4 \quad \text{2-65}$$

$$R_{lu} = \varepsilon_s\sigma_R T_s^4 \quad \text{2-66}$$

where C_{cloud} is a correction parameter for cloudiness, ε_a is the emissivity of the atmosphere in the clear sky condition, and σ_R is the Stefan-Boltzmann constant (5.67×10^{-8} W/m^2/K^4).

2.7 Horizontal capillary barrier systems

2.7.1 Working principle of horizontal capillary barrier systems

Capillary barrier systems (CBSs) have been primarily used for landfill cover systems to prevent water infiltration into waste (Mallants et al., 1999; Benson et al., 2007). CBSs generally consist of two layers with different soil particle sizes, a finer layer (F.L.) overlying a coarser layer (C.L.), placed over the ground to prevent percolation of water into the underlying soil. The working principle of CBSs is based on the difference in the unsaturated hydraulic properties (SWRC and SHCC) of the two materials (Rahardjo et al., 2012). The different values of hydraulic

conductivity k_l of the finer and coarser layers limit flow of water from the finer layer to the coarser layer and hence reduce or prevent percolation of water into the underlying soil (Stormont and Anderson, 1999; Khire et al., 2000; Rahardjo et al., 2012).

Figure 2-14 shows typical SWRCs and SHCCs for two capillary barrier materials. Under saturated conditions (see points A_1 and B_1 in Figure 2-14), the hydraulic conductivity of the coarser layer is much higher than that of the finer layer ($k_{s,c} > k_{s,f}$). On the other hand, under unsaturated conditions, for a given a value of suction (see points A_2 and B_2 in Figure 2-14), the coarser layer has a much lower value of hydraulic conductivity than the finer layer ($k_{l,c} < k_{l,f}$), because the coarser layer is at a much lower value of degree of saturation S_l. Hence the coarser layer acts as an almost impermeable barrier and rainwater infiltration is stored the upper finer layer.

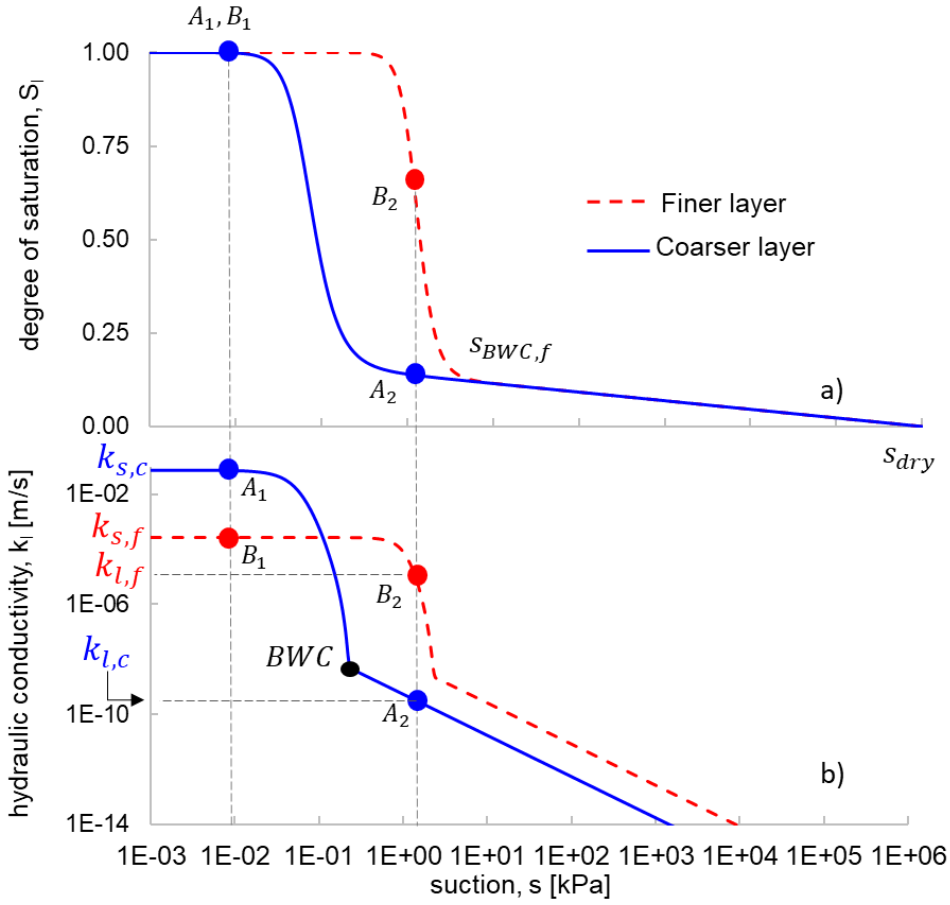

Figure 2-14 The main wetting a) SWRC and b) SHCC for capillary barrier system

There is, however, a maximum amount of infiltrating rainwater that can be stored in the finer layer. As more water fills the finer layer, and the value of S_l at the

bottom of the finer layer increases, the suction value at this interface with the coarser layer gradually reduces. If the suction value at the interface decreases sufficiently until it reaches the bulk water continuity value of the coarser layer (see BWC in Figure 2-14), the hydraulic conductivity of the coarser layer starts to increase dramatically, and water starts flowing down into the coarser layer. This point is called “breakthrough”, and it corresponds to failure of the capillary barrier.

2.7.2 Water storage capacity of horizontal capillary barrier systems

The water storage capacity WSC of a horizontal CBS (the volume of water stored in the finer layer per unit plan area at the time of breakthrough) can be calculated by integrating the profile of degree of saturation S_l over the thickness of the finer layer and multiplying by the soil porosity Φ:

$$WSC = \Phi \int_0^{t_f} S_l \, dz \qquad \text{2-67}$$

where z is the elevation above the interface between coarser and finer layers and t_f is the thickness of the finer layer. The variation of S_l with z, for use in Equation 2-67, can be obtained from the suction profile in the finer layer (the variation of s with z) at the time of breakthrough by using the appropriate wetting SWRC relationship (S_l: s) for the finer layer. Stormont and Morris (1998) proposed an approximate suction profile in the finer layer at the time of breakthrough, for a horizontal CBS subjected to continuous rainfall of constant intensity, leading to a simplified method of calculating WSC through Equation 2-67.

Breakthrough from the finer layer to the coarser layer occurs when the suction at the interface between the two layers falls to a value s_1 corresponding to the bulk water continuity value of the coarser layer $s_{BWC,c}$ (Scarfone et al., 2020a), and hence this sets the value of suction at the bottom of the finer layer (see Figure 2-15):

$$s_1 = s_{BWC,c} \qquad \text{2-68}$$

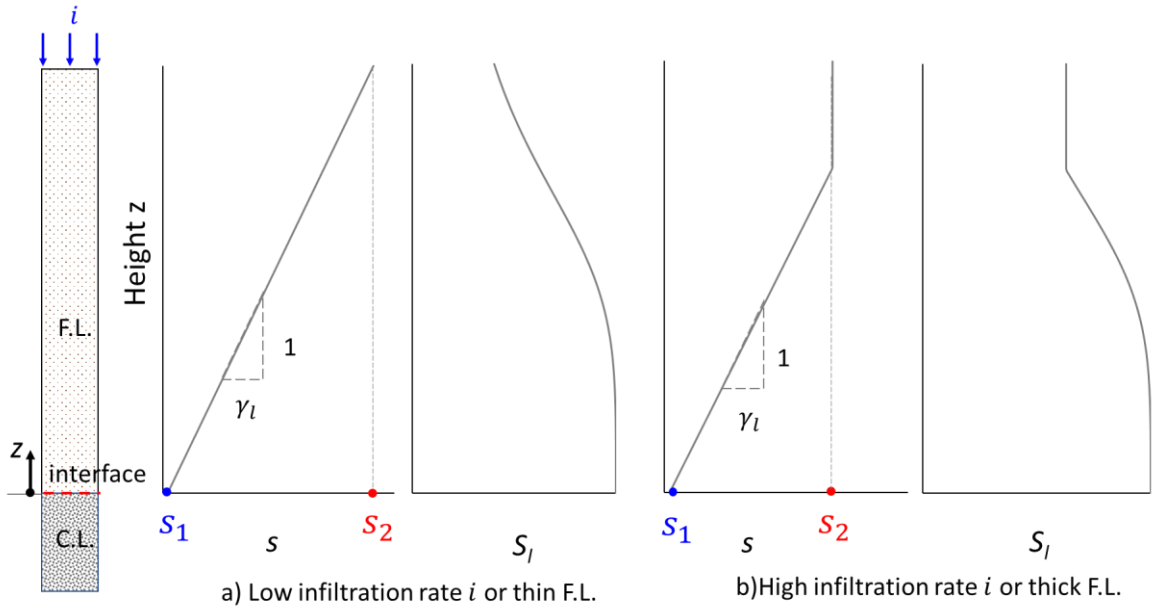

Figure 2-15 Approximate suction profile of CBS at breakthrough (after Stormont and Morris, 1998)

For the variation of suction through the rest of the finer layer, Scarfone (2020) sets out the logic of the approximate suction profile at breakthrough first proposed by Stormont and Morris (1998). Under continuous rainfall infiltration at the ground surface of constant intensity i (volumetric flow rate per unit plan area), breakthrough of water from the finer layer to the coarser layer occurs when the full water storage capacity of the finer layer has been occupied (i.e., when the soil of the finer layer is unable to store any more water at every depth z within the finer layer). Hence, at this time, a steady state flow situation is achieved within the finer layer, with the vertical seepage velocity q_v (volumetric flow rate per unit plan area) at all values of z within the finer layer equal to the rainfall infiltration rate i. However, q_v can be expressed by Darcy's law (see Equation 2-23):

$$q_v = k_l \frac{dh_l}{dz} \qquad \textbf{2-69}$$

where k_l is the hydraulic conductivity of the soil and h_l is the total head of the pore water, defined in Equation 2-24. Differentiating Equation 2-24:

$$\frac{dh_l}{dz} = 1 + \frac{1}{\gamma_l} \cdot \frac{dp_l}{dz} \qquad \textbf{2-70}$$

where p_l is the pore liquid pressure and γ_l is the unit weight of liquid water.

Given $s = p_g - p_l$, and p_g is assumed constant (and equal to atmospheric pressure), Equation 2-70 can be rewritten in terms of the suction gradient as:

$$\frac{dh_l}{dz} = 1 - \frac{1}{\gamma_l} \cdot \frac{ds}{dz} \quad \text{2-71}$$

Towards the bottom of the finer layer, at the time of breakthrough, the soil is at high degree of saturation S_l and hence the hydraulic conductivity k_l is high in this region, and much higher than the vertical seepage velocity $q_v = i$ (i.e. $k_l \gg i$). According to Darcy's law (see Equation 2-69), this means that the value of the vertical hydraulic gradient $\frac{dh_l}{dz}$ is much less than one (i.e., almost zero, $\frac{dh_l}{dz} \approx 0$). Equation 2-71 then indicates that the variation of suction s with elevation in this lower part of the finer layer is indistinguishable from a hydrostatic variation:

$$\frac{ds}{dz} \approx \gamma_l \quad \text{2-72}$$

Moving upwards through the finer layer, the value of suction increases, according to the (almost) hydrostatic variation, and hence the degree of saturation falls and so does the hydraulic conductivity k_l. However, there will typically be a significant part of the finer layer where the value of k_l is still much larger than the value of $q_v = i$, indicating that the value of $\frac{dh_l}{dz}$ is still much less than 1 and hence the suction variation is still approximately hydrostatic. If the rainfall infiltration rate is low or the thickness of the finer layer is small, this approximately hydrostatic variation of suction will continue right up to the ground surface (see Figure 2-15a). The maximum suction in the finer layer s_2 is then given by:

$$s_2 = s_1 + \gamma_l t_f \quad \text{2-73}$$

where γ_l is the unit weight of the liquid water and t_f is the thickness of the finer layer (see Figure 2-15a).

In contrast, when the rainfall infiltration rate is higher or the thickness of the finer layer is greater, moving upwards through the finer layer a situation is reached where the suction increases sufficiently, and the degree of saturation

reduces sufficiently, that it is no longer true to say that the hydraulic conductivity k_l is much greater than vertical seepage velocity $q_v = i$. This means that the hydraulic gradient becomes significantly greater than zero (see Equation 2-69) and hence the suction variation begins to diverge from a hydrostatic profile. Moving on upwards, the suction increases further, and degree of saturation and hydraulic conductivity decrease further until a critical value of suction s_f^* is reached. This critical value of suction corresponds to the value at which the hydraulic conductivity of the material of the finer layer is equal to the rainfall infiltration rate ($k_l = i$). At this point (and remembering $q_v = i$ at all values of z at the time of breakthrough), Darcy's law (see Equation 2-69) indicates that the hydraulic gradient has a value of one ($\frac{dh_l}{dz} = 1$). Consequently, the suction is not changing with elevation (see Equation 2-71), and from this point upwards to the ground surface the suction remains constant at s_f^*. For these higher values of infiltration rate i or greater thicknesses of finer layer, the suction profile should therefore show a gradual transition from an approximately hydrostatic profile in the lower part of the finer layer (where the value of k_l is much greater than i) to a constant value of suction in the upper part of the finer layer (where the value of k_l is equal to i). In practice, however, because the value of k_l for the material of the finer layer changes by several orders of magnitude for relatively modest changes of suction, the transition from the hydrostatic profile to the constant value of suction occurs over a very limited height of the finer layer. The approximate suction profile suggested by Stormont and Morris (1998) therefore corresponds to the bi-linear relationship shown in Figure 2-15b. Note that, in this case, the maximum value of suction in the finer layer s_2 is given by:

$$s_2 = s_f^*. \qquad \textbf{2-74}$$

Many authors have done numerical modelling, laboratory tests or field work to validate this simplified approach for calculating the water storage capacity of a horizontal CBS. Stormont and Anderson (1999) studied the behaviour of CBSs and determined the suction profile within the finer layer of a CBS at breakthrough by a series of laboratory infiltration tests conducted on CBSs composed of silty sand and pea gravel. Similarly, Yang et al. (2006) and Harnas et al. (2014) performed column infiltration tests to investigate the water storage capacity of CBSs.

Stormont and Morris (1998) and Khire et al. (2000) performed numerical analyses to investigate the effect of different parameter value on water storage capacity of horizontal CBSs and to study the hydraulic behaviour of horizontal CBSs when subject to different weather conditions. These studies showed that the water storage capacity mainly depends upon rainfall intensity, finer layer properties and finer layer thickness. They also found reasonable agreement with the simplified approach of Stormont and Morris (1998) for calculating water storage capacity. None of these studies however represented a comprehensive parametric investigation covering all possible combinations of the important variables.

Scarfone (2020) studied horizontal conventional capillary barrier systems through advanced hydraulic numerical modelling and laboratory experimental column tests. He demonstrated that the approximate suction profile at breakthrough proposed by Stormont and Morris (1998) and the associated prediction of water storage capacity were excellently matched to the corresponding numerical results and experimental column test results (for the limited number of cases that he considered).

2.8 Sloping capillary barrier systems

2.8.1 Working principle of sloping capillary barrier systems

CBSs on slopes have been used to prevent slope failure during intensive rainfall or under extreme weather condition by preventing or reducing rainfall infiltration into the underlying soil (Miyazaki, 1988; Oldenburg and Pruess, 1993; Rahardjo et al., 2012).

When rainfall occurs on a sloping CBS, the infiltrating rainwater is initially stored within the finer layer and then increasing amounts of water are diverted down the slope as flow within the lower part of the finer layer. During continuous rainfall of constant intensity, a final steady state is achieved, where the water storage capacity of the finer layer is fully occupied and hence all infiltrating rainwater is either diverted down the slope within the finer layer or breaks through into the coarser layer (if this breakthrough occurs, the CBS has failed). In this steady state condition shown in Figure 2-16, the amount of water transferred down the slope within the finer layer increases moving down the slope because in this steady state

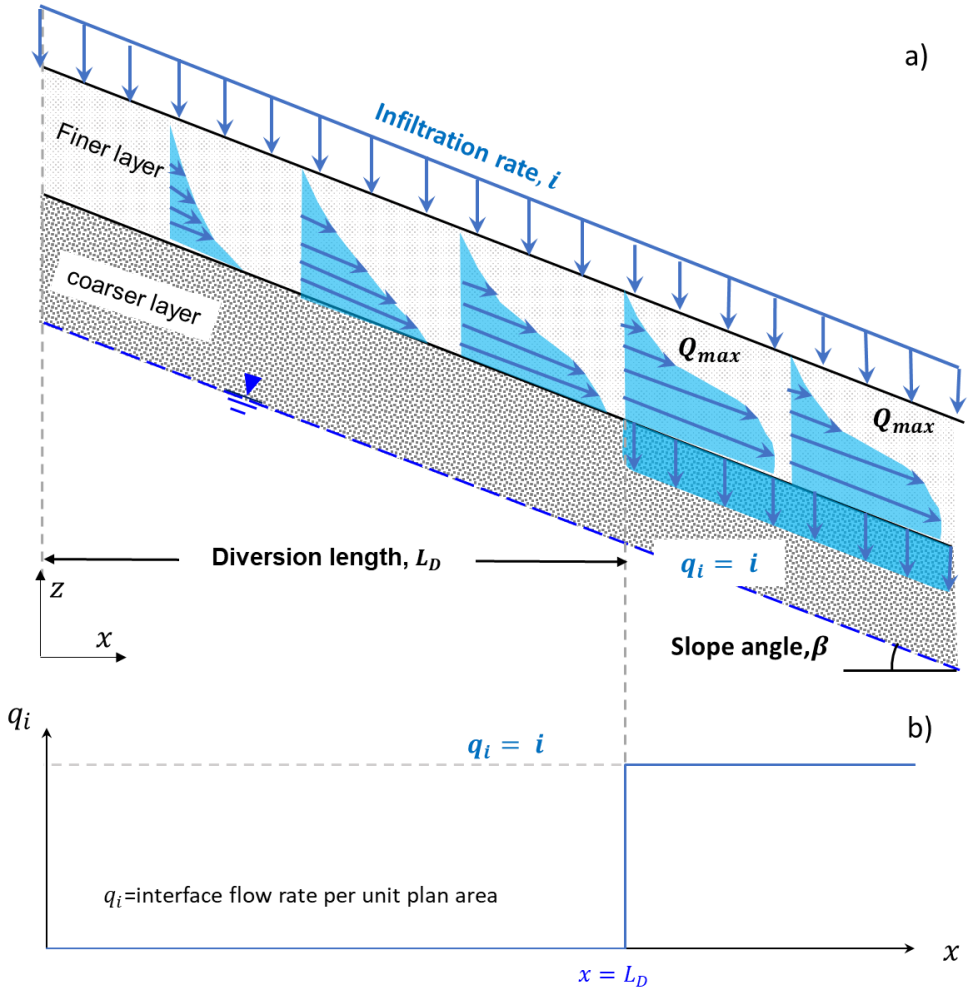

Figure 2-16 Schematic steady state water flow within sloping CBS subjected to rainfall of constant intensity (after Parent and Cabral, 2006)

condition, if no breakthrough has occurred, each vertical slice of the finer layer must be transferring all the rainfall infiltrating the slope surface from this slice to the top of the slope. However, there is a maximum amount of water that can be transferred down the slope within the finer layer without breakthrough to the coarser layer occurring. This is known as the water transfer capacity Q_{max} of the CBS (Ross, 1990). The horizontal distance from the top of the slope to the point where the water flow down the slope reaches this water transfer capacity is known as the diversion length L_D (see Figure 2-16). If the slope is shorter than the diversion length L_D, no breakthrough to the coarser layer will occur. However, if the slope is longer than the diversion length L_D, the final steady state situation will involve no breakthrough over the upper part of the slope (to the diversion length), and then breakthrough into the coarser layer for the lower part of the slope (from the diversion length onwards). In this final steady state, the water transferred down the slope within the finer layer is equal to the water transfer capacity Q_{max} for the entire lower part of the slope (from the diversion length

onwards) and in this part of the slope the vertical seepage velocity q_i across the interface is equal to the rainfall infiltration rate $(q_i = i)$(see Figure 2-16).

The effective performance of sloping capillary barrier systems subjected to realistic (intermittent) rainfall infiltration depends upon both the water storage capacity (WSC) and the water transfer capacity down the slope (Ross, 1990; Steenhuis et al., 1991; Oldenburg and Pruess, 1993; Stormont, 1995). Water storage capacity and water transfer capacity are both dependent on the hydraulic properties of the capillary barrier materials (SWRC and SHCC), slope geometry (i.e., length of slope, angle of slope, number and thicknesses of CBS layers (multi-layered CBSs are possible). Moreover, the performance of a CBS on a slope also depends upon meteorological conditions, and soil-atmosphere interaction phenomena, which determine the variations of rainwater infiltration and evaporation (Stormont and Morris, 1998; Bussière et al., 2007; Zhan et al., 2013).

2.8.2 Water transfer capacity and diversion length of sloping CBSs subjected to rainfall of constant intensity

The water transfer capacity Q_{max} represents the maximum flow rate down the slope (m^3/s per metre run along the slope) that can be achieved within the finer layer without breakthrough occurring into the coarser layer. It can be calculated by considering a vertical cross-section of the CBS taken at the diversion length and then integrating over this vertical cross-section the horizontal component q_h of the final steady state seepage velocity within the finer layer, which varies with the vertical height z above the bottom of the finer layer:

$$Q_{max} = \int_0^{t_f} q_h \, dz \qquad \textbf{2-75}$$

The diversion length L_D under continuous rainfall of constant intensity i can then be calculated as:

$$L_D = \frac{Q_{max}}{i} \qquad \textbf{2-76}$$

The variation of the final steady state horizontal seepage velocity q_h with z in Equation 2-75 will depend upon the steady state suction profile on the vertical

cross-section corresponding to the diversion length (the same suction profile will also apply to all vertical cross-sections further down the slope). According to Darcy's law:

$$q_h = -k_l \frac{\partial h_l}{\partial x} \quad \text{2-77}$$

where the hydraulic conductivity k_l is a function of suction s and the horizontal hydraulic gradient $\frac{\partial h_l}{\partial x}$ (where x is the horizontal coordinate measured from the top of the slope) is also dependent on the suction profile on vertical cross-sections.

Several analytical or semi-analytical methods have been proposed to evaluate the water transfer capacity Q_{max} and hence diversion length L_D of a sloping CBS when subjected to continuous rainfall of constant intensity (or steady state condition) (Ross, 1990; Steenhuis et al., 1991; Oldenburg and Pruess, 1993; Morel-Seytoux, 1994; Morel-Seytoux et al., 1996; Kampf and Montenegro, 1997).

Ross (1990) was the first author to study the water transfer capacity of a sloping CBS. He obtained a complete analytical solution, by solving the relevant governing equations, without having to make any assumption in advance of an appropriate suction profile. In order to do this, however, he assumed that the finer layer of the CBS was infinitely thick and he also assumed a highly unrealistic exponential form (Gardner, 1958) for the SHCC of each layer:

$$k_l = k_s exp(-\alpha s) \quad \text{2-78}$$

where α is a soil constant. Ross (1990) defined "breakthrough" as corresponding to the point when suction at the interface between finer and coarser layers reached zero (with the exponential form of SHCC given in Equation 2-78, there is no bulk water continuity value of suction for the coarser layer at which the value of k_l for this layer suddenly starts increasing dramatically).

The full analytical solution of Ross (1990) for water transfer capacity Q_{max} is:

$$Q_{max} = \frac{k_{s,f} \tan\beta}{\alpha_f \gamma_l} \left[\left(\frac{i}{k_{s,c}} \right)^{\alpha_f/\alpha_c} - \frac{i}{k_{s,f}} \right] \quad \text{2-79}$$

where $k_{s,f}$ and $k_{s,c}$ are the saturated hydraulic conductivity of the finer and coarser layers respectively, α_f and α_c are the values of the soil constant α in the exponential SHCC expression (see Equation 2-78) for the finer and coarser layers respectively, β is the slope angle, i is the rainfall intensity and γ_l is the unit weight of water. For typical CBSs, there is significant contrast between the SHCC curves of the finer and coarser layers ($\alpha_f \ll \alpha_c$) and also $k_{s,f} \gg i$. For these conditions, Equation 2-79 simplifies to:

$$Q_{max} = \frac{k_{s,f} \tan\beta}{\alpha_f \gamma_l} \qquad \textbf{2-80}$$

Using this simplified expression for Q_{max}, diversion length L_D is given by:

$$L_D = \frac{Q_{max}}{i} = \frac{k_{s,f} \tan\beta}{\alpha_f \gamma_l i} \qquad \textbf{2-81}$$

Unfortunately, the unrealistic assumptions employed by Ross (1990) to derive his fully analytical solution (finer layer of infinite thickness and exponential form for the SHCCs of the two layers) mean that his resulting analytical expressions for Q_{max} and L_D (Equations 2-79, 2-80, and 2-81) are of limited use.

Subsequently, several authors developed revised analytical or semi-analytical solutions for calculation of water transfer capacity Q_{max} and hence diversion length L_D based on modifications to Ross' solution. For example, Steenhuis et al. (1991) assumed a modified exponential form for the SHCC of the finer layer:

$$\begin{aligned} k_{l,f} &= k_{s,f} && s < s_{AEX,f} \\ k_{l,f} &= k_{s,f} exp\left[-\alpha_f \left(s - s_{AEX,f}\right)\right] && s \geq s_{AEX,f} \end{aligned} \qquad \textbf{2-82}$$

where $s_{AEX,f}$ is the air exclusion value of suction for the finer layer. They also assumed that breakthrough corresponded to achievement of a suction value at the interface equal to the bulk water continuity value of the coarser layer $s_{BWC,c}$. This led to the following expressions for Q_{max} and L_D:

$$Q_{max} = \frac{k_{s,f} \tan\beta}{\gamma_l} \left[\frac{1}{\alpha_f} + \left(s_{AEX,f} - s_{BWC,c}\right)\right] \qquad \textbf{2-83}$$

$$L_D = \frac{k_{s,f} \tan \beta}{\gamma_l i} \left[\frac{1}{\alpha_f} + \left(s_{AEX,f} - s_{BWC,c} \right) \right] \quad \text{2-84}$$

As expected, these converge to the expressions of Ross (1990) (Equations 2-80 and 2-81) if $s_{AEX,f} = 0$ and $s_{BWC,c} = 0$.

Stormont (1995) extended the solution of Ross (1990) by accounting for the effect of anisotropy in hydraulic conductivity of the finer layer of the CBS. Stormont's solution for calculation of water transfer capacity and hence diversion length consisted of two terms: the first term represents the capillary barrier effect (the same as Ross' solution) and the second term refers to the additional transfer capacity attributable to the anisotropy of the finer layer.

Parent and Cabral (2006) developed a semi-analytical method, by assuming an approximate suction profile at breakthrough. This method has the advantage over the approach of Ross (1990) or Steenhuis et al. (1991) that it is can be used with any chosen SHCC model. Parent and Cabral (2006) assumed that the suction profile in the finer layer on all vertical cross-sections from the diversion length onwards corresponded to the approximate suction profile at breakthrough for a horizontal CBS described earlier in Section 2.7.2 and shown in Figure 2-15. This approximate suction profile, with $\frac{ds}{dz} = \gamma_l$ in the lower part of the finer layer, occurring on all vertical cross-sections from the diversion length onwards, results in the following expression for the horizontal hydraulic gradient in this lower part of the finer layer from the diversion length onwards:

$$\frac{\partial h_l}{\partial x} = -\tan \beta \quad \text{2-85}$$

where β is the slope angle. Hence, from Equation 2-77, from the diversion length onwards, the horizontal seepage velocity in this lower part of the finer layer is given by:

$$q_h = k_l \tan \beta \quad \text{2-86}$$

For a thick finer layer or high infiltration rate (see Figure 2-15), in the upper part of the finer layer, where the assumed approximate suction profile involves a

constant value of suction s_f^*, the corresponding predicted value of q_h is zero. Consequently, the Parent and Cabral (2006) method for predicting water transfer capacity Q_{max} (and hence diversion length L_D) can be expressed as:

$$Q_{max} = \frac{\tan\beta}{\gamma_l}\int_{s_1}^{s_2} k_l \, ds \qquad \textbf{2-87}$$

$$L_D = \frac{\tan\beta}{i \cdot \gamma_l}\int_{s_1}^{s_2} k_l \, ds \qquad \textbf{2-88}$$

where s_1 is the suction at the bottom of the finer layer at the time of breakthrough (the bulk water continuity suction of the coarser layer) and s_2 is the suction at the top of the finer layer, which, with this assumed suction profile, is given by either $s_1 + \gamma_l t_f$ or s_f^*, whichever is the smaller (see Figure 2-15).

Various attempts have been made to validate the analytical or semi-analytical solutions for Q_{max} and L_D by experimental tests, field tests or numerical modelling (Bussiere et al., 2003; Tami et al., 2004; Bussière et al., 2007; Aubertin et al., 2009; Li et al., 2013; Harnas et al., 2014; Liu et al., 2015). For instance, Oldenburg and Pruess (1993) performed numerical analyses using the finite element method to study the behaviour of sloping capillary barriers and they compared their results of diversion length at final steady state with the predictions of Ross (1990) (Equations 2-80 and 2-81). In their numerical simulations, the diversion length was identified as the location where large downward flux through the interface commenced in the final steady state. The numerical modelling employed a hydraulic conductivity expression based on Richards's equation, whereas Ross's prediction used the exponential form of hydraulic conductivity variation of Equation 2-78. The numerical experiments showed that diversion length identification was more complicated than assumed in the theoretical analysis. Moreover, Ross's prediction of L_D was found to be slightly conservative.

2.8.3 Behaviour of sloping CBSs subjected to realistic weather conditions

The previous section presented studies of the behaviour of sloping CBSs when subjected to continuous rainfall of constant intensity. This section presents the behaviour of sloping CBSs when subjected to intermittent rainfall. Typically, when

rainfall is discontinuous, the location within the slope where breakthrough occurs varies with time. At the start of a period of rainfall, the infiltrating rainwater goes into storage within the finer layer. If the duration of rainfall is short, breakthrough might not occur anywhere in the slope, whereas longer duration of rainfall may cause breakthrough in the lower part of the slope. During periods without rainfall, water can be removed from the finer layer by a combination of evaporation from the ground surface and water transfer down the slope in the lower part of the finer layer, leading to partial restoration of the storage capacity. There may also be vertical redistribution of water within the finer layer. Hence, when rainfall starts again, the initial state of the CBS will depend upon the previous history of intermittent rainfall. This means that the behaviour of a sloping CBS subjected to realistic intermittent rainfall is very complex.

Many researchers have attempted to study the effects of intermittent rainfall patterns on the behaviour of sloping CBSs (e.g. Morris and Stormont, 1999; Aubertin et al., 2009; Lacroix Vachon et al., 2015; Ng et al., 2015b; Chen et al., 2019; Scarfone, 2020; Scarfone et al., 2022). Aubertin et al. (2009) investigated the effect of the main factors, including climate conditions, hydraulic properties of CBS materials, and CBS configuration, on the behaviour of sloping CBSs and breakthrough prediction. Lacroix Vachon et al. (2015) compared results from numerical simulations under transient rainfall with the results obtained by experiment (Abdolahzadeh et al., 2011), steady state numerical simulations, analytical solution (Ross, 1990), and semi-analytical solution (Parent and Cabral, 2006). Ng et al. (2015b) and Chen et al. (2019) performed numerical modelling of a newly proposed three-layered sloping CBS by using CODE_BRIGHT finite element software to back-analyse physical experiments performed under humid climatic conditions.

Although, many researchers have attempted to develop numerical prediction tools to study sloping CBSs under transient state realistic weather conditions (including whether breakthrough will occur and, if so, subsequent restoration of the CBS effect after rainfall ceases), there were often limitations in the research, such as exclusion of water retention hysteresis (important under real meteorological conditions) or ignoring soil-atmosphere interaction (i.e., evaporation, and vegetation).

Scarfone (2020) and Scarfone et al. (2022) performed numerical modelling of sloping CBSs subjected to long-term meteorological conditions including soil-atmosphere interaction and impact on factor of safety (FoS). This study captured the variability of the climate (i.e. temperature, relative humidity, radiation and rainfall) through two different climate areas: Cagliari (dry and warm) and London (wet and cool), represented by annual sinusoidal cycles of temperature, relative humidity and radiation but with daily rainfall totals covering a full 10 year period. Thermo-hydraulic FE modelling (including retention hysteresis and soil-atmosphere interaction) was performed using the advanced multi-physics CODE_BRIGHT software (see Chapter 3), and separate stability analyses performed with the limit analysis software LimitState: GEO. Values of the product of degree of saturation S_l and suction s were exported from the CODE_BRIGHT software to the LimitState: GEO software at times corresponding to the most critical rainfall events with the 10 year period. Values of factor of safety were then calculated for each of these events, with the LimitState: GEO software, assuming that shear strength under unsaturated conditions was given by Equation 2-59. The results of this investigation showed that sloping CBSs were effective in maintaining slope stability by preventing decreases of suction in the underlying soil during extreme rainfall events. This applied whether the finer layer was made of silty sand or fine sand, with both types of finer layer equally effective in maintaining slope stability. If the finer layer was made of silty sand, the CBS strongly relied on the water storage capacity, whereas if the finer layer was made of fine sand, the CBS relied much more on water transfer capacity for performance. Moreover, the results demonstrated that the sloping CBSs were effective at maintaining slope stability even if they did not completely prevent breakthrough at all times. A small amount of breakthrough, of limited duration and limited extent (at the bottom part of slope) during an extreme rainfall event was acceptable, because the critical failure surface still remained within the CBS (rather than extending into the underlying soil) and hence the slope remained stable. Unfortunately, however, the type of complex multi-physics numerical modelling employed by Scarfone (2020) and Scarfone et al. (2022) is impractical as a standard design method of analysis for use by practising geotechnical engineers.

2.9 Multi-layered capillary barrier systems

Multi-layered CBSs have been proposed to increase the effectiveness of CBSs, by increasing either water storage capacity or water transfer capacity or both. Figure 2-17 shows types of capillary barrier, including a conventional CBS (Figure 2-17a), with one finer layer and one coarser layer, a multi-layer capillary barrier (Figure 2-17b), with additional alternating coarser and finer layers (more than two layers of each type are possible) and a three-layered CBS proposed by Ng et al. (2015a) with a third layer of compacted clay below a conventional CBS (Figure 2-17c).

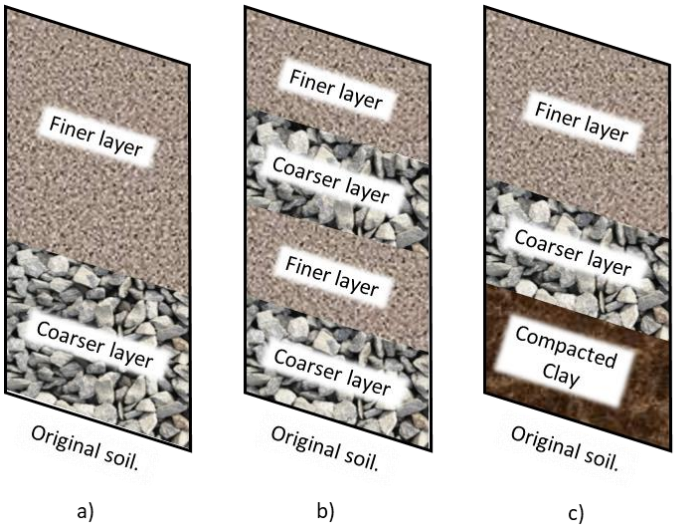

Figure 2-17 Types of capillary barrier systems: a) conventional CBS, b) multi-layered CBS and c) three-layered CBS

Multi-layered CBSs (Figure 2-17b) provide increase water storage capacity and water transfer capacity by increasing the number of finer layers. According to Harnas et al. (2014), their research aimed to increase water storage of capillary barrier systems by an experimental study comparing a multi-layered CBS (with two finer layers and two coarser layers) against a conventional CBS. The results showed that multi-layered CBS provided higher water storage capacity and slower breakthrough flow rate than conventional CBSs.

Three-layered CBSs (see Figure 2-17c) have been proposed, with the addition of a low hydraulic conductivity base soil layer (i.e. compacted clay), to provide an additional barrier when the overlying CBS fails. Ng et al. (2015b) presented physical and numerical modelling of an inclined three-layered CBS (Figure 2-17c) under extreme rainfall. The results confirmed that the three-layered capillary barrier performed well under extreme rainfall when breakthrough occurred in the

overlying CBS. However, the effects of slope angle, rainfall intensity, clay thickness and long-term performance were not examined in this project. Chen et al. (2019) presented physical test results and numerical modelling of a three-layered sloping capillary barrier (Figure 2-17c) in humid climates. Both experimental and numerical results showed that water transfer rate down the slope increased with increase of slope angle.

Scarfone (2020) applied similar concepts to those set out in Section 2.7.2 to propose an approximate suction profile at steady state for horizontal multi-layered CBSs (see Figure 2-17b). For low infiltration rate or thin finer layers (see in Figure 2-18a), the approximate suction profile proposed by Scarfone (2020) involves a hydrostatic suction profile (Equation 2-72) in each finer layer, with the value of suction s_1 ($s_1 = s_{BWC,c}$, Equation 2-68) at the bottom of the lowest finer layer and a constant value of suction s_3 within each intermediate coarser layer:

$$s_3 = s_c^* \quad \textbf{2-89}$$

where s_c^* is the value of suction at which the hydraulic conductivity of the coarser layer is equal to the rainfall infiltration rate i. In this case, the suction s_2 at top of the lowest finer layer is given by $s_2 = s_1 + \gamma_l t_f$ (given in Equation 2-73) where t_f is the thickness of an individual finer layer, and the suction at the top of all remaining finer layers s_4 is given by:

$$s_4 = s_c^* + \gamma_l t_f \quad \textbf{2-90}$$

For the case of a higher infiltration rate or thicker finer layers (see Figure 2-18b), there is an upper part of each finer layer that is at a constant value of suction s_f^*. The value of suction at the top of each finer layer s_2 is then given by $s_2 = s_f^*$ (Equation 2-74). The variation of degree of saturation S_l with elevation throughout the various finer layers and the intermediate coarser layers, for determining the water storage capacity of the multi-layered CBS, can be determined from the assumed suction profile by using the SWRC of the two materials of the CBS. For multi-layered CBSs the water storage capacity is given by integrating the final steady state volumetric water content over the thicknesses of all finer layers and all intermediate coarser layers (i.e. all layers of the CBS except the lowest coarser layer).

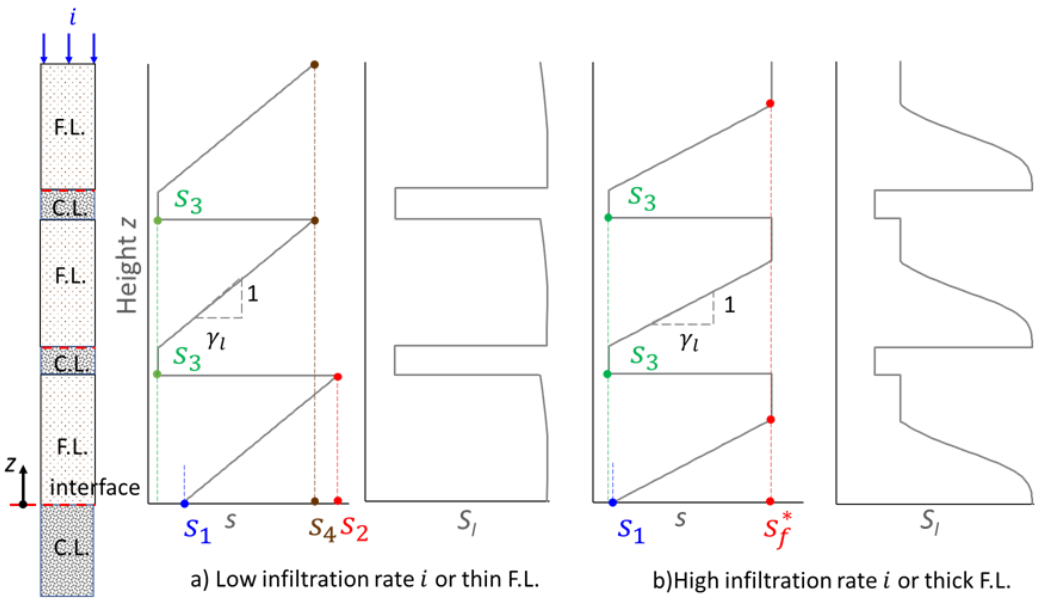

Figure 2-18 Approximate suction profile of horizontal multi-layered CBS at breakthrough (after Scarfone, 2020)

The simplified method of analysis for horizontal multi-layered CBSs proposed by Scarfone (2020) was validated by numerical modelling and laboratory column tests. Results from the three different methods (simplified method of analysis, numerical analyses, and experimental tests) showed good agreement with each other. The results confirmed that using multi-layered CBSs leads to significant increase of water storage capacity and, for a CBS of a specified total thickness, there is an optimum number of finer layers to maximise the water storage capacity.

Chapter 3 Numerical code: CODE_BRIGHT software

The CODE_BRIGHT multi-physics finite element software (Olivella et al., 1994; Olivella et al., 1996) used for the numerical modelling undertaken within this thesis, is presented in this chapter. Hydraulic and coupled thermo-hydraulic numerical analyses are a major part of this thesis because these have been used to investigate the hydraulic behaviour of horizontal CBSs and sloping CBSs under continuous rainfall of constant intensity (Chapters 4 and 5), to investigate the thermo-hydraulic behaviour of sloping CBSs subject to intermittent or varying intensity rainfall (Chapter 6) and to validate a proposed simplified method of analysis for sloping CBSs subjected to extreme rainfall events (Chapter 7).

3.1 CODE_BRIGHT

The 'CODE_BRIGHT' multi-physics finite element code was developed at the Universität Politècnica de Catalunya (UPC) in Barcelona (UPC., 2019). This program can be used for modelling thermo-hydro-mechanical-chemical (THMC) processes in three-phase (unsaturated) geological media. Within this thesis, only hydraulic (H) and thermo-hydraulic (TH) modelling was performed (see Section 1.3) and therefore the mechanical and chemical aspects of CODE_BRIGHT are not fully described in this chapter. CODE_BRIGHT v.8.2 was used throughout this thesis. Pre-processing and post-processing was performed with the 'GiD' program, developed by the International Center for Numerical Methods in Engineering (CIMNE) in Barcelona (Ribo et al., 1999). Pre-processing refers to the process of defining and preparing the problem (i.e. the definition of geometry, material properties, boundary conditions, initial conditions, solution information and other parameters). This pre-processing included automatic meshing by GiD, subject to information on the required mesh refinement provided by the user. Post-processing refers to presentation and visualization of the results of numerical simulations (i.e. deformed mesh, minimum and maximum values of variables, vector distributions, and presentation of variables through contour fields and contour lines). GiD v.13.04 was used in this thesis.

Many simultaneous interaction phenomena are considered in the CODE_BRIGHT formulation. For example, variation of temperature affects liquid density, liquid viscosity, vapour density and surface tension and these in turn affect hydraulic conductivity, water retention behaviour (water storage), liquid water transfer and water vapour transfer.

The following assumptions and aspects are included in the general (THMC) formulation:

- Dry air is considered as a single species (i.e. no separate consideration of the constituent gases, nitrogen, oxygen, carbon dioxide, etc).

- The assumption of thermal equilibrium between phases is considered. This means that, at any given location, the three phases (solid, liquid, and gas) are at the same temperature.

- Water vapour concentration is in equilibrium with the liquid phase (Psychrometric law, see Equation 2-4).

- Dissolved air concentration is in equilibrium with the gas phase (Henry's law, see Section 2.3.1)

- Primary unknowns are solid displacement $\boldsymbol{u}$ (in three spatial directions: x, y, and z), pore liquid pressure p_l, pore gas pressure p_g, and temperature T.

- Balance of momentum for the porous medium is reduced to the equation of stress equilibrium (i.e. dynamic effects are not considered), with a mechanical constitutive model to relate stress with strain (which defines displacement).

- Small strain and small strain rate are assumed for solid deformation.

- Balance of momentum for liquid and gas phases and for dissolved species (water vapour and dissolved air) are reduced to constitutive equations (Darcy's law and Fick's law)

- Physical parameters in constitutive laws are functions of pressure and temperature; for example, saturated vapour pressure (involved in the psychrometric law and in Fick's law for diffusion of water vapour), surface tension (involved in the SWRC constitutive model), and dynamic viscosity (involved in Darcy's law) all depend on temperature.

3.2 Governing equations

The primary objective of the numerical modelling described in Chapters 4-7 was hydraulic modelling of capillary barrier systems. However, some of this hydraulic modelling was to include the influence of vapour transfers (see Section 2.3.1) and evaporation from the ground surface (see Section 2.6) and it was therefore necessary to also include thermal modelling and relevant thermo-hydraulic coupling (i.e. thermo-hydraulic (TH) modelling). Thus, the governing equations within CODE_BRIGHT relevant to TH modelling are presented in this section.

All the governing equations considered within CODE_BRIGHT are presented by Olivella et al. (1994) and Olivella et al. (1996). There are four types of governing equations in CODE_BRIGHT: balance equations, constitutive equations, equilibrium relationships, and definition constraints. Numerous equations can be applied in CODE_BRIGHT (for full THMC modelling), but this section focuses on the equations that have been used in this thesis. A list of these equations and corresponding variables is shown in Table 3-1.

3.2.1 Balance equations

Mass balance equations are established following a compositional approach and performed for three species: soil particles, water and air.

The mass balance of solid can be expressed:

$$\frac{\partial}{\partial t}\left(\rho_s(1-\Phi)\right) + \nabla \cdot \boldsymbol{j_s} = 0 \qquad \textbf{3-1}$$

where ρ_s is the density of the solid particles (kgm^{-3}), Φ is porosity and $\boldsymbol{j}_s$ is the mass flux of solid (kgm^{-2}s^{-1}) which is expressed as:

$$\boldsymbol{j_s} = \rho_s(1-\Phi)\frac{d\boldsymbol{u}}{dt} \quad \textbf{3-2}$$

This mass balance of solid equation expresses the variation of porosity Φ caused by volumetric deformation and any variation of solid density ρ_s.

Table 3-1 Equations and variables in CODE_BRIGHT (after Olivella et al., 1994)

Equation name	Variable	Equations
Balance equations		
Solid mass balance	Φ	3-1
Water mass balance	p_l	3-3
Air mass balance	p_g	3-6
Internal energy	T	3-9
Stress equilibrium	$\dot{\boldsymbol{u}}$	3-10
Definition Constraints		
Deformation $\dot{\boldsymbol{\varepsilon}} = \frac{\mathbf{1}}{\mathbf{2}}(\boldsymbol{\nabla}\dot{\boldsymbol{u}} + \boldsymbol{\nabla}\dot{\boldsymbol{u}}^t)$	$\dot{\boldsymbol{\varepsilon}}$	3-11
Liquid phase and gas phase		
$\boldsymbol{\omega_l^w} + \boldsymbol{\omega_l^a} = \mathbf{1}$	ω_l^w	3-12
$\boldsymbol{\omega_g^w} + \boldsymbol{\omega_g^a} = \mathbf{1}$	ω_g^a	3-13
$\boldsymbol{S_l} + \boldsymbol{S_g} = \mathbf{1}$	S_g	3-14
$\boldsymbol{i_g^w} + \boldsymbol{i_g^a} = \mathbf{1}$	$\boldsymbol{i_g^a}$	3-15
$\boldsymbol{i_l^w} + \boldsymbol{i_l^a} = \mathbf{1}$	$\boldsymbol{i_l^w}$	3-16
Equilibrium restrictions		
Henry's law	Dissolved air mass fraction (ω_l^a)	3-17
Psychrometric law	Vapour mass fraction (ω_g^w)	3-18
Constitutive equations		
Darcy's law	Liquid and gas advective flux ($\boldsymbol{q_l}, \boldsymbol{q_g}$)	3-26,3-28
Fick' law	Vapour and air non- advective fluxes ($\boldsymbol{i_g^w}, \boldsymbol{i_l^a}$)	3-32
Fourier's law	Conductive heat flux ($\boldsymbol{i_c}$)	3-34

The mass balance of water present in liquid and gas phases is expressed as:

$$\frac{\partial}{\partial t}\left(\left(\theta_l^w S_l + \theta_g^w S_g\right)\Phi\right) + \nabla\cdot\left(\boldsymbol{j_l^w} + \boldsymbol{j_g^w}\right) = f^w \quad \textbf{3-3}$$

$$\frac{\partial}{\partial t}(\text{mass of water stored in liquid and gas phases}) + \nabla\cdot(\text{total flux of water}) = (\text{external source or sink of water})$$

where θ_l^w is mass of water per unit volume in liquid phase (kgm^{-3}) , θ_g^w is mass of water vapour per unit volume in gas phase (kgm^{-3}) (i.e. $\theta_g^w = \rho_v$), S_l and S_g are degree of saturation of liquid and gas phases respectively (S_g=1-S_l), Φ is porosity, $\boldsymbol{j}_g^w$ and $\boldsymbol{j}_l^w$ are mass fluxes of water in gas and liquid phases (kgm^{-2}s^{-1}), respectively, and f^w is external source (positive) or sink (negative) of water (kgm^{-3}s^{-1}).

The total mass fluxes of water in both liquid phase $\boldsymbol{j}_l^w$ and gas phase $\boldsymbol{j}_g^w$ are each the sum of three components: a non-advective (diffusive) component $\boldsymbol{i}_l^w$, an advective component due to fluid motion and an advective component due to the solid motion:

$$\boldsymbol{j}_l^w = \boldsymbol{i}_l^w + \theta_l^w \boldsymbol{q}_l + \theta_l^w S_l \Phi \frac{d\boldsymbol{u}}{dt} \quad \textbf{3-4}$$

$$\boldsymbol{j}_g^w = \boldsymbol{i}_g^w + \theta_g^w \boldsymbol{q}_g + \theta_g^w S_g \Phi \frac{d\boldsymbol{u}}{dt} \quad \textbf{3-5}$$

where $\boldsymbol{i}_l^w$ and $\boldsymbol{i}_g^w$ are non-advective mass fluxes of water in the liquid phase and the gas phase respectively (kgm^{-2}s^{-1}) and $\boldsymbol{q}_l$ and $\boldsymbol{q}_g$ are advective volume fluxes of liquid and gas phases respectively (ms^{-1}).

The unknown degree of saturation S_l in Equations 3-3 to 3-5 is related to the primary unknowns of liquid pressure p_l, gas pressure p_g and temperature T through the SWRC model (noting that temperature is involved because of the dependence of surface tension (and hence SWRC) on temperature).

Air mass balance is given by:

$$\frac{\partial}{\partial t}\left(\left(\theta_l^a S_l + \theta_g^a S_g\right)\Phi\right) + \nabla \cdot \left(\boldsymbol{j}_g^a + \boldsymbol{j}_l^a\right) = f^a \quad \textbf{3-6}$$

$$\frac{\partial}{\partial t}(\text{mass of air in liquid and gas phases}) + \nabla \cdot (\text{total flux of air}) = (\text{external source or sink of air})$$

where θ_l^a is the mass of air per unit volume of liquid (kgm^{-3}), θ_g^a is the mass of air per unit volume of gas, $\boldsymbol{j}_l^a$ and $\boldsymbol{j}_g^a$ are the total mass fluxes of air in the liquid phase and the gas phase (kgm^{-2}s^{-1}) respectively, and f^a is the external source or

sink of air ($kgm^{-3}s^{-1}$). The mass fluxes of air in both liquid and gas phases can be expressed as:

$$\boldsymbol{j}_l^a = \boldsymbol{i}_l^a + \theta_l^a \boldsymbol{q}_l + \theta_l^a S_l \Phi \frac{d\boldsymbol{u}}{dt} \quad \textbf{3-7}$$

$$\boldsymbol{j}_g^a = \boldsymbol{i}_g^a + \theta_g^a \boldsymbol{q}_g + \theta_g^a S_g \Phi \frac{d\boldsymbol{u}}{dt} \quad \textbf{3-8}$$

Internal energy balance can be expressed as:

$$\frac{\partial}{\partial t}\left(e_s\rho_s(1-\Phi) + e_l\rho_l S_l \Phi + e_g\rho_g S_g \Phi\right) - \frac{\Phi S_g p_g}{\rho_g}\frac{\partial \rho_g}{\partial t} + \nabla \cdot \left(\boldsymbol{i}_c + \boldsymbol{j}_{es} + \boldsymbol{j}_{el} + \boldsymbol{j}_{eg}\right) = f^Q \quad \textbf{3-9}$$

$$\frac{\partial}{\partial t}(\text{internal energy in solid, liquid and gas phases}) + \nabla \cdot (\text{total flux of energy}) = (\text{external source or sink of heat})$$

where e_l, e_g and e_s are internal energies (per unit mass) of liquid, gas and solid phases respectively (m^2s^{-2}), $\boldsymbol{i}_c$ is the energy flux due to conduction through the porous medium, $\boldsymbol{j}_{es}$, $\boldsymbol{j}_{eg}$ and $\boldsymbol{j}_{el}$ are the energy fluxes due to advection of solid, gas and liquid respectively (kgs^{-3}) and f^Q is an internal/external energy source or sink ($kgm^{-1}s^{-3}$)

Momentum balance for the porous medium is reduced to a statement of equilibrium:

$$\nabla \cdot \boldsymbol{\sigma} + \mathbf{b} = 0 \quad \textbf{3-10}$$

where $\boldsymbol{\sigma}$ is the stress tensor ($kgm^{-1}s^{-2}$) and $\mathbf{b}$ is the vector of body forces ($kgm^{-2}s^{-2}$).

3.2.2 Definition constraints

The deformation definition constraint (compatibility) is expressed by:

$$\dot{\boldsymbol{\varepsilon}} = \frac{1}{2}(\nabla \dot{\boldsymbol{u}} + \nabla \dot{\boldsymbol{u}}^t) \quad \textbf{3-11}$$

where $\dot{\boldsymbol{\varepsilon}}$ is the strain rate tensor and $\dot{\boldsymbol{u}} = \frac{d\boldsymbol{u}}{dt}$ is the solid displacement rate.

The liquid phase consists of water and dissolved air and the following definition constraint is used:

$$\theta_l^w + \theta_l^a = \rho_l \quad \textbf{3-12}$$

Similarly, the following definition constraint for the gas phase is used:

$$\theta_g^w + \theta_g^a = \rho_g \quad \textbf{3-13}$$

The volume of voids comprises of either liquid phase or gas phase, the following definition constraint is used:

$$S_l + S_g = 1 \quad \textbf{3-14}$$

The binary diffusion concept is applied to diffusive fluxes in gas phase. This means that the diffusive flux of water vapour in the gas phase is balanced by an equal and opposite diffusive flux of air in the gas phase:

$$\boldsymbol{i}_g^w + \boldsymbol{i}_g^a = 0 \quad \textbf{3-15}$$

The same concept applies to diffusive fluxes of water and dissolved air in the liquid phase:

$$\boldsymbol{i}_l^w + \boldsymbol{i}_l^a = 0 \quad \textbf{3-16}$$

3.2.3 Equilibrium restrictions

The concentration of each species (i.e. air or water) in each phase (i.e. liquid or gas) is governed by equilibrium restrictions: Henry's law or the psychrometric law.

Henry's law governs the concentration of dissolved air in the liquid phase, expressed as:

$$\frac{\theta_l^a}{\rho_l} = p_a \cdot \left(\frac{1}{H}\frac{M_a}{M_w}\right) \quad \textbf{3-17}$$

where p_a is the partial pressure of air in the gas phase, M_a is the molecular mass of air, M_w is the molecular mass of water and H is Henry's constant. The following default values are used in CODE_BRIGHT: M_a = 0.02895 kg/mol M_w = 0.01801kg/mol and H = 10000 MPa.

The psychrometric law governs the concentration of water vapour in the gas phase and in CODE_BRIGHT, this is expressed in term of the vapour density in the gas phase ρ_v as:

$$\rho_v = \rho_{v0} \exp\left(\frac{-(p_g - p_l)M_w}{RT\rho_l}\right) \quad \textbf{3-18}$$

where ρ_{v0} is the saturated vapour density in the gas phase in contact with a planar gas-liquid interface, R is the universal gas constant (8.314 J/(molK)) and T is the absolute temperature. The law of idea gases is used to calculated ρ_{v0} as below:

$$\rho_{v0} = \frac{p_{v0}M_w}{RT} \quad \textbf{3-19}$$

where p_{v0} is the saturated vapour pressure in a gas phase in contact with a planar gas-liquid interface, calculated using the empirical relationship:

$$p_{v0}\,(\text{MPa}) = 136075 \exp\left(-\frac{5239.7}{T}\right) \quad \textbf{3-20}$$

CODE_BRIGHT can solve full thermo-hydro-mechanical problems, but in this thesis, mechanical aspects were not considered. Therefore, Equations 3-1, 3-2, 3-10, and 3-11 were not used. The porosity Φ was taken as constant, equal to the initial value specified by the user and all term involving deformation rate $d\boldsymbol{u}/dt$ in Equations 3-4, 3-5, 3-7, and 3-8 were considered equal to zero ($d\boldsymbol{u}/dt = 0$) i.e. the mechanical and hydraulic governing equations were effectively decoupled in the software.

All numerical simulations in this thesis were performed excluding the solving of air mass balance equations, consequently, Equations 3-6 and 3-7, and 3-8 were not used. The pore gas pressure was considered as uniform and constant (p_g= 0.1

MPa). Thus, dissolved air in the liquid phase was not considered (i.e. θ_l^a = 0 and $\theta_l^w = \rho_l$).

Numerical simulations presented in Chapters 4 and 5, and some of these presented in later chapters involved only hydraulic modelling (rather than thermo-hydraulic modelling). In these cases, the energy balance equation (Equation 3-9) was excluded, temperature was considered as uniform and constant, and water vapour in the gas phase was not considered. In contrast, some of the numerical simulations presented in Chapter 6 involved full thermo-hydraulic modelling.

3.2.4 Constitutive equations

CODE_BRIGHT provides many options for the forms of the various constitutive equations. Only the relevant constitutive equations are presented here.

The phase properties relevant to the numerical simulations presented in this thesis are the specific heat capacity of the solid phase, liquid density, liquid viscosity, gas density, gas viscosity and thermal properties relevant to the internal energy of the liquid and gas phases. Table 3-2 shows the default laws and parameter values for these phase properties suggested in CODE_BRIGHT by Olivella et al. (1996) and which were used in all simulations presented in this thesis.

In CODE_BRIGHT, the type of constitutive law is defined by the value of index ICL. This ICL number indicates the type of constitutive law or model, such as SWRC (ICL = 6) or SHCC (ICL = 14). The value of a second index ITYCL then indicates which specific version of that type of constitutive law or model is used. For example, ICL = 6, ITYCL = 1 would correspond to the van Genuchten (VG) SWRC model. Each constitutive law or model can then involve up to 10 parameter values (P1 to P10). The meaning of these different parameters will be different for the different constitutive laws or models, as illustrated in Table 3.3. For example, with ICL = 6 and ITYCL = 1, the parameters P1 to P5 would be the soil constants required in the van Genuchten SWRC model and the parameters P6 to P10 would be unused (see Table 3-3).

In CODE_BRIGHT, there are many SWRC models (ICL = 6) available. In this thesis, four different SWRC models have been used namely: van Genuchten model (SWRC-

Table 3-2 Default laws and parameter values for phase properties in CODE_BRIGHT (after Olivella et al., 1996)

Solid phase specific heat $C_s = 1000$ Jkg^{-1}K^{-1}		
Liquid density $\rho_{l0} = 1002.6$ kgm^{-3} $\beta_\rho = 4.5\text{x}10^4$ MPa-1 $p_{l0} = 0.1$ MPa $\alpha_T = -3.4\text{x}10^{-4}\text{K}^{-1}$	$\rho_l = \rho_{l0}\exp\left(\beta_\rho(p_l - p_{l0}) + \alpha_T(T - 273.15)\right)$	**3-21**
Liquid viscosity $A = 2.1\text{x}10^{-12}$ MPa s $B = 1808.5$ K	$\mu_l = A\exp\left(\frac{B}{T}\right)$	**3-22**
Gas density	Law of ideal gases	
Gas viscosity $A = 1.48\text{x}10^{-12}$MPa s $B = 119.4$ K $C = 0.14$ MPa $D = 1.2\text{x}10^{15}$ kg	$\mu_g = \frac{A\sqrt{T}}{\left(1 + \frac{B}{T}\right)\left(1 + \frac{C - Dk_i}{p_g}\right)}$ k_i:intrinsic permeability	**3-23**

VG), modified van Genuchten model (SWRC-modVG), hysteretic van Genuchten model (SWRC-hysteretic VG) and hysteretic modified van Genuchten model (SWRC-hysteretic modVG).

The conventional van Genuchten (SWRC-VG) model (ICL = 6, ITYCL = 1) can be expressed as:

$$S_{le} = S_{lr} + S_{ls} - S_{lr} = \left(1 + \left(\frac{p_g - p_l}{P_0}\right)^{\frac{1}{1-m}}\right)^{-m}, P_0 = \bar{P}_0\frac{\sigma_s}{\bar{\sigma}_s} \quad \textbf{3-24}$$

where S_{lr} is the residual degree of saturation (a soil constant), S_{ls} is the maximum degree of saturation (at s = 0) and P_0 is a material parameter which is dependent on temperature because surface tension σ_s varies with temperature. The parameter $\bar{P}_0$ represents the value of P_0 at a reference temperature of 20°C and $\bar{\sigma}_s$ represents the value of σ_s at this reference temperature. If the user sets $\bar{\sigma}_s$ = 0, P_0 is considered, independent of temperature and equal to $\bar{P}_0$. $\bar{\sigma}_s$ = 0.072 N/m at 20°C was applied in the thermo-hydraulic numerical modelling i.e. temperature-dependence of the SWRC (through temperature-dependence of surface tension σ_s) was included in the thermo-hydraulic numerical modelling presented in Chapter 6. As the soil was assumed to be non-deforming (rigid), the

Table 3-3 Parameter requirements for constitutive equations in thermo-hydraulic numerical modelling in CODE_BRIGHT (after Olivella et al., 1996)

Model	P1	P2	P3	P4	P5	P6	P7	P8	P9	P10
SWRC-VG (ICL=6, ITYCL=1) Equation 3-24	$\bar{P}_0$ (MPa)	$\bar{\sigma}_s$ $\left(\frac{\mathrm{N}}{\mathrm{m}}\right)$	m (-)	S_{lr} (-)	S_{ls} (-)	-	-	-	-	-
SWRC-modVG (ICL=6, ITYCL=17) Equation 3-25	$\bar{P}_0$ (MPa)	$\bar{\sigma}_s$ $\left(\frac{\mathrm{N}}{\mathrm{m}}\right)$	m (-)	S_{lr} (-)	S_{ls} (-)	s_{dry} (MPa)	ξ (-)	-	-	-
SWRC-hysteretic VG (ICL=6, ITYCL=1)	$\bar{P}_{0d}$ (MPa)	$\bar{\sigma}_s$ $\left(\frac{\mathrm{N}}{\mathrm{m}}\right)$	m (-)	S_{lr} (-)	S_{ls} (-)	$\bar{P}_{0w}$ (MPa)	γ_d (-)	s_0 (MPa)	S_{l0} (-)	γ_w (-)
SWRC-hysteretic modVG (ICL=6, ITYCL=17)	$\bar{P}_{0d}$ (MPa)	$\bar{\sigma}_s$ $\left(\frac{\mathrm{N}}{\mathrm{m}}\right)$	m (-)	ξ (-)	S_{ls} (-)	$\bar{P}_{0w}$ (MPa)	γ_d (-)	s_0 (MPa)	S_{l0} (-)	γ_w (-)
Intrinsic permeability, $\boldsymbol{k_i}$ (ICL=7, ITYCL=1) Equation 3-27	$k_{11,0}$ (m^2)	$k_{22,0}$ (m^2)	$k_{33,0}$ (m^2)	-	-	-	-	-	-	-
SHCC-M (ICL=14, ITYCL=1) Equation 3-29	-	-	m (-)	S_{lr} (-)	S_{ls} (-)	-	-	-	-	-
SHCC-modM+LF (ICL=14, ITYCL=1) Equation 3-30	-	C_r^{Film} (MPa^{-dfilm})	m (-)	$S_{l,BWC/BWD}$ (-)	S_{ls} (-)	a^{Film} (MPa)	d^{Film} (-)	-	-	-
Diffusive water in gas, $\boldsymbol{i_g^w}$ (ICL=11, ITYCL=1) Equations 3-32,3-33	D $\left(\frac{\mathrm{m^2Pa}}{\mathrm{sK^n}}\right)$	n (-)	τ_0 (-)	-	-	-	-	-	-	-
Thermal conductivity (ICL=9, ITYCL=1) Equations 3-36, 3-37	λ_{dry} $\left(\frac{\mathrm{W}}{\mathrm{mK}}\right)$	λ_{sat} $\left(\frac{\mathrm{W}}{\mathrm{mK}}\right)$	$(\lambda_{dry})_0$ $\left(\frac{\mathrm{W}}{\mathrm{mK}}\right)$	λ_{gas} $\left(\frac{\mathrm{W}}{\mathrm{mK}}\right)$	λ_{liq} $\left(\frac{\mathrm{W}}{\mathrm{mK}}\right)$	a_1 (-)	a_2 (-)	a_3 (-)		

SWRC was not affected by porosity variation. Thus, the parameters P6, P7 and P9 of this model which are the parameters for porosity influence on the SWRC (see Table 3-3), were not used in this model.

The modified van Genuchten SWRC model (SWRC-modVG) first developed by Fayer and Simmons (1995) and described in Sections 2.2.3 and 2.4.1, was implemented in CODE_BRIGHT by Scarfone (2020). This model is not available in the standard version of CODE_BRIGHT, but it is available in the version modified by Scarfone (2020) as ICL = 6, ITYCL = 17. In this new modified model, the residual degree of

saturation S_{lr} is not constant, but varies with matric suction, $S_{lr} = \xi \ln\left(\frac{s_{dry}}{s}\right)$ (see Section 2.2.3). Thus, the degree of saturation S_l can be expressed see Equation 2-38, as:

$$S_l = \xi \ln\left(\frac{s_{dry}}{s}\right) + \left(\frac{1}{1+\left(\frac{s}{P_0}\right)^n}\right)^m \cdot \left(S_{ls} - \xi \ln\left(\frac{s_{dry}}{s}\right)\right), P_0 = \bar{P}_0 \frac{\sigma_s}{\bar{\sigma}_s} \quad \textbf{3-25}$$

When using this SWRC model in CODE_BRIGHT, a value of 1 (rather than S_{lr}) is used in P4 and then the values of s_{dry} and ξ are provided as P6 and P7 respectively (see Table 3-3). s_{dry} = 1000 MPa would be the standard value.

Scarfone (2020) also implemented the new hysteretic SWRC model described in Section 2.4.1 in his copy of CODE_BRIGHT, which was used for all the work presented in this thesis. Within this version of CODE_BRIGHT, there is a hysteretic version of the van Genuchten SWRC model (ICL = 6, ITYCL = 1) and the hysteretic modified van Genuchten SWRC model (ICL = 6, ITYCL = 17). The following constraints were necessary for the implementation of the hysteretic SWRC models in CODE_BRIGHT (because of the limitation of a maximum of 10 input parameters, P1-P10).

- For both the hysteretic VG model and the hysteretic modVG model, the maximum degree of saturation is the same for drying and wetting ($S_{ls,d} = S_{ls,w} = S_{ls}$)

- For both the hysteretic VG model and the hysteretic modVG model, the parameter m has the same value for the main drying curve and the main wetting curve ($m_d = m_w = m$)

- For the hysteretic VG model, the residual degree of saturation is the same for drying and wetting ($S_{lr,d} = S_{lr,w} = S_{lr}$)

- For the hysteretic modVG model, the main drying curve and the main wetting curve coincide in the pendular state ($\xi_d = \xi_w = \xi$)

- For the hysteretic modVG model, the suction at oven-dryness is fixed as s_{dry} = 1000 MPa

For these hysteretic SWRC models, the user has to provide the values of soil constants defining the main drying and main wetting curves ($\bar{P}_{0d}$, $\bar{P}_{0w}$, $\bar{\sigma}_s$, m, S_{ls} and either S_{lr} (hysteretic VG) or ξ (hysteretic modVG)) and the additional parameters defining the shapes of scanning drying curves and scanning wetting curves (γ_d and γ_w respectively). For the hysteretic models, P1 and P6 are $\bar{P}_{0d}$ and $\bar{P}_{0w}$, respectively, for both models (ITYCL = 1 and 17). P7 and P10 are γ_d and γ_w respectively; these values have to be greater than zero, otherwise the model is considered non-hysteretic. In addition, however, it is also necessary for the user to provide information on whether the initial state is on the main drying curve, the main wetting curve, or a specific scanning curve. This is done by providing values for initial state parameters s_0 and S_{l0} as input data P8 and P9 respectively (see Table 3-3). s_0 and S_{l0} are not the initial values of suction and degree of saturation. Initial values of suction at different locations in the finite element mesh are given by a user-defined initial suction profile (see Section 3.5). The values of s_0 and S_{l0} within the hysteretic SWRC model then define the specific scanning curve for this initial state, with a point with coordinates s_0 and S_{l0} being an arbitrary reference point on this scanning curve. If, at a particular location, in the FE mesh, the initial value of s is greater than s_0, the initial state is on a scanning drying curve passing through the point (s_0, S_{l0}), whereas, if the initial value of s is less than s_0, the initial state is on a scanning wetting curve passing through the point (s_0, S_{l0}). In particular:

- For the hysteretic VG model, s_0 = 1000 MPa and $S_{l0} = S_{lr}$ will result in initial states on the main wetting curve at all locations in the FE mesh, whereas s_0 = 0, $S_{l0} = S_{ls}$ will result in initial states on the main drying curve at all locations

- For the hysteretic modVG model, s_0 = 1000 MPa and $S_{l0} = 0$ will result in initial states on the main wetting curve at all locations, whereas s_0 = 0, $S_{l0} = S_{ls}$ will result in initial states on the main drying curve at all locations

The advective volume flux of liquid $\boldsymbol{q}_l$ (occurring in Equations 3-4 and 3-7) is given in CODE_BRIGHT by Darcy's law (see Equation 2-23):

$$\boldsymbol{q}_l = \frac{-\boldsymbol{k}_i k_{lr}}{\mu_l}(\nabla p_l - \rho_l \mathbf{g}) \quad \textbf{3-26}$$

where $\boldsymbol{k}_i$ is intrinsic permeability, k_{lr} is the relative hydraulic conductivity of the liquid phase, μ_l is the dynamic viscosity of the liquid, ρ_l is the density of the liquid and $\mathbf{g}$ is a vector of gravity forces.

CODE_BRIGHT includes the possibility that intrinsic permeability is anisotropic, in which case $\boldsymbol{k}_i$ is a vector quantity. However, throughout the work presented in this thesis, intrinsic permeability (ICL = 7, ITYCL = 1) was modelled as constant and isotropic (k_{11}= k_{22}= k_{33}= k_i). Note that the saturated value of hydraulic conductivity k_s is related to intrinsic permeability k_i by Equation 2-31:

$$k_s = k_i \frac{\rho_l \mathrm{g}}{\mu_l} \quad \textbf{3-27}$$

The advective volume flux of gas $\boldsymbol{q}_\mathrm{g}$ occurring in Equations 3-5 and 3-8 is also given by Darcy's law (see Equation 2-25):

$$\boldsymbol{q}_\mathrm{g} = \frac{-\boldsymbol{k}_i k_\mathrm{gr}}{\mu_\mathrm{g}}\left(\nabla p_\mathrm{g} - \rho_\mathrm{g}\mathbf{g}\right) \quad \textbf{3-28}$$

where k_gr is the relative conductivity of the gas phase, μ_g is the dynamic viscosity of the gas and ρ_g is the density of gas.

Two SHCC models (ICL = 14) were used to define the relative hydraulic conductivity k_{lr}: the conventional Mualem model (SHCC-M, ICL = 14, ITYCL = 1) model which is presented in the standard version of CODE_BRIGHT and the modified Mualem plus liquid film model (SHCC-modM+LF, ICL = 14,ITYCL = 1) which is the new hydraulic conductivity model described in Section 2.4.2 and which was implemented by Scarfone (2020) in the version of CODE_BRIGHT used for the numerical modelling described in Chapters 4 to 7 of this thesis.

The conventional Mualem (M) SHCC model (ICL = 14, ITYCL = 1) was typically used in combination with the conventional or hysteretic van Genuchten (VG or hysteretic VG) SWRC model (ICL = 6, ITYCL = 1). It only represents the bulk water component of hydraulic conductivity k_l^{Bulk}, with the expression presented in Equation 2-35, which involves the following expression for the relative hydraulic conductivity k_{lr} :

$$k_{lr} = \sqrt{S_{le}\left(1-\left(1-S_{le}^{\frac{1}{m}}\right)^{m}\right)^{2}} \qquad \textbf{3-29}$$

where the effective degree of saturation S_{le} is given by Equation 2-6. The parameter value required for this SHCC model are m, S_{lr} and S_{ls} (see Table 3-3).

The modified Mualem with liquid film SHCC (SHCC-modVG +LF, ICL = 14, ITYCL = 1) model was implemented by Scarfone (2020) in the version of CODE_BRIGHT used in this thesis. This SHCC model involves two components of hydraulic conductivity: the bulk water component k^{Bulk} and the liquid film flow k^{Film}. This new hydraulic conductivity model was typically used in combination with the conventional or hysteretic modified van Genuchten SWRC models (SWRC-modVG or SWRC-hysteretic modVG, ICL=6, ITYCL=17).

The new conductivity model (see Equations 2-52 and 2-55) can be re-written as:

$$k_l = k_s\left(\sqrt{S_l^C}\left(1-\left(1-(S_l^B)^{1/m}\right)^{m}\right)^{2} + C_r^{Film}\cdot\left(a^{Film}+s\right)^{d^{Film}}\right) \qquad \textbf{3-30}$$

where $S_l^C = (S_l - S_{l,BWD})/(1 - S_{l,BWD})$; $S_l^B = (S_l - S_{l,BWEX})/(1 - S_{l,BWEX})$ for drying and $S_l^C = (S_l - S_{l,BWC})/(1 - S_{l,BWC})$; $S_l^B = (S_l - S_{l,BWE})/(1 - S_{l,BWE})$ for wetting, $S_{l,BWD}$, $S_{l,BWC}$, $S_{l,BWEX}$ and $S_{l,BWE}$ are the value of degree of saturation at BWD, BWC, BWEX and BWE points, respectively (see Section 2.4.2). In the implementation of the new SHCC model in CODE_BRIGHT, Scarfone (2020) had to assume $S_{l,BWD} = S_{l,BWC} = S_{l,BWEX} = S_{l,BWE}$ meaning $S_l^C = S_l^B$ and these values are identical for wetting and drying. In Equation 3-30, d^{Film} is the exponent of -1.5 appearing in Equation 2-55 and C_r^{Film} is related to the parameter C^{Film} appearing in Equations 2-55 and 2-56 by:

$$C_r^{Film} = \frac{C^{Film}}{k_s} \quad \textbf{3-31}$$

The input parameters for the new- SHCC model in CODE_BRIGHT are the values of C_r^{Film}, m, $S_{l,BWC/BWD,}$, S_{ls}, a^{Film}, and d^{Film}(always taken as -1.5), as shown in Table 3-3. The dummy parameter a^{Film} (see Section 2.4.2) can be selected as any value between $s_{BWD}/100$ and $s_{BWD}/10$ for drying and between $s_{BWC}/100$ and $s_{BWC}/10$ for wetting (Scarfone, 2020). The conventional Mualem (M) or modified Mualem (modM) SHCC model excluding the liquid film flow effect could be modelled by switching off (leaving blank) liquid film flow parameters P2, P6, and P7. Moreover, the modM SHCC model could convert to the conventional M SHCC model by providing S_{lr} = $S_{l,BWC/BWD}$ in P4.

Diffusive mass fluxes (of water vapour in the gas phase $\boldsymbol{i}_g^w$ and of dissolved air in the liquid phase $\boldsymbol{i}_l^a$) are governed by Fick's law (see Section 2.3.1). Fick's law for diffusive flux of water vapour in the gas phase (ICL=11, ITYCL=1) is written (see Equation 2-27) as:

$$\boldsymbol{i}_g^w = -\left(\tau\Phi\rho_g S_g D_g^w \mathbf{I}\right)\nabla\omega_g^w \quad \textbf{3-32}$$

where τ is a tortuosity parameter, Φ is porosity, ρ_g is gas density, S_g is degree of gas saturation ($S_g = 1 - S_l$), $\mathbf{I}$ is the identity matrix, ω_g^w is the mass fraction of water in the gas phase and D_g^w is the diffusion coefficient of vapour in the gas phase, given by Equation 2-29:

$$D_g^w = \mathrm{D}\left(\frac{(T)^n}{p_g}\right) \quad \textbf{3-33}$$

where p_g is absolute gas pressure (Pa), D and n are parameters which are recommended by Olivella et al. (1996) as: D = 5.9x10^{-6} m^{2}s^{-1}K^{-n}Pa, n = 2.3. Tortuosity τ, was assumed as a constant value of 1, as recommended by Olivella et al. (1996).

Thermal conductivity model (ICL = 9, ITYCL = 1) used Fourier's law to compute conductive heat flux $\boldsymbol{i}_c$ which is expressed as:

$$\boldsymbol{i}_c = -\lambda_T \nabla T \quad \textbf{3-34}$$

where $\boldsymbol{i}_c$ is the energy flux due to conduction, λ_T is the thermal conductivity which depends on porosity Φ and ∇T is the temperature gradient.

Within CODE_BRIGHT, thermal conductivity λ_T is assumed to depend on degree of saturation S_l as follows:

$$\lambda_T = \lambda_{sat}\sqrt{S_l} + \lambda_{dry}\left(1 - \sqrt{S_l}\right) \quad \textbf{3-35}$$

where λ_{sat} is the thermal conductivity in a fully saturated condition (S_l = 1) and λ_{dry} is the thermal conductivity in dry condition (S_l = 0). λ_{dry} and λ_{sat} depend upon λ_{solid}, λ_{gas} and λ_{liq} , the thermal conductivities of the solid phase, gas phase and liquid phase, respectively, and the porosity Φ according to:

$$\lambda_{dry} = {\lambda_{solid}}^{(1-\Phi)}\lambda_{gas}^{\Phi} \quad \textbf{3-36}$$

$$\lambda_{sat} = {\lambda_{solid}}^{(1-\Phi)}\lambda_{liq}^{\Phi} \quad \textbf{3-37}$$

The thermal conductivity of the solid phase λ_{solid} depends on mineralogy. The sands and gravels used in CBSs are typically composed of quartz minerals. Thus, the thermal conductivity of the phases were determining by assuming the following parameters values: λ_{solid} = 7.7 $Wm^{-1}K^{-1}$, λ_{gas} = 0.024 $Wm^{-1}K^{-1}$ and λ_{liq} = 0.6 $Wm^{-1}K^{-1}$,which were suggested by Laloui and Loria (2019).

3.3 Numerical approach

In CODE_BRIGHT, the system of coupled governing partial differential equations (PDEs), described in Section 3.2, is solved numerically. The numerical approach can be divided into two parts: spatial and temporal discretization. The finite element method is used for spatial discretization whereas the finite difference method is used for time discretization. The main features of the numerical approach are:

- Linear interpolation functions are used on segment elements (1-D), triangular, quadrilateral or tetrahedral elements (2-D), or triangular prism

or quadrilateral prism elements (3-D). Two-dimensional quadrilateral elements were used in this thesis. For the elements, flow equations are solved using element-wise and cell-wise approximations.

- Finite difference and an implicit scheme are used for time integration. Two intermediate points are defined between the two points of the time interval. The time discretization is linear, and the implicit scheme uses two intermediate point, $t^{k+\varepsilon}$ and $t^{k+\theta}$ between the initial t^k and final t^{k+1} times. As the problem is non-linear, the Newton-Raphson method is adopted in an iterative scheme.

In terms of the spatial discretization, the concept of a cell is used in CODE_BRIGHT (see Figure 3-1). Once space is discretized, with a mesh defined by the user, assigned nodes i and elements e, the code assigns a cell to each node of the mesh. The cell is centred on the corresponding node (see node i in Figure 3-1) and the cell is made of fractions of the different elements which share this node. The balance equations are written for each cell associated to each node. In CODE_BRIGHT, the unknowns $\boldsymbol{u}$, p_l, p_g and T are nodal quantities whereas many dependent variables such as degree of saturation S_l, intrinsic permeability k_i, relative hydraulic conductivity k_{lr}, relative gas conductivity k_{gr}, thermal conductivity λ, etc., are element quantities. When balance equations are solved for a cell, the contributions of the different elements to a single cell are summed. As a result, a sort of "average" of the elemental qualities are considered for each node cell.

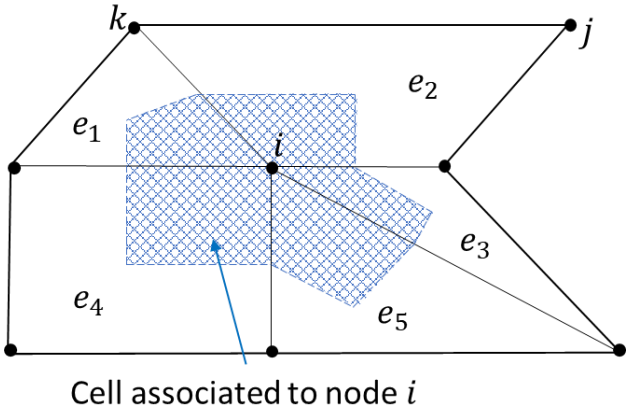

Figure 3-1 Concept of cell in a finite element mesh (after Olivella et al., 1996)

For calculating element qualities of hydraulic conductivity k_l and gas conductivity k_g, five different options have been provided in CODE_BRIGHT, selected by the user by the parameter IOPTPC in the CODE_BRIGHT pre-processor (see more details in CODE_BRIGHT manual (UPC., 2019)) as follows:

- IOPTPC=0, the suction value on each node is calculated by $p_g - p_l$, these are averaged to get a value of suction for each element, which is then used to calculate the degree of saturation S_l for each element (using the SWRC model). The elemental values of k_l and k_g are computed as functions of the elemental values of S_l. The derivative of hydraulic conductivity $\partial k_l/\partial S_l$ is calculated as a function of this elemental value of S_l.

- IOPTPC=-1, (default option), the suction value on each node is calculated by $p_g - p_l$, and this is then used to calculate the degree of saturation on each node (using the SWRC model). These values of S_l at each node are then used to calculate a value of S_l for each element by taking an appropriate average of the nodal values of S_l. Then, the elemental values of k_l and k_g are computed as a function of the elemental value of S_l. The derivative of hydraulic conductivity $\partial k_l/\partial S_l$ is calculated as a function of this element value of S_l.

- IOPTPC=-2, the suction value on each node is used to calculate a value of S_l on each node. These nodal values of S_l are then used to calculate the values of k_l and k_g on each node. Then, the elemental values of k_l and k_g are computed by averaging nodal values of k_l and k_g. The derivative of hydraulic conductivity $\partial k_l/\partial S_l$ is calculated as a function of the elemental value S_l, which is obtained from averaging nodal values of S_l.

- IOPTPC=-3, same as IOPTPC=-2, but nodal values of the derivative of hydraulic conductivity $\partial k_l/\partial S_l$ are calculated, for the values of S_l on each node. Then the element value of $\partial k_l/\partial S_l$ is calculated as the average of the nodal values.

- IOPTPC=-4, the suction value on each node use to calculate S_l on each node. These values of S_l at each node are then used to calculate the values of k_l

and k_g on each node. Then, the elemental values of k_l and k_g are set equal to the maximum nodal value of k_l or k_g. The derivative of hydraulic conductivity $\partial k_l/\partial S_l$ also set equal to the maximum nodal value of k_l or k_g.

Further details about the options can be found from CODE_BRIGHT manual 2019 (UPC., 2019).

Only two options were used in the numerical modelling presented in this thesis: IOPTPC = -1 and IOPTPC = -3. The standard default option IOPTPC = -1 was used for most of the simulations presented in Chapter 4, because it has the shortest computing time and led to physically sensible results and no evidence of numerical problems for these initial simulations. However, in some subsequent simulations, numerical problems were experienced with IOPTPC= -1. After investigating all five options, IOPTPC=-3 was selected for all remaining simulations, at it was least prone to experiencing numerical problems whilst also always producing physically sensible results. Figure 3-2 shows an example of a simulation (a sloping CBS subjected to rainfall intensity i = 10^{-6} m/s from t = 0) where significant numerical instability occurred around the onset of breakthrough when IOPTPC -1 was used (note the major oscillations of interface flow rate per unit plan area q_i around the time of breakthrough ($t \approx$ 24 hours)). Figure 3-2 shows that this transient numerical instability was greatly reduced by the use of IOPTPC -3 but that crucially the results of the two simulations were almost identical in other important aspects, such as the time to breakthrough and the final steady state at the end of the simulation.

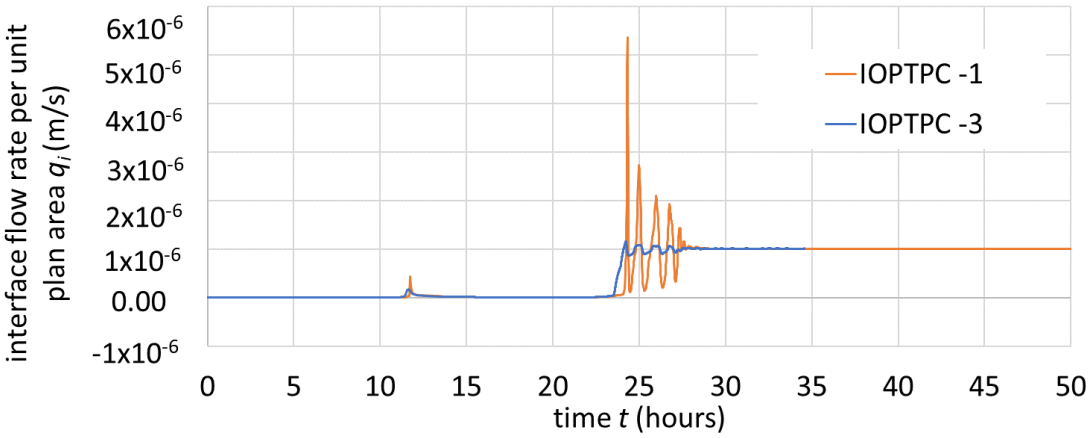

Figure 3-2 Comparison of simulations with IOPTPC -1 and IOPTPC -3 (β=35°, FSGV, t_f = 40 cm, i = 10^{-6} m/s, x>L_D)

The finite element mesh for space discretization is generated automatically by GiD following user preferences set in the pre-processing stage. A structured mesh follows a regular topological pattern, where all inner nodes have the same number of elements. In this thesis, linear quadrilateral elements were used in structured meshes. This avoids locking when the medium is highly incompressible (UPC., 2019). The size of elements can also be defined in different ways in CODE_BRIGHT. One is to assign the number of elements in each boundary line and the code will automatically assign the same number of elements to the opposite boundary line in each surface. A mesh refinement gradient can be defined by assigning the concentration at the two ends of each line, with the size of elements reduced or enlarged towards the two ends of the lines. For example, the concentration assignment along a given boundary line could be (0.2/-0.3). In this case positive number 0.2 means that elements will be concentrated (smaller elements) towards the initial extremity of the line. The second number (-0.3) in this case means that elements will be enlarged toward the final extremity of the line. As the magnitude of the weight increase from zero, the difference between element sizes will be greater.

3.4 Boundary modelling

When thermo-hydraulic numerical modelling is performed, both hydraulic and thermal boundary conditions must be specified on each boundary of the FE model. Hydraulic boundary conditions involve specification of either boundary values of liquid and gas pressures (p_l and p_g) or relevant water and air fluxes. Similarly, thermal boundary conditions consist of either a boundary value of temperature T or relevant energy fluxes on the boundary.

In CODE_BRIGHT, both types of boundaries (specified values of p_l, p_g and T or specified fluxes) are incorporated by adding a flux or flow rate at the boundary nodes of the mesh (see Section 3.4.1), directed perpendicular to boundaries. Positive values indicate flow entering model, while negative values are for fluxes leaving the model. Two types of boundaries are available in CODE_BRIGHT: standard boundary and atmosphere boundary.

3.4.1 Standard boundary

On standard boundaries, the boundary condition is incorporated by adding a flux or flow rate (water, air or energy), even if the required boundary condition is a specified value of p_l, p_g or T . For example, the mass boundary flux of water in the gas phase (vapour) $\boldsymbol{j}_g^w$ and the mass boundary flux of air in the gas phase $\boldsymbol{j}_g^a$ are expressed, respectively, as:

$$\boldsymbol{j}_g^w = \left(\omega_g^w\right)^0 \boldsymbol{j}_g^0 + \left(\omega_g^w\right)^0 \gamma_{g,n}\left(p_g^0 - p_g\right) + \beta_g \left(\left(\rho_g \omega_g^w\right)^0 - \left(\rho_g \omega_g^w\right)\right) \quad \textbf{3-38}$$

$$\boldsymbol{j}_g^a = \left(\omega_g^a\right)^0 \boldsymbol{j}_g^0 + \left(\omega_g^a\right)^0 \gamma_{g,n}\left(p_g^0 - p_g\right) + \beta_g \left(\left(\rho_g \omega_g^a\right)^0 - \left(\rho_g \omega_g^a\right)\right) \quad \textbf{3-39}$$

$$\left(\omega_g^a\right)^0 = 1 - \left(\omega_g^w\right)^0 \quad \textbf{3-40}$$

where the superscript ^{0} denotes a prescribed value, ω is mass fraction, ρ_g is gas density, p_g is gas pressure, $\boldsymbol{j}_g^0$ is a prescribed gas flow and $\gamma_{g,n}$ and β_g are gas leakage coefficients for boundary conditions (numerical factors).

The general form of standard boundary condition includes three terms (see Equation 3-38 or Equation 3-39). Two of these will always be zero. The first term of Equation 3-38 represents the mass flow of water vapour which take place when a prescribed mass flow rate of gas $\boldsymbol{j}_g^0$ is defined at the boundary. The second term represents the mass flow of water vapour which take place when a prescribed value of phase pressure (the prescribed gas pressure p_g^0) is defined at the boundary. The third term represents the mass flow of water vapour which takes place when a prescribed species mass fraction (a prescribed water mass fraction ω_g^w) is defined at the boundary. When a user wants to define a prescribed gas flow rate $\boldsymbol{j}_g^0$ at the boundary, the following parameter values should be used for the numerical leakage coefficients: $\gamma_{g,n} = 0$ and $\beta_g = 0$. If a prescribed gas pressure p_g^0 is required at the boundary the following parameter values should be used $\boldsymbol{j}_g^0 = 0$, $\gamma_{g,n} \neq 0$ and $\beta_g = 0$. Finally, if a prescribed species mass fraction ω_g^w is required at the boundary the following parameter values should be used $\boldsymbol{j}_g^0 = 0$, $\gamma_{g,n} = 0$ and $\beta_g \neq 0$. The numerical leakage coefficient parameters $\gamma_{g,n}$ and β_g represent the strength with which prescribed boundary values of fluid pressure or species mass fraction are applied. For instance, when a prescribed gas pressure is assigned

at the boundary, if $\gamma_{g,n}$ was selected as a very high value, the resulting boundary value of gas pressure will be very close to the prescribed value. However, if $\gamma_{g,n}$ was too high, this would lead to numerical difficulties (matrix ill-conditioned). In contrast, a value of $\gamma_{g,n}$ that was inappropriately low would results in inaccurate prescription of gas pressure at the boundary. If $\boldsymbol{j}_g^0 = 0$ is applied together with a negative value of leakage coefficient, $\gamma_{g,n}$ then this represent a "seepage boundary condition", where outflow is allowed, and it occurs when $p_g = p_g^0$ whereas for $p_g < p_g^0$ an impermeable boundary condition is applied ($\boldsymbol{j}_g^0 = 0$).

Similar concepts apply for the mass flux of water in the liquid phase $\boldsymbol{j}_l^w$ and the mass flux of air in the liquid phase $\boldsymbol{j}_l^a$, which can be expressed as:

$$\boldsymbol{j}_l^w = (\omega_l^w)^0 \boldsymbol{j}_l^0 + (\omega_l^w)^0 \gamma_{l,n}(p_l^0 - p_l) + \beta_l\left((\rho_l \omega_l^w)^0 - (\rho_l \omega_l^w)\right) \quad \textbf{3-41}$$

$$\boldsymbol{j}_l^a = (\omega_l^a)^0 \boldsymbol{j}_g^0 + (\omega_l^a)^0 \gamma_{l,n}(p_l^0 - p_l) + \beta_l\left((\rho_l \omega_l^a)^0 - (\rho_l \omega_l^a)\right) \quad \textbf{3-42}$$

$$(\omega_l^w)^0 = 1 - (\omega_l^a)^0 \quad \textbf{3-43}$$

Appropriate values of the numerical leakage coefficients $\gamma_{g,n}$, $\gamma_{l,n}, \beta_g$, and β_l can be obtained easily by a few trials. Values of leakage coefficient of gas phase $\gamma_{g,n}$ = 10^{-6} m/s, and leakage coefficient of liquid phase $\gamma_{l,n}$ = 10^{-6} m/s have been used in this thesis (these values have been confirmed from Scarfone (2020)). β_g and β_l were not used in this thesis, therefore, both were always set to zero.

The boundary condition for energy flux $\boldsymbol{j_e}$ can be expressed as the general form:

$$\boldsymbol{j}_e = \boldsymbol{j}_e^0 + \gamma_{e,n}(T^0 - T) + E_g^w\left(\boldsymbol{j}_g^w\right) + E_g^a\left(\boldsymbol{j}_g^a\right) + E_l^w(\boldsymbol{j}_l^w) + E_l^a(\boldsymbol{j}_l^a) \quad \textbf{3-44}$$

where $\boldsymbol{j}_e^0$ is the energy flux prescribed at the boundary, T^0 is the temperature prescribed at the boundary and $\gamma_{e,n}$ is the corresponding numerical leakage coefficient. The terms $E_g^w\left(\boldsymbol{j}_g^w\right), E_g^a\left(\boldsymbol{j}_g^a\right), E_l^w(\boldsymbol{j}_l^w)$ and $E_l^a(\boldsymbol{j}_l^a)$ are advective energy fluxes related to the mass fluxes $\boldsymbol{j}_g^w, \boldsymbol{j}_g^a, \boldsymbol{j}_l^w$ and j_l^a. In numerical analysis, either $\boldsymbol{j}_e^0 \neq 0$ and $\gamma_{e,n} = 0$ (energy flux at boundary, in excess of contributions associated

with mass fluxes, is defined) or $\boldsymbol{j}_e^0 = 0$ and $\gamma_{e,n} \neq 0$ (temperature at boundary is defined).

3.4.2 Atmosphere boundary

Soil-atmosphere interaction (see detail in Section 2.6) was imposed in the numerical modelling by atmospheric boundary conditions. In simulating complex soil-atmosphere interactions in CODE_BRIGHT, this option allows boundary conditions to be imposed in terms of evaporation, rainfall, radiation and heat exchange (UPC., 2019). These phenomena are expressed as flux boundary conditions for three components (i.e. water, air and energy) as functions of state variables for the soil at the ground surface (e.g. temperature T, degree of saturation S_l, gas pressure p_g, fraction of water in the gas phase) and meteorological data that can vary with time.

When atmosphere boundary conditions are considered, the general parameters required are set out in Table 3-4. The latitude, time when autumn begins, time at noon, dry albedo and wet albedo are used in one of the options for calculating net radiation (they were not used in this thesis). Roughness length z_0, screen height z_a and stability factor ψ are used for estimating evaporation and advective energy flux (see below). In addition to the general parameters listed in Table 3-4, meteorological atmospheric parameters are required for modelling the atmosphere boundary, namely: atmospheric temperature T_a (°C), atmospheric gas pressure p_{ga} (MPa), atmospheric relative humidity R_h (-), net radiation R_n(Jm^{-2}s^{-1}), rainfall P (kgm^{-2}s^{-1}) and wind velocity v_a (m/s). Each of these meteorological parameters can either be constant with time or can vary with time.

The total mass flux of water at a boundary ($\boldsymbol{j}_w$) accounts for rainfall $\boldsymbol{P}$, evaporation $\boldsymbol{E}$, advective flux of water vapour in the gas phase $\boldsymbol{j}_g^w$ and surface runoff $\boldsymbol{j}_{sr}$ (all expressed as mass fluxes):

$$\boldsymbol{j}_w = k_{rain}\boldsymbol{P} - k_{evap}\boldsymbol{E} + \boldsymbol{j}_g^w - \boldsymbol{j}_{sr} \qquad \textbf{3-45}$$

where k_{rain} and k_{evap} are numerical coefficients, provided as input data, used to disable their respective flux.

Table 3-4 General parameters required for atmosphere boundary condition

Parameters	symbol
Latitude	λ (rad)
Time when autumn starts	t_s (s)
Time at noon	t_m(s)
Roughness length	z_0(m)
Screen height	z_a(m)
Stability factor	ψ(-)
Atmosphere gas density	ρ_{ga}(kg/m^3)
Dry albedo	A_d(-)
Wet albedo	A_w(-)
Gas leakage coefficient	$\gamma_{g,n}$(kg.m^{-2}.s^{-1}.MPa^{-1})
Liquid leakage coefficient	$\gamma_{l,n}$(kg.m^{-2}.s^{-1}.MPa^{-1})

Rainfall $\boldsymbol{P}$ and its variation with time, are specified directly by the user in terms of mass flow rate per unit plan area in units of kg·m^{-2}·s^{-1}. $\boldsymbol{P}$ can be either constant with time or varying sinusoidally with time or as a data file of specific values over specified time intervals. In this thesis, constant values of $\boldsymbol{P}$ were used in Chapters 4 and 5, and different constant values of $\boldsymbol{P}$ over specific time intervals were used in Chapters 6 and 7.

Evaporation $\boldsymbol{E}$ is given by an aerodynamic diffusion relation (see Equation 2-62):

$$\boldsymbol{E} = \frac{K^2 v_a \psi}{\left(\ln \frac{z_a}{z_0}\right)^2} (\rho_v - \rho_{va}) \qquad \textbf{3-46}$$

where K is the Von Karman constant (K = 0.4), z_a is the screen height, v_a is the wind speed at the screen height, ψ is a stability of factor, z_0 is the roughness length of the boundary surface, ρ_{va} is the atmospheric absolute humidity at the screen height and ρ_v is the absolute humidity in the soil voids at the soil surface, which varies with the temperature and the suction at the ground surface (see Section 2.6.2).

The advective mass flux of vapour in the gas phase across the boundary $\boldsymbol{j}_g^w$ is given by:

$$\begin{cases} \boldsymbol{j}_g^w = \theta_g^w \boldsymbol{q}_g \text{ if } p_g > p_{ga} \\ \boldsymbol{j}_g^w = \rho_{va} \boldsymbol{q}_g \text{ if } p_g \leq p_{ga} \end{cases} \quad \textbf{3-47}$$

where p_g is the pore gas pressure in the soil at the ground surface, p_{ga} is atmospheric gas pressure, θ_g^w is the mass of water vapour per unit volume in the gas phase within the soil voids at the ground surface, ρ_{va} is the vapour density in the atmosphere (at the screen height) and $\boldsymbol{q}_g$ is the volume flux of gas phase across the boundary. The volume flux of gas at the boundary $\boldsymbol{q}_g$ is calculated as:

$$\boldsymbol{q}_g = \gamma_g (p_g - p_{ga}) \quad \textbf{3-48}$$

where γ_g is a numerical leakage coefficient for gas flow.

Surface runoff $\boldsymbol{j}_{sr}$ is given as:

$$\begin{cases} \boldsymbol{j}_{sr} = \gamma_w (p_l - p_{ga}) \text{ if } p_l > p_{ga} \\ \boldsymbol{j}_{sr} = 0 \qquad\qquad\quad \text{if } p_l \leq p_{ga} \end{cases} \quad \textbf{3-49}$$

where p_l is the pore liquid pressure in the soil at the ground surface and γ_w is a numerical leakage coefficient. When assuming no ponding, a very high value for γ_w can be used. If $p_l > p_{ga}$, all liquid is unable to infiltrate and will runoff.

The total energy flux $\boldsymbol{j}_e$ at the boundary, which includes the sensible heat flux H_s, the convective heat flux H_c and the net radiation R_n, can be calculated as:

$$\boldsymbol{j}_e = R_n + H_s + H_c \quad \textbf{3-50}$$

In CODE_BRIGHT, different options are available for specifying the net radiation R_n and its variation with time. In some of these options, R_n and its variation with time are specified directly by the user, either as constant with time or as varying sinusoidally with time or as a data file of specific values over specified time intervals. In this thesis, only constant values of R_n were considered. In another option (not used in this thesis), R_n is calculated by CODE_BRIGHT as the combination of different terms:

$$R_n = R_s(1 - A_l) + \varepsilon_s R_{ld} - R_{lu} \quad \textbf{3-51}$$

where R_s is global short-wave solar radiation, A_l is the surface albedo, ε_s is the emissivity of the surface (which depends on the surface properties), R_{ld} is the downward atmospheric long-wave radiation and R_{lu} is the upward long-wave radiation from soil surface. If this option is used, R_s and its variation with time are calculated by CODE_BRIGHT based on the latitude λ, time when autumn starts t_s and time at noon t_m (see Table 3-4).In addition, for this option, the surface albedo A_l is calculated from the value of S_l at the ground surface and values of dry albedo A_d and wet albedo A_w (see Table 3-4).Finally, for this option, R_{ld} and R_{lu} are given by:

$$R_{ld} = C_{cloud}\varepsilon_a\sigma_R T_a^4 \quad \textbf{3-52}$$

$$R_{lu} = \varepsilon_s\sigma_R T_s^4 \quad \textbf{3-53}$$

where C_{cloud} is a correction parameter for cloudiness, ε_a is the emissivity of the atmosphere in the clear sky condition, σ_R is the Stefan-Boltzmann constant ($5.67\text{x}10^{-8}$ W/m^2/K^4) and T_a and T are the atmosphere temperature and soil surface temperature respectively.

The sensible heat flux H_s is calculated (see Equation 2-63) as:

$$H_s = \frac{K^2 v_a \psi}{\left(\ln\frac{z_a}{z_0}\right)^2}\rho_{ga}C_a(T_a - T) \quad \textbf{3-54}$$

where ρ_{ga} is the atmospheric gas density, C_a is the specific heat of the gas, T_a is the atmospheric temperature at the screen height, T is the temperature of the soil at the ground surface and $K = 0.4$ (Von Karman's constant).

The convective heat flux H_c is the sum of convective components related to liquid water, vapour, and dry air:

$$H_c = h_v\left(\boldsymbol{E} + \boldsymbol{j}_g^w\right) + h_{lv}(\boldsymbol{P} + \boldsymbol{j}_{sr}) + h_a\boldsymbol{j}_a \quad \textbf{3-55}$$

where h_v, h_{lv} and h_a are free energy of vapour, liquid water and dry air which depend on temperature.

3.5 Initial conditions

Initial conditions are expressed in terms of profiles of liquid pressure p_l, gas pressure p_g, and temperature T. These are assigned on surface/volume in CODE_BRIGHT, available as two options: uniform or linear distribution.

In all the work presented in this thesis, the initial value of p_g was imposed as uniform (p_g = 0.1 MPa) and p_g was then maintained constant at 0.1 MPa throughout all analyses. Initial liquid pressure profiles assigned by the user were converted by CODE_BRIGHT to initial suction profiles ($p_g - p_l$). Typically, these initial suction profiles were either uniform (within a given zone of soil) or varying with vertical elevation z (see Figure 3-3). Then the initial distribution of degree of saturation was determined by CODE_BRIGHT by calculating from the SWRC constitutive model.

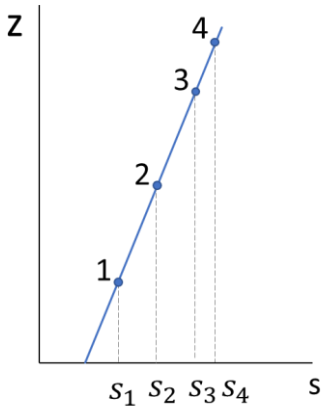

Figure 3-3 Initial suction profile

If a hysteretic SWRC constitutive model was employed, the initial value of S_l depended on the values of the initial state parameters s_0 and S_{l0} as well as the initial value of s and the values of the SWRC soil constants ($\bar{P}_{0d}$, $\bar{P}_{0w}$, m, ξ, S_{ls}, γ_d and γ_w) (see Table 3-3). For example, given an initial suction profile, as shown in Figure 3-3, with points 1,2,3 and 4 at four different heights, corresponding to four different suction values (s_1, s_2 , s_3 and s_4), the initial values of S_l would be calculated as shown in Figure 3-4. If any initial suctions values are less than the specified initial state parameter s_0 (i.e. s_1 and s_2 in Figure 3-4), the initial state for those points (1 and 2) was on the scanning wetting curve passing through point A (s_0, S_{lo}), and the initial values of degree of saturation S_{l1} and S_{l2} would be calculated accordingly. If any points were at initial suction values higher than s_0 (i.e. s_3 and s_4 in Figure 3-4), then CODE_BRIGHT calculated the corresponding

initial values of S_l (S_{l3} and S_{l4}) from the scanning drying curve passing through point A. In all the numerical simulations involving hysteretic modelling presented in this thesis, initial state values were set at s_0 = 1000 MPa and $S_{lo} = S_{lr}$ (hysteretic VG model) or $S_{lo} = 0$ (hysteretic modVG model), so that initial states were on the main wetting curve throughout the entire FE mesh.

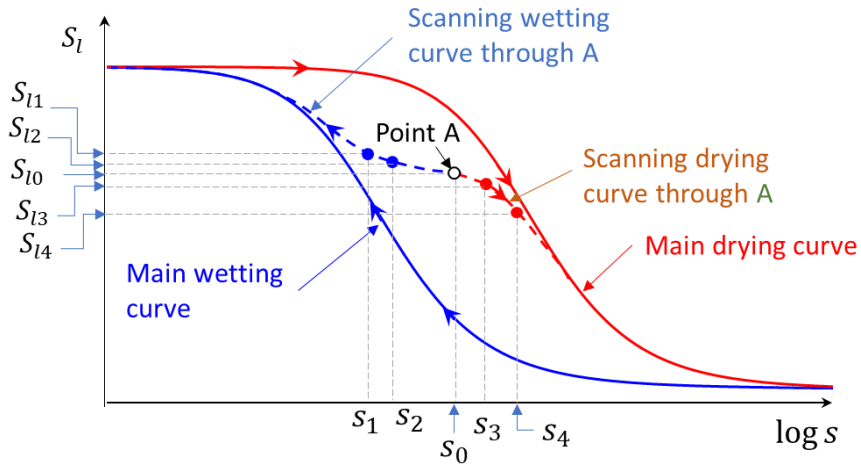

Figure 3-4 Calculation of initial values of degree of saturation for SWRC-hysteretic model

In the thermo-hydraulic numerical modelling described in this thesis, the initial value of temperature T was always set at a uniform value (of either 20°C or 6.32°C, see Section 6.1.2). In all the hydraulic numerical modelling, a uniform value of T = 20°C was imposed, not just as an initial state but throughout all analyses.

Chapter 4 Horizontal CBSs subjected to continuous rainfall of constant intensity

This chapter describes numerical simulations of one-dimensional models, used to validate the existing simplified method of Stormont and Morris (1998) for calculating water storage capacity of conventional horizontal CBSs when subjected to continuous rainfall of constant intensity (and the corresponding extended simplified method for horizontal multi-layered CBSs proposed by Scarfone (2020)). These numerical simulations were performed with the advanced hydraulic constitutive model (modVG-modM+LF) developed by Scarfone (2020) and Scarfone et al. (2020a), described earlier in Section 2.4. The aims of these analyses were: i) to validate the existing simplified method (including validating the simplified suction profile assumed within the method) by performing a comprehensive parametric study to confirm that the simplified method works for all realistic values of key parameters or to demonstrate any limitation on its validity, and ii) to investigate the development of the hydraulic response of horizontal CBSs subjected to continuous rainfall of constant intensity over time, towards the final steady-state.

The work presented in this chapter represents an advance over the numerical modelling of horizontal CBSs performed by Scarfone (2020) in two main aspects. Firstly, the work reported here represents a far more comprehensive parametric study than performed by Scarfone (2020). Secondly, Scarfone (2020) only reported results relating to the final steady state, whereas this chapter also includes investigation of the behaviour of the CBS prior to final steady state, which provides important new insights.

This chapter consists of six sub-sections, starting with a review of the existing simplified method for calculating water storage capacity of a horizontal CBS at the final steady state (Section 4.1). This is followed by a description of the numerical model of horizontal CBSs (Section 4.2), and then the results of numerical parametric studies of the behaviour of conventional horizontal CBSs (Section 4.3) and multi-layered CBSs (Section 4.4) at the final steady state. Section 4.5 presents the development of hydraulic behaviour of both conventional

and multi-layered horizontal CBSs over time towards the final steady-state. The chapter finishes with some remarks and conclusions (Section 4.6).

4.1 Simplified method for calculating water storage capacity.

The existing simplified method of Stormont and Morris (1998) for calculating the water storage capacity of a horizontal CBS subjected to continuous rainfall of constant intensity uses the soil water retention curve (SWRC) of the finer layer of the CBS and an approximate profile of matric suction s in the finer layer (F.L.) at breakthrough (see Section 2.7.2).

Water storage capacity WSC is calculated by integrating over the thickness of the F.L the volumetric water content (degree of saturation multiplied by porosity), see Equation 2-67:

$$WSC = \Phi \int_0^{t_f} S_l \, dz \qquad \text{4-1}$$

where z is the elevation starting from the interface between F.L and C.L ($z_{interface} = 0$) , t_f is the thickness of the F.L, Φ is the porosity of the F.L and S_l is the degree of saturation at height z in the finer layer at the time of breakthrough. In the simplified method of Stormont and Morris (1998) (see Section 2.7.2), the variation of S_l with z is obtained from a simplified suction profile in the finer layer (the variation of s with z) at the time of breakthrough (final steady state) by using the SWRC relationship (S_l : s) for the finer layer.

The simplified suction profile at breakthrough, and the physical justification for it, was described in Section 2.7.2 and it is shown again in Figure 4-1. The value of suction s_1 at the bottom of finer layer (see Figure 4-1) corresponds to the bulk water continuity value of suction for the underlying coarser layer $s_{BWC,c}$:

$$s_1 = s_{BWC,c} \qquad \text{4-2}$$

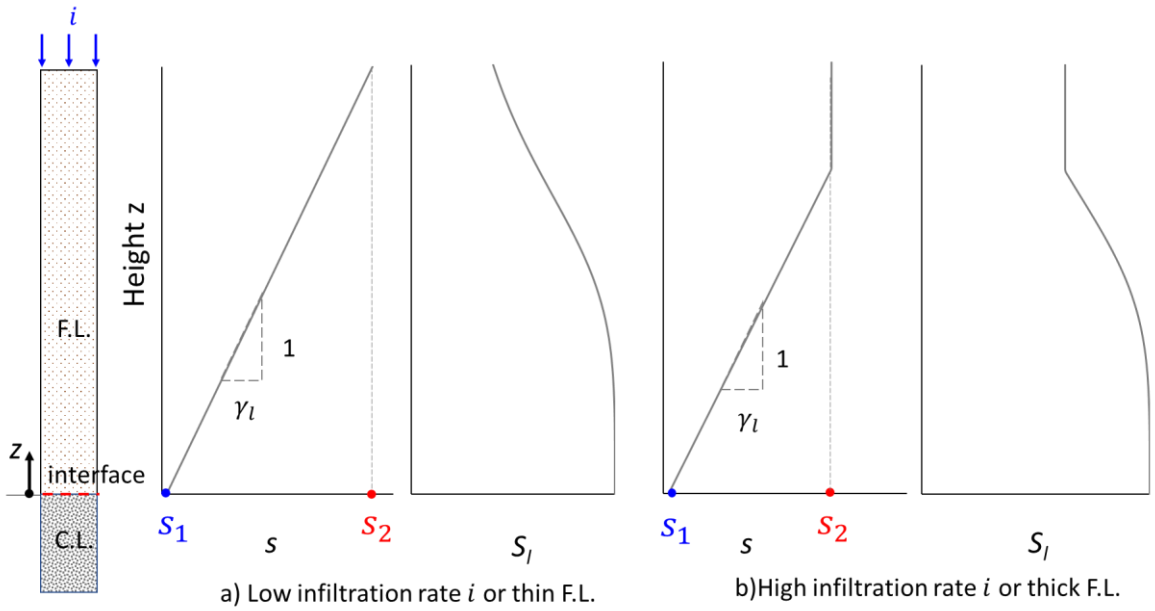

Figure 4-1 Approximate suction profile of horizontal CBS at breakthrough (after Stormont and Morris, 1998)

In the lower part of the F.L, the simplified suction profile corresponds to a hydrostatic distribution:

$$\frac{ds}{dz} = \gamma_l \qquad \text{4-3}$$

For a thin layer or a low rainfall infiltration rate i, the hydrostatic suction profile of Equation 4-3 applies over the full thickness of the finer layer (see Figure 4-1a) and the value of suction s_2 at the top of the F.L is given by:

$$s_2 = s_{BWC,c} + \gamma_l t_f \qquad \text{4-4}$$

For a thicker finer layer or a higher rainfall infiltration rate (see Figure 4-1b), the hydrostatic suction profile of Equation 4-3 applies over the lower part of the F.L, but with a constant value of suction in the upper part of the F.L. This constant value of suction in the upper part of F.L corresponds to s_f^*, the value of suction at which the hydraulic conductivity of the F.L is equal to the rainfall infiltration rate i (see Section 2.7.2). Hence, in this case of a thicker finer layer of higher rainfall intensity, the value of suction s_2 at the top of the finer layer is given by:

$$s_2 = s_f^* \qquad \text{4-5}$$

This situation applies if the F.L thickness is greater than a critical value t_f^* given by:

$$t_f^* = \frac{s_f^* - s_{BWC,c}}{\gamma_l} \quad \textbf{4-6}$$

The profile of degree of saturation S_l against elevation z within the finer layer, for use in Equation 4-1, can be determined from the assumed suction profile by using the SWRC of the finer layer. If the thickness of the F.L is less than the critical value of t_f^*, given by Equation 4-6, the hydrostatic suction profile of Equation 4-3 applies throughout the full thickness of the F.L and Equation 4-1 can be re-expressed as an integral with respect to suction rather than with respect to elevation z:

$$WSC = \frac{\Phi}{\gamma_l}\int_{s_1}^{s_2} S_l \; ds \quad \textbf{4-7}$$

where the limits of integration, s_1 and s_2, are given by Equations 4-2 and 4-4 respectively. It is clear from Equation 4-7 that calculation of WSC involves integration of the SWRC expression ($S_l : s$) between appropriate limits. If the thickness of the F.L is greater than the critical value of t_f^*, the equivalent expression for WSC is:

$$WSC = \frac{\Phi}{\gamma_l}\int_{s_1}^{s_f^*} S_l \; ds + \Phi S_l(s_f^*)(t_f - t_f^*) \quad \textbf{4-8}$$

where $S_l(s_f^*)$ is the value of degree of saturation at a suction value s_f^* and t_f^* is the critical thickness given by Equation 4-6.

Scarfone (2020) applied similar concepts to multi-layered CBSs, to derive the water storage capacity and approximate suction profile at final steady state for a horizontal multi-layered CBS (see Section 2.9). For multi-layered CBSs the water storage capacity is given by integrating the final steady state volumetric water content over the thicknesses of all finer layers and all intermediate coarser layers (i.e. all layers of the CBS except the lowest coarser layer).

For low infiltration rate or thin finer layers (see in Figure 4-2a), the simplified suction profile proposed by Scarfone (2020) involves a hydrostatic suction profile (Equation 4-3) in each finer layer, a value of suction s_1 (given by Equation 4-2) at the bottom of the lowest finer layer and a constant value of suction s_3 within each intermediate coarser layer:

$$s_3 = s_c^* \tag{4-9}$$

where s_c^* is the value of suction at which the hydraulic conductivity of the coarser layer is equal to the rainfall infiltration rate i. In this case, the suction s_2 at the top of the lowest finer layer is given by Equation 4-4, where t_f is the thickness of an individual finer layer, and the suction at the top of all remaining finer layers s_4 is given by:

$$s_4 = s_c^* + \gamma_l t_f \tag{4-10}$$

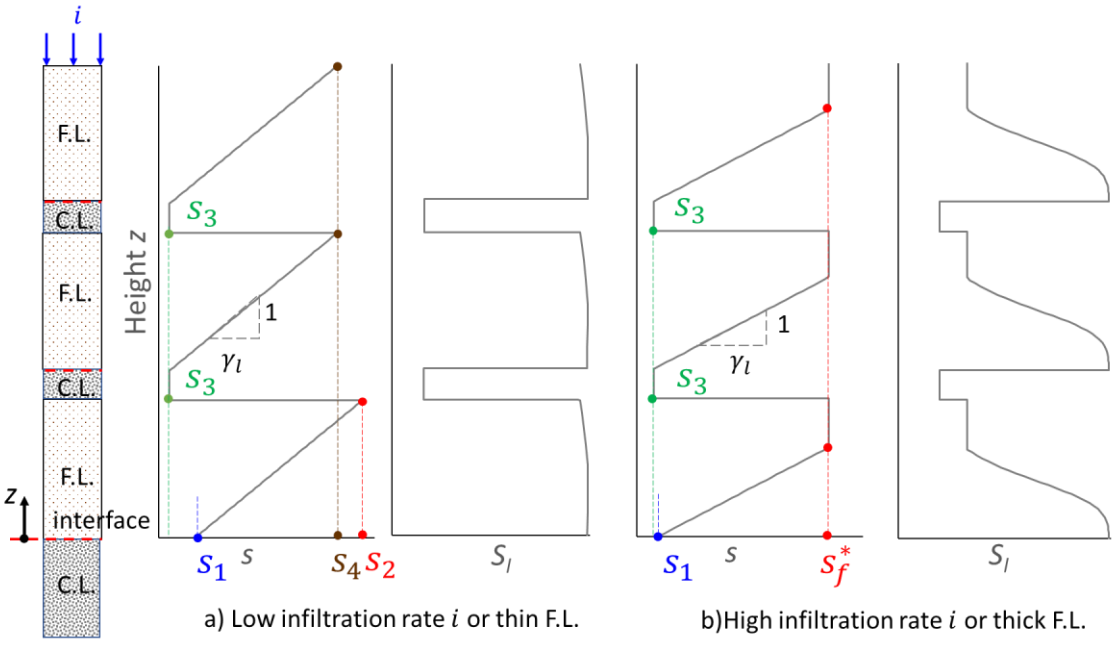

Figure 4-2 Approximate suction profile of horizontal multi-layered CBS at breakthrough (after Scarfone, 2020)

The variation of degree of saturation S_l with elevation throughout the various finer layers and the intermediate coarser layers, for determining the water storage capacity of the multi-layered CBS, can be determined from the assumed suction profile by using the SWRCs of the two materials of the CBS.

For the case of a higher infiltration rate or thicker finer layers (see Figure 4-2b), there is an upper part of each finer layer that is at a constant value of suction s_f^*. The value of suction at the top of each finer layer is then given by Equation 4-5.

4.2 Numerical model of horizontal CBSs

For validating the simplified method of calculating the WSC of conventional and multi-layered CBSs, described in Section 4.1, hydraulic numerical modelling was performed, using the advanced (non-hysteretic) hydraulic constitutive model modVG-modM+LF described in Section 2.4. A substantial number of numerical simulations were performed, with different values of key parameters, to form a parametric study and hence a more comprehensive numerical investigation of the validity of the existing simplified method for calculating WSC than achieved by previous researchers. These key parameters that were varied were the rainfall infiltration rate i, the material of the finer layer of the CBS, and the thickness of the finer layer. The numerical analyses also covered multi-layered CBSs as well as conventional CBSs.

In all the numerical modelling presented in Chapters 4 to 7, each CBS material was considered as a uniform non-deforming (rigid) material i.e. no deformation of the solid phase ($\boldsymbol{u}$ = 0) and gas pressure was imposed as constant as p_g = 100 kPa (as a consequence there was insignificant flow of gas and hence no advection of water vapour i.e. the only possible movement of vapour was by diffusion).

In addition, the numerical modelling presented in Chapter 4 was only hydraulic modelling (rather than thermo-hydraulic modelling). Temperature T was imposed as constant at 20°C. This meant that vapour diffusion was effectively excluded (as described in Section 2.3.1, in unsaturated soils at values of suction less than several MPa, significant diffusion of water vapour occurs only when there is a temperature gradient in the soil). There was also no inclusion of evaporation from the ground surface (this requires thermo-hydraulic modelling, to calculate the variation of ground surface temperature with time). Retention hysteresis was not included in the numerical modelling presented in Chapter 4 (i.e. the non-hysteretic modVG-modM+LF hydraulic constitutive model was used), with the

materials of the CBS assumed to be on the main wetting SWRC throughout. This was considered acceptable, as behaviour under continuous rainfall of constant intensity involved monotonic wetting of the CBS materials.

4.2.1 Geometry and mesh

The numerical models used for the horizontal conventional CBSs were a vertical column of CBS, comprised of two layers: top F.L. (thickness t_f = 80 cm, 40 cm, or 20 cm) and bottom C.L. (thickness t_c = 20 cm) (see Figure 4-3a, Figure 4-3b and Figure 4-3c). The range of thicknesses of F.L (t_f), between 20 cm and 80 cm, represent these actually used in practice (e.g. Tami et al., 2004; Aubertin et al., 2009; and Lacroix Vachon et al., 2015). The 20 cm thickness of the C.L was considered realistic and had little impact on the results, as it was sufficient to ensure no influence of the bottom boundary. This choice of t_c was made on the basis of results of preliminary numerical tests performed by Scarfone (2020).

Although a horizontal CBS is a one-dimensional problem, the numerical modelling was performed using a 2D numerical model (see Figure 4-3), but with boundary conditions and initial conditions that meant that all parameters varied in only the vertical direction.

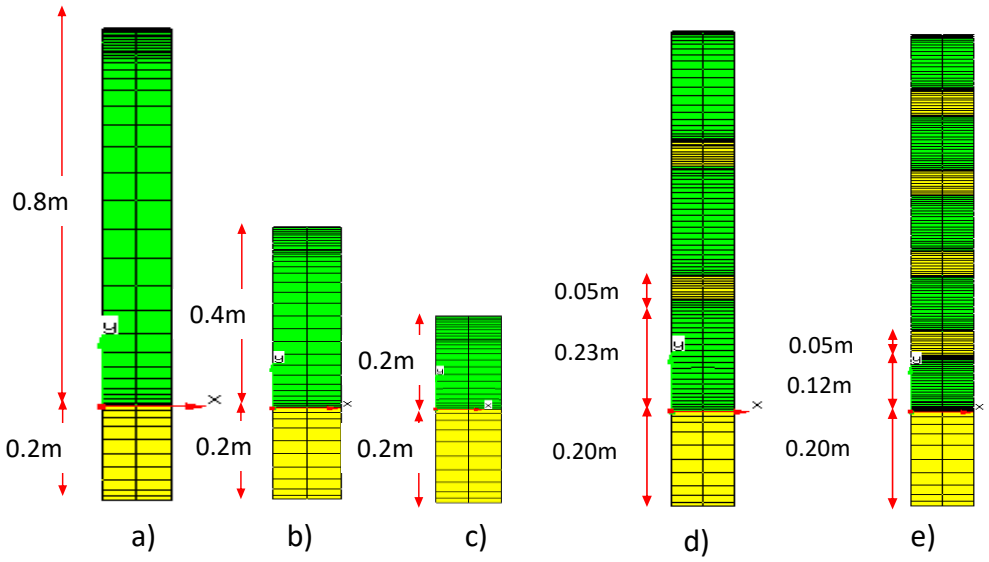

Figure 4-3 Geometry of numerical models of horizontal CBSs a) t_f = 80 cm, t_{CBS} = 100 cm, b) t_f= 40 cm, t_{CBS} = 60 cm, b) t_f = 20 cm, t_{CBS} = 40 cm, d) multi-layered CBS 3 finer layers, t_{CBS} = 100 cm, and e) multi-layered CBS 5 finer layers, t_{CBS} = 100 cm.

Quadrilateral elements were used (see Figure 4-3). For the C.L (z = 0 to z = -0.2 m), 10 elements were used in the vertical direction with mesh refinement 0.7/0.7 (finer towards the two ends). For the F.L (z = 0 to z = 0.8 m, 0.4 m or 0.2 m), 26 elements were used in the vertical direction; divided into an upper section of 10 elements and lower section of 16 elements to allow appropriate refinement close to the ground surface and close to the interface with the C.L. The upper section of 10 elements was always 0.05 m thick with a mesh gradient of 0/0.2, producing very fine elements close to ground surface. The lower section of 16 elements, with a thickness of 0.75 m, 0.35 m or 0.15 m had a mesh gradient of 0.6/0.6 (i.e. refinement at the top and bottom), to produce a reasonable match at the boundary with the upper section and a degree of refinement close to the interface with the C.L. The very concentrated mesh elements close to the ground surface were because the atmospheric boundary conditions (which were considered subsequently in Chapter 6) caused high gradients in the state variables (i.e. p_l and T) close to the ground surface. All models of horizontal CBSs models had two elements in the horizontal direction (which is the minimum requirement for CODE_BRIGHT).

Numerical modelling of multi-layered CBSs considered models with three finer layers (see Figure 4-3d) and models with five finer layers (see Figure 4-3e). In all modelling of multi-layered CBSs, the total thickness of the CBS was 100 cm and the thickness of the bottom C.L was 20 cm. The thickness of intermediate coarser layers was 5 cm , and the thickness of finer layers was adjusted to maintain the total thickness at 100 cm (see Figure 4-3d and Figure 4-3e). The mesh elements of the bottom C.L were the same as for the conventional CBS. Each intermediate C.L had 10 elements in the vertical direction with 0.6/0.6 refinement. Each finer layer had 26 elements in the vertical direction, with 0.6/0.6 refinement.

The mesh refinements used for both conventional and multi-layered CBSs were considered appropriate, because Scarfone (2020) also used very similar mesh and he showed that this is suitable mesh refinement to give results of high accuracy for conventional and multi-layered CBSs subjected to continuous rainfall of constant intensity. No specific study of mesh refinement was undertaken within the current project, which relied instead on the mesh refinement study undertaken by Scarfone (2020). This was probably a valid decision for the

numerical modelling of horizontal CBSs reported in this chapter, because the materials involved and the parameters investigated were no more demanding than those considered by Scarfone (2020). In hindsight, however, it was probably not a wise decision for the numerical modelling of sloping CBSs reported in Chapters 5 to 7, because some of these simulations may have involved more demanding requirements of mesh refinement than was the case for Scarfone (2020). This issue is discussed further in Section 5.3.1.

4.2.2 Material properties

Two different materials were used for the F.L, representative of silty sand (SS) and fine sand (FS). A single material was used for the C.L, representative of gravelly sand (GV). The F.L and C.L materials were modelled using the (non-hysteretic) advanced hydraulic constitutive model modVG-modM+LF described in Section 2.4. Retention hysteresis was not considered and the single SWRCs shown in Figure 4-4a should be considered as representing main wetting SWRCs.

Constitutive model parameter values for the three materials are shown in Table 4-1 and the corresponding SWRCs and SHCCs are shown in Figure 4-4. All three materials are the same materials as studied by Scarfone (2020).

For the finer layer materials, the parameter values for the silty sand were based on a real material, whereas the parameter values for fine sand were selected as realistic for a typical material with a D_{10} value 5 times larger than for the silty sand, after considering the relevant scaling relationships (values of $\bar{P}_0$, k_i and C_r^{Film} for fine sand were selected as respectively 5^{-1},5^{2} and 5^{-3} times the corresponding values for the silty sand). For the fine sand, the porosity value was simply assumed to be the same as for the silty sand.

The coarser layer material (i.e. gravelly sand) is a typical material for the C.L of a CBS (e.g. Chen et al., 2019). The material properties of the gravelly sand do not have a significant influence on the hydraulic behaviour of the CBS, provided there is significant contrast between the hydraulic behaviour of the finer layer and the coarser layer. Only the bulk water continuity value of suction $s_{BWC,c}$ has significant influence, as this defines the critical breakthrough value of suction at the

interface between C.L and F.L. This value of $s_{BWC,c}$ is specified by the SWRC of the C.L material and the value of the parameter $S_{l,BWC/BWD}$ given in Table 4-1.

Table 4-1 Material properties of the horizontal capillary barrier systems for numerical modelling

Materials	Constitutive Model		Physical parameters			
			Φ (-)	k_i (m^2)	k_s (m/s)	D_{10} (mm)
Silty sand (F.L.)	modVG-modM+LF		0.411	1.11×10^{-12}	1.08×10^{-5}	0.034
Fine sand (F.L.)	modVG-modM+LF		0.411	2.77×10^{-11}	2.70×10^{-4}	0.17
Gravelly sand (C.L.)	modVG-modM+LF		0.382	7.81×10^{-9}	7.62×10^{-2}	2.73
			SWRC parameters			
	$\bar{P}_0$ (MPa)	$\bar{\sigma}_{s0}$ (N/m)	m (-)	ξ (-)	S_{ls} (-)	
Silty sand (F.L.)	6.05E-3	0.072	0.779	1.36E-2	1	
Fine sand (F.L.)	1.21E-3	0.072	0.779	6.79E-3	1	
Gravelly sand (C.L.)	6.45E-5	0.072	0.688	3.27E-3	1	
			SHCC parameters			
	m (-)	$S_{l,BWC/BWD}$ (-)	S_{ls} (-)	C_r^{Film} ($MPa^{-1.5}$)	a^{Film} (MPa)	d^{Film} (-)
Silty sand (F.L.)	0.779	0.22	1	1.19E-7	2.0E-4	-1.5
Fine sand (F.L.)	0.779	0.18	1	9.54E-10	4.0E-5	-1.5
Gravelly sand (C.L.)	0.688	0.16	1	2.21E-13	1.5E-7	-1.5

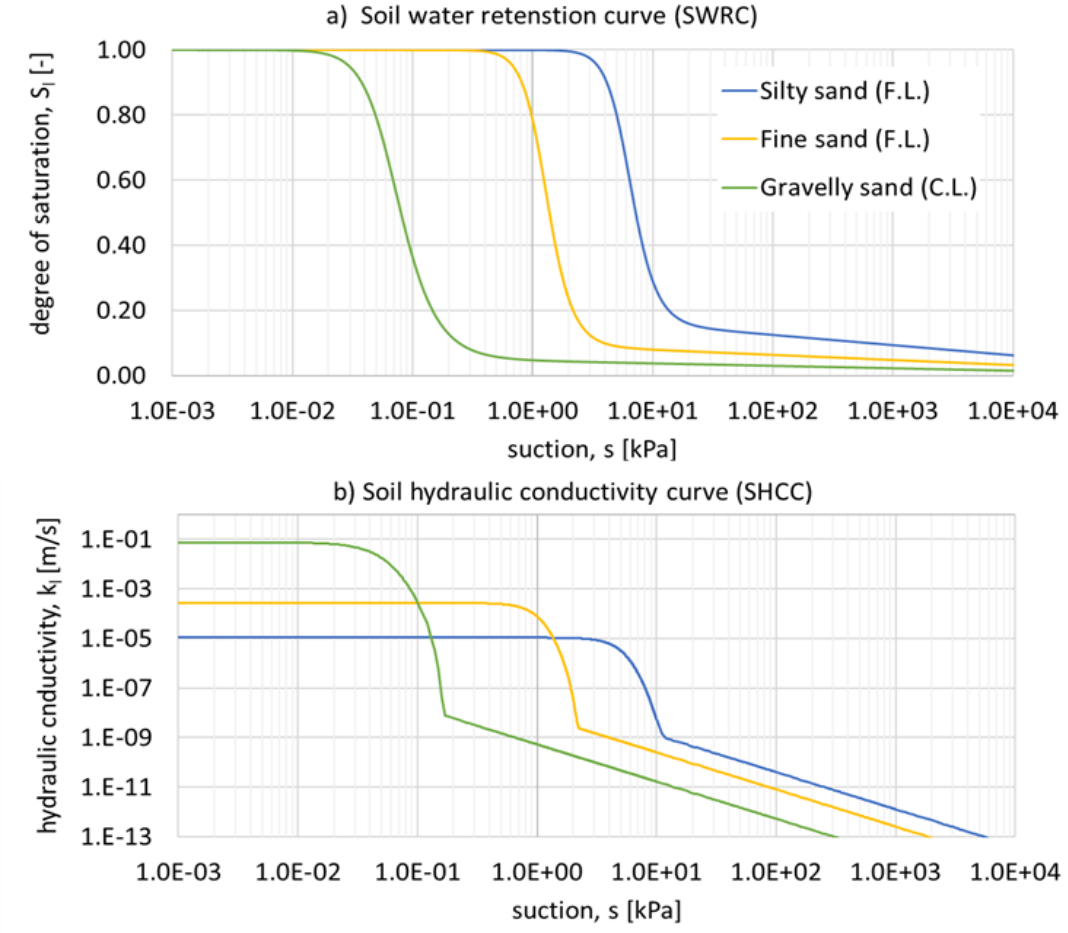

Figure 4-4 Hydraulic constitutive model for defining a) soil water retention curve (SWRC) and b) soil hydraulic conductivity curve (SHCC)

Some further points are worth noting in relation to the material properties:

- For the SWRCs, temperature was constant at T = 20°C in all numerical modelling presented in Chapter 4 and hence there was no variation of SWRC with temperature (i.e. $P_0 = \bar{P}_0$ throughout and $\bar{\sigma}_{s0}$ plays no role, see Section 3.2.4);

- For the SHCCs, values of saturated hydraulic conductivity k_s were calculated by CODE_BRIGHT from the intrinsic permeability k_i defined by the user (given in Table 4-1), and the density ρ_w and dynamic viscosity μ_w of water, using Equation 2-31. With no variation of temperature in the modelling presented in Chapter 4, ρ_w and μ_w were constant and hence k_s was constant for each material;

- For the SHCCs, values of C_r^{Film} shown in Table 4-1 (required as a material parameter in the version of CODE_BRIGHT modified by Scarfone (2020), see Section 3.2.4) were calculated by determining the values of C^{Film} from the value of D_{10} (see Table 4-1), using Equation 2-56 and the default value of X_D= 2.35x10^{-9} mm·ms^{-1}·kPa$^{1.5}$ (see Section 2.4.2) and then the required value of C_r^{Film} was determined from Equation 3-31. Scarfone (2020) showed that film flow could have significant influence on the suction distribution in the coarser layer of the CBS but it had negligible influence on the hydraulic behaviour within the finer layer and the onset of breakthrough across the interface between finer layer and coarser layer. Hence, the precise value selected for C_r^{Film} was unlikely to be crucial in the numerical modelling results.

4.2.3 Initial conditions and boundary conditions

Pore gas pressure p_g and temperature T were both imposed as constant and uniform, with p_g= 0.100 MPa and T = 20°C (293.15°K).

The initial condition for all numerical analyses presented in Chapter 4 was a hydrostatic variation of pore liquid pressure p_l, defined by p_l = 0.070 MPa (s = 30 kPa) at the bottom boundary, p_l = 0.068 MPa (s = 32 kPa) at the interface between

C.L and F.L and p_l = 0.060, 0.064 or 0.066 MPa (s = 40, 36 or 34 kPa) at the ground surface, depending on the total thickness of the CBS. In this initial condition, the coarser layer was at very low degree of saturation S_l (see Figure 4-4a). In particular, the initial suction in the upper part of the C.L was significantly greater than the bulk water continuity value of suction (s^c_{BWC}≈ 0.2 kPa, see Figure 4-4b), so the upper part of the C.L had an extremely low value of hydraulic conductivity k_l in this initial state. With initial suction values between 32 kPa and 34 kPa, 36 kPa or 40 kPa, the entire thickness of the F.L was initially at low S_l irrespective of whether the F.L was made of fine sand or silty sand (see Figure 4-4a). The assumed initial suction distribution was arbitrary, however, provided both layers of the CBS were initially in a relatively dry state, the precise detail of the initial distribution suction was unimportant for the subsequent hydraulic behaviour of the CBS.

For modelling of multi-layered CBSs, the same initial condition was applied as for the conventional CBSs i.e. a hydrostatic suction profile, with pore-liquid pressure defined by p_l = 0.070 MPa (s = 30 kPa) at the bottom, p_l = 0.068 MPa (s = 32 kPa) at the lowest interface between the bottom C.L and the first F.L, p_l = 0.060 MPa (s = 40kPa), at the top of the uppermost F.L and corresponding intermediate values of p_l and s at all intermediate interfaces.

In term of boundary conditions only hydraulic boundary conditions were required. No mechanical boundary conditions were required because displacement was imposed as zero ($\boldsymbol{u}$ = 0) at all locations within the FE model throughout all simulations.

The bottom boundary condition was imposed by a defined constant value of pore liquid pressure equal to the initial value at that location, namely p_l = 0.070 MPa. For the top boundary condition, vertical liquid water flow was imposed with different constant values of rainfall infiltration rate i as shown in Table 4-2 . In order to assess the influence of rainfall infiltration rate, for the conventional CBSs, three different values of infiltration rate were considered: i= 10^{-8} m/s, i = 10^{-6} m/s, and i = 10^{-5} m/s (see details in Table 4-2). The range of rainfall infiltration rates considered (10^{-8} m/s to 10^{-5} m/s) covered the full range of possible interest.

Table 4-2 Numerical simulations of horizontal conventional CBSs

No.	Analysis identifier	Finer layer (F.L.)	F.L. thickness t_f(m)	Infiltration rate i (m/s)
1	FSGV_F20_i105	Fine sand	0.2	10^{-5}
2	FSGV_F40_i105	Fine sand	0.4	10^{-5}
3	FSGV_F80_i105	Fine sand	0.8	10^{-5}
4	FSGV_F20_i106	Fine sand	0.2	10^{-6}
5	FSGV_F40_i106	Fine sand	0.4	10^{-6}
6	FSGV_F80_i106	Fine sand	0.8	10^{-6}
7	FSGV_F20_i108	Fine sand	0.2	10^{-8}
8	FSGV_F40_i108	Fine sand	0.4	10^{-8}
9	FSGV_F80_i108	Fine sand	0.8	10^{-8}
10	SSGV_F20_i105	Silty sand	0.2	10^{-5}
11	SSGV_F40_i105	Silty sand	0.4	10^{-5}
12	SSGV_F80_i105	Silty sand	0.8	10^{-5}
13	SSGV_F20_i106	Silty sand	0.2	10^{-6}
14	SSGV_F40_i106	Silty sand	0.4	10^{-6}
15	SSGV_F80_i106	Silty sand	0.8	10^{-6}
16	SSGV_F20_i108	Silty sand	0.2	10^{-8}
17	SSGV_F40_i108	Silty sand	0.4	10^{-8}
18	SSGV_F80_i108	Silty sand	0.8	10^{-8}

This is clear when the rates are converted into units of mm/day, as shown in Table 4-3. Infiltration rate i = 10^{-8} m/s (0.864 mm/day) represents extremely light drizzle. Even if this rainfall intensity was sustained without break for a full year, it would only represent an annual rainfall of 325 mm, which would be the annual rainfall of a moderately dry location (about 50 % of the average annual rainfall of London (615 mm, years 1991-2000). An infiltration rate i = 10^{-7} m/s (8.64 mm/day) represents light rainfall. If this rainfall intensity was sustained for 24 hours, the daily total would represent a typical wet day in many locations in the UK and if it was sustained for 10 days it would represent a sustained wet period in most locations. If this rainfall intensity was sustained without break for a full year, it would produce an annual rainfall of 3.15 m, representing one of the wettest locations in the world. Infiltration rate i = 10^{-6} m/s (86.4 mm/day) represents heavy rain. This rainfall intensity would occur reasonably frequently for periods

of minutes or perhaps a few hours, during intense rainfall events. If it was sustained for a full day, it would represent an extreme rainfall event, with a return period measured in years or decades in most locations in the UK. Infiltration rate i = 10^{-5} m/s (864 mm/day) is so extreme that it would never occur in most locations in the world and where it did, it would only be for very short periods of minutes or a few hours.

Table 4-3 Rainfall infiltration rates

Infiltration rate i (m/s)	Daily rainfall (mm/day)
10^{-8}	0.864
10^{-7}	8.64
10^{-6}	86.4
10^{-5}	864

For multi-layered CBS simulations (see Table 4-4), two different rainfall infiltration rates (10^{-6} m/s and 10^{-8} m/s) were imposed for the case where the finer layers were made of silty sand and three different rainfall infiltration rates (10^{-5} m/s, 10^{-6} m/s and 10^{-8} m/s) were imposed for the case where the finer layers were made of fine sand. Infiltration rate i = 10^{-5} m/s was not completed for the case of the finer layer made of silty sand, because this induced numerical problems. The value of i = 10^{-5} m/s is relatively close to the saturated hydraulic conductivity of the silty sand, which means that if rainfall of this rate was applied it might produce run-off (only for a sloping CBS) or ponding of water on the ground surface. The numerical modelling did not allow for the possibility of ponding, and hence numerical problems occurred. It is, however, unclear why these problems occurred when a multi-layered CBS with the finer layer made of silty sand was subjected to a rainfall intensity of 10^{-5} m/s, but they did not occur when the equivalent conventional CBS (also with the finer layer made of fine sand) was subjected to the same rainfall intensity.

Table 4-4 Numerical simulations of horizontal multi-layered CBSs

No	Analysis identifier	Finer layer F.L.	F.L. thickness t_f (m)	No. of F.L.(N)	Infiltration rate i (m/s)
3	FSGV_F80_i105	Fine sand	0.80	1	10^{-5}
19	FSGV_3NF23_i105	Fine sand	0.23	3	10^{-5}
20	FSGV_5NF12_i105	Fine sand	0.12	5	10^{-5}
6	FSGV_F80_i106	Fine sand	0.80	1	10^{-6}
21	FSGV_3NF23_i106	Fine sand	0.23	3	10^{-6}
22	FSGV_5NF12_i106	Fine sand	0.12	5	10^{-6}
9	FSGV_F80_i108	Fine sand	0.80	1	10^{-8}
23	FSGV_3NF23_i108	Fine sand	0.23	3	10^{-8}
24	FSGV_5NF12_i108	Fine sand	0.12	5	10^{-8}
15	SSGV_F80_i106	Silty sand	0.80	1	10^{-6}
25	SSGV_3NF23_i106	Silty sand	0.23	3	10^{-6}
26	SSGV_5NF12_i106	Silty sand	0.12	5	10^{-6}
18	SSGV_F80_i108	Silty sand	0.80	1	10^{-8}
27	SSGV_3NF23_i108	Silty sand	0.23	3	10^{-8}
28	SSGV_5NF12_i108	Silty sand	0.12	5	10^{-8}

4.3 Results: conventional horizontal CBSs at final steady state

This section presents the hydraulic response of conventional horizontal CBSs at final steady state from the numerical modelling and validation of the simplified suction profile proposed by Stormont and Morris (1998) and the corresponding simplified method of estimating water storage capacity, as described in Section 4.1.

Figure 4-5 shows the variation of water flow rate per unit plan area q_v across the interface between F.L and C.L plotted against time for the case of a finer layer with a thickness of 80 cm, with results shown for both different finer layer materials (FS and SS) and for all three rainfall infiltration rates (i = 10^{-5} m/s, i = 10^{-6} m/s, and i = 10^{-8} m/s).

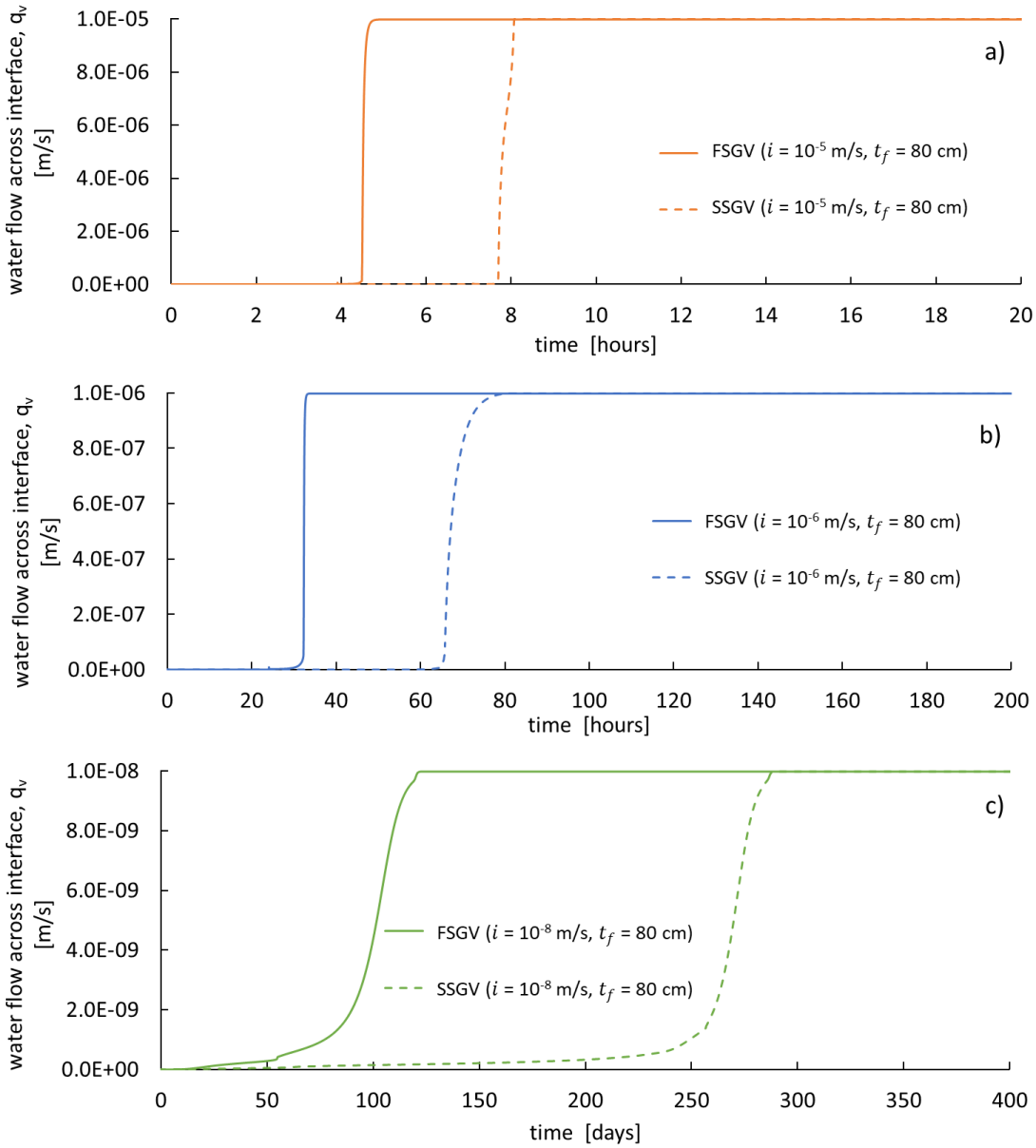

Figure 4-5 Development of interface flow rate for t_f = 80 cm and two types of finer layer material (fine sand and silty sand) and different rainfall infiltration rates: a) i = 10^{-5} m/s, b) i = 10^{-6} m/s, and c) i = 10^{-8} m/s

Figure 4-5a and Figure 4-5b show that, for infiltration rate of 10^{-5} m/s or 10^{-6} m/s, breakthrough of water from the finer layer to the coarser layer is a sudden phenomenon, with negligible flow across the interface until a rapid increase to a final flow rate across the interface equal to the rainfall infiltration rate i (the final steady state). At a low infiltration rate of i = 10^{-8} m/s (Figure 4-5c) the phenomenon of breakthrough is rather more gradual. Closer inspection of Figure 4-5a and Figure 4-5b also shows that, at higher infiltration rates, breakthrough is slightly more gradual when the F.L. made of silty sand (SSGV) than when the F.L is made of fine sand (FSGV).

Inspection of Figure 4-5 shows that, as expected, the time to breakthrough reduces as the rainfall infiltration rate increases. In addition, Figure 4-5 shows that, for any given infilltration rate, the time to breakthrough is greater when the F.L is made of silty sand (SSGV) than when the F.L is made of fine sand (FSGV).This suggests that a CBS with the F.L made of silty sand has greater water storage capacity than a CBS with the F.L made of fine sand (see later).

Figure 4-6 shows comparision of the development of water flow rate across the interface with time for CBSs with different thicknesses of finer layer (0.2 m, 0.4 m, and 0.8 m) when the finer layer is made of fine sand and the rainfall infiltration rate i = 10^{-6} m/s . As expected, time to breakthrough increases as the thickness of the finer layer increases, suggesting that, as expected, the water storage capacity of the CBS increases with increasing thickness of the F.L.

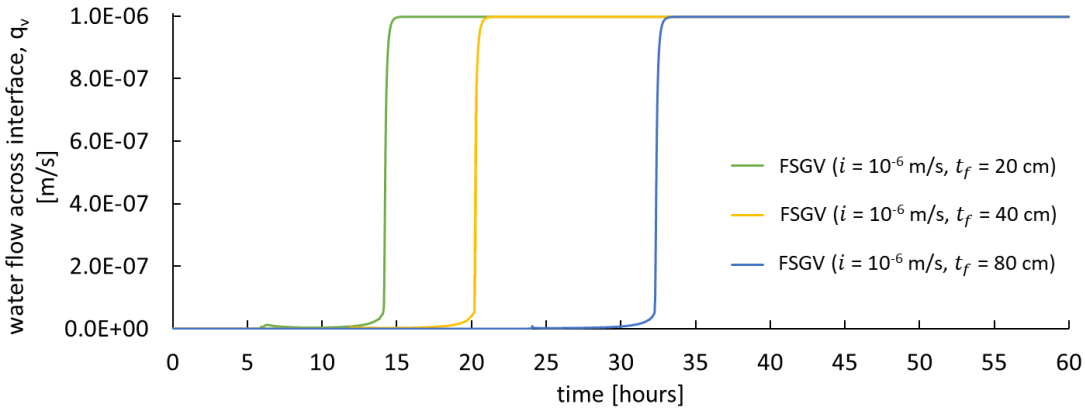

Figure 4-6 Development of interface flow rate for different finer layer thicknesses (t_f = 20 cm, 40 cm, and 80 cm) with the finer layer made of fine sand and infiltration rate i = 10^{-6} m/s

Validation of the simplified suction profiles suggested by Stormont and Morris (1998) (see Section 4.1) was performed by comparing with final steady state suction profiles from the finite element (FE) results (see Figure 4-7a and Figure 4-8a for the cases with t_f = 80 cm). In addition, degree of saturation profiles determined by the simplified method (obtained from the simplified suction profile by using the same modVG SWRC relationship as used in the FE modelling) were compared with corresponding final steady state degree of saturation profiles from the FE modelling (see Figure 4-7b and Figure 4-8b for the cases with t_f = 80 cm).

Figure 4-7 shows the final steady state profiles of suction and degree of saturation obtained in 80 cm thick F.L made of fine sand with three different rainfall

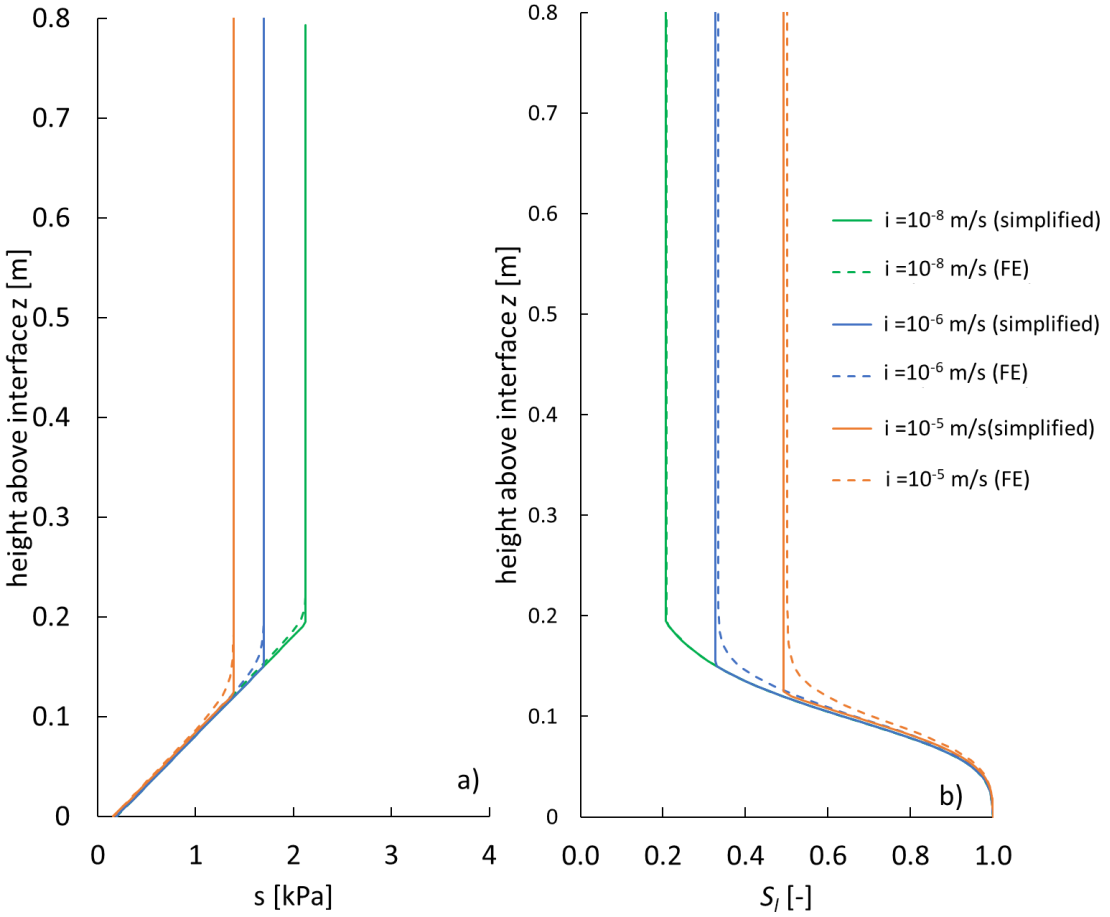

Figure 4-7 Comparison between simplified method results and FE numerical results at final steady state for horizontal CBS with F.L made of fine sand a) suction profiles and b) degree of saturation profiles (FSGV, t_f = 0.80m)

infiltration rates : 10^{-8} m/s, 10^{-6} m/s , and 10^{-5} m/s. For the simplified suction profiles, the consant value of suction s_f^* in the upper part of the F.L.was s_f^* = 2.1 kPa for i = 10^{-8} m/s, s_f^* = 1.7 kPa for i = 10^{-6} m/s, and s_f^* = 1.4 kPa for i = 10^{-5} m/s. Inspection of Figure 4-7a shows that, for all three infiltration rates, the simplified suction profiles are an excellent match to the corresponding final steady state suction profiles from the FE modelling. The only visible difference is that the simplified suction profiles slightly overestimate the values of suction in the region where the simplified suction profile involves a change from the hydrostatic profile to a constant value of suction s_f^*, because the FE results show that this sharp transition is, in reality, slightly rounded. Inspection of Figure 4-7b shows that the degree of saturation profiles predicted by the simplified method are also a good match to the corresponding final steady state from the FE modelling. Values of S_l are slightly under-predicted by the simplified method, particularly in the transition region described above, because of the slight overestimation of the suction values. This suggests that the simplifed method will slightly under-predict

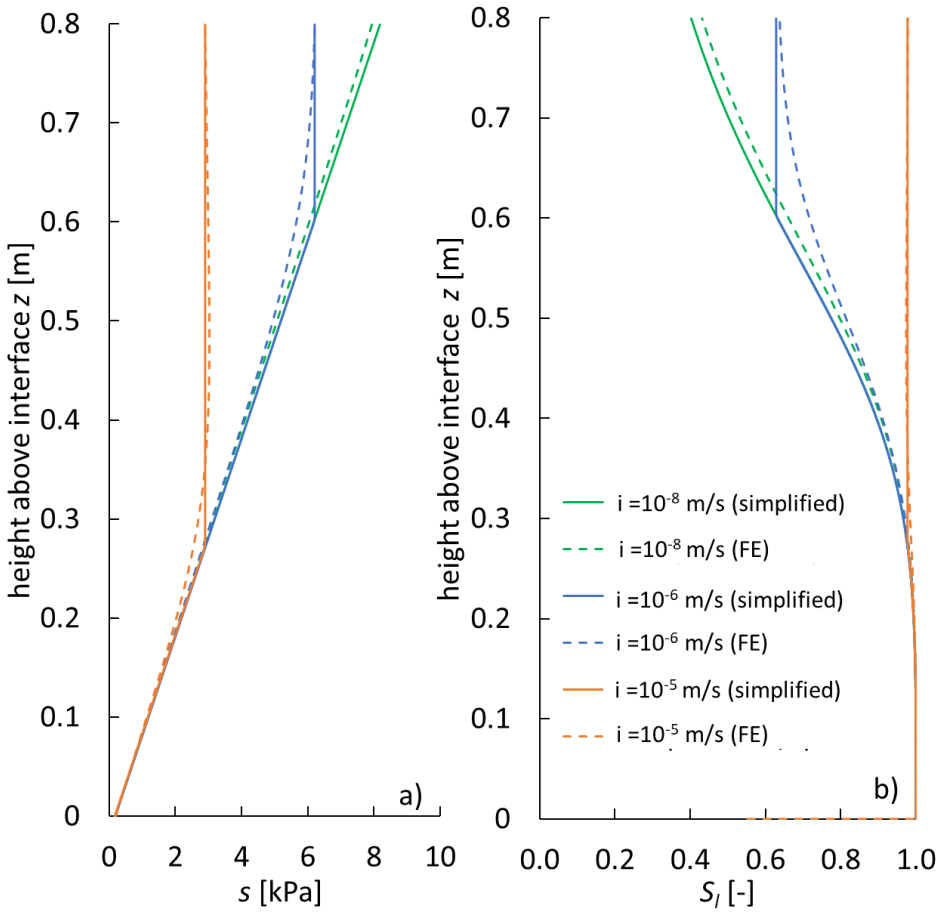

Figure 4-8 Comparison between simplified method and FE numerical results at final steady state for horizontal CBS with F.L made of silty sand a) suction profiles and b) degree of saturation profiles (SSGV, t_f = 0.80m)

the storage capacities of the CBS at the three different rainfall infiltration rates (see later). For the case of CBSs with F.L made of fine sand but finer layer thickness of 20 cm or 40 cm (see Appendix A), the quality of matching between simplified method and FE results, in terms of suction profiles and degree of saturation profiles, was similar to the results shown in Figure 4-7.

Figure 4-8 shows the final steady state suction profiles and degree of saturation profiles obtained in 80 cm thick F.L made of silty sand under the three different rainfall infiltration rates. In this case, the values of s_f^* (the value of suction at which the hydraulic conductivity of the F.L is equal to the rainfall infiltration rate i) are: s_f^* = 9.6 kPa for i = 10^{-8} m/s, s_f^* = 6.8 kPa for i = 10^{-6} m/s, and s_f^* = 2.9 kPa for i = 10^{-5} m/s. The predicted suction value never achieved 9.6 kPa , within the thickness of the finer layer, and hence there is no constant value of suction in the upper part of F.L for the simplified suction profile corresponding to i = 10^{-8} m/s. Inspection of Figure 4-8 shows again that the profiles of suction and degree of

saturation predicted by the simplified method are a reasonable match to the corresponding final steady state profiles from the FE modelling. Again, values of suction were generally slightly overestimated by the simplified method and values of degree of saturation were therefore slightly underestimated, suggesting slight underprediction of the water storage capacity (see below). Similar quality of match was achieved with finer layer thicknesses of 20 cm and 40 cm (see Appendix A).

Water storage capacity can be obtained by integrating the final steady state degree of saturation profile over the thickness of the finer layer and multiplying by the porosity Φ (see Equation 4-1). The water storage capacities (WSCs) of CBSs for different thickness of F.L and different rainfall infiltration rates are shown in Figure 4-9 (finer layer made of fine sand) and Figure 4-10 (finer layer made of silty sand).

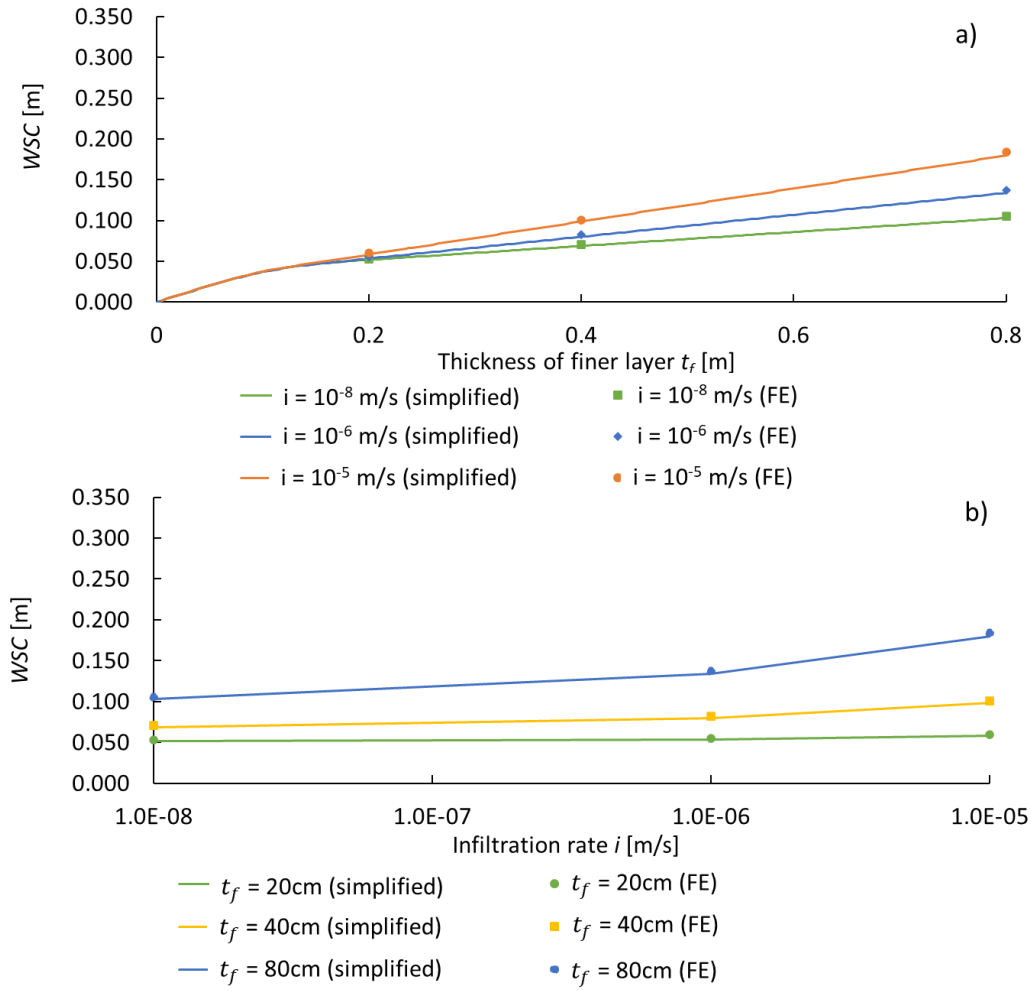

Figure 4-9 Water storage capacity of horizontal CBS with finer layer made of fine sand a) influence of fine layer thickness and b) influence of infiltration rate

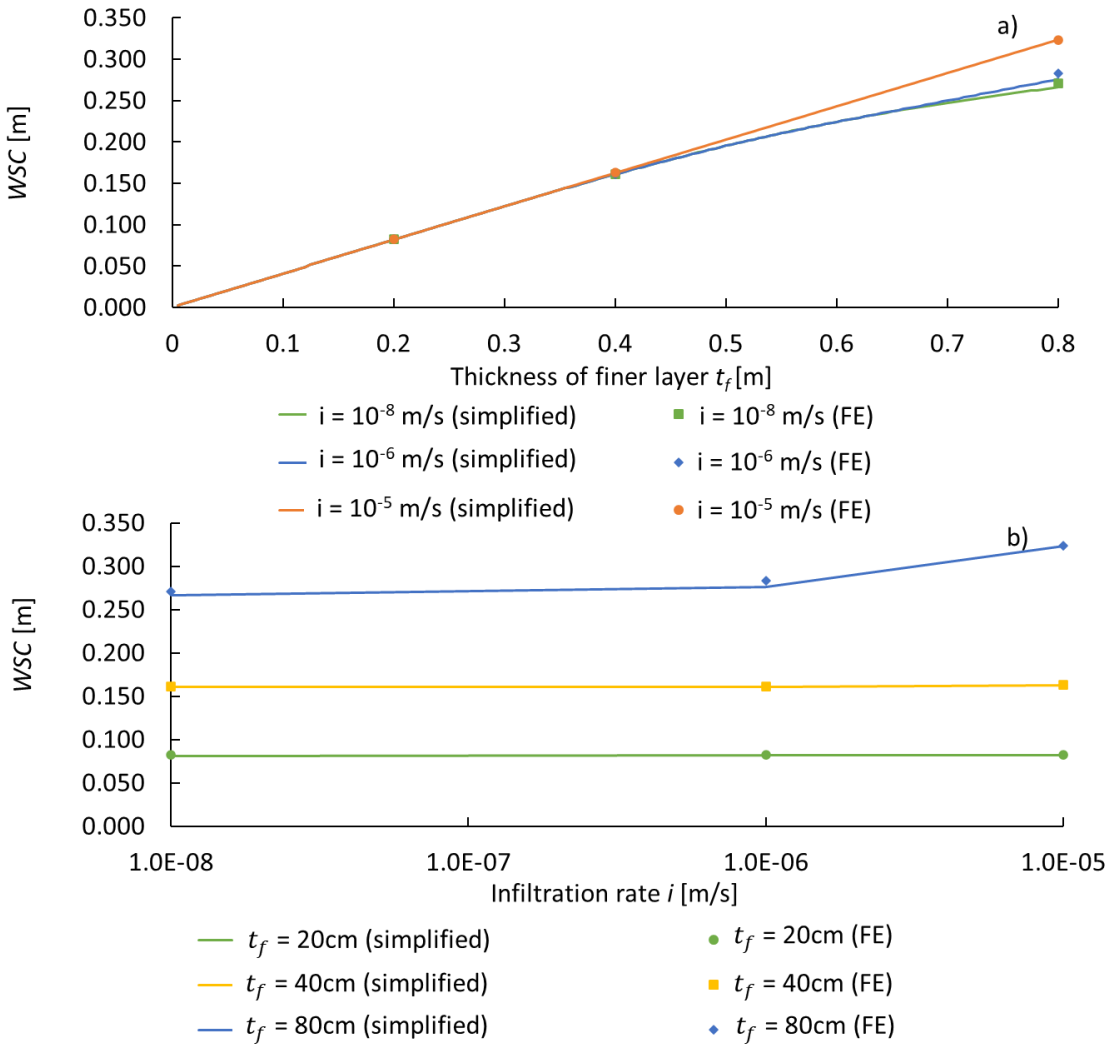

Figure 4-10 Water storage capacity of horizontal CBS with finer layer made of silty sand: a) influence of fine layer thickness and b) influence of infiltration rate

Inspection of Figures 4-9 and 4-10 shows that the simplified method provides accurate predictions of water storage capacity (WSC) in all cases, when compared with the corresponding FE result. The simplified method tends to be very slightly conservative (underestimating slightly the values of WSC), due to the slight overestimation of suction values and slightly underestimation of degree of saturation values shown in Figure 4-7 and Figure 4-8, but any differences in WSC between simplified method and FE results are always very small. The eighteen different cases shown in Figure 4-9 and Figure 4.10 represent the full range of rainfall intensities of interest, the full practical range of finer layer thickness and two different finer layer materials, spanning the range of realistic interest. The results presented in Figures 4-9 and 4-10 therefore represent a more comprehensive numerical validation of the simplified method of Stormont and

Morris (1998) for predicting WSC of a conventional horizontal CBS than previously reported in the literature.

Inspection of Figures 4-9 and 4-10 also highlights important differences in the variation of WSC for CBSs with the finer layer made of fine sand and for CBSs with finer layer made of silty sand. Firstly, comparison of Figures 4-9 and 4-10 shows that, for any given combination of infiltration rate and finer layer thickness, the WSC of a CBS with the F.L made of silty sand is greater than the WSC of a CBS with F.L made of fine sand. The reason for this is clear from inspection of Figures 4-7b and 4-8b, which shows that, under the relevant range of suction values, when the F.L is made of fine sand, high values of S_l are achieved only in a thin layer at the base of F.L, whereas when the F.L is made of silty sand, high values of S_l can be achieved over a much greater thickness of the F.L.

Secondly, inspection of Figure 4-9a shows that, for a CBS with the F.L made of fine sand, the variation of WSC with finer layer thickness t_f is non-linear at low values of t_f and then linear at higher values of t_f (with a low gradient that depends on infiltration rate i). The reason for this is apparent from Figure 4-7b, which shows S_l varying in the lowest 20 cm of the F.L and then, if the F.L is relatively thick, S_l is constant (at a low value, which is dependent on infiltration rate i) in the upper part of the F.L. In contrast, inspection of Figure 4-10a shows that, for a CBS with the F.L made of silty sand, WSC is proportional to finer layer thickness for low value of t_f, with the variation then becoming non-linear at high values of t_f, unless the infiltration rate is very high. This can be related to the degree of saturation profiles shown in Figure 4-8b, with WSC proportional to t_f for low values of t_f corresponding to situations where the F.L achieves full saturation over its complete depth.

Finally, inspection of Figures 4-9b and 4-10b shows that, for CBSs with the F.L made of fine sand or silty sand, WSC increases with increasing rainfall infiltration rate i, unless the finer layer thickness t_f is small. The reason for this is apparent from Figures 4-7 and 4-8. If t_f is sufficiently small, the simplified suction profile will be hydrostatic over the full height of the F.L for all relevant values of i, and hence WSC is independent of i. However, if t_f is greater, different values of s_f^*

for different values of i will apply in the upper part of the F.L, and hence WSC increases with increasing infiltration rate. Scarfone (2020) noted, however, that higher values of WSC obtained at high infiltration rates may not be reliable for design purposes, due to the effect of water redistribution occurring within the finer layer after rainfall infiltration ceases and hence the value of WSC corresponding to a very low infiltration rate (e.g. i = 10^{-8} m/s) should be used for design of horizontal CBSs.

4.4 Results: multi-layered horizontal CBSs at final steady state

Scarfone (2020) developed a simplified suction profile for multi-layered CBSs subjected to continuous rainfall of constant intensity (see Sections 2.9 and 4.1) and validated this for a few specific cases by laboratory column tests and numerical modelling. This section presents a more comprehensive numerical validation of the simplified method for multi-layered CBSs, covering an appropriate range of rainfall intensities, material properties of the F.L and number of finer layer (see Table 4-4). In all simulations, the total thickness of the CBS was 100 cm, with a bottom C.L of 20 cm thickness, so that the combined thickness of finer layers and intermediate coarser layers was always 80cm (see Table 4-4 and Section 4.2.1).

Figure 4-11 shows final steady state suction profiles and degree of saturation profiles for multi-layered CBSs with finer layers made of fine sand and different numbers of finer layers (N = 1, N = 3, and N = 5 where N is the number of finer layers). Results are shown for three different infiltration rates (10^{-8} m/s, 10^{-6} m/s and 10^{-5} m/s). Figure 4-12 shows the corresponding final steady state suction profiles and degree of saturation profiles for multi-layered CBSs with the finer layers made of silty sand, but in this case only two different infiltration rates were analysed (10^{-8} m/s and 10^{-6} m/s).

Inspection of Figures 4-11 and 4-12 shows that the suction profiles and degree of saturation profiles predicted by the simplified method of Scarfone (2020) are generally a good match to the corresponding FE results. Step changes of suction

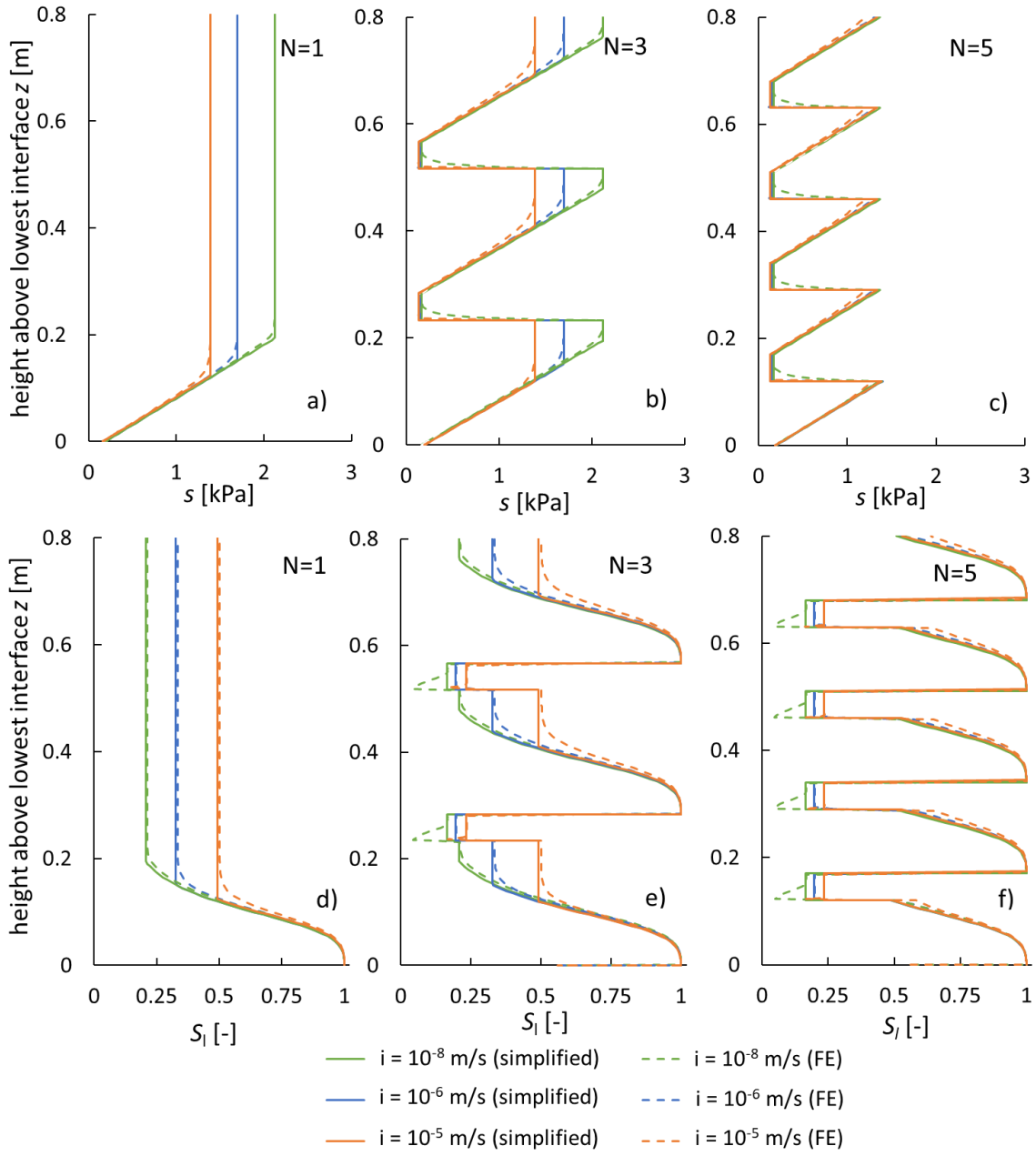

Figure 4-11 Final steady state suction profiles (a, b, and c) and degree saturation profiles (d, e, and f) within muti-layered CBSs with finer layers made of fine sand (N = 1, one F.L, N = 3 three F.Ls, and N = 5, five F.Ls)

predicted by the simplified method (at the bottom of each intermediate C.L) or sudden changes of gradient of the suction profile predicted by the simplified method are rounded off in the FE results. This produces some minor mis-matches in the values of S_l predicted by the simplified method, particularly in the intermediate coarser layers. The most significant mis-matches of degree of saturation arise because the simplified suction profile involves a step change of suction at the interface at the bottom of each intermediate coarser layer, which is physically impossible, whereas the FE results predict a more realistic steep gradient of suction in the lower part of each intermediate coarser layer.

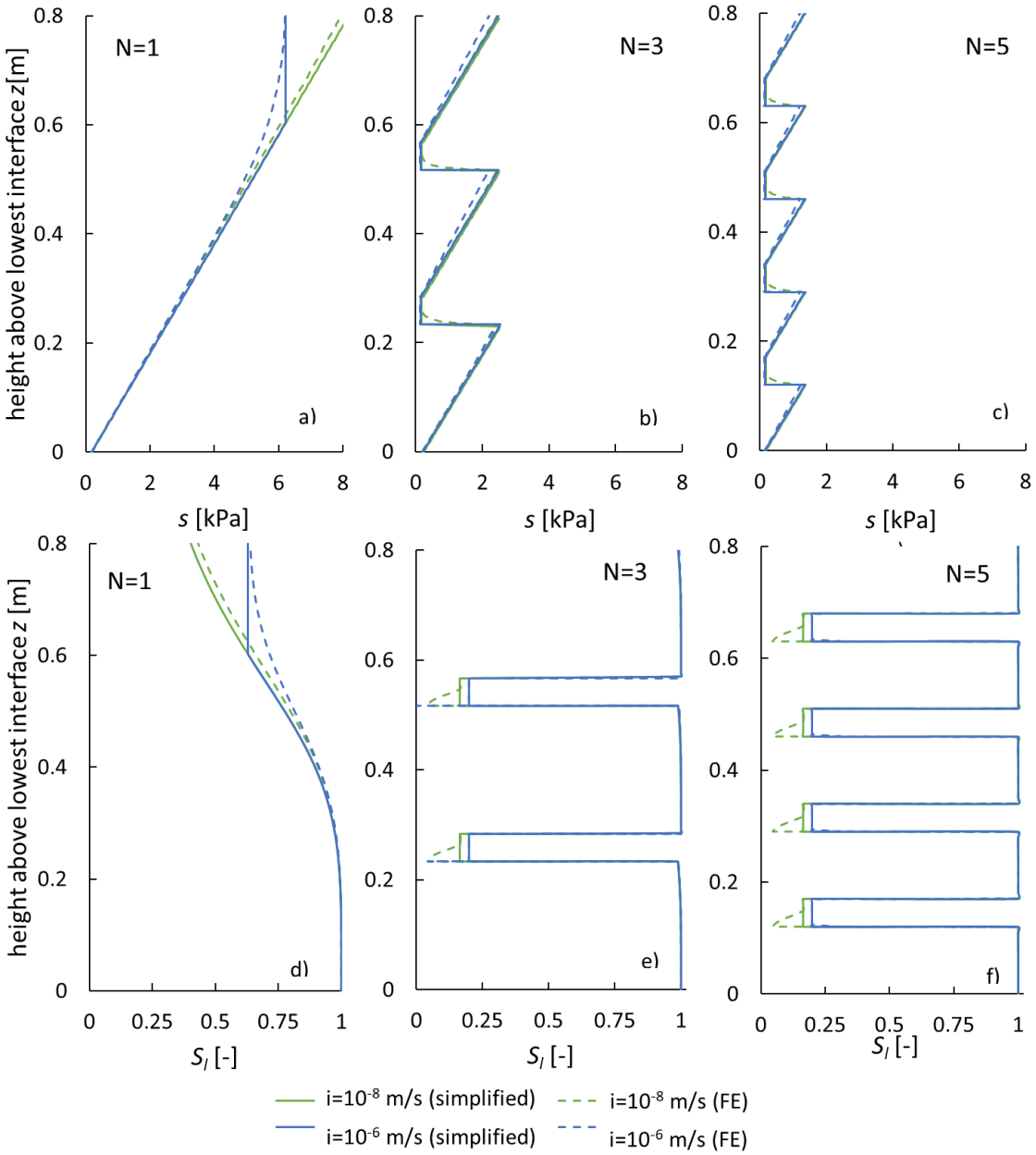

Figure 4-12 Final steady state suction profiles (a, b, and c) and degree saturation profiles (d, e, and f) within multi-layered CBSs with finer layers made of silty sand (N = 1, one F.L, N = 3 three F.Ls, and N = 5 , five F.Ls)

Figure 4-13 shows the effect of number of finer layers N on water storage capacity (WSC). The FE modelling has been done for N = 1,3 and 5 whereas the simplified method have been done for N = 1,2,3,4,5 and 6. The predictions of the simplified method of Scarfone (2020) are, in all cases, in excellent agreement with the corresponding results from the FE simulations. This represents a more comprehensive numerical validation of the simplified method for horizontal multi-layered CBSs than previously achieved by Scarfone (2020).

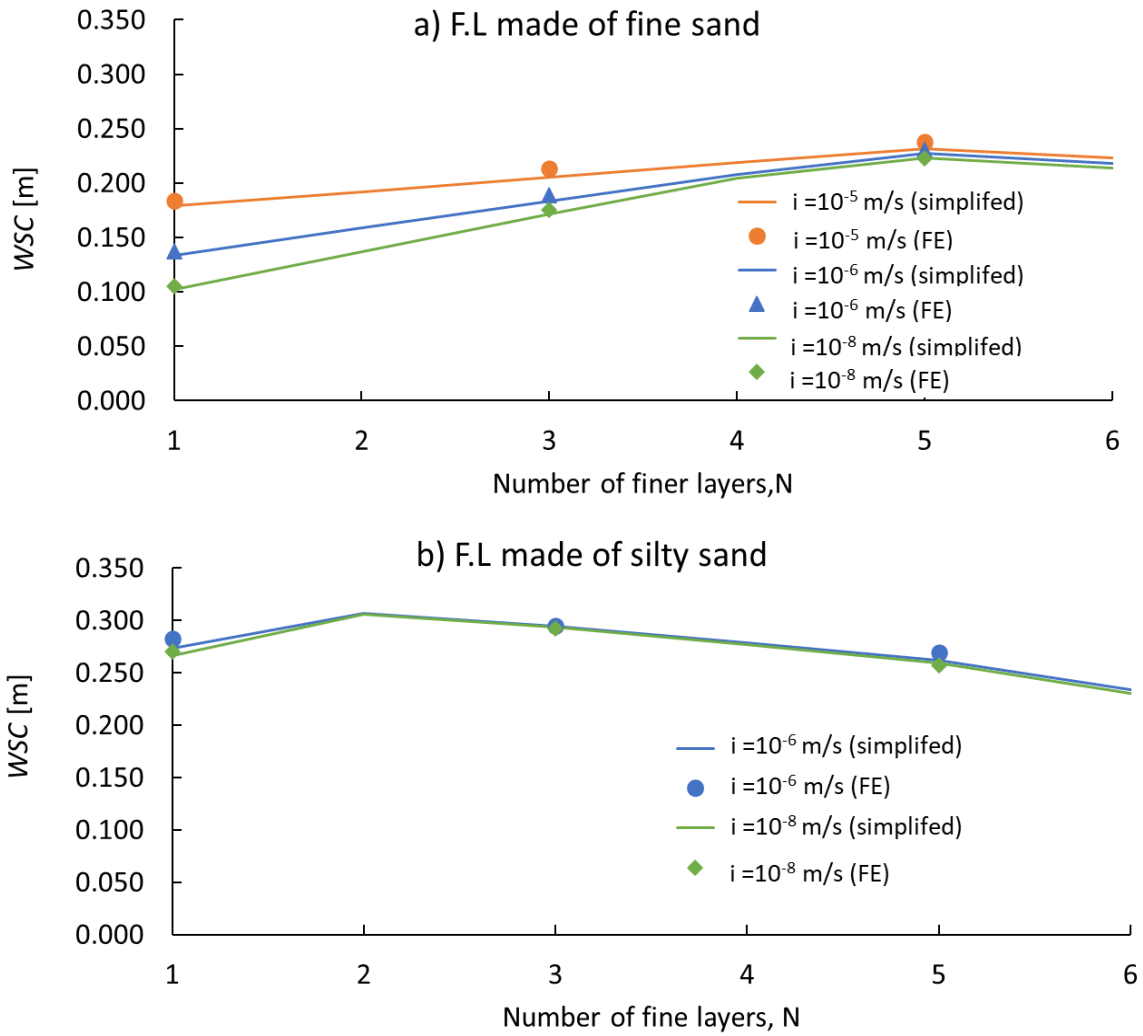

Figure 4-13 Water storage capacity of multi-layered CBSs a) finer layers made of fine sand, b) finer layers made of silty sand

Figure 4-13a shows that, with finer layers made of fine sand, the use of multi-layered barriers leads to increase of WSC over a conventional CBS and the optimum is a multi-layered CBS with five finer layers. The increase of WSC over a conventional CBS is significant if it is remembered that WSC values corresponding to a very low rainfall intensity (i.e. i = 10^{-8} m/s) should be used for design purposes. In contrast, with finer layers made of silty sand, any benefit of a multi-layered CBS over a conventional CBS is relatively minor and, according to the simplified method, the optimum is a multi-layered CBS with only two finer layers (see Figure 4-13b).

It can be remarked that the reduction of WSC as the number of finer layers is increased above the optimum value occurs because the degree of saturation within intermediate coarser layers is low (see Figures 4-11 and 4-12). If excessive numbers of finer layers are included, the low values of S_l within each intermediate

coarser layer more than offsets the high values of S_l achieved in the lower part of each finer layer (see Figures 4-12e and 4-12f).

4.5 Behaviour prior to final steady state

This section presents discussion of the development of hydraulic behaviour of the conventional and multi-layered horizontal CBSs, over time towards the final steady-state. Improved understanding of this development of the wetting process over time is helpful in subsequently understanding behaviour under more complex rainfall scenarios, including intermittent rainfall (Chapter 6) and extreme rainfall events (Chapter 7).

4.5.1 Conventional horizontal CBSs

The water flow rate q_v (volumetric flow rate per unit area) across the interface between F.L and C.L (at z = 0) varies with time within a typical conventional horizontal CBS, as shown in Figure 4-14. The corresponding vertical profiles of suction and degree of saturation at various times are shown in Figure 4-15.

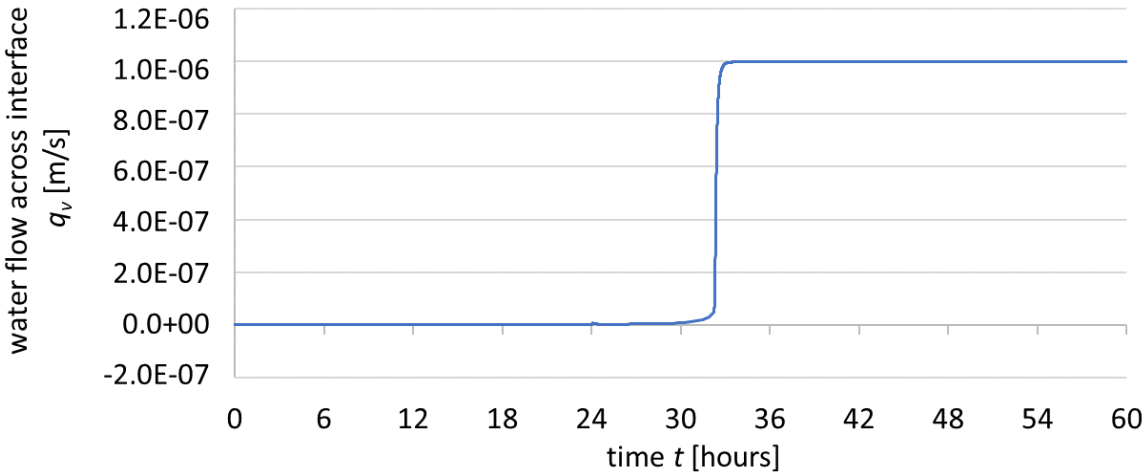

Figure 4-14 Liquid water velocity across the interface (FSGV, t_f = 80 cm, i = 10^{-6} m/s)

For the example shown in Figure 4-14, breakthrough occurs at about t = 33 hours. At this time the vertical liquid water velocity across the interface increases rapidly from very low values until it gradually reaches the rainfall infiltration rate i = 10^{-6} m/s. The occurrence of breakthrough at about t = 33 hours is also apparent in the degree of saturation profiles shown in Figure 4-15. At t = 0, t = 12 hours, t = 24 hours and t = 30 hours (Figures 4-15b, 4-15d, 4-15f, and 4-15h), the entire C.L

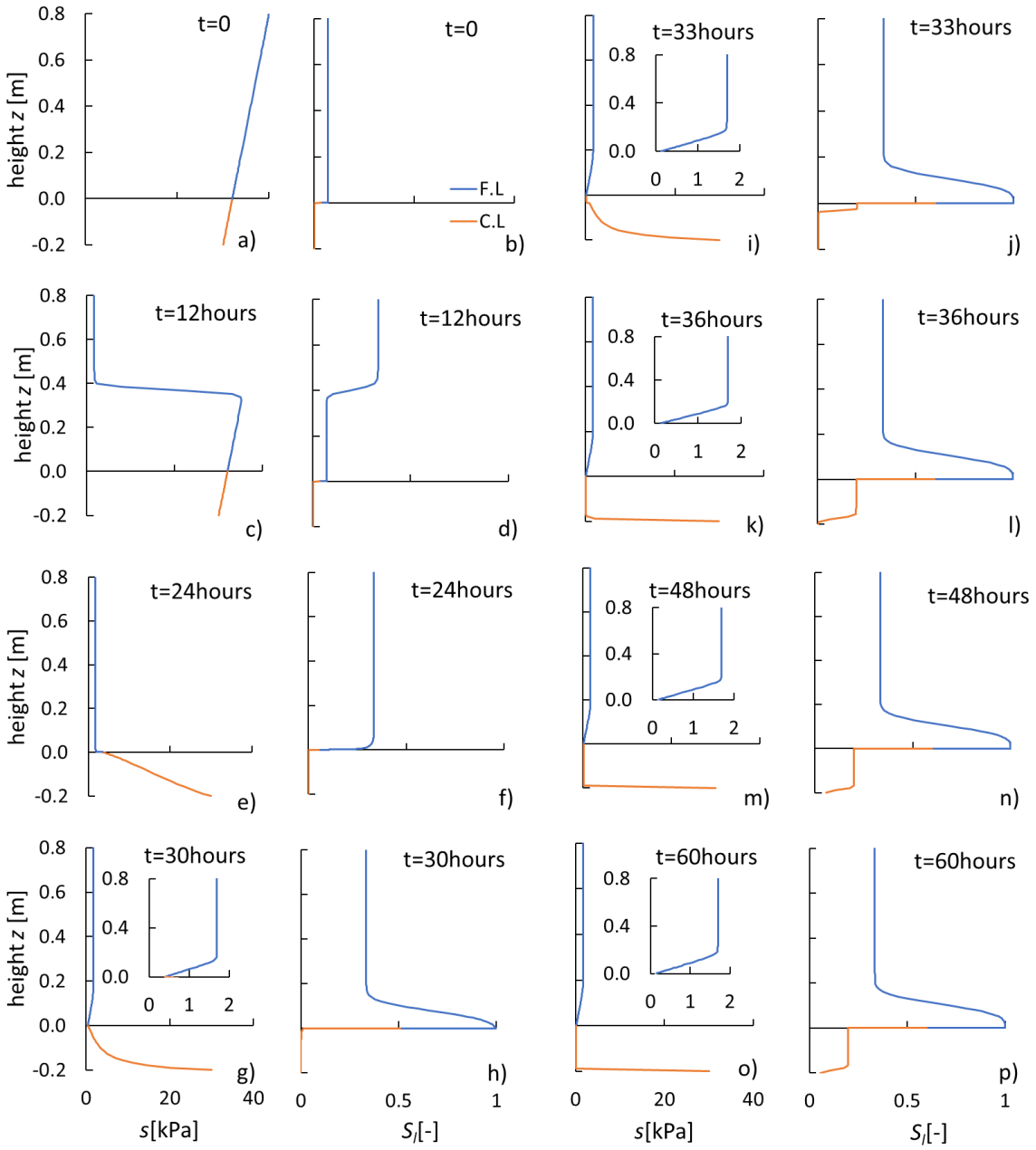

Figure 4-15 Profiles of suction and degree of saturation at different times (FSGV, t_f = 80 cm, i = 10^{-6} m/s)

(-0.2 < z < 0) is at very low degree of saturation. At t = 33 hours (Figure 4-15j), the upper part of the C.L has wetted to S_l = 0.20 (i.e. breakthrough has started). At t = 36 hours (Figure 4-15l), t = 48 hours (Figure 4-15n) and t = 60 hours (Figure 4-15p), almost the entire C.L has wetted to S_l = 0.20 (i.e. breakthrough is complete).

Detailed inspection of Figure 4-15 shows the behaviour of the CBS developing over time from the start of the rainfall until the final steady state (after breakthrough occurred). At t = 0, Figure 4-15a and 4-15b show the initial state, with the assumed

initial hydrostatic suction profile in both F.L and C.L and corresponding low values of S_l in the F.L and very low values of S_l in the C.L. In the early hours of rainfall infiltration (0< t<24 hours), a sharp wetting front progresses downward through the F.L from the ground surface. Above the wetting front, the material of F.L is at a constant suction value of suction $s = s_f^*$ = 1.7 kPa (the value of suction at which the hydraulic conductivity of the F.L is equal to the rainfall infiltration rate i = 10^{-6} m/s) and the degree of saturation is constant at the corresponding value of S_l = 0.33. Below the wetting front, the suction and degree of saturation profiles in the lower part of the F.L and in the C.L are unchanged from the initial profiles. At t = 12 hours (see Figures 4-15c and 4-15d) the wetting front has reached about z = 0.4 m i.e. halfway down from the ground surface). Note that during this initial wetting phase, as a wetting front moves down from the ground surface, the soil above the wetting front is only partially wetted, to S_l = 0.33.

At t = 24 hours (see Figures 4-15e and 4-15f), the initial wetting front reaches the bottom of the finer layer. The value of suction at the interface between F.L and C.L at this point has reduced to $s = s_f^*$ = 1.7 kPa. As this value of suction is still greater than the bulk water continuity value of the coarser layer ($s_{BWC,c}$ = 0.2 kPa), breakthrough does not occur. At this point, the only water flow across the interface and into the C.L is that due to film flow in the C.L, which is almost insignificant (associated with an extremely low value of hydraulic conductivity). Although this film flow is sufficient to change the suction profile in the C.L (see Figure 4-15e) from the initial suction profile, it is insufficient to cause any noticeable change of degree of saturation within C.L (see Figure 4-15f).

A second wetting stage now commences. In this second wetting stage, water passes through the upper part of the F.L, without any increase in the water stored in this upper part, and instead further filling of the F.L now occurs from the bottom of the layer. Figures 4-15g and 4-15h show the situation at t = 30 hours, with a thin zone at the base of the F.L now at significantly higher values of S_l and corresponding lower values of suction. At t = 30 hours, the value of suction at the base of the F.L, at the interface with the C.L, is still greater than $s_{BWC,c}$ = 0.2 kPa, and hence breakthrough has still not occurred. At t = 33 hours, however, the wetting of the lower part of the F.L has progressed a little further, the suction at the interface has fallen to $s_{BWC,c}$ = 0.2 kPa and breakthrough occurred.

For t = 36 hours (Figures 4-15k and 4-15l), t = 48 hours (Figures 4-15m and 4-15n) and t = 60 hours (Figures 4-15o and 4-15p), the final steady state has been reached. In the example shown in Figure 4-15, with the F.L made of fine sand, the high degree of saturation zone at the base of the F.L in the final steady state is of limited height, whereas this zone is of significantly greater depth in cases where the F.L is made of silty sand (as discussed earlier in Section 4.3).

4.5.2 Multi-layered horizontal CBSs

This section presents the hydraulic behaviour of multi-layered horizontal CBSs from the beginning of rainfall until the final steady state. A typical example of the development of water flow across the various interfaces at the bottoms of the different finer layers is shown in Figure 4-16 for a multi-layered horizontal CBS involving three finer layers (N=3). Figure 4-17 shows the corresponding profiles of suction and degree of saturation at selected times.

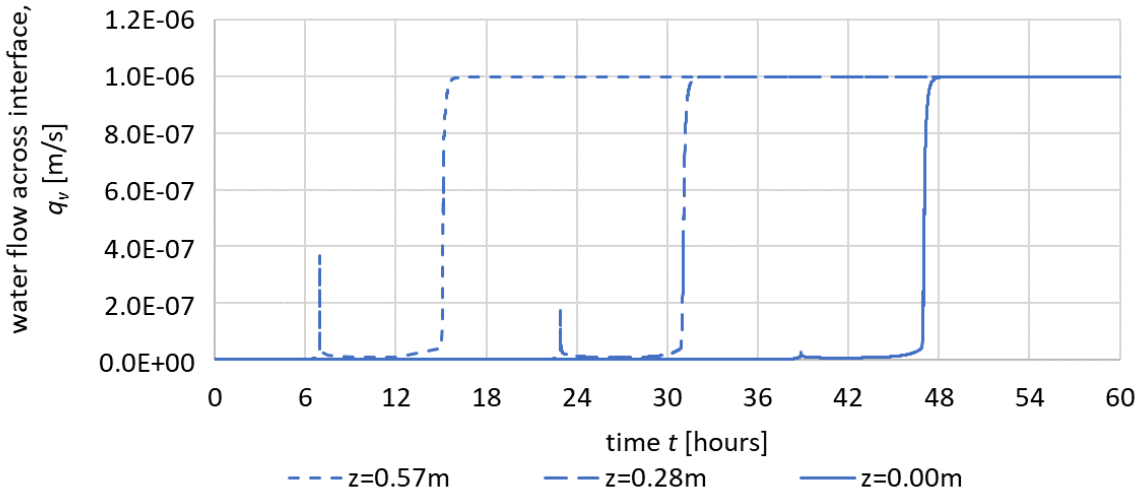

Figure 4-16 Liquid water velocity across interfaces at bottoms of finer layers (z = 0.57m, z=0.28m, and z=0) in multi-layered CBS with three finer layers (FSGV, N=3, i=10^{-6}m/s)

Figure 4-16 shows water breakthrough across the interfaces at different z values: z = 0.57 m, z = 0.28 m and z = 0, which represent the positions of the bottoms of the three finer layers. Breakthrough occurred at about t = 15 hours from the uppermost F.L, at about t = 32 hours from the second F.L, and at about t = 47 hours from the lowest F.L (breakthrough occurred at t = 33 hours in the corresponding conventional CBS with the same total thickness). These results indicate that multi-layered horizontal CBSs have the ability to substantially lengthen the time to final breakthrough from the lowest F.L into the bottom C.L.

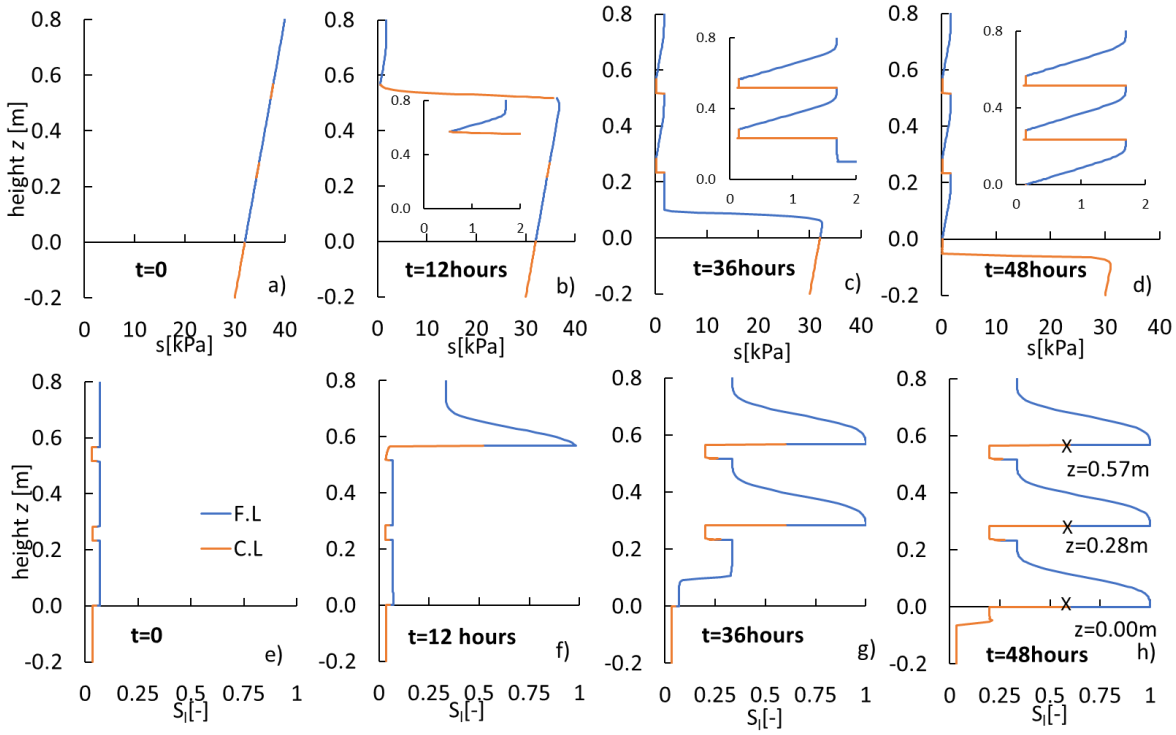

Figure 4-17 Profiles of suction (a, b, c, and d) and degree of saturation (e, f, g, and h) at different times in multi-layered horizontal CBS with three finer layers (FSGV, N=3, i=10^{-6}m/s)

The very brief spike in flow across each interface, visible in Figure 4-16 approximately 8 hours before full breakthrough occurred across the same interface, corresponded to the time when a wetting front progressing downwards through the F.L, during the first stage of partial wetting of the F.L, first reached the interface at the base of the F.L. These very short duration spikes may be numerical artefacts arising in the FE modelling.

Figure 4-17 shows the profiles of suction (a, b, c, and d) and degree of saturation (e, f, g, and h) within the horizontal multi-layered CBS at t = 0, t = 12 hours, t = 36 hours and t = 48 hours. t = 48 hours (Figures 4-17d and 4-17h) corresponds to the final steady state in all the finer layers and intermediate coarser layers but wetting to the final steady state has not yet progressed through the full depth of the bottom C.L (see Figure 4-17h). Inspection of Figures 4-17b and 4-17f for t = 12 hours show that the wetting of the uppermost F.L is complete before breakthrough occurs into the uppermost intermediate C.L and then into the second F.L. Similarly, wetting of the second F.L is complete before breakthrough occurs into the second intermediate C.L and then wetting of the lowest F.L commences (see Figures 4-17c and 4-17g, for t = 36 hours). Wetting of each F.L with the multi-layered CBS follows the same two-stage pattern as previously described for the

wetting of a conventional CBS i.e. a first partial wetting stage (to s = s_f^* and a corresponding value of S_l), involving a wetting front moving downwards from the top of the F.L and then a second wetting stage involving further filling progressing upwards from the bottom of the F.L, until the suction at the bottom of the F.L reaches s_{BWC}^c, at which time breakthrough occurs into the underlying C.L.

4.6 Conclusions

The main results of the work presented in this chapter can be summarised as follows:

1) For conventional horizontal CBSs, the approximate suction profile within the finer layer of the CBS at the time of breakthrough suggested by Stormont and Morris (1998) was an excellent match to the corresponding final steady state suction profile observed in the numerical analyses in all cases (see Figures 4-7 and 4-8 as examples).

2) As a consequence, the simplified semi-analytical method of Stormont and Morris (1998) for calculating the water storage capacity of a horizontal conventional CBS subjected to constant intensity rainfall produces results that agree very well with the corresponding results from the numerical analyses in all cases (see Figures 4-9 and 4-10). This represents a more comprehensive numerical validation of the simplified method of Stormont and Morris (1998) than previously reported in the literature.

3) For CBSs with the same thickness of finer layer, a CBS with the finer layer made of silty sand has significantly greater water storage capacity than a CBS with the finer layer made of fine sand, whatever the rainfall infiltration rate (see Figures 4-9 and 4-10). This is because when the finer layer is made of silty sand, high values of degree of saturation are achieved over a considerable thickness of the finer layer (see Figure 4-8b), whereas when the finer layer is made of fine sand, high values of degree of saturation are only achieved in a very limited thickness at the bottom of the finer layer (see Figure 4-7b).

4) For a CBS with a finer layer of a given thickness and made of a specified material, the water storage capacity is independent of rainfall infiltration rate i if the finer layer is relatively thin but increases with increasing i if the finer layer is thicker (see Figures 4-9a and 4-10a). This means that the value of water storage capacity (WSC) corresponding to a very low infiltration rate represents a conservative estimate of WSC, as noted by Scarfone (2020).

5) Increased water storage capacity can be achieved by using multi-layered CBSs (see Figure 4-13). This is particularly useful if the finer layers are made of fine sand, because, whereas little increase of storage capacity can be achieved by increasing the thickness of the finer layer of a conventional CBS beyond a certain thickness, increases of storage capacity can be achieved by adding additional finer layers.

6) The predictions of the simplified method of Scarfone (2020) for the water storage capacity of multi-layered CBSs are, in all cases, in excellent agreement with the corresponding results from the FE simulations. This is a more comprehensive numerical validation than has previously been achieved of the simplified semi-analytical method for calculation of WSC of multi-layered CBSs suggested by Scarfone (2020).

7) If the finer layers are made of fine sand, the optimum number of finer layers within a multi-layered CBS (to maximize WSC for a given total thickness of the CBS) is N = 5. If the finer layers are made of silty sand, the optimum number of finer layers is predicted by the simplified method to be N = 2. If excessive numbers of finer layers are included (above the optimum value), the low values of S_l within each intermediate coarser layer more than offset the high values of S_l achieved in the lower part of each finer layer.

8) Wetting of the F.L of a conventional horizontal CBS is a two-stage process. The first stage involves a wetting front moving downwards from the ground surface. Above the wetting front the soil of the F.L is partially wetted, at a suction $s = s_f^*$ and a corresponding degree of saturation. Once this initial partial wetting front reaches the bottom of the F.L, the second stage of wetting commences. This second stage involves further filling of the F.L. from

the bottom upwards. This continues until the suction at the bottom of F.L reaches $s = s_{BWC,c}$, at which point breakthrough occurs into the underlying C.L.

9) For a multi-layered CBS, each finer layer wets in turn, starting from the uppermost F.L, with wetting of any lower F.L only commencing once wetting of the F.L above is completed. Wetting of each F.L in a multi-layered CBS follows the same two-stage pattern as previously described for the wetting of a conventional CBS.

Chapter 5 Sloping CBSs subjected to continuous rainfall of constant intensity

This chapter presents numerical modelling of sloping CBSs subjected to continuous rainfall of constant intensity, together with development and numerical validation of a new simplified method for calculating water transfer capacity (and hence diversion length) and water storage capacity of sloping CBSs under different rainfall intensities.

The numerical modelling was performed with the advanced hydraulic constitutive model (modVG-modM+LF), developed by Scarfone (2020) and Scarfone et al. (2020a) and described in Section 2.4, and hence this numerical modelling represents an advance over most published work on numerical modelling of sloping CBSs (with the exception of Scarfone (2020) and Scarfone et al. (2022)). In addition, the numerical validation of the newly proposed simplified method is more comprehensive than any equivalent exercise previously reported in the literature.

The chapter starts (Section 5.1) with a review of an existing simplified method for calculating water transfer capacity (and hence diversion length) proposed by Parent and Cabral (2006), highlighting a fundamental weakness of this method. Section 5.2 then presents the development of a new simplified method for determining water transfer capacity, based on a more logical approach. Section 5.3 describes the numerical models used in the remainder of the chapter. This includes full geometry numerical models, involving the CBS and the underlying soil (CBS+US), and simplified geometry numerical models, involving only the CBS. In Section 5.4, the results of the full geometry and simplified geometry models are compared, to justify the use of only simplified geometry models throughout the rest of the chapter and Chapters 6 and 7. In Section 5.5 the new simplified method predictions of water storage capacity and water transfer capacity (and hence diversion length) are validated by comparing with the final steady state FE results. Section 5.6 presents the behaviour of sloping CBSs prior to final steady-state from the numerical modelling results. Numerical modelling of multi-layered sloping CBS is presented in Section 5.7, together with validation of the new

simplified method extended to multi-layered CBSs. Finally, Section 5.8 summarises the main conclusions of the work presented in the chapter.

5.1 Problem with existing simplified method for calculating water transfer capacity

As reviewed in Section 2.8.1, the performance of a CBS on a slope subjected to varying rainfall depends on both water storage capacity and water transfer capacity. Water storage capacity WSC under rainfall of constant intensity i can be calculated by integrating the final steady state volumetric water content over the finer layer thickness at a location on the slope where breakthrough has occurred (i.e. at or beyond the diversion length L_D). Water transfer capacity Q_{max} under rainfall of constant intensity i can be calculated by integrating the horizontal liquid water velocity q_h over a vertical cross-section through the finer layer of the CBS (taken at a location at or beyond the diversion length), as described in Section 2.8.2 and Equation 2-75:

$$Q_{max} = \int_0^{t_f} q_h \, dz \qquad \textbf{5-1}$$

The diversion length L_D can then be calculated from Equation 2-76:

$$L_D = Q_{max}/i \qquad \textbf{5-2}$$

The variation of horizontal seepage velocity q_h with z in Equation 5-1 will depend upon the steady state suction profile on the vertical cross-section corresponding to the diversion length (the same suction profile will also apply to all vertical cross-sections beyond the diversion length). According to Darcy's law:

$$q_h = -k_l \frac{\partial h_l}{\partial x} \qquad \textbf{5-3}$$

where the hydraulic conductivity k_l is a function of suction s and the horizontal hydraulic gradient $\frac{\partial h_l}{\partial x}$ (where x is the horizontal coordinate measured from the top of the slope) is also dependent on the suction profile on vertical cross-sections.

As described in Section 2.8.2, the existing simplified semi-analytical method of Parent and Cabral (2006) for predicting water transfer capacity Q_{max} (and hence diversion length L_D) calculates the variation of q_h with z by assuming an approximate steady state suction profile in the finer layer on vertical cross-sections at and beyond the diversion length that coincides with the approximate suction profile at breakthrough for a horizontal CBS (see Section 2.7.2 and Section 4.1). This approximate suction profile involves a hydrostatic suction gradient ($\frac{ds}{dz} = \gamma_l$) in the lower part of the finer layer (see Figure 5-1a). This results in the following expression (Equation 2-85) for the horizontal hydraulic gradient in this lower part of the finer layer:

$$\frac{\partial h_l}{\partial x} = -\tan\beta \qquad \textbf{5-4}$$

where β is the slope angle. The derivation of Equation 5-4 is illustrated in Figure 5-1b, which shows two points in this lower part of the F.L, A and A', both at the same elevation and both at values of x at or beyond the diversion length, but separated by a horizontal distance Δx. If z_A is the vertical height of point A above the interface with the C.L, then point A' is a vertical height ($z_A + \Delta x \tan\beta$) above the interface. Hence, the values of suction at points A and A' (s_A and $s_{A'}$ respectively) are given by:

$$s_A = s_1 + \gamma_l z_A \qquad \textbf{5-5}$$

$$s_{A'} = s_1 + \gamma_l(z_A + +\Delta x \tan\beta) \qquad \textbf{5-6}$$

The horizontal hydraulic gradient between points A and A' is therefore given by:

$$\frac{\partial h_l}{\partial x} = -\frac{1}{\gamma_l}\frac{\partial s}{\partial x} = \frac{-(s_{A'} - s_A)}{\gamma_l \Delta x} = -\tan\beta \qquad \textbf{5-7}$$

In the upper part of the finer layer, where the assumed approximate suction profile involves a constant value of suction s_f^* (see Figure 5-1a), the corresponding predicted horizontal hydraulic gradient is zero. This is clear from examination of Figure 5-1b, where the horizontal hydraulic gradient between two points B and

B', both at the same elevation and both in the upper part of the F.L, where s = s_f^*, is given by:

$$\frac{\partial h_l}{\partial x} = \frac{(s_B - s_{B'})}{\gamma_l \Delta x} = 0 \qquad \text{5-8}$$

Hence, there is no horizontal flow (q_h= 0) predicted in this upper part of the finer layer.

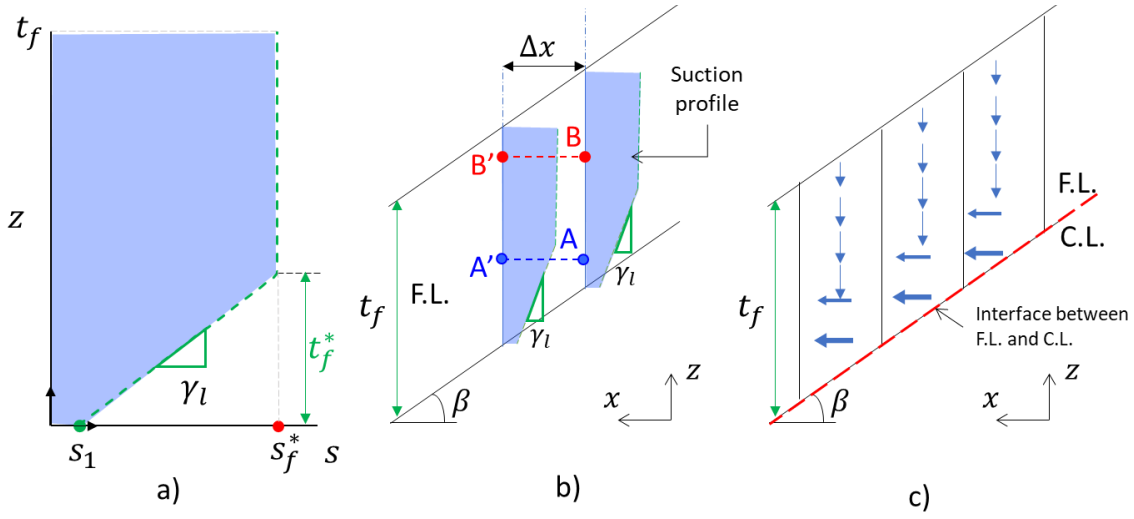

Figure 5-1 Simplified suction profile assumed by Parent and Cabral (2006): a) suction profile; b) determination of horizontal hydraulic gradient; c) predicted flow directions

Equations 5-7 and 5-8 result in the following expression (see Equation 2-87) for the water transfer capacity Q_{max}:

$$Q_{max} = \frac{\tan\beta}{\gamma_l} \int_{s_1}^{s_2} k_l \, ds \qquad \text{5-9}$$

where s_1 is the suction at the bottom of the finer layer at the time of breakthrough (the bulk water continuity suction of the coarser layer, $s_{BWC,c}$) and s_2 is the suction at the top of the finer layer, which, with this assumed suction profile, is given by either $s_1 + \gamma_l t_f$ or s_f^*, whichever is the smaller. The simplified method of Parent and Cabral (2006) for calculating water transfer capacity is described as "semi-analytical", because most SHCC expressions (relating k_l to s) cannot be integrated analytically, and hence the integration in Equation 5-9 must be performed numerically.

Unfortunately, the approximate suction profile assumed in the simplified semi-analytical method of Parent and Cabral (2006), leading to Equation 5-9, while realistic for a horizontal CBS, is physically unreasonable for a sloping CBS, because it implies an illogical flow direction in the lower part of the F.L. In this lower part of the F.L, the hydrostatic suction profile ($\frac{\partial s}{\partial z} = \gamma_l$, i.e. $\frac{\partial h_l}{\partial z} = 0$) assumed on each vertical cross-section implies no flow in the vertical direction, and hence the predicted vertical and horizontal water velocities in this region are given by:

$$q_v = 0 \qquad \textbf{5-10}$$

$$q_h = k_l \tan\beta \qquad \textbf{5-11}$$

For a horizontal CBS, the assumption $\frac{\partial h_l}{\partial z} = 0$ (which leads to Equation 5-10) is a reasonable approximation to the true situation ($q_v = i$), because the rainfall intensity i is much less than the hydraulic conductivity k_l in this high degree of saturation region at the bottom of the F.L. However, the combination of Equation 5-10 and Equation 5-11 is physically unreasonable for a sloping CBS, because it implies horizontal flow in the lower part of the F.L, as shown in Figure 5-1c. This horizontal flow would imply a lack of continuity of flow between adjacent vertical slices of the CBS (as shown in Figure 5-1c) and continuous flow of water across the interface, from the C.L to F.L (i.e. in the wrong direction across the interface). A more realistic approximation rather than horizontal flow in the lower part of the F.L, would be inclined flow, parallel to the interface ($\frac{q_v}{q_h} = \tan\beta$), in the lower part of the F.L. The vertical flow predicted in the upper part of the F.L (see Figure 5-1c) is, however, a reasonable approximation. In this upper part of the F.L, the predicted water velocities in horizontal and vertical direction are:

$$q_v = i \qquad \textbf{5-12}$$

$$q_h = 0 \qquad \textbf{5-13}$$

It should be noted that, quite correctly, the magnitude of the vertical velocity in the upper part of F.L, from Equation 5-12, which is transferring only the rainfall infiltrating above, is much smaller than the predicted horizontal water velocity in

the lower part of the F.L, from Equation 5-11, which is transferring all the rainfall infiltrating on the upper part of the slope (from the top of the slope to the diversion length L_D).

5.2 Development of a new simplified method

This section presents a proposal for a more physically realistic simplified suction profile in the F.L (corresponding to final steady state at vertical cross-sections at or beyond the diversion length), together with corresponding development of a revised simplified method for calculating water transfer capacity (and hence diversion length) and water storage capacity.

The new proposal for a simplified suction profile is based on the simplified flow pattern shown in Figure 5-2c. This involves flow parallel to the interface in the lower part of the F.L and vertical flow in the upper part of the F.L. Inclined flow, parallel to the interface, at the bottom of the F.L is rigorously true for values of x less than the diversion length (i.e. the upper part of the slope, where breakthrough is not occurring). However, inclined flow parallel to the interface is also approximately true at the bottom of the F.L for the lower part of the slope where breakthrough is occurring ($x \geq L_D$). An assumption of inclined flow parallel to the interface in the bottom part of the F.L for $x \geq L_D$ is much more realistic than the horizontal flow in the lower part of the F.L implied by the simplified suction profile assumed by Parent and Cabral (2006). In reality, at locations in the CBS at or beyond the diversion length (i.e. where breakthrough is occurring), flow at the bottom of the F.L will involve two components: a large component of velocity parallel to the interface (it is this component that is transferring down the slope the rainfall infiltration on the upper section of the slope, from the top of the slope to the diversion length); and a much smaller component of velocity perpendicular to the interface (the breakthrough flow). The vertical component of this velocity perpendicular to the interface must be equal to the rainfall infiltration rate i (this is simply transferring across the interface the rainfall infiltration on the part of the slope surface directly above). Provided that the diversion length L_D is much greater than the thickness of the lower part of the F.L over which the inclined flow down the slope is occurring, the velocity component parallel to the interface must be much larger than the velocity component perpendicular to the interface. This statement is justified in Appendix B. This

should always be the case for well-designed CBSs, and hence the assumption that flow at the bottom of the F.L is parallel to the interface is a good approximation.

Figure 5-2a shows the proposed simplified suction profile corresponding to the assumed simplified flow pattern shown in Figure 5-2c. The suction at the bottom of the F.L is given by $s = s_1 = s_{BWC,c}$ (the same as assumed by Parent and Cabral (2006)). In the lower part of the F.L, a linear variation of suction is assumed on each vertical cross-section, given by:

$$\frac{\partial s}{\partial z} = \alpha\gamma_l \qquad \textbf{5-14}$$

where α is a constant. The challenge now is to derive an expression for α that corresponds to inclined flow parallel to the interface. In the upper part of the F.L (if it is sufficiently thick), the proposed simplified suction profile involves a constant value of suction s_f^* (the same as assumed by Parent and Cabral (2006)).

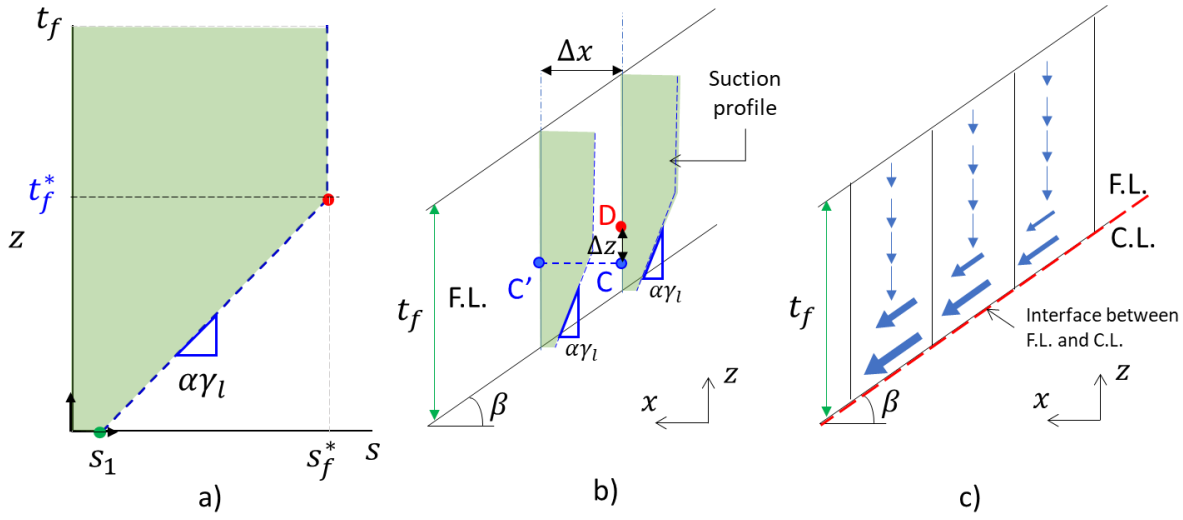

Figure 5-2 New proposal for simplified suction profile: a) suction profile; b) determination of horizontal and vertical hydraulic gradients; c) predicted flow directions

In order to derive an expression for the factor α in Equation 5-14, values of hydraulic gradient in vertical and horizontal directions, within the lower part of F.L, need to be calculated, using Figure 5-2b. The vertical hydraulic gradient is calculated by considering two points C and D, in the lower part of F.L, at the same value of x but separated by a vertical distance Δz. Considering the fundamental definition of hydraulic head h_l (see Equation 2-24), the vertical hydraulic gradient can be related to the vertical suction gradient by:

$$\frac{\partial h_l}{\partial z} = 1 - \frac{1}{\gamma_l}\frac{\partial s}{\partial z} \quad \textbf{5-15}$$

Therefore, for the simplified suction profile shown in Figure 5-2:

$$\frac{\partial h_l}{\partial z} = 1 - \frac{s_D - s_C}{\gamma_l \Delta z} = 1 - \alpha \quad \textbf{5-16}$$

Then by considering two points C and C' at the same elevation, but separated by a horizontal distance Δx (see Figure 5-2b), the horizontal hydraulic gradient is given by:

$$\frac{\partial h_l}{\partial x} = -\frac{1}{\gamma_l}\frac{\partial s}{\partial x} = \frac{-(s_{C'} - s_C)}{\gamma_l \Delta x} = -\alpha \tan\beta \quad \textbf{5-17}$$

Water velocities in vertical and horizontal directions, q_v and q_h, within the lower part of F.L are then given, from Darcy's law applied to Equations 5-16 and 5-17, as:

$$q_v = k_l(1 - \alpha) \quad \textbf{5-18}$$

$$q_h = k_l \alpha \tan\beta \quad \textbf{5-19}$$

where q_v is taken as positive downwards (i.e. in the opposite direction to the z axis) whereas q_h is taken as positive in the downslope direction (i.e. in the same direction as the x axis).

If the flow in the lower part of the F.L is parallel to the interface, then, within this part of the F.L:

$$\frac{q_v}{q_h} = \tan\beta \quad \textbf{5-20}$$

Inserting Equations 5-18 and 5-19 in Equation 5-20 gives the required expression for α:

$$\alpha = \frac{1}{1 + \tan^2\beta} \quad \textbf{5-21}$$

Using a standard trigonometric expression:

$$1 + \tan^2 \beta = \sec^2 \beta = \frac{1}{\cos^2 \beta} \quad \textbf{5-22}$$

Hence, Equation 5-21 can be re-written as:

$$\alpha = \cos^2 \beta \quad \textbf{5-23}$$

Inserting the expression for α from Equation 5-23 into Equations 5-18 and 5-19 shows that the new approximate suction profile leads to the following expressions for vertical and horizontal seepage velocities within the lower part of the finer layer:

$$q_v = k_l \sin^2 \beta \quad \textbf{5-24}$$

$$q_h = k_l \sin \beta \cos \beta \quad \textbf{5-25}$$

The new approximate suction profile suggests that the inclined flow (parallel to the slope) will occur over the lower part of the finer layer, over a thickness t_f^* (see Figure 5-2a) that is given by:

$$t_f^* = \frac{s_f^* - s_1}{\alpha \gamma_l} = \frac{s_f^* - s_1}{\gamma_l \cos^2 \beta} \quad \textbf{5-26}$$

In contrast, the approximate suction profile assumed by Parent and Cabral (2006), shown in Figure 5-1a, suggests that horizontal flow occurs over a smaller thickness:

$$t_f^* = \frac{s_f^* - s_1}{\gamma_l} \quad \textbf{5-27}$$

Note that both approximations assume that in the upper part of the finer layer, above a height t_f^*, the flow is vertical ($q_h = 0$, $q_v = i$). This upper part of the finer layer therefore makes no contribution to the water transfer capacity Q_{max}.

Use of the new approximate suction profile, together with the corresponding expression for q_h from Equation 5-25, within the expression of Equation 5-1 for the water transfer capacity Q_{max} leads to the following result:

$$Q_{max} = \frac{\tan\beta}{\gamma_l}\int_{s_1}^{s_4} k_l \, ds \qquad \textbf{5-28}$$

where s_4 is the new expression for the value of suction at the top of the finer layer (either $s_1 + \alpha\gamma_l t_f$ or s_f^*, whichever is the smaller). Note that, whereas Equations 5-25 and 5-11 indicate that the proposed new semi-analytical method predicts significantly different variations of horizontal seepage velocity q_h with z to the existing method of Parent and Cabral (2006), the final expressions for the water transfer capacity Q_{max} (Equations 5-28 and 5-9) are very similar. The only difference is the upper limit of suction (s_4 or s_2) in the integration. For high rainfall infiltration rates or thick finer layers (thicker than the value of t_f^* given by Equation 5-26, the values of s_4 and s_2 are identical (in this case, both s_4 and s_2 are equal to s_f^*) and the two semi-analytical methods predict identical values of water transfer capacity Q_{max}. For low infiltration rates or thinner finer layers, the proposed new semi-analytical method predicts lower values of Q_{max} than the existing semi-analytical method of Parent and Cabral (2006).

Figure 5-3 compares, for sloping CBSs with the finer layer made of fine sand, values of water transfer capacity Q_{max} predicted by the two simplified methods, with predictions of the Parent and Cabral (2006) simplified method shown by dotted lines and predictions of the new simplified method shown by dashed lines. The figure shows the predicted variations of Q_{max} with finer layer thickness t_f for the two simplified methods.

Figure 5-3a shows the influence of rainfall intensity i on the predicted values of Q_{max}, by presenting (for the case of slope angle $\beta = 35^{\circ}$) results for $i = 10^{-6}$m/s (blue lines) and $i = 5$x10^{-6}m/s (green lines). These two values of rainfall intensity were selected because they were the rainfall intensities subsequently investigated in the corresponding numerical simulations (see Section 5.3 for the justification of these selected values). The blue lines ($i = 10^{-6}$m/s) are not visible in Figure 5-3a, because they are hidden behind the corresponding green lines ($i = 5$x10^{-6}m/s),

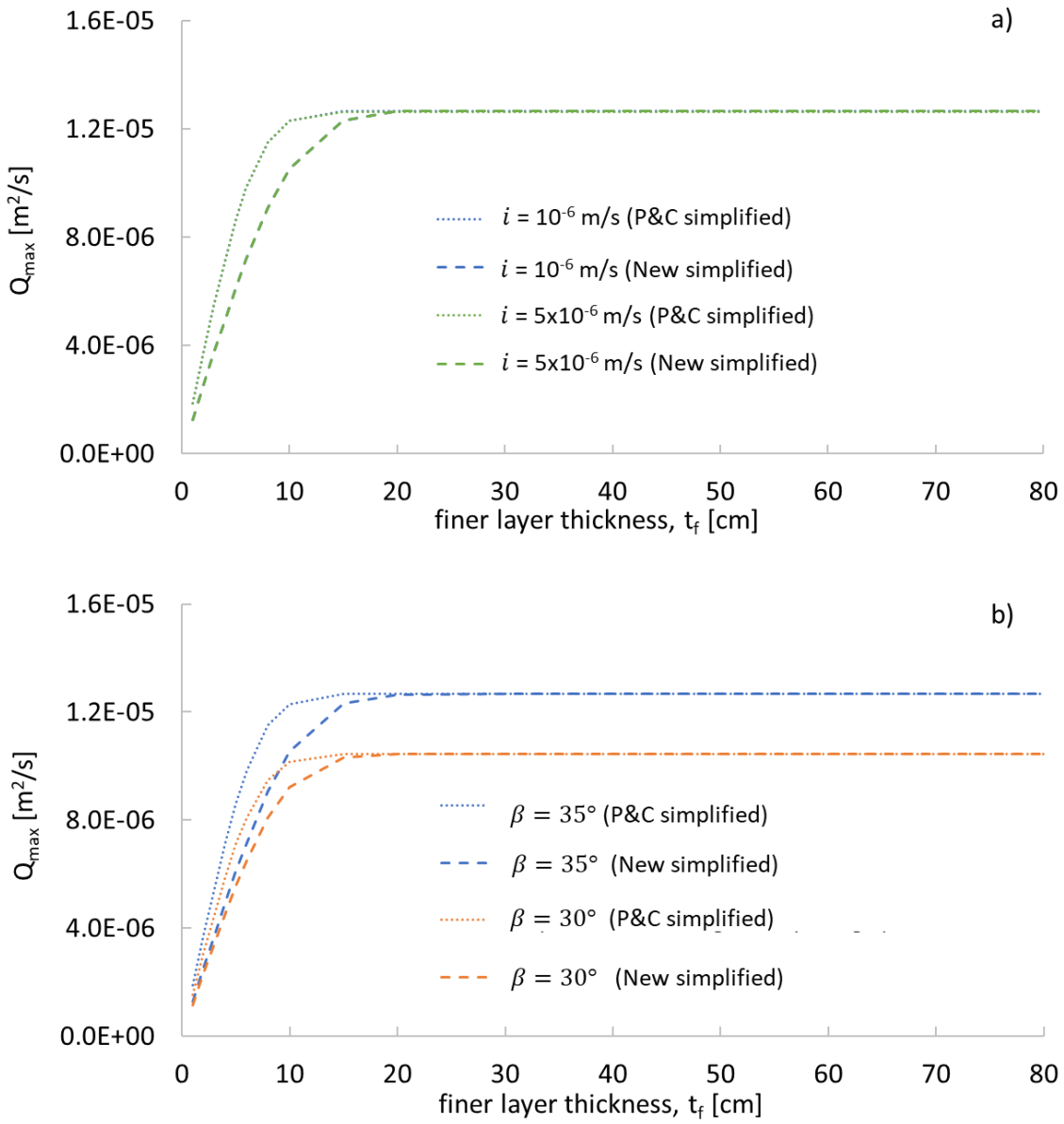

Figure 5-3 Predicted water transfer capacity Q_{max} of sloping CBSs with F.L made of fine sand: comparison of two simplified methods a) influence of rainfall intensity ($\beta = 35°$); b) influence of slope angle (i = 10⁻⁶ m/s)

showing that rainfall intensity has insignificant effect on predicted water transfer capacity of a sloping CBS when the finer layer is made of fine sand. This is true over the full range of conceivable rainfall intensities and is a consequence of the water transfer all taking place in the lowest part of the finer layer, where the predicted suction profile (for both simplified methods) is independent of rainfall intensity. Further inspection of Figure 5-3a shows that, if the finer layer is made of fine sand, the two simplified methods predict identical values of Q_{max} when the finer layer thickness t_f is greater than about 20cm, corresponding to the critical thickness t_f^* given by Equation 5-26. For values of t_f less than about 20cm, the new simplified method predicts lower values of Q_{max} than the simplified

method of Parent and Cabral (2006). It is notable that the simplified method of Parent and Cabral (2006) suggests that there is no benefit (in terms of increased water transfer capacity) in increasing the thickness of a finer layer made of fine sand beyond about 15cm, whereas the new simplified method suggests that there is benefit in increasing the finer layer thickness up to about 20cm.

Figure 5-3b shows the influence of slope angle β on the predicted values of Q_{max}, by presenting (for the case of rainfall intensity $i = 10^{-6}$m/s) results for $\beta = 30^{\circ}$ (orange lines) and $\beta = 35^{\circ}$ (blue lines). These two values of slope angle were selected because they were the slope angles subsequently investigated in the corresponding numerical simulations (see Section 5.3 for justification). Inspection of Figure 5-3b shows that both simplified methods predict that water transfer capacity Q_{max} increases with increasing slope angle.

Figure 5-4 shows the corresponding predictions of Q_{max} from the two simplified methods for sloping CBSs if the finer layer made of silty sand. The rainfall intensities ($i = 10^{-6}$m/s and $i = 2\text{x}10^{-7}$m/s in Figure 5-4a) and slope angles ($\beta = 30^{\circ}$ and $\beta = 35^{\circ}$) used in Figure 5-4 are again the values used subsequently in the corresponding numerical simulations (see Section 5.3 for justification). Comparison of Figure 5-4 with Figure 5-3 shows that, according to both simplified methods, any sloping CBS with the finer layer made of silty sand has significantly lower water transfer capacity Q_{max} than a corresponding CBS with the finer layer made of fine sand, as reported by Scarfone (2020).

Inspection of Figures 5-4a and 5-4b shows that the simplified method of Parent and Cabral (2006) predicts that, for a sloping CBS with the finer layer made of silty sand, Q_{max} increases with increasing finer layer thickness t_f up to a thickness of about 60cm, whereas the new simplified method predicts that Q_{max} increases with increasing t_f up to a thickness of more than 80cm. For all values of t_f up to at least 80cm, the new simplified method predicts lower values of Q_{max} than the simplified method of Parent and Cabral (2006). Comparing with Figure 5-3, it is clear that, according to either simplified method, greater thickness of finer layer is appropriate if the finer layer is made of silty sand than if the finer layer is made of fine sand.

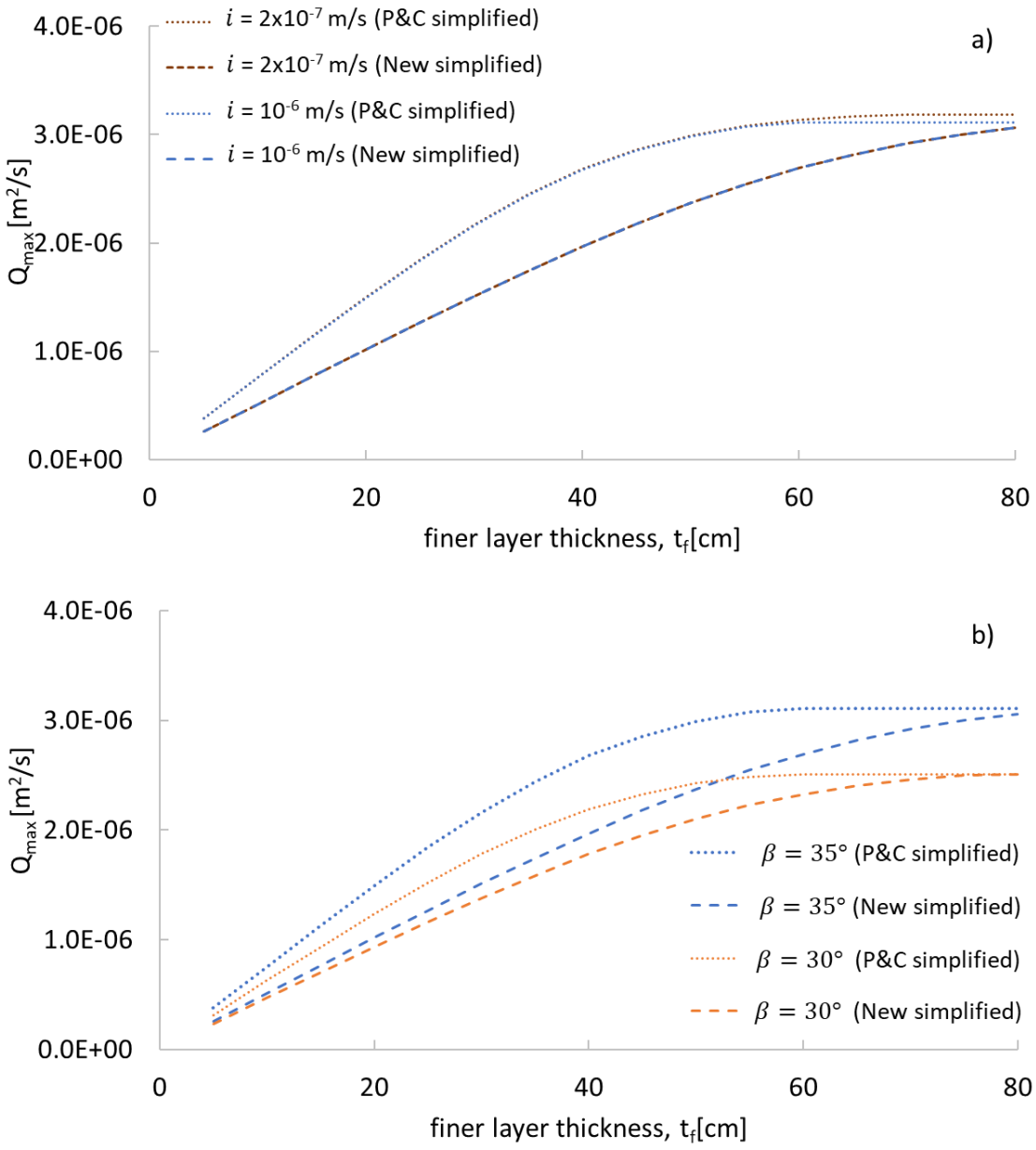

Figure 5-4 Predicted water transfer capacity Q_{max} of sloping CBSs with F.L made of silty sand: comparison of two simplified methods a) influence of rainfall intensity (β=35°); b) influence of slope angle (i = 10^{-6} m/s)

Figure 5-4a shows that, for sloping CBSs with the finer layer made of silty sand, up to a finer layer thickness of about 60cm, the simplified method of Parent and Cabral (2006) predicts no influence of rainfall intensity (the blue dotted line for $i = 10^{-6}$m/s and the brown dotted line for $i =$ 2x10^{-7}m/s coincide), but the predicted value of Q_{max} decreases slightly with increasing rainfall intensity (the blue dotted line is slightly below the brown dotted line) if the finer layer thickness is greater than about 60cm. In Figure 5.4a, there is no evidence of any influence of rainfall intensity on the predictions of Q_{max} from the new simplified method (the brown dashed line is invisible behind the bule dashed line over the full range of t_f), but a very slight influence of rainfall intensity would be apparent for very

thick finer layers at very extreme (unrealistically high) values of rainfall intensity. Comparing Figure 5-4a with Figure 5-3a, it can be seen that, for a sloping CBS with a very thick finer layer, there may be a small influence of rainfall intensity on predicted values of Q_{max} if the finer layer is made of silty sand, whereas there is no influence of rainfall intensity if the finer layer is made of fine sand. This is a consequence of the fact that water transfer occurs over a much greater thickness of the finer layer when the finer layer is made of silty sand, whereas the water transfer is restricted to only a very thin zone at the base of the finer layer if the finer layer is made of fine sand (see results presented in Section 5.5). For the case of a very thick finer layer made of silty sand, the water transfer may extend far enough up the finer layer to reach a region where the suction profile is affected by rainfall intensity.

Figure 5-4b confirms that, according to both simplified methods, water transfer capacity Q_{max} increases with increasing slope angle β.

Whereas the proposed new simplified method predicts values of water transfer capacity Q_{max} that are either the same or lower than those predicted by the method of Parent and Cabral (2006) (depending on whether the F.L thickness t_f is greater or less than the critical value of t_f^* of Equation 5-26), the new method always predicts values of water storage capacity WSC that are the same or greater than those predicted by Parent and Cabral (2006). For a sloping CBS, Parent and Cabral (2006) predict values of WSC that are identical to those for a horizontal CBS, given in Equation 4-7 (if t_f is less than the value of t_f^* from Equation 5-27) or Equation 4-8 (if t_f is more than the value of t_f^* from Equation 5-27). In contrast, the new method predicts that for values of t_f greater than t_f^* (now given by Equation 5-26):

$$WSC = \frac{\Phi}{\alpha\gamma_l}\int_{s_1}^{s_4} S_l \, ds \qquad \textbf{5-29}$$

where $s_1 = s_{BWC,c}$ and $s_4 = s_1 + \alpha\gamma_l t_f$. For values of t_f greater than t_f^* (given by Equation 5-26), the new method predicts:

$$WSC = \frac{\Phi}{\alpha\gamma_l}\int_{s_1}^{s_f^*} S_l\, ds + \Phi S_l\left(s_f^*\right)\left(t_f - t_f^*\right) \quad \textbf{5-30}$$

where $S_l\left(s_f^*\right)$ is the value of degree of saturation at a suction value s_f^* and t_f^* is the critical thickness given by Equation 5-26. It is interesting to note that the new method predicts higher values of WSC for a sloping CBS than for the equivalent horizontal CBS. It should also be noted that, for either the conventional simplified method of Parent and Cabral (2006) or the proposed new simplified method, for a sloping CBS, values of F.L thickness t_f (in Equations 4-8 and 5-30) are measured vertically, rather than perpendicular to the slope.

The variation of water storage capacity (WSC) with finer layer thickness t_f, rainfall intensity i and slope angle β predicted by the two simplified methods are illustrated in Figure 5-5 (finer layer made of fine sand) and Figure 5-6 (finer layer made of silty sand).

Comparison of Figures 5-5 and 5-6 shows that, according to both simplified methods, any sloping CBS with the finer layer made of silty sand has significantly greater water storage capacity WSC than a corresponding CBS with the finer layer made of fine sand, as reported by Scarfone (2020). According to both simplified methods, WSC increases with increasing finer layer thickness t_f over the full range of t_f shown in the figures. Values of WSC predicted by the two methods are identical at low values of t_f (up to about t_f = 8 cm if the finer layer is made of fine sand (Figure 5-5) or up to about t_f = 40 cm if the finer layer is made of silty sand (Figure 5-6)), whereas the new simplified method predicts greater values of WSC than the simplified method of Parent and Cabral (2006) for thicker finer layers.

Figure 5-5a shows that both simplified methods predict that WSC increases significantly with increasing rainfall intensity if the finer layer is made of fine sand. In contrast, Figure 5-6a shows that, when the finer layer is made of silty sand, the Parent and Cabral (2006) simplified method predicts only slight influence of rainfall intensity on WSC and according to the new simplified method the influence of rainfall intensity on WSC is so small that it is not visible.

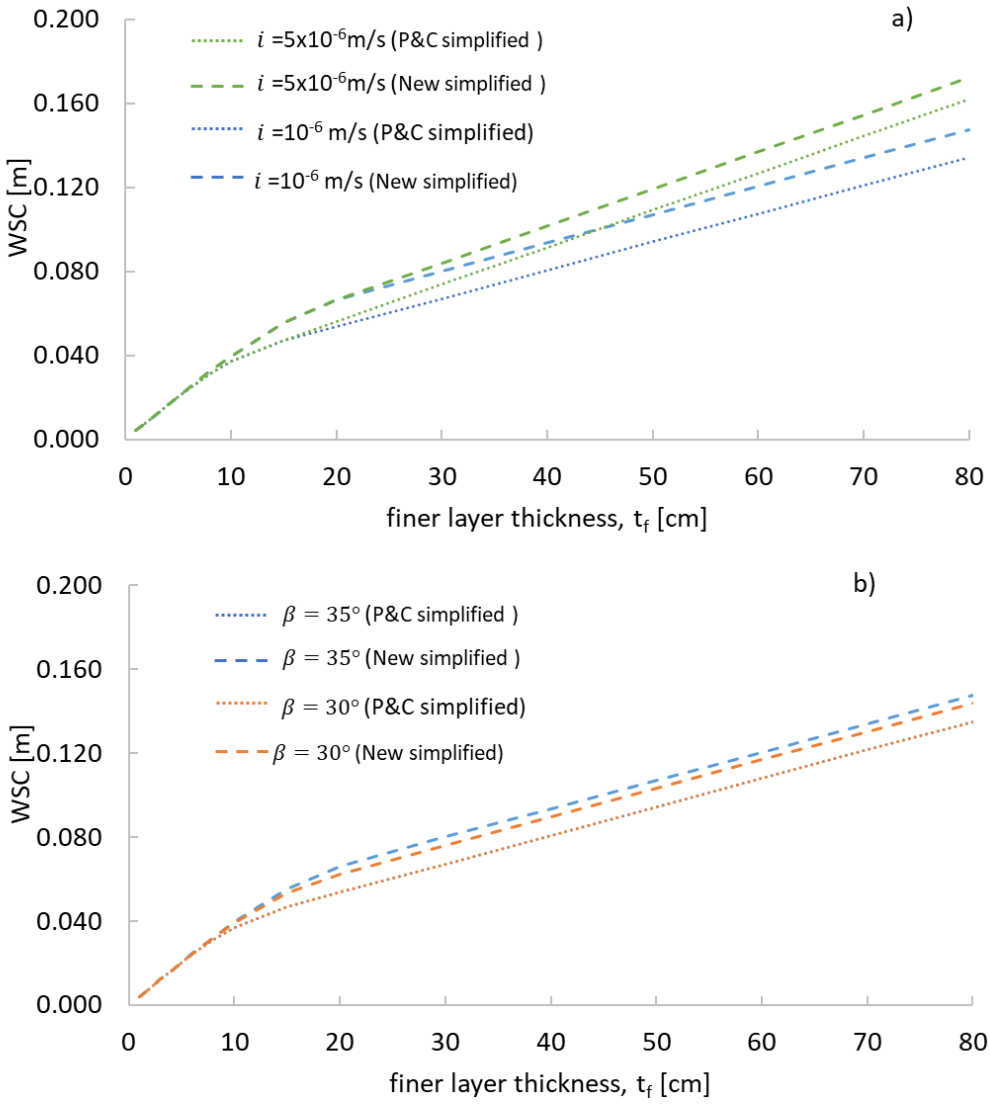

Figure 5-5 Predicted water storage capacity WSC of sloping CBSs with F.L made of fine sand: comparison of two simplified methods a) influence of rainfall intensity (β=35°); b) influence of slope angle i = 10^{-6} m/s

Figures 5-5b and 5-6b show that the Parent and Cabral (2006) simplified method predicts no influence of slope angle β on water storage capacity WSC, whereas the new simplified method predicts that WSC increases slightly with increasing slope angle, at least for higher values of finer layer thickness t_f.

5.3 Numerical model of sloping CBSs

2-D hydraulic numerical simulations were performed to validate the new simplified semi-analytical method for calculating water transfer capacity (and hence diversion length) and water storage capacity, including comparing with the predictions of the existing simplified semi-analytical method of Parent and Cabral

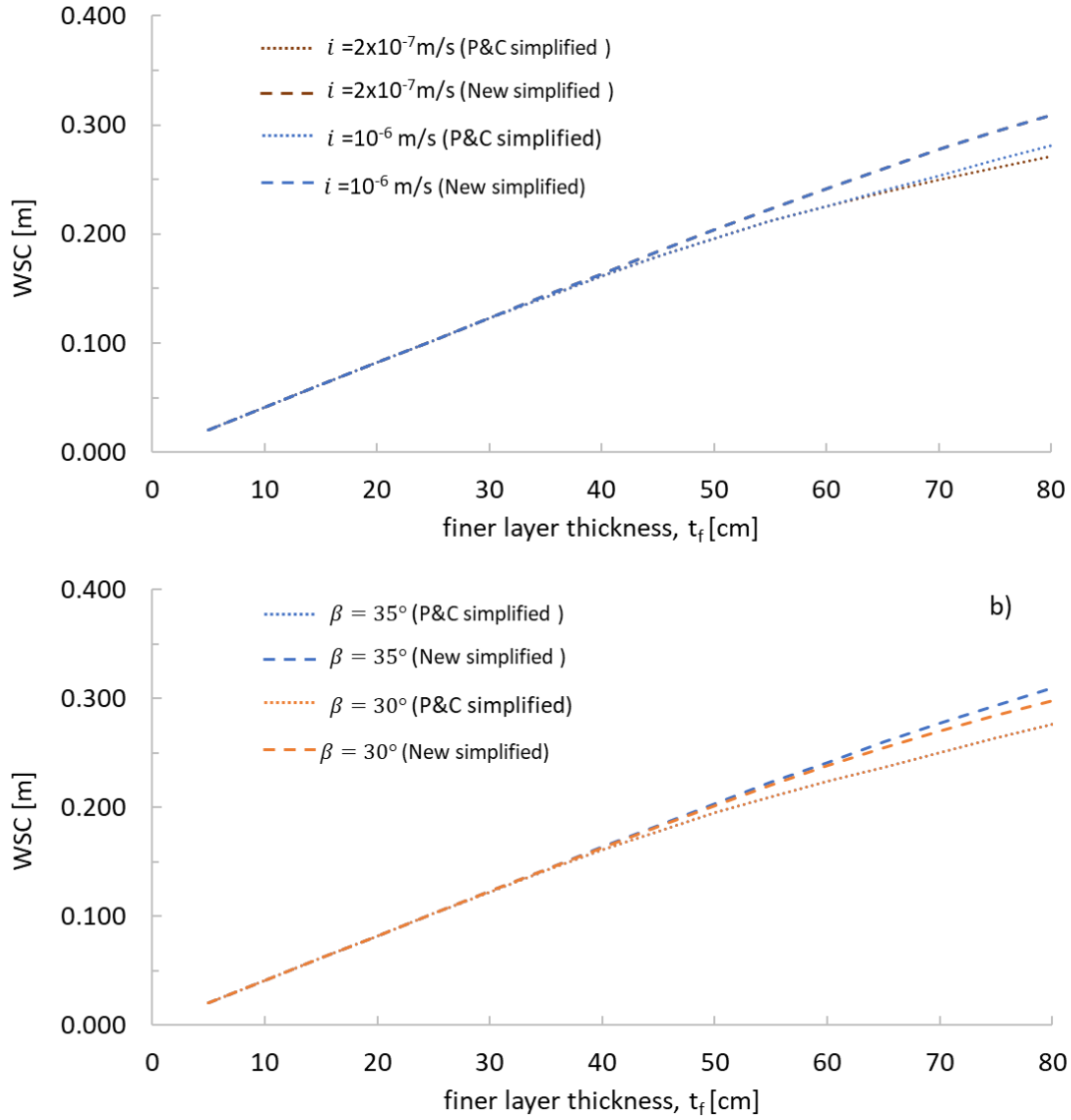

Figure 5-6 Predicted water storage capacity WSC of sloping CBSs with F.L made of silty sand: comparison of two simplified methods a) influence of rainfall intensity (β=35°); b) influence of slope angle (i = 10^{-6} m/s)

(2006). This involved an appropriate parametric study, comprising a total twenty-seven numerical simulations.

The numerical analyses were performed using the advanced hydraulic constitutive model (modVG-modM+LF) of Scarfone (2020) and Scarfone et al. (2020a), described in Section 2.4. Hydraulic hysteresis was not considered for the simulations in this chapter. In the analyses, the solid phase was considered as non-deformable and the gas phase as non-mobile. This means that there was no displacement of the solid phase ($\boldsymbol{u} = 0$) and pressure of the gas phase was uniform and constant (p_g = 100 kPa). Thermal numerical modelling was not considered. Thus, isothermal conditions were imposed with a constant uniform temperature

(T=20°C), implying negligible diffusion of water vapour and no evaporation from the slope surface.

The main parametric study varied the key parameters of slope angle β, rainfall intensity i, material of finer layer and thickness of F.L t_f (see Table 5-1). Further numerical simulations analysed multi-layered sloping CBSs (see Table 5-2 and Section 5.7).

Table 5-1 Finite element numerical simulations of sloping conventional CBSs

No	Analysis Identifier	F.L.	t_f (m)	U.S.	i (m/s)	β (°)
	Model type A (full geometry model)					
1	A_FSGV_F40i106S35	FS	0.4	S	10^{-6}	35
2	A_FSGV_F80i106S35	FS	0.8	S	10^{-6}	35
3	A_FSGV_F40i506S35	FS	0.4	S	$5x10^{-6}$	35
4	A_FSGV_F80i506S35	FS	0.8	S	$5x10^{-6}$	35
5	A_FSGV_F80i106S30	FS	0.8	S	10^{-6}	30
6	A_SSGV_F40i207S35	SS	0.4	S	$2x10^{-7}$	35
7	A_SSGV_F80i207S35	SS	0.8	S	$2x10^{-7}$	35
8	A_SSGV_F40i106S35	SS	0.4	S	10^{-6}	35
9	A_SSGV_F80i106S30	SS	0.8	S	10^{-6}	35
10	A_SSGV_F80i106S30	SS	0.8	S	10^{-6}	30
	Model type B (simple geometry model)					
11	B_FSGV_F10i106S35	FS	0.1	-	10^{-6}	35
12	B_FSGV_F40i106S35	FS	0.4	-	10^{-6}	35
13	B_FSGV_F80i106S35	FS	0.8	-	10^{-6}	35
14	B_FSGV_F20i506S35	FS	0.2	-	$5x10^{-6}$	35
15	B_FSGV_F40i506S35	FS	0.4	-	$5x10^{-6}$	35
16	B_FSGV_F80i506S35	FS	0.8	-	$5x10^{-6}$	35
17	B_FSGV_F80i106S30	FS	0.8	-	10^{-6}	30
18	B_SSGV_F40i207S35	SS	0.4	-	$2x10^{-7}$	35
19	B_SSGV_F80i207S35	SS	0.8	-	$2x10^{-7}$	35
20	B_SSGV_F20i106S35	SS	0.2	-	10^{-6}	35
21	B_SSGV_F40i106S35	SS	0.4	-	10^{-6}	35
22	B_SSGV_F80i106S35	SS	0.8	-	10^{-6}	35
23	B_SSGV_F80i106S30	SS	0.8	-	10^{-6}	30
24	B_MSGV_F40i106S35	MS	0.4	-	10^{-6}	35
25	B_CSGV_F40i106S35	CS	0.4	-	10^{-6}	35

Table 5-2 Finite element numerical simulations of sloping multi-layered CBSs

No	Analysis Identifier	F.L.	t_f (m)	No. of F.L.	C.L.	t_c (m)	i (m/s)	β (°)
14	B_FSGV_F20i506S35	FS	0.2	1	GV	0.2	$5x10^{-6}$	35
26	2M_FSGV_F20i506S35	FS	0.2	2	GV	0.2/0.05*	$5x10^{-6}$	35
20	B_SSGV_F20i106S35	SS	0.2	1	GV	0.2	10^{-6}	35
27	2M_SSGV_F20i106S35	SS	0.2	2	GV	0.2/0.05*	10^{-6}	35

0.05* m is the thickness of the intermediate coarser layer

5.3.1 Geometry and mesh

Two different types of two-dimensional model were analysed: "full geometry" models which consisted of the CBS and the underlying soil (Model type A) (see Figures 5-7a and 5-7b) and "simple geometry" model which included only the CBS (Model type B) (see Figure 5-7c). The intention was to investigate whether results from Model type B (only CBS) were always very similar to results from Model type A (CBS+US). If so, this would allow subsequent more demanding thermo-hydraulic numerical modelling (with atmosphere boundary conditions), described in Chapter 6, to be conducted using only the simple type of model (Model type B), thus avoiding excessive computational run times.

For both "full geometry" and "simple geometry" models, the numerical models did not extend horizontally beyond the top of the slope or the bottom of the slope (see Figures 5-7a, 5-7b, and 5-7c). This was intentional. The real situation in the field would typically involve horizontal ground surfaces extending from the top and bottom of the slope, with the CBS continued a short distance along each of these surfaces. It was decided, however, in the numerical analyses described in Chapters 5, 6, and 7, to ignore the potential complexities introduced by these features at the top and bottom of the slope. This was partly to avoid introducing further variables into the parametric study (e.g. the precise length and geometry of the section of CBS extending along the horizontal ground surface at the top of the slope). It was also to ensure that the geometry of the numerical models was more consistent with the geometry implicitly assumed in the existing and new simplified methods of analysis described in Sections 5.1 and 5.2. The practical issue of how to account, within the new simplified method, for the influence of the section of CBS extending along the horizontal ground surface at the top of the slope is considered further in Section 8.3. Omission of any horizontal ground surface at the bottom of the slope, within the numerical modelling, was less significant, because all numerical simulations were performed for situations where breakthrough was expected within the slope (i.e. the horizontal extent of the slope was greater than the expected diversion length, see Section 5.3.3). Provided the diversion length was significantly shorter than the horizontal extent of the slope, the unrealistic boundary at the base of the slope was expected to have little influence on the modelling of breakthrough further up the slope.

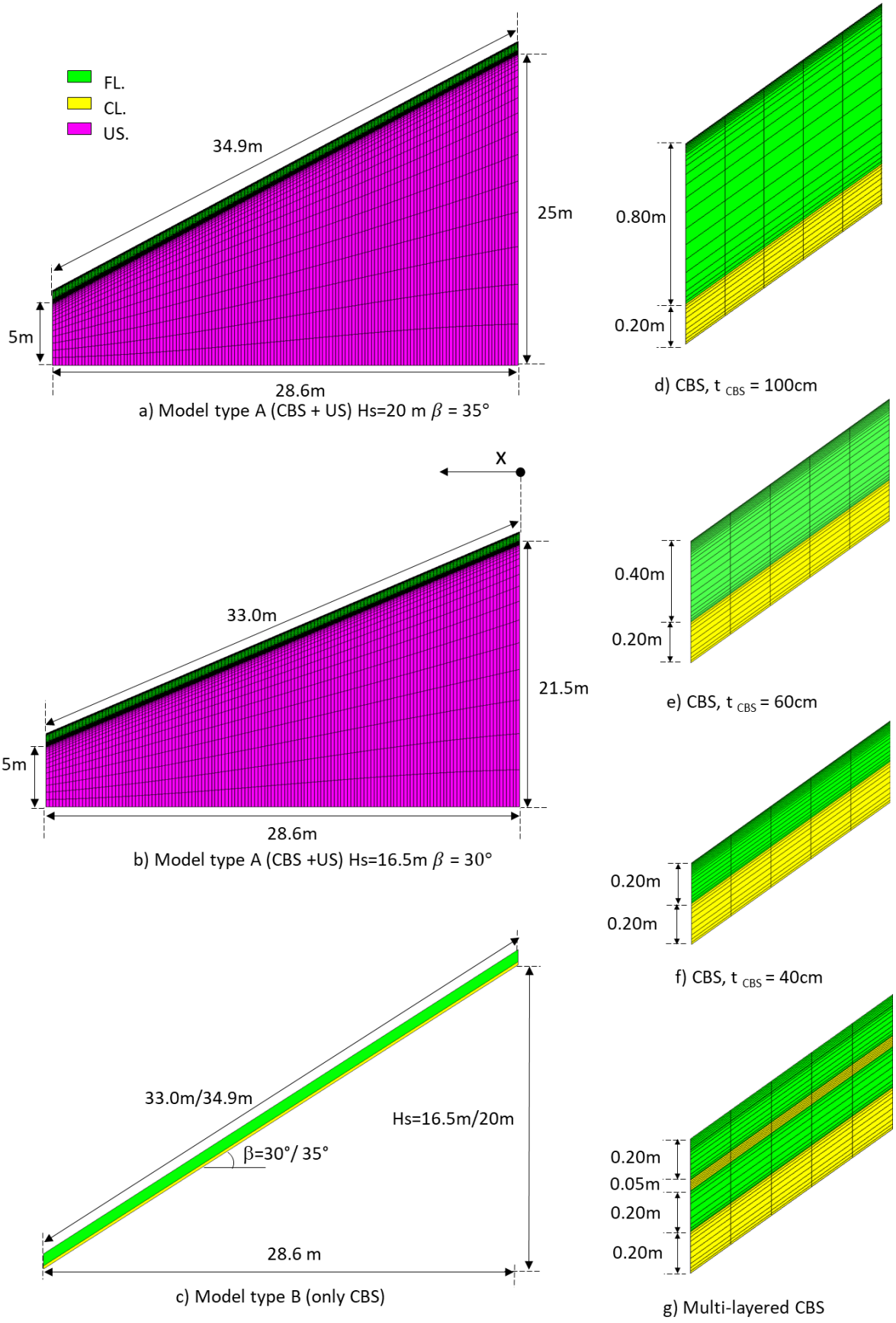

Figure 5-7 Geometry of numerical models and finite element mesh

Two different values of slope angle β were studied. As indicated in Table 5-1, the majority of analyses were performed with β = 35°, and the influence of slope angle

was then investigated through four analyses (two with full geometry models and two with the corresponding simple geometry models) performed with β = 30°. These represented reasonable values of slope angle for situations where a CBS might be considered. As described by Scarfone et al. (2022), if the concern is avoiding instability, CBSs are worth considering on slopes where the angle of the slope is greater than the friction angle of the underlying soil, but less than the friction angles of the two materials forming the CBS. If the slope angle is less than the friction angle of the underlying soil, a CBS is unlikely to be required, because the slope should be stable without a CBS, even during extreme rainfall. If the slope angle is greater than the friction angle of the materials forming the CBS, it is likely that the CBS will fail during extreme rainfall (see Section 8.2). Of course, to ensure a value of factor of safety against slope instability significantly greater than 1, CBSs may also be useful on slopes of lower angle (see Section 8.2).

For the numerical models with β = 35°, the vertical height of the slope was 20 m. This corresponded to a horizontal length of the slope of 28.6 m (see Figure 5-7a). For the numerical models with β = 30°, the horizontal length of slope was maintained at 28.6 m, thus reducing the vertical height of the slope to 16.5 m (see Figure 5-7b). For the "full geometry" models, the underlying soil was modelled down to a horizontal bottom boundary located 5 m below the elevation of the bottom of the slope (see Figures 5-7a and 5-7b).

In all numerical modelling of sloping conventional CBSs, the thickness of the C.L was 0.2 m (see Table 5-1 and Figures 5-7d, 5-7e and 5-7f). Four different values of F.L. thickness t_f were modelled, giving four different values of the total thickness t_{CBS} of the CBS: t_f = 0.1 m (giving t_{CBS} = 0.3 m), t_f = 0.2 m (giving t_{CBS} = 0.4 m), t_f = 0.4m (giving t_{CBS} = 0.6 m) and t_f = 0.8 m (giving t_{CBS} = 1.0 m), as shown in Table 5-1 and Figures 5-7d, 5-7e and 5-7f (t_f = 0.1 m is not shown).

The finite element mesh, for all simulations , was made of quadrilateral elements. Within the F.L and C.L the sides of the elements were vertical or parallel to the slope surface (e.g. see Figures 5-7d, 5-7e, 5-7f and 5-7g). In the horizontal direction, there were 143 elements, and hence each element had a horizintal width of 0.2 m. This width of 0.20 m was considered a reasonable compromise between the need to indentify diversion length L_D with a reasonable degree of

precision (i.e.± 0.20 m in this case) and avoiding excessive computational run times as the number of elements (and hence number of degrees of freedom) was increased (particularly in the more complex thermo-hydraulic numerical analyses described in Chapter 6). In the vertical direction, the number of elements within the F.L and C.L and mesh refinement within F.L and C.L followed the same arrangement as previously used for the modelling of horizontal CBSs (see Section 4.2.1). The horizontal and vertical dimensions of elements within the F.L and C.L meant that these elements had high values of aspect ratio (ratio of horizontal width to vertical height), ranging from 4 to 36. However, Scarfone (2020) and Scarfone et al. (2022) used elements with even larger values of aspect ratio for their equivalent numerical modelling of sloping CBSs using CODE_BRIGHT and they did not report any numerical difficuties that they attributed to the high values of aspect ratio. This is presumably because the gradients of most variables were much higher in the vertical direction than in a direction parallel to the slope. For the underlying soil (in Model type A), there were 16 elements in the vertical direction (see Figures 5-7a and 5-7b).

The choice of mesh refinement, for both type A and type B models, was based on a mesh refinement study performed by Scarfone (2020), with no additional study of mesh refinement undertaken as part of the current project. In hindsight, this was probably a mistake, because the numerical modelling of sloping CBSs performed within the current study included two features not present in the numerical simulations performed by Scarfone (2020), both of which might suggest a need for greater refinement of the FE mesh in the lowest part of the finer layer of the CBS (immediately above the interface with the coarser layer).

Firstly, water transfer within the finer layer becomes restricted to a thin zone at the bottom of the finer layer as the finer layer material becomes coarser and the current project included two additional possible materials for the finer layer (medium sand and coarse sand, see Section 5.3.2), in addition to the fine sand and silty sand considered by Scarfone (2020). When the finer layer was made of medium sand or coarse sand, water transfer at the base of the finer layer was concentrated in a very thin zone (see Section 5.5.4) and a greater degree of mesh refinement might have been desirable in this region.

Secondly, the numerical modelling performed within this project involved detailed investigation of the flow across the interface between finer and coarser layers, expressed as a flow rate across the interface per unit plan area q_i, a variable not examined by Scarfone (2020). The value of q_i, at a given value of horizontal coordinate x and a given value of time t, was determined from the results of a numerical simulation as the small difference between two much larger quantities output by CODE_BRIGHT (see Section 5.4). Hence accurate determination of the value of q_i required very precise numerical values of these outputs from the FE modelling at the interface between finer and coarser layers of the CBS.

The possible consequences of inadequate refinement of the FE mesh, in the zone close to the interface between finer and coarser layers of the CBS, in some of the numerical simulations, are discussed further in Sections 5.4 and 5.5.4.

5.3.2 Material properties

The materials of the CBS (F.L and C.L) were represented by the advanced non-hysteretic hydraulic constitutive model (modVG-modM+LF) developed by Scarfone (2020) and Scarfone et al. (2020a) and described in Section 2.4. For the "full geometry" models (Model type A), the underlying soil was represented by the conventional van Genuchten-Mualem model (VG-M), because accurate representation of behaviour at low values of degree of saturation was unneccessary for this material, because the values of suction were never sufficient to produce low value of S_l in this fine-grained material. No hysteresis was included in the hydraulic constitutive modelling for any of the materials, on the basis that the numerical modelling reported in this chapter was restricted to continuous rainfall of constant intensity. The unique SWRC assumed for each material should therefore be considered as representing the main wetting curve.

The parameter values of the various materials are shown in Table 5-3 and the SWRCs and SHCCS are shown in Figure 5-8, for the coarser layer of the CBS (C.L), all the numerical analyses were performed with the same gravelly sand (GV) as used in Chapter 4 for the horizontal CBSs (see Table 4-1), also used previously for sloping CBSs by Scarfone (2020) and Scarfone et al. (2022). Four different materials were used for the finer layer of the CBS (F.L) as shown in Table 5-1, Table 5-3 and Figure 5-8. Most of the simulations including both "full geometry"

Table 5-3 Material properties for sloping CBSs

Materials	Constitutive Model	Physical parameters			
		Φ (-)	k_i (m^2)	k_s (m/s)	D_{10} (mm)
Silty sand (F.L.)	modVG-modM+LF	0.411	1.11×10^{-12}	1.08×10^{-5}	0.034
Fine sand (F.L.)	modVG-modM+LF	0.411	2.77×10^{-11}	2.70×10^{-4}	0.170
Medium sand (F.L.)	modVG-modM+LF	0.411	1.11×10^{-10}	1.08×10^{-3}	0.340
Coarse sand (F.L.)	modVG-modM+LF	0.411	6.94×10^{-10}	6.77×10^{-3}	0.850
Gravelly sand (C.L.)	modVG-modM+LF	0.382	7.81×10^{-9}	7.62×10^{-2}	2.730
Silt (U.S.)	VG-M	0.480	3.80×10^{-14}	3.71×10^{-7}	-
		SWRC parameters			
	$\bar{P}_0$ (MPa)	$\bar{\sigma}_{s0}$ (N/m)	m (-)	ξ (-)	S_{lr} (-)	S_{ls} (-)
Silty sand (F.L.)	6.05×10^{-3}	0.072	0.779	1.36×10^{-2}	-	1
Fine sand (F.L.)	1.21×10^{-3}	0.072	0.779	6.79×10^{-3}	-	1
Medium sand (F.L.)	6.05×10^{-4}	0.072	0.779	6.40×10^{-3}	-	1
Coarse sand (F.L.)	2.42×10^{-4}	0.072	0.779	6.00×10^{-3}	-	1
Gravelly sand (C.L.)	6.45×10^{-5}	0.072	0.688	3.27×10^{-3}	-	1
Silt (U.S.)	2.52×10^{-2}	0.072	0.186	-	0.00	1

	SHCC parameters						
	m (-)	S_{lr} (-)	$S_{l,BWC./BWD}$ (-)	S_{ls} (-)	C_r^{Film} ($MPa^{-1.5}$)	a^{Film} (MPa)	d^{Film} (-)
Silty sand (F.L.)	0.779	-	0.22	1	1.19×10^{-7}	2.0×10^{-4}	-1.5
Fine sand (F.L.)	0.779	-	0.18	1	9.54×10^{-10}	4.0×10^{-5}	-1.5
Medium sand (F.L.)	0.779	-	0.18	1	1.19×10^{-10}	4.0×10^{-5}	-1.5
Coarse sand (F.L.)	0.779	-	0.18	1	7.62×10^{-12}	4.0×10^{-5}	-1.5
Gravelly sand (C.L.)	0.688	-	0.16	1	2.21×10^{-13}	1.5×10^{-7}	-1.5
Silt (U.S.)	0.186	0.00	0.00	1	-	-	-

and "simple geometry" analyses (see Table 5-1), used for the F.L either the silty sand (SS) or fine sand (FS) that were both employed in Chapter 4 and by Scarfone (2020) and Scarfone et al. (2022). However, two "simple geometry" simulations used medium sand (MS) or coarse sand (CS) (see Table 5-3 and Figure 5-8) for the F.L (see Table 5-1). These simulations were used for the part of the study reported in Section 5.5.4. For the "full geometry" simulations (Model type A), the underlying soil (US) was represented by the same silt as employed by Scarfone (2020) and Scarfone et al. (2022) (see Table 5-3 and Figure 5-8).

5.3.3 Initial conditions and boundary conditions

For the "full geometry" models (Model type A), the initial condition of the underlying soil was a hydrostatic distribution of pore liquid pressure p_l, with p_l = 100 kPa (s = 0) at the bottom boundary, i.e. a horizontal water table 5 m below the base of the slope and $p_l \approx$ 50 kPa (s = 50 kPa) at the base of the slope and $p_l \approx$ -150 kPa (s = 250 kPa) or $p_l \approx$ -115 kPa (s = 215 kPa) at the top of the slope (for β = 35° and β = 30° respectively), as shown in Figure 5-9. In all models (Type

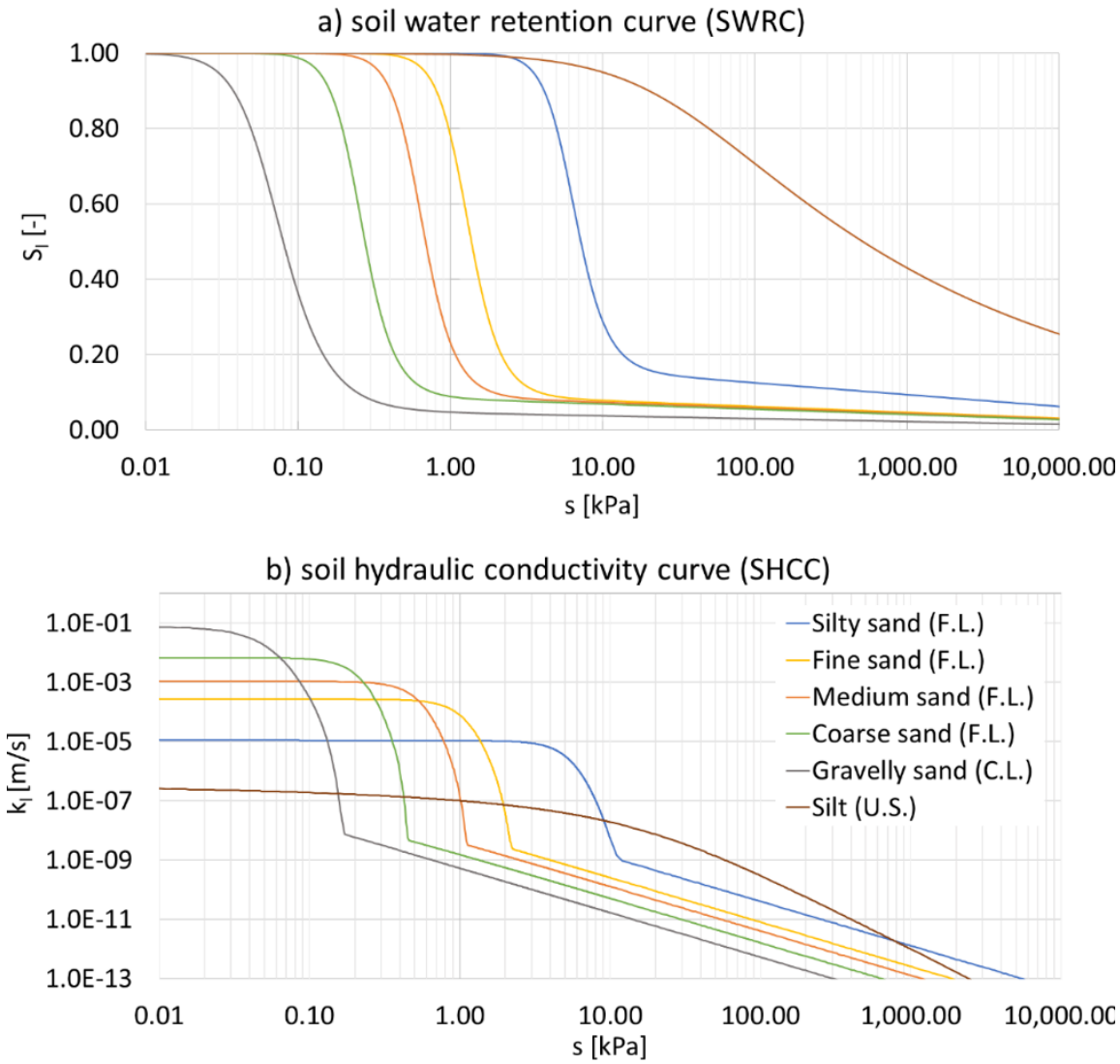

Figure 5-8 Hydraulic properties of materials a) soil water retention curve SWRC and b) soil hydraulic conductivity curve SHCC

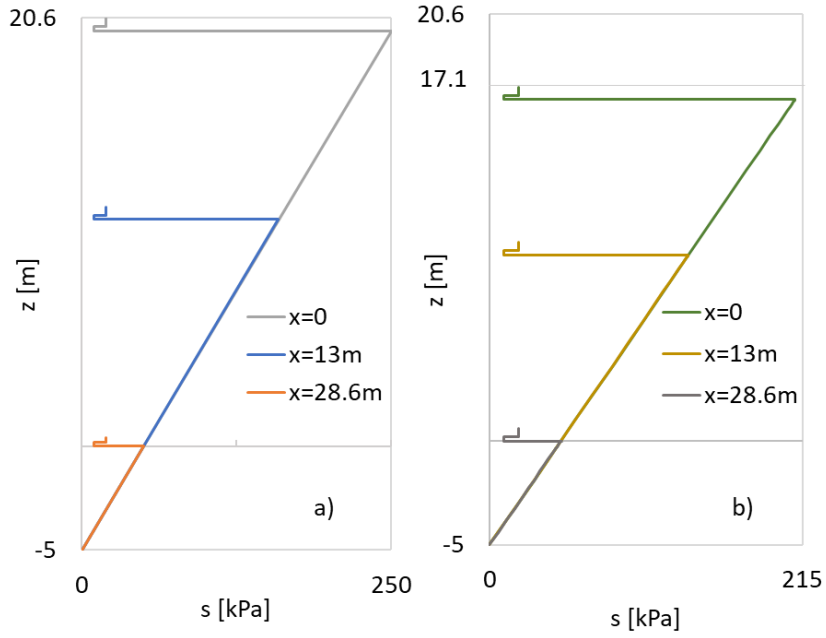

Figure 5-9 Initial suction profiles for Model type A a) β = 35° ; b) β = 30°

A and Type B), a uniform value of initial pore liquid pressure p_l = 90 kPa (s = 10 kPa) was assumed in the C.L and a different uniform value of initial pore liquid pressure p_l = 80 kPa (s = 20 kPa) was assumed in the F.L (see Figure 5.9). The corresponding initial values of degree of saturation S_l within the various materials (constant values of S_l in the C.L and in the F.L and vertical variation of S_l in the U.S in Model type A) were determined by CODE_BRIGHT from the relevant SWRC expression. Due to the initial values of suction in the C.L and F.L (10 kPa and 20 kPa respectively), the CBS was initially almost dry (see Figure 5-8a), with the materials of C.L and F.L in the pendular state (see Figure 2-3). In contrast, despite the much higher initial values of suction in the underlying soil (up to 250 kPa), the initial values of S_l in the underlying soil were significantly higher than in the CBS (see Figure 5-8a), because the underlying soil was a fine-grained soil (silt).

Standard type boundary conditions (see Section 3.4.1) were imposed on all boundaries. The boundary condition at the top boundary (the soil surface), in all models was a continuous water flux representing constant intensity rainfall infiltration i (volume flow rate per unit plan area). The infiltration rate $i = 10^{-6}$m/s (86.4mm/day), representing heavy rainfall, was selected as the standard rainfall intensity for the majority of simulations (see Table 5.1). In addition, with the finer layer made of fine sand, an additional rainfall intensity i =5x10^{-6}m/s was examined and, with the finer layer made of silty sand, a different additional rainfall intensity i = 2x10^{-7}m/s was examined (see Table 5.1). The reason that the second rainfall intensity that was selected was different for the fine sand and silty sand cases was that the same width of FE model (28.6m) and the same horizontal width of each FE element in the CBS (0.2m) were used for all simulations and the intention was to ensure that the diversion length could be accurately identified in all simulations. With the finer layer made of fine sand, if rainfall intensity i = 2x10^{-7}m/s had been employed, the diversion length predicted by the new simplified method would have been more than 60m (i.e. breakthrough would not have occurred within the FE model). With the finer layer made of silty sand, if rainfall intensity i=5x10^{-6}m/s had been employed, the diversion length predicted by the new simplified method would have been less than 0.6m (i.e. breakthrough would have occurred extremely close to the top of the slope). Hence, as a consequence of the decision to use the same FE geometry and mesh for all simulations, the range of rainfall intensities employed in the investigation of

sloping CBSs was less comprehensive than was employed in the investigation of horizontal CBSs reported in Chapter 4.

For the "simple geometry" models (Model type B, only CBS), the bottom boundary (at the bottom of the CBS) was modelled as impermeable to liquid water and water vapour. Other possible bottom boundary conditions were examined for Model type B (e.g. a constant value of p_l, corresponding to a constant value of suction) and it made no significant difference to the results except at the bottom of the coarser layer. For the "full geometry" models (Model type A, CBS+US), the boundary condition on the bottom boundary, at the base of underlying soil, was a constant value of pore liquid pressure p_l = 100 kPa (s = 0). The lateral boundaries, for both types of models (Types A and B) were modelled as impermeable to liquid and vapour flows, with the exception of the left lateral side of the CBS (F.L and C.L), which was modelled as a seepage boundary (see Section 3.4.1), with no liquid flow for p_l < 100 kPa (s > 0) but water allowed to flow out (with p_l on the boundary then maintained constant) when the pore pressure value reached p_l = 100 kPa (s = 0).

5.4 Results: comparison of Model types A and B and identifying diversion length

As computational runtime was a significant concern for the more complex thermo-hydraulic numerical modelling with atmospheric boundary conditions when moving on to Chapters 6 and 7, Model type B (only CBS) was investigated for the purpose of reducing the number of elements in the FE model, in order to reduce the runtime. The aim of comparing the results from Model type A (CBS+US) and Model type B (only CBS) was to confirm that the numerical results of Model type B (only CBS) were reliable i.e. the same as the results from Model type A. In addition, the numerical results of Model type A (CBS+US) also gave information of water percolation into and through the underlying soil. These results helped to justify the criterion adopted for the determination of breakthrough and hence diversion length in Model type B (only CBS).

An obvious way to determine breakthrough and diversion length from the numerical modelling results was to examine the water flow across the interface between F.L and C.L (given that breakthrough corresponds to the sudden onset of

large water flows across this interface). CODE_BRIGHT does not provide values of flow velocity across the interface, instead it outputs values of horizontal liquid water velocity q_h and vertical liquid water velocity q_v at each node. For a node on the interface between F.L and C.L, the component of liquid water velocity normal to the interface q_n (i.e. the flow across the interface) can be calculated as:

$$q_n = q_v \cos\beta - q_h \sin\beta \quad \text{5-31}$$

q_n from Equation 5-31 represents the flow rate entering the C.L across the interface expressed as a volumetric liquid water flow rate per unit area of the interface. It is, however, more convenient to express this flow rate entering the C.L from the F.L as a volumetric flow rate per unit plan area q_i, as this should equate to the rainfall infiltration rate i (also expressed as a volumetric flow rate per unit plan area) when breakthrough is fully established. This interface flow rate per unit plan area q_i is given by:

$$q_i = \frac{q_n}{\cos\beta} = q_v - q_h \tan\beta \quad \text{5-32}$$

Figure 5-10 shows final steady state values of interface flow rate per unit plan area q_i plotted against horizontal coordinate x (measured from the top of the slope) for three typical Model type A simulations and three corresponding Model type B simulations. All three cases shown in Figure 5-10 are for finer layer thickness t_f = 80 cm and rainfall intensity i = 10^{-6} m/s. In Figures 5-10a and 5-10b, the F.L. is made of fine sand, with slope angle β = 35° in Figure 5-10a and β = 30° in Figure 5-10b. In Figure 5-10c, the F.L. is made of silty sand and β = 35°.

The concept of diversion length is very clear from the simulation results presented in Figure 5-10. Each simulation shows very low values of final steady state interface flow velocity q_i up to a particular value of x (the diversion length L_D) and then a value of q_i further down the slope that is equal to or very close to the rainfall intensity (i = 10^{-6} m/s). Slightly elevated values of q_i close to the lateral boundaries at the top and bottom of the slope (x = 0 and x = 26.8 m), are probably just a consequence of the presence of the artificial lateral boundaries at x = 0 and x = 26.8 m in each numerical model (see Figure 5-7). Two other minor features of

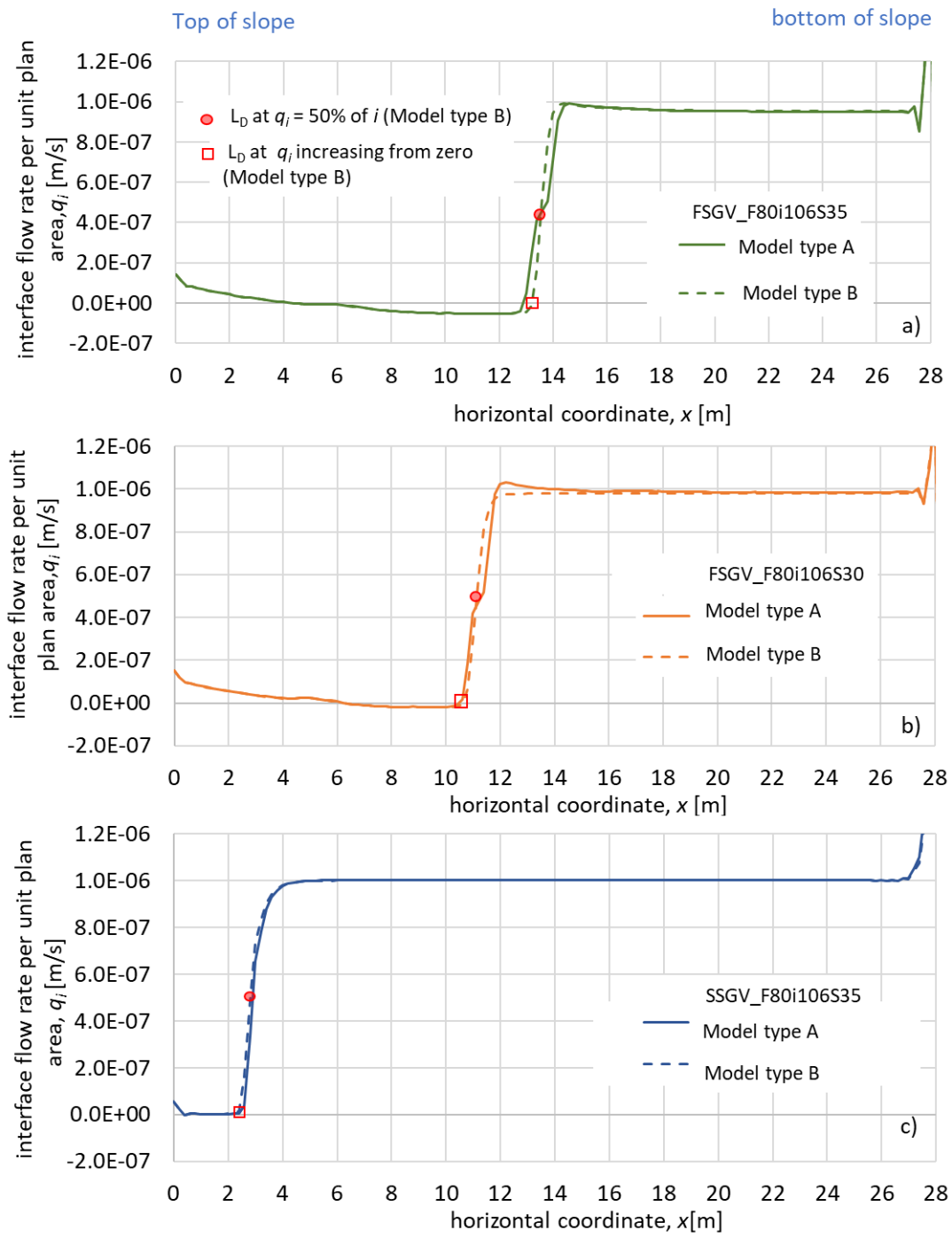

Figure 5-10 Final steady state interface flow rate per unit plan area for Model types A and B with t_f = 80 cm and i = 10^{-6} m/s: a) FS, β = 35°; b) FS, β = 30°; c) SS, β = 35°

the simulation results shown in Figure 5-10 were however unexpected and have not been entirely explained at this point. Firstly, for all simulations with the F.L made of fine sand (including those shown in Figures 5-10a and 5-10b), the values of q_i for x less than the diversion length always showed a gradual trend with x, decreasing from small positive values (i.e. flow from F.L to C.L) at low values of x to small negative values (i.e. flow from C.L to F.L) at values of x approaching the diversion length. Secondly, again for all simulations with the F.L made of fine

sand, the value of q_i at high values of x, well beyond the diversion length L_D, was consistently slightly lower than the rainfall infiltration rate i, even for simulations like those shown in Figure 5-10, where there was no evaporation and hence nowhere for the water to escape from the F.L other than flow across the interface or water transfer down the slope with the F.L. It is unclear whether these two small, unexpected features in the results of the numerical simulations represent a real physical phenomenon or are simply numerical issues, caused by the challenge of accurately modelling patterns of flow at the interface, where there are high gradients of most variables. This is going to be more severe in the cases involving fine sand than in those involving silty sand, because water transfer is concentrated into a thinner zone at the base of the F.L when the F.L is made of fine sand. This may suggest that greater mesh refinement was needed at the bottom of the F.L when the F.L was made of fine sand (see Section 5.3.1).This possibility of numerical error is increased in the case of the interface flow velocity q_i, which is calculated as a small difference between two much larger quantities (q_v and $q_h \tan\beta$), as shown in Equation 5-32.

Inspection of Figure 5-10 shows that, in all three pairs of simulations, the results from the "simply geometry" Model type B are very similar to those from the "full geometry" Model type A.

Further demonstration of close agreement between results from model type B and those from the corresponding Model type A is provided by Figure 5-11, which shows, for a value of x corresponding to the diversion length L_D, final steady state profiles of suction s, degree of saturation S_l and horizontal flow velocity q_h (crucial for determining water transfer capacity Q_{max}) for the same three pairs of simulations as in Figure 5-10. For the two pairs of simulations with the F.L. made of fine sand (Figures 5-11a, 5-11b, 5-11c and 5-11d, 5-11e and 5-11f) the results from Model type A and Model type B are indistinguishable. For the pair of simulations with the F.L made of silty sand (Figures 5-11g, 5-11h and 5-11i) there are slight differences between the results from Model type A and Model type B, in the values of S_l and q_h in the upper part of the F.L. These small differences were considered to be of little practical significance (they only occurred in cases where the F.L was made of silty sand and where the F.L was 80 cm thick, and where they occurred, Model type B was always conservative (underestimating values of S_l and q_h).

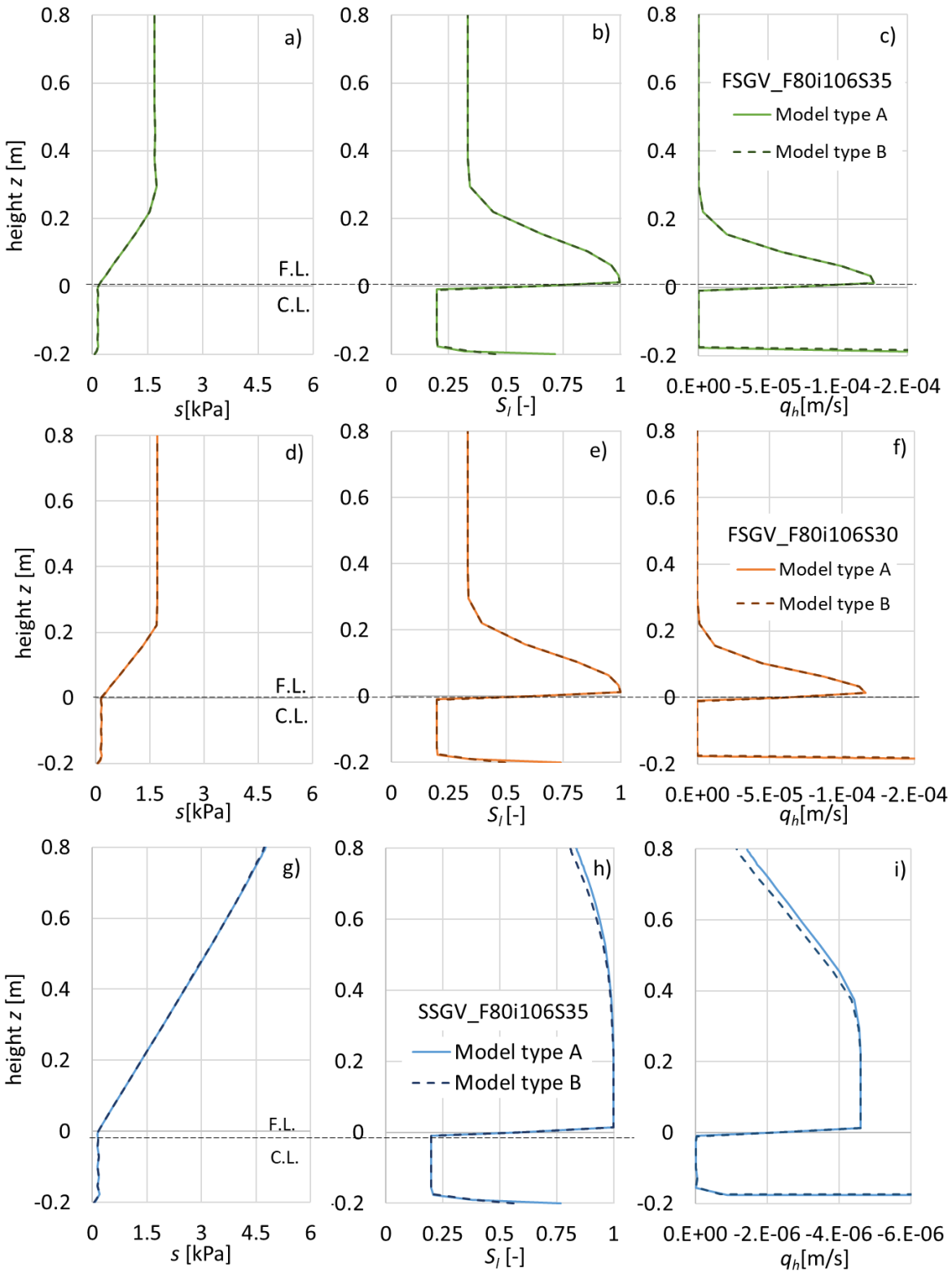

Figure 5-11 Final steady state profiles of suction, degree of saturation and horizontal liquid water velocity at $x \approx L_D$ for Model types A and B with t_f=80cm and i= 10^{-6}m/s:a) b) c) FS, β=35°; d) e) f) FS, β=30°; g) h) i) SS, β=35°

For the other seven cases where pairs of corresponding simulations were performed with Model type A and Model type B (see Table 5-1), results equivalent to Figures 5-10 and 5-11 are shown in Appendix C. The agreement, in terms of values of q_i, s , S_l, and q_h, was at least as good as illustrated for the three cases

shown in Figure 5-10 and Figure 5-11 (in many cases the results from Model type A and Model type B are indistinguishable). This justified the decision to use only Model type B going forward, to avoid excessive computational runtimes, particularly in the more computationally demanding simulations presented in Chapters 6 and 7 (involving thermo-hydraulic modelling, atmospheric boundary conditions, complex rainfall patterns and inclusion of hydraulic hysteresis). As an example of the reduction of computational runtime achieved by using Model type B rather than Model type A, the runtime to complete the simulation shown in Figure 5-10c (to t =200 hours, well beyond final steady state) was approximately 4 days for Model type A and approximately 3 hours for Model type B.

Plots of final steady state interface flow velocity q_i against horizontal coordinate x, such as those shown in Figure 5-10, are an ideal way to identify diversion length L_D from each simulation. Figure 5-10 illustrates two different ways in which this could be done, both applied to the Model type B results. The square data points in Figure 5-10 correspond to the point at which q_i first increases significantly and/or first goes above zero, whereas the circular data points are halfway up the sudden rise in q_i, at a value of q_i corresponding to half the rainfall intensity i. Clearly, use of the latter criterion would always suggest a slightly greater value of diversion length L_D than use of the former. For example, for the Model type B simulation shown in Figure 5-10a, the use of the square data point (q_i first increasing above zero) would suggest $L_D = 13.0$ m whereas use of the circular data point ($q_i = 0.5\text{x}10^{-6}$ m/s) would suggest $L_D = 13.6$ m.

To investigate further this identification of diversion length L_D, final steady state contour plots of degree of saturation and suction were examined for each simulation. An example is shown in Figures 5-12 and 5-13, corresponding to the Model type A and Model type B simulation shown in Figure 5-10a. Inspection of contour plots of this type confirmed that noticeable rises of S_l (see Figure 5-12) and decreases of s (see Figure 5-13) in the C.L (and also in the underlying soil in the Model type A simulations) commenced at x values closely matching the square data points in Figure 5-10 whereas these increases of S_l and decreases of s were more fully established from values of x matching the circular data points Figure 5-10. This suggests that the square data points would be more relevant if the purpose of defining diversion length L_D was to identify the location where any noticeable flow into the C.L (and therefore into the underlying soil) commenced.

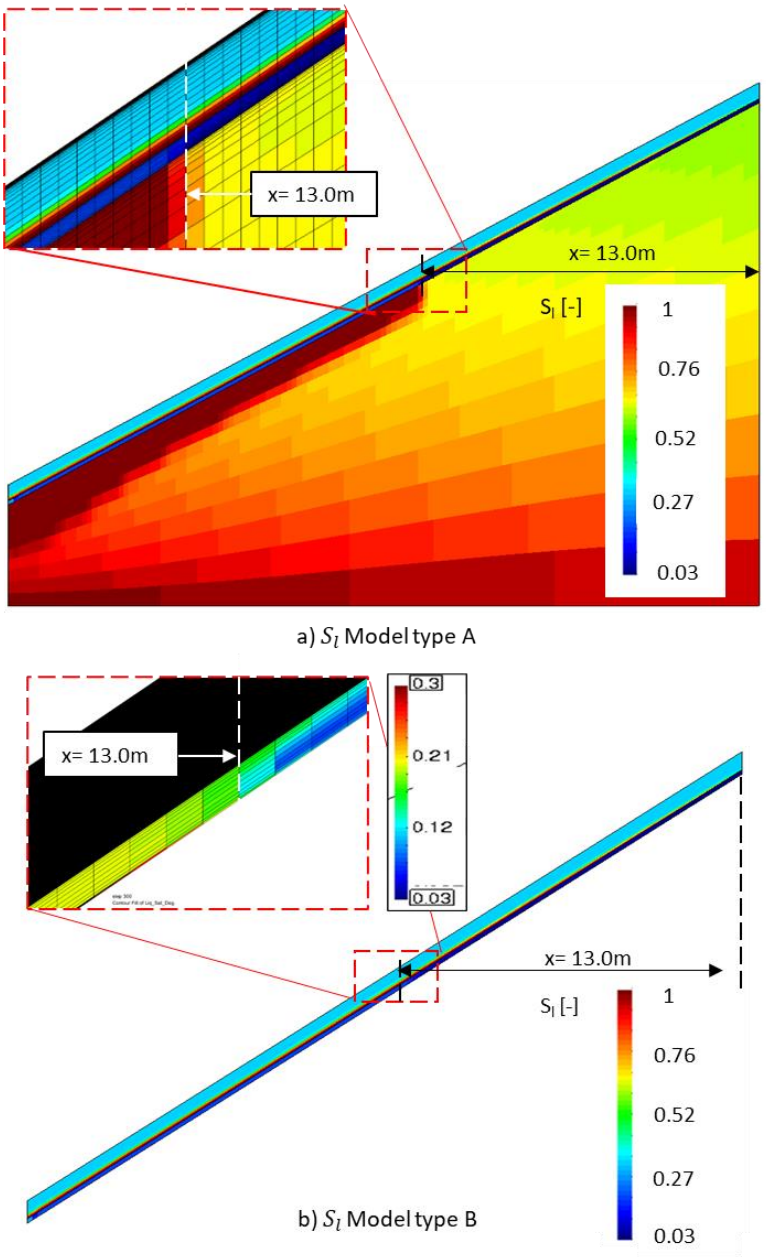

Figure 5-12 Contour plots of S_l at final steady state for β = 35°, FSGV, t_f= 80cm, i = 10^{-6} m/s ; a) Model type A; b) Model type B

In contrast, the circular data points would be more relevant if the purpose was to accurately estimate the total flow of water into the C.L of a CBS by assuming $q_i = 0$ for $0 < x < L_D$ and $q_i = i$ for $x \geq L_D$ as an approximation for integrating the true variation q_i over the full horizontal extent of the slope. For this project, it was decided to identify diversion length L_D as the horizontal coordinate where the final steady state value of interface flow velocity q_i reached 50% of the rainfall infiltration rate i (i.e. the circular data points in Figure 5-10).

With the selected criterion for identifying diversion length, the values of L_D for the three cases shown in Figure 5-10 were 13.6 m in Figure 5-10a (FS with β= 35°),

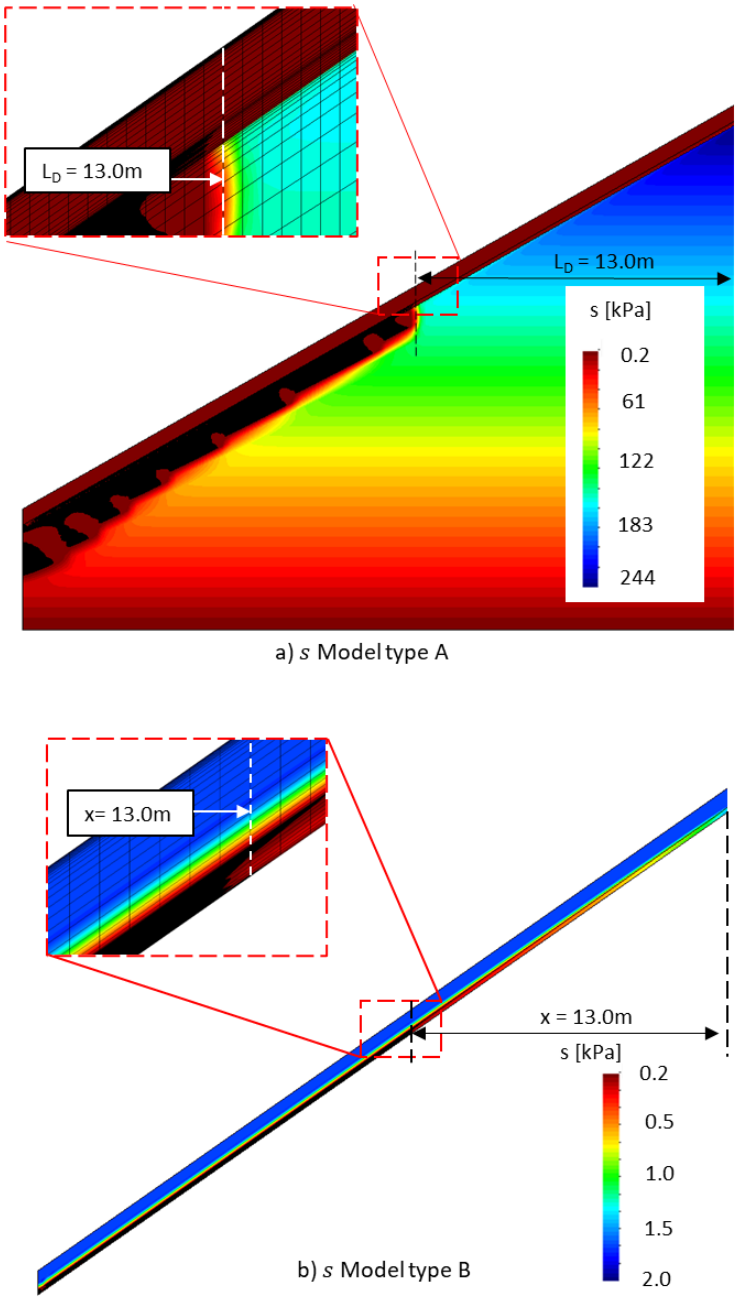

Figure 5-13 Contour plots of s at final steady state for β = 35°, FSGV, t_f= 80cm, i = 10^{-6} m/s; a) Model type A; b) Model type B

11.2 m in Figure 5-10b (FS with β = 30°), and 2.8 m in Figure 5-10c (SS with β = 35°). Comparing Figure 5-10a with Figure 5-10c, it is clear that the diversion length (and hence the water transfer capacity) is much greater for a CBS with the F.L. made of fine sand than for a CBS with the F.L. made of the silty sand (a slightly finer material), as previously reported by Scarfone (2020) and Scarfone et al. (2022). Comparing Figure 5-10a with Figure 5-10b, it is also clear that, for a given type of F.L. material, the diversion length (and hence water transfer capacity) increases with increasing slope angle (i.e. L_D is greater for β = 35° than for β = 30°). These issues are discussed further in Section 5.5.

5.5 Final steady state: suction profiles, transfer capacity and storage capacity

This section presents the final steady state results of the numerical analyses listed in Table 5-1, in terms of suction profiles, water transfer capacity and water storage capacity. The results of the numerical analyses are compared with those predicted by both simplified semi-analytical methods (the existing method of Parent and Cabral (2006), described in Section 5.1, and the proposed new method, described in Section 5.2). From now on the numerical analyses results presented are only those from Model Type B (the simplified geometry).

5.5.1 Suction profiles at x ≥ L_D

Figure 5-14 shows final steady state profiles of suction s, degree of saturation S_l and horizontal seepage velocity q_h at selected values of horizontal coordinates x, at and beyond the diversion length L_D, from FE results for one example simulation with the F.L made of fine sand (β = 35°, FSGV, t_f= 40 cm, i = 10^{-6} m/s). For this particular case, the diversion length was L_D = 13.6 m, so the profiles shown at x = 13.6 m in Figure 5-14 correspond to $x = L_D$, whereas the profiles shown at x = 16.0 m, x = 19.0 m and x = 25.0 m in Figure 5-14 correspond to $x > L_D$. Inspection of Figure 5-14 shows that, as predicted previously, within the F.L, the final steady state profiles of s, S_l and q_h are identical for all values of x equal to or greater than the diversion length L_D. Further inspection of Figure 5-14 shows that the final steady state profiles of s, S_l and q_h at different values of x do differ within the C.L, as the quantity of water flowing down the slope in the lower part of the C.L gradually increases with increasing x for $x > L_D$ (see Figure 5-14c). In a real CBS on a slope, some or all of this water flow within the C.L would percolate into the underlying soil of the slope.

Figures 5-15 and 5-16 show final steady state profiles of s, S_l and q_h within the F.L at x = $L_D$from the FE results for two different simulations. Figure 5-15 shows the same simulation as in Figure 5-14 (β = 35°, FSGV, t_f = 40 cm, i = 10^{-6} m/s), whereas Figure 5-16 shows the equivalent simulation with the F.L made of silty sand (β = 35°, SSGV, t_f = 40 cm, i = 10^{-6} m/s). Also shown in Figures 5-15 and 5-16 are the final steady state profiles of s, S_l and q_h within the F.L predicted by the

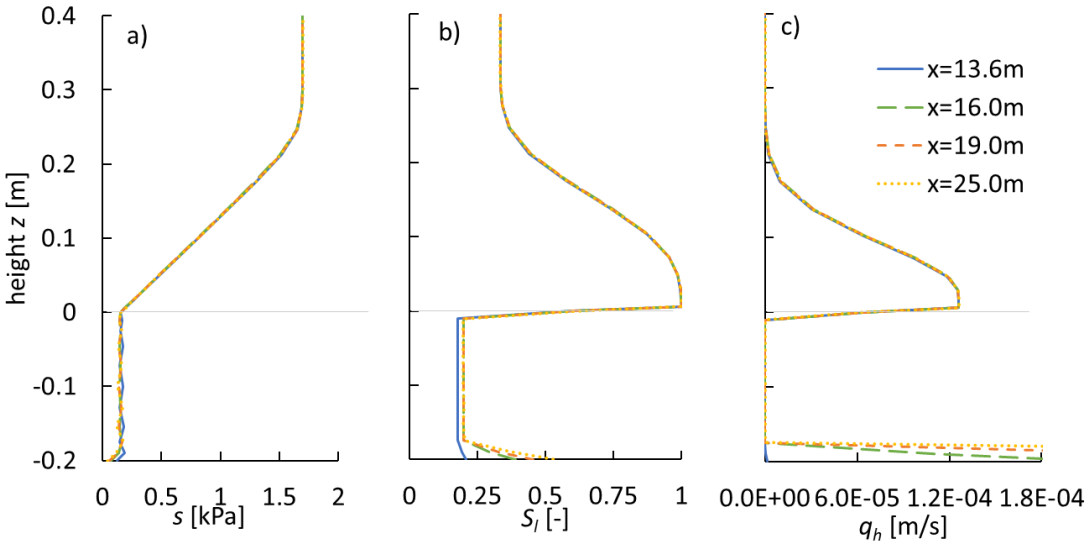

Figure 5-14 Final steady state profiles from FE analysis for x≥ L_D: a) suction b) degree of saturation c) horizontal water velocity (β =35°, FSGV, t_f = 40 cm, i = 10^{-6}m/s)

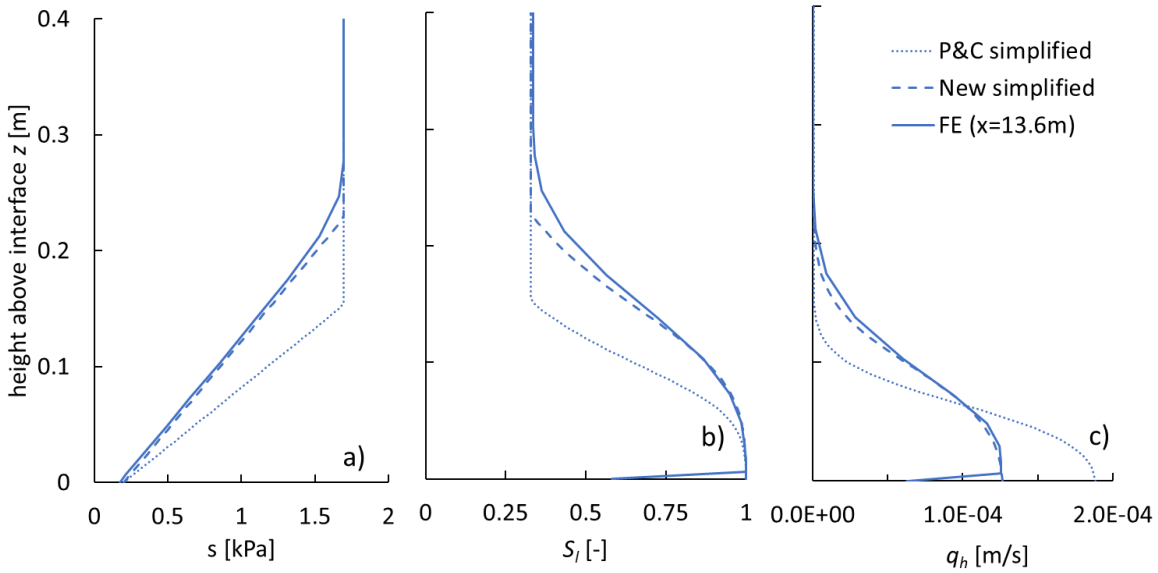

Figure 5-15 Final steady state profiles for x = L_D: a) suction; b) degree of saturation; and c) horizontal liquid water velocity (β=35°, FSGV, t_f = 40 cm, i = 10^{-6}m/s)

two simplified methods (the Parent and Cabral (2006) simplified method and the proposed new simplified method). The limiting value of suction s_f^* in the F.L (corresponding to the value of suction at which the hydraulic conductivity of the F.L material is equal to the rainfall intensity i) is much greater for the silty sand than for the fine sand (6.8 kPa, instead of 1.7 kPa). For the case of F.L made of fine sand, both simplified methods predict a linear increase of suction with elevation z only in a limited lower part of the F.L. (see Figure 5-15a). In contrast, because of the higher value of s_f^*, for the case of a F.L. made of silty sand, the predicted linear increase of suction with z extends over the full depth of the F.L for both simplified methods, as shown in Figure 5-16a.

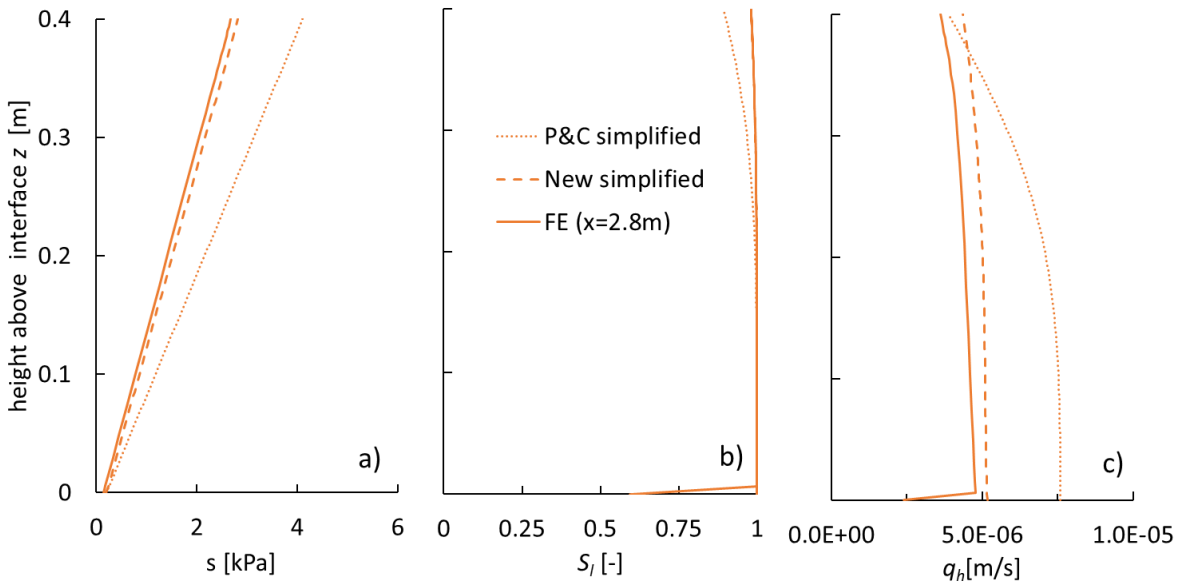

Figure 5-16 Final steady state profiles for x = L_D: a) suction; b) degree of saturation; and c) horizontal liquid water velocity (β=35°, SSGV, t_f = 40 cm, i = 10^{-6}m/s)

Inspection of Figures 5-15a and 5-16a shows that the suction profile predicted by the proposed new simplified method (described in Section 5.2) is, in both cases, an excellent match to the final steady state suction profile from the numerical simulation. In contrast, the suction profile predicted by Parent and Cabral (2006), which really applies to a horizontal CBS rather than a sloping CBS, shows significant errors in the part of the F.L where the new method is predicting a linear increase of suction with z. The excellent match of the new simplified method to the final steady state suction profiles from the numerical analyses was observed in all the simulations listed in Table 5-1.

Figures 5-15 and 5-16 also show the final steady state profiles of degree of saturation S_l (Figures 5-15b and 5-16b) and horizontal seepage velocity q_h (Figures 5-15c and 5-16c) from the numerical analyses, with the corresponding predictions from the two simplified methods. It is clear that, as a consequence of the more accurate representation of the suction profile, the proposed new simplified method predicts more accurately than the Parent and Cabral (2006) simplified method, the variations of both S_l and q_h with z, for the two cases illustrated in Figures 5-15 and 5-16. The same was true for all the other simulations listed in Table 5-1. It should be noted that the large reductions of S_l and q_h predicted by the numerical analyses at the very bottom of F.L (within the bottom element of the F.L.) are a numerical issue, arising from the numerical challenge of predicting the discontinuities in S_l and q_h that would occur at the interface between F.L and C.L.

5.5.2 Diversion length and water transfer capacity

This section presents numerical validation of water transfer capacity calculation by the new simplified method, by comparing with the finite element numerical results. Predictions from the Parent and Cabral (2006) simplified method are also shown, for comparison. Table 5-1 lists the numerical simulations with Type B models and the different parameter values that were used in the numerical validation.

Figure 5-17 shows the determination of the diversion length L_D from the finite element results, from the plots of final steady state interface flow velocity q_i against horizontal coordinate x, for the 7 simulations involving a F.L made of fine sand. Also shown in Figure 5-17 are the corresponding predictions from the two simplified methods, with $q_i = 0$ for $x < L_D$ and $q_i = i$ for $x \geq L_D$. Values of diversion length L_D for each simplified method were calculated from Equation 5-2, with transfer capacity Q_{max} calculated from Equation 5-28 (new method) or Equation 5-9 (Parent and Cabral (2006) method). Corresponding results for the 6 simulations involving a F.L made of silty sand are shown in Figure 5-18. Values of diversion length L_D determined from all the numerical simulations are also presented in **Error! Reference source not found.**.

Inspection of Figures 5-17 and 5-18 shows that, in all cases where the F.L is made of fine sand or silty sand, the values of diversion length L_D predicted by the new simplified method are reasonably consistent with those from the numerical analyses. When the F.L is made of fine sand (Figure 5-17), the simplified method tends to slightly underpredict the value of L_D (i.e. it is slightly conservative). In contrast, when the F.L is made of silty sand (Figure 5-18), the simplified method is typically very accurate and, in a few cases, slightly over-predicts L_D.

In many cases shown in Figures 5-17 and 5-18, the predictions of L_D from the Parent and Cabral simplified method are identical with those from the new simplified method. In a few cases however (those where the F.L is thinner), the Parent and Cabral method predicts greater values of L_D than the new simplified

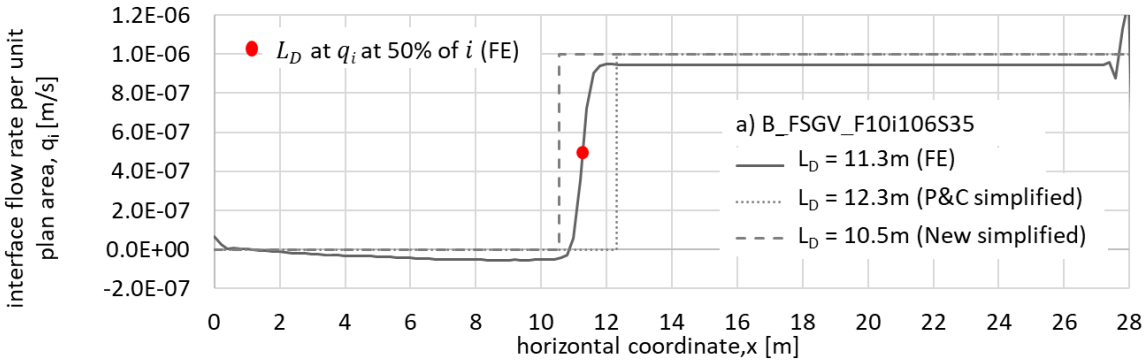
interface flow rate per unit plan area, q_i [m/s]
1.2E-06
1.0E-06
8.0E-07
6.0E-07
4.0E-07
2.0E-07
0.0E+00
-2.0E-07
L_D at q_i at 50% of i (FE)
a) B_FSGV_F10i106S35
L_D = 11.3m (FE)
L_D = 12.3m (P&C simplified)
L_D = 10.5m (New simplified)
0 2 4 6 8 10 12 14 16 18 20 22 24 26 28
horizontal coordinate,x [m]

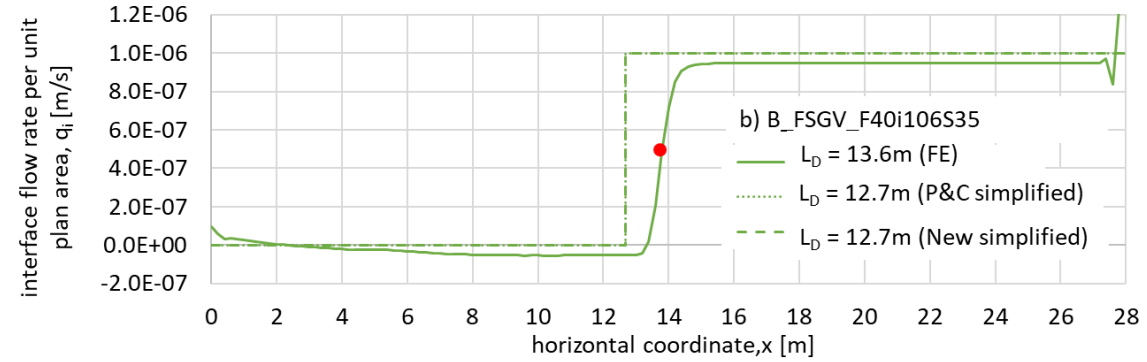
interface flow rate per unit plan area, q_i [m/s]
1.2E-06
1.0E-06
8.0E-07
6.0E-07
4.0E-07
2.0E-07
0.0E+00
-2.0E-07
b) B_FSGV_F40i106S35
L_D = 13.6m (FE)
L_D = 12.7m (P&C simplified)
L_D = 12.7m (New simplified)
0 2 4 6 8 10 12 14 16 18 20 22 24 26 28
horizontal coordinate,x [m]

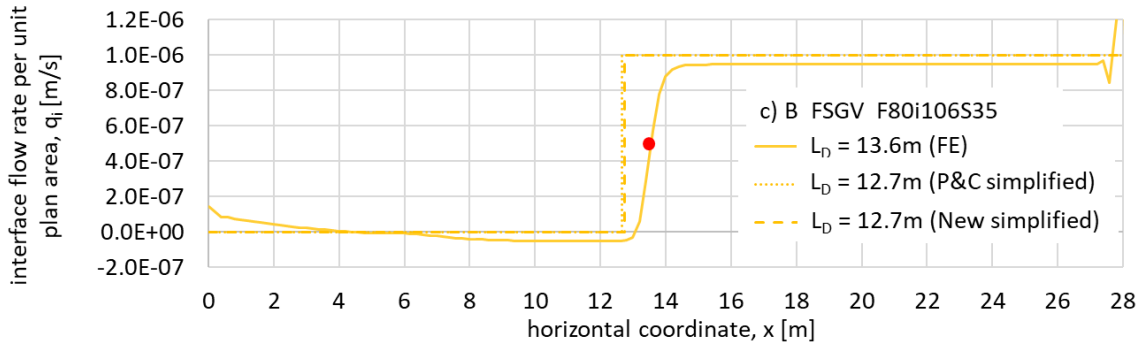
interface flow rate per unit plan area, q_i [m/s]
1.2E-06
1.0E-06
8.0E-07
6.0E-07
4.0E-07
2.0E-07
0.0E+00
-2.0E-07
c) B FSGV F80i106S35
L_D = 13.6m (FE)
L_D = 12.7m (P&C simplified)
L_D = 12.7m (New simplified)
0 2 4 6 8 10 12 14 16 18 20 22 24 26 28
horizontal coordinate, x [m]

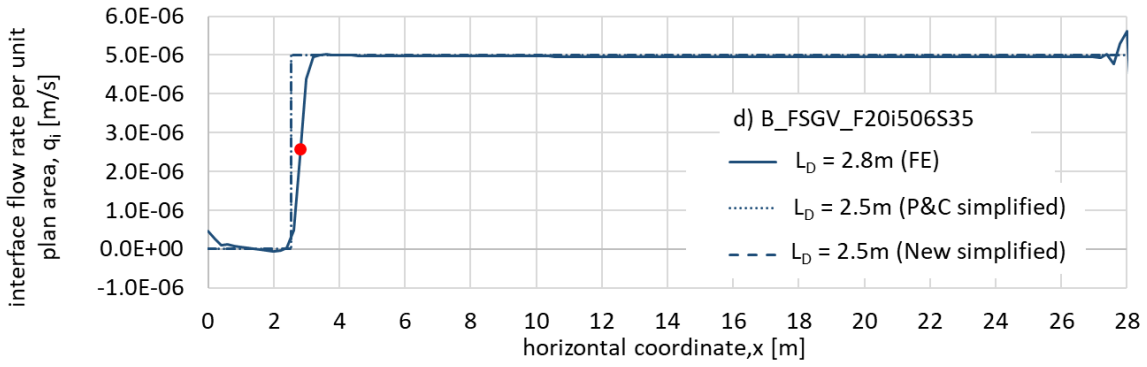
interface flow rate per unit plan area, q_i [m/s]
6.0E-06
5.0E-06
4.0E-06
3.0E-06
2.0E-06
1.0E-06
0.0E+00
-1.0E-06
d) B_FSGV_F20i506S35
L_D = 2.8m (FE)
L_D = 2.5m (P&C simplified)
L_D = 2.5m (New simplified)
0 2 4 6 8 10 12 14 16 18 20 22 24 26 28
horizontal coordinate,x [m]

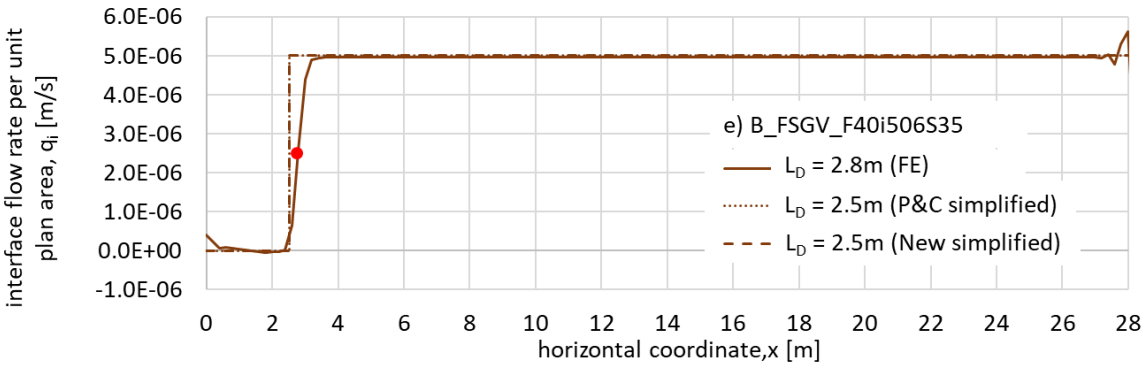
interface flow rate per unit plan area, q_i [m/s]
6.0E-06
5.0E-06
4.0E-06
3.0E-06
2.0E-06
1.0E-06
0.0E+00
-1.0E-06
e) B_FSGV_F40i506S35
L_D = 2.8m (FE)
L_D = 2.5m (P&C simplified)
L_D = 2.5m (New simplified)
0 2 4 6 8 10 12 14 16 18 20 22 24 26 28
horizontal coordinate,x [m]

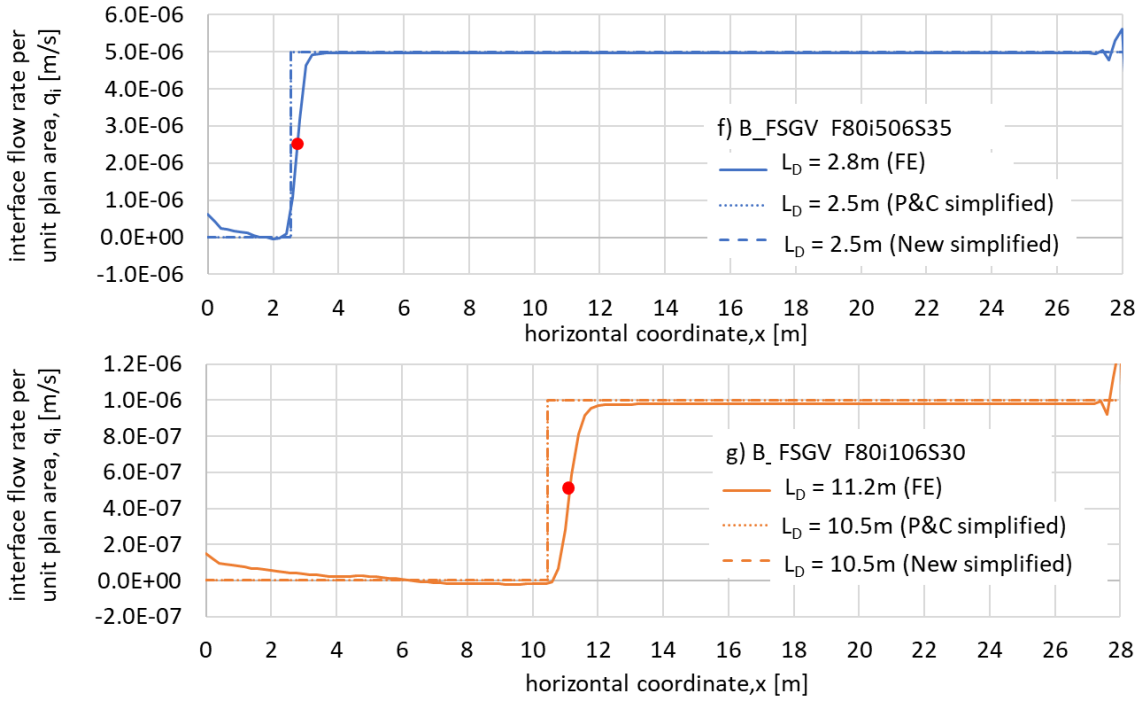

Figure 5-17 Final steady state interface flow velocity for analyses with F.L made of fine sand

method, and in these cases, it is the new simplified method that provides a better match to the results of the numerical simulations. The reason why the Parent and Cabral (2006) method often predicts the same values of L_D as the new simplified method, and hence is often able to accurately predict the values of L_D despite assuming a very unrealistic suction profile, is apparent from Equations 5-9 and 5--28 Inspection of Equations 5-9 and 5-28 shows that the only difference in the values of Q_{max} (and hence L_D) predicted by the two simplified methods is the value of suction at the top of the finer layer (s_2 or s_4). s_2 and s_4 will be identical if the F.L thickness t_f is greater than the critical value t_f^* for the new simplified method, given in Equation 5-26. Figure 5-15 illustrated a case where t_f is greater than the critical value. Figure 5-15c shows that the Parent and Cabral simplified method predicts that the value of horizontal seepage velocity q_h is too high at the very bottom of the F.L. (because it predicts a value of horizontal hydraulic gradient that is too high) but then it predicts that the height of the zone over which horizontal flow is occurring is too small. These two effects exactly compensate if t_f is greater than the critical value.

Variations of water transfer capacity Q_{max} with finer layer thickness are shown in Figure 5-19 (F.L made of fine sand) and Figure 5-20 (F.L made of silty sand), including both FE results and predictions from the two simplified methods (the

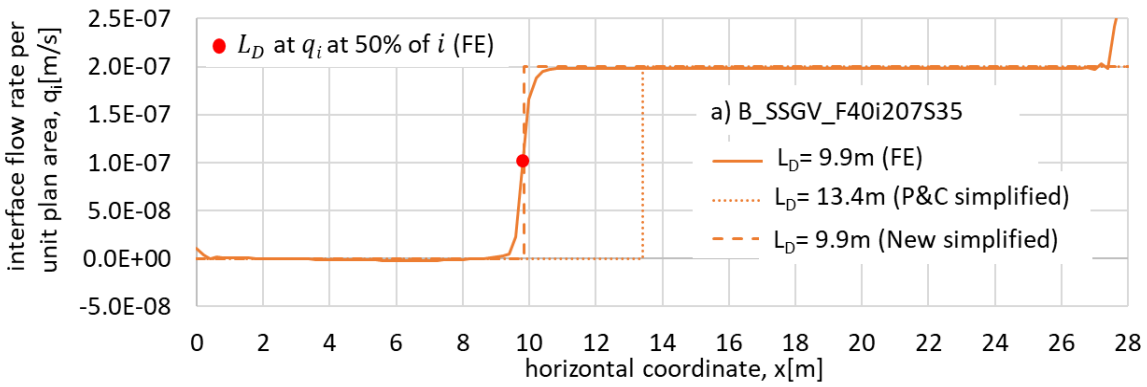
L_D at q_i at 50% of i (FE)
a) B_SSGV_F40i207S35
L_D= 9.9m (FE)
L_D= 13.4m (P&C simplified)
L_D= 9.9m (New simplified)
interface flow rate per unit plan area, q_i[m/s]
horizontal coordinate, x[m]

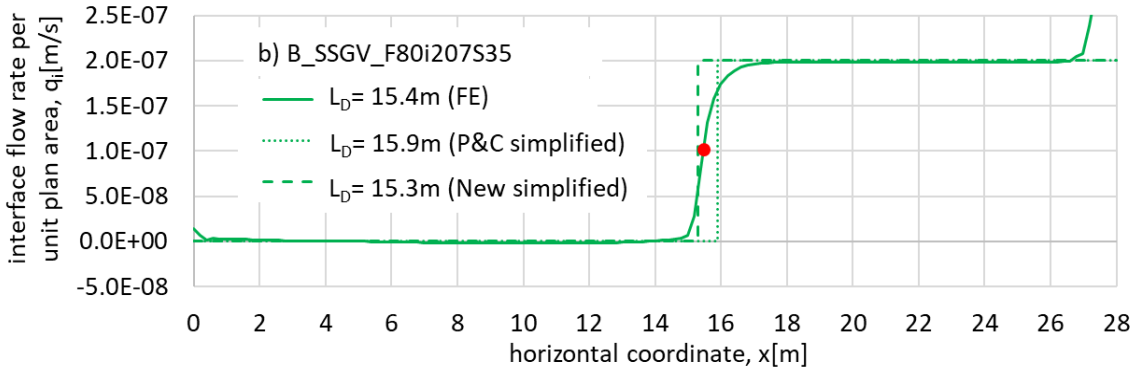
b) B_SSGV_F80i207S35
L_D= 15.4m (FE)
L_D= 15.9m (P&C simplified)
L_D= 15.3m (New simplified)
interface flow rate per unit plan area, q_i[m/s]
horizontal coordinate, x[m]

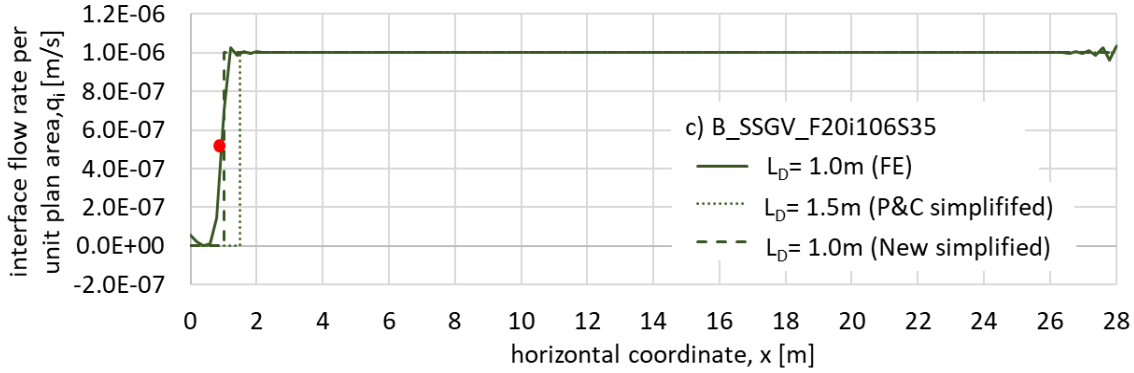
c) B_SSGV_F20i106S35
L_D= 1.0m (FE)
L_D= 1.5m (P&C simplifefed)
L_D= 1.0m (New simplified)
interface flow rate per unit plan area,q_i [m/s]
horizontal coordinate, x [m]

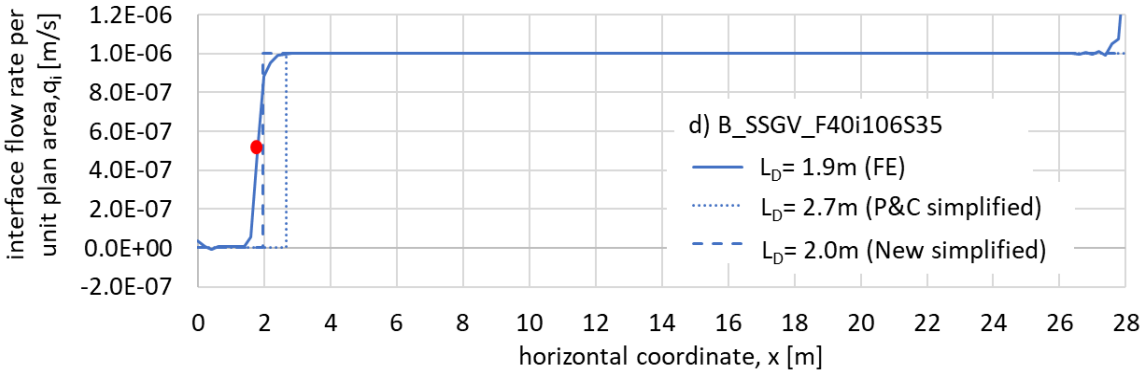
d) B_SSGV_F40i106S35
L_D= 1.9m (FE)
L_D= 2.7m (P&C simplified)
L_D= 2.0m (New simplified)
interface flow rate per unit plan area,q_i [m/s]
horizontal coordinate, x [m]

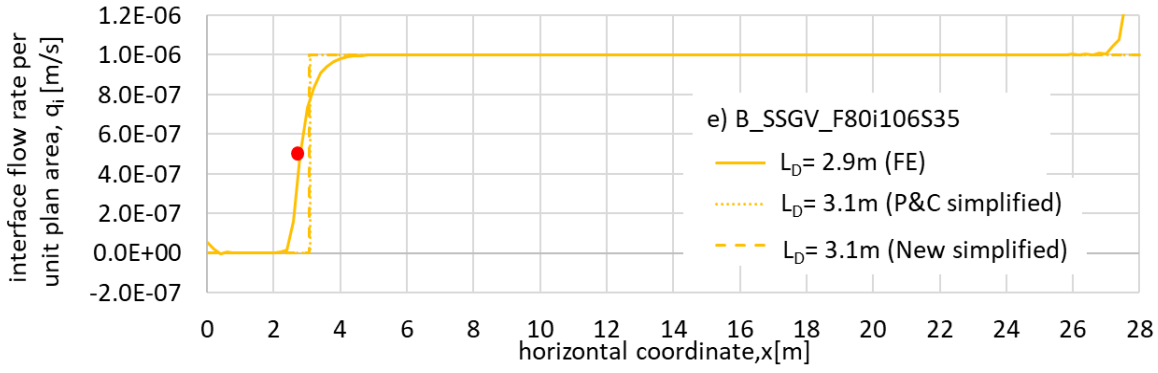
e) B_SSGV_F80i106S35
L_D= 2.9m (FE)
L_D= 3.1m (P&C simplified)
L_D= 3.1m (New simplified)
interface flow rate per unit plan area, q_i [m/s]
horizontal coordinate,x[m]

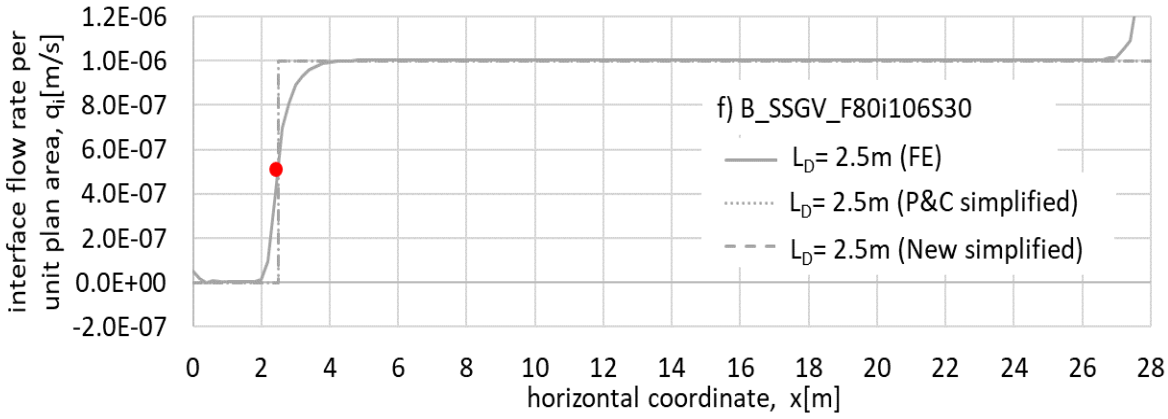

Figure 5-18 Final steady state flow velocity for analyses with F.L. made of silty sand

latter shown previously in Figures 5-3 and 5-4). Values of Q_{max} from the numerica simulations are shown by the individual data points. These values of Q_{max} from the numerical simulations, which are also presented in Table 5-4, have been determined from the corresponding values of L_D by inverting Equation 5-2:

$$Q_{max} = L_D i \qquad \textbf{5-33}$$

In Figure 5-19 , some of the data points correspond to FE simulations performed with a rainfall intensity i = 10^{-6} m/s and others correspond to i = 5x10^{-6} m/s. It is clear, however, that this difference in rainfall intensity had no influence on transfer capacity Q_{max} (compare, for slope angle β = 35°, individual data points for two different rainfall intensities for t_f = 40 cm and t_f = 80 cm). Similarly, in Figure 5-20, two different rainfall intensities i = 10^{-6} m/s and i = 2x10^{-7} m/s were used in the numerical analyses, but for a given slope angle and thickness of F.L, the transfer capacity was the same for two different values of rainfall intensities.

Inspection of Figures 5-19 and 5-20 shows that the new simplified method accurately predicts values of Q_{max} in all cases. This provides important numerical validation of the proposed new simplified method. In contrast, where the predictions of Q_{max} from the Parent and Cabral method differ from those from the new simplified method (for low values of F.L thickness), the Parent and Cabral method can significantly overestimate the value of Q_{max}.

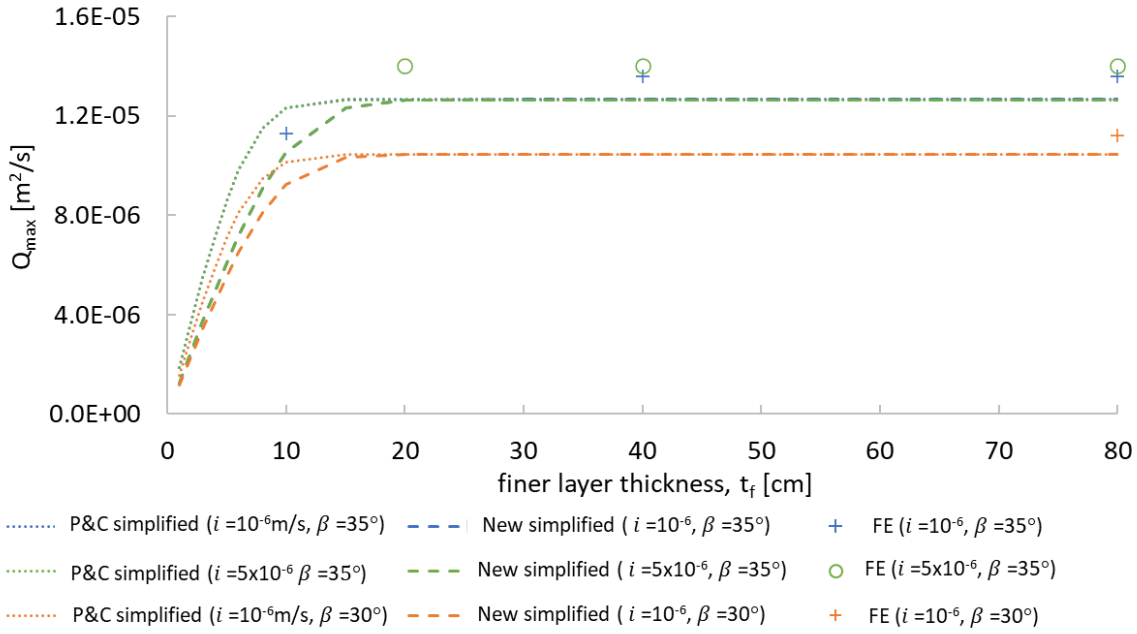

Figure 5-19 Water transfer capacity of sloping CBSs with F.L. made of fine sand

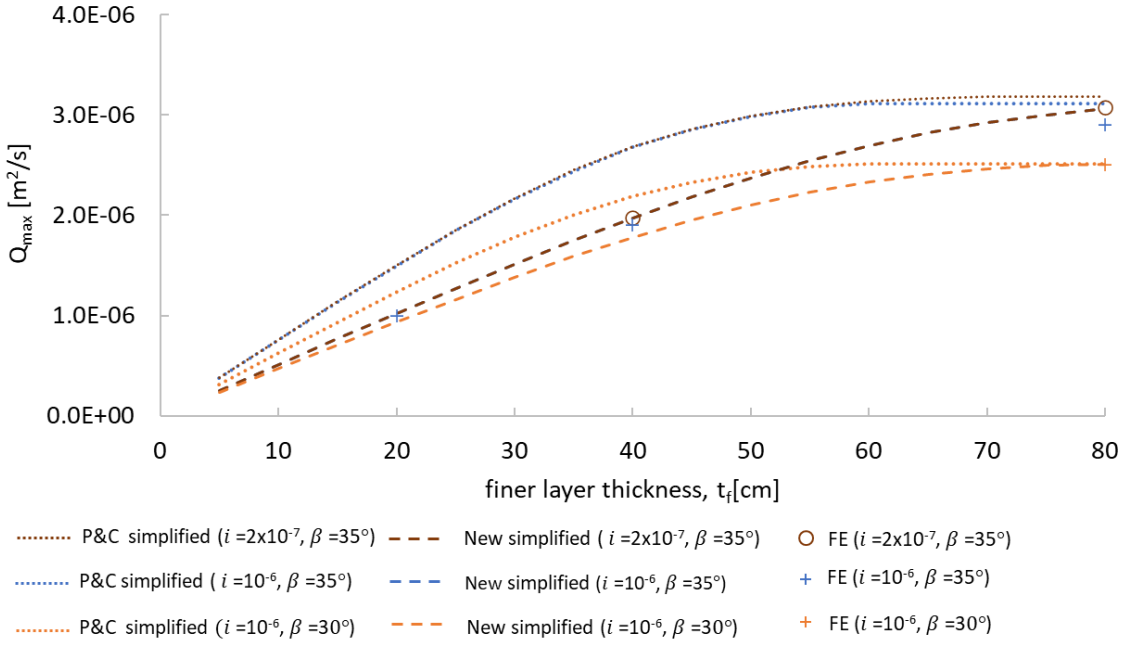

Figure 5-20 Water transfer capacity of sloping CBSs with F.L made of silty sand.

Various important trends are illustrated by the FE results in Figures 5-19 and 5-20 and Table 5-4. Firstly, the water transfer capacity Q_{max} is significantly greater when the F.L is made of fine sand than when the F.L is made of silty sand (as previously reported by Scarfone (2020) and Scarfone et al. (2022)). For example, with β = 35° and t_f = 40 cm, $Q_{max} \approx$ 1.4x10^{-5} m^2/s when the F.L is made of fine sand and Q_{max} ≈1.9x10^{-6} m^2/s when the F.L is made of silty sand. Secondly, when the F.L is made of fine sand, no significant gain in Q_{max} is achieved by increasing the thickness of the F.L beyond about 15 cm, whereas when the F.L is made of

silty sand, increasing the F.L thickness up to 80 cm can be beneficial. Finally, water transfer capacity Q_{max} increases with increasing slope angle (compare the results for β = 35° with those for β = 30° in Figures 5-19 and 5-20).

Table 5-4 Diversion length, water transfer capacity and water storage capacity from numerical simulations

Analysis identifier	β (°)	F.L. material	t_f (cm)	i (m/s)	L_D (m)	Q_{max} (m^2/s)	WSC (m)
B_FSGV_F10i106S35	35	FS	10	10^{-6}	11.3	$1.13x10^{-5}$	0.040
B_FSGV_F40i106S35	35	FS	40	10^{-6}	13.6	$1.36x10^{-5}$	0.096
B_FSGV_F80i106S35	35	FS	80	10^{-6}	13.6	$1.36x10^{-5}$	0.151
B_FSGV_F20i506S35	35	FS	20	$5x10^{-6}$	2.8	$1.40 x10^{-5}$	0.069
B_FSGV_F40i506S35	35	FS	40	$5x10^{-6}$	2.8	$1.40 x10^{-5}$	0.105
B_FSGV_F80i506S35	35	FS	80	$5x10^{-6}$	2.8	$1.40 x10^{-5}$	0.177
B_FSGV_F80i106S30	30	FS	80	$2x10^{-7}$	11.2	$1.12 x10^{-5}$	0.147
B_SSGV_F40i207S35	35	SS	40	$2x10^{-7}$	9.9	$1.98 x10^{-6}$	0.163
B_SSGV_F80i207S35	35	SS	80	$2x10^{-7}$	15.4	$3.08 x10^{-6}$	0.310
B_SSGV_F20i106S35	35	SS	20	10^{-6}	1.0	$1.00x10^{-6}$	0.082
B_SSGV_F40i106S35	35	SS	40	10^{-6}	1.9	$1.90x10^{-6}$	0.153
B_SSGV_F80i106S35	35	SS	80	10^{-6}	2.9	$2.90x10^{-6}$	0.310
B_SSGV_F80i106S30	30	SS	80	10^{-6}	2.5	$2.50x10^{-6}$	0.310

5.5.3 Water storage capacity

This section presents numerical validation of water storage capacity calculation by the new simplified method, by comparing with the finite element numerical results, with the predictions of the existing simplified semi-analytical method by Parent and Cabral method also shown for comparison. Table 5-1 lists the numerical simulations with Type B models and the different parameter values that were used in the numerical simulations. The water storage capacities ($WSCs$) of CBSs for different thickness of F.L. and rainfall infiltration rates are shown in Figure 5-21 (finer layer made of fine sand) and Figure 5-22 (finer layer made of silty sand).

Figure 5-21 shows the values of water storage capacity from the finite element (FE) results and from the two simplified methods (i.e. P&C simplified method and new simplified method). Values of water storage capacity from the FE results were determined from numerical integration (over the thickness of the F.L) of degree of saturation with respect to z (at $x = L_D$) and then multiplication by the porosity Φ (see Equation 4-1). Water storage capacity for each simplified method (shown previously in Figures 5-5 and 5-6) was calculated from Equations 4-7 and 4-8 (Parent and Cabral (2006) simplified method) or Equations 5-29 and 5-30 (new simplified method). Values of WSC determined from all the numerical simulations are also presented in Table 5-4.

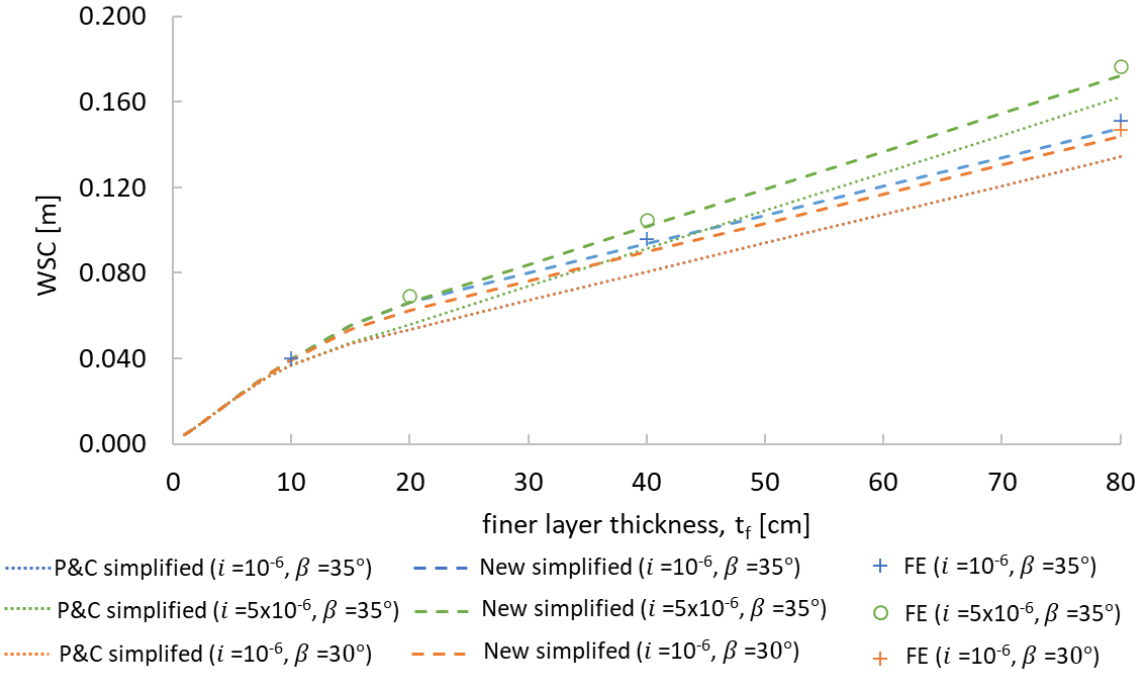

Figure 5-21 Water storage capacity of sloping CBSs with F.L made of fine sand

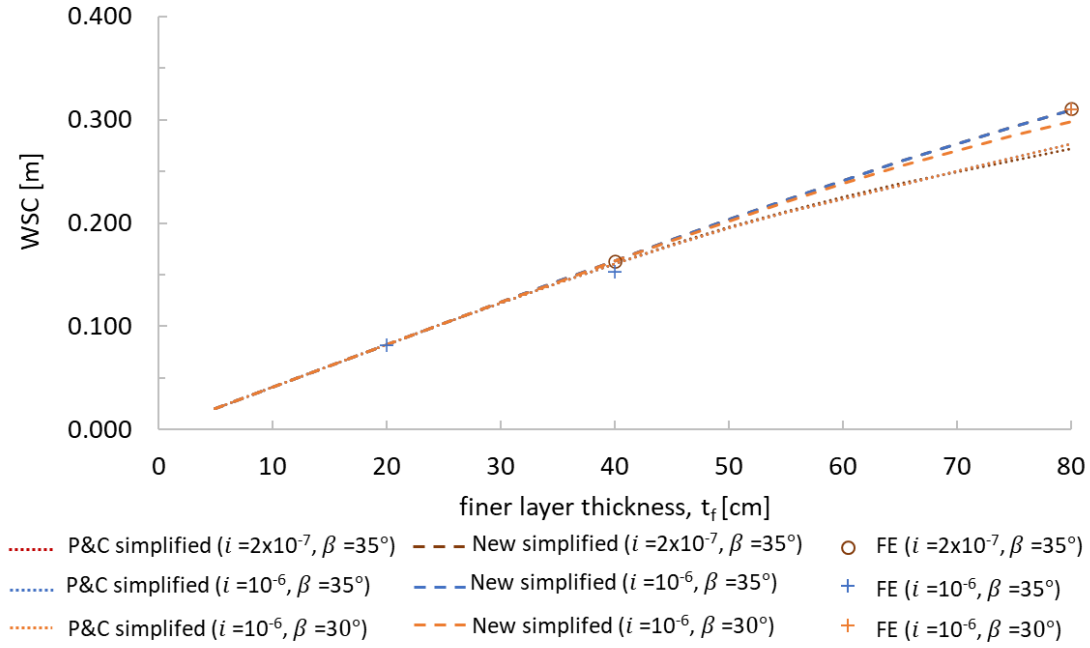

Figure 5-22 Water storage capacity of sloping CBSs with F.L made of silty sand

Inspection of Figures 5-21 and 5-22 shows that the values of WSC predicted by the new simplified method are a reasonable match with the FE results for all cases analysed whereas the Parent and Cabral simplified method results in significant under-prediction of WSC in a number of cases. When the F.L is made of fine sand (Figure 5-21), the new simplified method tends to slightly underpredict the value of WSC (i.e. it is slightly conservative). In contrast, when the F.L is made of silty

sand (Figure 5-22), the new simplified method matches the FE results in almost all cases, but slightly under-predicts WSC for β =30°, t_f= 80 cm, i =10^{-6} m/s and slightly over-predicts WSC for β =35°, t_f= 40 cm, i =10^{-6} m/s. The Parent and Cabral simplified method underestimates WSC in all cases when the F.L is made of fine sand (Figure 5-21) and in those cases involving the greatest thickness of F.L (t_f= 80 cm) when the F.L is made of silty sand (Figure 5-22).

Overall, the results presented in Figures 5-21 and 5-22 and Table 5-4 show that WSC is significantly greater when the F.L is made of silty sand than when the F.L is made of fine sand (as previously reported for horizontal CBSs in Section 4.3 and as reported for sloping CBSs by Scarfone (2020) and Scarfone et al. (2022)). For example, with β = 35°, t_f= 40 cm and i = 10-6m/s, WSC = 0.096 m when the F.L is made of fine sand and WSC = 0.153 m when the F.L is made of silty sand. Moreover, WSC can be increased by increasing the thickness of the finer layer for both types of finer layer material (fine sand and silty sand). Finally, WSC increases slightly with increasing slope angle β if the F.L is thicker (compare the results for β = 35° with those for β = 30° in Figures 5-21 and 5-22).

5.5.4 Influence of F.L material on transfer capacity and storage capacity

Table 5-1 shows that Model Type B numerical simulations with β = 35°, t_f = 40 cm and i = 10^{-6} m/s were performed using four different finer layers materials: silty sand; fine sand; medium sand; and coarse sand. The results of these simulations, and the corresponding predictions of the new simplified method, were used to investigate the influence of F.L material on water transfer capacity Q_{max} and water storage capacity WSC. In all cases, the C.L material was the gravelly sand. The only influence of the C.L material on transfer capacity and storage capacity is through the breakthrough value of suction s_1 at the bottom of the F.L, which is equal to the bulk water continuity value of suction for the C.L. material $s_{BWC,c}$.

The SWRC and SHCC properties of the four different F.L materials are shown in Table 5-3 and Figure 5-8. The silty sand parameter values were taken from a real material (see Scarfone (2020)). The parameter values for the other three fictitious F.L materials were then simply scaled appropriately (according to relevant

physical relationships) using the different values of D_{10}, which were selected as 5,10, and 25 times the D_{10} value of the silty sand (see Table 5-3). The value of porosity Φ was considered the same for all four soils, as was the value of the parameter m in the SWRC and SHCC expressions. In reality, porosity may vary slightly for the different F.L materials, but this would have a modest effect on the results presented here. Values of intrinsic permeability k_i and hence saturated hydraulic conductivity k_s were considered proportional to $(D_{10})^2$. Values of $\bar{P}_0$ in the SWRC expression were selected as proportional to $(D_{10})^{-1}$ and values of the SWRC parameter ξ were then selected by appropriate curve-fitting. Values of C^{Film} were assumed proportional to $(D_{10})^{-1}$(see Equation 2-56), meaning that values of C_r^{Film} were proportional to $(D_{10})^{-3}$ (see Equation 3-31).

Figure 5-23 shows final steady state profiles of suction s, degree of saturation S_l and horizontal seepage velocity q_h for the four numerical simulations (at $x = L_D$) and the corresponding predictions of the new simplified method. The match between simplified predictions of s, S_l and q_h and corresponding results from the FE simulations is generally very good, with the most significant mis-matches being the values of S_l and q_h for the case with the F.L made of coarse sand (CS), at the very bottom of the F.L (where most of the water transfer is occurring). It is worth noting that, for the coarse sand, very small errors in the prediction of the suction (see Figure 5-23a) can result in much more significant errors in the predictions of S_l and q_h (see Figures 5-23b and 5-23c). As noted previously, it is also possible that when the F.L is made of coarse sand, the underlying implicit assumption of the new simplified method of a dramatic contrast of hydraulic properties between F.L and C.L is no longer fully justified. Finally, (as noted in Section 5.3.1) it is also possible that even greater refinement of the FE mesh in the very bottom part of the F.L would have been appropriate for the simulation involving coarse sand, because in this case all the water transfer occurs in an extremely thin band at the bottom of the F.L.

Figures 5-24 and 5-25 show values of water transfer capacity Q_{max} and water storage capacity WSC respectively plotted against D_{10} particle size for the four different F.L materials. Results from the numerical simulations are shown, together with the corresponding predictions from the new simplified method. For the numerical simulations involving fine sand and silty sand, the values of Q_{max}

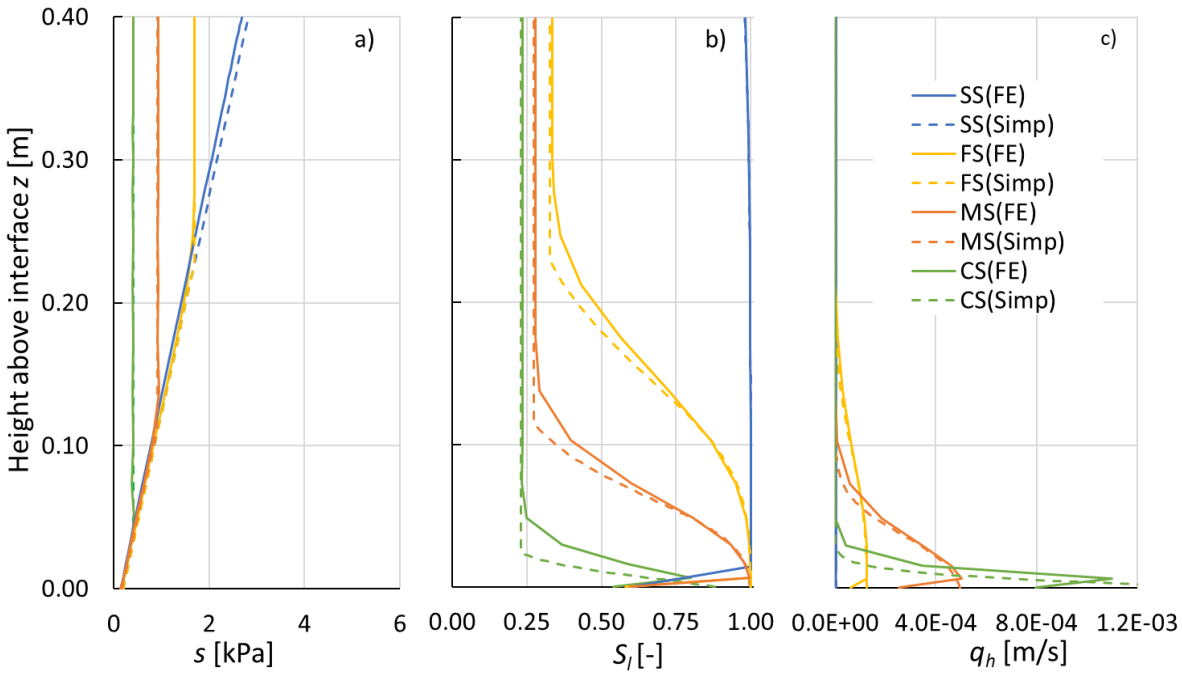

Figure 5-23 Final steady state profiles for x ≥ L_D for different F.L materials: a) suction; b) degree of saturation; and c) horizontal liquid water velocity (β =35°, t_f = 40 cm, i = 10^{-6} m/s)

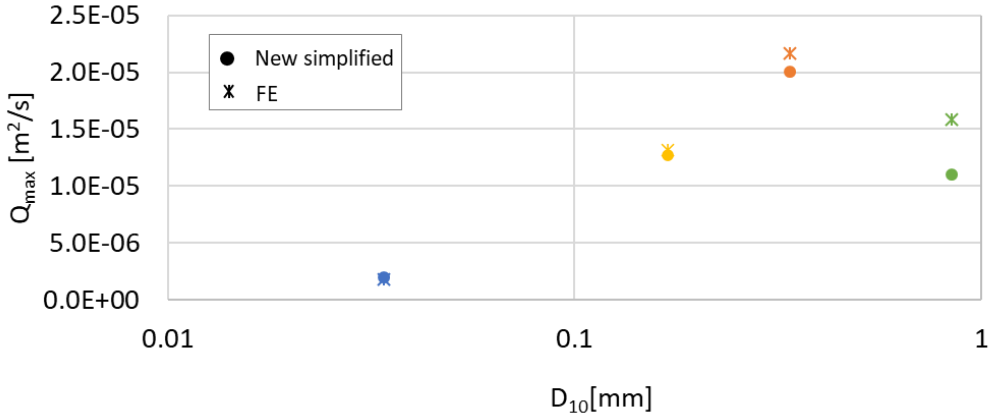

Figure 5-24 Influence of F.L. material on water transfer capacity ($\beta = 35°, t_f$ = 40 cm, i = 10^{-6} m/s)

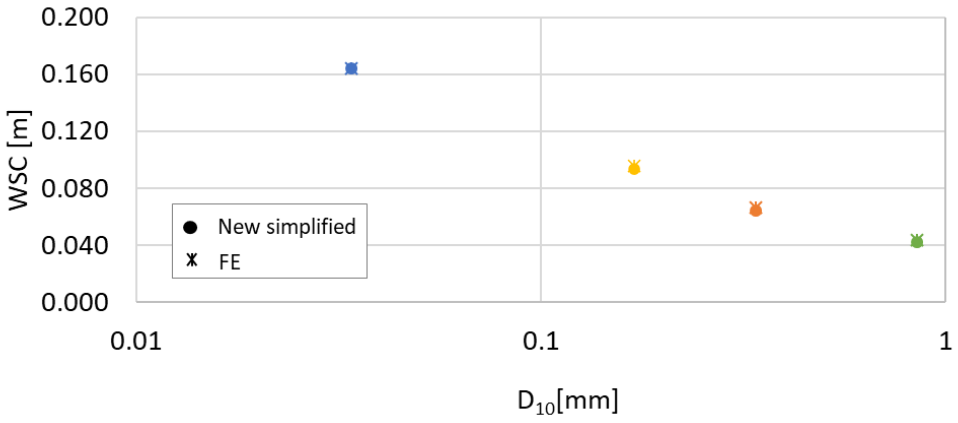

Figure 5-25 Influence of F.L. material on water storage capacity ($\beta = 35°, t_f$ = 40 cm, i = 10^{-6} m/s)

were determined by the method described in Section 5.5.2, using Equation 5-33, with the diversion length L_D determined from the plot of final steady interface flow velocity q_i against horizontal coordinate x. However, for the numerical simulations involving medium sand and coarse sand, the plots of q_i against x were considered unreliable (indicating numerical instabilities, possibly due to insufficient mesh refinement in the lower part of the F.L and calculation of a q_i as a very small difference between two much larger quantities (q_v and $q_h \tan\beta$), as described in Section 5.4). In these four cases, values of water transfer capacity Q_{max} from the FE simulations were determined by numerically integrating the corresponding profiles of horizontal water velocity shown in Figure 5-23c (values of q_h were not subject to numerical instabilities).

Inspection of Figure 5-24 shows that the new simplified method provides a reasonable match to the values of Q_{max} from the numerical analyses when the F.L is made of silty sand or fine sand, but it slightly underestimates Q_{max} from the numerical analyses when the F.L is made of medium sand, and significantly underestimates Q_{max} from the numerical analyses when the F.L is made of coarse sand. As described earlier, this could represent a weakness of the simplified method (if the underlying assumption of a dramatic contrast between hydraulic properties of F.L and C.L is no longer valid). Alternately, it could represent a weakness of the numerical analyses, with greater mesh refinement required at the bottom of the F.L, because water transfer is increasingly concentrated into a narrow zone at the base of the F.L, when the F.L materials get coarser (see Section 5.3.1).

Considering both FE results and simplified method predictions, it is clear from Figure 5-24 that Q_{max} is greatest when the F.L is made of medium sand (D_{10}= 0.34 mm), Q_{max} is slightly lower if the F.L is made of fine sand (D_{10}= 0.17 mm) or coarse sand (D_{10}= 0.85 mm) and Q_{max} is much lower if the F.L is made of silty sand (D_{10}= 0.034 mm). The reason for this is clear from examination of Figure 5-23c. As the F.L become coarser, the peak value of q_h, at the bottom of the F.L, increases (because of the increased hydraulic conductivity at high value of S_l), but the depth of the zone over which horizontal flow is occurring decreases (because of the more rapid drop of S_l with elevation z). Q_{max} is given by integrating q_h with respect to

z (i.e. the area under the curve) and this reaches a maximum for the case of medium sand.

Inspection of Figure 5-25 shows, in all four cases, a good match between predicted values of water storage capacity WSC from the new simplified method and the corresponding values of WSC from the numerical analyses. The results show that WSC increases as the F.L material become finer. The reason for this is clear from Figure 5-23b, with high values of S_l achieved over greater depths as the F.L is made finer.

For a sloping CBS subjected to realistic rainfall conditions (i.e. intermittent and of varying intensity, as considered in Chapters 6 and 7), the performance of the CBS depends upon both water transfer capacity Q_{max} and water storage capacity WSC. The relative importance of Q_{max} and WSC will depend upon climatic conditions. Inspection of Figures 5-24 and 5-25 suggests that, as stated by Scarfone (2020) and Scarfone et al. (2022), for many climatic conditions, fine sand may be a suitable material for the F.L of a sloping CBS, as it provides reasonable values of both Q_{max} and WSC. If, however, the climate is generally dry with occasional intense short-duration extreme rainfall events, it may be possible to rely entirely on storage capacity and hence silty sand maybe more suitable for the F.L (as stated by Scarfone (2020) and Scarfone et al. (2022)). Finally, if the climate involves very long duration extreme rainfall events, where CBS performance relies entirely on water transfer capacity, medium sand may be the most suitable material for the F.L.

5.5.5 Behaviour at x < L_D: suction profiles, water transfer and water storage

The aim of this section is to understand the hydraulic behaviour within a sloping CBS at the final steady state at cross sections further up the slope than the diversion length ($x < L_D$). The data points in Figure 5-26 show final steady state suction profiles from a typical FE simulation (β = 35°, FSGV, t_f = 40 cm, i = 10^{-6} m/s) taken at three different cross-sections, corresponding to $x = L_D$ (x = 13.6 m) and $x < L_D$ (x = 9.6 m and x = 4.0 m). It is clear, from inspection of Figure 5-26, that for $x < L_D$ the steady state suction value at the interface at the bottom of

the F.L is, as expected, greater than the critical value corresponding to breakthrough ($s_{BWC,c}$ = 0.2 kPa). It is also clear that, for $x < L_D$, the gradient of the suction profile in the lower part of F.L is the same as the corresponding gradient of the suction profile at $x = L_D$. This shows that, in this lower part of the F.L, flow is approximately parallel to the interface at $x < L_D$ as well as at $x \geq L_D$. In the upper part of the F.L, the suction profile is constant at s_f^* for all cross-sections.

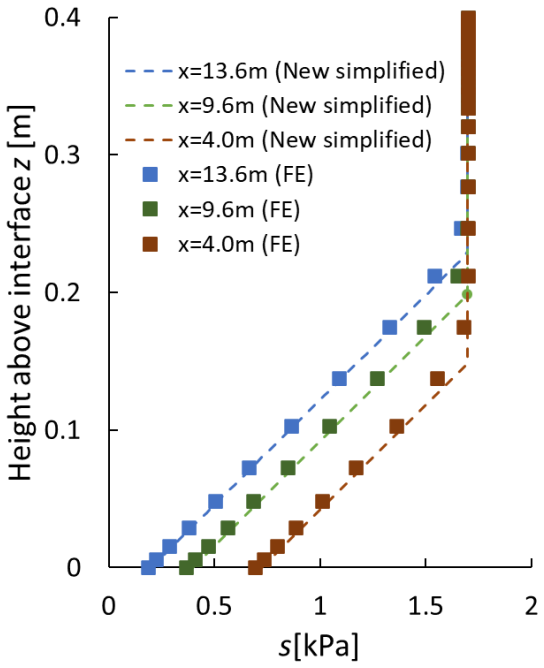

Figure 5-26 Final steady state suction profiles at x≤ L_D (β=35°,FSGV, t_f=40cm and i=10^{-6} m/s)

The new simplified method can be extended to cross-sections at $x < L_D$, to predict suction profiles, values of water transfer Q_x and water storage WS at different values of x, by assuming flow parallel to the interface in the lower part of the F.L and hence a vertical suction gradient given by Equation 5-14 in this part of the F.L. For $x < L_D$, water transfer Q_x and water storage WS are defined by:

$$Q_x = \int_0^{t_f} q_h \, dz \qquad \text{5-34}$$

$$WS = \Phi \int_0^{t_f} S_l \, dz \qquad \text{5-35}$$

For $x < L_D$, Q_x is less than the water transfer capacity Q_{max} and WS is less than the water storage capacity WSC.

The new simplified method procedure for predicting suction profiles and corresponding values of Q_x and WS for different values of x less than the diversion length L_D, starts by assuming a value of suction at the interface s_i lying between the breakthrough value $s_{BWC,c}$ and the limiting value of s_f^*. The calculation process is performed for different value of s_i, with each value of s_i subsequently calculated as referring to a different value of x between zero and the diversion length L_D (see Equation 5-37 below). For each value of suction at the interface s_i, and the corresponding assumed suction profile, the value of water transfer Q_x is calculated, using the SHCC of the F.L, as:

$$Q_x = \frac{\tan\beta}{\gamma_l}\int_{s_i}^{s_5} k_l\, ds \qquad \textbf{5-36}$$

where s_5 is the value of suction at the top of the F.L, given by either s_f^* or $s_i + \alpha\gamma_l t_f$, whichever is the smaller. The horizontal coordinate x of the cross-section with this suction profile is then given by:

$$x = Q_x/i \qquad \textbf{5-37}$$

Finally, the value of water storage WS corresponding to this value of x and this suction profile is calculated, using the SWRC of the F.L, as:

$$WS = \frac{\Phi}{\alpha\gamma_l}\int_{s_i}^{s_f^*} S_l\, ds + \Phi S_l\left(s_f^*\right)\left(t_f - \frac{s_f^* - s_i}{\alpha\gamma_l}\right), \text{if } s_f^* < s_i + \alpha\gamma_l t_f \qquad \textbf{5-38}$$

or

$$WS = \frac{\Phi}{\alpha\gamma_l}\int_{s_i}^{s_i+\alpha\gamma_l t_f} S_l\, ds\,, \text{if } s_f^* \geq s_i + \alpha\gamma_l t_f \qquad \textbf{5-39}$$

Figure 5-26 shows for a typical case, the suction profiles calculated by the new simplified method for different values of x plotted together with the corresponding results from the numerical simulation. It is clear that the agreement between the predictions of the simplified method and the results of the FE simulations is excellent.

Figures 5-27 and 5-28 show results, from the new simplified method and from the corresponding FE simulations, of water transfer Q_x and water storage WS plotted against horizontal coordinate x for different values of rainfall infiltration rate i (for the case β = 35°, FSGV, t_f = 40 cm, i = 1x10^{-6}, 2x10^{-6}, and 5x10^{-6} m/s). The values of Q_x and WS from the FE simulations shown in Figures 5-27 and 5-28 were calculated from Equations 5-34 and 5-35 respectively, using numerical integration and values of q_h and S_l from the FE results. As a consequence, the FE values of Q_{max} shown in Figure 5-27 (for $x \geq L_D$) are not necessarily identical to those listed in Table 5-4 and shown in Figure 5-14, which were calculated from Equation 5-33 and the values of diversion length L_D determined from the FE simulations. It is clear from Figures 5-27 and 5-28 that the agreement between the predictions of the simplified method and the results of the FE simulations is excellent. Generally, the predictions of Q_x and WS from the simplified method are slightly conservative when compared with the FE results (i.e. values of Q_x and WS are slightly under-predicted by the simplified method). This was true for all the numerical simulations involving finer layers made of fine sand or silty sand. It is also worth noting from Figures 5-27 and 5-28 that, for a given CBS (i.e. given materials and fixed values of β and t_f), the water transfer capacity Q_{max} is independent of rainfall intensity i (at least over a realistic range of rainfall intensities) whereas the water storage capacity WSC increases slightly with increasing rainfall intensity i.

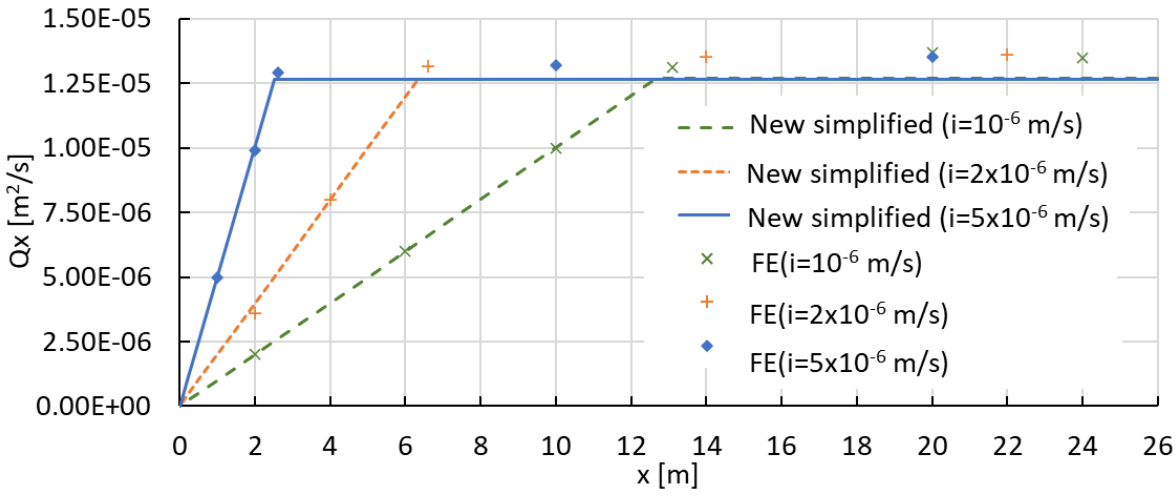

Figure 5-27 Steady state water transfer at different x values (β = 35°, FSGV, t_f = 40cm)

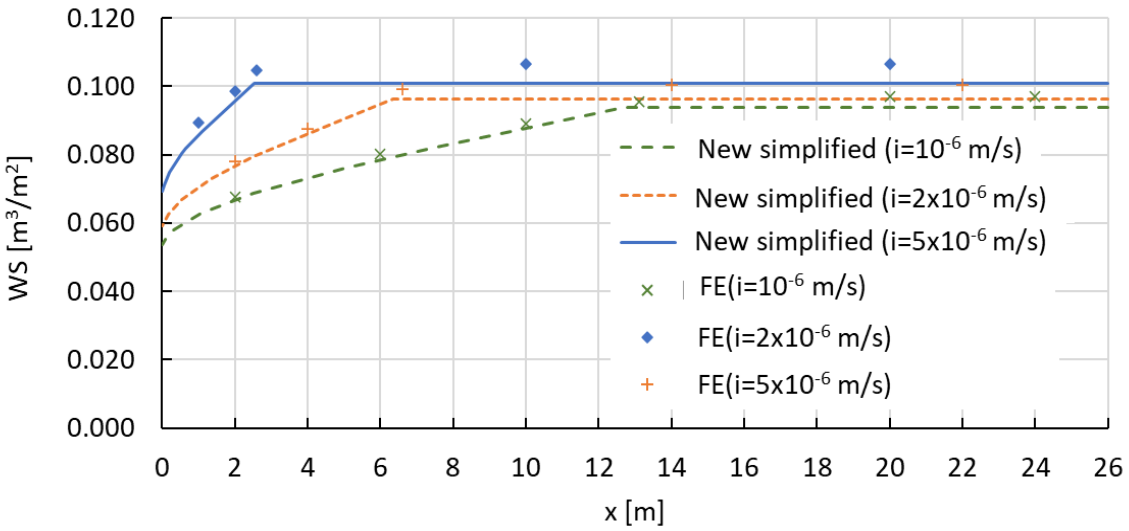

Figure 5-28 Steady state water storage at different x values (β = 35°, FSGV, t_f = 40cm)

5.6 Behaviour prior to final steady state

This section presents the development of the hydraulic behaviour of sloping CBSs prior to reaching final steady state, through examination of one specific FE simulation, corresponding to β = 35°, FSGV, t_f = 40 cm, i = 10^{-6} m/s). The diversion length in this simulation was L_D = 13.6 m, according to the FE simulation.

Figure 5-29 shows that for $x < L_D$ (x = 6 m and x = 13 m), no breakthrough occurred and the value of q_i remained very small throughout. For $x > L_D$ (x = 19 m and x = 24 m) breakthrough occurred at $t \approx$ 35 hours, with a sudden rise in q_i to a final steady state value almost equal to the rainfall intensity (i =10^{-6} m/s). The variation of q_i immediately after the sudden rise showed temporary numerical instability, which was identical at x = 19 m and x = 24 m. This probably reflects the challenge of accurately determining q_i as the small difference between two much larger quantities (q_v and $q_h \tan\beta$) and perhaps a need for greater mesh refinement in the lower part of the F.L (see Section 5.3.1). It is important to note that, while small errors arising from insufficient mesh refinement could produce large error of q_i; they would have a much smaller influence on corresponding values of s, S_l, q_h, Q_x, or WS.

It is clear from Figure 5-29 that the time to breakthrough was identical for x = 19 m and x = 24m (the variations of q_i for these two values of x are indistinguishable). The same behaviour occurred for all simulations listed in Table 5-1,with the time

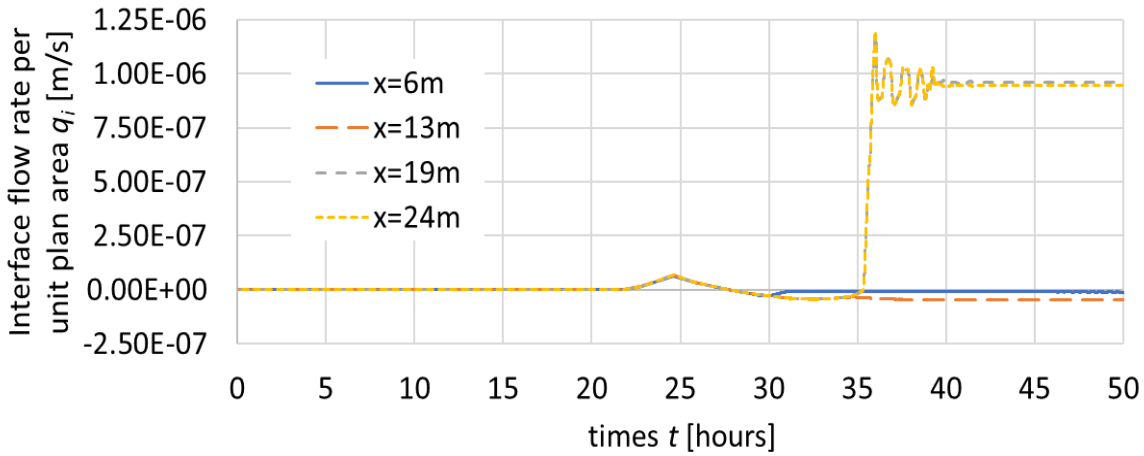

Figure 5-29 Development of interface flow velocity with time at different cross-sections (β = 35°, FSGV, t_f = 80 cm and i = 10^{-6} m/s)

to breakthrough independent of x for all values of x greater than or equal to the diversion length L_D. This is a very important observation. It had always been expected that every cross section at $x \geq L_D$ would behave in an identical fashion after breakthrough, but this observation suggests that even before breakthrough, and right up to the time of breakthrough, every cross-section at $x \geq L_D$ is behaving in an identical fashion. This suggests that rainfall infiltration entering at a given cross-section initially goes entirely into increasing the water stored at that cross-section and diversion down the slope of this infiltrating water only commences when the cross-section has reached its final steady state value of water stored. If cross-sections at $x \geq L_D$ began diverting water down the slope (within the F.L) prior to achieving their final steady state water stored, cross-sections at different values of x would be expected to achieve breakthrough at different times, with breakthrough occurring first at the bottom of the slope and breakthrough then gradually progressing back up the slope to the final steady state diversion length L_D. This observation, that water infiltrating at a given cross-section only begins to be diverted down the slope when the cross-section reaches a final steady state value of water stored, is used in the development of a simplified method of analysis for extreme rainfall events described in Chapter 7.

Figure 5-30 shows profile of suction s, degree of saturation S_l and horizontal seepage velocity q_h at different times for the cross-section at x = 19 m ($x > L_D$). Examination of Figure 5-30 shows that behaviour during the early stage (t = 10 hours and t = 20 hours) is identical to a horizontal CBS (see Section 4.5.1), with a partial wetting front (to $s = s_f^*$ and the corresponding value of S_l) progressing

downward from the ground surface and no horizontal water flow (q_h = 0). Arrival of this first partial wetting front at the interface at the bottom of F.L corresponds to the small peak in the value of q_i seen in Figure 5-29 at $t \approx$ 25 hours.

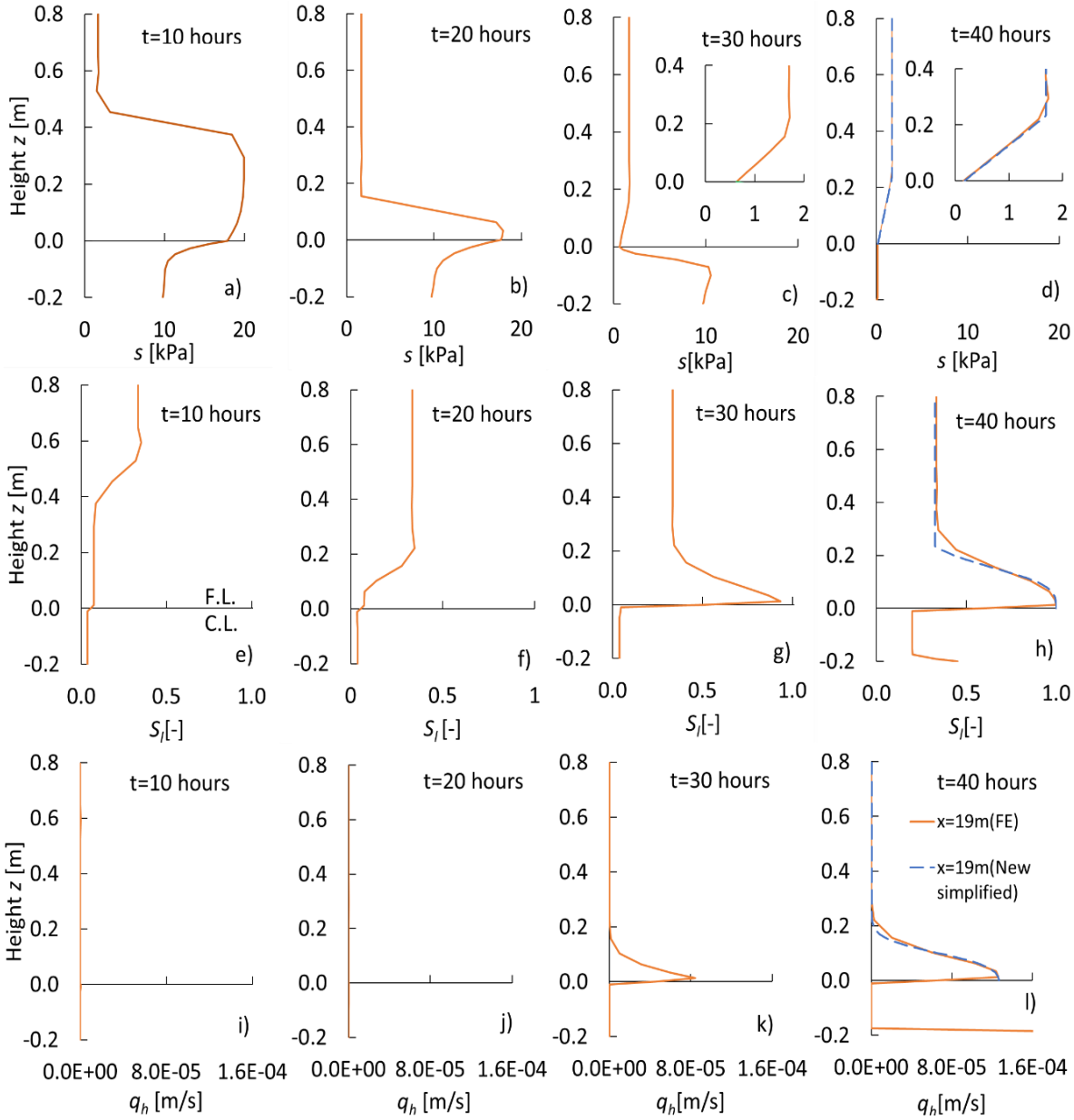

Figure 5-30 Profiles of suction, degree of saturation and horizontal seepage velocity at different times ($\beta = 35°$, FSGV, t_f = 80 cm, i = 10^{-6} m/s)

As with the horizontal CBSs, a second stage of additional wetting then occurs, with the additional water filling the cross-section from the bottom of the F.L (see t = 30 hours in Figure 5-30). It is during this stage that horizontal water transfer across the cross-section first begins to occur (see the plot of q_h for t = 30 hours). However, this does not necessarily mean that rainwater infiltrating at the top of the cross-section has started diverting down the slope. It is more likely that, at t = 30 hours, the rainwater infiltrating at the top of the cross-section at x = 19 m is

still going entirely into increasing the water stored in the cross-section and, at this time, the transfer flow at the bottom of the F.L simply represents water transfer across the cross-section, arising from rainwater infiltration into the parts of the CBS further up the slope, at values of x< L_D. These cross-sections further up the slope, at $x < L_D$, complete filling to lower final steady state values of WS (see Figure 5-28) at earlier times than those cross-sections at x≥ L_D and hence begin transferring water down the slope at earlier times.

The results at t = 40 hours in Figure 5-30 represent the final steady state profiles at x = 19 m, with water breakthrough at the interface now occurring (see Figure 5-29) water transfer down the slope occurring at full capacity ($Q_x = Q_{max}$) and water storage at full capacity ($WS = WSC$). Note that the final steady state profile of q_h for $x > L_D$ includes significant water transfer occurring at the bottom of the C.L (as a consequence of water breakthrough into the C.L from $x = L_D$ to x = 19m). In a real CBS on a slope, some or all of this water would be percolating into the underlying soil. Also shown in Figure 5-30 for t = 40 hours are the final steady state profiles within the F.L calculated by the new simplified method for $x \geq L_D$. These show excellent agreement with the corresponding FE results.

5.7 Multi-layered sloping CBSs

FE simulations were performed for two sloping multi-layered CBSs, as shown in Table 5-2 and Figure 5-7. Both involved two finer layers, each with a thickness of 20 cm (FSGV with i = 5x10^{-6} m/s in one case and SSGV with i = 10^{-6} m/s in the other). Corresponding simulations for conventional CBSs (also with t_f = 20 cm) can be found in Table 5-1. Values of diversion length L_D from the FE analyses, identified from the variations of final steady state q_i for the interface at the bottom of the lowest F.L plotted against horizontal coordinate x, are listed in Table 5-5 for the two multi-layered CBSs and the corresponding conventional CBSs. It is clear that, in both cases, use of a multi-layered CBS has doubled the value of diversion length L_D i.e. doubled the water transfer capacity Q_{max}. In contrast, use of a thicker F.L within a conventional CBS would have produced very little increase of Q_{max} in the case where the F.L was made of fine sand (see Figure 5-19)

Table 5-5 Diversion length of sloping multi-layered CBSs

β = 35 °, FSGV, t_f = 20 cm, i = 5x10^{-6} m/s			
No. of finer layers	**Diversion length L_D (m)**		
	FE	New simplified	Parent & Cabral simplified
1	2.60	2.53	2.53
2	5.20	5.26	5.26
β = 35 °, SSGV, t_f = 20 cm, i = 1x10^{-6} m/s			
No. of finer layers	**Diversion length L_D (m)**		
	FE	New simplified	Parent & Cabral simplified
1	1.00	1.02	1.50
2	2.00	2.03	3.02

Figures 5-31 and 5-32 show the final steady state profiles of s, S_l, and q_h for $x = L_D$ from the two multi-layered CBS simulations. Also shown in Figure 5-31 and Figure 5-32 are the corresponding profiles predicted by the new simplified method and by the simplified method of Parent and Cabral, both extended to multi-layered CBSs following the logic developed by Scarfone (2020) for horizontal multi-layered CBSs, described in Sections 2.9 and 4.1. In both cases, the simplified suction profile assumes a uniform value of suction $s_3 = s_c^*$ in each intermediate C.L. It is clear from Figures 5-31 and 5-32 that, in both cases, the extended version of the new simplified method provides an excellent match to the FE results, whereas the extended version of the Parent and Cabral simplified method (which assumes a simplified suction profile more appropriate to a horizontal multi-layered CBS) produces significant errors.

Values of diversion length L_D predicted by the two extended simplified methods are listed in Table 5-5, for comparison with the corresponding FE results. The extended new simplified method provides an excellent match to the FE results in all cases (conventional and multi-layered CBSs, with F.L made of either fine sand or silty sand). In contrast, the extended version of the Parent and Cabral simplified method provides accurate predictions of diversion length L_D when the finer layers are made of fine sand, but significantly over-predicts the values of L_D (for both conventional and multi-layered CBSs) when the finer layers are made of silty sand. The reasons for this are apparent from the profiles of horizontal seepage velocity q_h shown in Figure 5-31c and Figure 5-32c.

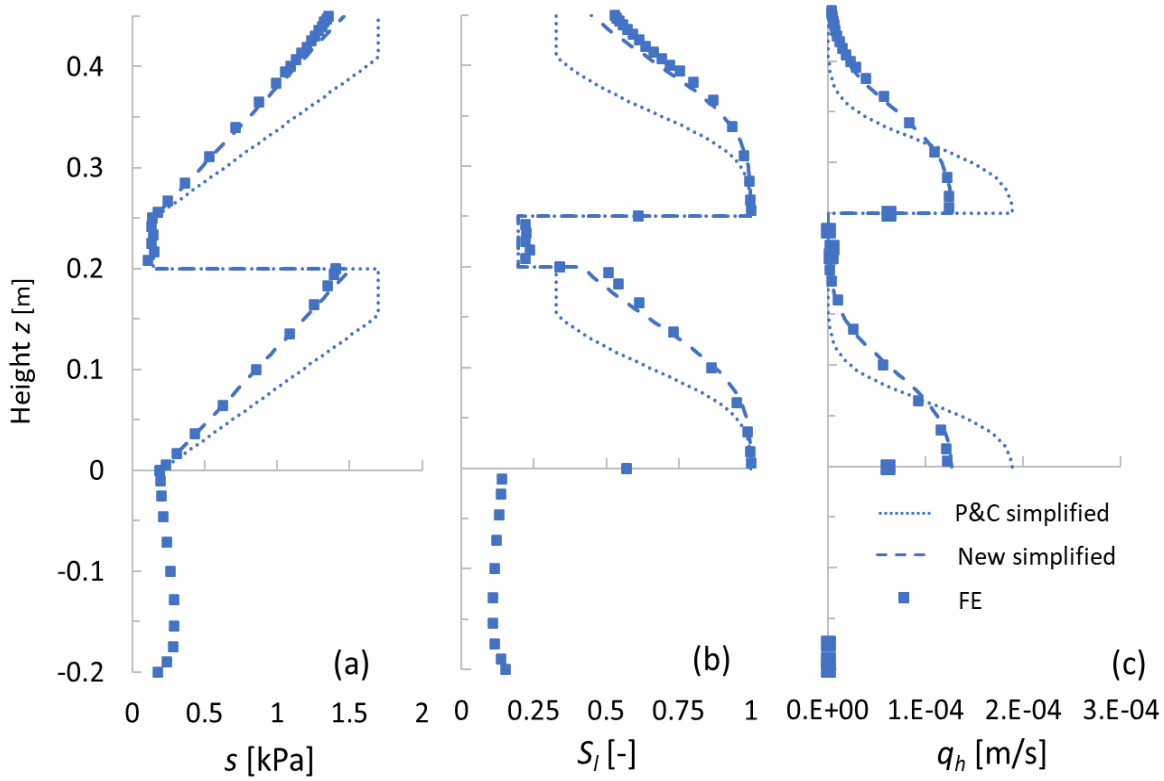

Figure 5-31 Final steady state profiles of: a) suction; b) degree of saturation; (c) horizontal seepage velocity at $x = L_D$ ($\beta = 35°$, FSGV, t_f = 20 cm, i = 5x10^{-6} m/s)

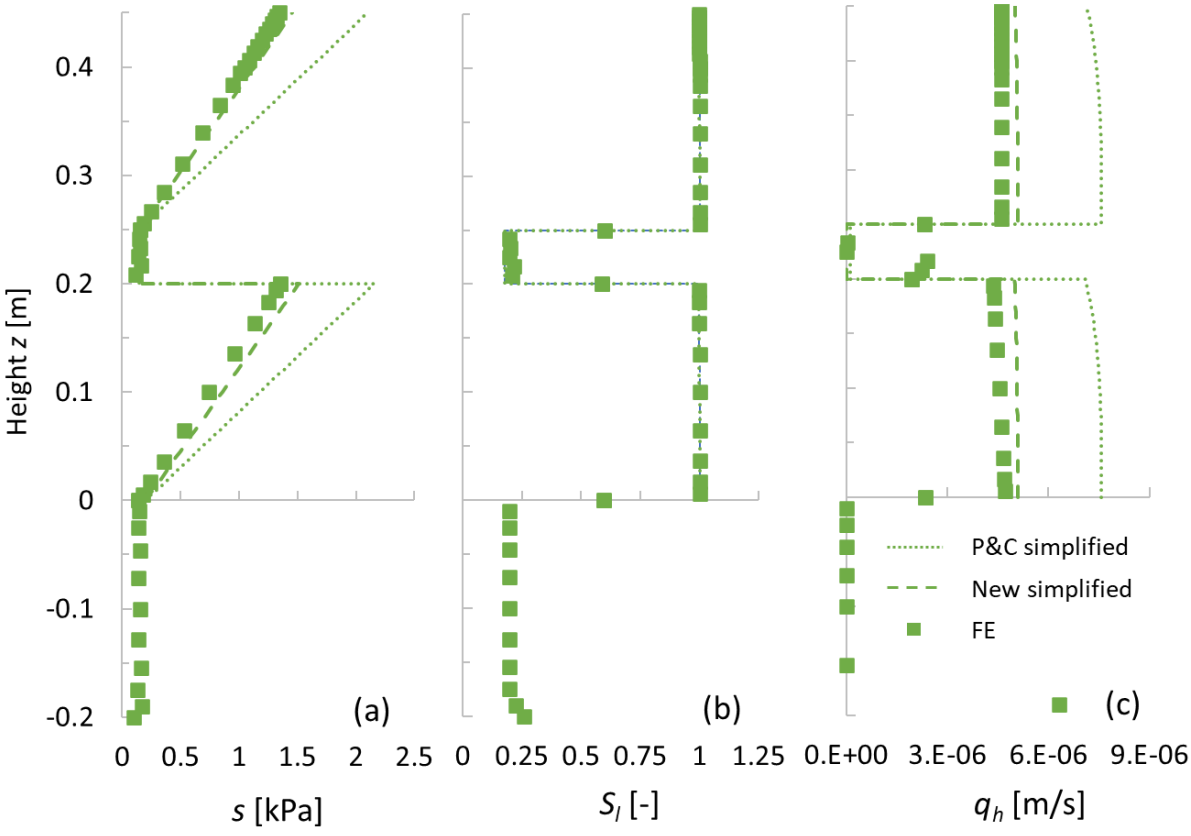

Figure 5-32 Final steady state profiles of: a) suction; b) degree of saturation; (c) horizontal seepage velocity at $x = L_D$ ($\beta = 35°$, SSGV, t_f = 20 cm, i = 10^{-6} m/s)

5.8 Conclusions

The main achievements and conclusions arising from the study of sloping CBSs subjected to continuous rainfall of constant intensity presented in this chapter are summarized below.

1) A new simplified method of analysis has been developed for determining the water transfer capacity Q_{max}, diversion length L_D and water storage capacity WSC of sloping CBSs subjected to continuous rainfall of constant intensity. The new simplified method assumes an approximate steady state suction profile on vertical cross-sections of the F.L at and beyond the diversion length L_D that is appropriate for sloping CBSs, with flow parallel to the slope in the lower part of the F.L. This contrasts with an existing simplified method from Parent and Cabral (2006), which incorrectly assumes a simplified suction profile appropriate to horizontal CBSs.

2) In all cases analysed, the proposed new form of approximate steady state suction profile on vertical cross-sections at and beyond the diversion length L_D is a much better match with the corresponding final steady state suction profiles from FE results than the approximate suction profile used in the existing simplified method of Parent and Cabral (2006) (e.g., see Figures 5-15 and 5-16).

3) In all cases where the F.L is made of fine sand or silty sand, the water transfer capacity Q_{max} (and hence diversion length L_D) predicted by the new simple semi-analytical method (Equation 5-28) is an excellent match to the water transfer capacity determined from the FE results (see Figures 5-19 and 5-20). Where the values of Q_{max} predicted by the two simple semi-analytical methods differ (this occurs when the finer layer is thin), the value of Q_{max} predicted by the existing semi-analytical method of Parent and Cabral (2006) overestimates the value determined from the FE results (see Figures 5-19 and 5-20). The method of Parent and Cabral (2006) overestimates the value of horizontal seepage velocity q_h at the very bottom of the finer layer but underestimates the thickness of the zone at

the bottom of the finer layer over which significant values of q_h occur (see Figures 5-15c).

4) Although the predictions of water transfer capacity Q_{max} from the two simplified semi-analytical methods are often identical and rarely differ by very much, the new simplified semi-analytical method predicts significantly higher values of water storage capacity (WSC) for sloping CBSs than the existing method of Parent and Cabral (2006) and these higher values of water storage capacity are in agreement with the FE results (see Figures 5-21 and 5-22).

5) Whereas the method of Parent and Cabral (2006) predicts that a sloping CBS has the same water storage capacity as a horizontal CBS, the new method correctly predicts that a sloping CBS has a higher water storage capacity than a horizontal CBS. This is important, because the performance of a sloping CBS under realistic intermittent rainfall will depend upon both water transfer capacity and water storage capacity.

6) For a slope of given gradient β and a CBS with a finer layer of given thickness and material, the water transfer capacity Q_{max} is almost independent of rainfall infiltration rate i (see Figures 5-19 and 5-20), whereas the water storage capacity WSC increases slightly with increasing rainfall infiltration rate i (see Figures 5-21 and 5-22).

7) For a slope of given gradient β and a CBS with a finer layer of a given material, the water transfer capacity Q_{max} initially increases with increasing thickness t_f of the finer layer, but the value of Q_{max} ultimately reaches a limiting value and does not increase further with further increases of t_f (see Figures 5-19 and 5-20). If the F.L is made of fine sand, Q_{max} reaches this limiting value when the thickness of the finer layer is less than 20 cm (see Figure 5-19), whereas if the F.L made of silty sand the limiting value of Q_{max} is only reached for t_f about 80 cm (see Figure 5-20)

8) The results of the FE simulations and the corresponding simplified method predictions show that a sloping CBS with the F.L made of fine sand will have

lower water storage capacity WSC but higher water transfer capacity Q_{max} than a sloping CBS with the F.L made of silty sand (i.e. a slightly finer material). WSC will decrease further and Q_{max} increase further if the F.L is made of medium sand (i.e. slightly coarser again). However, if the F.L is made of coarse sand (i.e. even coarser) Q_{max} begins to decrease as well as WSC i.e. there is no possible argument for using coarse sand for the F.L.

9) The new simplified method can be extended to cross-sections at $x < L_D$, to predict suction profiles (see Figure 5-26), values of water transfer Q_x (see Figure 5-27) and values of water storage WS (see Figure 5-28) at different values of x, by assuming flow parallel to the interface in the lower part of the F.L. and hence a vertical suction gradient given by $\partial s/\partial z = \alpha\gamma_l$ in this part of the F.L.

10) Behaviour prior to achieving final steady state involves two stages of wetting of the F.L, similar to horizontal CBSs. An initial partial wetting stage (to $s = s_f^*$) progress downwards from the top of the F.L and this is then followed by further wetting progressing upwards from the bottom of the F.L. The behaviour observed in the FE simulations suggests that rainfall infiltration entering at a given cross-section of the CBS initially goes entirely into increasing the water stored at that cross-section and diversion down the slope of this infiltrating water only commences when the cross-section has reached its final steady value of water stored.

11) Increased water transfer capacity can be achieved by the use of multi-layered CBSs. This is particularly effective for a CBS where the finer layer is made of fine sand, where increases of Q_{max} cannot be achieved by increasing the thickness of a single finer layer beyond about 20 cm but increases of Q_{max} can be achieved by adding additional number of finer layers.

Chapter 6 Sloping CBSs subjected to intermittent or varying intensity rainfall

This chapter presents numerical modelling of sloping CBSs subjected to simple patterns of intermittent or varying intensity rainfall (i.e. closer to real weather conditions than the continuous rainfall off constant intensity studied in Chapter 5). The aim was to develop improved understanding of the behaviour of sloping CBSs under intermittent or varying intensity rainfall, to aid the subsequent development of a new simplified method of analysis for sloping CBSs subjected to extreme rainfall events (see Chapter 7).

The numerical modelling described in this chapter involved three changes to the numerical modelling described in Chapter 5, as set out in the following three paragraphs.

Firstly, as described above, the applied rainfall was intermittent or of varying intensity rather than continuous and of constant intensity. Three different types of rainfall pattern were applied: single constant intensity rainfall events of limited duration (followed by zero rainfall), as shown in Figure 6.1a; various simple cyclic patterns of rainfall, as shown in Figure 6.1b; and various simple representations of extreme rainfall events, as illustrated by the example in Figure 6-1c.

Secondly, because of the intermittent or varying intensity rainfall, it was considered important to include the effects of evaporation from the ground surface (it was thought that water removed by evaporation during pauses between rainfall could be important). Modelling of evaporation at the ground surface was achieved through the use of an atmospheric boundary condition (see Section 3.4.2) at the ground surface. This required a change to thermo-hydraulic numerical modelling (rather than the simpler hydraulic numerical modelling used in Chapters 4 and 5), because the rate of evaporation from the ground surface depended upon the absolute humidity (or vapour density) ρ_v in the soil voids at the ground surface (see Equations 2-62 and 3-46), which depended in turn on both the suction and temperature of the soil at the ground surface (see Equations 2-5 and 2-4). Use of thermo-hydraulic numerical modelling meant that vapour diffusion within the CBS

due to temperature gradient (see Section 2.3.1) was included, whereas this was omitted in the hydraulic numerical modelling described in Chapters 4 and 5.

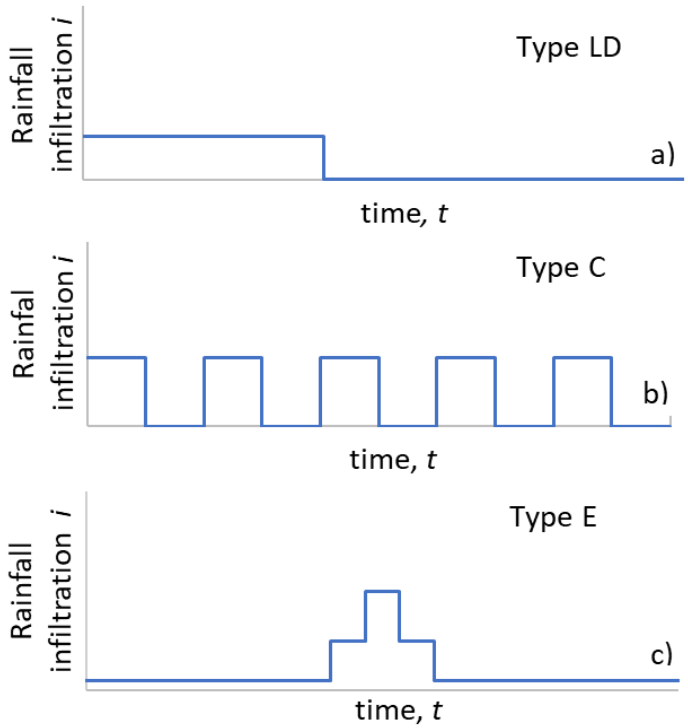

Figure 6-1 Typical rainfall patterns employed in Chapter 6: a) single rainfall event of limited duration; b) cyclic rainfall pattern; a) extreme rainfall event

Thirdly, because of the intermittent or varying intensity rainfall, it was considered important to include the effects of retention hysteresis (see Section 2.2.2) (whereas this was omitted in the modelling described in Chapters 4 and 5). Retention hysteresis was included by use of the hysteretic modVG-modM+LF advanced hydraulic constitutive model described in Sections 2.4 and 3.2.4).

This chapter consists of five sub-sections. Section 6.1 describes the thermo-hydraulic numerical modelling. The following three sub-sections present and discuss the results of the numerical simulations of sloping CBSs subjected to single rainfall events of limited duration (Section 6.2), cyclic rainfall patterns (Section 6.3) and extreme rainfall events (Section 6.4). Section 6.5 summarises the main conclusions of the work presented in the chapter.

6.1 Thermo-hydraulic numerical modelling

Some of the numerical simulations presented in this chapter involved 2-D thermo-hydraulic numerical modelling with atmosphere boundary condition at the ground

surface. A number of equivalent 2-D hydraulic numerical modelling simulations (with standard boundary conditions at the ground surface) were also performed, to explore the influence of evaporation at the ground surface, by comparing the results of thermo-hydraulic simulations (with evaporation) against equivalent hydraulic simulations (without evaporation).

In both types of numerical modelling (thermo-hydraulic and hydraulic), the pore gas pressure p_g was imposed as constant (at p_g = 100 kPa) throughout the analyses, the same as in Chapters 4 and 5. This meant that, in all analyses, movement of the gas phase was not calculated and hence advection of water vapour (see Section 2.3.1) was omitted (this would typically be in significant). Transport of water vapour by diffusion (see Section 2.3.1) was, however, included in all analyses, although thermally-driven vapour diffusion (likely to be the dominant mechanism of vapour diffusion) was included only in the thermo-hydraulic simulations. Temperature T was imposed as constant (at T = 20°C) in the hydraulic analyses.

6.1.1 Geometry, mesh, and material properties

Simple geometry model type B (see Figure 5-3c) with β = 35°, t_f = 40 cm and t_{CBS} = 60 cm, the same as previously used in Chapter 5, was used throughout this chapter and Chapter 7. The finite element mesh, for all simulations, was made of quadrilateral elements, following the same arrangement as previously used for the modelling in Chapter 5 (see Section 5.3.1).

In the simulations within this chapter, the F.L of the CBS was modelled as either a fine sand (FS) or a silty sand (SS), whereas the C.L was always modelled as a gravelly sand (GV). These three materials were directly equivalent to the coresponding materials studied in Chapters 4 and 5.

The majority of the simulations presented in this chapter employed the advanced hysteretic hydraulic constitutive model (hysteretic modVG-modM+LF) developed by Scarfone (2020) and Scarfone et al. (2020b) and described in Section 2.4. The materials properties of three materials are listed in Table 6.1. The values of the parameters $\bar{P}_{od}$ and $\bar{P}_{ow}$ in Table 6.1 control the locations of the main drying SWRC and main wetting SWRC respectively and additional parameters γ_d and γ_w control

the shapes of scaning drying SWRCs and scanning wetting SWRCs respectively (see Section 2.4.1). The SWRCs and SHCCs are shown in Figure 6-2, where the continuous lines represent the main wetting and main drying curves and dashed lines represent typical scanning curves. The values of $\bar{P}_{ow}$ in Table 6.1 corresponded to the values of $\bar{P}_o$ used for the non-hysteretic modelling in Chapters 4 and 5, which assumed that the soil state was always on the main wetting SWRC.

Table 6-1 Material properties for sloping CBSs including hydraulic hysteresis modelling

Materials		**Physical parameters**			
		Φ	k_i	$k_{s\ at\ T=20°C}$	D_{10}
	Constitutive Model	(-)	(m^2)	(m/s)	(mm)
Silty sand (F.L)	hysteretic modVG-modM+LF	0.411	$1.11x10^{-12}$	$1.08x10^{-5}$	0.034
Fine sand (F.L)	hysteretic modVG-modM+LF	0.411	$2.77x10^{-11}$	$2.70x10^{-4}$	0.170
Gravelly sand (C.L)	hysteretic modVG-modM+LF	0.382	$7.81x10^{-9}$	$7.62x10^{-2}$	2.730

	SWRC parameters							
	$\bar{P}_{0d}$	$\bar{P}_{0w}$	$\bar{\sigma}_{s0}$	m	ξ	S_{ls}	γ_d	γ_w
	(MPa)	(MPa)	(N/m)	(-)	(-)	(-)	(-)	(-)
Silty sand (F.L)	1.16E-2	6.05E-3	0.072	0.779	$1.36\ x10^{-2}$	1	8	8
Fine sand (F.L)	2.31E-3	1.21E-3	0.072	0.779	$6.79\ x10^{-3}$	1	8	8
Gravelly sand (C.L)	1.93E-5	6.45E-5	0.072	0.688	$3.27\ x10^{-3}$	1	6	6

	SHCC parameters					
	m	$S_{l,BWC/BWD}$	S_{ls}	C_r^{Film}	a^{Film}	d^{Film}
	(-)	(-)	(-)	($MPa^{-1.5}$)	(MPa)	(-)
Silty sand (F.L)	0.779	0.22	1	$1.19\ x10^{-7}$	$2.0\ x10^{-4}$	-1.5
Fine sand (F.L)	0.779	0.18	1	$9.54\ x10^{-10}$	$4.0\ x10^{-5}$	-1.5
Gravelly sand (C.L)	0.688	0.16	1	$2.21\ x10^{-13}$	$1.5\ x10^{-7}$	-1.5

In Section 6.4 a small number of simulations were performed with the non-hysteretic hydraulic constitutive model modVG-modM+LF. The results of these simulations were compared with the corresponding results from simulations performed with the hysteretic modVG-modM+LF hydraulic constitutive model, to investigate the influence of retention hysteresis. For some of the non-hysteretic simulations, the values of $\bar{P}_o$ were taken as $\bar{P}_{ow}$ from Table 6.1 (i.e. soil state always on the main wetting curve), whereas for other non-hysteretic simulations, the values of $\bar{P}_o$ were taken as $\bar{P}_{od}$ from Table 6.1 (i.e. soil state always on the main drying curve).

For thermo-hydraulic numerical modelling, thermal conduction and vapour diffusion were modelled by using Fourier's law and Fick's law respectively (see Section 3.2.4). The thermal conductivity λ (see Equations 3-35, 3-36 and 3-37) was determined by assuming the following parameters values: λ_{solid} = 7.7 $Wm^{-1}K^{-1}$, λ_{gas}

= 0.024 $Wm^{-1}K^{-1}$ and λ_{liq} = 0.6 $Wm^{-1}K^{-1}$,which were suggested by Laloui and Loria (2019). The diffusion coefficient of vapour in the gas phase (see Equations 3-32 and 3-33) was determined using default parameter values, recommended by Olivella et al. (1996): D = 5.9x10^{-6} $m^2s^{-1}K^{-n}Pa$, n = 2.3. Tortuosity was fixed at τ = 1, as recommended by Olivella et al. (1996).

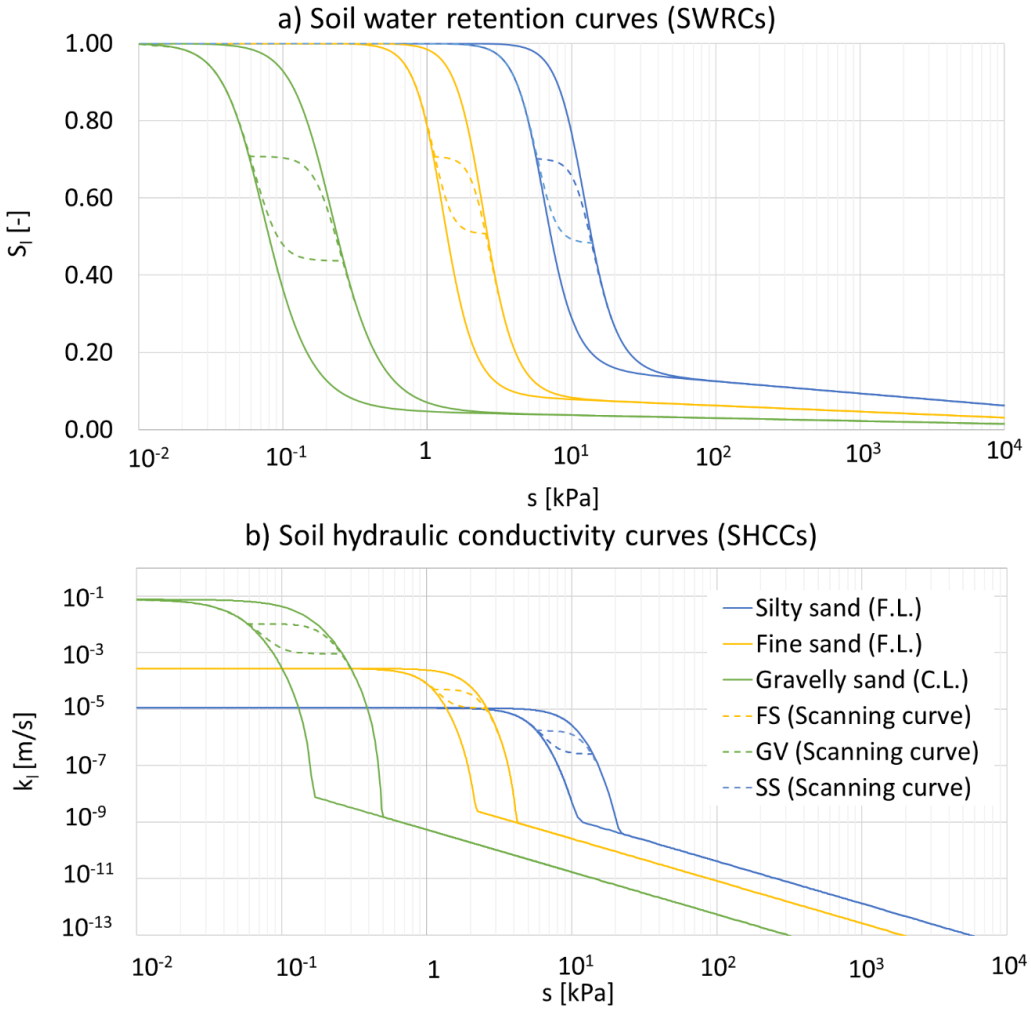

Figure 6-2 Hydraulic properties of materials at T = 20℃, including hydraulic hysteresis modelling: a) SWRCs and b) SHCCs including hydraulic hysteresis modelling

6.1.2 Initial and boundary conditions

The initial distribution of pore liquid pressure p_l within the CBS was the same as employed within the simulations reported in Chapter 5 (see Section 5.3.3), corresponding to a uniform initial value of suction s = 10 kPa in the C.L and a different uniform value of initial suction s = 20 kPa in the F.L. For the thermo-hydraulic numerical modelling a uniform initial value of temperature T was applied throughout the CBS. Two different initial values of temperature were used, corresponding to two different climate conditions (described below): “hot

humid" and "cool humid". For the hot humid simulations, an initial uniform temperature T = 20°C was applied, whereas for the cool humid simulations, an initial uniform temperature T = 6.32°C was applied.

For the numerical simulations using the hysteretic hydraulic constitutive model, the initial values of the parameters s_0 and S_{lo}, describing the previous suction reversal point, were taken as s_0 = 1000 MPa and S_{lo} = 0. This meant that initial states (for both F.L and C.L) were on the main wetting curve (see Section 3.2.4). On the main wetting curve at s = 10 kPa (C.L) or s = 20 kPa (F.L), the materials of the CBS were at a relatively dry initial state, as shown in Figure 6-2a.

For all simulations (thermo-hydraulic modelling and hydraulic modelling), standard boundary conditions (see Section 3.4.1) were applied on the bottom boundary and on the lateral boundaries (at the top and bottom of the slope). The boundary conditions on these boundaries were identical to those imposed on the corresponding boundaries for the simple type B models in Chapter 5 (see Section 5.3.3) i.e. impermeable to liquid and vapour flows on the bottom boundary and up-slope lateral boundary and a seepage boundary conditions on the down-slope lateral boundary.

For the thermo-hydraulic numerical simulations, the top boundary (i.e. the ground surface) was represented by an atmospheric boundary (see Section 3.4.2), to allow the inclusion of evaporation to the atmosphere. On this boundary, constant values of atmospheric temperature T_a, atmospheric pressure p_{ga}, atmospheric relative humidity R_{ha}, net radiation R_n and wind speed v_a were imposed. These constant values of T_a, p_{ga}, R_{ha}, R_n and v_a are listed in Table 6-2 for the 'hot humid' simulations and the 'cool humid' simulations. The hot humid values represent average annual values for Phuket, Thailand from the Thai Meteorological Department (Thai Meteorological Department, 2020), whereas the cool humid values represent average values for London, UK from the Meteorological Office (Met Office, 2020). Values of further parameters required in applying the atmospheric boundary condition (see Section 3.4.2) are listed in Table 6-3.

Rainfall was imposed on the ground surface, as part of the atmospheric boundary condition, in terms of a specified variation with time of the precipitation rate P (expressed as a mass flow rate of liquid per unit plan area). The required variation of P with time for the desired rainfall pattern (see Figure 6-1) was calculated by

converting values of rainfall infiltration rate i (expressed as volumetric flow rate of liquid per unit plan area) to values of P by multiplying by the density of water at the atmospheric temperature T_a.

Table 6-2 Atmospheric parameters for thermo-hydraulic numerical simulations

	Atmospheric temperature, T_a (˚C)	Atmospheric gas pressure, p_{ga} (MPa)	Atmospheric relative humidity, R_{ha} (-)	Net radiation R_n (J/m^2/s)	Wind speed, v_a (m/s)
Hot humid	27.00	0.10	0.77	271	3.66
Cool humid	10.98	0.10	0.77	174	2.91

Table 6-3 General parameters for atmosphere bounday modelling

Parameters	Symbol	Input values
Roughness length	z_0(m)	0.001
Screen height	z_a(m)	1.5
Stability factor	φ(-)	1.0
Atmospheric gas density	ρ_{ga}(kg·m^{-3})	0.1
Numerical gas leakage coefficient	$\gamma_{g,n}$(kg·m^{-2}·s^{-1}·MPa^{-1})	1E+06
Numerical liquid leakage coefficient	$\gamma_{l,n}$(kg·m^{-2}·s^{-1}·MPa^{-1})	-1E+06

For the hydraulic numerical simulations, the top boundary (i.e. the ground surface) was represented by a standard boundary condition (see Section 3.4.1) with a specified variation with time of rainfall infiltration rate i (volumetric flow rate of liquid per unit plan area) and impermeable to vapour i.e. using the same approach as for the hydraulic numerical modelling in Chapters 4 and 5.

6.2 Single constant intensity rainfall events of limited duration

This section presents the results and discussions of simulations of single rainfall events of limited duration. Three different rainfall patterns were considered, as shown in Figure 6-3. All three involved a constant rainfall intensity i = 10^{-6} m/s starting at t = 0. The duration of the rainfall was either 12 hours (rainfall pattern LD1), 24 hours (LD2) or 48 hours (LD3). After this there was no further rainfall (i = 0).

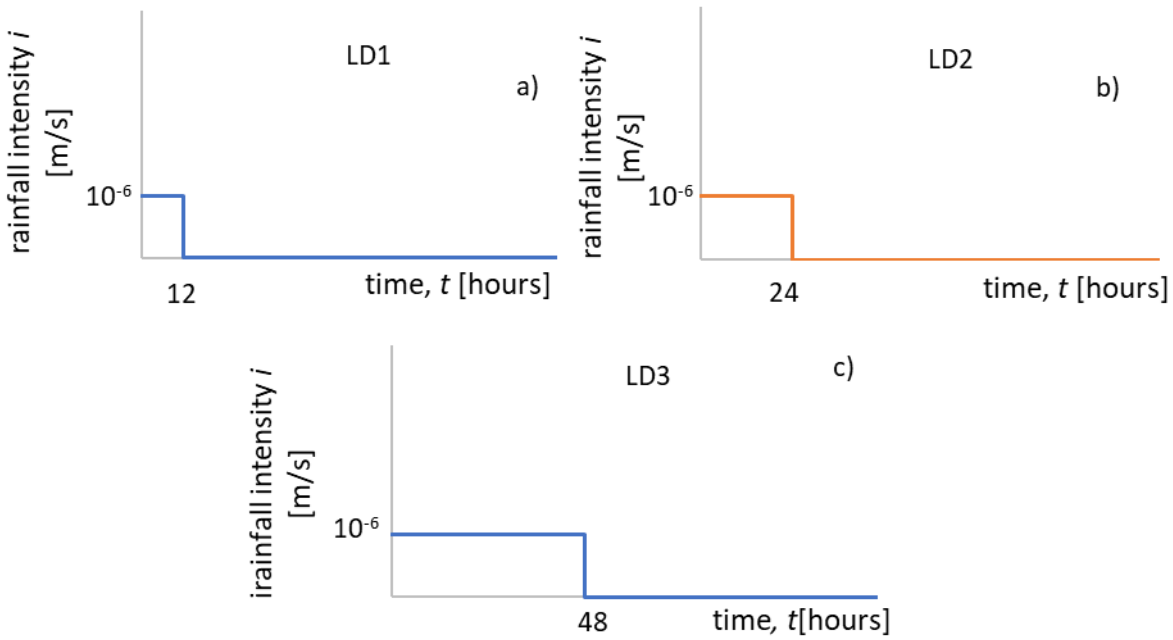

Figure 6-3 Rainfall patterns for single rainfall events of limited duration

Table 6.4 lists the full set of simulations of rainfall events of limited duration. Four thermo-hydraulic simulations (with evaporation) were performed, involving three with the F.L of the CBS made of fine sand (rainfall patterns LD1, LD2 and LD3) and a single simulation with the F.L made of silty sand (rainfall pattern LD3). In all four thermo-hydraulic simulations, the atmospheric conditions corresponded to the 'hot-humid' climate. Table 6.4 shows that three hydraulic simulations (without evaporation) were also performed, all with the F.L made of fine sand (rainfall patterns LD1, LD2 and LD3). In the following sub-sections, selected results are presented from the seven thermo-hydraulic or hydraulic simulations, to highlight key aspects of behaviour that were observed.

Table 6-4 Numerical simulations of sloping CBSs subjected to single rainfall events of limited duration (β = 35°, t_f = 40cm)

No.	Analysis Identifier	Evaporation	F.L material	Climate	Rainfall pattern
1	1C12P	Yes	Fine sand	Hot-humid	LD1
2	1C24P	Yes	Fine sand	Hot-humid	LD2
3	1C48PFS	Yes	Fine sand	Hot-humid	LD3
4	1C48PSS	Yes	Silty sand	Hot-humid	LD3
5	1C12PNOE	No	Fine sand	-	LD1
6	1C24PNOE	No	Fine sand	-	LD2
7	1C48PNOE	No	Fine sand	-	LD3

6.2.1 Excluding evaporation

Figure 6-4 shows the interface flow velocity q_i (volumetric flow rate of liquid across the interface per unit plan area) plotted against time for different values of horizontal coordinate x for the three hydraulic modelling simulations (i.e. no evaporation from the ground surface). For this particular situation (β = 35°, t_f = 40 cm and F.L made of fine sand), the value of diversion length L_D if the rainfall intensity i =10^{-6} m/s was maintained indefinitely was 12.7 m according to new simplified method developed in Chapter 5 or 13.6 m according to the results of the numerical modelling in Chapter 5 (see Figure 5-17b).

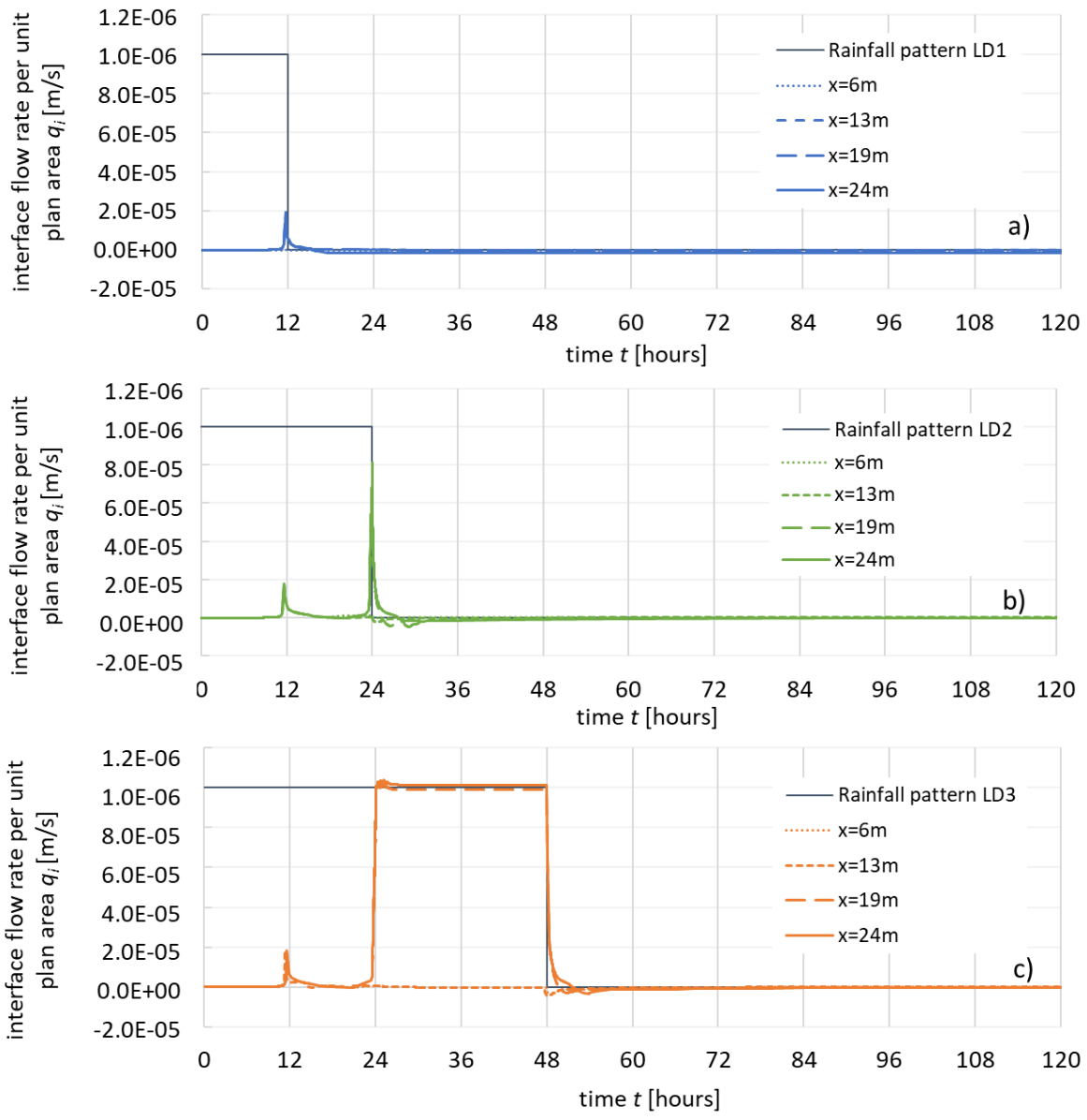

Figure 6-4 Variation of interface flow velocity with time during rainfall events of limited duration if evaporation is excluded: a) rainfall pattern LD1; b) rainfall pattern LD2; c) rainfall pattern LD3 (β = 35°, FSGV, t_f = 40cm)

Inspection of Figure 6-4 shows that in all cases (all three rainfall patterns and all values of x), a small spike in the value of interface flow velocity q_i occurred at $t \approx 12$ hours. This corresponded to the arrival at the interface of the initial partial-wetting front, which progresses downwards from the ground surface during the first 12 hours of rainfall, as described in Section 5.6.

Inspection of Figure 6-4c (rainfall pattern LD3) shows that, when the rainfall was maintained for a duration of 48 hours, breakthrough occurred at $t \approx 24$ hours at x = 19 m and x = 24 m (with q_i rapidly increasing to the rainfall intensity i = 10^{-6} m/s), but no breakthrough occurred at x = 6 m or x = 13 m. This is consistent with the observation reported above, from Figure 5-17b, that the diversion length L_D (if the rainfall intensity i = 10^{-6} m/s was maintained indefinitely) was 13.6 m according to the numerical modelling results presented in Chapter 5. Figure 6.4b (rainfall pattern LD2) shows that when the duration of the rainfall event was only 24 hours, breakthrough was just starting at x = 19 m and x = 24 m when the rainfall finished, and breakthrough then stopped. In Figure 6.4a (rainfall pattern LD1), when the duration of the rainfall event was only 12 hours, the rainfall finished before breakthrough commenced, and hence no breakthrough occurred.

The most important new information to emerge from the numerical simulations of rainfall events of limited duration is what happens within the CBS when the rainfall stops. Inspection of Figure 6.4c shows that, at x = 19 m and x = 24 m, where the breakthrough had occurred, as soon as the rainfall stopped (at t = 48 hours), the value of the interface flow velocity q_i immediately dropped very dramatically and after only a very short time the value of q_i was almost zero (corresponding to the new rainfall rate). The fact that, if breakthrough has previously occurred and there is then a drop in rainfall intensity, the interface flow velocity drops immediately, with no time-lag, is a very significant observation.

6.2.2 Influence of evaporation

This section presents selected results from the thermo-hydraulic modelling numerical simulations (with evaporation) of rainfall events of limited duration and compares these with the corresponding results from hydraulic modelling

simulations (without evaporation), to explore the role of evaporation from the ground surface.

Figure 6-5 shows the variation with time of soil-atmosphere interactions and ground surface conditions during the three thermo-hydraulic numerical simulations with the F.L made of fine sand (with rainfall patterns LD1, LD2 and LD3). Results are shown for x = 13 m, but the variations of soil-atmosphere interactions and ground surface conditions were very similar at other values of x.

The soil-atmosphere interactions included in Figure 6-5 are the precipitation rate P and evaporation rate E, both expressed as mass flow rate per unit plan area to aid comparison. Values of evaporation rate E were converted from mass flow rate per unit slope area (the data provided by CODE_BRIGHT). The ground surface conditions presented in the figure are the suction s in the soil at the ground surface, the temperature T of the soil at the ground surface and the relative humidity R_h of the gas phase in the soil voids at the ground surface.

It is important to realise that the evaporation rate E calculated within CODE_BRIGHT and shown in Figure 6-5, is calculated from Equation 2-62, which represents the actual rate of evaporation (Brutsaert, 1982) from the ground surface (which depends on the combination of atmospheric conditions and conditions of the soil at the ground surface). This actual rate of evaporation may be lower than the potential evaporation rate (Bond and Willis, 1969), which depends only on atmospheric conditions and represents the evaporation rate for those atmospheric conditions that would occurs from a saturated ground surface with zero suction at the ground surface. The actual evaporation rate will be lower than the potential evaporation rate as the soil dries from a saturated condition.

The results shown in Figure 6-5 are very similar for the three rainfall patterns (LD1, LD2 and LD3) after accounting for the different rainfall durations. During the period of rainfall, relatively steady state conditions are reached (in terms of soil-atmosphere interactions and ground surface conditions) in less than 12 hours. Then during the subsequent period when rainfall had finished, the behaviour was very similar for the three different rainfall patterns if time was measured from the point where the rainfall stopped. By considering the physical processes occurring and the relationships between different variables, it is possible to

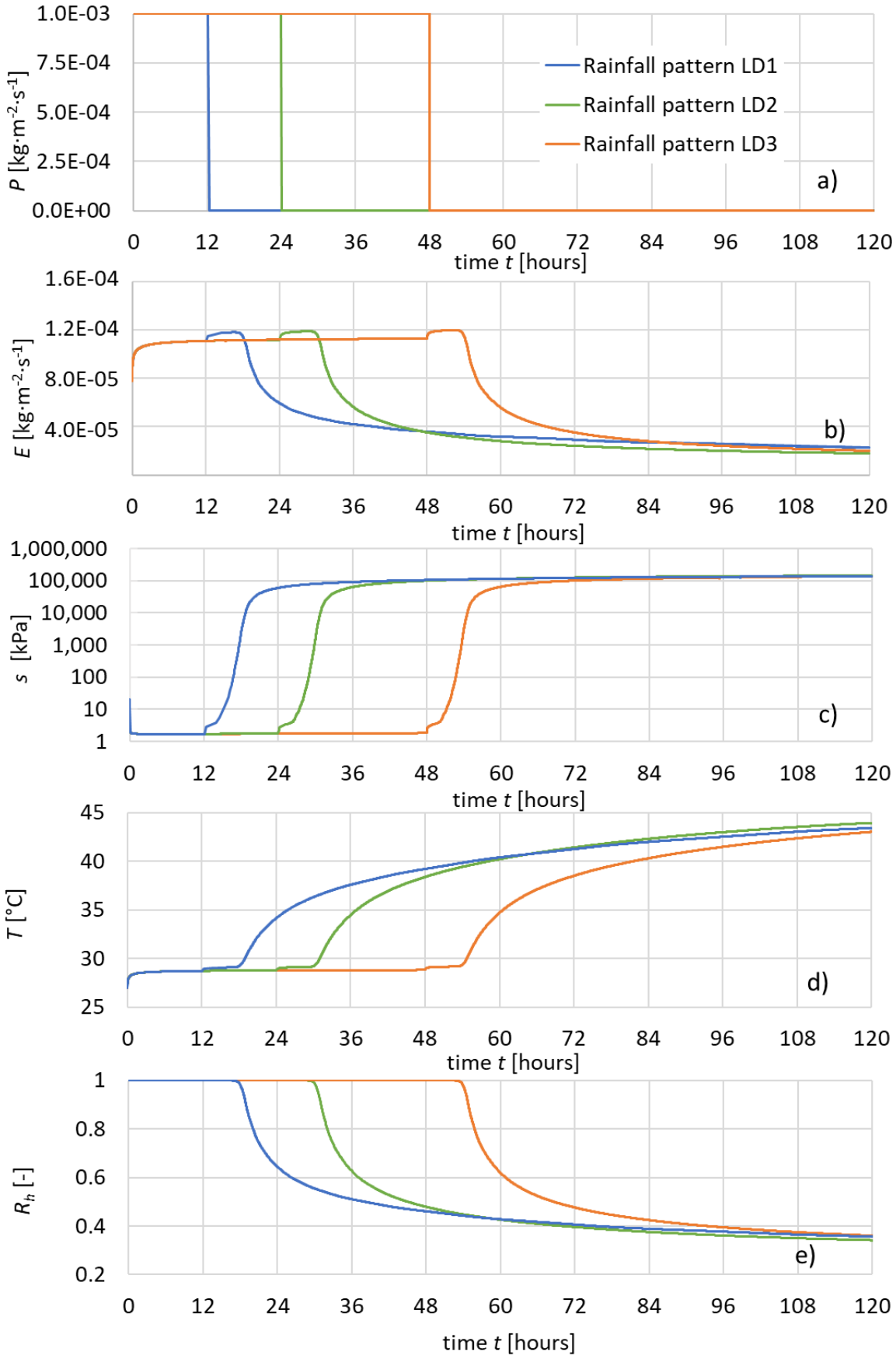

Figure 6-5 Soil-atmosphere interactions and ground surface conditions at x=13m during rainfall events of limited duration: a) precipitation *P*; b) evaporation *E*; c) suction *s* at ground surface ; d) temperature *T* at ground surface; and e) relative humidity R_h in soil voids at ground surface (β = 35°, FSGV, t_f = 40cm, hot-humid climate)

explain the complex variations with time of the different variables shown in Figure 6-5.

Inspection of Figure 6-5 shows that, during the initial period of rainfall, evaporation rate E initially increases (because of increasing temperature of the ground surface) before quickly stabilising, suction s at the ground surface drops almost immediately from its initial value of 20 kPa to a lower stable value of $s \approx$ 1.7 kPa, ground surface temperature T increases from its initial value of 20℃ and stabilizes at $T \approx$ 28.3℃ (slightly higher than the atmospheric temperature of 27℃) and relatively humidity R_h in the soil voids at the ground surface remains indistinguishable from 1 throughout the period of rainfall. The initial drop of suction, from s = 20 kPa to $s = s_f^*$= 1.7 kPa is a consequence of the initial partial-wetting front (to $s = s_f^*$) progressing downwards from the ground surface from t = 0. However, this change of suction has negligible effect on the relative humidity R_h in the soil voids at the ground surface because the psychrometric law (Equation 2-4) indicates that R_h only begins to drop noticeably below 1 when the suction is several MPa. The initial rise in temperature T at ground surface is a consequence of a net input of energy to the soil at the ground surface, because the combination of net radiation arriving at the surface and sensible heat transfer from the atmosphere (at T_a = 27℃) to the ground (initially at a temperature lower than 27℃) initially exceeds the sum of the energy required for evaporation and the heat transfer deeper into the ground. This increasing temperature of the ground surface causes an increase of evaporation rate E, because the saturated vapour density ρ_{vo} increases with increasing temperature, which implies an increase in the vapour density ρ_v in the soil voids at the ground surface if the relative humidity has not changed (see Equation 2-5), which in turn leads to an increase in evaporation rate E (see Equation 2-62). A steady state is reached when the temperature T and evaporation E have risen sufficiently for the combination of net radiation and sensible heat transfer from the atmosphere to the ground (the latter now negative as the ground is at a higher temperature than the atmosphere) to equate with the energy required for evaporation (now increased, because of the increased evaporation rate) and the heat transferred deeper into the ground.

Inspection of Figure 6-5 shows that when the rainfall finished (at t = 12 hours, t = 24 hours or t = 48 hours) there were almost immediate small rises of evaporation

rate E, suction s and temperature T, but with R_h still essentially unchanged (because R_h will only drop noticeably below 1 when suction is several MPa). The immediate small rise of suction s is thought to be a consequence of retention hysteresis, which means that, as the rainfall ceases and drying of the soil commences at the ground surface (due to evaporation), the very low initial gradient of a scanning drying SWRC means that a finite increase of suction can occur with negligible drop in the degree of saturation S_l (i.e. requiring negligible extraction of water from the soil). The small increase in temperature as soon as the rainfall ceases is thought to be due to the cessation of the previous small cooling effect of rainwater at the atmospheric temperature T_a = 27°C entering the slightly hotter ground surface. It is this small increase of ground surface temperature that causes the small increase of evaporation rate E (by increasing the saturated vapour pressure ρ_{vo} and hence increasing the vapour density ρ_v, as described earlier).

After the initial small changes of E, s and T when rainfall finishes, Figure 6-5 then shows a period of about 6 hours during which evaporation rate E remains approximately constant, suction s increases steadily, temperature T remains approximately constant and relative humidity R_h remains indistinguishable from 1. The rise of suction is a consequence of the falling value of degree of saturation S_l in the soil at ground surface, as water is extracted by evaporation. However, for about 6 hours this increase of suction is insufficient to cause any noticeable change of relative humidity R_h (a consequence of the psychrometric law of Equation 2-4) and hence there is nothing to cause a change in the evaporation rate E or the ground surface temperature T.

Finally, about 6 hours after the rainfall has finished, sufficient water has been extracted from the soil at the ground surface by evaporation to increase the suction there to several MPa, which is sufficient (according to the psychrometric law) for the relative humidity R_h to begin dropping noticeably below 1. This means that the vapour density ρ_v in the soil voids at the ground surface begins to drop (see Equation 2-5) and hence the evaporation rate E begins to drop (Equation 2-62). As the evaporation rate drops, the energy required to drive this evaporation reduces, and the excess energy (the difference between net radiation and the sum of sensible heat loss to the atmosphere, energy required for evaporation and heat

transfer to deeper into the soil) leads to heating of the ground surface and an increase in ground surface temperature T.

In summary, inspection of Figure 6-5 shows that, while the rainfall is occurring, at i = 10^{-6} m/s ($P \approx 10^{-3}$ kg/m^{2}s), the evaporation rate E quickly stabilises at $E \approx 10^{-4}$ kg/m^{2}s i.e. at approximately 10% of the rainfall rate. When the rainfall finishes, the evaporation continues at approximately this rate (even slightly increased) for a further 6 hours before beginning to decrease significantly. This decrease in evaporation rate is associated with decreasing vapour density ρ_v in the soil voids at the ground surface as the soil there dries, but the reduction of ρ_v only commences when the soil at the surface has dried to a suction of several MPa. Suction values in excess of several MPa are perfectly possible in a coarse-grained soil, such as the fine sand forming the F.L of a CBS. At these values of suction, the soil will be at a very low value of S_l, well into the pendular range (see Figure 5.4a), with the small amount of pore water restricted to very thin water films on the surfaces of the sand particles. To a casual observer, the soil may appear completely dry. In the case of the sloping CBS shown in Figure 6-5, this surface condition of suction in excess of several MPa is initially restricted to a very thin zone at the ground surface.

The influence of evaporation at the ground surface on any occurrence of breakthrough within the CBS can be observed by comparing Figure 6-6 with Figure 6-4. These two figures show the variation of interface flow velocity q_i for corresponding thermo-hydraulic and hydraulic simulations respectively (i.e. with and without evaporation). Figure 6-7 shows a direct comparison of results with and without evaporation when a CBS is subjected to 48 hours of rainfall (rainfall pattern LD3).

Inspection of Figure 6-7 shows that, at x = 19 m and x = 24 m, inclusion of evaporation has reduced the value of q_i after breakthrough by about 10%. This is consistent with the observation from Figure 6-5 that, during the period of rainfall, evaporation reduced the net mass flow rate of water from the atmosphere into the ground by about 10%. It is also clear from Figure 6-7 that inclusion of evaporation delayed onset of breakthrough by about 10% (from $t \approx$ 24 hours to $t \approx$ 26.3 hours), consistent with the 10% reduction of net mass flowrate of water from

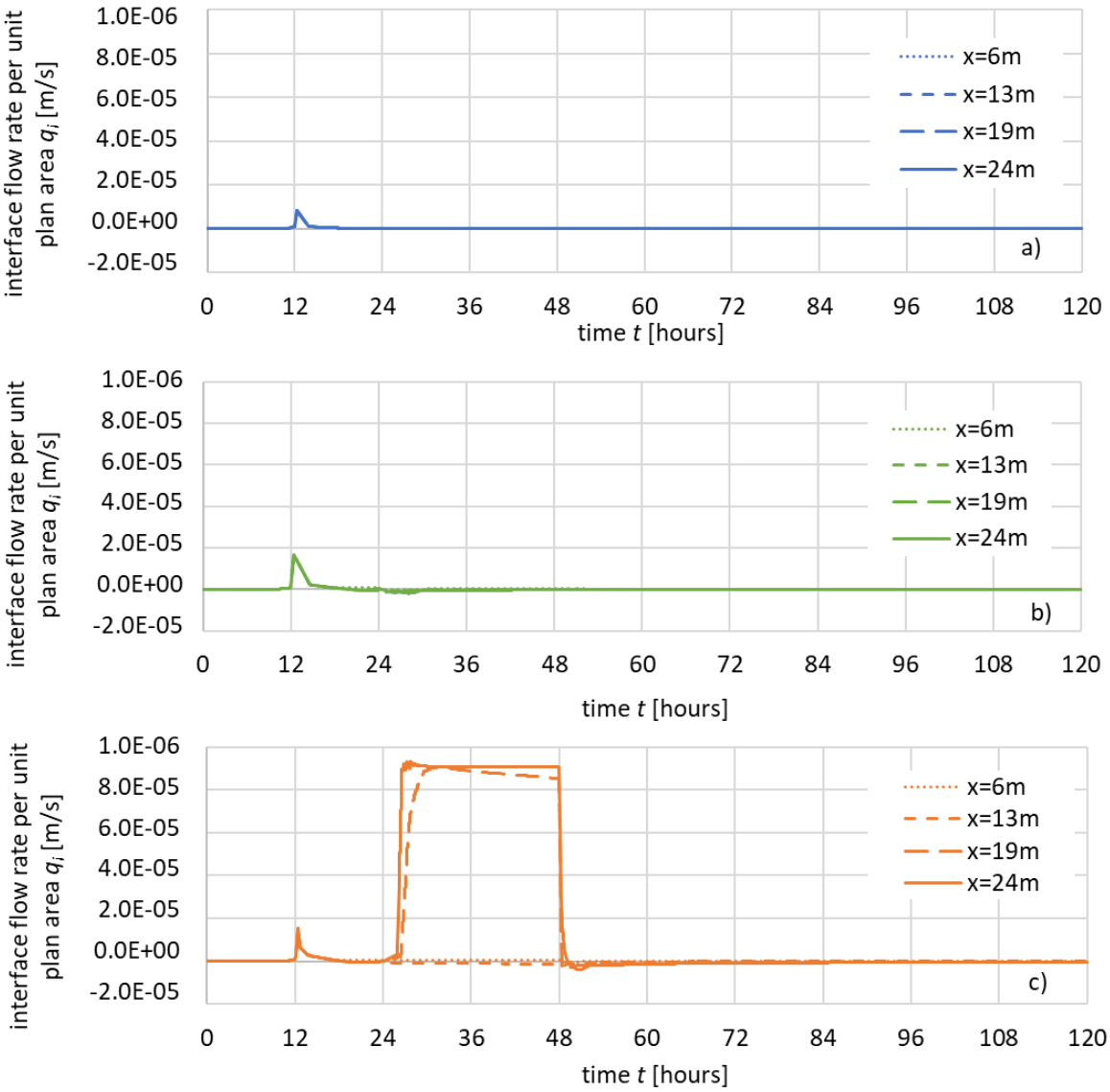

Figure 6-6 Variation of interface flow velocity with time during rainfall events of limited duration if evaporation is included; a) rainfall pattern LD1; b) rainfall pattern LD2 and c) rainfall pattern LD3 (β = 35°, FSGV , t_f = 40cm, hot-humid climate)

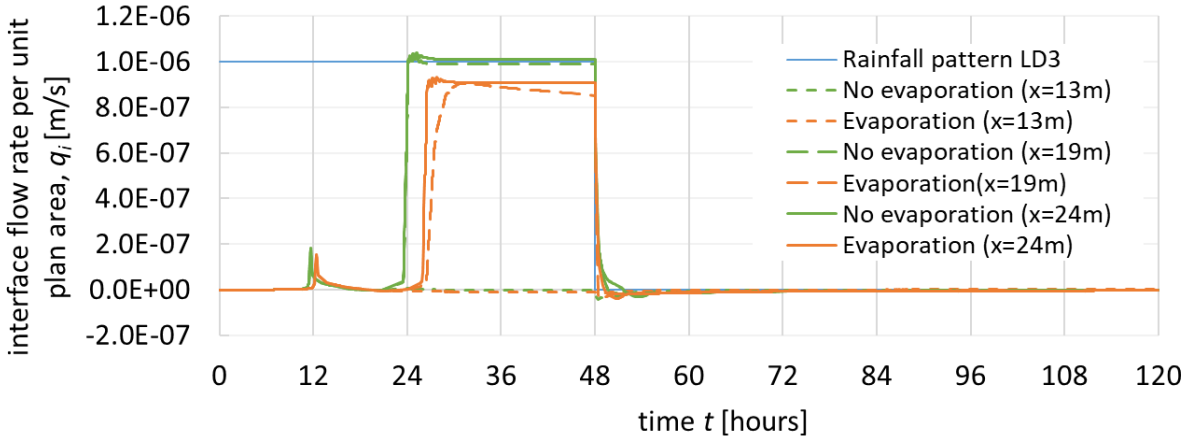

Figure 6-7 Influence of evaporation on variation of interface flow velocity (β = 35°, FSGV, t_f = 40cm, hot-humid climate, rainfall pattern LD3)

the atmosphere into the ground (i.e. it took about 10% longer to fill the storage capacity of the CBS). Comparison of Figure 6-6b with Figure 6-4b shows that this slight delay in the onset of breakthrough caused by inclusion of evaporation was sufficient to avoid any start of breakthrough under rainfall pattern LD2. An important point to emphasise from Figures 6-6 and 6-7 is that the key observation from Section 6.2.1 of what happens if breakthrough has occurred and then rainfall stops remains unchanged i.e. the value of interface flow velocity q_i immediately drops dramatically and within a very short time duration q_i has reduced to the new rainfall rate (zero in this case).

For the same two simulations as presented in Figure 6-7 (rainfall pattern LD3, with and without evaporation), Figure 6-8 shows profiles of suction s, degree of saturation S_l and horizontal seepage velocity q_h within the CBS at x = 13 m at different times. Comparing the results while the rainfall is ongoing (t = 12 hours, t = 24 hours and t = 48 hours), it can be seen that the only impact of evaporation is slight slowing of the process of wetting the CBS, due to the 10% reduction of net mass flowrate of water into the ground surface. For example, at t = 12 hours, the profiles of S_l show that without evaporation the initial partial-wetting front has reached the bottom of the F.L, and further filling of the F.L from the bottom upwards has just commenced, whereas with evaporation the initial partial wetting front has not quite reached the bottom of the F.L. Similarly, at t = 24 hours, without evaporation the profiles of S_l and q_h show that final steady state conditions under the rainfall intensity i = 10^{-6} m/s have been reached (the results at t = 24 hours are identical with those at t = 48 hours), whereas with evaporation final steady state conditions have not been reached at t = 24 hours (there are noticeable differences with the results at t = 48 hours).

Examining the results in Figure 6-8 at t = 60 hours and t = 120 hours, it can be seen that, after the rainfall ceases, significant influence of evaporation is limited to the upper part of the F.L. In particular, if evaporation is included, a drying front slowly progresses downwards from the surface, as water is extracted from the ground surface by evaporation, whereas this drying front is absent if evaporation is not included. By t = 60 hours (12 hours after rainfall has finished), when evaporation is included, the soil at the ground surface is in a very dry state, with very low value of degree of saturation S_l and very high value of suction s

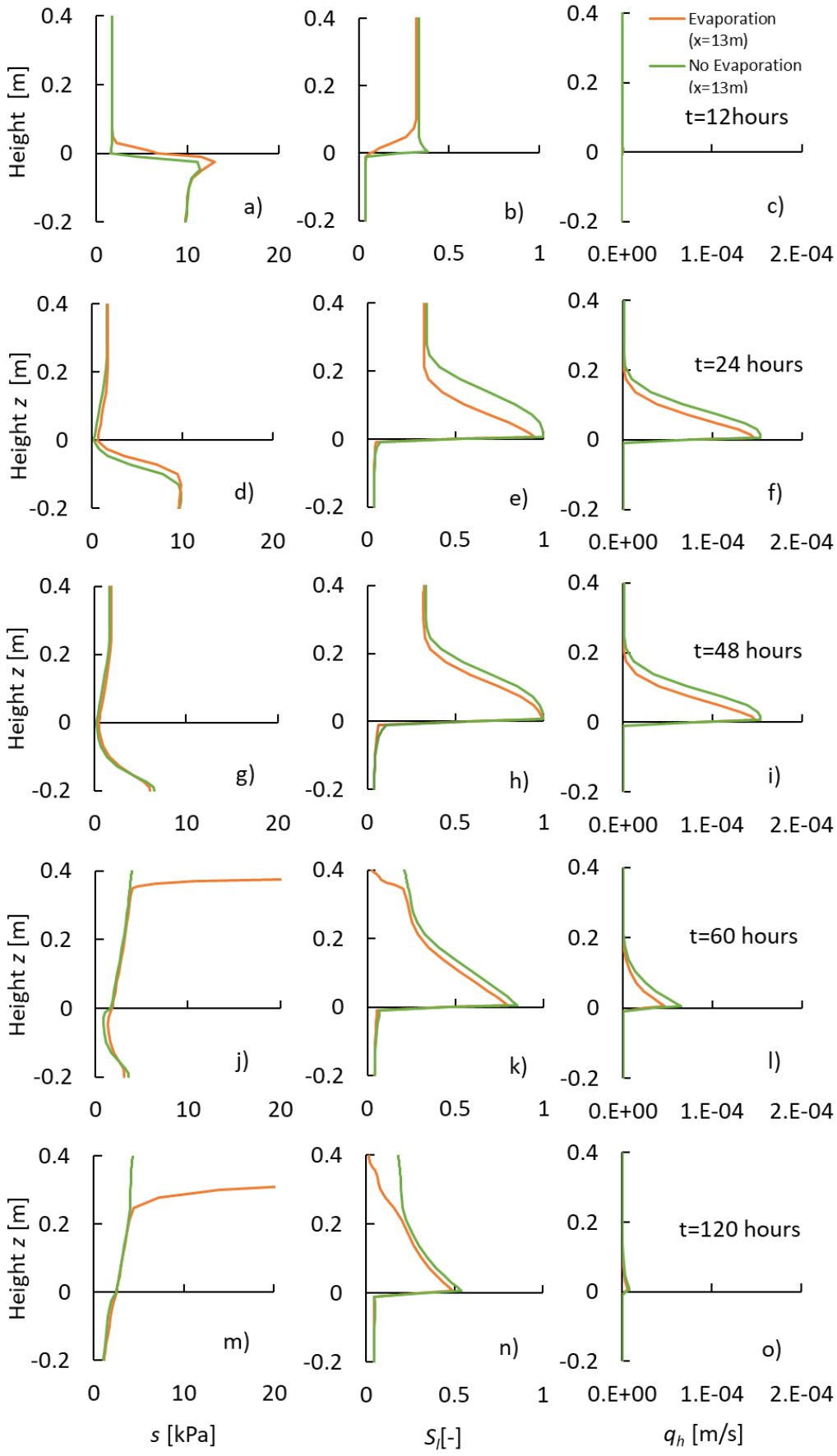

Figure 6-8 Influence of evaporation on profiles of suction *s*, degree of saturation S_l and horizontal seepage velocity q_h at *x* = 13m (β = 35°, FSGV, t_f = 40cm, hot-humid climate, rainfall pattern LD3)

(many MPa), resulting in the significant drop of evaporation rate E from the ground surface seen in Figure 6-5.

As time advances (see t = 60 hours and t = 120 hours in Figure 6-8), the drying front slowly progresses further down into the F.L, but below the drying front the profiles of s, S_l and q_h are almost unaffected by the inclusion of evaporation at the ground surface. This indicates that any drying of the lower part of the F.L, below the drying front, is caused by water drainage down the slope (in the lower part of the F.L) (see the profiles of q_h at t = 48 hours and t = 60 hours), rather than by water drawn up to the ground surface by the evaporation. Negligible water is drawn up to the ground surface below the drying front, because water struggles to flow through the upper part of F.L, which has very low hydraulic conductivity (because of low values of S_l).

By t = 120 hours, any water drainage down the slope in the lower part of the F.L has almost ceased (see the profile of q_h) and hence any significant further drying of the lowest part of the F.L would only occur when the drying front progressing downwards from the ground surface reached this depth. This would take a very long time because the rate of evaporation from the ground surface is now relatively low (see Figure 6-5).

6.2.3 Influence of material of finer layer

All the simulations presented in Sections 6.2.1 and 6.2.2 involved CBSs with the F.L made of fine sand. This section presents the results of the single simulation involving a CBS with the F.L made of silty sand (with evaporation and rainfall pattern LD3, see Table 6-4) and investigates the influence of the material of the F.L by comparing with the results of the corresponding simulation of a CBS with the F.L made of fine sand.

Figure 6-9 shows the soil-atmosphere interactions (precipitation rate P and evaporation rate E) and ground surface conditions (suction s, temperature T and relative humidity R_h) for two simulations (one involving fine sand, the other involving silty sand) all taken at x = 13 m.

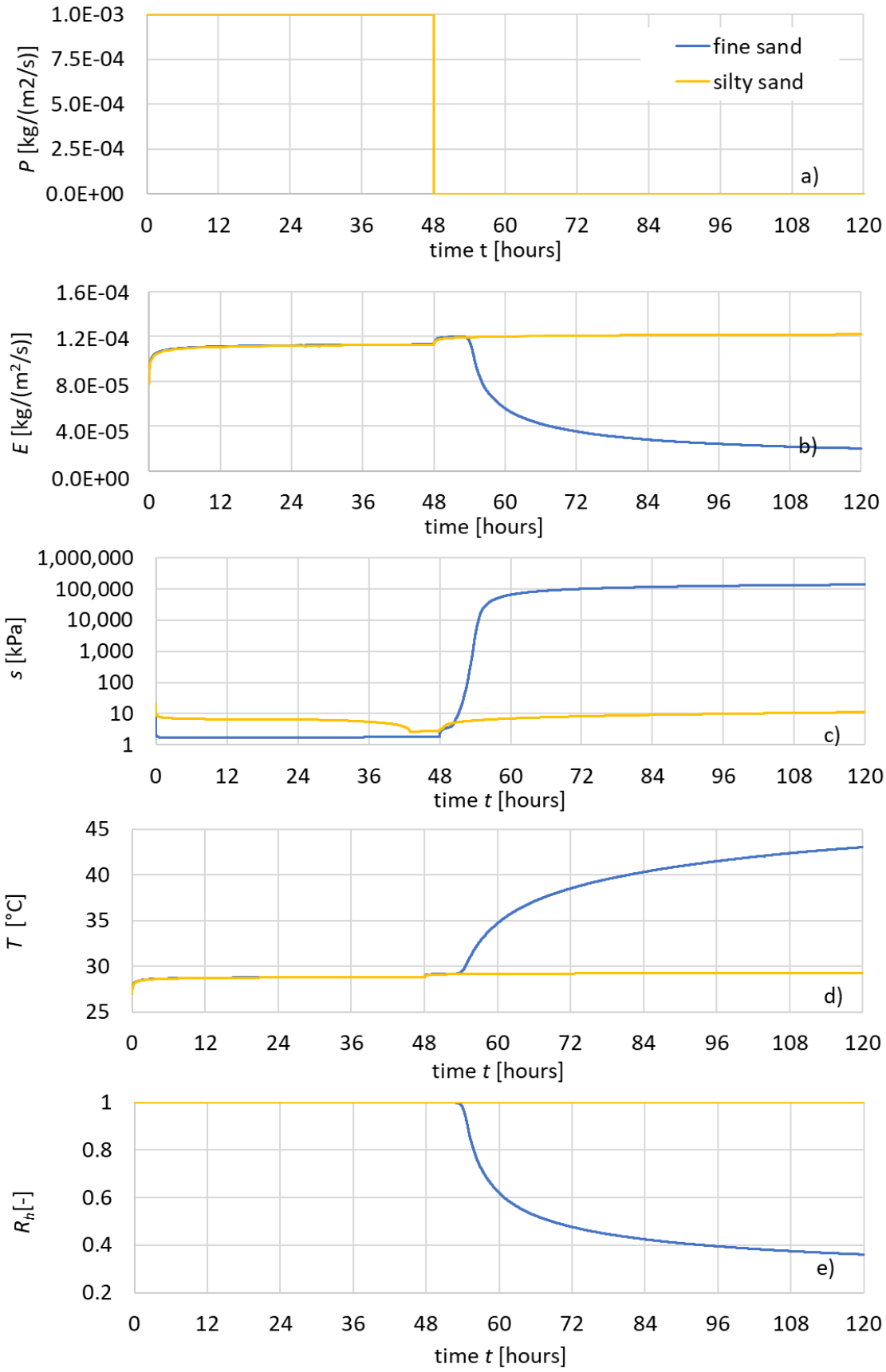

Figure 6-9 Influence of material of F.L on soil-atmosphere interactions and ground surface conditions at x=13m: a) precipitation P; b) evaporation E; c) suction s at ground surface; d) temperature T at ground surface, and e) relative humidity R_h in soil voids at ground surface (β = 35°, FSGV, t_f = 40cm, hot-humid climate, rainfall pattern LD3)

During the period of rainfall (up to t = 48 hours) and for approximately 6 hours after the rainfall finished, the variations of evaporation rate E, temperature at the ground surface T and relative humidity at the ground surface R_h are indistinguishable for the two simulations in Figure 6-9. In this period up to about t = 54 hours, it is only the suction s at the ground surface that is different for the two simulations.

For the simulation involving a F.L made of silty sand, the value of s at ground surface dropped very quickly after the start of rainfall (t = 0) from the initial value s = 20 kPa to a value $s = s_f^*$ = 6.8 kPa, as the initial partial-wetting front progressed downward from the ground surface. This was directly equivalent to what happened in the case where the F.L was made of fine sand (but is that case s_f^* = 1.7 kPa). However, for the simulation involving a F.L made of silty sand, during the later part of the rainfall period (from t = 24 hours to t = 48 hours) there was a further gradual drop in the value of s at the ground surface. This was a consequence of the second stage of wetting, involving additional filling of the F.L from the bottom upwards, arriving back at the ground surface. In contrast, when the F.L was made of fine sand, the second stage of wetting of the F.L (from the bottom upwards) did not progress right back up to ground surface. These differences can be seen in the profiles of s and S_l at t = 24 hours and t = 48 hours in Figure 6-10. From t = 43 hours to t = 48 hours, a steady state had been reached under the rainfall intensity i = 10^{-6} m/s, with s = 2.8 kPa at the ground surface. While the rainfall was occurring (up to t = 48 hours), the different values of suction s at the ground surface in the two simulations caused no differences in evaporation rate E (and hence no differences in ground surface temperature T), because the values of suction in both simulations remained relatively low during this period, and hence they were insufficient to cause any noticeable drop in the relative humidity R_h in the soil voids at the ground surface (R_h remaining indistinguishable from 1).

In Figure 6-9, the main differences between the two simulations occurred after the rainfall finished. After rainfall stopped (t = 48 hours), the suction s at the ground surface increased in both simulations, due to drying of the soil by evaporation. With the F.L made of fine sand, the increase of suction rapidly accelerated and after about 6 hours the suction had increased to many MPa, which

was sufficient to cause the relative humidity R_h at the ground surface to start decreasing significantly, which in turn (as described in Section 6.2.2) caused the rate of evaporation E to decrease significantly and hence the temperature T at the ground surface to increase considerably. In contrast, with the F.L made of silty sand, the increase of suction s at the ground surface after the rainfall ceased was much slower and even at t = 120 hours (72 hours after the rainfall stopped), the value of s was still very modest (s = 11 kPa). This modest increase of suction was much less than required to cause any noticeable drop of relative humidity R_h at the ground surface and hence there was no decrease in evaporation rate E or increase of ground surface temperature T when the F.L was made of silty sand. In summary, whereas, with a F.L made of fine sand, the evaporation rate decreased significantly, starting 6 hours after the rainfall finished, with a F.L made of silty sand, the evaporation rate remained unchanged long after rainfall finished.

The dramatic difference in the post-rainfall increase in suction at the ground surface caused by the change of F.L material, which was responsible for the major difference in evaporation rates from 6 hours after the rainfall stopped can be explained by examining the profiles of suction s and degree of saturation S_l shown in Figure 6-10. At t = 60 hours and t = 120 hours, the F.L made of fine sand was at very low values of S_l and very high values of s at the ground surface. This was because the value of S_l at the ground surface was relatively low even as the rainfall stopped (t = 48 hours) and surface-drying by evaporation then led to a shallow surface zone of very dry soil, which could not be fed by water drawn from deeper in the F.L, because the hydraulic conductivity of the upper part of the F.L was already very low. In contrast, with the F.L made of silty sand, the value of S_l at the ground surface remained relatively high at t = 60 hours and t = 120 hours, and the value of suction remained correspondingly low. This was because the value of S_l at the ground surface was high when the rainfall stopped (t = 48 hours) and it did not decrease dramatically as water was extracted by evaporation, because it could be continuously replenished by water drawn from deeper in the F.L, because the hydraulic conductivity of the F.L remained relatively high over the full depth. In summary, whereas the water extracted by evaporation from a F.L made of fine sand was drawn almost entirely from a shallow surface zone of the F.L, leading to extreme drying of this shallow surface zone, the water extracted

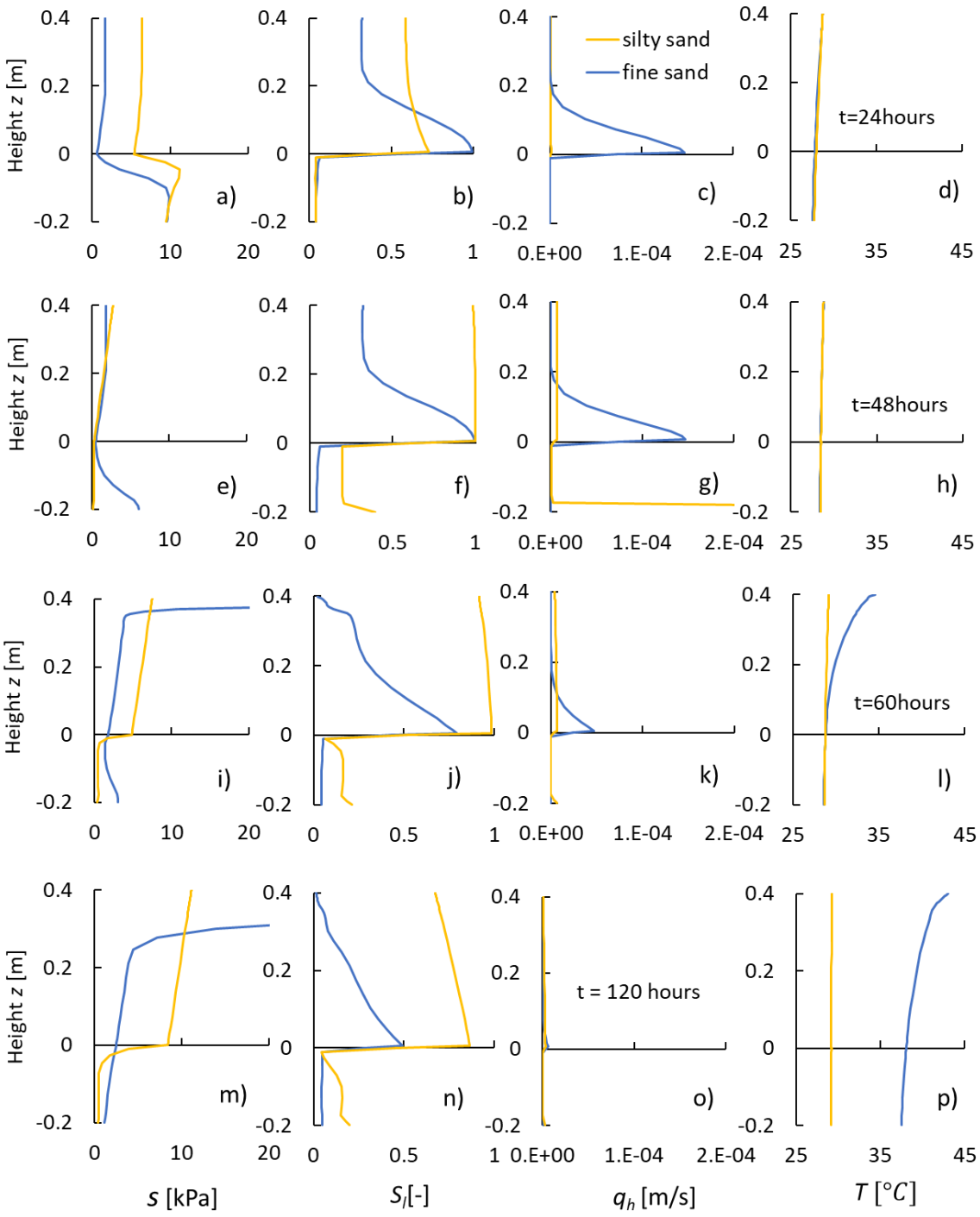

Figure 6-10 Influence of F.L material on profiles of suction *s*, degree of saturation S_l, and horizontal seepage velocity q_h at x = 13m (β = 35°, FSGV, t_f = 40 cm, hot-humid climate, rainfall pattern LD3)

by evaporation from a F.L made of silty sand was drawn from the entire thickness of the F.L, leading to only relatively modest drying of the surface zone.

Figure 6-11 compares the variations of interface flow velocity q_i (at x = 13 m and x = 24 m) for the simulation involving a F.L made of silty sand and the corresponding simulation involving a F.L made of fine sand. As previously noted in Section 6.2.2, with the F.L made of fine sand, breakthrough occurs at x = 24 m

but not at x = 13 m. In contrast, Figure 6-11 shows that, with the F.L made of silty sand, breakthrough occurs at both x = 13 m and x = 24 m. This is because the diversion length L_D for the CBS with the F.L made of silty sand ($L_D \approx$ 1.9 m, see Figure 5-18d) is much less than for the CBS with the F.L made of fine sand ($L_D \approx$ 13.6 m, see Figure 5-17b), because a CBS with the F.L made of silty sand has much lower water transfer capacity Q_{max} than a CBS with the F.L made of fine sand (compare Figures 5-20 and 5-19). Figure 6-11 also shows that, for both types of F.L, when breakthrough does occur, the value of q_i is approximately 10% less than the rainfall infiltration rate, because the evaporation rate E stabilises at about 10% of the precipitation rate P while the rain is ongoing (see Figure 6-9).

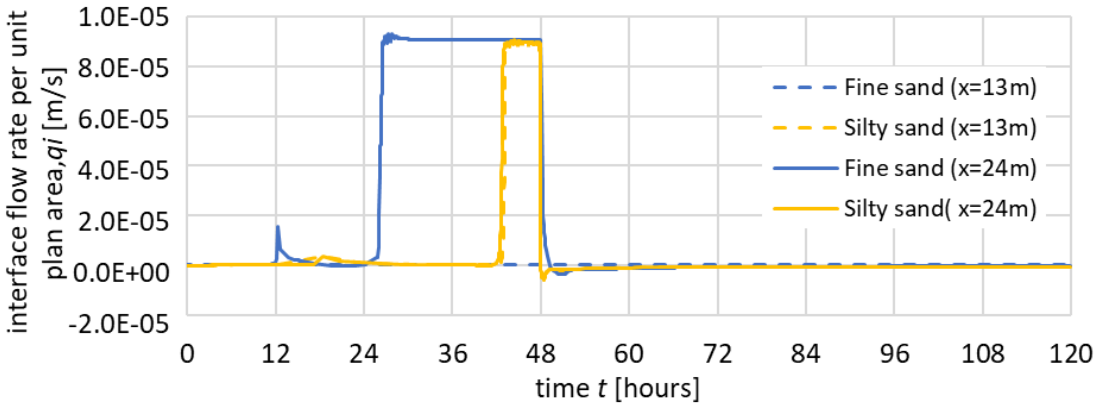

Figure 6-11 Influence of F.L material on variation of interface flow velocity (β = 35°, FSGV, t_f = 40cm, hot-humid climate, rainfall pattern LD3)

Inspection of Figure 6-11 shows that, where breakthrough occurs with the F.L made of silty sand (at x = 13 m and x = 24 m), the time required for breakthrough to commence ($t \approx$ 42.7 hours) is considerably longer than when breakthrough occurs with the F.L made of fine sand ($t \approx$ 26.3 hours). This difference occurs because the water storage capacity WSC of a CBS with the F.L made of silty sand is significantly greater than the WSC of a CBS with the F.L made of fine sand (compare Figures 5-22 and 5-21). Hence, Figure 6-11 shows the combined impact of the high water storage capacity and low water transfer capacity of a CBS with the F.L made of silty sand: breakthrough is delayed by the high water storage capacity, but when breakthrough does occur it extends to lower values of x (i.e. over more of the slope) because of the low water transfer capacity.

Inspection of Figure 6-11 also shows that with both types of F.L (fine sand or silty sand), the interface flow velocity drops almost immediately to the new rainfall intensity (zero in this case) when the rainfall intensity reduces.

Another important issue is how quickly and effectively the quantity of water stored WS in the F.L reduces after rainfall ceases and how this is affected by the material of the F.L. This is important because it represents restoration of storage capacity within the F.L, which is obviously beneficial for any future rainfall event. This issue can be examined by inspection of the profiles of degree of saturation S_l in Figure 6-10 from the time rainfall ends (i.e. for t = 48 hours, t = 60 hours and t = 120 hours).

For a CBS with the F.L made of fine sand, extraction of water from the F.L by evaporation from the ground surface to the atmosphere after the rainfall ends removes water from only a shallow surface zone (see the profile of S_l in Figure 6-10). As seen previously, after about 6 hours this extraction of water by evaporation begins to reduce substantially. In addition, however, for a CBS with the F.L made of fine sand, after the rainfall ends, removal of water from the lower part of the F.L (see the profile of S_l in Figure 6-10) occurs by water transfer down the slope in the bottom part of the F.L (see the profiles of horizontal seepage velocity q_h at t = 48 hours and t = 60 hours in Figure 6-10). However, this mode of water removal also slows and then stops within a few days of rainfall finishing (see the profile of q_h at t = 120 hours in Figure 6-10).

In contrast, for a CBS with the F.L made of silty sand, there is insignificant removal of water by water transfer down the slope (see the profiles of q_h in Figure 6-10), but removal of water by evaporation to the atmosphere, as seen previously, extracts water from the entire thickness of the F.L and this process occurs without diminishing for many days or weeks.

In the early hours after rainfall stops, the rate of water removal from a F.L made of fine sand will be greater than for a F.L made of silty sand, because the combination of water extraction from the top of the F.L by evaporation and water extraction from the lower part of the F.L by transfer down the slope, in the case of a F.L made of fine sand, will initially exceed the water extraction from the entire F.L by evaporation in the case of a F.L made of silty sand. However, both modes of water extraction reduce after relatively short times in the case of a F.L made of fine sand, whereas the single mode of extraction (by evaporation) remains undiminished for many days or weeks in the case of a F.L made if silty

sand. This means that, during dry periods lasting days or weeks, restoration of water storage capacity will be more effective if the F.L is made of silty sand than if the F.L is made of fine sand.

6.3 Cyclic patterns of rainfall

This section presents the results and discussions of simulations of simple cyclic rainfall patterns. Six different cyclic rainfall patterns were considered, as shown in Figure 6-12, involving different rainfall intensities, different rainfall durations and different durations of dry periods between the periods of rainfall. The intention within this section was to investigate how behaviour during an individual period of rainfall was affected by previous alternating rainfall periods and dry periods.

Table 6-5 lists the full set of simulations of sloping CBSs subjected to cyclic rainfall patterns. All simulations involved CBSs with the F.L made of fine sand. Seven thermo-hydraulic simulations (with evaporation) were performed. Six of these (covering all six cyclic rainfall patterns) involved the "hot-humid" climatic conditions (see Table 6-2) and there was a single simulation (with cyclic rainfall pattern C3) with the "cool-humid" climatic conditions. Each thermo-hydraulic simulation with a cyclic rainfall pattern was intended to involve 5 cycles of rainfall, but in a few simulations the full set of five cycles was not completed (see Table 6-5), because a data storage limit was reached. In most cases, however, sufficient cycles were completed to achieve a repeating cyclic response of the CBS. Table 6-5 shows that four hydraulic simulations (without evaporation), directly corresponding to four of the thermo-hydraulic simulations (with evaporation), were also performed (with 5 or 10 cycles of rainfall).

6.3.1 Typical behaviour under a cyclic rainfall pattern

Figures 6-13 and 6-14 show the results of a typical thermo-hydraulic simulation (cyclic rainfall pattern C1 with hot-humid climate), in terms of interface flow velocity q_i (Figure 6-13) and soil-atmosphere interactions and ground surface conditions (Figure 6-14). Cyclic rainfall pattern C1 involved 24 hours periods of rainfall of intensity i =10^{-6} m/s alternating with 24 hours periods with no rainfall i.e. alternating wet and dry days (see Figure 6-12).

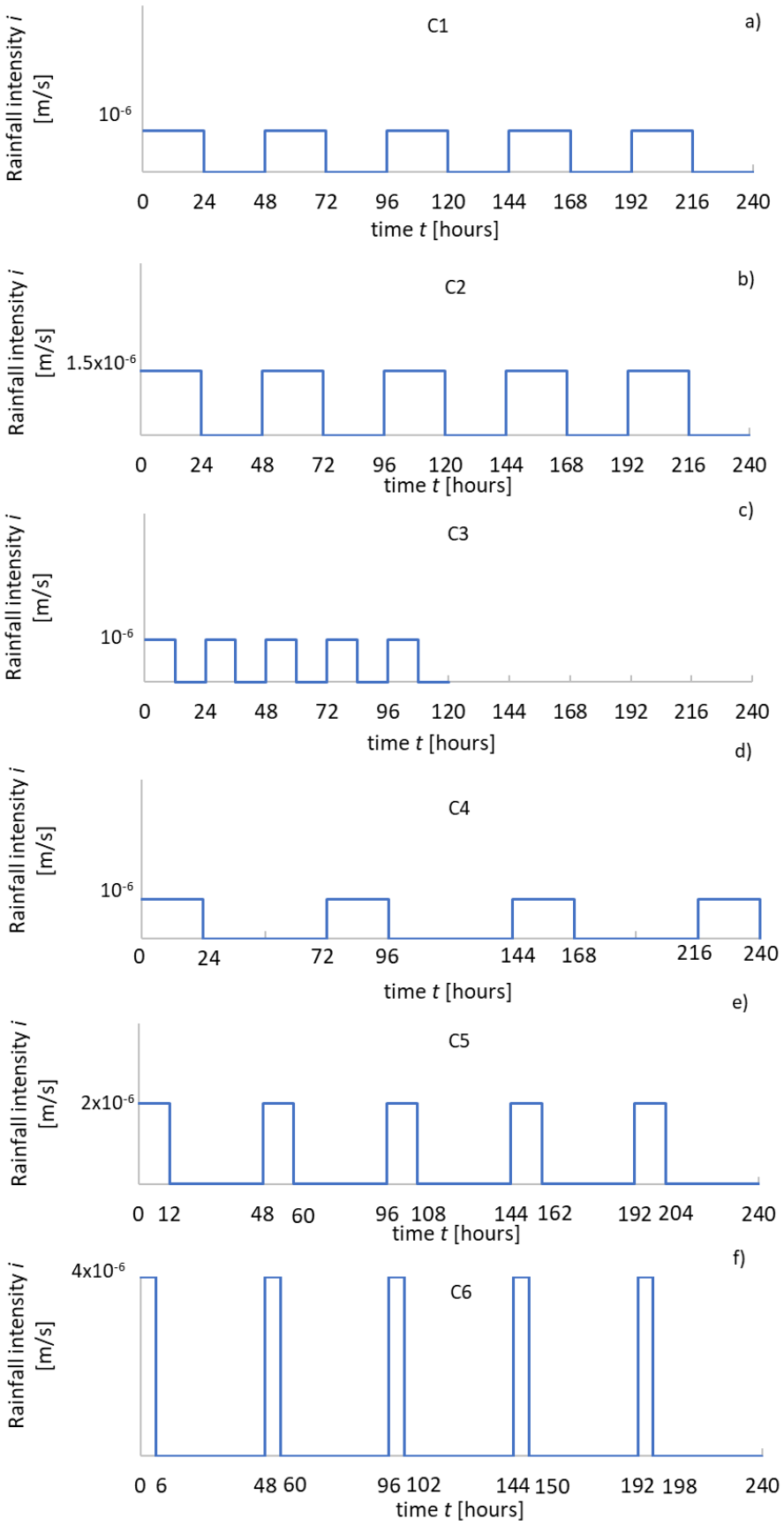

Figure 6-12 Cyclic rainfall patterns

Figure 6-13 shows no breakthrough at any value of x during the first 24 hours period of rainfall. This is consistent with the earlier observation from Section 6.2.2. (see Figure 6-6) that, if this form of CBS was subjected to a single rainfall

Table 6-5 Numerical simulations of sloping CBSs subjected to cyclic rainfall patterns (β = 35°, t_f = 40 cm)

No.	Analysis Identifier	Evaporation	F.L. material	Climate	Rainfall pattern	Number of cycles
8	5C24ON24OFF	Yes	Fine sand	Hot-humid	C1	5
9	5C24ON24OFF15P	Yes	Fine sand	Hot-humid	C2	3
10	5C12ON12OFFPK	Yes	Fine sand	Hot-humid	C3	5
11	5C24ON48OFF	Yes	Fine sand	Hot-humid	C4	3
12	5C12ON36OFF2P	Yes	Fine sand	Hot-humid	C5	3
13	5C6ON42OFF4P	Yes	Fine sand	Hot-humid	C6	1
14	5C12ON12OFFLN	Yes	Fine sand	Cool-humid	C3	5
15	10C24ON24OFFPKNOE	No	Fine sand	-	C1	10
16	10C12ON12OFFPKNOE	No	Fine sand	-	C3	10
17	5C12ON36OFF2PKNOE	No	Fine sand	-	C5	5
18	5C6ON42OFF4PKNOE	No	Fine sand	-	C6	5

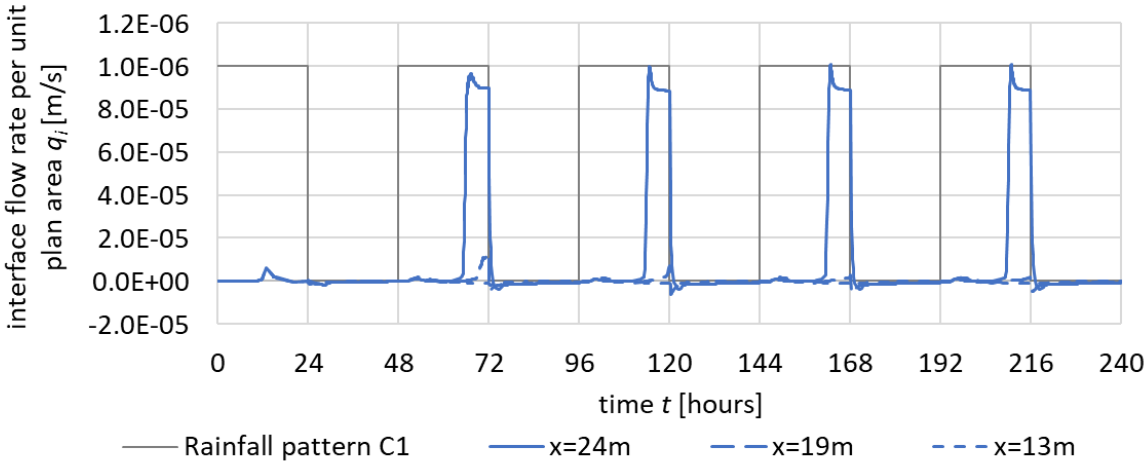

Figure 6-13 Variation of interface flow velocity with time at different values of x for cyclic rainfall pattern C1 (β = 35°, FSGV, t_f = 40 cm, hot-humid climate)

event of limited duration, under the hot-humid climate conditions, the rainfall duration had to be greater than about 26.3 hours for breakthrough to occur (at x values greater than the diversion length L_D = 13.6 m corresponding to the rainfall intensity i =10^{-6} m/s).

Figure 6-13 shows that breakthrough did occur during the second 24 hour period of rain and during all subsequent 24 hour periods of rain but only at x = 24 m of the three values of x shown in the figure. The fact that, at x = 24 m, breakthrough

did occur during the second and subsequent 24 hours periods of rain but not during the first 24 hours period of rain indicates that less of the water storage capacity of the F.L was available at the start of the second and subsequent 24 hour periods of rain than at the start of the first 24 hour period of rain. This makes sense, because the CBS was in a very dry initial state at t = 0, with very little water stored in the F.L. It is noteworthy that at x = 24 m, the pattern of breakthrough (i.e. the variation of q_i with time) was identical within each 24 hour period of rainfall from the second rainfall period onwards. This pattern involved breakthrough commencing approximately 17 hours after the start of rainfall and q_i then quickly settling (after an initial spike) at about 10% less than the rainfall intensity i (consistent with a 10% reduction of the net mass flowrate of water into the ground surface, due to evaporation). The fact that, at x = 24 m, the pattern of breakthrough was identical within each 24 hour period of rainfall from the second rainfall period onwards means that the state of the CBS (i.e. the variation of water stored with x) was identical at the start of each of these rainfall periods.

It also noteworthy from Figure 6-13 that breakthrough did not occur at x = 19m during the second and subsequent periods of rainfall, despite the fact that this value of x is greater than the diversion length L_D = 13.6 m which would apply if the rainfall intensity i = 10^{-6} m/s was sustained indefinitely. The fact that breakthrough did occur during second and subsequent periods of rainfall at x = 24 m but not at x = 19 m, despite the fact that both these values of x are greater than the diversion length L_D = 13.6 m, indicates that the amount of water stored within F.L at the start of the second and subsequent periods of rainfall varied with x. This is entirely consistent with the fact that previous rainfall produces amounts of water storage within the slope that vary with x, at least in the upper part of slope (i.e lower values of x), as shown for example in Figure 5-28. This was in contrast with conditions at the start of first period of rainfall, because the initial state of the CBS (at t = 0) was the same for all values of x.

Figure 6-14 shows the variation with time of soil-atmosphere interactions (precipitation rate P and evaporation rate E) and ground surface conditions (suction s, temperature T and relative humidity R_h within the soil voids) at x = 13 m for the same simulation as shown in Figure 6-13. The results shown in Figure 6-14 were for x= 13m, where no breakthrough occurred, however equivalent plots

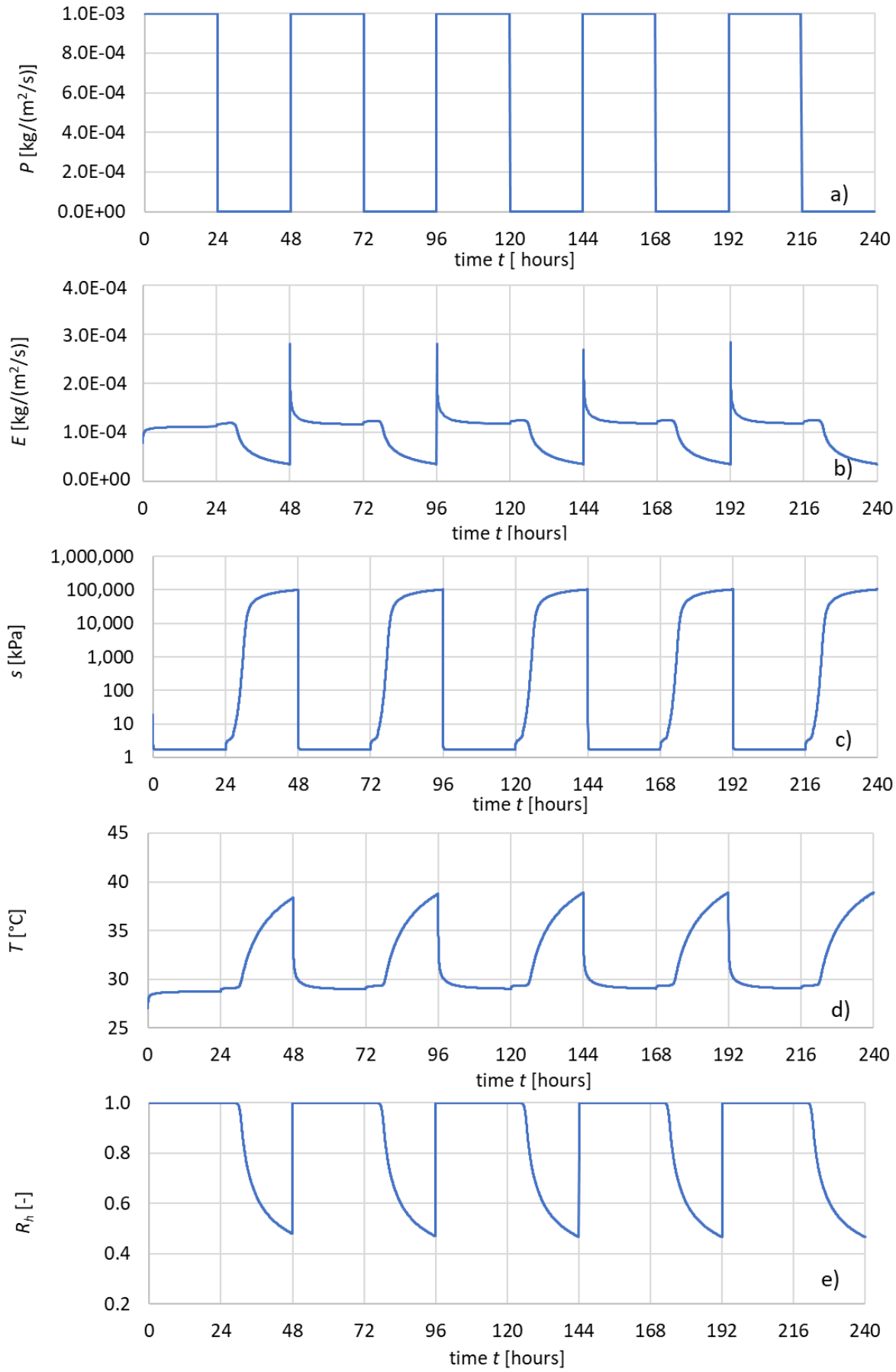

Figure 6-14 Variation of soil-atmosphere interactions and ground surface conditions at x=13m during cyclic rainfall pattern C1: a) precipitation P; b) evaporation E; c) suction s at ground surface; d) temperature T at ground surface; and e) relative humidity R_h in soil voids at ground surface (β = 35°, FSGV, t_f = 40cm, hot-humid climate)

at x = 19 m and x = 24 m, where there was breakthrough, showed results that were almost identical to those in Figure 6-14.

The behaviour shown in Figure 6-14 during the first 24-hour period of rainfall and the following 24-hour period without rain (i.e. t = 0 to t = 48 hours) is identical to the corresponding results from Figure 6-5 for the equivalent single rainfall event of 24 hours duration.

Figure 6-14 shows that, from the end of the first 24 hour-period of rainfall (i.e. from t = 24 hours onwards) the variation with time of the soil-atmosphere interactions and ground surface conditions follows a cyclic pattern, repeating every 48 hours, covering a 24-hour period with no rainfall and a 24-hour period of rainfall. This is consistent with the observation from Figure 6-13 that the breakthrough pattern simply repeated from the second 24-hour period of rain onwards. Inspection of Figure 6-14 shows that, during each 24-hour period of rainfall from the second rainfall period onwards, the evaporation rate E briefly spikes, the suction s at the ground surface drops immediately the rainfall starts (and the relative humidity returns to 1 as a consequence) and the temperature T at the ground surface quickly drops. Soon after the start of each of these rainfall periods, the values of E, s, T and R_h have all returned to steady state values consistent with the rainfall infiltration rate i = 10^{-6} m/s.

6.3.2 Influence of cyclic rainfall patterns

In this section, results of the thermo-hydraulic simulations for the various cyclic rainfall patterns (C1-C6 in Figure 6-12) are compared, to investigate the influence of the cyclic rainfall pattern. All the simulations considered in this section involved the hot-humid climate conditions (see Table 6-5).

Figure 6-15 compares the variations of interface flow velocity q_i (at x = 13 m, x = 19 m and x = 24 m) for the simulations involving cyclic rainfall patterns C1 and C2. Results are shown for the first three cycles of rainfall. Both rainfall patterns involved repeated cycles of 24 hours of rainfall alternating with 24 hours periods of no rainfall. The difference was that cyclic rainfall pattern C2 involved a rainfall intensity i = 1.5x10^{-6} m/s, 50% greater than the rainfall intensity i = 10^{-6} m/s in cyclic rainfall pattern C1 (see Figure 6-12).

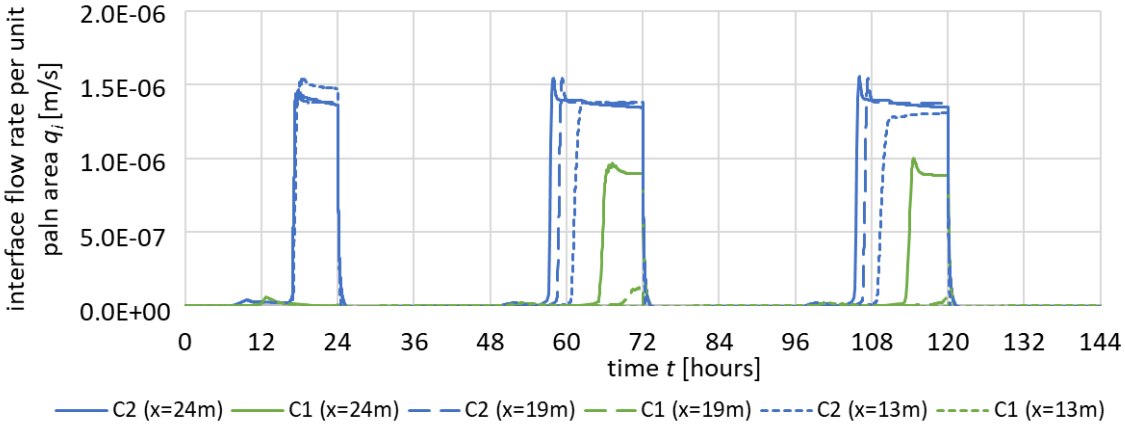

Figure 6-15 Influence of cyclic rainfall intensity on variation of interface flow velocity (β = 35°, FSGV, t_f = 40cm, hot-humid climate, cyclic rainfall patterns C1 and C2)

Inspection of Figure 6-15 shows that, when breakthrough occurred under rainfall pattern C2, after a brief initial spike in the value of q_i, the interface flow velocity q_i quickly settled at a value that was generally slightly smaller than the rainfall intensity i = 1.5x10^{-6} m/s (consistent with the slight reduction of net mass flowrate of water into the ground surface caused by evaporation). Whereas rainfall pattern C1 produced no breakthrough in the first 24-hour period of rainfall and then, breakthrough only at x = 24 m (of the three values of x shown in Figure 6-15) during the second and subsequent periods of rainfall, cyclic rainfall pattern C2 produced breakthrough at all three values of x, even during the first 24-hour period of rainfall. The fact that breakthrough occurred at all three values of x under rainfall pattern C2, is consistent with the higher rainfall intensity resulting in a shorter diversion length L_D, so that even x = 13 m was less that L_D. The higher rainfall intensity in rainfall pattern C2 also meant that the water storage capacity was filled more quickly than water rainfall pattern C1. This explains why breakthrough was able to occur during the first 24-hour period of rainfall under rainfall pattern C2 and it also explains why breakthrough occurred earlier under rainfall pattern C2 than under rainfall pattern C1 in the second and subsequent periods of rainfall.

It can be observed in Figure 6-15 that, under rainfall pattern C2, during the second and subsequent periods of rainfall breakthrough occurred at different times at different values of x, with breakthrough occurring earlier the higher the value of x. This pattern is consistent with the suggestion from Section 6.3.1 that at the start of the second and subsequent periods of rainfall the amount of water stored in the F.L of the CBS varied with x as a consequence of the variation with x of

water stored at the end of that first rainfall period (see for example Figure 5-28). This contrasts with the first 24-hour period of rainfall, where the initial state of the CBS (at t = 0) is the same for all values of x, and hence breakthrough occurred at the same time for all values of x (see Figure 6-15).

Figure 6-16 shows that the variation of interface flow velocity q_i (at x = 13 m, x = 19 m and x = 24 m) for the simulation with cyclic rainfall pattern C3. This rainfall pattern involved the same rainfall intensity as rainfall pattern C1 (i = 10^{-6} m/s), but with rainfall periods of only 12 hours and intervening periods of 12 hours with no rainfall (see Figure 6-12). This cyclic rainfall pattern therefore represents cycles of identical days of rainfall, but with all the rain falling within a 12-hour period in each day.

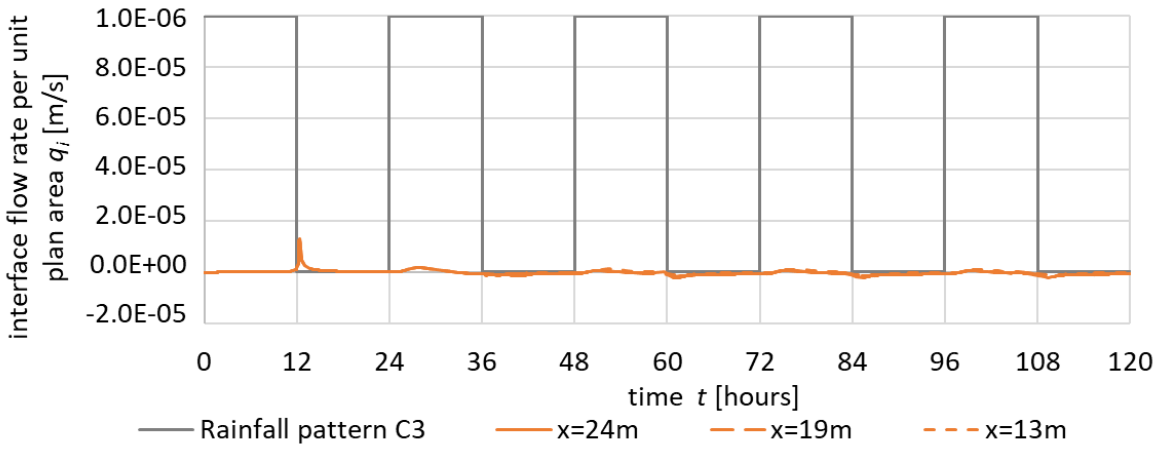

Figure 6-16 Variation of interface flow velocity with time at different values of x for cyclic rainfall pattern C3 (β = 35°, FSGV, t_f = 40cm, hot-humid climate)

Inspection of Figure 6-16 shows that, under cyclic rainfall pattern C3, there was no breakthrough in any of the rainfall periods at any of the three values of x. This indicates that there was sufficient restoration of water storage capacity during each 12-hour period without rain to ensure that breakthrough did not occur at any value of x during the subsequent 12-hour period of rain.

Cyclic rainfall pattern C3 and C1 involved the same value of rainfall intensity (i = 10^{-6} m/s) and the same total amount of rainfall in any 48-hour period. Results for rainfall pattern C3 from Figure 6-16 (no breakthrough) can be compared with results for rainfall pattern C1 from Figure 6-13 (breakthrough at x = 24 m during second and subsequent periods of rainfall). This comparison indicates that, for the

same rainfall intensity (when it is raining) and the same total amount of rainfall over many days, a CBS with the F.L made of fine sand will be more successful at preventing breakthrough if rainfall periods are of relatively short duration, with these separated by dry periods of relatively short duration. This is because, with the F.L made of fine sand, as reported in Section 6.2.3, restoration of water storage capacity during periods when it is not raining, by a combination of evaporation from the ground surface and water transfer down the slope, occurs most rapidly during the first few hours after rainfall stops with both processes slowing dramatically after only a few hours. Hence, longer intervening periods without rainfall do not greatly increase the restoration of water storage capacity to cope with subsequent proportionally longer periods of rainfall.

Figure 6-17 shows the results of the simulation with cyclic rainfall pattern C4, for comparison with the corresponding results for cyclic rainfall pattern C1 presented previously in Figure 6-13. Rainfall pattern C4 involves the same rainfall intensity as rainfall pattern C1 (i = 10^{-6} m/s) and the same duration for each period of rainfall (24 hours). The only difference between rainfall patterns C4 and C1 is the duration of the intervening time periods of no rainfall (48 hours in the case of C4, compared to 24 hours in the case of C1), as shown in Figure 6-12. This means that whereas rainfall pattern C1 involves alternating wet and dry days, rainfall pattern C4 involves two dry days between each wet day.

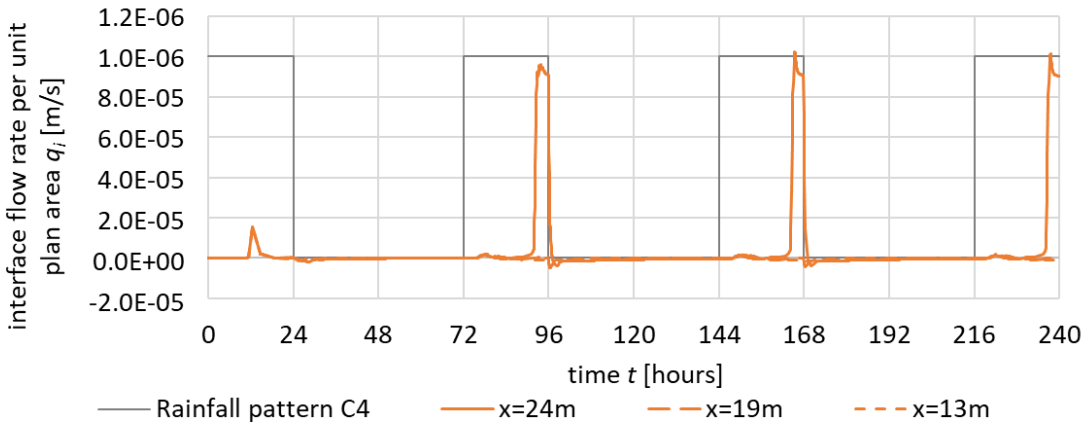

Figure 6-17 Variation of interface flow velocity with time at different values of x for cyclic rainfall pattern C4 (β = 35°, FSGV, t_f = 40cm, hot-humid climate)

Comparison of Figure 6-17 with Figure 6-13 shows that the only significant difference in the results is that the breakthrough that occurs at x = 24m during the second and subsequent 24-hour periods of rainfall occurs slightly later under

rainfall pattern C4 than under rainfall pattern C1 (approximately 20 hours after the start of each rainfall period rather than approximately 17 hours after the start of each rainfall period). This difference is consistent with additional restoration of water storage capacity during the longer intervening dry periods in rainfall pattern C4 (48 hours without rain, compared to only 24 hours without rain in rainfall pattern C1). The increase in breakthrough time at x = 24 m is however relatively modest, because, as noted previously, within a CBS with the F.L made of fine sand, the processes responsible for restoration of storage capacity (evaporation to atmosphere and water transfer down the slope) both slow down significantly within a few hours of rainfall stopping.

Figure 6-18 compares the results from simulations involving cyclic rainfall patterns C1, C5 and C6 (see Figure 6-12). All three rainfall patterns involve alternating wet days (with rainfall) and dry days (without rainfall) and all three involves the same total amount of rainfall in each wet day. The difference is that, in rainfall patterns C5 and C6, the rainfall is concentrated in only part of each wet day. C5 involves rainfall intensity i = 2x10^{-6} m/s for 12 hours every alternate day, whereas C6 involves rainfall intensity i = 4x10^{-6} m/s for 6 hours every alternate day (see Figure 6-12). The objective in comparing the results of simulations of rainfall patterns C1, C5 and C6 was to investigate how the distribution of rain within wet days affects the performance of a sloping CBS. All three simulations shown in Figure 6-18 involved hydraulic modelling (without evaporation), rather than thermo-hydraulic modelling (with evaporation). This was because the attempt to perform a thermo-hydraulic numerical simulation with cyclic rainfall pattern C6 reached the data storage limit after only 1 cycle (see Table 6-5).

Figure 6-18b shows a magnified view of the results for the second cycle of rainfall, with this also representative of all subsequent cycles. Inspection of Figure 6-18b indicates that at x = 24 m and x = 19 m, breakthrough occurred under all three cycle rainfall patterns (C1, C5 and C6). However, at x = 13 m, breakthrough occurred only under rainfall patterns C5 and C6 and at x = 6 m breakthrough occurred only under rainfall pattern C6.

The area under each curve in Figure 6-18b (the integral of interface flow velocity q_i with respect to time t) gives the total liquid water flow across the interface per

unit plan area at that value of x (in a single rainfall cycle). Figure 6-19 shows the results of this integration, at each of the four values of x shown in Figure 6-18, for cyclic rainfall patterns C1, C5 and C6. It is clear from Figure 6-19 that, at x = 24 m and x = 19 m, where breakthrough occurs under all three rainfall patterns, the integrated total of water flow across the interface (per unit plan area) at each of these values of x is similar for the three rainfall patterns (slightly less for C1 than for the other two rainfall patterns at x = 19 m). Inspection of Figure 6-18 shows that this is because, in rainfall patterns such as C5 and C6, the higher value of interface flow rate velocity q_i (compared to rainfall pattern C1) is compensated by the shorter duration of breakthrough. It is also clear however from Figure 6-19 that the integrated totals of water flow across the interface at x = 13 m and x = 6 m are very different for the three rainfall patterns, because breakthrough occurred at both these values of x for rainfall pattern C6, whereas breakthrough does not occur at x = 6 m for rainfall pattern C5 and breakthrough occurs at neither of these values of x for rainfall pattern C1.

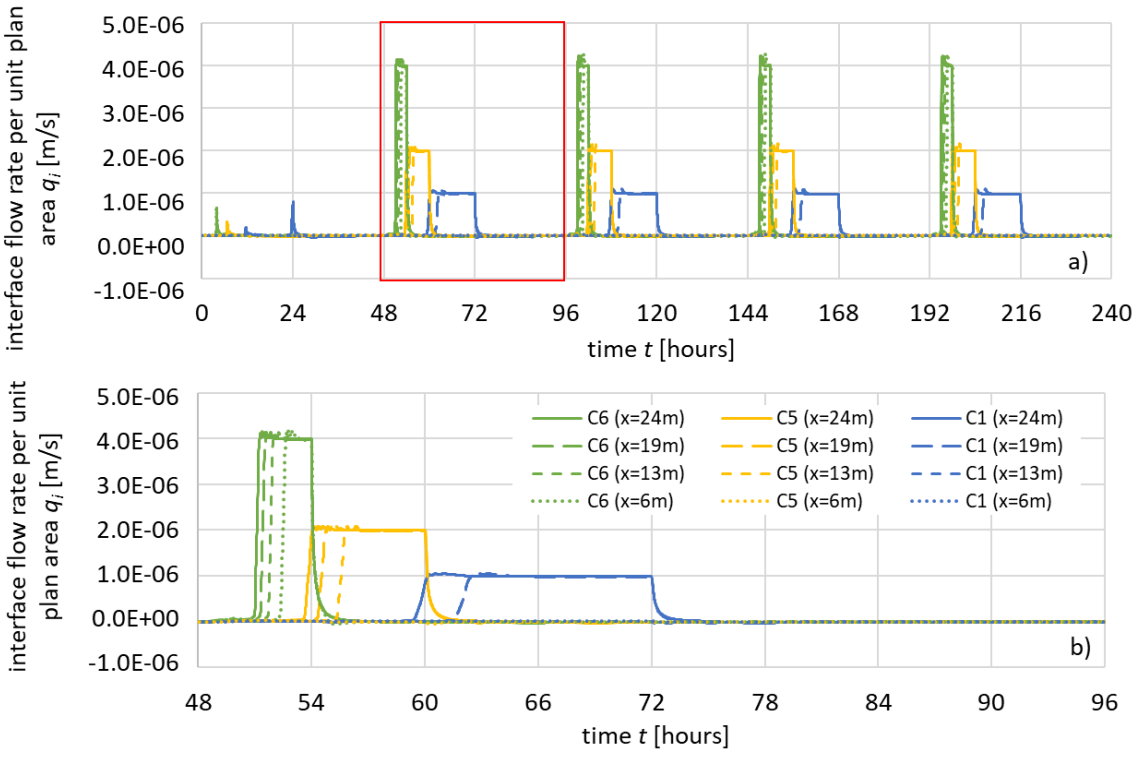

Figure 6-18 Variation of interface flow velocity for cyclic rainfall patterns C1, C5 and C6: a) all 5 cycles; b) second cycle only (β = 35°, FSGV, t_f = 40cm)

Rainfall data provided in meteorological records typically consists simply of daily totals of rainfall (hourly rainfall data are available on special request from the UK Meteorological Office, but this is rarely used by practicing engineers and was not

known at the time of conducting the current research). This means that, when analysing the behaviour of a sloping CBS under real rainfall conditions, it will normally be difficult to do anything other than assume that each daily total of rainfall is uniformly distributed throughout that day (see for example, Scarfone (2020) and Scarfone et al. (2022)). The results presented in Figure 6-19 for rainfall patterns C1, C5 and C6 suggest that this approach is likely to lead to an underestimate of the total flow of water across the interface over the entire slope, because the extent of breakthrough within the slope (i.e. the range of values of x over which some breakthrough occurs) will be greater if the rainfall is concentrated within only part of each day.

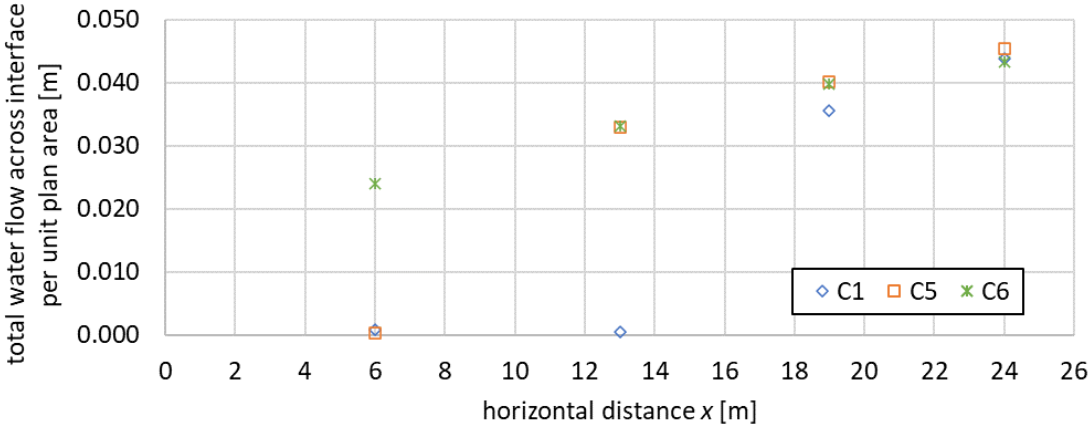

Figure 6-19 Variation of total water flow across interface per unit plan area during second cycle of cyclic rainfall patterns C1, C5 and C6 (β = 35°, FSGV, t_f = 40 cm)

Figure 6-20 shows the variation of evaporation rate E during the first 48 hours (i.e. the first rainfall cycle) of thermo-hydraulic simulations with rainfall patterns C1, C2, C5 and C6. These four cyclic rainfall patterns involved four different values of rainfall intensity i (10^{-6} m/s, $1.5\text{x}10^{-6}$ m/s, $2\text{x}10^{-6}$ m/s and $4\text{x}10^{-6}$ m/s respectively). It is notable however, from Figure 6-20, that the steady state evaporation rate E while rain was occurring was very similar in all four cases, at approximately $E \approx 10^{-4}$ kg/m^{2}s, i.e. the steady state evaporation rate was almost independent of rainfall intensity. In addition, in all four cases, the evaporation rate was slightly higher for 6-12 hours after rainfall stopped (the longer times applying when the rainfall was more concentrated) and only then, for reasons described earlier, did the evaporation rate begin to reduce significantly.

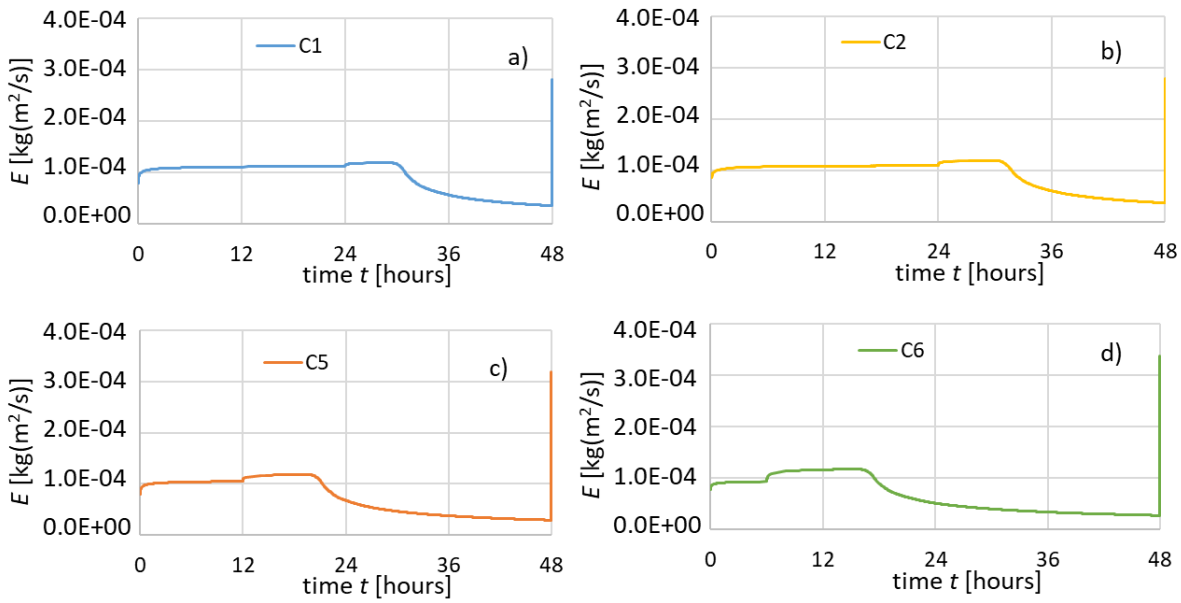

Figure 6-20 Variation of evaporation rate with time during first cycle of selected cyclic rainfall patterns (β = 35°, FSGV, t_f = 40 cm, hot-humid climate)

6.3.3 Influence of atmospheric temperature and radiation

As set out in Table 6-5, a single thermo-hydraulic numerical simulation was performed with the cool-humid climate conditions. This involved cyclic rainfall pattern C3 (cycles of 12 hours of rainfall of intensity i = 10^{-6} m/s alternating with 12 hours of no rainfall). The influence of climate conditions was investigated by comparing the results of this simulation with the results from the corresponding simulation involving the hot-humid climate conditions. As noted in Section 6.1.2, the cool-humid climate conditions represented average annual values for London, UK, whereas the hot-humid climate conditions represented average annual values for Phuket, Thailand. Inspection of Table 6-2 shows that the main differences between the two sets of climate conditions were that the cool-humid climate involved a lower value of atmospheric temperature T_a (10.98°C instead of 27.00°C) and a lower value of net radiation R_n (174 J/m²s instead of 271 J/m²s). In addition, the cool-humid climate also involved a slightly lower value of wind speed v_a (2.91 m/s instead of 3.66 m/s).

Figure 6-21 shows variations of soil atmosphere interactions (P and E) and ground surface conditions (s, T and R_h) at x = 13 m for the simulations with the two different climate conditions. It is notable that the steady state evaporation rate E during rainfall was approximately 5x10^{-5} kg/m²s under the cool-humid climate

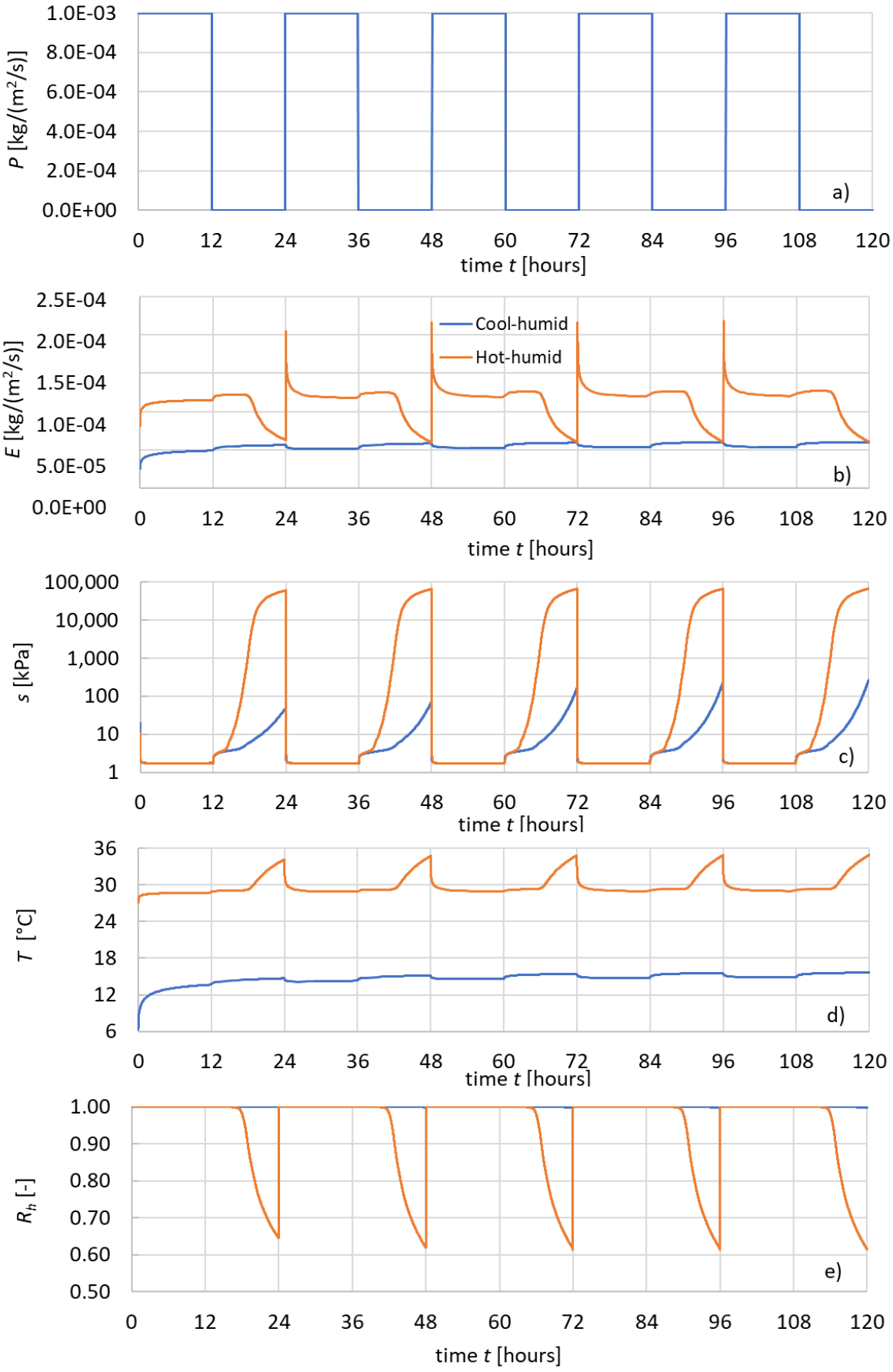

Figure 6-21 Influence of climate on variations of soil-atmosphere interactions and ground surface conditions at x= 13m during cyclic rainfall pattern C3: a) precipitation rate *P*; b) evaporation rate *E*; c) suction *s* at ground surface; d) temperature *T* at ground surface; and c) relative humidity R_h in soil voids at ground surface (β = 35°, FSGV, t_f = 40 cm)

conditions i.e. roughly 50% of the corresponding value under the hot-humid conditions.

As in the hot-humid conditions, the evaporation rate under the cool-humid conditions increases slightly each time the rainfall stopped. However, in contrast to the hot-humid conditions, the evaporation rate under the cool-humid climate remained at this slightly elevated value for the full 12 hour-period when there was no rainfall, rather than starting to decrease significantly 6 hours after the rainfall finished. Inspection of Figure 6-21 shows that this was because the gradual increase of suction after the rainfall stopped occurred more slowly under the cool-humid conditions than under the hot-humid conditions, so that it would have taken significantly more than 12 hours without rainfall before the suction reached several MPa and the evaporation rate started to decrease. As a consequence, with cyclic rainfall pattern C3, the evaporation rate remained relatively constant under the cool-humid climate conditions.

Figure 6-22 compares the variations of interface flow velocity q_i for the simulations of cyclic rainfall pattern C3 with the two different climate conditions. Whereas there was no breakthrough at x = 24 m, x = 19 m or x = 13 m under the hot-humid conditions, from the third cycle of rainfall onwards there was breakthrough at x = 24 m and x = 19 m under the cool-humid conditions. This difference can be attributed to the lower evaporation rate under the cool-humid climate conditions (both during rainfall and during each 12hour-period without rainfall, see Figure 6-21). The reason that breakthrough occurred in the third cycle under rainfall pattern C3 (Figure 6-22a), whereas breakthrough occurred in the second cycle under rainfall pattern C1 (Figure 6-13) was that there was only half as much rain per cycle in rainfall pattern C3 and hence the first two cycles involved an equivalent amount of rainfall as the first cycle in C1.

The lower evaporation rate during rainfall means that the effective rainfall infiltration rate (after accounting for evaporation) was slightly higher under cool-humid conditions: about 95% of the rainfall infiltration rate, compared to about 90% of the rainfall infiltration rate under the hot-humid conditions. This means that the amount of water stored in the F.L when each 12-hour period of rainfall finished was slightly higher under cool-humid conditions than under the hot-humid conditions. The fact that the evaporation rate during the 12-hour periods of no

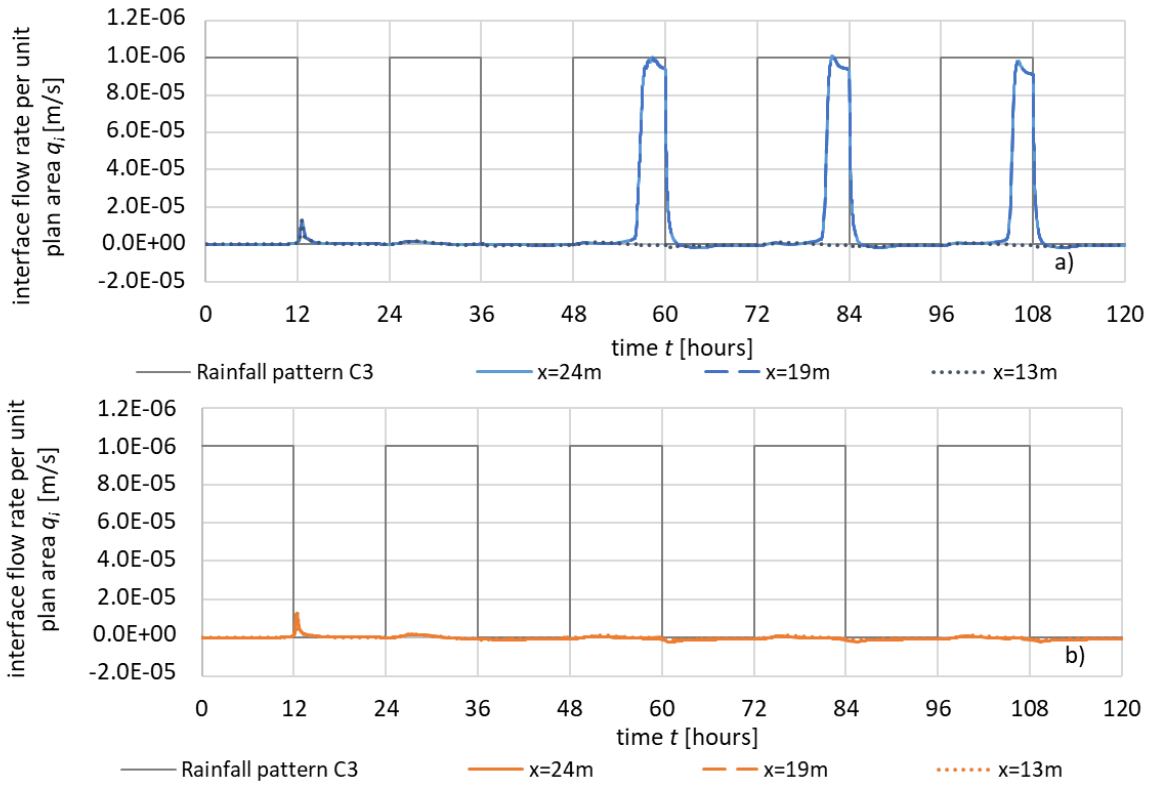

Figure 6-22 Influence of climate conditions on variation of interface flow velocity with time at different value of x for cyclic rainfall pattern C3: a) cool-humid; and b) hot humid (β = 35°, FSGV, t_f = 40 cm)

rainfall was also lower under cool-humid conditions than under hot-humid conditions then meant that restoration of storage capacity occurred more slowly under the cool-humid conditions. Together, these two effects meant that the amount of water stored in the F.L at the start of each rainfall period was higher under cool-humid conditions than under hot-humid conditions and hence breakthrough was more likely during the subsequent 12 hours of rainfall.

The results presented in Section 6.2 and 6.3 show that the evaporation rate is almost constant during periods when rainfall is occurring (and for some time after rainfall finishes). This evaporation has the effect of reducing the effective rainfall infiltration rate, by an amount corresponding to the mass flow rate of water from the ground to the atmosphere due to evaporation (converted to an equivalent volumetric flow rate of liquid water per unit plan area). This steady state evaporation rate during rainfall has been shown to be dependent on climate conditions (see this section), but almost independent of rainfall intensity (see Section 6.3.2) or the material of the F.L (Section 6.2.3).

6.4 Extreme rainfall events

This section presents and discusses the results of numerical simulations involving the extreme rainfall events shown in Figure 6-23. Each of the three extreme rainfall events involved a sustained period of moderate or low intensity rain (the antecedent rain), followed by a few days or a single day of extreme rainfall, before a return to the initial rainfall intensity. Consideration of the behaviour of a sloping CBS subjected to an extreme rainfall event appropriate for the location of the slope is likely to be a key feature of a rational methodology for the design and assessment of a sloping CBS (see Chapters 7 and 8).

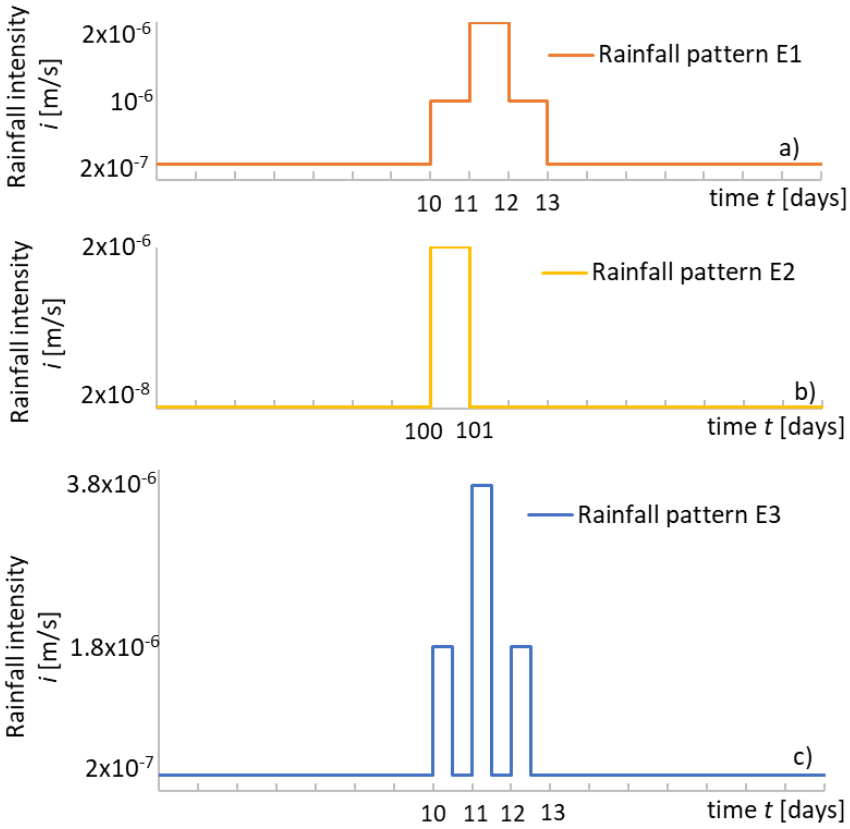

Figure 6-23 Extreme rainfall events

The original intention had been to conduct thermo-hydraulic numerical simulations (with evaporation) of the extreme rainfall events. However, numerical instabilities occurred in the first attempt at one of these thermo-hydraulic simulations. Previous experience suggested that these numerical difficulties could be solved, but that finding a solution would probably be time-consuming. Given that time was limited, it was decided to proceed with hydraulic simulations

(without evaporation) of the extreme rainfall events, which largely avoided the numerical instabilities.

Further consideration also suggested that there was good justification for only performing hydraulic simulations (without evaporation) of the extreme rainfall events. Each of the extreme rainfall events shown in Figure 6-23 involved continuous rainfall (i.e. no periods without rainfall) and commenced with a long period of antecedent rain. Previous results for single rainfall events of limited duration (see Section 6.2) and for cyclic rainfall patterns (see Section 6.3) had indicated that, under continuous rainfall and constant atmospheric conditions, the evaporation rate quickly reached a constant steady state value, which was almost independent of rainfall intensity and the material of F.L (but which did depend on the atmospheric conditions). These previous results also showed that, in terms of the behaviour of the CBS, the constant rate of evaporation simply reduced the effective rainfall infiltration rate by an amount corresponding to the evaporation rate. Hence, hydraulic numerical analyses (without evaporation) of the extreme rainfall events shown in Figure 6-23 would be adequate if the applied rainfall infiltration rate in the hydraulic numerical simulations represented the effective rainfall infiltration rate (i.e. after subtracting the constant evaporation rate from the true rainfall infiltration rate).

6.4.1 Behaviour of a CBS with F.L made of fine sand

Figure 6-24 shows the results of simulations of a sloping CBS with the F.L made of fine sand subjected to extreme rainfall event E1 (see Figure 6-23). This extreme rainfall event involved 10 days of antecedent rain of intensity i = 2x10^{-7} m/s (i.e. a total of 172.8 mm of rain over the 10 days). This would represent a sustained wet period in most locations in the UK. The 10 days of antecedent rain was followed by three days of extreme (i = 10^{-6} m/s) or very extreme (i = 2x10^{-6} m/s) rainfall (i = 10^{-6} m/s from t = 10 days to t = 11 days, i = 2x10^{-6} m/s from t = 11 days to t = 12 days and i = 10^{-6} m/s from t = 12 days to t = 13 days). This would represent a very extreme rainfall event (345.6 mm of rain in only three days), with a return period well in excess of 100 years in most locations in the UK. After the three days of extreme rain, the rainfall intensity returned to the initial value of i = 2x10^{-7} m/s.

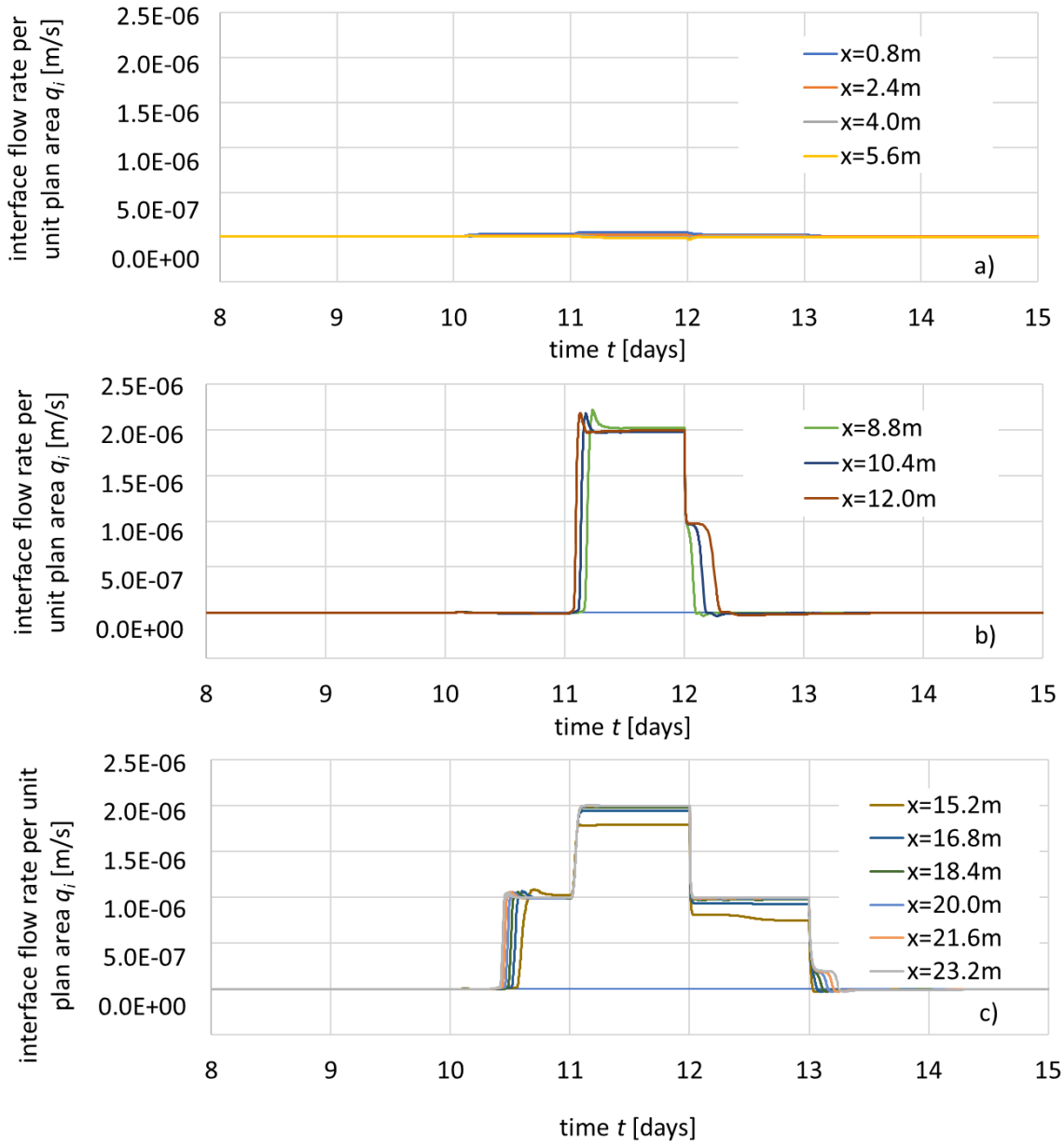

Figure 6-24 Variation of interface flow velocity with time at different values of x for CBS with F.L made of fine sand under extreme rainfall pattern E1 (β = 35°, FSGV, t_f = 40 cm)

Inspection of Figure 6-24 shows that no breakthrough occurred at x = 0.8 m, x = 2.4 m, x = 4.0 m or x = 5.6 m (see Figure 6-24a), breakthrough started under the highest rainfall intensity (of i = 2x10^{-6} m/s), between t = 11 days and t = 12 days, at x = 8.8 m, x = 10.4 m and x = 12.0 m (see Figure 6-24b) and breakthrough started under the rainfall intensity i = 10^{-6} m/s, between t = 10 days and t = 11 days, at x = 15.2 m, x = 16.8 m, x = 18.4 m, x = 20.2 m, x = 21.6 m and x = 23.2 m (see Figure 6-24c). This was consistent with expectations, because the diversion length L_D under a rainfall intensity i = 10^{-6} m/s (if this rainfall intensity was sustained indefinitely) was previously found to be 13.6 m (see Figure 5-12b) and the corresponding values of L_D for i = 2x10^{-6} m/s and i = 2x10^{-7} m/s would be expected to be 6.8 m and 68.0 m respectively.

Inspection of Figures 6-24b and 6-24c shows that, when breakthrough did occur, it commenced some hours after the increase in rainfall intensity that caused the breakthrough. For example, in Figure 6-24b breakthrough started some hours after the increase of rainfall intensity to i = 2x10^{-6} m/s at t = 11 days. Similarly, in Figure 6-24c breakthrough started some hours after the increase of rainfall intensity to i = 10^{-6} m/s at t = 10 days. These time-lags before breakthrough started were associated with the time required to fill the F.L to the appropriate value of water storage capacity WSC from the lower value of water stored WS at that value of x under the previous (lower) rainfall intensity. Inspection of Figures 6-24b and 6-24c shows that these time-lags before the start of breakthrough were of different durations at different values of x, with shorter time-lags at higher values of x. This can be attributed to different values of WS under the previous rainfall intensity at different values of x, with higher previous values of WS at higher values of x (see Figure 5-28).

Figure 6-24c shows that if breakthrough has already occurred under one rainfall intensity and the rainfall intensity then increases, there is a second (short) time-lag before the value of interface flow velocity increases further in response to the increase of rainfall intensity i.e. a short time-lag after the second increase of rainfall intensity at t = 11 days in Figure 6-24c. This time-lag is associated with the time to fill the F.L from the value of water storage capacity WSC corresponding to the previous (lower) rainfall intensity to the slightly higher value of WSC corresponding to new (higher) rainfall intensity (see Figure 5-28). As a consequence, the duration of this time-lag is the same for all values of x where it occurs.

Inspection of Figures 6-24b and 6-24c shows that, when breakthrough first occurs or when it subsequently increases after a further increase of rainfall intensity, after an initial spike the value of interface flow velocity q_i quickly stabilises at a value that is generally equal to the rainfall intensity i. This is consistent with expectations, given that the results shown in Figure 6-24 are from a hydraulic numerical simulation (with no evaporation). The sole exception is at x = 15.2 m (see Figure 6-24c) where values of q_i between t = 11 days and t = 13 days are slightly lower than expected. No reason has been found for this, as the values of

q_i follow expected patterns at the two adjacent values of x (x = 12.0 m in Figure 6-24b and x = 16.8 m in Figure 6-24c).

Figures 6-24b and 6-24c show that if breakthrough has previously occurred, when the rainfall intensity decreases the value of interface flow velocity q_i immediately reduces to the new (lower) rainfall intensity i.e. with no time-lag (see decrease in rainfall intensity to i = 10^{-6} m/s at t = 12 days in Figures 6-24b and 6-24c and the second decrease in rainfall intensity to i = 2x10^{-7} m/s at t = 13 days in Figure 6-24c). This absence of any time-lag before q_i reduces following a reduction of rainfall intensity is consistent with observations for single rainfall events of limited duration (Section 6.2) and for cyclic rainfall patterns (Section 6.3).

The final observation from Figures 6-24b and 6-24c is that, if breakthrough has previously occurred, when the rainfall intensity decreases to a new (lower) value that is insufficient to maintain breakthrough indefinitely at that value of x (i.e. the value of x is less than the new (increased) value of diversion length L_D), there is a time-lag before the value of interface flow velocity q_i reduces from the new rainfall rate to zero. Examples of this time-lag can be seen in Figure 6-24b after the rainfall intensity drops to i = 10^{-6} m/s at t = 12 days and in Figure 6-24c after the rainfall intensity drops to i = 2x10^{-7} m/s at t = 13 days. The duration of this final time-lag, to the time where interface flow ceases, is dependent on the value of x, with longer durations of time-lag for higher values of x.

6.4.2 Behaviour of a CBS with F.L made of silty sand

Earlier results had indicated that a sloping CBS with the F.L made of silty sand was not well-suited for use in climatic regions with sustained wet conditions, because of the low value of water transfer capacity Q_{max} (see Section 5.5.4). This was confirmed by a hydraulic numerical simulation involving extreme rainfall event E1 (see Figure 6-23). This simulation indicated that a significant part of the slope experienced breakthrough even during the antecedent rain (the diversion length L_D corresponding to i = 2x10^{-7} m/s was 9.9 m (see Figure 5-18a)). In addition, during the three days of extreme rainfall most of the slope had a variation of interface flow velocity q_i that was little different to the variation of rainfall intensity i (i.e. the CBS was not serving any useful function during these three days).

A sloping CBS with the F.L made of silty sand may however be more useful in climatic conditions that are generally relatively dry but that involve occasional extreme rainfall events of short duration. This is because a CBS with the F.L made of silty sand has high storage capacity (see Section 5.5.4) and also because restoration of storage capacity during long duration intervening dry periods without rain is effective if the F.L is made of silty sand, because evaporation continues at an undiminished rate for many days or weeks after rainfall ceases (see Section 6.2.3). Hence, it was decided to conduct a hydraulic numerical simulation of a sloping CBS with the F.L made of silty sand under the alternative extreme rainfall event E2 shown in Figure 6-23, more representative of a relatively dry climate with occasional short duration extreme rainfall events. Extreme rainfall event E2 involved low intensity antecedent rain at i = 2x10^{-8} m/s maintained for 100 days (sufficient to reach steady state conditions throughout the slope) and a single day of very extreme rain (i = 2x10^{-6} m/s) from t = 100 days to t = 101 days.

Figure 6-25 shows the results of the hydraulic numerical simulation (without evaporation) of a sloping CBS with the F.L made of silty sand subjected to extreme rainfall pattern E2. No breakthrough occurred, at any value of x, during the antecedent rain (t = 0 to t = 100 days), consistent with an expected value of diversion length L_D of about 99 m for the low rainfall intensity i = 2x10^{-8} m/s. Under the extreme rainfall intensity i = 2x10^{-6} m/s from t = 100 days to t = 101 days, results for x = 1.6 m (Figure 6-25a) and for higher values of x (Figures 6-25b and 6-25c) show that full breakthrough occurred at all values of x equal to or greater than 1.6 m. This is consistent with an expected value of L_D of only about 1.0 m if a rainfall intensity i = 2x10^{-6} m/s was maintained indefinitely. At these values of x ($x \geq$ 1.6m), there was a time-lag of several hours after the rainfall intensity increased (at t = 100 days) before breakthrough occurred (see Figure 6-25). As expected, the duration of this time-lag reduced as the value of x increased (consistent with the observations reported in Section 6.4.1).

Figure 6-25a shows that at x = 0.6 m, x = 0.8 m and x = 1.0 m partial breakthrough occurred some hours after the rainfall intensity increased at t = 100 days, with q_i rising towards a final steady state value less than the rainfall intensity i. This is consistent with the fact that the diversion length L_D, which is simplified as a sharp

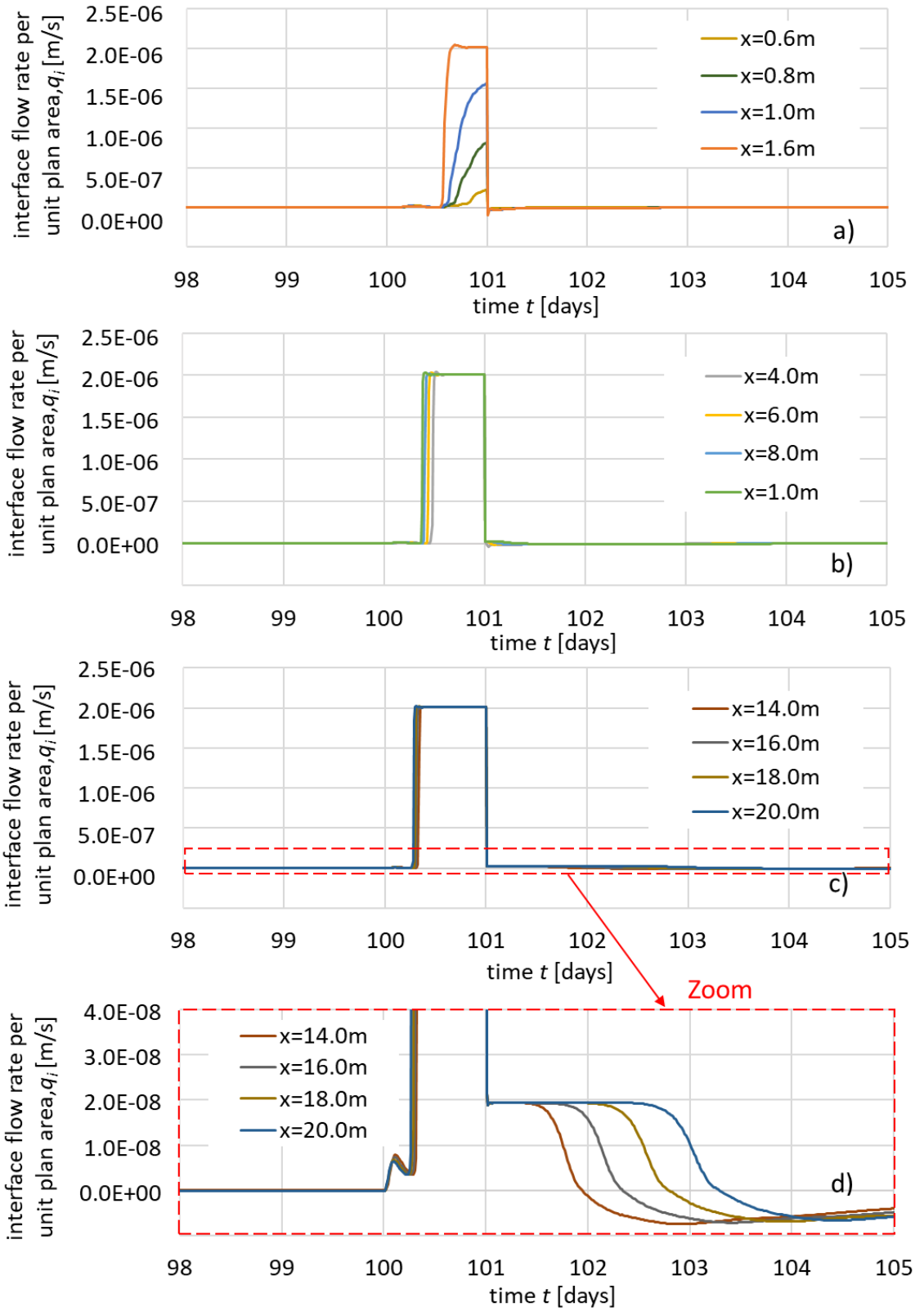

Figure 6-25 Variation of interface flow velocity with time at different values of x for CBS with F.L made of silty sand under extreme rainfall pattern E2 (β = 35°, FSGV, t_f = 40 cm)

transition between no breakthrough (q_i= 0) and full breakthrough (q_i= i) in reality represents the average location of a zone, covering a range of x, over which the final steady state value of q_i increases from zero to the rainfall intensity i (see Figure 5-18). With the diversion length L_D for i = 2x10^{-6} m/s predicted as 1.0 m,

it is entirely consistent that the results in Figure 6-25a show final steady state values of q_i increasing from zero to i over a range of x from about x = 0.6 m to x =1.6 m.

Figures 6-25a, 6-25b and 6-25c show that, if breakthrough had previously occurred, a decrease in rainfall intensity (at t = 101 days) resulted in an immediate reduction in the value of interface flow velocity q_i (i.e. no time-lag). Inspection of the magnified view shown in Figure 6-25d indicates that this immediate reduction of q_i was to a value corresponding to the new (reduced) rainfall intensity i = 2x10^{-8} m/s. Then sometime later (after a time-lag) the value of q_i reduced to zero (or even a very small negative value), because the rainfall intensity i = 2x10^{-8} m/s was insufficient to maintain breakthrough indefinitely at any of the relevant values of x (because L_D = 99 m for this rainfall intensity). This behaviour was consistent with the results for a sloping CBS with the F.L made of fine sand previously discussed in Section 6.4.1.

6.4.3 Influence of rainfall distribution within each day

For the same CBS as investigated in Section 6.4.1 (F.L made of fine sand), an additional hydraulic numerical simulation was performed with extreme rainfall pattern E3 (see Figure 6-23). Rainfall pattern E3 involved the same antecedent rainfall as pattern E1, and the same total daily rainfall as pattern E1 in each day of the three-day extreme rainfall event. The difference was that whereas for extreme rainfall event E1 each day of extreme rainfall was at a constant rate throughout the day, in rainfall pattern E3 the additional rainfall (in excess of the background antecedent rainfall rate) was entirely concentrated in the first 12 hours of each day). The intention was to compare the results of the simulations for extreme rainfall patterns E3 and E1, to see if the distribution of rainfall within each day of an extreme rainfall event was important for the total water flow across the interface of a sloping CBS.

Figure 6-26 shows the results for the simulation involving extreme rainfall pattern E3. The qualitative behaviour observed is entirely consistent with that reported previously in Sections 6.4.1 and 6.4.2. The first and third days of extreme rainfall involved the same rainfall, but the response of the CBS is, as expected, different

on these two days because the initial state of the CBS is different at the start of these two periods of rainfall.

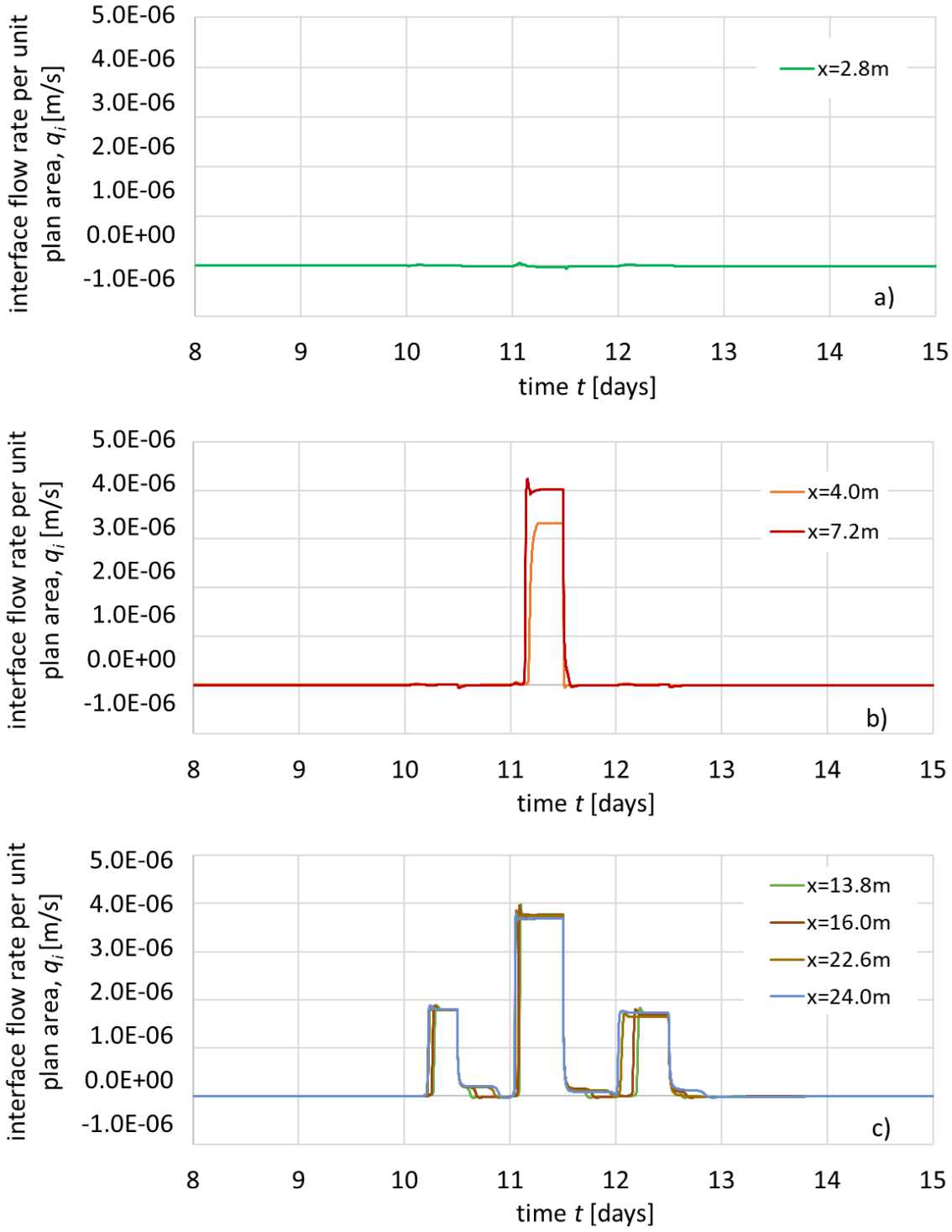

Figure 6-26 Variation of interface flow velocity with time at different value of x for CBS with F.L made of fine sand under extreme rainfall pattern E3 (β = 35°, FSGV, t_f = 40 cm)

Figure 6-27 compares the two simulations (extreme rainfall patterns E1 and E3), in terms of the total flow of water across the interface per unit plan area at

different values of x (obtained by integrating the plots of q_i against time shown in Figures 6-24 (rainfall pattern E1) and 6-26 (rainfall pattern E3). Inspection of Figure 6-27 shows that, if the rainfall during each day of an extreme rainfall event was concentrated in only part of the day (rainfall pattern E3), but it was analysed assuming that each daily total of rainfall was uniformly distributed throughout that day (rainfall pattern E1) this would result in an underestimate of the range of values of x at which breakthrough was predicted (e.g. there would be an incorrect prediction of no breakthrough at x = 5.6 m). More generally, values of total water flow across the interface per unit plan area would be underpredicted at low values of x, but overpredicted at higher values of x (see Figure 6-27).

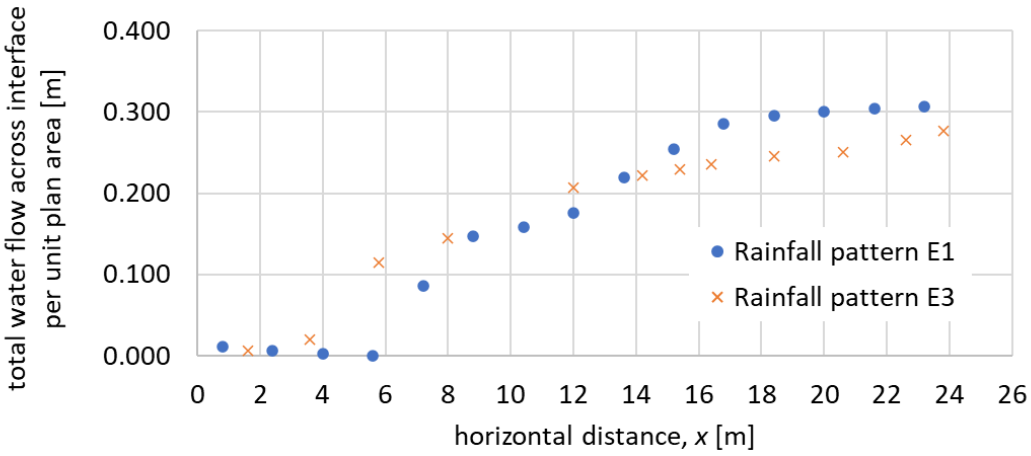

Figure 6-27 Variation of total water flow across interface per unit plan area for a CBS with F.L made of fine sand during extreme rainfall events E1 and E3 (β = 35°, FSGV, t_f = 40 cm)

6.4.4 Influence of water retention hysteresis

All the thermo-hydraulic and hydraulic simulations presented so far in Chapter 6 included retention hysteresis, through use of the hysteretic-modVG-modM+LF constitutive model. Two further hydraulic simulation were performed of a CBS with the F.L made of fine sand subjected to extreme rainfall event E1, but this time without retention hysteresis (i.e. with the non-hysteretic modVG-modM+LF constitutive model). In one of these non-hysteretic simulations, the values of the SWRC input parameter $\bar{P}_0$ (for the F.L and C.L) were taken as the values of $\bar{P}_{0w}$ from Table 6.1 i.e. the soil state was always on the main wetting SWRC. In the other non-hysteretic simulation, the values of $\bar{P}_0$ were taken as the values of $\bar{P}_{0d}$ from Table 6.1, i.e. the soil state was always on the main drying SWRC. The intention was to compare the results from the corresponding hysteretic and non-

hysteretic simulations, to investigate the role of retention hysteresis in the response of a sloping CBS to an extreme rainfall event.

Figure 6-28 shows the results of the full hysteretic simulation (full HMW) and the two non-hysteretic simulations (main wetting MW and main drying MD) at x = 12 m and x = 24 m. It is notable that the MW non-hysteretic simulation suffered from numerical instability immediately after the onset of breakthrough, whereas this did not occur in either of the other simulations. It should be emphasised however that the numerical instability was apparent only in the value of interface flow velocity q_i, because q_i was calculated as the small difference between two much larger quantities ($q_i = q_v - q_h \tan\beta$, as shown in Equation 5-32). The numerical instabilities in the separate values of q_v and q_h were very small (in percentage terms) but these small instabilities in q_v and q_h produced the much larger percentage variations of q_i shown in Figure 6-28.

After discounting the numerical instabilities, inspection of Figure 6-28 shows that the MW non-hysteretic simulation provides an excellent match to the full hysteretic simulation (at both values of x) in terms of the onset of breakthrough. This is to be expected, as the soil behaviour during the full hysteretic simulation would be expected to be on the main wetting SWRC up to and including the onset of breakthrough. It is also notable however that the MW non-hysteretic model provides a reasonable match to the full hysteretic simulation (at both values of x) even as the rainfall intensity reduces. The only significant error in the MW non-hysteretic simulation is slight overestimation of the time-lag before breakthrough ceases (after the decrease of rainfall intensity to i = 10^{-6} m/s at t = 12 days in Figure 6-28a and after the drop in rainfall intensity to i = $2\text{x}10^{-7}$ m/s at t = 13 days in Figure 6-28b). In contrast, the results of the MD non-hysteretic simulation differ significantly from the results of the full hysteretic simulation (at both value of x) in several important respects. This is because during an extreme rainfall event it is the wetting behaviour of the F.L material that is most crucial in controlling key aspects of the CBS behaviour, such as whether breakthrough occurs at a particular value of x and, if so when this breakthrough occurs. In contrast, the drying behaviour of the material is only relevant in influencing the timing when breakthrough ceases, and this is relatively unimportant, because the main reductions in interface flow velocity q_i occur instantaneously when the rainfall

intensity reduces and it is only the final reduction of q_i to zero that is influenced by whether the soil behaviour is assumed to be an a drying curve or a wetting curve (see Figure 6-28).

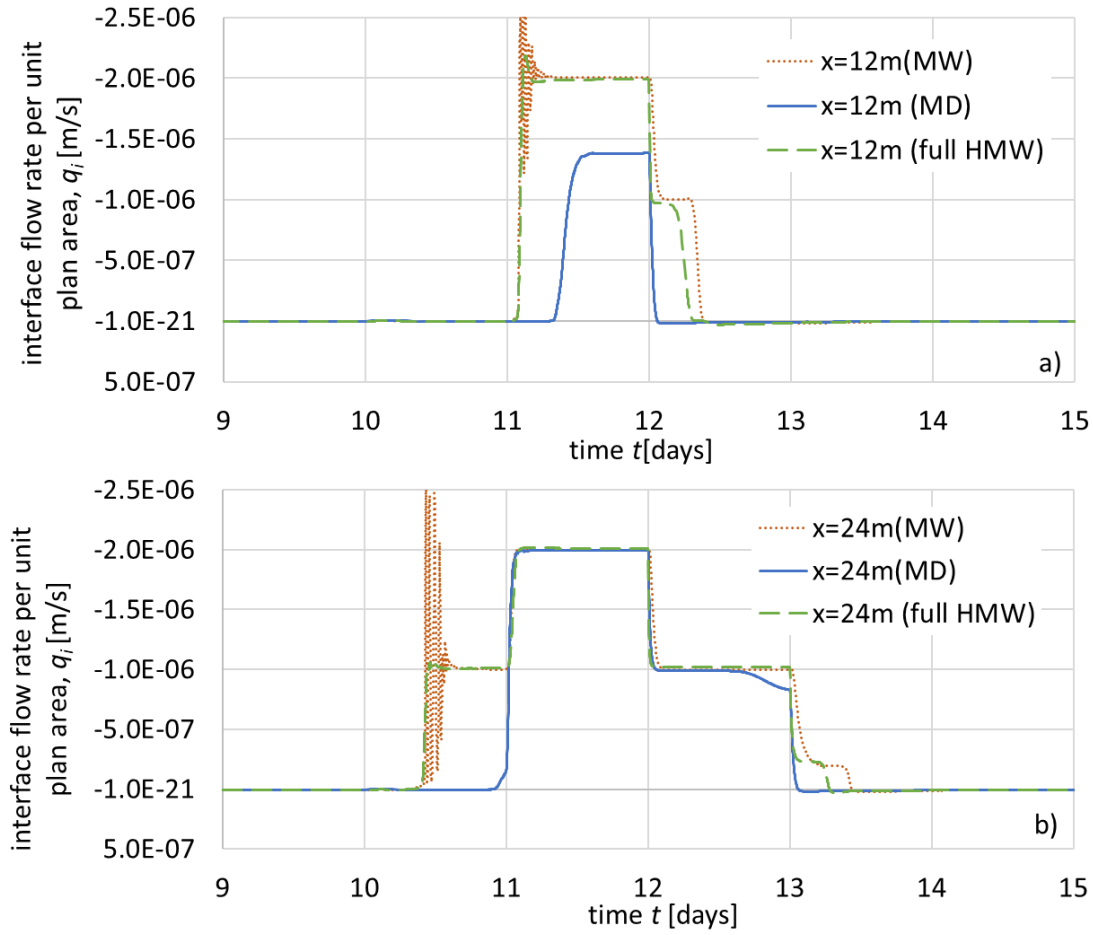

Figure 6-28 Variation of interface flow velocity for hysteretic and non-hysteretic simulations of CBS with F.L made of fine sand subjected to extreme rainfall event E1 (β = 35°, FSGV, t_f = 40 cm)

Figure 6-29 shows the variation of total water flow across the interface per unit plan area for the three different simulations, calculated by integrating the plots of interface flow velocity q_i against time t at different values of x. The results for the MW non-hysteretic simulation in Figure 6-29 are considered reasonably reliable, despite the numerical instability apparent in Figure 6-28, because the integration process averaged out the effects of the numerical oscillations.

Figure 6-29 shows that the MW non-hysteretic simulation slightly overestimated the total water flow across the interface per unit plan area at most values of x, when compared with the full hysteretic simulation. This slight overestimation can be attributed to the over-prediction of the time-lags before the final cessation of breakthrough shown in Figure 6-28. In contrast, Figure 6-29 shows that the MD

non-hysteretic simulation greatly underpredicted the total water flow across the interface when compared with the full hysteretic simulation.

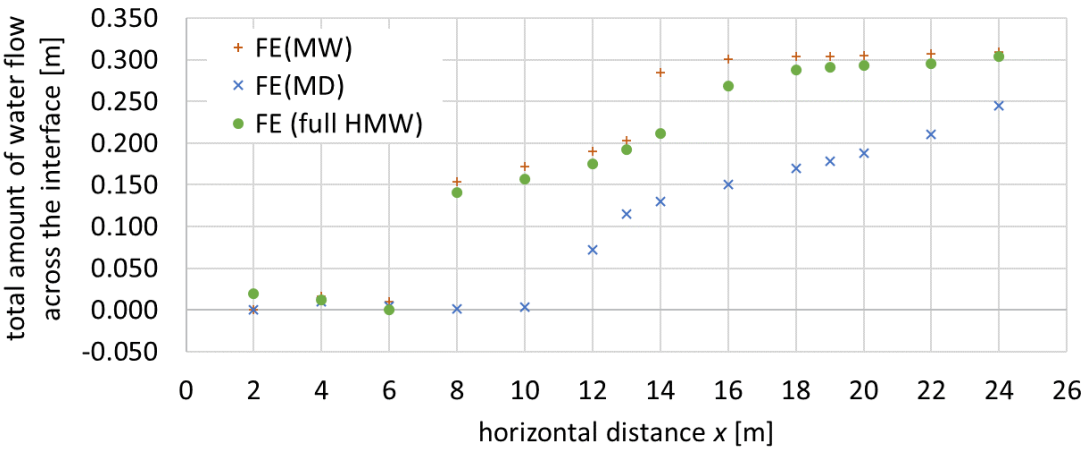

Figure 6-29 Variation of total water flow across interface per unit plan area for hysteretic and non-hysteretic simulations of CBS with F.L made of fine sand subjected to extreme rainfall event E1 (β = 35°, FSGV, t_f = 40 cm)

Overall, the results presented in Figures 6-28 and 6-29 suggest that it may be acceptable to ignore retention hysteresis when analysing the response of a sloping CBS subjected to an extreme rainfall event, by assuming that the soil state remains on the main wetting SWRC throughout the extreme rainfall event. A non-hysteretic analysis based on use of the main wetting SWRC will be slightly conservative, as it should slightly underpredict the total water flow across the interface of the CBS.

6.5 Conclusions

The main achievements and conclusions of the work presented in this chapter can be summarised as follows.

1) Thermo-hydraulic numerical simulations (with evaporation from the ground surface) and hydraulic numerical simulations (without evaporation) have been performed for sloping CBSs subjected to: rainfall events of limited duration; cyclic rainfall patterns; and extreme rainfall events. The results of these simulations have provided important new insights into the behaviour of sloping CBSs subjected to intermittent or varying intensity rainfall.

2) Thermo-hydraulic simulations indicate that, during rainfall, the rate of evaporation from the ground surface quickly reaches a steady state value. When rainfall ceases, the evaporation rate remains almost unchanged from this steady state value for a period of hours, days, or weeks (the duration depends upon the climate conditions and the material of the F.L). The steady state value of evaporation rate during rainfall is dependent on the atmospheric conditions (atmospheric temperature, atmospheric relative humidity, net radiation, and wind speed) but is almost independent of rainfall intensity and material of the F.L.

3) Comparison of thermo-hydraulic simulations and hydraulic simulations shows that, while rainfall is occurring, the effect of evaporation from the ground surface is to simply reduce the effective rainfall infiltration rate by an amount equal to the steady state evaporation rate (after conversion of the evaporation rate from a mass flow rate per unit slope area to an equivalent volumetric flow rate of liquid water per unit plan area). This means that, for rainfall events where there are no periods without rain, analyses can be performed without explicitly including evaporation, by simply using effective rainfall infiltration rates that are calculated by subtracting the steady state evaporation rate from the real rainfall infiltration rates.

4) Rainfall of constant effective intensity i will, if sustained for sufficient time, cause breakthrough at all values of horizontal coordinate x greater than the diversion length L_D corresponding to the effective rainfall intensity i. This breakthrough at $x \geq L_D$ will involve interface flow velocity q_i equal to the effective rainfall intensity i. If the initial state of the CBS, at the start of the current effective rainfall intensity i, is the same for all values of x, the time to breakthrough will be the same for all values of x where breakthrough occurs. This time to breakthrough is associated with the time to fill the F.L from the initial value of water stored WS to the value of water storage capacity WSC corresponding to the current effective rainfall intensity i.

5) If however, the current effective rainfall intensity i has been preceded by previous cycles of rainfall or other forms of antecedent rain, the initial state of the CBS at the start of the current rainfall will vary with x and hence the time to breakthrough will vary with x. The time to breakthrough will generally be lower for larger values of x (i.e. breakthrough occurs earlier further down the slope).

6) If breakthrough has already occurred at a particular value of x and the effective rainfall intensity increases, there will be a time-lag before the interface flow velocity q_i increases to the new (higher) value of effective rainfall intensity. This time-lag is associated with the time to fill the F.L from the value of water storage capacity WSC corresponding to the previous effective rainfall intensity to the (slightly higher) value of WSC corresponding to the new (higher) effective rainfall intensity. As a consequence, the duration of this time-lag is independent of x.

7) If breakthrough has already occurred at a particular value of x and the effective rainfall intensity decreases, the value of interface flow velocity q_i decreases immediately (with no time-lag) to the new (lower) effective rainfall intensity.

8) If breakthrough has already occurred at a particular value of x and the effective rainfall intensity decreases to a value that is insufficient to maintain breakthrough indefinitely at this value of x (i.e. if x is less than the increased value of diversion length L_D corresponding to the new (lower) effective rainfall intensity), breakthrough ceases (q_i falls to zero) some time later than the decrease of effective rainfall intensity (i.e. after a further time-lag).

9) If rainfall ceases, restoration of water storage capacity within the F.L occurs gradually. This is a consequence of two processes: evaporation from the ground surface and water transfer down the slope in the lower part of F.L.

10) After rainfall ceases, evaporation initially continues at a similar (even slightly higher) rate than the steady state value of evaporation rate during

rainfall. After some time, the evaporation rate begins to decrease, as the material of the F.L becomes dryer at the ground surface. However, this decrease in evaporation rate only commences when the suction in the soil at the ground surface reaches several MPa (because only then does the relative humidity in the soil voids begin to fall noticeably below 1). The time for this to happen depends upon the soil type of the F.L and the atmospheric conditions. It will happen more quickly under hot (and dry) atmospheric conditions, and it will also happen more quickly if the F.L is made of fine sand rather than silty sand. This because drying of the surface of the F.L occurs more slowly if it is made of silty sand, because the water there is replenished by water flowing up from deeper in the F.L, whereas this is unable to happen if the F.L is made of fine sand.

11) After rainfall ceases, the initial contribution of water transfer down the slope to restoration of water storage capacity is greater if the F.L is made of fine sand than if the F.L is made of silty sand. However, this water transfer down the slope ceases relatively quickly after the rainfall finishes.

12) Overall, therefore, restoration of water storage capacity during extended dry periods between rainfall is more effective if the F.L is made of silty sand than if the F.L is made of fine sand. If the F.L is made of silty sand, even though the contribution of water transfer down the slope is small, restoration of water transfer capacity by evaporation from the ground surface continues at an undiminished rate for many days or weeks after the rainfall ceases. In contrast, if the F.L is made of fine sand, the contributions of both water transfer down the slope and evaporation from the ground surface begin to decrease significantly just hours after the rainfall ceases.

13) Hysteresis in the retention behaviour is relatively unimportant to the behaviour of a sloping CBS subjected to an extreme rainfall event. For an extreme rainfall event, it will be acceptable (and slightly conservative) to ignore retention hysteresis and assume that the soil state within the CBS is always on the main wetting SWRC.

14) If rainfall is unevenly distributed within individual days, but the performance of a sloping CBS is analysed by assuming that each daily total

of rainfall is evenly distributed within that day, this will lead to some errors in predicted total water flows across the interface of the CBS. In particular, values of total water flow across the interface per unit plan area will generally be underestimated at low values of x (towards the top of the slope) but overestimated at higher values of x (towards the bottom of slope).

Chapter 7 Development and numerical validation of a simplified method of analysis for extreme rainfall events

This chapter presents the development of a simplified method of analysis for capillary barrier systems when subjected to extreme rainfall events. The intention is that this simplified method could be used within a practical design methodology for sloping CBSs, suitable for use by practising geotechnical engineers in industry i.e. not involving complex multi-physics FE modelling. The simplified method of analysis was developed based on understanding arising from the numerical modelling presented in Chapters 5 and 6 and it has been validated against the results of appropriate numerical simulations.

Section 7.1 presents the proposed simplified method of analysis for sloping CBSs subjected to extreme rainfall patterns, based on understanding and knowledge gained from previous advanced thermo-hydraulic and hydraulic numerical simulations in Chapters 5 and 6. Sections 7.2 present numerical validation of the simplified method, by comparison against appropriate FE simulations. Section 7.3 is a brief summary of the main developments and conclusions from the chapter.

7.1 Development of simplified method

7.1.1 Overall approach of simplified method

The simplified method described here is intended for analysing extreme rainfall events, because this is likely to be key to the design of sloping CBSs for prevention of rainfall-induced slope instabilities. The method starts with a decision by the user on what constitutes an appropriate design extreme rainfall event for the slope location (with an appropriately long return period, allowing for predictions of any climate change effects, see Section 8.3). Typical design extreme rainfall events are illustrated by the continuous blue lines in Figure 7-1, showing the variation of effective rainfall intensity i with time t, where effective rainfall intensity is the adjusted rainfall intensity after subtracting the steady state evaporation rate during rainfall from the real rainfall intensity (see Section 6.4).

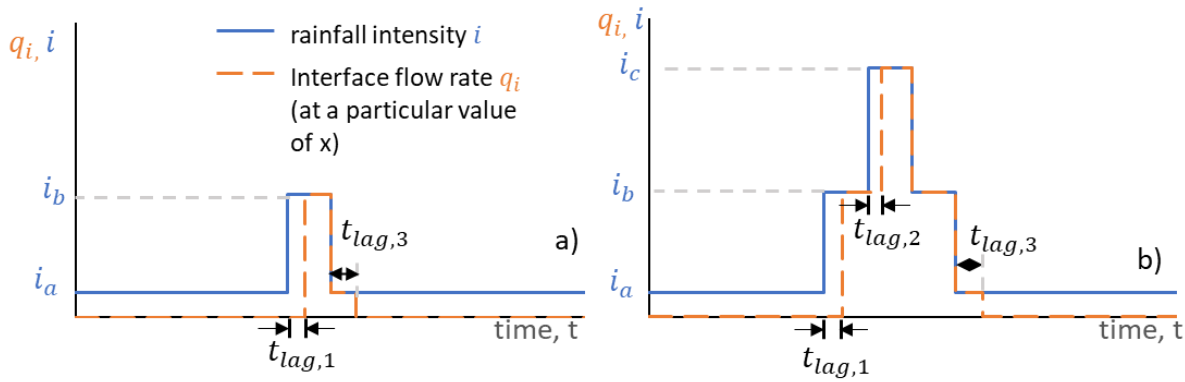

Figure 7-1 Schematic of rainfall intensities and interface flow rates for design extreme rainfall events

A typical design extreme rainfall event will consist of one or more days of extreme rainfall intensity following immediately after a sustained wet period of lower effective rainfall intensity i_a (the antecedent rain). Figure 7-1a shows an extreme rainfall event consisting of a single day of extreme effective intensity i_b, whereas Figure 7-1b shows an alternative extreme rainfall event of three days duration, of effective intensity i_b during the first and third days and even more extreme effective intensity i_c during the middle day.

The purpose of the simplified method of analysis is to determine, for the design rainfall pattern, the variation with time of interface flow velocity per unit plan area q_i (defined by Equation 5-32) at different values of x (the horizontal coordinate from the top of the slope). The designer can then decide whether, for this design extreme rainfall event, it is appropriate to design for no breakthrough, by ensuring that no breakthrough occurs for values of x up to the horizontal extent of the slope or by installing collector drains at horizontal separations down the slope that are less than the value of x corresponding to any occurrence of breakthrough. Alternatively, the designer may decide that, for this design extreme rainfall event, a limited amount of breakthrough is acceptable (i.e. a limited total volume water flow across the interface over a limited range of x at the bottom of the slope is acceptable), as described in Section 8.3. In the latter case, the simplified method would be used to determine the expected flow pattern across the interface i.e. variations of q_i with time t and horizontal coordinate x) for the design rainfall event.

The dashed orange lines in Figure 7-1 illustrate the qualitative forms of variation of interface flow velocity q_i with time (at a particular value of x) predicted by the simplified method, based on understanding resulting from the numerical modelling results presented in Chapters 5 and 6. In Figure 7-1, the initial (antecedent) effective rainfall intensity i_a is insufficient to cause breakthrough at the particular value of x illustrated in the figure even if this rainfall intensity is maintained indefinitely (i.e. the value of x is less than the diversion length L_{Da} corresponding to the effective rainfall intensity i_a). In contrast, the extreme effective rainfall intensities i_b, and i_c are both sufficient, if maintained indefinitely, to cause breakthrough at the particular value of x (i.e. x is greater than the diversion lengths L_{Db} and L_{Dc}).

Inspection of Figure 7-1 shows that the predicted variation of q_i (at the particular value of x) involves a time-lag $t_{lag,1}$ after the increase of effective rainfall intensity from i_a to i_b before q_i increases from zero to the new effective rainfall intensity i_b, as observed in Sections 5.6 and 6.4. If the rainfall subsequently increases further to effective intensity i_c (see Figure 7-1b), a further time-lag $t_{lag,2}$ is observed between the increase of rainfall intensity and the increase of q_i from i_b to the new effective rainfall intensity i_c. If the effective rainfall intensity decreases from i_c to i_b (Figure 7-1b) or from i_b to i_a (Figures 7-1a and Figure 7-1b), the interface flow velocity q_i reduces immediately (with no time-lag) to the new lower effective rainfall intensity, consistent with observations reported in Sections 6.2, 6.3, and 6.4. Finally, if the effective rainfall intensity has reduced to a value i_a which is insufficient to maintain breakthrough indefinitely at the particular value of x (e.g. the reduction of effective rainfall intensity from i_b to i_a in Figures 7-1a and 7-1b), the value of q_i will reduce from i_a to zero after a time-lag $t_{lag,3}$. The challenge for the simplified method is to provide predictions of the durations of the time-lags $t_{lag,1}$, $t_{lag,2}$ and $t_{lag,3}$.

The time-lags $t_{lag,1}$ and $t_{lag,2}$ in Figure 7-1 are associated with the times required to increase the water stored in the finer layer WS at various values of x from the value of WS associated with the previous (lower) rainfall intensity to the higher value of WS associated with the new (higher) rainfall intensity. This is illustrated in Figure 7-2a, which shows the predicted variations of final steady state water stored WS plotted against x for the three different effective rainfall intensities

i_a, i_b and i_c, if each of these were sustained indefinitely, as presented previously in Figure 5-28. In Figure 7-2a, L_{Da}, L_{Db} and L_{Dc} are the final steady state diversion lengths corresponding to effective rainfall intensities i_a, i_b and i_c respectively, and WSC_a, WSC_b, and WSC_c are the water storage capacities corresponding to these three effective rainfall intensities. Note that, as reported in Section 5.5.3, WSC increases with increasing rainfall intensity. The three data points marked in Figure 7-2a illustrate how the water stored WS at a particular value of x needs to increase if the effective rainfall intensity increases from i_a to i_b or from i_b to i_c, because WS has to reach a new steady state value in equilibrium with the new effective rainfall intensity. It is important to note that the time-lag $t_{lag,1}$ at a particular value of x is not solely associated with the time required to increase WS at that particular value of x. $t_{lag,1}$ can also be affected by the times necessary to increase WS at values of x further up the slope, as described in Section 7.1.2.

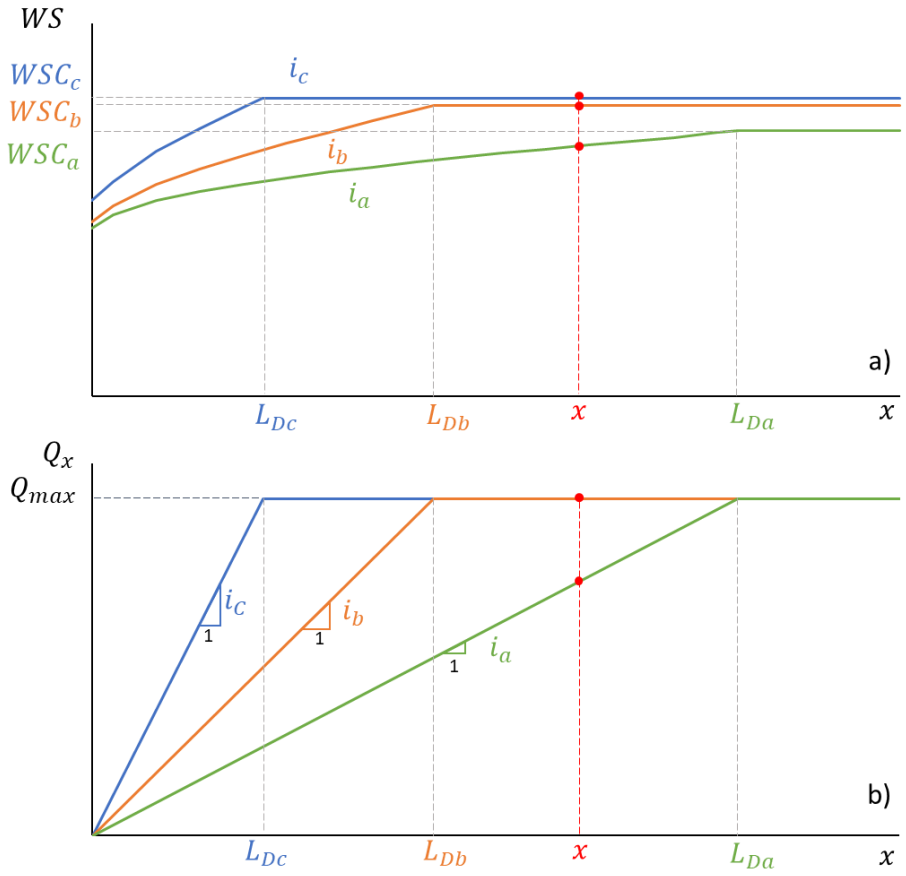

Figure 7-2 Design charts of final steady state variations of a) water storage WS and b) water transfer Q_x plotted against x for different effective rainfall intensities

The time-lags $t_{lag,3}$ in Figure 7-1 are associated with the times required to reduce the water stored WS at various values of x from high steady state values of WS associated with a (higher) previous rainfall intensity to lower steady state values

of WS associated with a (lower) current rainfall intensity (see Figure 7-2a). The duration of time-lag $t_{lag,3}$ at a particular value of x is not, however, associated with the time required to reduce WS at that particular value of x. $t_{lag,3}$ is instead controlled by the times necessary to reduce WS at values of x further up the slope, as described in Section 7.1.3.

Figure 7-2b shows water transfer Q_x at final steady state plotted against x for the same three effective rainfall intensities as in Figure 7-2a. The form of Figure 7-2b was shown previously in Figure 5-27, with Q_{max} being the water transfer capacity. Note that, as stated in Section 5.5.5, the water transfer capacity Q_{max} is independent of rainfall intensity i (at least for a realistic range of rainfall intensities). Note also that, at final steady state under a given effective rainfall intensity i, for values of x less than the diversion length L_D, the gradient of the plot of Q_x against x is given by:

$$\frac{\partial Q_x}{\partial x} = i \qquad \textbf{7-1}$$

The corresponding diversion length L_D is then given by:

$$L_D = \frac{Q_{max}}{i} \qquad \textbf{7-2}$$

For a design extreme rainfall event involving effective rainfall intensities i_a, i_b, and i_c (each sustained over a finite length of time), the plots of final steady WS against x and Q_x against x if each of these effective rainfall intensities was sustained indefinitely, shown in Figure 7-2, are a key starting point of the proposed simplified method for analysing extreme rainfall events. These plots in Figure 7-2 should be derived according to the methodology set out in Chapter 5, which involves the new simplified steady state suction profiles at different values of x set out in Sections 5.2 and 5.5.5. In deriving the plots shown in Figure 7-2, the SWRC used for the finer layer should represent the main wetting curve, as it is reasonable to assume that the material of the F.L is on the main wetting curve during an extreme rainfall event (see Section 6.4.4).

A key assumption in the proposed simplified method for analysing extreme rainfall events is that two requirements must be satisfied if the interface flow velocity q_i

at a particular value of x is to be equal to the current effective rainfall intensity i (i.e. for breakthrough to be fully established at the value of x):

(a) the water stored WS at that value of x must be at least equal to the water storage capacity WSC_i corresponding to the current effective rainfall intensity i (WS can exceed WSC_i if the rainfall intensity decreases, as explained in Section 7.1.3);

(b) the water transfer Q_x at that value of x must be equal to the water transfer capacity Q_{max}.

It is realistic to assume that both these conditions must be satisfied if breakthrough is to commence ($t_{lag,1}$) or if q_i is to increase to the current effective rainfall infiltration rate ($t_{lag,2}$). If WS is less than WSC_i, there is still unoccupied water storage capacity at the cross-section and no need for breakthrough to occur or q_i to increase (if breakthrough has already occurred under a previous rainfall intensity). If Q_x is less than Q_{max}, there is still unused water transfer capacity at the cross-section and therefore again no need for breakthrough or increase of q_i.

The proposed simplified method for analysing extreme rainfall events is based on a method of slices, where the finer layer of the CBS is divided into slices of horizontal width Δx, as shown in Figure 7-3. In Figure 7-3, i is the current effective rainfall infiltration rate (per unit plan area) at the top of the slice, q_i is the current interface flow rate (per unit plan area) at the bottom of the slice and WS is the current value of water stored in the slice (per unit plan area). Q_x is the water transfer (per unit length in the out-of-plane direction) into the slice across the upslope vertical boundary of the slice and $\partial Q_x/\partial x$ is the gradient of Q_x across the slice. Continuity of water mass (ignoring any changes of water density, any changes of water phase or any water vapour transfers, all of which are likely to be of minor importance during extreme rainfall events) means that, at any time:

$$\frac{\partial (WS)}{\partial t}\Delta x + \frac{\partial Q_x}{\partial x}\Delta x + q_i \Delta x = i\Delta x$$

$$\frac{\partial (WS)}{\partial t} + \frac{\partial Q_x}{\partial x} + q_i = i \qquad \text{7-3}$$

It is clear from Equation 7-3 that the sum of the rate of increase of WS with time $\partial(WS)/\partial t$, the gradient of Q_x with respect to x, $\partial Q_x/\partial x$ and the interface flow velocity q_i must always be equal to the effective rainfall infiltration rate i. It is important to note that it is only the gradient $\partial Q_x/\partial x$ that is diverting down the slope any of the effective rainfall infiltration rate i entering the slice directly above. In contrast, the water transfer Q_x represent water simply carried across the slice, originating from rainfall infiltration further up the slope. Hence, for the remainder of this chapter, $\partial Q_x/\partial x$ is termed water diversion whereas Q_x is termed water transfer.

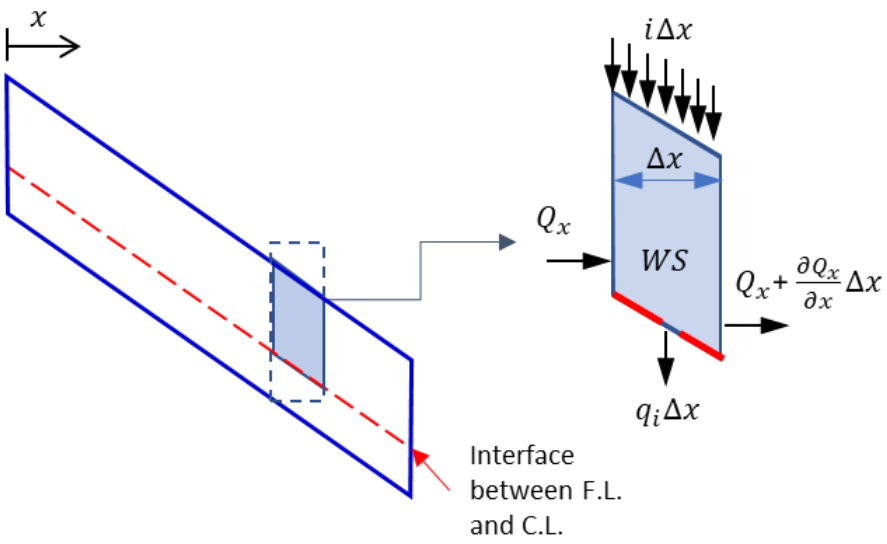

Figure 7-3 Schematic of method of slices

The proposed simplified method for analysing extreme rainfall events involves satisfying Equation 7-3 for each individual slice whilst following various rules. Slices are considered in sequence, starting at the top of the slope (x = 0), because changes of $\partial Q_x/\partial x$ in an individual slice will influence values of Q_x in all slices further down the slope and hence may affect the time at which the transfer capacity Q_{max} is reached in some of these slices further down the slope. The rules that are followed after an increase of rainfall intensity are described in Section 7.1.2, whereas the rules that are followed after a decrease of rainfall intensity are described in Section 7.1.3. In Sections 7.1.2 and 7.1.3 slices are assumed to be of infinitesimal width dx. Further issues of how the method is applied in practice to slices of finite width Δx are set out in Section 7.1.4.

7.1.2 Rules for application following an increase of rainfall intensity

The rules that are applied following an increase of effective rainfall intensity were established from a mix of logic and observations of behaviour from the FE simulations presented in Chapters 5 and 6. The rules are as follows:

- Initially, each slice fills (WS increasing), with no change of water diversion $\partial Q_x/\partial x$ and no change of interface flow velocity q_i from the values immediately before the increase of rainfall intensity.

- When filling of the slice is complete (WS reaches its final steady state value for the current effective rainfall intensity i, as shown in Figure 7-2a) or Q_x = Q_{max}, then water diversion $\partial Q_x/\partial x$ changes.

- If filling of the slice is complete and Q_x is less than Q_{max}, $\partial Q_x/\partial x$ changes to the current effective rainfall infiltration rate i (i.e. all the rainfall infiltrating the slice is diverted down the slope).

- If Q_x = Q_{max}, $\partial Q_x/\partial x$ goes to zero, irrespective of whether filling of the slice is complete or still ongoing. $\partial Q_x/\partial x$ must go to zero if Q_x = Q_{max}, to prevent Q_x exceeding the water transfer capacity Q_{max} at the downslope boundary of the slice.

- For breakthrough to commence ($t_{lag,1}$) or q_i to increase ($t_{lag,2}$), the two conditions set out previously in Section 7.1.1 must be satisfied: WS = WSC_i and Q_x = Q_{max}. If both these conditions are satisfied, q_i changes to the current effective rainfall infiltration rate i.

Of the two conditions that must be satisfied for breakthrough or increase of q_i, WS=WSC_i depends only on what is happening in the individual slice, whereas Q_x = Q_{max} depends on filling of slices further up the slope (because when one of these slices further up the slope completes filling, $\partial Q_x/\partial x$ across that slices changes, hence affecting the values of Q_x in slices further down the slope).

The rules for application following an increasing of rainfall intensity set out above are sufficient if the previous rainfall intensity was sustained for sufficiently long duration to reach final steady state for that effective rainfall intensity in all slices. This applied to all extreme rainfall events analysed in this chapter. Further rules would be required if the previous rainfall intensity was applied for a duration that was insufficient to reach steady state. Further work is required on developing the rules to cover such situations.

Figures 7-4, 7-5 and 7-6 show the application of the rules set out above to a case where the effective rainfall intensity increases from a previous value i_a to a higher current value i_b, and the previous effective rainfall intensity i_a had been applied for sufficiently long duration to reach final steady state in all slices.

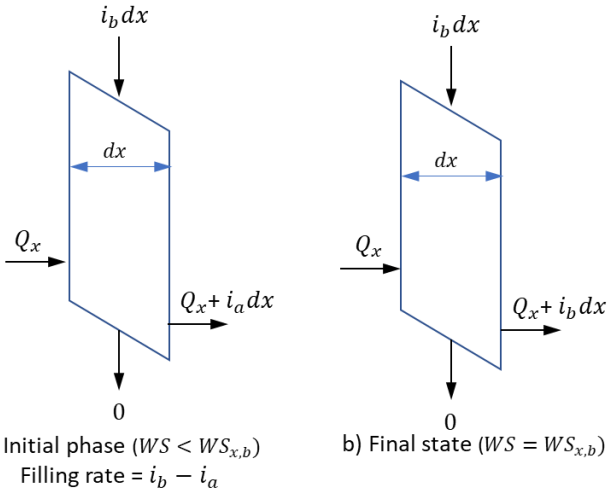

Figure 7-4 Schematic filling process within slices at $x < L_{Db}$ following increase of effective rainfall intensity from i_a to i_b

Figure 7-4 shows the situation for a slice at $x < L_{Db}$, i.e. a slice which will not experience breakthrough under effective rainfall intensity i_a or effective rainfall intensity i_b, even if this effective rainfall intensity is applied indefinitely. Figure 7-4a shows the initial filling phase of the slice, with $\partial Q_x/\partial x$ and q_i unchanged from their previous values ($\partial Q_x/\partial x = i_a$ and $q_i = 0$) and Equation 7-3 then giving the filling rate $\partial(WS)/\partial t$ of the slice as $i_b - i_a$. Hence, the filling time for this slice is given by:

$$Filling\ time = \frac{WS_{x,b} - WS_{x,a}}{i_b - i_a} \quad \text{7-4}$$

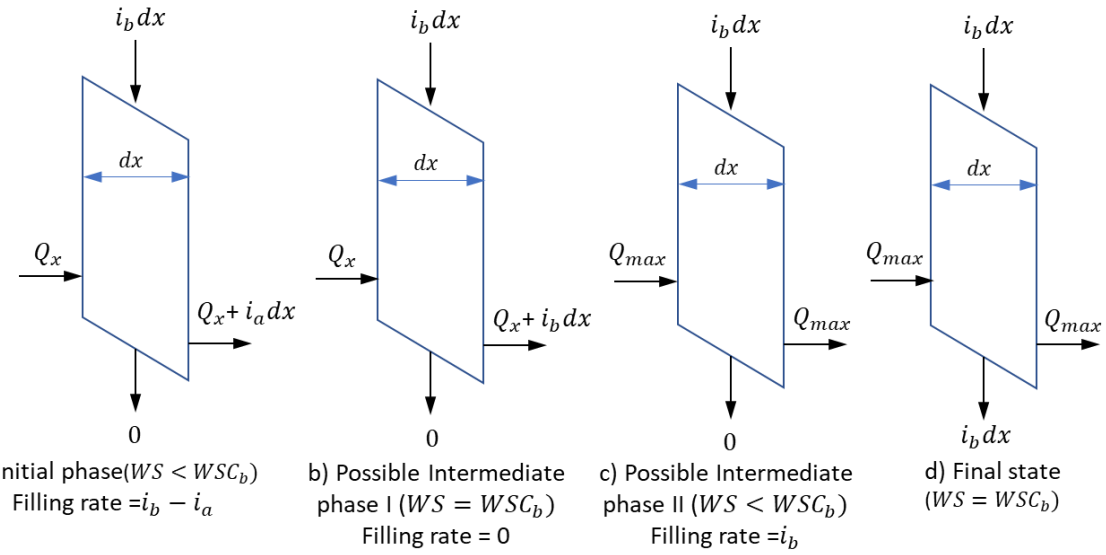

Figure 7-5 Schematic filling process within slices at $L_{Db} < x < L_{Da}$ following increase of effective rainfall intensity from i_a to i_b

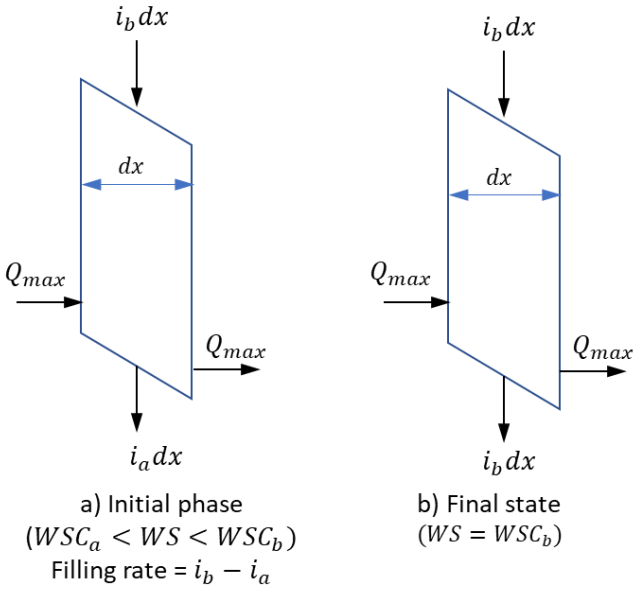

Figure 7-6 Schematic filling process within slices at $x > L_{Da}$ following increase of effective rainfall intensity from i_a to i_b

where $WS_{x,a}$ and $WS_{x,b}$ are the final steady state values of WS at the particular value of x for the effective rainfall intensities i_a and i_b respectively (see Figure 7-2a). Because $x < L_{Db} < L_{Da}$, $WS_{x,a}$ is less than the corresponding water storage capacity WSC_a and $WS_{x,b}$ is less than the corresponding water storage capacity WSC_b (see Figure 7-2a). Figure 7-4b shows the final steady state for the slice, which commences after the filling time given by Equation 7-4. In this final steady state, $WS = WS_{x,b}$, $\partial(WS)/\partial t = 0$, $q_i = 0$ and Equation 7-3 then gives $\partial Q_x/\partial x = i_b$ (i.e. the water diversion $\partial Q_x/\partial x$ has increased to the current effective rainfall infiltration rate i_b).

Figure 7-5 shows the situation for a slice at $L_{Db} \leq x < L_{Da}$ i.e. a slice which did not experience breakthrough under the previous effective rainfall intensity i_a but which will experience breakthrough under the current effective rainfall intensity i_b, if this current effective rainfall intensity continues indefinitely. Figure 7-5a shows an initial phase, with $\partial Q_x/\partial x$ and q_i unchanged from their previous values ($\partial Q_x/\partial x = i_a$ and $q_i = 0$) and the filling rate $\partial(WS)/\partial t = i_b - i_a$, from Equation 7-3.

There will then be an intermediate phase (Figure 7-5b or Figure 7-5c) before reaching a final steady state (Figure 7-5d). Two different possibilities exist for the intermediate phase. If the water stored WS reaches the water storage capacity WSC_b, corresponding to the current effective rainfall intensity i_b, before the water transfer Q_x reaches the water transfer capacity Q_{max}, intermediate phase I occurs (see Figure 7-5b). In intermediate phase I, $WS = WSC_b$, $q_i = 0$ (because the second condition required for breakthrough has not yet been satisfied, $Q_x \neq Q_{max}$) and hence $\partial Q_x/\partial x = i_b$ from Equation 7-3. If, however, as a consequence of changes of $\partial Q_x/\partial x$ across slices further up the slope, the water transfer Q_x reaches the water transfer capacity Q_{max} before WS reaches WSC_b, intermediate phase II occurs (see Figure 7-5c), instead of intermediate phase I. In intermediate phase II, $Q_x = Q_{max}$, $\partial Q_x/\partial x = 0$, $q_i = 0$ (because the first condition required for breakthrough has not yet been satisfied, $WS \neq WSC_b$) and hence according to Equation 7-3, the filling rate $\partial(WS)/\partial t$ increases to i_b (from $i_b - i_a$).

Figure 7-5d shows the final steady state, with breakthrough having occurred ($WS = WSC_b, Q_x = Q_{max}, \partial(WS)/\partial t = 0,\ q_i = i_b$). The time required to reach this final state corresponds to $t_{lag,1}$ (see Figure 7-1). The value of $t_{lag,1}$ cannot be calculated from consideration of the individual slice alone, as it also depends upon what happens in slices further up the slope (e.g. filling times of slices at $x < L_{Db}$ given by Equation 7-4). If intermediate phase I occurs (WS reaches WSC_b before Q_x reaches Q_{max}):

$$t_{lag,1} > \frac{WSC_b - WS_{xa}}{i_b - i_a} \tag{7-5}$$

Equation 7-5 applies because, if intermediate phase I occurs, $(WSC_b - WS_{xa})/(i_b - i_a)$ is the time required for the initial phase shown in Figure 7-5a and additional time is then required for intermediate phase I. In contrast, if intermediate phase II occurs (Q_x reaches Q_{max} before WS reaches WSC_b):

$$t_{lag,1} < \frac{WSC_b - WS_{xa}}{i_b - i_a} \quad \text{7-6}$$

Equation 7-6 applies because, if intermediate phase II occurs, the early part of filling the slice (the initial phase shown in Figure 7-5a) occurs at a filling rate $i_b - i_a$, but the later part of filling the slice (intermediate phase II) occurs at a higher filling rate i_b.

Figure 7-6 shows the situation for a slice at $x \geq L_{Da} > L_{Db}$, i.e. a slice which was already experiencing breakthrough under the previous effective rainfall intensity i_a and which will ultimately experience an increase of interface flow velocity (q_i increasing from i_a to i_b) if the higher current effective rainfall intensity i_b is continued indefinitely. Figure 7-6a shows the initial filling phase, with $\partial Q_x/\partial x$ and q_i unchanged from their previous values ($\partial Q_x/\partial x = 0,\ Q_x = Q_{max},\ q_i = i_a$) and hence the filling rate $\partial(WS)/\partial t = i_b - i_a$ from Equation 7-3. Figure 7-6b shows the final steady state, with $WS = WSC_b,\ Q_x = Q_{max},\ \partial(WS)/\partial t = 0,\ \partial Q_x/\partial x = 0$ and hence $q_i = i_b$ from Equation 7-3 i.e. the interface flow velocity has increased to the current effective rainfall intensity i_b. The time to reach this final state corresponds to $t_{lag,2}$ (see Figure 7-1). The value of $t_{lag,2}$ is given by:

$$t_{lag,2} = \frac{WSC_b - WSC_a}{i_b - i_a} \quad \text{7-7}$$

7.1.3 Rules for application following a decrease of rainfall intensity

The rules that are applied following a decrease of effective rainfall intensity were established from a mix of logic and observations of behaviour from the FE simulations presented in Chapter 6. The rules are:

- Immediately following the decrease in rainfall intensity, there is no change in water diversion $\partial Q_x/\partial x$ from the previous value, but if the interface flow velocity q_i was previously equal to the previous effective rainfall intensity (i.e. breakthrough had occurred under the previous rainfall intensity), q_i immediately reduces to the lower current effective rainfall intensity (as seen, for example, in Sections 6.2 , 6.3, and 6.4). If q_i was previously zero, it remains at zero.

- When emptying of the slice is complete (WS reaches its final steady state value for the current effective rainfall intensity i) or Q_x falls below Q_{max} (if it had previously been at Q_{max}), the water diversion $\partial Q_x/\partial x$ changes.

- If emptying of the slice is complete and Q_x is less than Q_{max}, $\partial Q_x/\partial x$ changes to the current effective rainfall infiltration rate i.

- If Q_x falls below Q_{max}, having previously been at Q_{max}, and emptying of the slice is not yet complete (or has not yet started), the diversion $\partial Q_x/\partial x$ changes to the previous effective rainfall intensity.

- Breakthrough ceases and interface flow velocity q_i goes to zero ($t_{lag,3}$) if $Q_x < Q_{max}$ or $WS < WSC_i$ ($Q_x = Q_{max}$ and $WS \geq WSC_i$ must both be satisfied in order to sustain any breakthrough ($q_i > 0$)).

The rules for application following a decrease of rainfall intensity set out above are sufficient if the previous effective rainfall intensity was sustained for a sufficiently long duration to reach final steady state in all slices. This applied to all extreme rainfall events analysed in this chapter. Possible future extension of the rules to also cover situations where the previous effective rainfall intensity was applied for a duration insufficient to reach final steady state in all slices is discussed further in Section 9.2.

Figures 7-7, 7-8 and 7-9 show the application of the rules set out above to a case where the effective rainfall intensity decreases from a previous value i_b to a lower current value i_a.

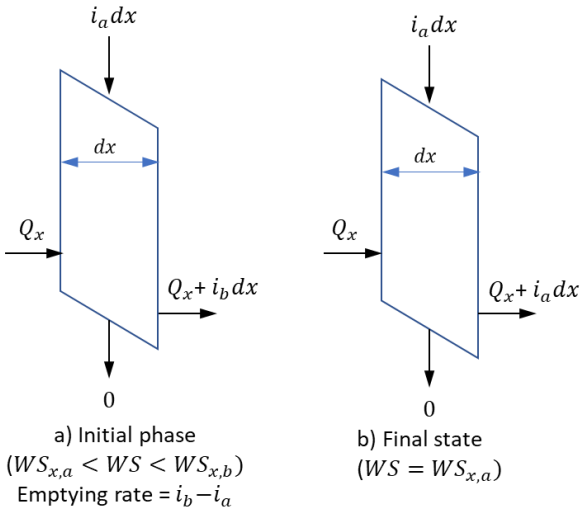

Figure 7-7 Schematic emptying process within slices at $x < L_{Db}$ following decrease of effective rainfall intensity from i_b to i_a

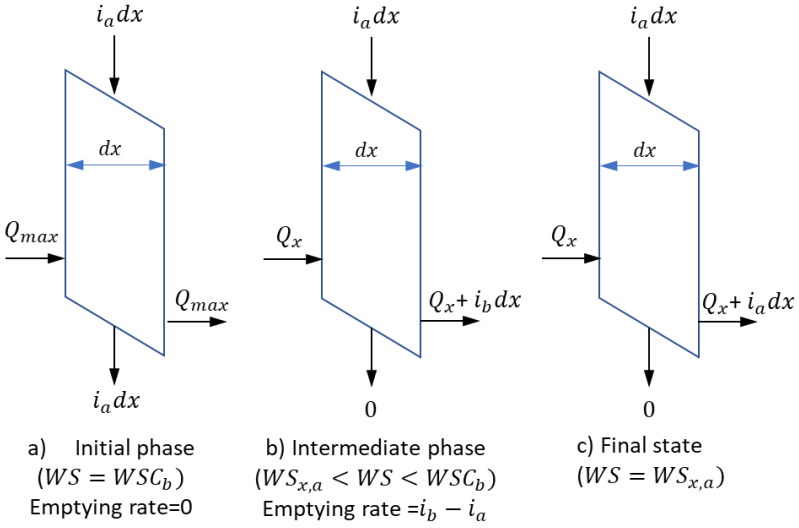

Figure 7-8 Schematic emptying process within slices at $L_{Db} < x < L_{Da}$ following decrease of effective rainfall intensity from i_b to i_a

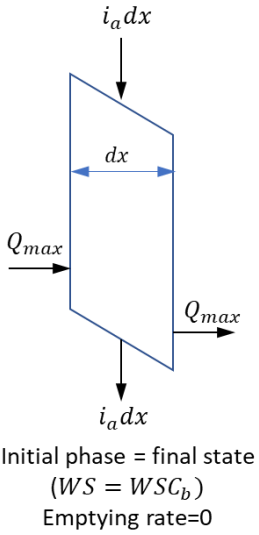

Figure 7-9 Schematic emptying process within slices at $x > L_{Da}$ following decrease of effective rainfall intensity from i_b to i_a

Figure 7-7 shows the situation for a slice at $x < L_{Db}$ i.e. a slice which had not experienced breakthrough under the higher previous effective rainfall intensity i_b. Figure 7-7a shows an initial emptying phase, with $\partial Q_x/\partial x$ and q_i unchanged from their previous values ($\partial Q_x/\partial x = i_b$ and $q_i = 0$) and Equation 7-3 giving the emptying rate $\partial(WS)/\partial t$ as $i_b - i_a$. Hence, the emptying time of the slice is given by:

$$Emptying\ time = \frac{WS_{x,b} - WS_{x,a}}{i_b - i_a} \quad \textbf{7-8}$$

Figure 7-7b shows the final steady state for the slice, which is reached after the emptying time from Equation 7-8. In this final steady state, $WS = WS_{x,a}$, $\partial(WS)/\partial t = 0$, $q_i = 0$ and $\partial Q_x/\partial x = i_a$.

Figure 7-8 shows the situation for a slice at $L_{Db} \leq x < L_{Da}$ i.e. a slice which had experienced breakthrough under the previous effective rainfall intensity i_b but which will not sustain breakthrough indefinitely under the current (lower) effective rainfall intensity i_a. Figure 7-8a shows an initial phase, with $\partial Q_x/\partial x$ unchanged from its previous value ($\partial Q_x/\partial x = 0, Q_x = Q_{max}$) and q_i reduced from its previous value $q_i = i_b$ to its current value $q_i = i_a$ (consistent with an immediate drop in interface flow rate as the effective rainfall intensity decreases). During this initial phase, no emptying of the slice occurs ($\partial Q_x/\partial x = 0$, $q_i = i_a$ and hence $\partial(WS)/\partial t = 0$ from Equation 7-3), with WS remaining constant at its previous value $WS = WSC_b$.

The initial phase shown in Figure 7-8a continues until Q_x reduces below Q_{max}, as a consequence of $\partial Q_x/\partial x$ reducing in some slices further up the slope, as the emptying phase of these slices further up the slope is completed. The duration of the initial phase shown in Figure 7-8a corresponds to the time-lag $t_{lag,3}$ shown in Figure 7-1. Hence the time-lag duration $t_{lag,3}$ is entirely associated with emptying of slices further up the slope, rather than emptying of the individual slice.

Figure 7-8b shows an intermediate emptying phase, with Q_x now less than Q_{max}, $\partial Q_x/\partial x = i_b$ (the previous rainfall rate), $q_i = 0$ (i.e. breakthrough has ceased, because the second condition required for breakthrough is no longer satisfied,

$Q_x \neq Q_{max}$) and hence the emptying rate is given by $-\partial(WS)/\partial t = (i_b - i_a)$. The duration of this intermediate emptying phase is given by:

$$Emptying\ time = \frac{WSC_b - WS_{x,a}}{i_b - i_a} \quad \text{7-9}$$

The emptying times given in Equations 7-8 and 7-9 (for slices at $x < L_{Db}$ and for slices at $L_{Db} \leq x < L_{Da}$ respectively) are relevant for the determination of $t_{lag,3}$ for slices further down the slope.

Figure 7-8c shows the final state, for a slice at $L_{Db} \leq x < L_{Da}$, with $WS = WS_{x,a}$, $\partial(WS)/\partial t = 0$, $\partial Q_x/\partial x = i_a$ and $q_i = 0$.

Figure 7-9 shows the situation for a slice at $x \geq L_{Da}$ i.e. a slice which experiences breakthrough under both previous effective rainfall intensity i_b and current (lower) effective rainfall intensity i_a. The interface flow velocity q_i reduces from i_b to i_a immediately, as the rainfall intensity reduces, and the slice achieves its final state immediately, with WS unchanged ($WS = WSC_b$, $\partial(WS)/\partial t = 0$, $Q_x = Q_{max}$, $\partial Q_x/\partial x = 0$ and $q_i = i_a$). Note that the simplified method predicts that those slices at $x \geq L_{Da}$ remain permanently at the water storage capacity WSC_b, corresponding to the previous (higher) rainfall intensity (where $WSC_b > WSC_a$). This is because the only ways to reduce WS to WSC_a would be by having $\partial Q_x/\partial x > 0$ (which is not possible, because $Q_x = Q_{max}$) or by having q_i greater than the current rainfall intensity i_a (which does not fit with the observation in Section 6.4 that, when effective rainfall intensity is reduced, q_i decreases immediately to the new effective rainfall intensity. The apparent anomaly of WS remaining permanently above WSC_a for slices at $x \geq L_{Da}$ when effective rainfall intensity is reduced to i_a can be explained if the retention behaviour of the F.L material is hysteretic i.e. WSC_a and WSC_b (shown in Figure 7-2a) have been calculated assuming that the soil state is still on the main wetting curve, but this is unlikely to be true if the rainfall intensity is decreasing. This issue is discussed further in Section 7.2.

7.1.4 Implementation of method of slices

This sub-section describes how the simplified method is applied in practice, to slices of finite width Δx. To illustrate the calculation procedure, Table 7-1 shows part of a large Excel worksheet used for application of the simplified method to a sloping CBS subjected to an extreme rainfall event. The extreme rainfall event was of the form illustrated in Figure 7-1b, with i_a = 2x10^{-7} m/s (applied from t = 0 to t = 10 days and from t = 13 days onwards), i_b = 10^{-6} m/s (applied from t = 10 days to t = 11 days and from t = 12 days to t = 13 days) and i_c = 2x10^{-6} m/s (applied from t = 11 days to t = 12 days). The details of the slope and CBS were: β = 35°, FSGV, t_f = 40 cm. The CBS was analysed as a large number of slices, each of width Δx = 2.11 m. This slice width was selected because it resulted in exactly six slices to the diversion length L_{Db} = 12.66 m, corresponding to the second effective rainfall intensity i_b = 10^{-6} m/s. The influence of the slice width has not yet been examined properly, to investigate how small the slice width needs to be in order to get results of acceptable accuracy. This should be investigated further in the future.

Table 7-1 Part of Excel spreadsheet for implementation of method of slices

t = 10-11 days after rise in rainfall intensity				i_a[m/s]=	i_b[m/s]=	
Slice width[m] 2.11				2.00E-07	1.00E-06	
Slice no. 8			L_D[m]	63.30	12.66	
$WS_{x,a}$ at steady state[m] 0.0646			WSC[m]	0.0896	0.0937	
WSC_b at steady state[m] 0.0937			Q_{max}[m^2/s]	1.266E-05	1.266E-05	
time	x=14.77m	WS	dQx/dx	q_i	dWS/dt	x=16.88m
[x10^3 s]	Q_x [x10^{-6}m^2/s]	[m]	[x10^{-6}m/s]	[x10^{-6}m/s]	[x10^{-6}m/s]	Q_x [x10^{-6}m^2/s]
0	2.95	0.0646	0.20	0.00	0.80	3.38
17.42	4.64	0.0785	0.20	0.00	0.80	5.06
22.36	6.33	0.0824	0.20	0.00	0.80	6.75
26.32	8.02	0.0856	0.20	0.00	0.80	8.44
30.01	9.71	0.0886	0.20	0.00	0.80	10.13
33.63	11.39	0.0915	0.20	0.00	0.80	11.82
36.39	11.39	0.0937	0.60	0.40	0.00	12.66
37.32	12.66	0.0937	0.00	1.00	0.00	12.66

Table 7-1 shows the part of the spreadsheet applying to slice 8 from t = 10 days to t = 11 days, when the effective rainfall intensity was i_b = 10^{-6} m/s, having increased from i_a = 2x10^{-7} m/s at t = 10 days. Slice 8 extended from x = 14.77 m to x = 16.88 m, i.e. $x \geq L_{Db}$ (where L_{Db} = 12.66 m), meaning that breakthrough

was expected in this slice under the effective rainfall intensity i_b = 10^{-6} m/s. The calculations within the part of the Excel spreadsheet shown in Table 7-1 were only performed once the parts of the spreadsheet referring to slices 1-7 (i.e. the slices further up the slope) had been completed.

The first column in Table 7-1 shows the time since the increase of effective rainfall intensity from i_a = 2x10^{-7} m/s to i_b = 10^{-6} m/s. At zero time, the value of WS for slice 8 (see column 3 of Table 7-1) was at the final steady state value $WS_{x,a}$ = 0.0646 m corresponding to the previous effective rainfall intensity i_a = 2x10^{-7} m/s and a value of x corresponding to the mid-point of the slice (x = 15.825 m). Most of the subsequent times listed in the first column of Table 7-1 correspond to times at which the value of water transfer Q_x at the upslope boundary of the slice (x = 14.77 m), given in the second column of the table, experienced a step increase, because one of the slices further up the slope (slices 1-7) completed filling and the water diversion $\partial Q_x/\partial x$ across the slice further up the slope increased from i_a to i_b. The times of 17.42x10^3 s (4.84 hours), 22.36 x10^3 s (6.21 hours), 26.32 x10^3 s (7.31 hours), 30.01 x10^3 s (8.34 hours) and 33.63x10^3 s (9.34 hours) corresponded to completion of filling of slices 1,2,3,4 and 5 respectively. The next time of 36.39x10^3 s (10.11 hours) shown in the first column of Table 7-1, corresponded to the completion of filling of slice 8 itself, to the water storage capacity WSC_b= 0.0937 m corresponding to the current effective rainfall intensity i_b = 10^{-6} m/s. This completion of filling of slice 8 occurred before completion of filling of slices 6 and 7. Up to this time of 36.39x10^3 s, slice 8 was in the initial filling phase shown in Figure 7-5a, with $\partial Q_x/\partial x = i_a$ = 0.2x10^{-6} m/s, q_i = 0 and $\partial(WS)/\partial t = i_b - i_a$ = 0.8x10^{-6} m/s, as shown in columns 4, 5 and 6 of Table 7-1.

As slice 8 completed filling at t = 36.39x10^3 s, the expectation might be that the water diversion $\partial Q_x/\partial x$ across the slice would increase from $\partial Q_x/\partial x = i_a$ = 0.2x10^{-6} m/s to $\partial Q_x/\partial x = i_b$ = 10^{-6} m/s (corresponding to intermediate phase I in Figure 7-5b). However, $\partial Q_x/\partial x = i_b$ = 10^{-6} m/s was not possible across the entire width of slice 8, because this would have produced a value of Q_x at the downslope boundary of the slice (x = 16.88 m) that exceeded the water transfer capacity Q_{max} = 12.66x10^{-6} m^2/s. Instead, therefore, the average value of $\partial Q_x/\partial x$ across the slice had to be limited to 0.6x10^{-6} m/s (see column 4 of Table 7-1), in order

to limit the value of Q_x at the downslope boundary of the slice to the water transfer capacity Q_{max} = 12.66x10^{-6} m^2/s (see column 7 of Table 7-1). Application of Equation 7-3 to the slice then results in an average value of interface flow velocity q_i across the slice of 0.4x10^{-6} m/s (see column 5 of Table 7-1). In practice, this meant that, going forward from a time 36.39x10^3 s, 60% of slice 8 was in intermediate phase I with $Q_x < Q_{max}$, $\partial Q_x/\partial x = i_b$ = 10^{-6} m/s, $\partial(WS)/\partial t$ = 0 and q_i = 0 (see Figure 7-5b) and the remaining 40% of the slice (the part further down the slope) was already in the final state, with $Q_x = Q_{max}$, $\partial Q_x/\partial x$ = 0, $\partial(WS)/\partial t$ = 0 and $q_i = i_b$ = 10^{-6} m/s (see Figure 7-5d). This illustrates the fact that, when the simplified method of slices is applied to slices of finite width Δx, there will sometimes be periods when part of a slice is in one phase while the remainder of the same slice is in another phase.

The final time of 36.39x10^3 s (10.37 hours) shown in Table 7-1, corresponded to completion of filling of slice 6, resulting in an increase of the value of Q_x at the upslope boundary of slice 8 (x = 14.77 m) to $Q_x = Q_{max}$ = 12.66x10^{-6} m^2/s (see column 2 of Table 7-1). This meant that $\partial Q_x/\partial x$ now had to be zero across the entire width of slice 8, meaning that, from a time of 37.32x10^3 s onwards, the entire slice 8 was in the final state shown in Figure 7-5d (with $Q_x = Q_{max}$, $\partial Q_x/\partial x$ = 0, $\partial(WS)/\partial t$ = 0 and $q_i = i_b$ = 10^{-6} m/s) i.e. breakthrough was now fully established over the full width of slice 8. Hence, $t_{lag,1}$ = 36.39x10^3 s for 40% of the slice (16.04 m $< x \leq$ 16.88 m) and $t_{lag,1}$ = 37.32x10^3 s for the remaining 60% of the slice (14.77 m $< x \leq$ 16.04 m).

7.2 Numerical validation of simplified method of analysis for extreme rainfall events

Numerical validation of the simplified method of analysis for extreme rainfall events was performed in this section by comparing simplified method results with FE numerical analysis results. All the numerical modelling involved hydraulic modelling (i.e. without evaporation), with the hysteretic hydraulic constitutive model (hysteretic modVG-ModM+LF), as described previously in Chapter 6. The use of hydraulic numerical modelling (without evaporation), rather than thermo-hydraulic numerical modelling (with evaporation), meant that the effective

rainfall intensities were equal to the real rainfall intensities. The details of the numerical models (geometry, FE mesh, materials properties, initial conditions, and boundary conditions) were presented previously in Section 6.1.

7.2.1 CBS with F.L made of fine sand

Figure 7-10a shows the extreme rainfall pattern E1 that was applied to a sloping CBS with the F.L made of fine sand. This involved a period of 10 days ($0< t < 10$ days) of antecedent rain of intensity i = 2x10^{-7} m/s, corresponding to an unusually sustained wet period (17.26 mm per day for 10 days). The 10 day period of antecedent rain was sufficient to ensure that the entire CBS had reached final steady state under the rainfall intensity i = 2x10^{-7} m/s, with no breakthrough in the slope, because the diversion length under this rainfall intensity (68.0 m) was considerably greater than the horizontal extent of the slope in the FE model (26.8m). This was followed by an extreme rainfall event of three days duration, with i = 10^{-6} m/s (86.4 mm per day) for first and third days and i = 2x10^{-6} m/s (172.8 mm per day) for the central day. Rainfall intensity returned to i = 2x10^{-7} m/s after 3 days of extreme rainfall. Details of the sloping CBS were as follows: β =35°, FSGV, t_f = 40 cm. The numerical modelling of this CBS subjected to this particular extreme rainfall pattern was presented previously in Section 6.4.1.

The simplified method of analysis for extreme rainfall events was used to predict the variation with time of interface flow velocity q_i at different values of x by the method of slices, following the logic provided earlier in Section 7.1. This involved use of the predicted plots of final steady state variation of water transfer Q_x against x and water stored WS against x , if the three rainfall intensities relevant to extreme rainfall pattern E1 were each sustained indefinitely. These plots, shown in Figure 7-11, were determined following the logic presented in Sections 5.1 and 5.5.5.

Figures 7-10b, 7-10c and 7-10d show the comparison of simplified method predictions and FE results, in terms of the variation with time of interface flow rate per unit plan area q_i at five selected values of x. The values of x from the simplified method and the FE simulations do not exactly coincide, because each of the former was taken at the centre of a slice whereas each of the latter was

taken at the corresponding closest node on the interface in the FE mesh. The Excel spreadsheet for the simplified method calculations for this particular case (β =35°, FSGV, t_f = 40 cm, rainfall pattern E1) is shown in full as Appendix D.

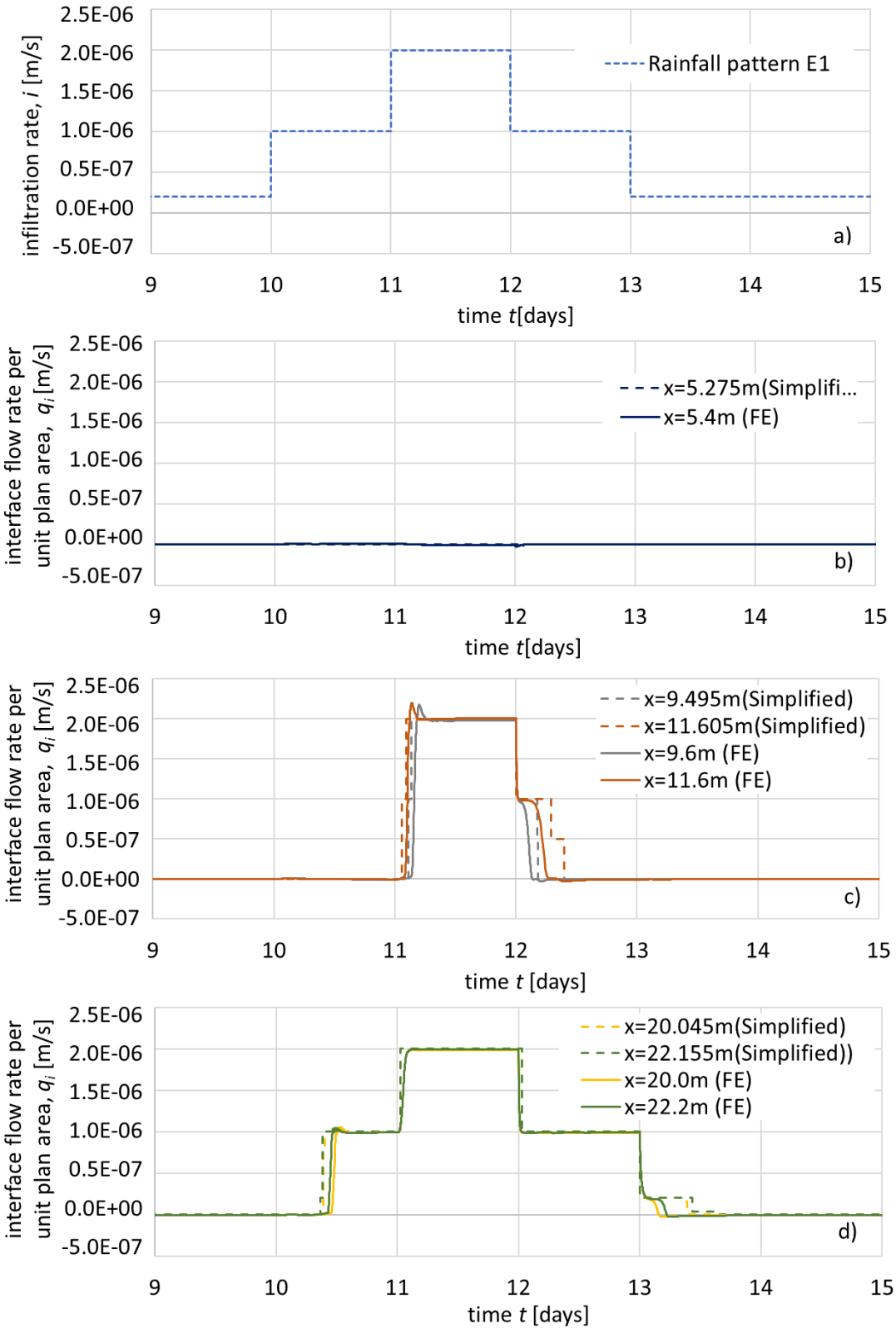

Figure 7-10 Sloping CBS with F.L. made of fine sand subjected to extreme rainfall pattern E1 comparison of FE results and simplified method predictions (β = 35°, FSGV, t_f = 40 cm)

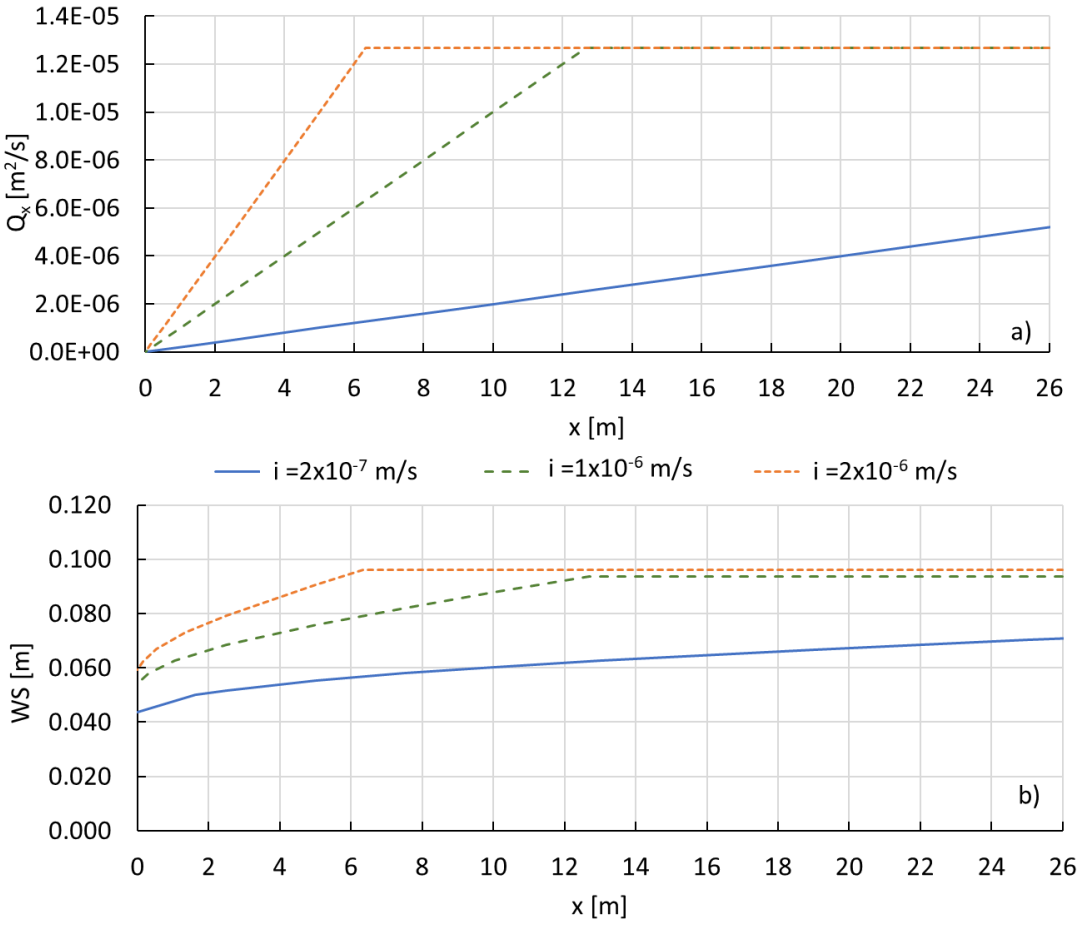

Figure 7-11 Final steady state plots of a) water transfer and b) water storage from simplified method for three rainfall intensities relevant to extreme rainfall pattern E1 (β = 35°, FSGV, t_f = 40 cm)

Figure 7-10b compares simplified method predictions with FE results for a relatively low value of x ($x \approx$ 5.3 m). The simplified method correctly predicts no occurrence of breakthrough at this value of x during the extreme rainfall event. This value of x is less than the final steady state diversion length predicted if the most extreme rainfall intensity (i_c = 2x10^{-6} m/s) had been sustained indefinitely (L_{Dc} = 6.33 m from simplified method).

Figure 7-10c shows simplified method predictions and corresponding FE results for intermediate values of x ($x \approx$ 9.5 m and $x \approx$ 11.6 m), corresponding to $L_{Dc} < x < L_{Db}$) i.e. where breakthrough was expected under the most extreme rainfall intensity (i_c = 2x10^{-6} m/s) but not under the intermediate rainfall intensity (i_b = 10^{-6} m/s). The comparison shows that the simplified method provides excellent predictions of the variation of q_i with time at both these values of x. Values of $t_{lag,1}$, after the rainfall intensity increased from i_b = 10^{-6} m/s to i_c = 2x10^{-6} m/s at t = 11 days, are slightly under-predicted by the simplified method at both values

of x, indicating that the simplified method is slightly conservative when applied to an increase of rainfall intensity

Figure 7-10d shows corresponding results for two higher values of x ($x \approx$ 20.0m and $x \approx$ 22.2m), corresponding to $x > L_{Db} > L_{Dc}$ i.e. where breakthrough is expected under both i_b = 10^{-6} m/s and i_c = 2x10^{-6} m/s. The simplified method provides excellent predictions of the duration of time-lags $t_{lag,1}$ (after the increase of rainfall intensity from i_a = 2x10^{-7} m/s to i_b = 10^{-6} m/s at t = 10 days) and $t_{lag,2}$ (after the increase of rainfall intensity from i_b = 10^{-6} m/s to i_c = 2x10^{-6} m/s at t = 11 days). Again, the simplified method seems slightly conservative when applied to an increase of rainfall intensity, as values of $t_{lag,1}$ and $t_{lag,2}$ are slightly under-predicted.

Figures 7-10c and 7-10d also provide evidence of the performance of the simplified method when applied to a decrease of rainfall intensity. Inspection of these figures show that the simplified method accurately predicts the immediate reduction of q_i to the new rainfall intensity as rainfall is reduced from i_c = 2x10^{-6} m/s to i_b = 10^{-6} m/s (at t = 12 days) or from i_b = 10^{-6} m/s to i_a = 2x10^{-7} m/s (at t = 13 days). The simplified method also correctly predicts the occurrence of a time-lag $t_{lag,3}$ before q_i drops to zero after a decrease in rainfall intensity to a new value of i that is insufficient to maintain breakthrough indefinitely at that value of x i.e. after reduction to i_b = 10^{-6} m/s at t = 12 days in Figure 7-10c and after the reduction to i_a = 2x10^{-7} m/s at t = 13 days in Figure 7-10d. The simplified method does, however, significantly over-predict the duration of these time-lags $t_{lag,3}$. This over-prediction of $t_{lag,3}$ is again conservative because it results in over-prediction of the total volume of water that flows across the interface (for the entire extreme rainfall event) at a particular value of x.

The significant over-prediction of $t_{lag,3}$ by the simplified method was attributed to ignoring the influence of retention hysteresis in the simplified method (whereas retention hysteresis was included in the FE simulations). The simplified method assumes that the soil state remains on the main wetting SWRC throughout. This is a reasonable assumption during the early period of an extreme rainfall event (when the rainfall intensity is increasing), but it is unrealistic once the rainfall

intensity begins to decrease. Attempts were made to modify the simplified method to account for the influence of retention hysteresis when the rainfall intensity was decreasing. Unfortunately, these attempted changes added considerably to the complexity of the method and produced results that were often not conservative (i.e. $t_{lag,3}$ was sometimes significantly underestimated). It was therefore decided to retain the simplified method in its original form (ignoring retention hysteresis) as this was judged to produce results of acceptable quality and which always erred on the conservative side.

Figure 7-12 compares the total amount of water flow (per unit plan area) across the interface, at a particular value of x, between simplified and FE methods. The total flow across the interface is obtained by integrating the interface flow velocity q_i over time. The simplified method predicts two step changes in the total flow across the interface per unit plan area, corresponding to x = L_{Dc} = 6.33 m and x = L_{Db} = 12.66 m. The FE results confirm two significant increases in total flow across the interface at approximately the same two values of x as predicted by the simplified method. Overall, the simplified method provides reasonable estimates of the total flow across interface at all values of x (when compared with the FE results) and generally always errs on the side of caution (overestimating the flow across the interface).

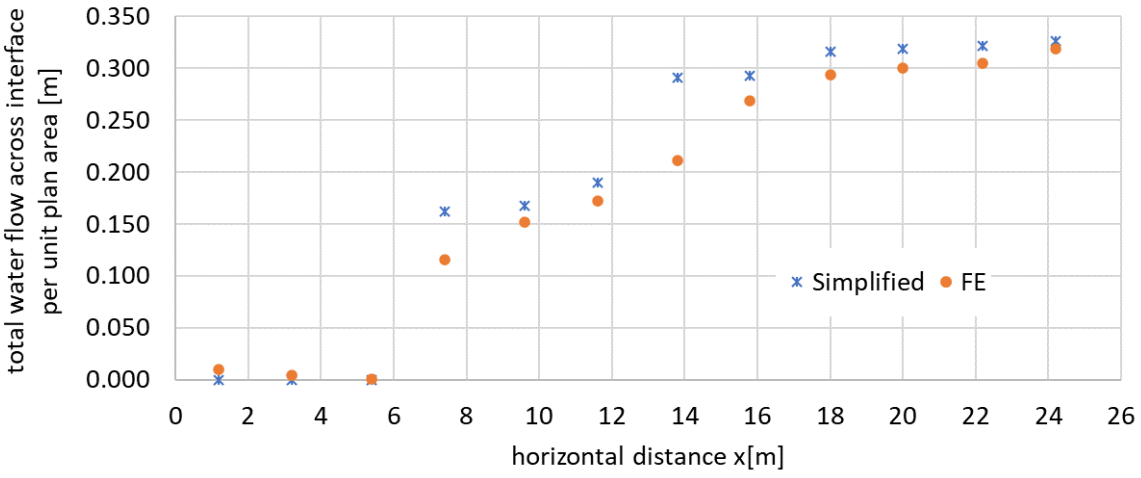

Figure 7-12 Variation of total water flow across interface per unit plan area: comparison of simplified method and FE results for a CBS with the F.L made of fine sand (β = 35°, FSGV, t_f = 40 cm, extreme rainfall pattern E1)

The total flow across the interface per unit plan area shown in Figure 7-12 represents the total water percolation (per unit plan area) into the C.L of the CBS during the extreme rainfall event and hence therefore the potential percolation into the underlying soil of the slope. For comparison, with no CBS this total percolation of water into the soil per unit plan area would be simply the integral of the rainfall intensity i with respect to time over the duration of the extreme rainfall event. For extreme rainfall pattern E1, this would equate to 0.536 m if the integral was performed from t = 0 to t = 14 days (i.e. including the 10 days of antecedent rain, the three-day extreme rainfall event and a further day of lower intensity rain at the end. Comparison with Figure 7-12 indicates that the CBS has been fully successful at preventing rainwater percolation into the C.L (and hence into the underlying soil) during the extreme rainfall event for x values from zero (the top of the slope) to about 6.3 m. It has reduced rainwater percolation during the extreme rainfall event by about 60%-75% for x values between about 6.3 m and 12.6 m and it has reduced percolation by at least 40% for x values up to about 24 m. This type of information would be extremely helpful in assessing the effectiveness of a given design of CBS in reducing rainwater percolation into the underlying soil during a specific design extreme rainfall event on a slope of a given horizontal extent (or with a given horizontal spacing between collector drains).

7.2.2 CBS with F.L made of silty sand

Section 6.4.2 described FE modelling of an extreme rainfall event applied to a sloping CBS with the F.L made of silty sand. Simplified method predictions for this case are now compared with the FE results. Details of the sloping CBS are: β =35°, SSGV, t_f = 40 cm and the rainfall pattern for the extreme rainfall event E2 is shown in Figure 7-13a. As described in Section 6.4.2, a sloping CBS with the F.L made of silty sand is suitable only for relatively dry climates, with occasional extreme rainfall events, because the low value of water transfer capacity Q_{max} makes this type of sloping CBS unsuitable for use in regions that experience sustained wet weather (if the antecedent rainfall is high, the high water storage capacity is of little benefit, because much of it is filled at the start of any extreme rainfall event). Hence, the extreme rainfall event E2 shown in Figure 7-13a has a relatively

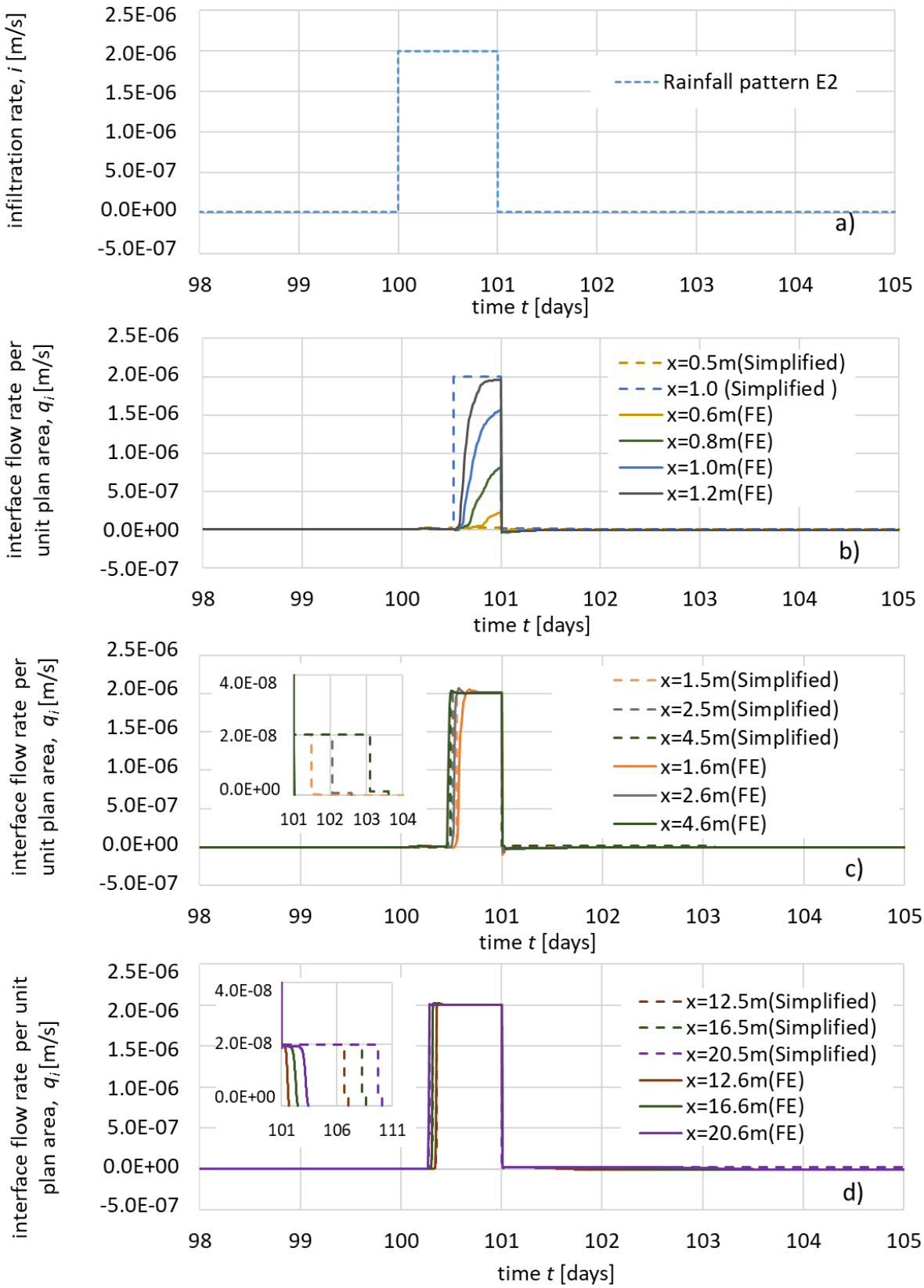

Figure 7-13 Sloping CBS with F.L. made of fine sand subjected to extreme rainfall pattern E2 comparison of FE results and simplified method prediction (β = 35°, FSGV, t_f = 40 cm)

low antecedent rainfall intensity i = 2x10^{-8} m/s, followed by a single day of extremely intense rainfall (i = 2x10^{-6} m/s). The antecedent rainfall (i = 2x10^{-8} m/s) was sustained for a duration of 100 days, to ensure that the CBS had reached steady state conditions under this rainfall intensity prior to the single day extreme rainfall event.

Figure 7-14 shows the predicted plots of final steady state variation of Q_x against x and WS against x for the CBS with the F.L made of silty sand and the two rainfall intensities relevant to extreme rainfall pattern E2 (i_a= 2x10^{-8} m/s and i_b= 2x10^{-6} m/s), for use in the simplified method of analysis for extreme rainfall events (method of slices). The predicted water transfer capacity Q_{max} was 1.97x10^{-6} m^2/s and the predicted diversion lengths corresponding to the two rainfall intensities were L_{Da} = 98.5 m and L_{Db} = 1.0 m. The predicted water storage capacities were WSC_a = 0.1638 m and WSC_b= 0.1638 m (i.e. WSC_b was so little greater than WSC_a that the difference was not apparent when the values were quoted to 4 significant figures).

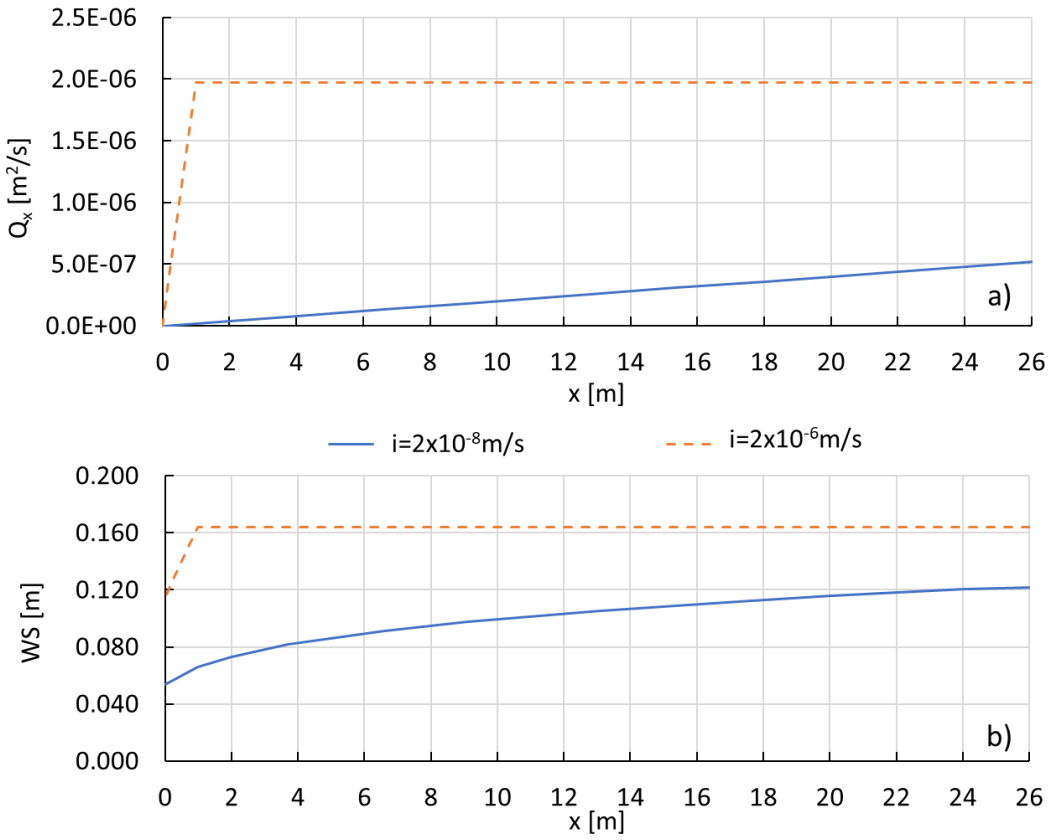

Figure 7-14 Final steady state plots of a) water transfer and b) water storage from simplified method for two rainfall intensities relevant to extreme rainfall pattern E2 (β = 35°, SSGV, t_f = 40 cm)

Figure 7-13b shows FE results and simplified method predictions in terms of the variation of interface flow velocity q_i with time, for low values of x ($x \leq$ 1.2 m). The simplified method predicts L_{Db} = 1.0 m and hence the method predicts breakthrough during the single day of extreme rainfall for $x \geq$ 1.0 m and no breakthrough for $x <$ 1.0 m. For x = 1.0 m, the simplified method predicts a time-lag $t_{lag,1}$ = 12.48 hours before the onset of breakthrough. In contrast, the FE results show that the change from no breakthrough at very low values of x to full breakthrough (q_i = i_b=2x10^{-6} m/s) at higher values of x is a slightly more diffuse phenomenon. For x = 0.6 m, x = 0.8 m, x = 1.0 m and x = 1.2 m, the FE results show partial breakthrough, with a time-lag before q_i increases from zero and then q_i final stabilizing at a value less than the rainfall intensity i_b=2x10^{-6} m/s. The reason that, for these values of x, q_i stabilises at an intermediate value (more than zero but less than i_b = 2x10^{-6} m/s) is clear from examination of Figure 5-18d, which shows the final steady state variation of q_i with x when continuous rainfall of constant intensity i = 10^{-6} m/s (half the intensity i_b = 2x10^{-6} m/s relevant to Figure 7-13b) was applied to the same sloping CBS. In Figure 5-18d, the simplified method predicts L_D = 2.0 m whereas the FE results show q_i increasing from zero from values of x slightly less than 2.0 m and final reaching full breakthrough ($q_i = i$) at a values of x slightly greater than 2.0 m (the corresponding values of x would be halved of the rainfall intensity was doubled, as was the case in Figure 7-13b). The results shown in Figure 7-13b mean that the simplified method under-predicts the total flow across the interface for x = 0.6 m and x = 0.8 m but over-predicts the total flow across the interface for x = 1.0 m and x = 1.2 m.

Figure 7-13c shows FE results and simplified method predictions for intermediate values of x ($x \approx$ 1.5 m, $x \approx$ 2.5 m and $x \approx$ 4.5 m) and Figure 7-13d shows corresponding results for higher values of x ($x \approx$ 12.5 m,$x \approx$ 16.5 m and $x \approx$ 20.5 m). The simplified method predictions are an excellent match to the FE results in all cases shown in Figures 7-13c and 7-13d. Values of $t_{lag,1}$ (the onset of breakthrough) are accurately predicted in all cases. Time-lags (before q_i reduces to zero, some time after the rainfall intensity reduces from i_b = 2x10^{-6} m/s to i_a = 2x10^{-8} m/s at t = 101 days) are difficult to see in the main figures of Figures 7-13c and 7-13d, because the value of q_i during $t_{lag,3}$ (q_i = i_a= 2x10^{-8} m/s) is so low. These time-lags $t_{lag,3}$ can be seem more clearly in the inset diagrams in Figures 7-

13c and 7-13d, which involve a magnified scale for q_i. Inspection of these inset diagrams shows that values of $t_{lag,3}$ are greatly overestimated by the simplified method (because of the failure to account for the role of retention hysteresis). For example, in Figure 7-13c the simplified method predicts $t_{lag,3}$ = 0.49 days at x = 1.5 m, $t_{lag,3}$ = 1.06 days at x = 2.5 m and $t_{lag,3}$ = 2.11 days at x = 4.5 m, whereas the FE results show values of $t_{lag,3}$ less than 1 hour in all 3 cases. Similarly, in Figure 7-13d the simplified method predicts $t_{lag,3}$ = 5.67 days at x = 12.5 m, $t_{lag,3}$ = 7.24 days at x = 16.5 m and $t_{lag,3}$ = 8.72 days at x = 20.5 m, whereas the corresponding values of $t_{lag,3}$ from the FE results are approximately 0.54 days, 1.24 days and 2.17 days respectively. Despite the considerable overestimation of the values of $t_{lag,3}$ by the simplified method, it is clear from the main parts of Figures 7-13c and 7-13d that this has little impact on the total estimate of water flow across the interface at different values of x, because the value of q_i is so low during $t_{lag,3}$ ($q_i = i_a$ = 2x10^{-8} m/s).

Comparison of the total amount of water flow across the interface predicted by the FE modelling and the simplified method is presented in Figure 7-15. The total amount of water flow across interface is obtained by integrating the areas under the curves in Figure 7-13. The simplified method (blue crosses) provides an accurate match to the results from the FE simulations (orange dots) and is conservative (slightly overestimating the total flow across the interface for all values of x greater than 1.0 m). For comparison, if there was no CBS, the total water percolation into the soil slope (given by integrating the rainfall intensity with respect to time, from t = 0 to t = 102 days) would have been 0.345 m. This means that the CBS has almost entirely prevented percolation into the slope only for $x < 1.0$ m, but at x = 2.0 m it has reduced percolation into the slope by about 77% and even at x = 20 m it has reduced percolation by about 63%.

7.2.3 Additional extreme rainfall events

To extend the numerical validation of the new simplified method of analysis for extreme rainfall events, additional FE simulations and corresponding simplified method calculations were performed for four additional extreme rainfall events. All four cases involved the same CBS as studied in Section 7.2.1, with the F.L made

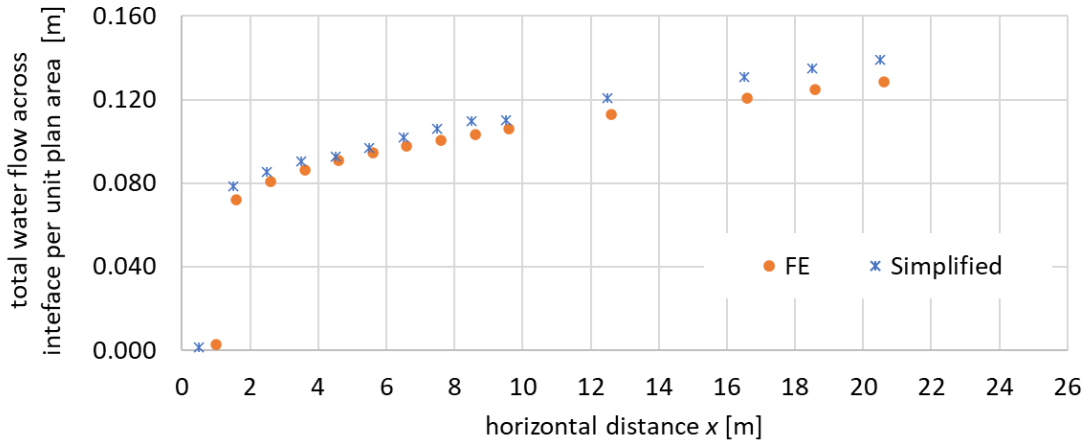

Figure 7-15 Variation of total water flow across interface per unit plan area: comparison of simplified method and FE results for a CBS with F.L. made of silty sand (β = 35°, SSGV, t_f = 40 cm, extreme rainfall pattern E2)

of fine sand (β =35°, FSGV, t_f = 40 cm). All four additional extreme rainfall events (E4, E5, E6 and E7), shown in Figure 7-16, involved the same three rainfall intensities as used in extreme rainfall event E1 (i_a = 2x10^{-7} m/s, i_b = 10^{-6} m/s, i_c = 2x10^{-6} m/s). Hence, the final steady state plots of Q_x against x and WS against x shown in Figure 7-11 were used within the simplified method.

Extreme rainfall events E4, E5, E6 and E7 were more complex than extreme rainfall event E1 and each one involved a double peak in the rainfall intensity. A particular objective was to investigate how well the simplified method coped with a second peak in rainfall intensity, given that the simplified method assumes that the soil of the F.L is on the main wetting SWRC throughout, whereas the soil states at the start of the second peak might be expected to be on scanning drying SWRCs, following the drop in rainfall intensity from the first peak. The FE simulations took full account of retention hysteresis, through use of the hysteretic modVG-modM+LF hydraulic constitutive model.

Figure 7-17 shows the comparison of simplified method predictions and FE results for the variation of interface flow velocity q_i with time at different values of x for extreme rainfall event E6. Corresponding results for extreme rainfall events E4, E5, and E7 are shown in Appendix E. The results shown in Figure 7-17 and Appendix E indicate that the simplified method predictions are an excellent match to the FE results in all cases. The simplified method always errs slightly on the conservative side, with values of $t_{lag,1}$ and $t_{lag,2}$ (after an increase of rainfall

intensity) slightly underpredicted and values of $t_{lag,3}$ (prior to breakthrough completely stopping after an appropriate decrease of rainfall intensity) overpredicted. This was true even during the second peak of rainfall intensity.

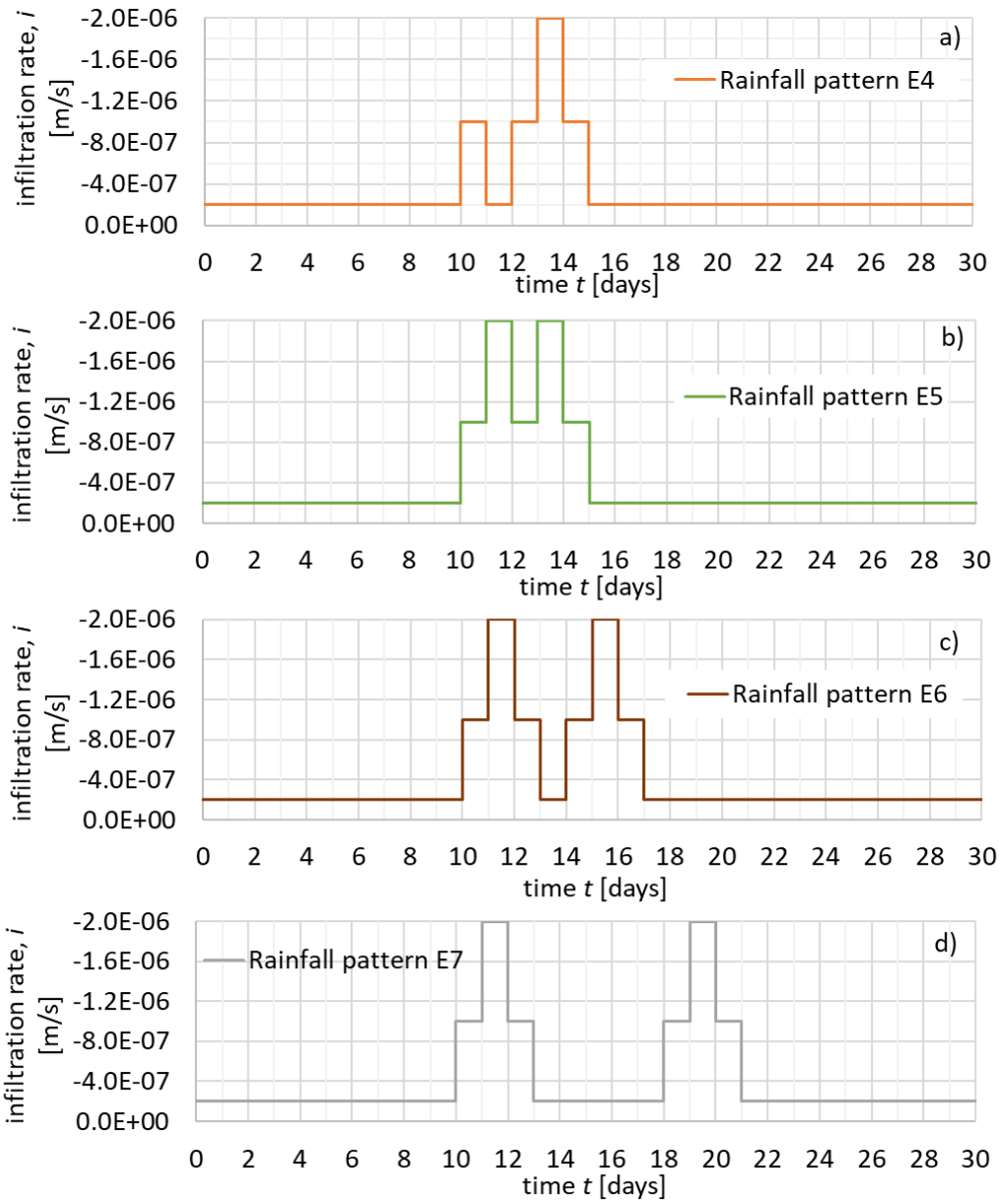

Figure 7-16 Additional extreme rainfall events E4, E5, E6 and E7

The excellent match between simplified method predictions and FE results is further emphasised by Figure 7-18, which shows the total flow across the interface (per unit plan area) plotted against x for extreme rainfall event E6. Similar results for extreme rainfall events E4, E5 and E7 are included in Appendix E. As expected, the predictions of the simplified method shown in Figure 7-18 and Appendix E err on the conservative side, with slightly larger quantities of flow across the interface predicted than according to the FE results.

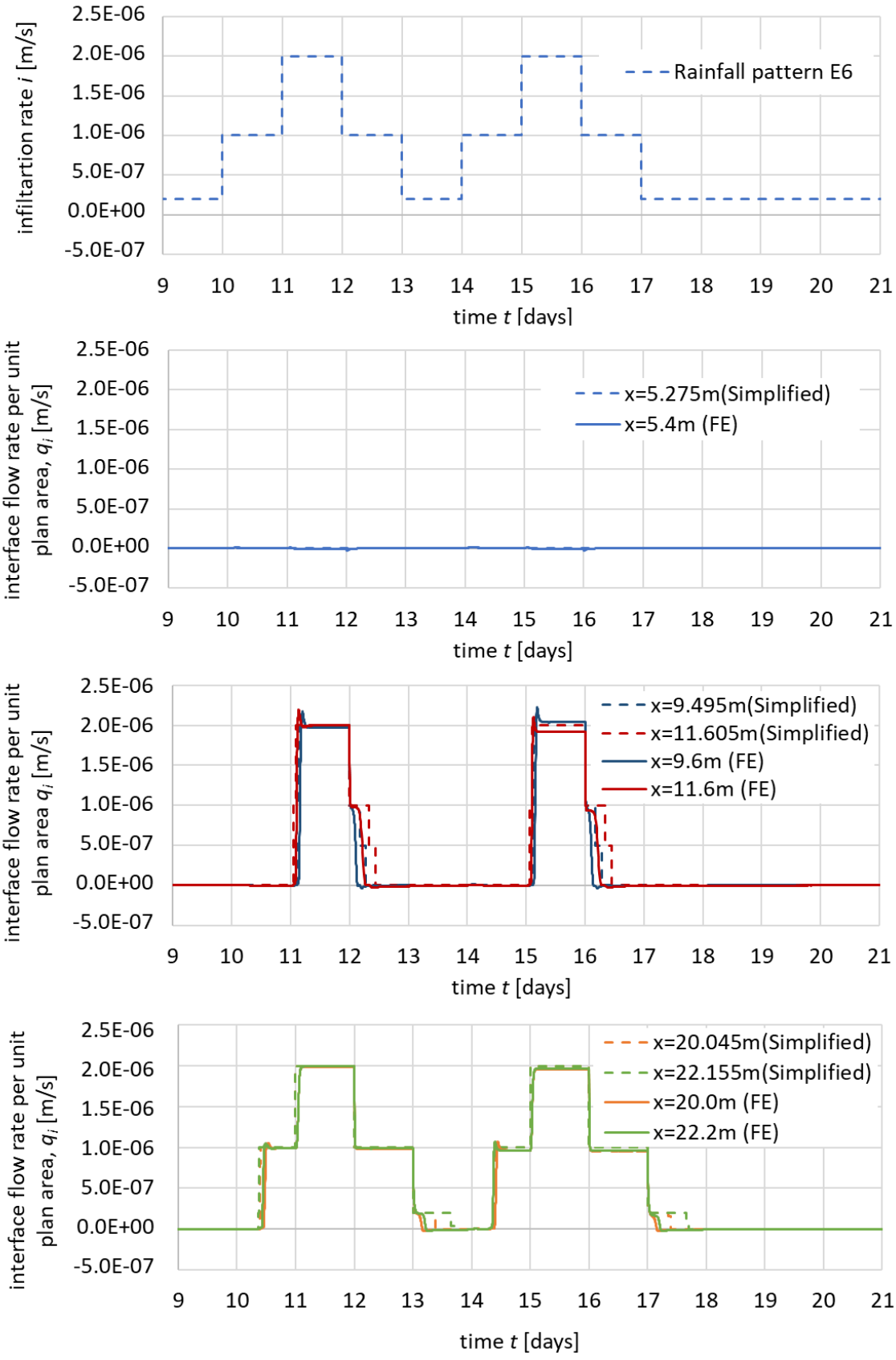

Figure 7-17 Sloping CBS with F.L. made of fine sand subjected to extreme rainfall pattern E6: comparison of FE results and simplified method predictions (β = 35°, FSGV, t_f = 40 cm)

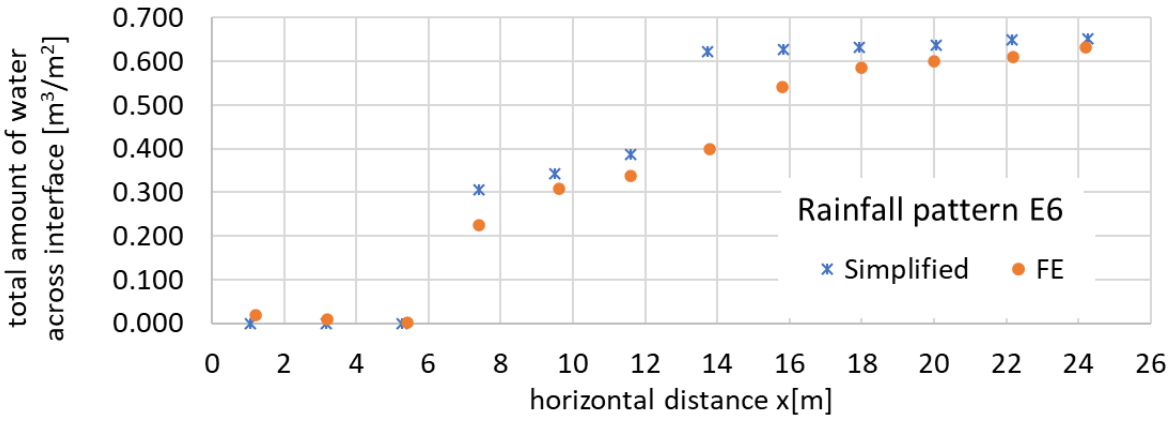

Figure 7-18 Variation of total water flow across interface per unit plan area: comparison of simplified method and FE results(β = 35°, FSGV, t_f = 40 cm, extreme rainfall pattern E6)

The excellent match between simplified method predictions and FE results in Figures 7-17 and 7-18 and in Appendix E confirms that the simplified method is suitable for use even with relatively complex extreme rainfall events, involving more than one peak of rainfall intensity, despite the fact that the simplified method assumes that the soil of the F.L is on the main wetting SWRC throughout (i.e. ignoring any influence of retention hysteresis).

7.3 Conclusions

The key achievements of this chapter can be summarized as follows:

1) A simplified method of analysis has been developed for sloping CBSs subjected to extreme rainfall events (see Section 7.1). The simplified method allows calculation of the variation with time of interface flow velocity q_i at any value of x (the horizontal distance from the top of the slope) for any specified extreme rainfall event (specified variation of effective rainfall intensity i with time). The simplified method employs a method of slices. A key starting point for the method is calculation of the final steady variation of water transfer Q_x against x and water storage WS against x for each of the effective rainfall intensities involved in the extreme rainfall event if each of these rainfall intensities were continued indefinitely. These final steady state plots of Q_x against x and WS against x make use of the approximate final steady state suction profiles for sloping CBSs developed earlier in Chapter 5.

2) Numerical validation of the simplified method of analysis was performed by comparison with FE simulations of corresponding extreme rainfall events (see Section 7.2). These FE simulations involved hydraulic numerical modelling and incorporated potentially important aspects of behaviour, such as accurate constitutive modelling of hydraulic behaviour of the materials of the CBSs at low degree of saturation and hysteresis of retention behaviour. None of these aspects of behaviour are explicitly included in the simplified method of analysis.

3) In all cases investigated, there was excellent match between the predictions of the simplified method (in terms of the predicted variation of q_i with time) and the corresponding FE results. This suggests that aspects of behaviour such as the influence of retention hysteresis are relatively unimportant during extreme rainfall events. The influence of evaporation from the ground surface can be incorporated in the simplified method by using effective rainfall infiltration rates that are calculated by subtracting the steady state evaporation rate during rainfall (which depends upon atmospheric conditions but not rainfall intensity or finer layer material) from the real rainfall infiltration rates.

4) Time lags $t_{lag,1}$ and $t_{lag,2}$, which are seen in the variation of q_i following increase of rainfall intensity, are slightly underpredicted by the simplified method. Time lags $t_{lag,3}$, which are seen when breakthrough ceases after an appropriate reduction of rainfall intensity, are more significantly over-predicted by the simplified method. This is attributed to the influence of retention hysteresis when rainfall intensity decreases in the later part of an extreme rainfall event. The significant over-prediction of time lags $t_{lag,3}$ is, however, relatively unimportant for the total flow across the interface per unit plan area, because the value of q_i is always low during $t_{lag,3}$.

5) The slight underprediction of values of $t_{lag,1}$ and $t_{lag,2}$ and the significant overprediction of values of $t_{lag,3}$ means that the simplified method is always conservative when compared with the FE results, in terms of the total water flow across the interface.

6) The match between simplified method predictions and FE results is excellent even for extreme rainfall events involving two peaks of rainfall intensity. This confirms that retention hysteresis remains relatively unimportant even during a second rise of rainfall intensity following quickly after a previous fall in rainfall intensity.

7) The rules followed during application of the simplified method are sufficient provided that each rainfall intensity within the extreme rainfall event is applied for sufficient duration to reach final steady state under that rainfall intensity at all values of x. This applied to all cases considered in the numerical validation presented in Section 7.2. Further complexity occurs if the extreme rainfall event involves very short durations of different rainfall intensities. This issue is discussed further in Section 9.2.

8) Overall, the proposed simplified method of analysis for sloping CBSs subjected to extreme rainfall events is highly promising. It has the potential to form part of a practical design methodology for sloping CBSs, suitable for use by practising geotechnical engineers in industry, without recourse to complex multi-physics FE modelling (see Chapter 8).

Chapter 8 Suggestions for practical design of sloping CBSs

This chapter uses the understanding gained in Chapters 4 to 7 to provide suggestions for the practical design of sloping CBSs subjected to realistic weather conditions, without use of complex multi-physics FE modelling (such as CODE_BRIGHT). The suggestions include use of the simplified method of analysis for sloping CBSs subjected to extreme rainfall events developed in Chapter 7.

This chapter comprises seven sub-sections: selection of CBS materials, layer thicknesses and geometry; checking factor of safety of a successful CBS; simplified analysis of extreme rainfall patterns; spacing of collector drains; possible development of design charts; use of multi-layered CBSs; and surface protection.

8.1 Selection of CBS materials, layer thicknesses and geometry

The performance of a sloping CBS depends primarily on the hydraulic properties (SWRC and SHCC) of the F.L (as well as the contrast with the corresponding properties of the C.L). In the majority of this thesis, two different materials were considered as candidates for the F.L: silty sand (the finer of the two) or fine sand (slightly coarser than the silty sand). These two materials were selected for investigation because they covered the range conventionally employed for the F.L of CBSs used in landfill cover systems (Rahardjo et al., 2016).

It was shown in Section 5.5.4 that sloping CBSs with the F.L made of silty sand have high water storage capacity WSC, but low water transfer capacity Q_{max}, whereas sloping CBSs with the F.L made of fine sand have lower WSC but significantly higher Q_{max}. For a horizontal CBS used in a landfill cover system, only WSC is relevant. In contrast, for sloping CBSs subjected to realistic rainfall patterns, including extreme rainfall events, high WSC and high Q_{max} are both desirable (see Chapters 6 and 7). If heavy rainfall is sustained for long durations, even high values of WSC will be completely filled before an extreme rainfall event is finished and continued performance of the CBS then depends solely on water

transfer capacity Q_{max}. Hence, it was concluded in Chapters 5-7 that sloping CBSs with the F.L made of silty sand are likely to be effective only in relatively dry climates (with occasional extreme rainfall events), whereas sloping CBSs with the F.L made of fine sand should be effective under almost all climatic conditions.

It was also shown in Section 5.5.4 that sloping CBSs with the F.L made of medium sand (i.e. slightly coarser again) would have higher water transfer capacity Q_{max} than even a sloping CBS with the F.L made of fine sand, although the water storage capacity WSC would be even lower. In the future, therefore it would worth investigating further whether medium sand or fine sand would be the most appropriate material for the F.L of sloping CBSs in different climatic conditions (with different design extreme rainfall events). This investigation would not be too onerous, as it could be done with the simplified method of analysis for extreme rainfall events developed in Chapter 7, rather than requiring multi-physics FE modelling. Another possible advantage of using medium sand rather than fine sand for the F.L would be that the surface of the CBS would be less prone to erosion (because of the slightly coarser material) and hence there would be less need for surface protection (see Section 8.7)

Section 5.5.4 indicates that there would be no point in using a material coarser than medium sand for the F.L of a sloping CBS, because values of both WSC and Q_{max} would be reduced if the F.L was made of coarse sand.

In terms of the thickness of the F.L, Sections 5.5.2 and 5.5.3 showed that, if the F.L was made of fine sand, the water transfer capacity Q_{max} would not increase with increasing thickness t_f of the finer layer once t_f exceeded about 15 cm, although the water storage capacity WSC would continue to increase. Given that performance of a sloping CBS with the F.L made of find sand depends mainly on Q_{max} (rather than WSC), it would seem that 15 cm would be adequate for the thickness of the F.L. However, practical risk of construction tolerances (unintended variations of F.L thickness over the slope), surface damage of the F.L (see Section 8.6) or some loss of F.L material into the C.L (see below) would suggest that 20 cm might normally be appropriate for the thickness of a F.L made of fine sand.

Sections 5.5.2 and 5.5.3 indicate that, if the F.L of a sloping CBS was made of silty sand, water transfer capacity Q_{max} would increase with increasing finer layer thickness t_f up to about t_f = 80 cm, and water storage capacity WSC would increase to even higher values of t_f. Hence, for a sloping CBS with the F.L made of silty sand, greater thicknesses of finer layer (than if the F.L were made of fine sand) would be desirable. The requirement for larger volumes of F.L material is another possible disadvantage of using silty sand rather than fine sand for the F.L of a sloping CBS.

In terms of material selection for the C.L of a sloping CBS, the only material property of the C.L that directly affects the performance of a sloping CBS is the bulk water continuity value of suction $s_{BWC,c}$, because this controls the value of suction at the interface with the F.L when breakthrough occurs. Ideally, the value of $s_{BWC,c}$ should be as small as possible, implying that the material of the C.L should be as coarse as possible. This would also ensure appropriate contrast between the hydraulic properties of the C.L and F.L, so that the capillary barrier phenomenon was effective. If, however, the C.L material was made too coarse relative to the F.L material, there would be a risk of particles from the F.L being carried into the C.L by the downward flow of water, hence negatively impacting on the capillary barrier effect. To avoid this effect, the maximum contrast between the particle sizes of the C.L and F.L materials should be governed by conventional filter rules, as used for example in design of embankment dams. According to Sherard and Dunnigan (1985), the standard filter rule is:

$$D_{15,c} < 5D_{85,f} \qquad \textbf{8-1}$$

where $D_{15,c}$ is the 15% passing point on the particle size distribution of the C.L material and $D_{85,f}$ is the 85% passing point on the particle size distribution of the F.L material.

Having selected the materials of the F.L, the appropriate way to select the material of the C.L would be to choose a material which has a $D_{15,c}$ value slightly less than five times the $D_{85,f}$ value of the F.L material. This should minimize $s_{BWC,c}$ and maximise the hydraulic contrast between F.L and C.L whilst ensuring that the filter rule of Equation 8-1 is satisfied.

For the single C.L material investigated in this thesis (gravelly sand), the value of $D_{15,c}$ is not available. Similarly, for the four different F.L materials investigated in the thesis (silty sand, fine sand, medium sand and coarser sand), values of $D_{85,f}$ are not available. Values of D_{10} are however available for all five materials (see Table 5-3). If it is assumed that, for all five materials, $D_{85}/D_{15} \approx 3$ (corresponding to relatively uniform materials, as would be typical of the materials used in CBSs) and if it is also assumed that all five particle size distributions are of the same shape (simply translated horizontally) in the conventional semi-logarithmic plot, then the value of $D_{15,c}/D_{85,f}$ appearing in Equation 8-1 can be estimated from:

$$\frac{D_{15,c}}{D_{85,f}} = \frac{1}{3}\frac{D_{10,c}}{D_{10,f}} \qquad \textbf{8-2}$$

Values of $D_{15,c}/D_{85,f}$ estimated from Equation 8-2, if each of the four materials were used in combination with a C.L made of gravelly sand ($D_{10,c}$ = 2.730 mm) are listed in Table 8-1. It is clear from Table 8-1 that the gravelly sand would be an unsuitable material for the C.L if the F.L was made of silty sand, because the estimated value of 26.8 for $D_{15,c}/D_{85,f}$ far exceeds the allowable value of 5 from Equation 8-1. Table 8-1 also suggests that the gravelly sand would be borderline suitable if the F.L was made of fine sand. Finally, if the F.L was made of medium sand or coarse sand, it would possible to use a slightly coarser material than the gravelly sand for the C.L, and this would be desirable as it would slightly reduce the value of $s_{BWC,c}$ (hence, slightly increasing WSC and Q_{max}) and it would ensure better hydraulic contrast between the F.L and C.L.

Table 8-1 Estimated values of $D_{15,c}/D_{85,f}$ if different F.L materials are used in combination with a C.L made of gravelly sand

F.L materials	$D_{10,f}$ (mm)	$D_{10,c}$ (mm)	Estimated $D_{15,c}/D_{85,f}$
Silty sand	0.034	2.730	26.8
Fine sand	0.170	2.730	5.35
Medium sand	0.340	2.730	2.68
Coarse sand	0.850	2.730	1.07

Experimental confirmation of the relevance to CBSs of the conventional filter rule of Equation 8-1 comes from laboratory column infiltration tests, representing horizontal conventional or multi-layered CBSs, performed by Scarfone (2020). From the particle size distributions of the F.L material and C.L material employed

by Scarfone (2020) in these column tests, the value of $D_{15,c}/D_{85,f}$ was calculated as 7.1 i.e. the filter rule of Equation 8-1 was exceeded, but not by a great margin. This is consistent with the fact that Scarfone (2020) reported some migration of F.L particles into the top few centimetres of the C.L, but not to the extent that it prevented achievement of the capillary barrier effect.

The numerical modelling presented in Chapters 5 to 7 would suggest that a thickness of only a few centimetres should be adequate for the C.L. However, allowing for construction tolerances (unintended variations of C.L thickness over the slope) and some migration of material from the F.L into the top few centimetres of the C.L, a C.L thickness of about 15 cm might be a reasonable choice.

To avoid water ingress into the underlying soil at the top of a slope, the CBS should extend a short distance along the horizontal ground surface at the top of the slope (see Figure 8-1). Scarfone (2020) performed numerical modelling which suggested that, for the cases he examined, 1.3 m horizontal extension of the CBS at the top of a slope was sufficient to prevent water ingress into the slope. However, this requires further investigation. It would be worth including anisotropy of permeability of the underlying soil in this investigation because this would influence whether the wetting zone extended into the slope. At the bottom of the slope, the CBS should again extend a short distance beyond the slope and there should be a toe drain (see Figure 8-1) to take away the water carried down the slope by water transfer within the F.L and any breakthrough into the C.L. If necessary, for a long slope (longer than the diversion length), there will need to be longitudinal collector drains along the slope at intervals down the slope (see Figure 8-1 and Section 8.4).

8.2 Checking factor of safety of a successful sloping CBS

The intention of a CBS on a slope is to prevent or limit rainwater percolation into the underlying soil of the slope, in order to avoid rainfall-induced instability of the slope. Scarfone (2020) and Scarfone et al. (2022) performed thermo-hydraulic FE modelling with CODE_BRIGHT of slopes covered by CBSs subjected to long-term

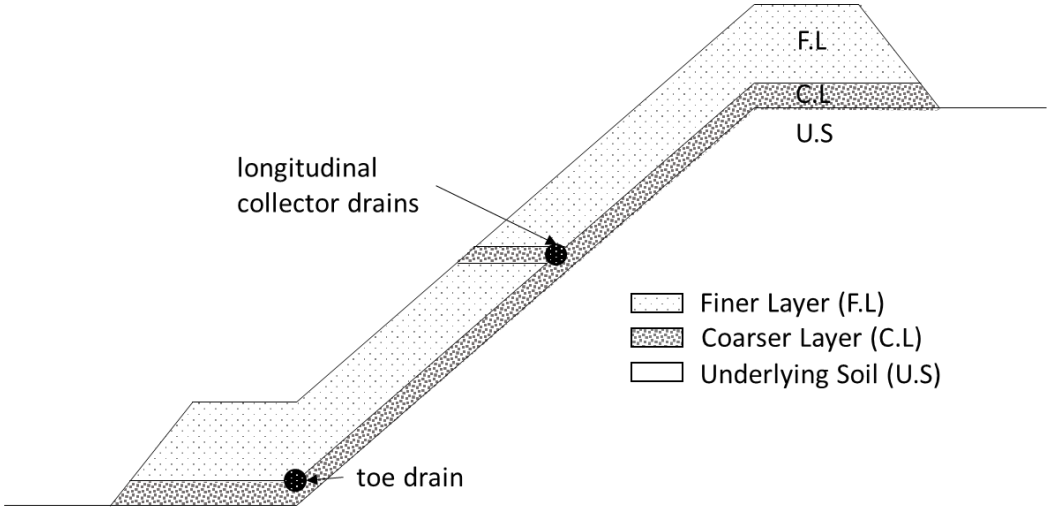

Figure 8-1 Sloping CBS geometry

realistic meteorological conditions, which they then combined with limit analyses of slope stability performed with the LimitState: GEO software (see Section 2.8.3). They showed that, provided the CBS was successful in preventing breakthrough or in restricting breakthrough to only limited extent (at the bottom of slope) and limited time duration (typically less than 24 hours on a few isolated days of extreme rain), the most critical failure surface was within the CBS, along the interface between F.L and C.L, rather than extending into the underlying soil. Analysing a planar potential failure surface along the interface within a CBS should be relatively straightforward. Hence, it makes sense to check the factor of safety (FoS) for such a failure surface before attempting the more difficult task of designing a sloping CBS to prevent or limit breakthrough, because if this FoS is inadequate there is no point in proceeding with the CBS design and an alternative solution must be sought for achieving stability of the slope.

In assessing the FoS of a CBS on a slope, where the failure surface is restricted to the interface between F.L and C.L, a conservative assumption is to assume that the suction at the interface has fallen to the critical breakthrough value $s_{BWC,c}$ along the entire length of the interface. This is a conservative assumption because, in reality, for a successful CBS design, either breakthrough would not have occurred anywhere in the slope or breakthrough would only have occurred in the lower part of the slope. Wherever breakthrough had not occurred, the suction at the interface would be greater than $s_{BWC,c}$. Given the planar nature of the failure surface, the shallow depth of the failure surface relative to the slope length and the assumption of a constant value of suction $s_{BWC,c}$ along the entire

length of the failure surface, the FoS can be calculated by performing an infinite slope analysis.

It can be assumed that failure at the interface will occur within the F.L material, rather than the C.L material, because both materials are likely to be cohesionless (c'= 0) and the F.L material is likely to have the lower value of friction angle $\emptyset'$. It can also be assumed that, if a breakthrough condition has been reached, with a very low value of suction $s_{BWC,c}$ at the interface, the F.L material at the interface will be in an almost saturated condition, so that the conventional saturated principle of effective stress applies on the failure surface.

Infinite slope analysis, for a planar failure surface parallel to the slope at a vertical depth t_f below the slope (where t_f is the thickness of the F.L), with cohesionless soil in a saturated condition at the failure surface and a value of pore water pressure u_w at the failure surface, gives the factor of safety (FoS) as:

$$\mathrm{FoS} = \frac{\tan \phi'_f}{\tan \beta}\left(1 - \frac{u_w}{\gamma_f t_f \cos^2 \beta}\right) \qquad \textbf{8-3}$$

where ϕ'_f is the friction angle of the F.L material, γ_f is the bulk unit weight of the F.L material and β is the slope angle. Equation 8-3 is derived in Appendix F. Given that the pore gas pressure can be assumed equal to atmospheric pressure throughout the CBS, the conservative assumption that $s = s_{BWC,c}$ on the entire failure surface corresponds to a value of pore water pressure u_w on the failure surface given by $u_w = -s_{BWC,c}$, so that Equation 8-3 becomes:

$$\mathrm{FoS} = \frac{\tan \phi'_f}{\tan \beta}\left(1 + \frac{s_{BWC,c}}{\gamma_f t_f \cos^2 \beta}\right) \qquad \textbf{8-4}$$

Equation 8-4 assumes that the bulk unit weight γ_f of the F.L material is constant throughout the vertical thickness t_f of the F.L. To account for variation of γ_f with height z within the F.L (arising from the variation of degree of saturation S_l with z), $\gamma_f t_f$ in Equation 8-4 could be replaced by the integral of γ_f with respect to z over the F.L thickness t_f. However, this level of detail would not be justified (it would have minimal impact on the calculated value of FoS, see below) and hence it would be acceptable to simply use an estimated average value for γ_f in Equation

8-4, or it would even be acceptable to conservatively assume a saturated value of γ_f.

The validity of Equation 8-4 was investigated by comparing with the values of FoS calculated by Scarfone (2020) and Scarfone et al. (2022) from their thermo-hydraulic FE modelling and associated limit analysis. Scarfone (2020) and Scarfone et al. (2022) performed FE modelling and associated limit analysis for the four different CBS designs shown in Table 8-2. In all four cases, the slope angle β was 35°, the slope height H was 10 m and the C.L was made of a gravelly sand ($s_{BWC,c}$ = 0.2 kPa). Two of the four cases involved a F.L made of fine sand (with ϕ'_f = 40°, γ_f = 17 kN/m^3 and hydraulic properties given in Table 6-1), and the other two cases involved a F.L made of silty sand (with ϕ'_f = 35°, γ_f = 19 kN/m^3 and hydraulic properties given in Table 6-1). For each F.L material, two different thicknesses of F.L were analysed (t_f = 0.4 m and t_f = 0.8 m). For each of the four CBS designs, analyses were performed with two different weather conditions, representing London, UK and Cagliari, Italy.

Table 8-2 FoS calculations for slopes covered by CBSs analysed by Scarfone (2020) and Scarfone et al. (2022) (H=10m)

β	Material of F.L.	ϕ'_f	t_f	γ_f	Scarfone (2020) London weather		Scarfone (2020) Cagliari weather		FoS from
(°)		(°)	(m)	(kN/m^3)	Breakthrough	FoS	Breakthrough	FoS	Eq 8-4
35	Fine sand	40	0.40	17.0	Yes, limited	1.26	Yes, limited	1.29	1.251
35	Fine sand	40	0.80	17.0	No	1.28	Yes, limited	1.31	1.225
35	Silty sand	35	0.40	19.0	Yes, limited	1.17	Yes, limited	1.16	1.039
35	Silty sand	35	0.80	19.0	No	1.26	No	1.32	1.020

In the thermo-hydraulic FE modelling performed by Scarfone (2020) and Scarfone et al. (2022), long-term rainfall patterns were modelled in great detail by representing real daily rainfall totals for a full 10-year period (selected from the meteorological records as an unusually wet decade). Other atmospheric parameters (temperature, relatively humidity, net radiation, and wind speed) were modelled as annual cyclic variations. Outputs of the product of degree of saturation S_l and suction s from the CODE_BRIGHT FE modelling at the end of selected wettest days within the decade (9 different days in the case of the London weather and 13 different days in the case of the Cagliari weather) were exported to the LimitState: GEO software for limit analysis calculations. In the

limit analysis calculations, the shear strength of the soil τ_f was given by Equation 2-59:

$$\tau_f = \left((\sigma - u_a) + S_l s\right) \tan \phi' \qquad \textbf{8-5}$$

and pore air pressure u_a was taken as zero (i.e. equal to atmospheric pressure). The limit analysis calculations considered extremely large numbers of possible failure surfaces, passing through the F.L of the CBS, the C.L of the CBS, the underlying soil of the slope or any combination of these. Without exception, the critical failure surface for every one of the 9 or 13 critical rainfall events was close to the interface between F.L and C.L for the majority of its length.

Table 8-2 shows the values of FoS calculated by Scarfone (2020) and Scarfone et al. (2020) for the most critical rainfall event within the 10-year period (for each of the two weather conditions). Also shown in Table 8-2 is whether breakthrough occurred within the CBS in the FE modelling. In three of the eight cases no breakthrough occurred. In the other five cases, breakthrough did occur, but this was of limited extent (just the lower part of the slope) and limited duration (just a few hours during days of extreme rainfall). Also shown in Table 8-2 are the values of FoS calculated from the simplified infinite slope expression of Equation 8-4.

Inspection of Table 8-2 shows that the values of FoS calculated by the simplified infinite slope expression of Equation 8-4 are always more conservative than the more accurate values of FoS calculated from the FE modelling and limit analysis. This is to be expected, because the simplified expression of Equation 8-4 assumes that the breakthrough value of suction s = $s_{BWC,c}$ is achieved along the entire length of the interface between F.L and C.L, whereas in reality there will be higher values of suction on the interface, either along the entire length of the interface (if no breakthrough occurred) or along much of the length of the interface (if only limited breakthrough occurred). Consistent with this explanation, it is notable from Table 8-2 that the simplified expression of Equation 8-4 gave values of FoS that were only 1%-11% less than the corresponding values from the FE modelling and limit analysis in those cases where limited breakthrough occurred, whereas this difference was as much as 23% in one of the cases where no breakthrough occurred (F.L made of silty sand, t_f = 0.8 m, Cagliari weather).

It is also worth noting that, when using the simplified infinite slope expression of Equation 8-4, the contribution to FoS of the breakthrough value of suction $s_{BWC,c}$ is relatively minor and an even simpler (and even more conservative) estimate of FoS would be given by assuming s = 0 along the entire interface:

$$\text{FoS} = \frac{\tan \phi'_f}{\tan \beta} \qquad \textbf{8-6}$$

For the cases analysed in Table 8-2, Equation 8-6 would suggest FoS = 1.20 if the F.L was made of fine sand (ϕ'_f = 40°) and FoS = 1.00 if the F.L made of silty sand (ϕ'_f = 35°). Comparison with the values of FoS from Equation 8-4 given in Table 8-2, shows that inclusion of the suction $s_{BWC,c}$ in Equation 8-4 increased calculated values of FoS by only about 2%-4%.

If Equation 8-4 suggests that the FoS of the proposed sloping CBS is acceptable, the next stage would be to consider how to design the CBS to prevent breakthrough or restrict breakthrough to limited extent and duration for appropriate design extreme rainfall events (see next section). If, however, Equation 8-4 indicates that the FoS of the proposed sloping CBS is unacceptable, it would be necessary to change the choice of F.L material (to increase the value of ϕ'_f), reduce the slope angle β (if this was feasible) or find an alternative solution (other than a CBS) for achieving stability of the slope.

The values of FoS shown in Table 8-2 (whether calculated by Equation 8-4 or by the FE modelling and limit state analysis performed by Scarfone (2020)) are all about 1.0 to 1.3. These values of FoS, which all relate to cases with a slope angle of 35°, would generally be considered unacceptable in practice. A value of approximately 1.5 for the FoS might generally be considered acceptable. Inspection of Table 8-2 suggests that, if the friction angle of the material of the F.L. of a CBS was 40° (fine sand) or 35° (silty sand), a sloping CBS would typically only produce an acceptable value of FoS if the slope angle was significantly less than 35°.

8.3 Simplified analysis of extreme rainfall events

The simplified method of analysis for extreme rainfall events developed in Chapter 7 can be used to analyse the performance of a proposed sloping CBS (employing F.L and C.L materials selected as suggested in Section 8.1), with a view to designing a CBS that prevents breakthrough or limits breakthrough to acceptable extent and duration (see below). Key to this will be selection of appropriate extreme rainfall events, appropriate to the location and the meteorological conditions of this location. It is likely that at least two different extreme rainfall events should be analysed for any slope location: one an extreme rainfall event, with a long return period; the other an even more extreme rainfall event with an even longer return period. Extreme and very extreme rainfall patterns should be selected based on past meteorological records for the location, but also taking account of the future effects of climate change (increasing frequency of extreme rainfall events of increasing severity). Each extreme rainfall event analysed should include an appropriate period and intensity of antecedent rainfall, applied for sufficient duration for the CBS to reach steady state under this antecedent rainfall intensity.

In applying the simplified method of analysis of extreme rainfall events developed in Chapter 7, account should be taken of the rainwater diverted down the sloping CBS by the extension of the CBS onto the horizontal ground surface at the top of the slope (see Figure 8-2). Scarfone (2020) showed that rainwater falling on the part of this horizontal section of the CBS up to the point A (see Figure 8-2) was diverted down the sloping CBS, whereas rainfall falling beyond point A (i.e. directly onto the C.L) infiltrated into the underlying soil at the top of the slope (see the shaded region in Figure 8-2). Hence, in applying the simplified method of analysis, values of x should be measured from point A, rather than from the top of the slope.

The key result of the simplified method of analysis of extreme rainfall events will be a plot of the form shown in Figure 8-3 i.e. a plot of total water flow across the interface (between F.L and C.L) per unit plan area for the various extreme and very extreme rainfall events selected for analysis.

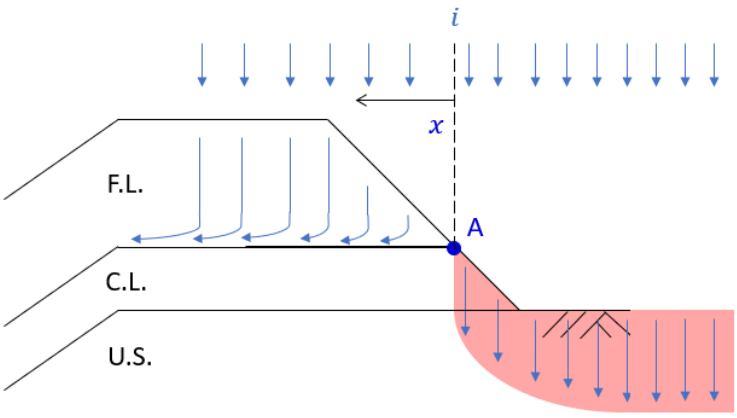

Figure 8-2 Schematic water flow within upper part of CBS on slope

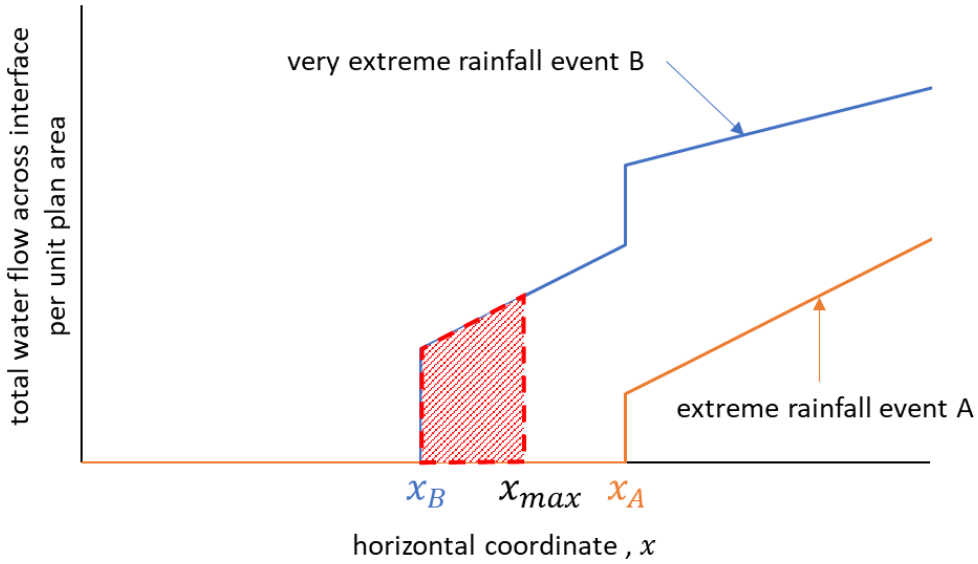

Figure 8-3 Output from simplified method of analysis of extreme rainfall events

Decisions would need to be taken on whether the CBS should be designed for no breakthrough or for limited breakthrough for each of the extreme rainfall events analysed with the simplified method. For example, it might be decided that there should be no breakthrough under extreme rainfall event A in Figure 8-3, but that limited breakthrough would be acceptable under very extreme rainfall event B. It would be necessary to decide what extent and duration of breakthrough under extreme rainfall event B would be acceptable. If it was decided that the acceptable quantity of breakthrough flow corresponded to the shaded red area shown in Figure 8-3, this would mean that the horizontal extent of the slope would need to be limited to x_{max} or that collector drains would need to be installed on the slope at a horizontal spacing no greater than x_{max} (see Section 8.4).

A question requiring further research in the future (see Section 9.2) is how to assess what extent of breakthrough is acceptable under the most extreme rainfall

event considered relevant to the particular slope. The point requiring further investigation is what amount of breakthrough (both spatial extent and time duration) can occur with the most critical failure surface still remaining along the interface between F.L and C.L, so that Equation 8-4 still represents a conservative estimate of the FoS of the slope covered by the CBS. Clearly, the simplified method developed in Chapter 7 could be used in combination with a requirement that no breakthrough should occur under the most extreme design rainfall event. However, it seems likely that this would be unnecessarily conservative, because it is clear from the work of Scarfone (2020) and Scarfone et al. (2022) that non-trivial amounts of breakthrough can occur within a sloping CBS without the critical failure surface extending into the underlying soil.

8.4 Spacing of collector drains

The output of the simplified method of analysis for the selected extreme rainfall events, illustrated in Figure 8-3, can be used to decide if longitudinal collector drains are required (in addition to a drain at the toe of slope) and, if so what spacing is required between collector drains. Figure 8-4 shows a possible collector drain layout on a slope, for a situation where collector drains are required. Collector drains would run almost longitudinally along the slope, but with a slight down-slope inclination, to carry away the water collected from the water transfer within the section of CBS above the drain. If the slope is very long in the longitudinal direction, down-slope drains (see Figure 8-4) might be constructed at regular intervals along the slope to take the water from the collector drains down to the toe drain.

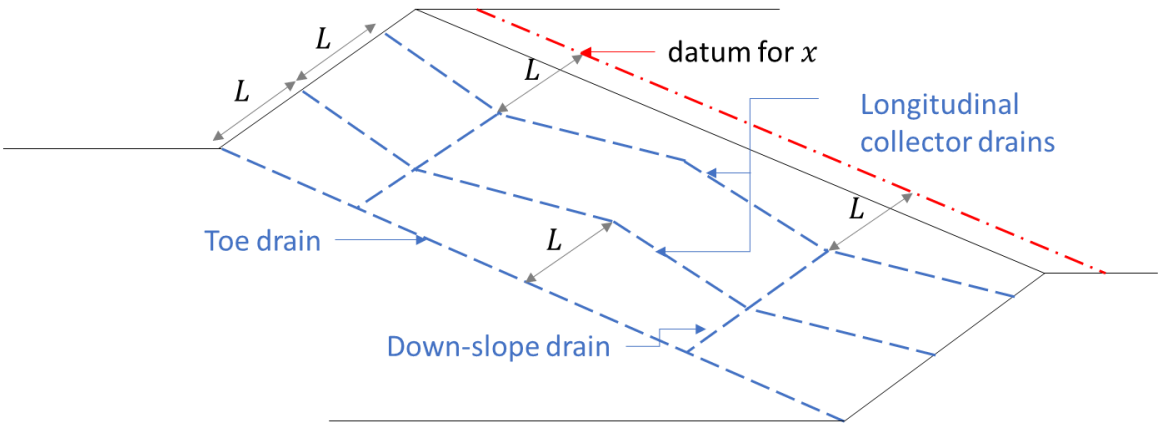

Figure 8-4 Possible arrangement of collector drains

If the horizontal extent of the slope (measured from the datum illustrated in Figure 8-2) was less than x_{max} (see Figure 8-3), no collector drains would be required, provided the red shaded extent of water breakthrough under very extreme rainfall event B in Figure 8-3 was considered acceptable. If the horizontal extent of the slope was greater than x_{max}, then collector drains would be required at spacing L (see Figure 8-4) given by:

$$L = \frac{x_{max}}{\cos\beta} \quad \text{8-7}$$

8.5 Potential development of design charts

For practising geotechnical engineers in industry, it would be ideal if the simplified method of analysis for sloping CBSs subjected to extreme rainfall events, discussed in Section 8.3, together with the associated ideas presented in Section 8.1 (selection of CBS materials and layer thicknesses), Section 8.2 (checking FoS) and Section 8.4 (spacing of collector drains), could all be combined and presented in the form of design charts. Ideally these design charts would allow a geotechnical designer to select appropriate CBS materials, layer thicknesses and (if necessary) collector drain spacing to achieve a required value of FoS for a slope of given angle subjected to a given design extreme rainfall event. Attempting to develop such design charts would be a challenging task, because of the number of different input variables involved, including slope angle β, F.L material properties, C.L. material properties, F.L. thickness and design extreme rainfall event. Perhaps the greatest challenges would arise from trying to capture the range of possible F.L. materials and the range of possible design extreme rainfall events in relatively simple fashion. For the F.L. material, the relevant properties are the SWRC and the SHCC, and probably these would need to be represented in the design charts by a limited number of possible SWRC/SHCC combinations, covering the full range of material types that might be considered for the F.L. of a sloping CBS. Similarly, for the design rainfall event, it is probable that this would need to be represented in the design charts through a limited number of possible design extreme rainfall events, covering the full range of possible scenarios for different climatic zones.

8.6 Multi-layered CBSs

The numerical modelling results presented in Section 5.7 showed that increased values of both water storage capacity and water transfer capacity can be achieved if multi-layered sloping CBSs are used instead of conventional sloping CBSs. This suggests that multi-layered sloping CBSs could be used to increase collector drain spacing or even remove the need for collector drains. This would result in cost-savings of the drains, but this would be offset by increased cost of the multi-layered CBSs. To explore this possibility further, it would be useful in future to extend the simplified method of analysis of extreme rainfall events, developed in Chapter 7, to cover multi-layered CBSs.

8.7 Surface protection

Sloping CBSs would probably require some form of surface protection, to prevent long-term surface erosion of the F.L material. Rainfall runoff should not occur with a well-designed sloping CBS, because surface runoff should only occur if the rainfall intensity i approaches or exceeds the saturated hydraulic conductivity k_s of the F.L material (Blanco-Canqui et al., 2002). Values of k_s for all possible F.L materials (see Table 5-3) exceed all realistic values of rainfall intensity i (see Table 4-3). Although there should be no runoff to cause surface erosion, it is possible that surface erosion could be produced by other causes. For example, under extreme rainfall, the impact of raindrops could be sufficient to cause surface damage. In addition, under very dry conditions there might be the risk of surface erosion by wind.

The most likely method of surface protection would be to use vegetation (Coppin and Richards, 1990). The roots of the vegetation would bind the surface together to provide surface protection. A vegetation cover would have the added advantage that evapo-transpiration would increase the rate of drying to the atmosphere, leading to greater restoration of water storage capacity of a CBS after rainfall. There might however also be disadvantages to the use of a vegetation cover. For example, if vegetation covers the surface, then the effects of shading the surface would reduce the temperature at the ground surface, leading to a decrease of evaporation rate. In addition, a root system within the F.L may change the

hydraulic properties of the F.L material (e.g. bulk hydraulic conductivity and water retention), adversely affecting the performance of the CBS. Various previous authors have studied the use of vegetation on CBSs through field trials (e.g. Zhan et al., 2017; Li et al., 2021). In the simplified methods of analyses in this thesis, the impact of vegetation on ground surface has been ignored. This should be studied further (see Section 9.2).

Chapter 9 Conclusions and recommendations

9.1 Conclusions

The global warming situation means that geotechnical applications with sustainable materials and construction are crucially important. Most civil and geotechnical applications which are widely used increase the concentration of CO_2 in the atmosphere, which contributes to climate change. The development of sustainable materials and applications of low-carbon solutions in geotechnical engineering practice are essential for reducing climate change.

Capillary barrier systems (CBSs) are soil cover systems for preventing percolation of water into the underlying soil. They can be used for a variety of purposes, including maintaining slope stability. CBSs are an example of sustainable geotechnical application because they use only naturally occurring geomaterials (sands and gravels), whereas many conventional methods of enhancing slope stability involve manufactured materials with high embedded carbon, such as concrete or geopolymers. The function of a CBS is based on the contrast between the hydraulic properties (soil water retention curve (SWRC) and soil hydraulic conductivity curve (SHCC)) of the finer and coarser layers. The performance of a CBS on a slope depends upon both the water storage capacity of the CBS and the water transfer capacity down the slope. The research presented in this thesis investigated the behaviour of CBSs on slopes through numerical modelling and the development of simplified methods of analysis.

The original research presented in the thesis can be divided into four major parts. The first part (Chapter 4) investigated horizontal CBSs subjected to continuous rainfall of constant intensity. This involved hydraulic FE numerical analyses and numerical validation of an existing simplified method for calculating water storage capacity at steady state. The second part (Chapter 5) investigated sloping CBSs subjected to continuous rainfall of constant intensity and involved hydraulic FE numerical analysis and development and numerical validation of a new simplified method for calculating water storage capacity and water transfer capacity (and hence diversion length) at steady state. The third part (Chapter 6) used thermo-hydraulic FE numerical analyses and hydraulic FE analyses to investigate the

behaviour of sloping CBSs subjected to various simple patterns of intermittent rainfall of varying intensity, to provide improved understanding of the behaviour of sloping CBSs under more realistic rainfall conditions, including the effects of evaporation from the ground surface and hysteresis in the hydraulic behaviour of the CBS materials. The final major original part of the work (Chapter 7) involved the development and numerical validation of a simplified method of analysis for sloping CBSs subjected to extreme rainfall events.

9.1.1 Horizontal CBSs subjected to continuous rainfall of constant intensity

A key performance aspect of a horizontal CBS is the water storage capacity i.e. the amount of water that can be stored in the finer layer before breakthrough of water occurs into the coarser layer (and hence into the underlying soil).

Stormont and Morris (1998) proposed a simplified semi-analytical method for calculating the water storage capacity WSC of a horizontal CBS subjected to continuous rainfall of constant intensity. This method is based on an assumed simplified suction profile within the finer layer at the time of breakthrough. Several previous authors have provided limited validation of this simplified method, by performing experimental column tests in the laboratory or by numerical modelling. These previous validation exercises have tended to be somewhat limited, involving only small numbers of laboratory tests or numerical simulations, rather than a full parametric study covering a realistic range of key geometrical, material and environmental parameter values. In addition, previous attempts at validation by numerical modelling have typically involved conventional hydraulic constitutive models (SWRC and SHCC) that are unrealistic at very low values of degree of saturation (in the pendular range). This may be an important shortcoming, because the phenomenon of breakthrough is crucially dependent on the hydraulic behaviour of the coarser layer at low degree of saturation.

Hydraulic numerical modelling of horizontal CBSs subjected to continuous rainfall of constant intensity was performed to investigate the validity of the simplified method for calculating water storage capacity WSC first proposed by Stormont

and Morris (1998). The numerical modelling was performed with the multi-physics finite element software CODE_BRIGHT and employed an advanced hydraulic constitutive model (Scarfone (2020) and Scarfone et al. (2020a)) giving improved modelling at low degree of saturation, including the contribution of film flow to hydraulic conductivity. Numerical simulations were performed with different combinations of key variables (rainfall intensity, thickness of finer layer and hydraulic properties of finer layer), representing a more comprehensive investigation than previously reported in the literature. In addition, the numerical modelling was extended from conventional CBSs to multi-layered CBSs, involving multiple pairs of alternating finer and coarser layers.

The results for conventional CBSs showed that the approximate suction profile within the finer layer of the CBS at the time of breakthrough suggested by Stormont and Morris (1998) was an excellent match to the corresponding suction profile observed in the numerical analyses in all cases. Consequently, the simplified semi-analytical method of Stormont and Morris (1998) for calculating the water storage capacity of a horizontal conventional CBS produces results that agree very well with the corresponding results from the numerical analyses in all cases. For multi-layered CBSs, the results showed that an extended simplified suction profile proposed by Scarfone (2020) and a corresponding simplified method of calculating water storage capacity were again excellent matches to the results from the numerical analyses in all cases. Overall, the results presented in the thesis provide increased confidence in the use of the simplified semi-analytical methods for calculating water storage capacities of conventional and multi-layered horizontal CBSs subjected to continuous rainfall of constant intensity.

The numerical modelling also demonstrated that wetting of the finer layer of a conventional horizontal CBS is a two-stage process. The first stage involves a wetting front moving downwards from the ground surface. Above the wetting front the soil of the finer layer is partially wetted, at a suction $s = s_f^*$ (and associated degree of saturation) corresponding to a state where the value of hydraulic conductivity k_l is equal to the rainfall intensity i. Once this initial partial wetting front reaches the bottom of the finer layer, the second stage of wetting commences. This second stage involves further filling of the finer layer from the bottom upwards. This continues until the suction at the bottom of the finer layer

reaches the bulk water continuity value of the coarser layer, at which point breakthrough occurs into the underlying coarser layer.

9.1.2 Sloping CBSs subjected to continuous rainfall of constant intensity

A new simplified method has been developed for determining the water storage capacity WSC and water transfer capacity Q_{max} (and hence diversion length L_D) of sloping CBSs subjected to continuous rainfall of constant intensity. The new simplified method assumes an appropriate steady state suction profile on vertical cross-sections of the finer layer at and beyond the diversion length L_D that is appropriate to a sloping CBS, with flow parallel to the slope in the lower part of the finer layer. This contrasts with an existing simplified method from Parent and Cabral (2006), which assumes an approximate suction profile appropriate to a horizontal CBS (i.e. the approximate suction profile of Stormont and Morris (1998)).

Two-dimensional hydraulic numerical modelling was performed of sloping CBSs subjected to continuous rainfall of constant intensity, using the CODE_BRIGHT FE software and the same advanced hydraulic constitutive model as employed previously for the numerical modelling of horizontal CBSs. There were two purposes of the numerical modelling. Firstly, to provide numerical validation (including an appropriate parametric study) of the proposed new simplified method for predicting WSC, Q_{max} and L_D. Secondly, to gain deeper understanding of the hydraulic behaviour of sloping CBSs subjected to rainfall.

In all cases analysed, the proposed new form of approximate steady state suction profile on vertical cross-sections at and beyond the diversion length was an excellent match to the corresponding final steady state suction profile from the FE results. As a consequence, in all cases, the proposed new method for predicting values of water storage capacity WSC and water transfer capacity Q_{max} (and hence diversion length L_D) for a sloping CBS subjected to continuous rainfall of constant intensity i provided an excellent match to the corresponding values from the FE results. This contrasted with the existing simplified method of Parent and Cabral (2006), which mis-predicted the suction profiles and, as a consequence, under-

predicted values of WSC in some cases and over-predicted values of Q_{max} (and hence L_D) in some cases. The development and numerical validation of the new simplified method of analysis for sloping CBSs subjected to continuous rainfall of constant intensity is a significant achievement, because this method can be easily used for hand-calculation or it could be implemented in simple commercial software (e.g. Excel or MATLAB), thus avoiding the need for expensive software and time-consuming FE analyses.

The results of FE analyses and corresponding simplified method predictions show that a sloping CBS with the finer layer (F.L) made of fine sand will have lower water storage capacity WSC but higher water transfer capacity Q_{max} than a sloping CBS with the F.L made of silty sand (i.e. a slightly finer material). WSC will decrease further and Q_{max} increase further if the F.L is made of medium sand (i.e. slightly coarser again). However, if the F.L is made of coarse sand (i.e. even coarser), Q_{max} begins to decrease as well as WSC i.e. there is no reason to use coarse sand for the F.L.

For a given choice of CBS materials, water storage capacity WSC increases with increasing thickness t_f of the F.L. However, water transfer capacity Q_{max} does not increase with t_f beyond a limiting thickness. This limiting thickness of F.L is only about 20 cm if the F.L is made of fine sand but is about 80 cm if the F.L is made of silty sand. For a given design of sloping CBS (i.e. a given combination of F.L material and F.L thickness), WSC increases slightly with increasing rainfall intensity i, but Q_{max} is almost independent of i.

A method was proposed for predicting approximate final steady state suction profiles on vertical cross-sections of a CBS in the upper part of a slope, at values of horizontal coordinate x less than the diversion length L_D. These predicted suction profiles were an excellent match to the corresponding results from the FE analyses. This led to a simplified method for predicting final steady state variations of water storage WS with x and water transfer Q_x with x for continuous rainfall of any constant intensity i. The results of these predictions ($WS{:}\,x$ and $Q_x{:}\,x$) were a good match to the corresponding results from the FE simulations.

For sloping CBSs subjected to continuous rainfall of constant intensity, wetting followed the same type of two-stage process as for a horizontal CBS. Significant

water transfer down the slope, within the lower part of the finer layer, only commences in the later part of the second stage of the wetting process.

For sloping CBSs, increased values of WSC and Q_{max} could be achieved by using multi-layered CBSs. The new simplified method of analysis, for predicting WSC and Q_{max}, was extended to multi-layered CBSs and successfully validated against numerical simulations.

9.1.3 Sloping CBSs subjected to intermittent or varying intensity rainfall

Thermo-hydraulic numerical simulations (with evaporation from the ground surface) and hydraulic numerical simulations (without evaporation) were performed for sloping CBSs subjected to various simple forms of intermittent or varying intensity rainfall, including rainfall of limited duration, cyclic rainfall patterns and extreme rainfall events. The numerical simulations also included modelling of retention hysteresis within the CBS materials, through use of the advanced hysteretic hydraulic constitutive model developed by Scarfone (2020) and Scarfone et al. (2020b). The results of the simulations provided important new insights into the behaviour of sloping CBSs subjected to intermittent or varying intensity rainfall.

Thermo-hydraulic numerical simulations indicated that, during rainfall, the rate of evaporation quickly reaches a steady state value, that is dependent on atmospheric conditions (atmospheric temperature, atmospheric relative humidity, net radiation, and wind speed) but is almost independent of rainfall intensity and materials of the CBS. Comparison of simulations with and without evaporation showed that, while rainfall is occurring, the effects of evaporation from the ground surface is simply to reduce the effective rainfall infiltration rate by an amount equal to the steady state evaporation rate. Hence, the behaviour of sloping CBSs during rainfall can be analysed without explicitly including evaporation in the analysis, by using an effective rainfall infiltration rate, given by subtracting the steady state evaporation rate from the real rainfall infiltration rate.

Numerical simulations with and without retention hysteresis showed that hysteresis in the retention behaviour of the CBS materials is relatively unimportant to the behaviour of a sloping CBS during an extreme rainfall event. For an extreme rainfall event, it will be acceptable (and slightly conservative) to ignore retention hysteresis and assume that the soil state within the CBS is always on the main wetting SWRC.

Rainfall of constant effective intensity i will, if sustained for sufficient time, cause breakthrough at all values of horizontal coordinate x greater than the diversion length L_D corresponding to the effective rainfall intensity i. The time-lag $t_{lag,1}$ to this occurrence of breakthrough is associated with the time to fill the F.L from the initial value of water stored WS to the value of water storage capacity WSC corresponding to the current effective rainfall intensity i. Once breakthrough occurs, the interface flow velocity q_i is equal to the effective rainfall intensity i.

If breakthrough has already occurred at a particular value of x and the rainfall intensity increases, there will be a time-lag $t_{lag,2}$ before the interface flow velocity q_i increases to the new (higher) value of effective rainfall intensity. This time-lag is associated with the time to fill the F.L from the value of water storage capacity WSC corresponding to the previous effective rainfall intensity to the slightly higher value of WSC corresponding to new (higher) effective rainfall intensity.

If breakthrough has already occurred at a particular value of x and the rainfall intensity decreases, the value of interface flow velocity q_i decreases immediately (with no time-lag) to the new (lower) effective rainfall intensity. If the new (lower) effective rainfall intensity is insufficient to maintain breakthrough indefinitely at this value of x (i.e. if x is less than the value of diversion length L_D corresponding to the new effective rainfall intensity), breakthrough ceases (q_i falls to zero) after a time-lag $t_{lag,3}$.

If rainfall ceases, restoration of water storage capacity within the F.L occurs gradually, as a consequence of evaporation from the ground surface and water transfer down the slope in the lower part of the F.L. If the F.L is made of fine sand, both of these processes slow down significantly within a few hours of rainfall

ceasing. In contrast, if the F.L is made of silty sand, the process of evaporation from the ground surface will continue at an unreduced rate for many days or weeks. Hence, restoration of water storage capacity during dry periods is more effective if the F.L is made of silty sand than if the F.L is made of fine sand.

9.1.4 Development of a simplified method of analysis for extreme rainfall events

A simplified method of analysis has been developed for sloping CBSs subjected to extreme rainfall events. The simplified method allows calculation of the variation with time of interface flow velocity q_i at any value of horizontal coordinate x for any specified extreme rainfall event (specified variation of effective rainfall intensity i with time). The influence of evaporation from the ground surface is accounted for in the method by using effective rainfall intensities (after subtracting the steady state evaporation rate during rainfall from the real rainfall infiltration rate). A key starting point for the method is calculation of final steady state variations of water storage WS with x and water transfer Q_x with x, for each of the effective rainfall intensities involved in the extreme rainfall event, if each of these effective rainfall intensities was continued indefinitely (see Section 9.1.2). Retention hysteresis of the CBS materials is ignored within the method, by assuming that the soil state is on the main wetting SWRC throughout. The simplified method of analysis for extreme rainfall events employs a method of slices. The rules employed within the method of slices assume that breakthrough within an individual vertical slice of the CBS occurs only if two conditions are satisfied: firstly, that the water stored WS at that value of x must be at least equal to the value of water storage capacity WSC corresponding to the current effective rainfall intensity i; and secondly that the water transfer Q_x at that value of x must be equal to the water transfer capacity Q_{max}.

Numerical validation of the proposed new simplified method of analysis for extreme rainfall events was performed by comparison with corresponding FE simulations. In all cases, there was an excellent match (in terms of the predicted variation of q_i with time at different values of x) between the predictions of the simplified method and the FE results. Time-lags $t_{lag,1}$ and $t_{lag,2}$, prior to the start of breakthrough or prior to an increase of interface flow velocity q_i, were slightly

under-predicted. Values of time-lag $t_{lag,3}$, before breakthrough ceased, were more significantly over-predicted (as a consequence of ignoring retention hysteresis). These errors in prediction of the various time-lags, mean that the new simplified method of analysis for extreme rainfall events is slightly conservative.

The rules followed during application of the simplified method are sufficient provided that each effective rainfall intensity within the extreme rainfall event (including the antecedent rain) is applied for sufficient duration to reach final steady state under that effective rainfall intensity at all values of x. Further complexity occurs if the extreme rainfall event involves very short durations of different rainfall intensities, and the simplified method has not yet been developed to cope with this issue (see Section 9.2).

9.1.5 Suggestions for practical design of sloping CBSs

Chapter 8 of this thesis covered a number of issues related to the practical design of sloping CBSs and various conclusions arose from this work.

In terms of selection of materials of a CBS, the majority of the thesis investigated the use of either silty sand or fine sand for the finer layer, because these represent the range of materials conventionally employed for the F.L in horizontal CBSs. However, for sloping CBSs, it was shown that, silty sand is likely to be a suitable material for the F.L only in relatively dry climates (with occasional extreme rainfall events), because of the low water transfer capacity (the high water storage capacity is only useful if it is not already largely filled by sustained antecedent rain). In contrast, sloping CBSs with the F.L made of fine sand, with their higher water transfer capacity (but lower water storage capacity), are more effective under a wider range of climate conditions. The work also suggests that medium sand (slighter coarser again) would be worthy of further investigation as a possible material for the F.L of sloping CBSs, because the water transfer capacity is even higher. The thickness of the F.L can be as low as 20 cm if the F.L is made of fine sand (or medium sand) but should be significantly greater if it is made of silty sand.

Having selected the material of the F.L, the material of the coarser layer (C.L) should be selected as coarse as possible while still satisfying standard filter rules at the interface with F.L. The thickness of the C.L can be as low as 15 cm.

A simple expression was derived for the factor of safety of a slope covered by a CBS, on the assumption that the CBS was successful in limiting breakthrough, so that the critical failure surface remained within the CBS, rather than extending into the underlying soil. This simple expression for factor of safety is based on an infinite slope analysis and assumes that the failure surface occurs within the F.L of the CBS, at the interface with the C.L, with a suction value equal to the critical breakthrough value (the bulk water continuity value of the C.L) along the entire length of this interface. Comparison with numerical modelling results from Scarfone (2020) and Scarfone et al. (2022), involving thermo-hydraulic FE modelling and associated limit analysis for long-term real meteorological conditions, indicated that the proposed simple expression for factor of safety was slightly conservative in those extreme rainfall events where limited breakthrough occurred within the CBS but could be very conservative in cases where no breakthrough occurred. The simple expression for factor of safety should be checked early in the design process of a sloping CBS, to confirm whether it is worth progressing with analysis of the CBS or whether the CBS materials need to be adjusted or alternative solutions explored for maintaining slope stability.

If the simple expression indicates that the factor of safety of a sloping CBS would be adequate if it can successfully limit breakthrough, so that the critical failure surface remains within the CBS, the new simplified method of analysis for extreme rainfall events (see Section 9.1.4) can then be applied. In applying this method, a crucial aspect will be the selection of appropriate design extreme rainfall events for the slope location (with appropriate very long return periods, after allowing for climate change effects). Important outputs from the simplified method of analysis will be plots of the variation of total water flow across the interface per unit plan area with horizontal coordinate x for each design extreme rainfall event. These plots can be used to assess whether longitudinal collector drains are required within the sloping CBS and, if so, what spacing is required for these collector drains.

9.2 Recommendations for future work

This final section discusses ideas and suggestions for further research work relating to the topics addressed in this thesis.

1. Further investigation (numerical modelling and use of the simplified method of analysis for extreme rainfall events) would be useful to examine under what climate conditions medium sand would be more suitable than fine sand for the material of the F.L of sloping CBSs

2. For all future numerical modelling, appropriate mesh refinement studies, should be performed, to investigate the level of mesh refinement required before further refinement causes no further change in results. It is likely that finer meshes are required at the base of the F.L for fine sand, medium sand and coarse sand. It would be useful to investigate whether greater mesh refinement at the base of the F.L removes some of small unexpected variations of interface flow velocity q_i seen in the simulations involving fine sand (see, for example, Figures 5-10a and 5-10b) and improved the mis-match between FE results and predictions of the new simplified method for values of water transfer capacity Q_{max} when the F.L was made of medium sand or coarse sand (see Figure 5-24).

3. The simplified method of analysis for extreme rainfall events currently requires considerable manual intervention in Excel worksheets. It would be useful to code the method (e.g. in MATLAB) to avoid the need for this type of laborious manual intervention and to a provide a user-friendly interface for input and output. This would be desirable, to allow practical application, in a commercial environment, of the simplified method of analysis of extreme rainfall events.

4. It would be useful to investigate the influence of slice width Δx in the method of slices used as part of the simplified method for extreme rainfall events (see Section 7.1.4), in order to provide recommendations on how to select appropriate slice width.

5. The simplified method of analysis for extreme rainfall events can currently only deal with situations where each rainfall intensity (including the antecedent rain) is sustained for sufficient duration to reach steady state under that effective rainfall intensity. It would be useful to develop the method to also apply to situations where steady state is not reached under each rainfall intensity. Initial brief attempts at this were unsuccessful, and a more sustained investigation is required.

6. Further investigation is required of the influence of the atmospheric conditions applicable during extreme rainfall events on the steady state evaporation rate during rainfall (this steady state evaporation rate during rainfall needs to be subtracted from the real rainfall intensity to give the effective rainfall intensity, for use in the simplified method of analysis of extreme rainfall events). In particular, the thermo-hydraulic numerical modelling presented in Chapter 6 assumed annual average values of atmospheric temperature T_a, atmospheric relative humidity R_{ha}, net radiation R_n and wind speed v_a, whereas it would be more appropriate to use values of T_a, R_{ha}, R_n and v_a corresponding to periods of extreme rainfall in determining an appropriate steady state evaporation rate during rainfall. For example, the value of atmospheric relative humidity R_{ha} during an extreme rainfall event would typically be significantly higher than the average annual value (approaching R_{ha} = 1). Also, the value of net radiation R_n during an extreme rainfall event would typically be significantly lower than the average annual value, because of high values of cloud cover during extreme rainfall events. A lower value of net radiation R_n would lead to lower values of ground surface temperature. A higher value of atmospheric relative humidity and a lower value of net radiation would therefore both lead to a lower estimate of the steady state evaporation rate during rainfall.

7. The work presented by Scarfone (2020) and Scarfone et al. (2022) suggests that it is unnecessarily conservative to design a CBS to completely prevent breakthrough under the most extreme foreseeable rainfall event, because the critical failure surface will remain within the CBS even if a limited amount of breakthrough occurs. It is however unclear what constitutes an

acceptable limited amount of breakthrough i.e. how much breakthrough can be allowed before the critical failure surface extends into the underlying soil of the slope. This issue requires further investigation.

8. Chapter 5 showed that multi-layered sloping CBSs could achieve greater values of both water storage capacity WSC and water transfer capacity Q_{max} than conventional sloping CBSs. The simplified method of analysis of sloping CBSs subjected to extreme rainfall events should be extended to multi-layered sloping CBSs, with appropriate numerical validation.

9. The proposed simplified methods of analysis for sloping CBSs (the method for continuous rainfall of constant intensity and the method for extreme rainfall events) should be validated against slope test data in the laboratory and in the field. Existing test data from laboratory slopes covered by CBSs (e.g. Zhan et al. (2014); Qian et al. (2010)) and from monitoring of field slopes covered by CBSs (e.g. Kampf and Montenegro (1997); Rahardjo (2015); Zhang et al. (2016)) should be investigated first, but it is possible that full physical validation will require new lab or field data from purpose-designed slope testing programmes.

10. Further investigation is required on whether any of the simplified methods developed in the thesis would require modifications to account for the role of any vegetation cover system employed to provide surface protection of sloping CBSs. In particular, it would be useful to see how vegetation (in combination with the atmospheric conditions) controls the steady state rate of evapo-transpiration under rainfall, which needs to be subtracted from the real rainfall intensity to give the effective rainfall intensity, for use in the simplified method of analysis for extreme rainfall events. Information on the influence of different types of vegetation (in combination with different atmospheric conditions) on the steady state evapo-transpiration rate during rainfall may already be available from the existing literature (e.g. Tang et al., 2018; Pedone et al., 2022) or may require new research.

11. It would be useful to investigate the feasibility of developing design charts, to represent the output of the simplified method of analysis for extreme

rainfall events in a fashion that was easy to use by practising geotechnical engineers (see Section 8.5).

Appendix A Additional results for horizontal CBSs subjected to continuous rainfall of constant intensity

This appendix shows the final steady state profiles of suction and degree of saturation from the FE simulations and the corresponding predictions of the simplified method for the remaining cases of horizontal CBSs subjected to continuous rainfall of constant intensity referred to in Section 4.3.

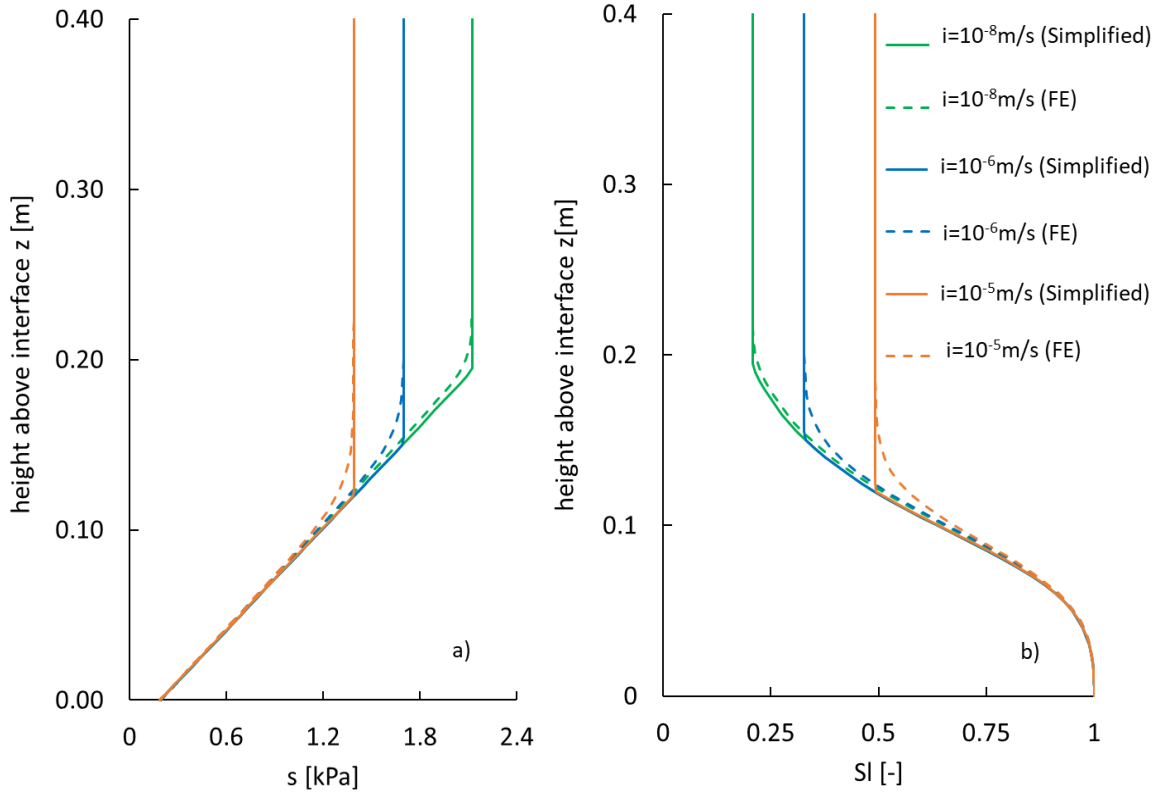

Figure A- 1 Comparison between simplified method and FE numerical results at final steady state a) suction profiles b) degree of saturation profiles (β=35°, FSGV, t_f=0.40m)

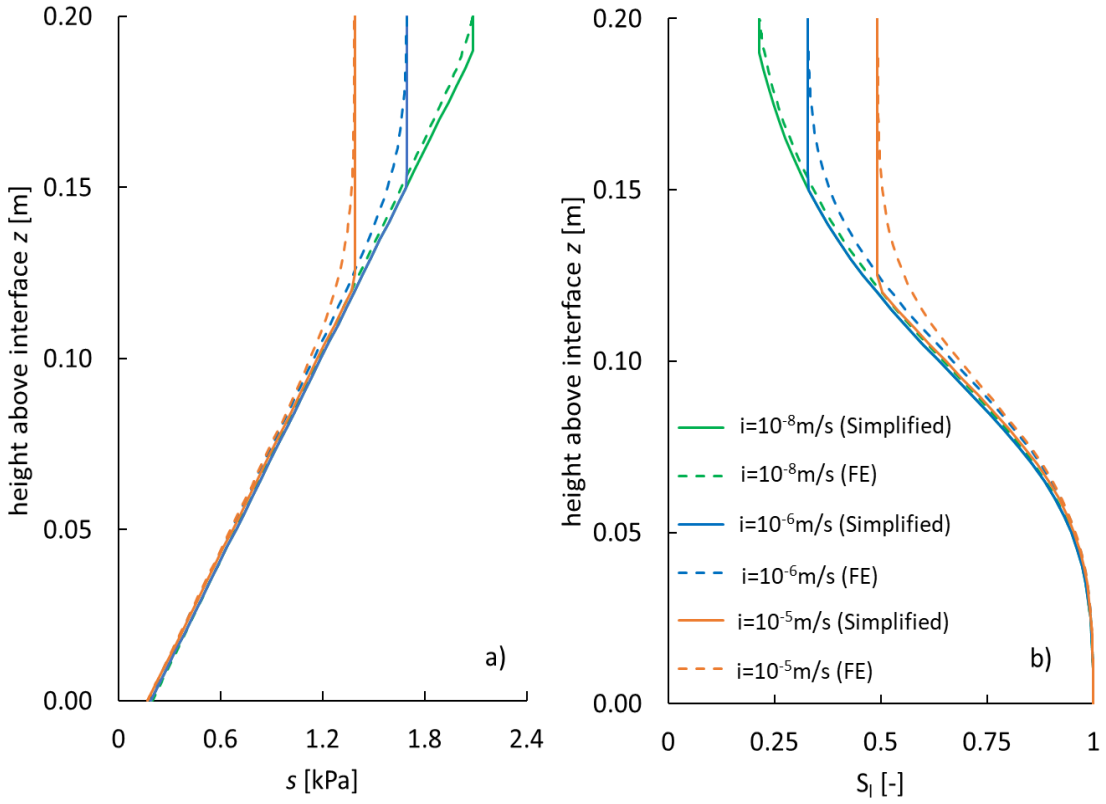

Figure A- 2 Comparison between simplified method and FE numerical results at final steady state a) suction profiles b) degree of saturation profiles (β=35°, FSGV, t_f=0.20m)

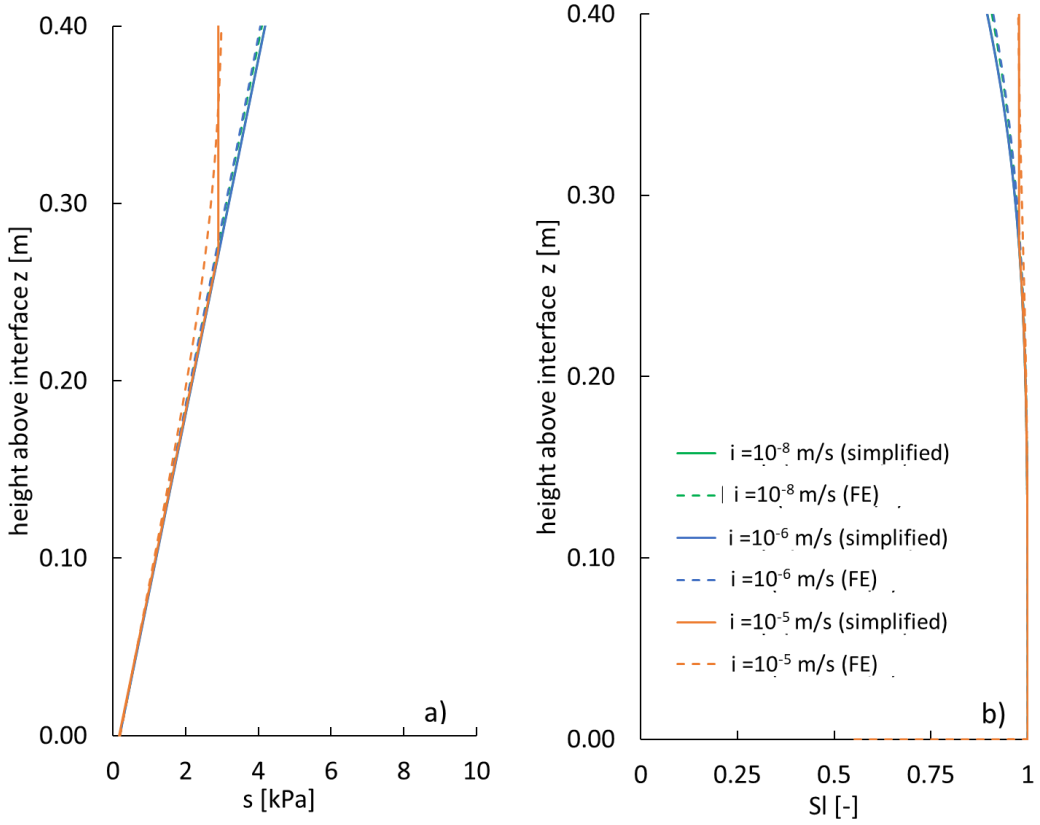

Figure A- 3 Comparison between simplified method and FE numerical results at steady state a) suction profiles b) degree of saturation profiles (β=35°, SSGV, t_f=0.40m)

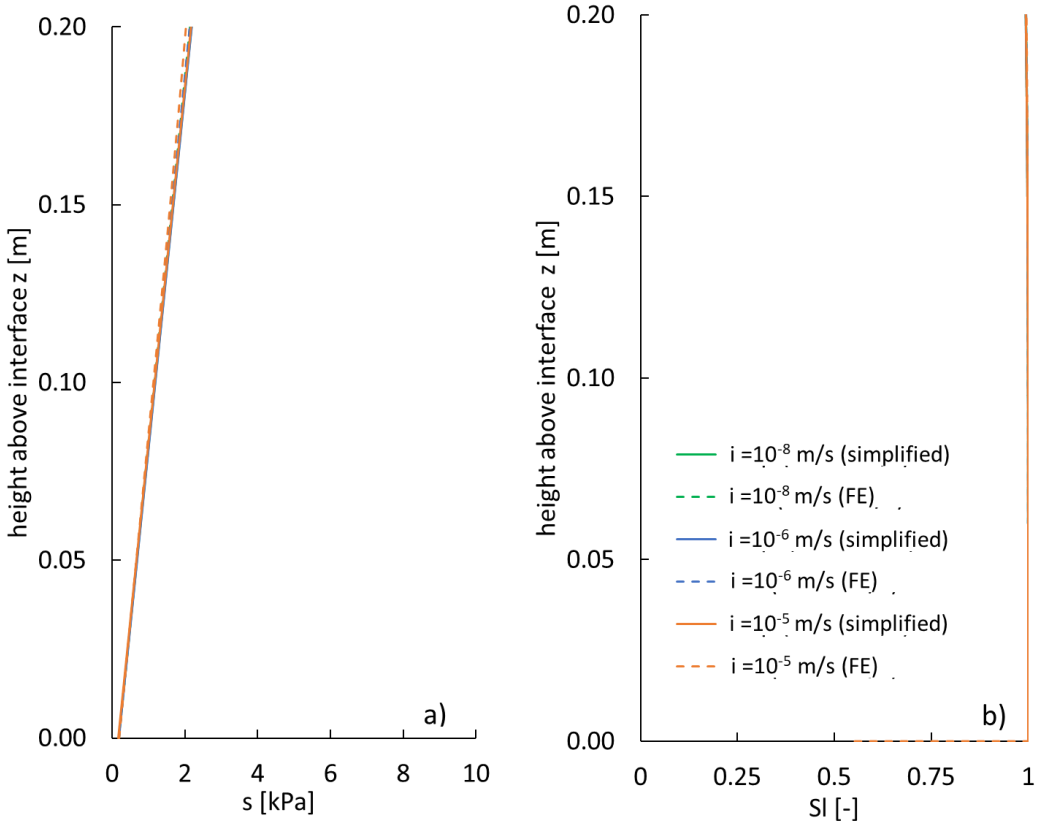

Figure A- 4 Comparison between simplified method and FE numerical results at final steady state a) suction profiles b) degree of saturation profiles (β=35°, SSGV, t_f=0.20m)

Appendix B Flow direction in lower part of finer layer for $x \geq L_D$

This appendix justifies the assumption made within the new simplified method of analysis for sloping CBSs developed in Section 5.2 that, at final steady state, the flow direction in the lower part of the F.L is approximately parallel to the interface with the C.L even at values of x equal to or greater than the diversion length (i.e. that the component of flow velocity perpendicular to the interface is small compared to the component parallel to the interface).

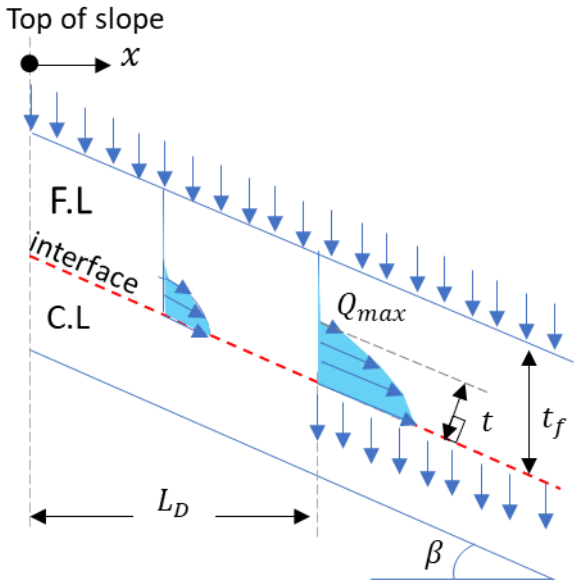

Figure B- 1 Schematic of liquid water flow within sloping CBS

At and beyond the diversion length ($x \geq L_D$), the mean value of tangential flow velocity (parallel to the interface) $\bar{q}_t$ within the bottom part of the finer layer, where water transfer is occurring, given by:

$$\bar{q}_t = (Q_{max}/t) \quad \text{B-1}$$

where t is the thickness of the lower part of the finer layer over which water transfer is occurring (measured perpendicular to the interface) as shown in Figure B-1. But $Q_{max} = L_D i$ (see Equation 5-2) and hence:

$$\bar{q}_t = L_D i/t \quad \text{B-2}$$

The normal flow velocity (perpendicular to the interface) q_n is the breakthrough flow rate per unit area of the interface (see Equation 5-32), given by:

$$q_n = q_i \cos\beta = i \cos\beta \qquad \text{B-3}$$

The ratio of mean tangential flow velocity to normal flow velocity within this zone is then given by:

$$\frac{\bar{q}_t}{q_n} = \frac{(L_D i/t)}{(i \cos\beta)} = \frac{L_D}{t \cos\beta} \qquad \text{B-4}$$

Therefore, if L_D/t is very large, the tangential flow velocity is much higher than normal velocity, i.e. the flow in this zone is approximately parallel to the interface even when some breakthrough flow is occurring across the interface.

Appendix C Additional comparison of numerical results between Model Type A and Model Type B

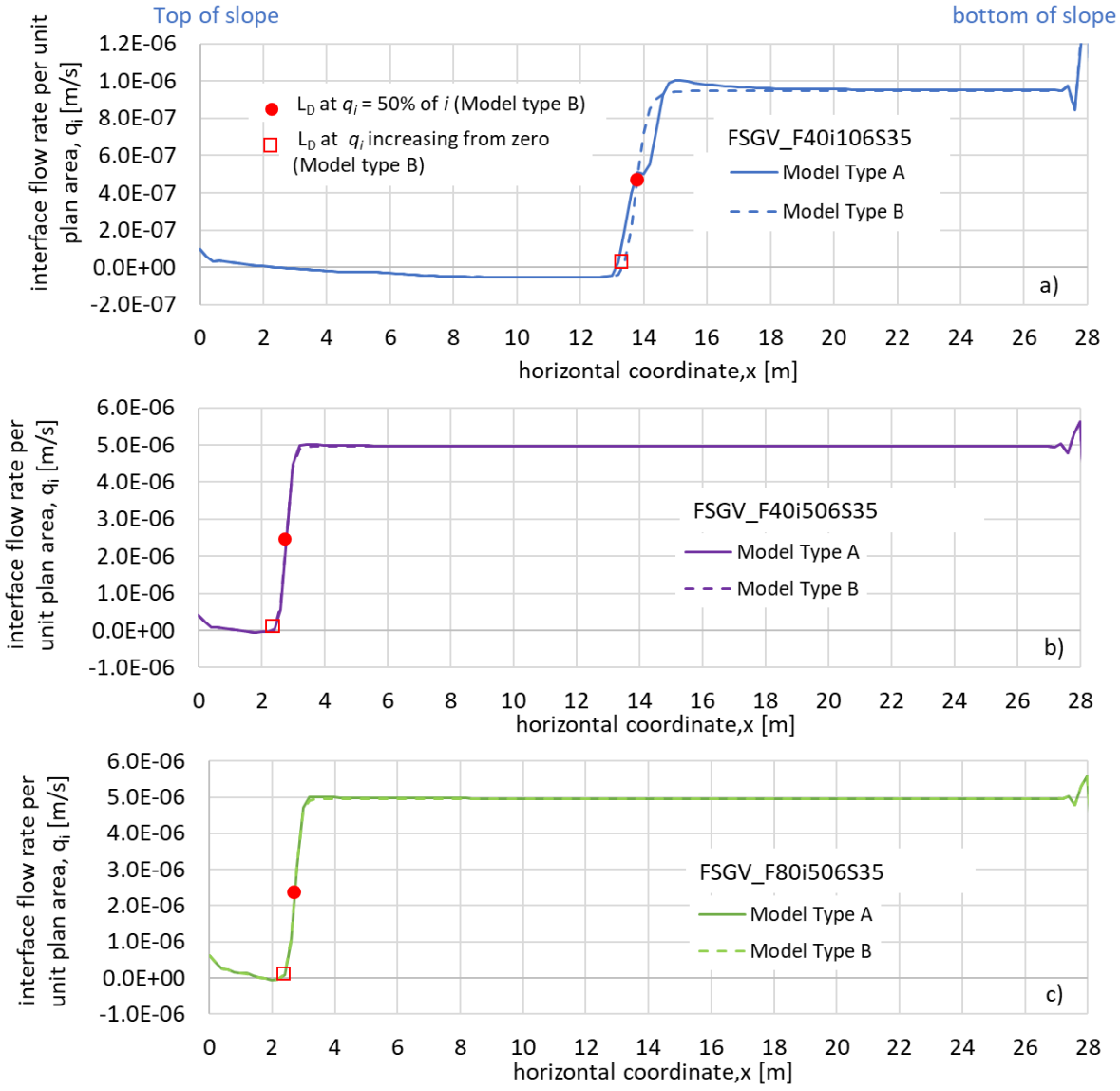

Figure C- 1 Final steady state interface flow rate per unit plan area for Model types A and B with FSGV a) β = 35°, t_f = 40 cm, i = 10^{-6} m/s; b)) β = 35°, t_f = 40 cm, i = 5x10^{-6} m/s; c) β = 35°, t_f = 80 cm, i = 5x10^{-6} m/s

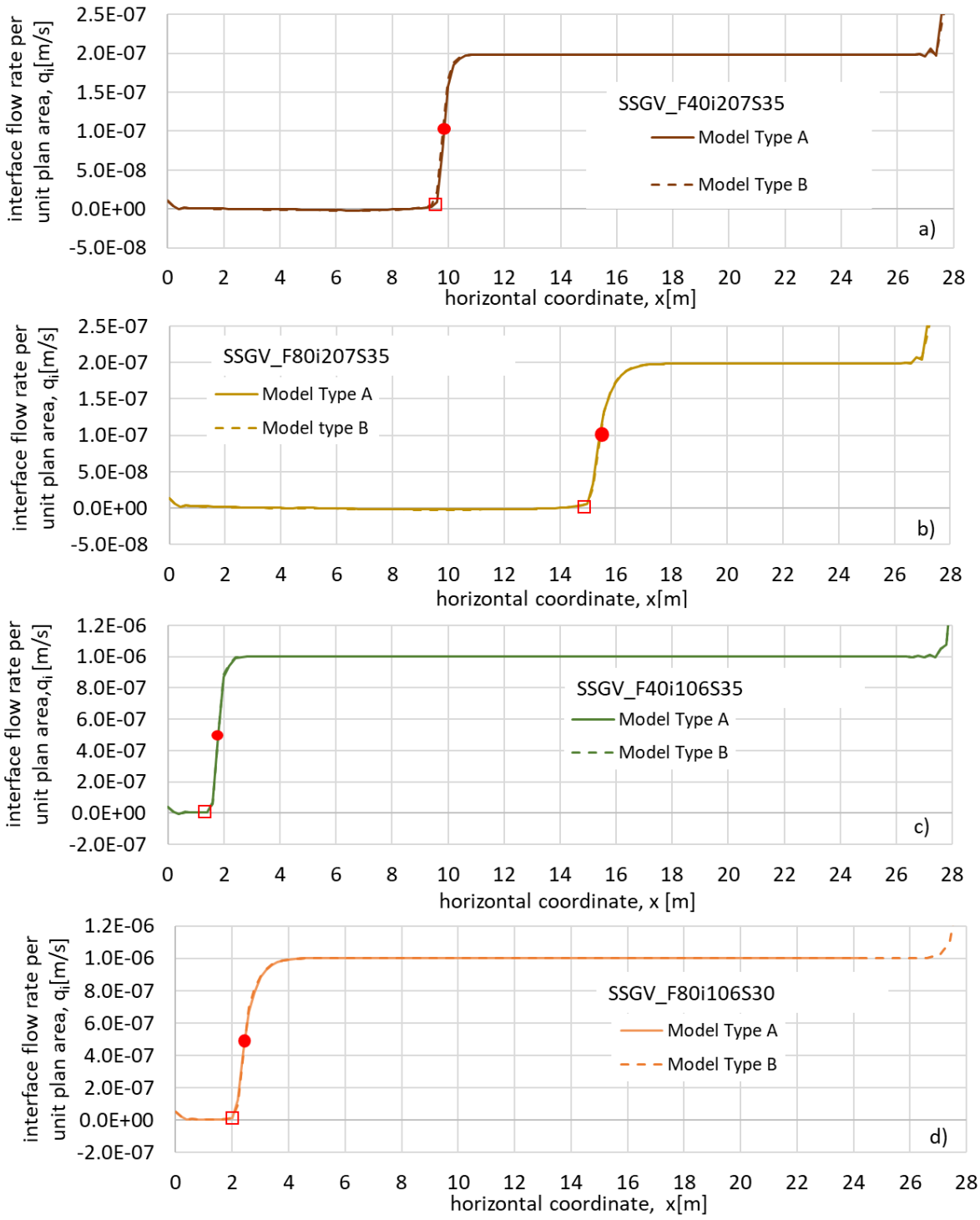

Figure C-2 Final steady state interface flow rate per unit plan area for Model types A and B with SSGV a) β = 35°, t_f = 40 cm, i = 2x10^{-7} m/s; b) β = 35°, t_f = 80 cm, i = 2x10^{-7} m/s; c) β = 35° t_f = 40 cm, i = 10^{-6} m/s; d) β $= 30°, t_f$ = 80 cm, i = 10^{-6} m/s

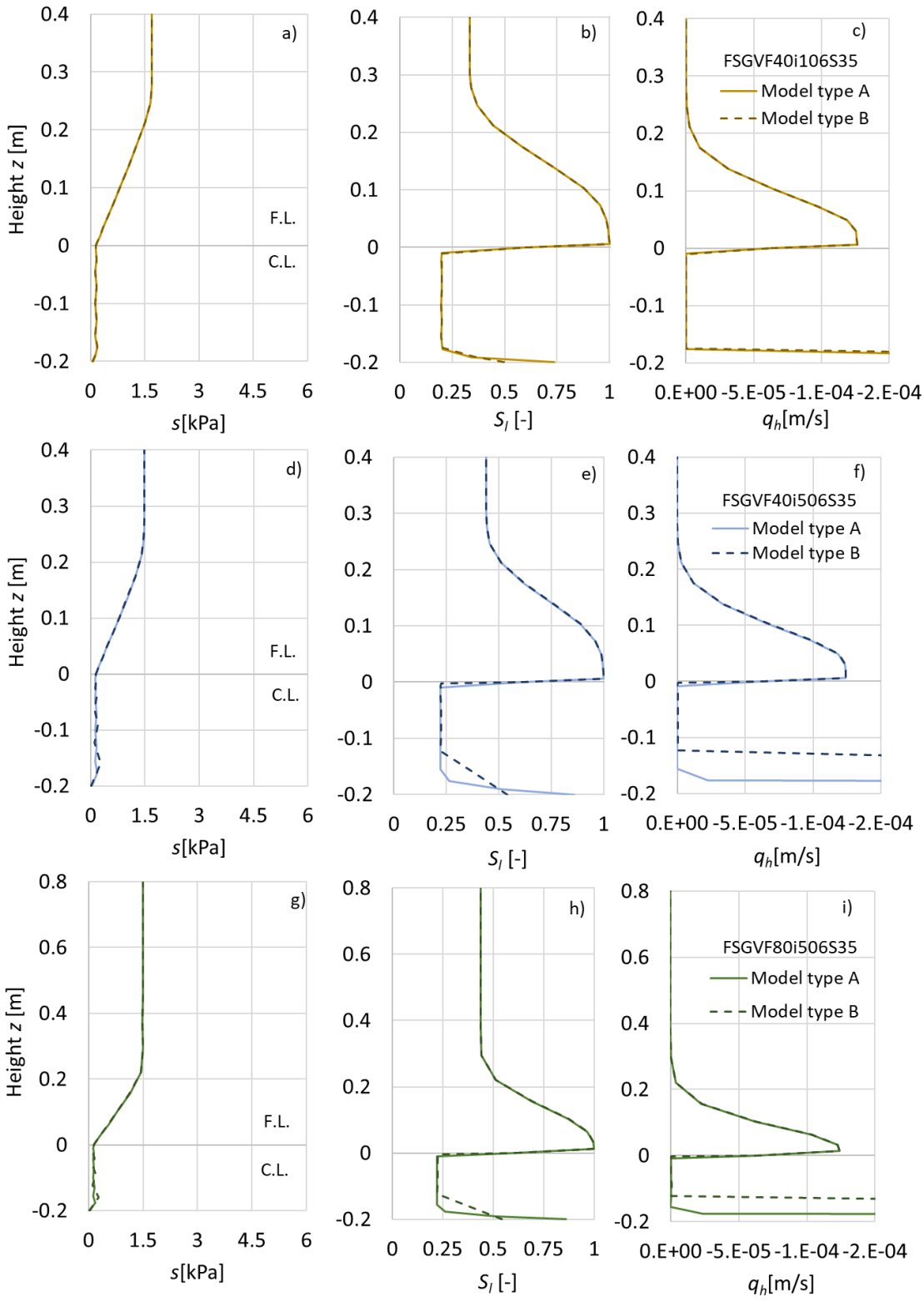

Figure C- 3 Final steady state profiles of suction, degree of saturation and horizontal liquid water velocity at x ≈ L_D for Model types A and B with FSGV: a)b)c) β = 35°, t_f = 80 cm and i = 5x10^{-6} m/s; d) e) f) β = 35°, t_f = 40 cm and i = 10^{-6} m/s; g) h) i) $\beta = 35°$, t_f = 40 cm and i = 5x10^{-6} m/s

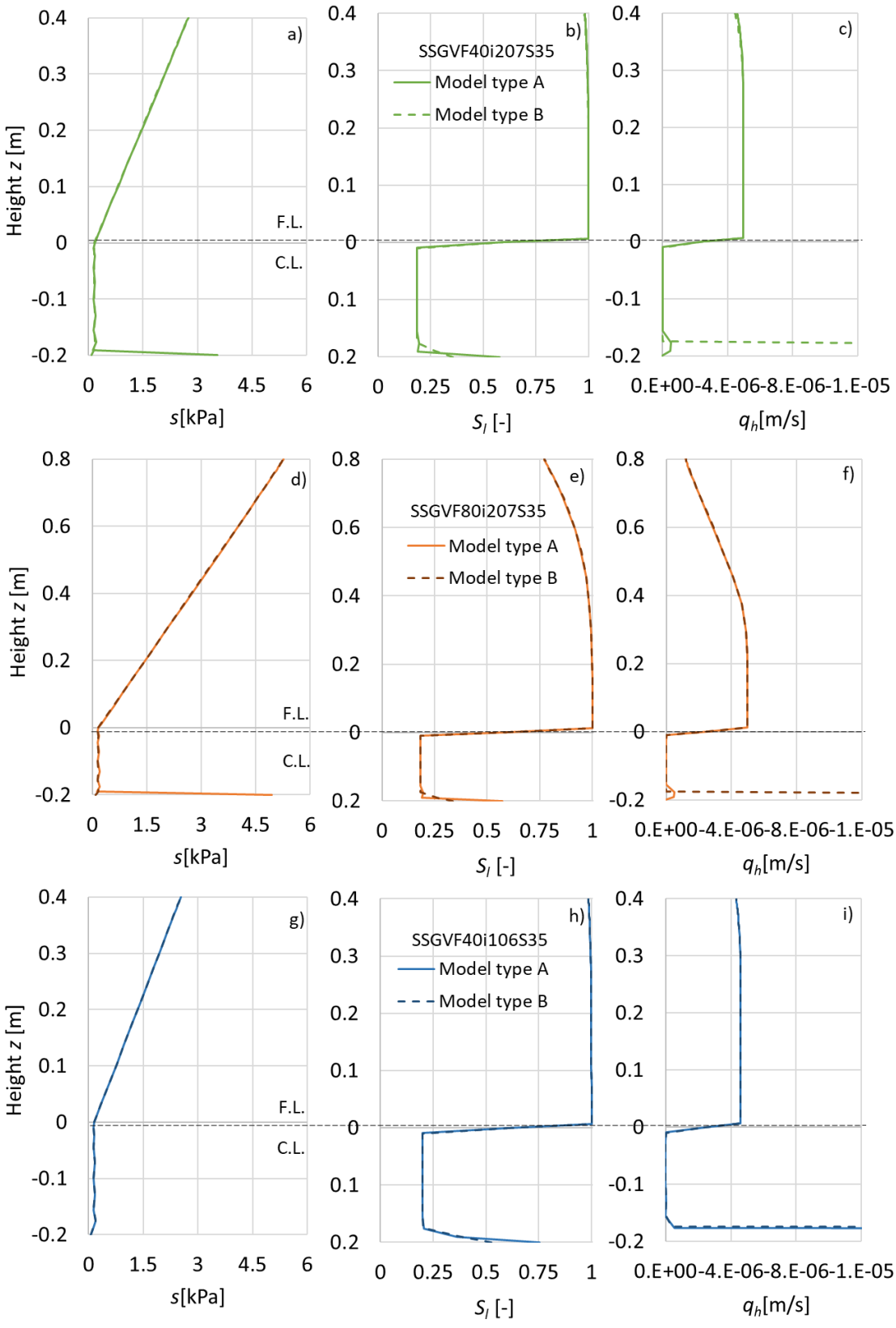
a)
b)
c)
SSGVF40i207S35
Model type A
Model type B
d)
e)
f)
SSGVF80i207S35
Model type A
Model type B
g)
h)
i)
SSGVF40i106S35
Model type A
Model type B
Height z [m]
F.L.
C.L.
s[kPa]
S_l [-]
q_h[m/s]
0.E+00-4.E-06-8.E-06-1.E-05

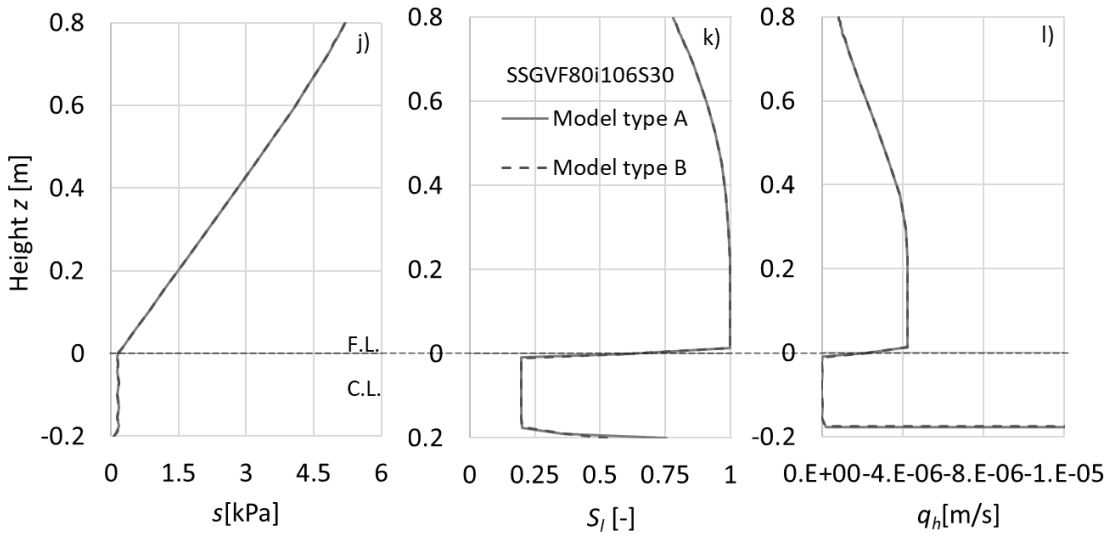

Figure C- 4 Final steady state profiles of suction, degree of saturation and horizontal liquid water velocity at x ≈ L_D for Model types A and B with SSGV: a) b) c) β=35°, t_f= 40 cm and i = 2x10^{-7} m/s; d) e) f) β=35°, t_f= 80 cm and i = 2x10^{-7} m/s; g) h) i) β=35°, t_f= 40 cm and i = 10^{-6} m/s; j) k) l) β=30° t_f= 80 cm and i = 10^{-6} m/s

Appendix D Simplified method of analysis for extreme rainfall events: example Excel worksheet for method of slices

Tables D-1 to D-4 show the detailed calculation of variation with time of interface flow velocity q_i for extreme rainfall event E1 applied to a sloping CBS with the F.L made of fine sand (β = 35°, FSGV, t_f= 40 cm). Table D-1 covers t = 10 days to t = 11 days ($i = i_b = 10^{-6}$ m/s, having increased from $i = i_a = 2\text{x}10^{-7}$ m/s at t = 10 days). Table D-2 covers t = 11 days to t = 12 days ($i = i_c = 2\text{x}10^{-6}$ m/s), Table D-3 covers t = 12 days to t = 13 days ($i = i_b = 10^{-6}$m/s) and Table D-4 covers t = 13 days to t = 14 days ($i = i_a = 2\text{x}10^{-7}$ m/s).

Table D- 1 Interface flow rates calculated by simplified method between t = 10 days and 11 days (after rise in rainfall intensity)

t = 10-11 days after rise in rainfall intensity				i_a[m/s]=	i_b[m/s]=	
Slice width[m] 2.11				2.00E-07	1.00E-06	
Slice no. 1		L_D[m]		63.30	12.66	
$WS_{x,a}$ at steady state[m] 0.0485		WSC[m]		0.0896	0.0937	
$WS_{x,b}$ at steady state[m] 0.0625		Qmax[m^2/s]		1.266E-05	1.266E-05	
time	x=0m	WS	dQx/dx	qi	dWS/dt	x=2.11m
[$x10^3$ s]	Q_x [$x10^{-6}m^2$/s]	[m]	[$x10^{-6}$m/s]	[$x10^{-6}$m/s]	[$x10^{-6}$m/s]	Q_x [$x10^{-6}m^2$/s]
0	0	0.0485	0.20	0.00	0.80	0.422
17.42	0	0.0625	1.00	0.00	0.00	2.110

t = 10-11 days after rise in rainfall intensity				i_a[m/s]=	i_b[m/s]=	
Slice width[m] 2.11				2.00E-07	1.00E-06	
Slice no. 2		L_D[m]		63.30	12.66	
$WS_{x,a}$ at steady state[m] 0.0527		WSC[m]		0.0896	0.0937	
$WS_{x,b}$ at steady state[m] 0.0706		Qmax[m^2/s]		1.266E-05	1.266E-05	
time	x=2.11m	WS	dQx/dx	qi	dWS/dt	x=4.22m
[$x10^3$ s]	Q_x [$x10^{-6}m^2$/s]	[m]	[$x10^{-6}$m/s]	[$x10^{-6}$m/s]	[$x10^{-6}$m/s]	Q_x [$x10^{-6}m^2$/s]
0	0.422	0.0527	0.20	0.00	0.80	0.84
17.42	2.11	0.0667	0.20	0.00	0.80	2.53
22.36	2.11	0.0706	1.00	0.00	0.00	4.22

t = 10-11 days after rise in rainfall intensity				i_a[m/s]=	i_b[m/s]=	
Slice width[m] 2.11				2.00E-07	1.00E-06	
Slice no. 3		L_D[m]		63.30	12.66	
$WS_{x,a}$ at steady state[m] 0.0556		WSC[m]		0.0896	0.0937	
$WS_{x,b}$ at steady state[m] 0.0766		Qmax[m^2/s]		1.266E-05	1.266E-05	
time	x=4.22m	WS	dQx/dx	qi	dWS/dt	x=6.33m
[$x10^3$ s]	Q_x [$x10^{-6}m^2$/s]	[m]	[$x10^{-6}$m/s]	[$x10^{-6}$m/s]	[$x10^{-6}$m/s]	Q_x [$x10^{-6}m^2$/s]
0	0.84	0.0556	0.20	0.00	0.80	1.27
17.42	2.53	0.0695	0.20	0.00	0.80	2.95
22.36	4.22	0.0735	0.20	0.00	0.80	4.64
26.32	4.22	0.0766	1.00	0.00	0.00	6.33

t = 10-11 days after rise in rainfall intensity				i_a[m/s]=	i_b[m/s]=	
Slice width[m] 2.11				2.00E-07	1.00E-06	
Slice no. 4		L_D[m]		63.30	12.66	
$WS_{x,a}$ at steady state[m] 0.0578		WSC[m]		0.0896	0.0937	
$WS_{x,b}$ at steady state[m] 0.0818		Q_{max}[m^2/s]		1.266E-05	1.266E-05	
time	x=6.33m	WS	dQx/dx	qi	dWS/dt	x=8.44m
[$x10^3$ s]	Q_x [$x10^{-6}m^2$/s]	[m]	[$x10^{-6}$m/s]	[$x10^{-6}$m/s]	[$x10^{-6}$m/s]	Q_x [$x10^{-6}m^2$/s]
0	1.27	0.0578	0.20	0.00	0.80	1.69
17.42	2.95	0.0718	0.20	0.00	0.80	3.38
22.36	4.64	0.0757	0.20	0.00	0.80	5.06
26.32	6.33	0.0789	0.20	0.00	0.80	6.75
30.01	6.33	0.0818	1.00	0.00	0.00	8.44

t = 10-11 days after rise in rainfall intensity				i_a[m/s]=	i_b[m/s]=	
Slice width[m] 2.11				2.00E-07	1.00E-06	
Slice no. 5		L_D[m]		63.30	12.66	
$WS_{x,a}$ at steady state[m] 0.0597		WSC[m]		0.0896	0.0937	
$WS_{x,b}$ at steady state[m] 0.0866		Q_{max}[m^2/s]		1.266E-05	1.266E-05	
time	x=8.44m	WS	dQx/dx	qi	dWS/dt	x=10.55m
[$x10^3$ s]	Q_x [$x10^{-6}m^2$/s]	[m]	[$x10^{-6}$m/s]	[$x10^{-6}$m/s]	[$x10^{-6}$m/s]	Q_x [$x10^{-6}m^2$/s]
0.00	1.69	0.0597	0.20	0.00	0.80	2.11
17.42	3.38	0.0737	0.20	0.00	0.80	3.80
22.36	5.06	0.0776	0.20	0.00	0.80	5.49
26.32	6.75	0.0808	0.20	0.00	0.80	7.17
30.01	8.44	0.0837	0.20	0.00	0.80	8.86
33.63	8.44	0.0866	1.00	0.00	0.00	10.55

t = 10-11 days after rise in rainfall intensity				i_a[m/s]=	i_b[m/s]=	
Slice width[m] 2.11				2.00E-07	1.00E-06	
Slice no. 6		L_D[m]		63.30	12.66	
$WS_{x,a}$ at steady state[m] 0.0615		WSC[m]		0.0896	0.0937	
$WS_{x,b}$ at steady state[m] 0.0913		Q_{max}[m^2/s]		1.266E-05	1.266E-05	
time	x=10.55m	WS	dQx/dx	qi	dWS/dt	x=12.66m
[$x10^3$ s]	Q_x [$x10^{-6}m^2$/s]	[m]	[$x10^{-6}$m/s]	[$x10^{-6}$m/s]	[$x10^{-6}$m/s]	Q_x [$x10^{-6}m^2$/s]
0	2.11	0.0615	0.20	0.00	0.80	2.53
17.42	3.80	0.0754	0.20	0.00	0.80	4.22
22.36	5.49	0.0794	0.20	0.00	0.80	5.91
26.32	7.17	0.0825	0.20	0.00	0.80	7.60
30.01	8.86	0.0855	0.20	0.00	0.80	9.28
33.63	10.55	0.0884	0.20	0.00	0.80	10.97
37.32	10.55	0.0913	1.00	0.00	0.00	12.66

Table D-1 Interface flow rates calculated by simplified method between t = 10 days and 11 days (after rise in rainfall intensity) (continued)

t = 10-11 days after rise in rainfall intensity				i_a[m/s]=	i_b[m/s]=	
Slice width[m]	2.11			2.00E-07	1.00E-06	
Slice no.	7	L_D[m]		63.30	12.66	
$WS_{x,a}$ at steady state[m]	0.0631	WSC[m]		0.0896	0.0937	
WSC_b at steady state[m]	0.0937	Q_{max}[m^2/s]		1.266E-05	1.266E-05	
time	x=12.66m	WS	dQx/dx	q_i	dWS/dt	x=14.77m
[$x10^3$ s]	Q_x [$x10^{-6}m^2$/s]	[m]	[$x10^{-6}$m/s]	[$x10^{-6}$m/s]	[$x10^{-6}$m/s]	Q_x [$x10^{-6}m^2$/s]
0	2.53	0.0631	0.20	0.00	0.80	2.95
17.42	4.22	0.0770	0.20	0.00	0.80	4.64
22.36	5.91	0.0810	0.20	0.00	0.80	6.33
26.32	7.60	0.0841	0.20	0.00	0.80	8.02
30.01	9.28	0.0871	0.20	0.00	0.80	9.71
33.63	10.97	0.0900	0.20	0.00	0.80	11.39
37.32	12.66	0.0929	0.00	0.00	1.00	12.66
38.06	12.66	0.0937	0.00	1.00	0.00	12.66
		intermediate phase II				

t = 10-11 days after rise in rainfall intensity				i_a[m/s]=	i_b[m/s]=	
Slice width[m]	2.11			2.00E-07	1.00E-06	
Slice no.	8	L_D[m]		63.30	12.66	
$WS_{x,a}$ at steady state[m]	0.0646	WSC[m]		0.0896	0.0937	
WSC_b at steady state[m]	0.0937	Q_{max}[m^2/s]		1.266E-05	1.266E-05	
time	x=14.77m	WS	dQx/dx	q_i	dWS/dt	x=16.88m
[$x10^3$ s]	Q_x [$x10^{-6}m^2$/s]	[m]	[$x10^{-6}$m/s]	[$x10^{-6}$m/s]	[$x10^{-6}$m/s]	Q_x [$x10^{-6}m^2$/s]
0	2.95	0.0646	0.20	0.00	0.80	3.38
17.42	4.64	0.0785	0.20	0.00	0.80	5.06
22.36	6.33	0.0824	0.20	0.00	0.80	6.75
26.32	8.02	0.0856	0.20	0.00	0.80	8.44
30.01	9.71	0.0886	0.20	0.00	0.80	10.13
33.63	11.39	0.0915	0.20	0.00	0.80	11.82
36.39	11.39	0.0937	0.60	0.40	0.00	12.66
37.32	12.66	0.0937	0.00	1.00	0.00	12.66

t = 10-11 days after rise in rainfall intensity				i_a[m/s]=	i_b[m/s]=	
Slice width[m]	2.11			2.00E-07	1.00E-06	
Slice no.	9	L_D[m]		63.30	12.66	
$WS_{x,a}$ at steady state[m]	0.0660	WSC[m]		0.0896	0.0937	
WSC_b at steady state[m]	0.0937	Q_{max}[m^2/s]		1.266E-05	1.266E-05	
time	x=16.88m	WS	dQx/dx	q_i	dWS/dt	x=18.99m
[$x10^3$ s]	Q_x [$x10^{-6}m^2$/s]	[m]	[$x10^{-6}$m/s]	[$x10^{-6}$m/s]	[$x10^{-6}$m/s]	Q_x [$x10^{-6}m^2$/s]
0	3.38	0.0660	0.20	0.00	0.80	3.80
17.42	5.06	0.0799	0.20	0.00	0.80	5.49
22.36	6.75	0.0838	0.20	0.00	0.80	7.17
26.32	8.44	0.0870	0.20	0.00	0.80	8.86
30.01	10.13	0.0900	0.20	0.00	0.80	10.55
33.63	11.82	0.0929	0.20	0.00	0.80	12.24
34.64	11.82	0.0937	0.40	0.60	0.00	12.66
36.39	12.66	0.0937	0.00	1.00	0.00	12.66

t = 10-11 days after rise in rainfall intensity				i_a[m/s]=	i_b[m/s]=	
Slice width[m]	2.11			2.00E-07	1.00E-06	
Slice no.	10	L_D[m]		63.30	12.66	
$WS_{x,a}$ at steady state[m]	0.0673	WSC[m]		0.0896	0.0937	
WSC_b at steady state[m]	0.0937	Q_{max}[m^2/s]		1.266E-05	1.266E-05	
time	x=18.99m	WS	dQx/dx	q_i	dWS/dt	x=21.1m
[$x10^3$ s]	Q_x [$x10^{-6}m^2$/s]	[m]	[$x10^{-6}$m/s]	[$x10^{-6}$m/s]	[$x10^{-6}$m/s]	Q_x [$x10^{-6}m^2$/s]
0	3.80	0.0673	0.20	0.00	0.80	4.22
17.42	5.49	0.0812	0.20	0.00	0.80	5.91
22.36	7.17	0.0852	0.20	0.00	0.80	7.60
26.32	8.86	0.0883	0.20	0.00	0.80	9.28
30.01	10.55	0.0913	0.20	0.00	0.80	10.97
32.96	10.55	0.0937	1.00	0.00	0.00	12.66
33.63	12.24	0.0937	0.20	0.80	0.00	12.66
34.64	12.66	0.0937	0.00	1.00	0.00	12.66

t = 10-11 days after rise in rainfall intensity				i_a[m/s]=	i_b[m/s]=	
Slice width[m]	2.11			2.00E-07	1.00E-06	
Slice no.	11	L_D[m]		63.30	12.66	
$WS_{x,a}$ at steady state[m]	0.0686	WSC[m]		0.0896	0.0937	
WSC_b at steady state[m]	0.0937	Q_{max}[m^2/s]		1.266E-05	1.266E-05	
time	x=21.1m	WS	dQx/dx	q_i	dWS/dt	x=23.21m
[$x10^3$ s]	Q_x [$x10^{-6}m^2$/s]	[m]	[$x10^{-6}$m/s]	[$x10^{-6}$m/s]	[$x10^{-6}$m/s]	Q_x [$x10^{-6}m^2$/s]
0	4.220	0.0686	0.20	0.00	0.80	4.64
17.42	5.908	0.0825	0.20	0.00	0.80	6.33
22.36	7.596	0.0865	0.20	0.00	0.80	8.02
26.32	9.284	0.0896	0.20	0.00	0.80	9.71
30.01	10.972	0.0926	0.20	0.00	0.80	11.39
31.35	10.972	0.0937	0.80	0.20	0.00	12.66
32.96	12.660	0.0937	0.00	1.00	0.00	12.66

t = 10-11 days after rise in rainfall intensity				i_a[m/s]=	i_b[m/s]=	
Slice width[m]	2.11			2.00E-07	1.00E-06	
Slice no.	12	L_D[m]		63.30	12.66	
$WS_{x,a}$ at steady state[m]	0.0698	WSC[m]		0.0896	0.0937	
WSC_b at steady state[m]	0.0937	Q_{max}[m^2/s]		1.266E-05	1.266E-05	
time	x=23.21m	WS	dQx/dx	q_i	dWS/dt	x=25.32m
[$x10^3$ s]	Q_x [$x10^{-6}m^2$/s]	[m]	[$x10^{-6}$m/s]	[$x10^{-6}$m/s]	[$x10^{-6}$m/s]	Q_x [$x10^{-6}m^2$/s]
0	4.64	0.0698	0.20	0.00	0.80	5.06
17.42	6.33	0.0838	0.20	0.00	0.80	6.75
22.36	8.02	0.0877	0.20	0.00	0.80	8.44
26.32	9.71	0.0909	0.20	0.00	0.80	10.13
29.80	9.71	0.0937	1.00	0.00	0.00	11.82
30.01	11.39	0.0937	0.60	0.40	0.00	12.66
31.35	12.66	0.0937	0.00	1.00	0.00	12.66

Table D- 2 Interface flow rates calculated by simplified method between t = 11 days and 12 days (after rise in rainfall intensity)

t = 11-12 days after rise in rainfall intensity			i_b[m/s]=	i_c[m/s]=		**t = 11-12 days after rise in rainfall intensity**			i_b[m/s]=	i_c[m/s]=		**t = 11-12 days after rise in rainfall intensity**			i_b[m/s]=	i_c[m/s]=	
Slice width[m] 2.11			1.00E-06	2.00E-06		Slice width[m] 2.11			1.00E-06	2.00E-06		Slice width[m] 2.11			1.00E-06	2.00E-06	
Slice no. 1		L_D[m]	12.66	6.33		Slice no. 2		L_D[m]	12.66	6.33		Slice no. 3		L_D[m]	12.66	6.33	
$WS_{x,b}$ at steady state[m] 0.0625		WSC[m]	0.0937	0.0961		$WS_{x,b}$ at steady state[m] 0.0706		WSC[m]	0.0937	0.0961		$WS_{x,b}$ at steady state[m] 0.0766		WSC[m]	0.0937	0.0961	
$WS_{x,c}$ at steady state[m] 0.0707		Qmax[m^2/s]	1.266E-05	1.266E-05		$WS_{x,c}$ at steady state[m] 0.0824		Qmax[m^2/s]	1.266E-05	1.266E-05		$WS_{x,c}$ at steady state[m] 0.0917		Qmax[m^2/s]	1.266E-05	1.266E-05	
time	x=0m	WS	dQx/dx	qi	dWS/dt	x=2.11m	time	x=2.11m	WS	dQx/dx	qi	dWS/dt	x=4.22m	time	x=4.22m	WS	dQx/dx	qi	dWS/dt	x=6.33m
[x10^3 s]	Q_x [x$10^{-6}m^2$/s]	[m]	[x10^{-6}m/s]	[x10^{-6}m/s]	[x10^{-6}m/s]	Q_x [x$10^{-6}m^2$/s]	[x10^3 s]	Q_x [x$10^{-6}m^2$/s]	[m]	[x10^{-6}m/s]	[x10^{-6}m/s]	[x10^{-6}m/s]	Q_x [x$10^{-6}m^2$/s]	[x10^3 s]	Q_x [x$10^{-6}m^2$/s]	[m]	[x10^{-6}m/s]	[x10^{-6}m/s]	[x10^{-6}m/s]	Q_x [x$10^{-6}m^2$/s]
0.00	0	0.0625	1.00	0.00	1.00	2.11	0.00	2.11	0.0706	1.00	0.00	1.00	4.22	0.00	4.22	0.0766	1.00	0.00	1.00	6.33
8.26	0	0.0707	2.00	0.00	0.00	4.22	8.26	4.22	0.0789	1.00	0.00	1.00	6.33	8.26	6.33	0.0849	1.00	0.00	1.00	8.44
							11.72	4.22	0.0824	2.00	0.00	0.00	8.44	11.72	8.44	0.0883	1.00	0.00	1.00	10.55
														15.05	8.44	0.0917	2.00	0.00	0.00	12.66

t = 11-12 days after rise in rainfall intensity			i_b[m/s]=	i_c[m/s]=		*t = 11-12 days after rise in rainfall intensity*			i_b[m/s]=	i_c[m/s]=		**t = 11-12 days after rise in rainfall intensity**			i_b[m/s]=	i_c[m/s]=	
Slice width[m] 2.11			1.00E-06	2.00E-06		Slice width[m] 2.11			1.00E-06	2.00E-06		Slice width[m] 2.11			1.00E-06	2.00E-06	
Slice no. 4		L_D[m]	12.66	6.33		Slice no. 5		L_D[m]	12.66	6.33		Slice no. 6		L_D[m]	12.66	6.33	
$WS_{x,b}$ at steady state[m] 0.0818		WSC[m]	0.0937	0.0961		$WS_{x,b}$ at steady state[m] 0.0866		WSC[m]	0.0937	0.0961		$WS_{x,b}$ at steady state[m] 0.0913		WSC[m]	0.0937	0.0961	
WSC_c at steady state[m] 0.0961		Qmax[m^2/s]	1.266E-05	1.266E-05		WSC_c at steady state[m] 0.0961		Qmax[m^2/s]	1.266E-05	1.266E-05		WSC_c at steady state[m] 0.0961		Qmax[m^2/s]	1.266E-05	1.266E-05	
time	x=6.33m	WS	dQx/dx	qi	dWS/dt	x=8.44m	time	x=8.44m	WS	dQx/dx	qi	dWS/dt	x=10.55m	time	x=10.55m	WS	dQx/dx	qi	dWS/dt	x=12.66m
[x10^3 s]	Q_x [x$10^{-6}m^2$/s]	[m]	[x10^{-6}m/s]	[x10^{-6}m/s]	[x10^{-6}m/s]	Q_x [x$10^{-6}m^2$/s]	[x10^3 s]	Q_x [x$10^{-6}m^2$/s]	[m]	[x10^{-6}m/s]	[x10^{-6}m/s]	[x10^{-6}m/s]	Q_x [x$10^{-6}m^2$/s]	[x10^3 s]	Q_x [x$10^{-6}m^2$/s]	[m]	[x10^{-6}m/s]	[x10^{-6}m/s]	[x10^{-6}m/s]	Q_x [x$10^{-6}m^2$/s]
0.00	6.33	0.0818	1.00	0.00	1.00	8.44	0.00	8.44	0.0866	1.00	0.00	1.00	10.55	0.00	10.55	0.0913	1.00	0.00	1.00	12.66
8.26	8.44	0.0901	1.00	0.00	1.00	10.55	8.26	10.55	0.0949	1.00	0.00	1.00	12.66	4.78	10.55	0.0961	1.00	1.00	0.00	12.66
11.72	10.55	0.0935	1.00	0.00	1.00	12.66	9.46	10.55	0.0961	1.00	1.00	0.00	12.66	8.26	12.66	0.0961	0.00	2.00	0.00	12.66
14.28	10.55	0.0961	1.00	1.00	0.00	12.66	11.72	12.66	0.0961	0.00	2.00	0.00	12.66							
15.05	12.66	0.0961	0.00	2.00	0.00	12.66														

Table D-2 Interface flow rates calculated by simplified method between t = 11 days and 12 days (after rise in rainfall intensity) (continued)

t = 11-12 days after rise in rainfall intensity				i_b[m/s]=	i_c[m/s]=		t = 11-12 days after rise in rainfall intensity				i_b[m/s]=	i_c[m/s]=		t = 11-12 days after rise in rainfall intensity				i_b[m/s]=	i_c[m/s]=	
Slice width[m] 2.11				1.00E-06	2.00E-06		Slice width[m] 2.11				1.00E-06	2.00E-06		Slice width[m] 2.11				1.00E-06	2.00E-06	
Slice no. 7		L_D[m]		12.66	6.33		Slice no. 8		L_D[m]		12.66	6.33		Slice no. 9		L_D[m]		12.66	6.33	
WSC_b at steady state[m] 0.0937		WSC[m]		0.0937	0.0961		WSC_b at steady state[m] 0.0937		WSC[m]		0.0937	0.0961		WSC_b at steady state[m] 0.0937		WSC[m]		0.0937	0.0961	
WSC_c at steady state[m] 0.0961		Qmax[m^2/s]		1.266E-05	1.266E-05		WSC_c at steady state[m] 0.0961		Qmax[m^2/s]		1.266E-05	1.266E-05		WSC_c at steady state[m] 0.0961		Qmax[m^2/s]		1.266E-05	1.266E-05	
time	x=12.66m	WS	dQx/dx	qi	dWS/dt	x=14.77m	time	x=14.77m	WS	dQx/dx	qi	dWS/dt	x=16.88m	time	x=16.88m	WS	dQx/dx	qi	dWS/dt	x=18.99m
x10^3 s]	Q_x [x$10^{-6}m^2$/s]	[m]	[x10^{-6}m/s]	[x10^{-6}m/s]	[x10^{-6}m/s]	Q_x [x$10^{-6}m^2$/s]	[x10^3 s]	Q_x [x$10^{-6}m^2$/s]	[m]	[x10^{-6}m/s]	[x10^{-6}m/s]	[x10^{-6}m/s]	Q_x [x$10^{-6}m^2$/s]	[x10^3 s]	Q_x [x$10^{-6}m^2$/s]	[m]	[x10^{-6}m/s]	[x10^{-6}m/s]	[x10^{-6}m/s]	Q_x [x$10^{-6}m^2$/s]
0.00	12.66	0.0937	0.00	1.00	1.00	12.66	0	12.66	0.0937	0.00	1.00	1.00	12.66	0	12.66	0.0937	0.00	1.00	1.00	12.66
2.44	12.66	0.0961	0.00	2.00	0.00	12.66	2.44	12.66	0.0961	0.00	2.00	0.00	12.66	2.44	12.66	0.0961	0.00	2.00	0.00	12.66

t = 11-12 days after rise in rainfall intensity				i_b[m/s]=	i_c[m/s]=		t = 11-12 days after rise in rainfall intensity				i_b[m/s]=	i_c[m/s]=		t = 11-12 days after rise in rainfall intensity				i_b[m/s]=	i_c[m/s]=	
Slice width[m] 2.11				1.00E-06	2.00E-06		Slice width[m] 2.11				1.00E-06	2.00E-06		Slice width[m] 2.11				1.00E-06	2.00E-06	
Slice no. 10		L_D[m]		12.66	6.33		Slice no. 11		L_D[m]		12.66	6.33		Slice no. 12		L_D[m]		12.66	6.33	
WSC_b at steady state[m] 0.0937		WSC[m]		0.0937	0.0961		WSC_b at steady state[m] 0.0937		WSC[m]		0.0937	0.0961		WSC_b at steady state[m] 0.0937		WSC[m]		0.0937	0.0961	
WSC_c at steady state[m] 0.0961		Qmax[m^2/s]		1.266E-05	1.266E-05		WSC_c at steady state[m] 0.0961		Qmax[m^2/s]		1.266E-05	1.266E-05		WSC_c at steady state[m] 0.0961		Qmax[m^2/s]		1.266E-05	1.266E-05	
time	x=18.99m	WS	dQx/dx	qi	dWS/dt	x=21.1m	time	x=21.1m	WS	dQx/dx	qi	dWS/dt	x=23.21m	time	x=23.21m	WS	dQx/dx	qi	dWS/dt	x=25.32m
x10^3 s]	Q_x [x$10^{-6}m^2$/s]	[m]	[x10^{-6}m/s]	[x10^{-6}m/s]	[x10^{-6}m/s]	Q_x [x$10^{-6}m^2$/s]	[x10^3 s]	Q_x [x$10^{-6}m^2$/s]	[m]	[x10^{-6}m/s]	[x10^{-6}m/s]	[x10^{-6}m/s]	Q_x [x$10^{-6}m^2$/s]	[x10^3 s]	Q_x [x$10^{-6}m^2$/s]	[m]	[x10^{-6}m/s]	[x10^{-6}m/s]	[x10^{-6}m/s]	Q_x [x$10^{-6}m^2$/s]
0	12.66	0.0937	0.00	1.00	1.00	12.66	0	12.66	0.0937	0.00	1.00	1.00	12.66	0	12.66	0.0937	0.00	1.00	1.00	12.66
2.44	12.66	0.0961	0.00	2.00	0.00	12.66	2.44	12.66	0.0961	0.00	2.00	0.00	12.66	2.44	12.66	0.0961	0.00	2.00	0.00	12.66

Table D- 3 Interface flow rates calculated by simplified method between t = 12 days and 13 days (after fall in rainfall intensity)

t = 12-13days after fall in rainfall intensity			i_c[m/s]=	i_b[m/s]=		t = 12-13days after fall in rainfall intensity			i_c[m/s]=	i_b[m/s]=		t = 12-13days after fall in rainfall intensity			i_c[m/s]=	i_b[m/s]=	
Slice width[m] 2.11			2.00E-06	1.00E-06		Slice width[m] 2.11			2.00E-06	1.00E-06		Slice width[m] 2.11			2.00E-06	1.00E-06	
Slice no. 1		L_D[m]	6.33	12.66		Slice no. 2		L_D[m]	6.33	12.66		Slice no. 3		L_D[m]	6.33	12.66	
$WS_{x,c}$ at steady state[m] 0.0707		WSC[m]	0.0961	0.0937		$WS_{x,c}$ at steady state[m] 0.0824		WSC[m]	0.0961	0.0937		$WS_{x,c}$ at steady state[m] 0.0917		WSC[m]	0.0961	0.0937	
$WS_{x,b}$ at steady state[m] 0.0625		Qmax[m^2/s]	1.266E-05	1.266E-05		$WS_{x,b}$ at steady state[m] 0.0706		Qmax[m^2/s]	1.266E-05	1.266E-05		$WS_{x,b}$ at steady state[m] 0.0766		Qmax[m^2/s]	1.266E-05	1.266E-05	
time	x=0m	WS	dQx/dx	qi	dWS/dt	x=2.11m	time	x=2.11m	WS	dQx/dx	qi	dWS/dt	x=4.22m	time	x=4.22m	WS	dQx/dx	qi	dWS/dt	x=6.33m
[x10^3 s]	Q_x [x$10^{-6}m^2$/s]	[m]	[x10^{-6}m/s]	[x10^{-6}m/s]	[x10^{-6}m/s]	Q_x [x$10^{-6}m^2$/s]	[x10^3 s]	Q_x [x$10^{-6}m^2$/s]	[m]	[x10^{-6}m/s]	[x10^{-6}m/s]	[x10^{-6}m/s]	Q_x [x$10^{-6}m^2$/s]	[x10^3 s]	Q_x [x$10^{-6}m^2$/s]	[m]	[x10^{-6}m/s]	[x10^{-6}m/s]	[x10^{-6}m/s]	Q_x [x$10^{-6}m^2$/s]
0	0	0.0707	2.00	0.00	-1.00	4.22	0.00	4.22	0.0824	2.00	0.00	-1.00	8.44	0.00	8.44	0.0917	2.00	0.00	-1.00	12.66
8.26	0	0.0625	1.00	0.00	0.00	2.11	8.26	2.11	0.0741	2.00	0.00	-1.00	6.33	8.26	6.33	0.0834	2.00	0.00	-1.00	10.55
							11.72	2.11	0.0706	1.00	0.00	0.00	4.22	11.72	4.22	0.0799	2.00	0.00	-1.00	8.44
														15.05	4.22	0.0766	1.00	0.00	0.00	6.33

t = 12-13days after fall in rainfall intensity			i_c[m/s]=	i_b[m/s]=		t = 12-13days after fall in rainfall intensity			i_c[m/s]=	i_b[m/s]=		t = 12-13days after fall in rainfall intensity			i_c[m/s]=	i_b[m/s]=	
Slice width[m] 2.11			2.00E-06	1.00E-06		Slice width[m] 2.11			2.00E-06	1.00E-06		Slice width[m] 2.11			2.00E-06	1.00E-06	
Slice no. 4		L_D[m]	6.33	12.66		Slice no. 5		L_D[m]	6.33	12.66		Slice no. 6		L_D[m]	6.33	12.66	
WSC_c at steady state[m] 0.0961		WSC[m]	0.0961	0.0937		WSC_c at steady state[m] 0.0961		WSC[m]	0.0961	0.0937		WSC_c at steady state[m] 0.0961		WSC[m]	0.0961	0.0937	
$WS_{x,b}$ at steady state[m] 0.0818		Qmax[m^2/s]	1.266E-05	1.266E-05		$WS_{x,b}$ at steady state[m] 0.0866		Qmax[m^2/s]	1.266E-05	1.266E-05		$WS_{x,b}$ at steady state[m] 0.0913		Qmax[m^2/s]	1.266E-05	1.266E-05	
time	x=6.33m	WS	dQx/dx	qi	dWS/dt	x=8.44m	time	x=8.44m	WS	dQx/dx	qi	dWS/dt	x=10.55m	time	x=10.55m	WS	dQx/dx	qi	dWS/dt	x=12.66m
[x10^3 s]	Q_x [x$10^{-6}m^2$/s]	[m]	[x10^{-6}m/s]	[x10^{-6}m/s]	[x10^{-6}m/s]	Q_x [x$10^{-6}m^2$/s]	[x10^3 s]	Q_x [x$10^{-6}m^2$/s]	[m]	[x10^{-6}m/s]	[x10^{-6}m/s]	[x10^{-6}m/s]	Q_x [x$10^{-6}m^2$/s]	[x10^3 s]	Q_x [x$10^{-6}m^2$/s]	[m]	[x10^{-6}m/s]	[x10^{-6}m/s]	[x10^{-6}m/s]	Q_x [x$10^{-6}m^2$/s]
0.00	12.66	0.0961	0.00	2.00	-1.00	12.66	0.00	12.66	0.0961	0.00	1.00	0.00	12.66	0.00	12.66	0.0961	0.00	1.00	0.00	12.66
8.26	10.55	0.0878	1.00	0.50	-0.50	12.66	8.26	12.66	0.0961	0.00	1.00	0.00	12.66	8.26	12.66	0.0961	0.00	1.00	0.00	12.66
11.72	8.44	0.0861	2.00	0.00	-1.00	12.66	11.72	12.66	0.0961	0.00	1.00	0.00	12.66	11.72	12.66	0.0961	0.00	1.00	0.00	12.66
15.05	6.33	0.0828	2.00	0.00	-1.00	10.55	15.05	10.55	0.0961	1.00	0.50	-0.50	12.66	15.05	12.66	0.0961	0.00	1.00	0.00	12.66
16.01	6.33	0.0818	1.00	0.00	0.00	8.44	16.01	8.44	0.0956	2.00	0.00	-1.00	12.66	16.01	12.66	0.0961	0.00	1.00	0.00	12.66
86.4	6.33	0.0818	1.00	0.00	0.00	8.44	24.99	8.44	0.0866	1.00	0.00	0.00	10.55	24.99	10.55	0.0961	1.00	0.50	-0.50	12.66
														34.54	10.55	0.0913	1.00	0.00	0.00	12.66

Table D-3 Interface flow rates calculated by simplified method between t = 12 days and 13 days (after fall in rainfall intensity) (continued)

t = 12-13days after fall in rainfall intensity				i_c[m/s]=	i_b[m/s]=	
Slice width[m]	2.11			2.00E-06	1.00E-06	
Slice no.	7	L_D[m]		6.33	12.66	
WSC_c at steady state[m]	0.0961	WSC[m]		0.0961	0.0937	
WSC_b at steady state[m]	0.0937	Q_{max}[m/s]		1.266E-05	1.266E-05	
time	x=12.66m	WS	dQx/dx	qi	dWS/dt	x=14.77m
x10^3 s]	Q_x [x10^{-6}m^2/s]	[m]	[x10^{-6}m/s]	[x10^{-6}m/s]	[x10^{-6}m/s]	Q_x [x10^{-6}m^2/s]
0.00	12.66	0.0961	0.00	2.00	-1.00	12.66
2.44	12.66	0.0937	0.00	1.00	0.00	12.66
8.26	12.66	0.0937	0.00	1.00	0.00	12.66
11.72	12.66	0.0937	0.00	1.00	0.00	12.66
15.05	12.66	0.0937	0.00	1.00	0.00	12.66
16.01	12.66	0.0937	0.00	1.00	0.00	12.66
24.99	12.66	0.0937	0.00	1.00	0.00	12.66
34.54	12.66	0.0937	0.00	1.00	0.00	12.66

t = 12-13days after fall in rainfall intensity				i_c[m/s]=	i_b[m/s]=	
Slice width[m]	2.11			2.00E-06	1.00E-06	
Slice no.	8	L_D[m]		6.33	12.66	
WSC_c at steady state[m]	0.0961	WSC[m]		0.0961	0.0937	
WSC_b at steady state[m]	0.0937	Q_{max}[m/s]		1.266E-05	1.266E-05	
time	x=14.77m	WS	dQx/dx	qi	dWS/dt	x=16.88m
[x10^3 s]	Q_x [x10^{-6}m^2/s]	[m]	[x10^{-6}m/s]	[x10^{-6}m/s]	[x10^{-6}m/s]	Q_x [x10^{-6}m^2/s]
0.00	12.66	0.0961	0.00	2.00	-1.00	12.66
2.44	12.66	0.0937	0.00	1.00	0.00	12.66
8.26	12.66	0.0937	0.00	1.00	0.00	12.66
11.72	12.66	0.0937	0.00	1.00	0.00	12.66
15.05	12.66	0.0937	0.00	1.00	0.00	12.66
16.01	12.66	0.0937	0.00	1.00	0.00	12.66
24.99	12.66	0.0937	0.00	1.00	0.00	12.66
34.54	12.66	0.0937	0.00	1.00	0.00	12.66

t = 12-13days after fall in rainfall intensity				i_c[m/s]=	i_b[m/s]=	
Slice width[m]	2.11			2.00E-06	1.00E-06	
Slice no.	9	LD[m]		6.33	12.66	
WSC_c at steady state[m]	0.0961	WSC[m]		0.0961	0.0937	
WSC_b at steady state[m]	0.0937	Qmax[m/s]		1.266E-05	1.266E-05	
time	x=16.88m	WS	dQx/dx	qi	dWS/dt	x=18.99m
[x10^3 s]	Q_x [x10^{-6}m^2/s]	[m]	[x10^{-6}m/s]	[x10^{-6}m/s]	[x10^{-6}m/s]	Q_x [x10^{-6}m^2/s]
0.00	12.66	0.0961	0.00	2.00	-1.00	12.66
2.44	12.66	0.0937	0.00	1.00	0.00	12.66
8.26	12.66	0.0937	0.00	1.00	0.00	12.66
11.72	12.66	0.0937	0.00	1.00	0.00	12.66
15.05	12.66	0.0937	0.00	1.00	0.00	12.66
16.01	12.66	0.0937	0.00	1.00	0.00	12.66
24.99	12.66	0.0937	0.00	1.00	0.00	12.66
34.54	12.66	0.0937	0.00	1.00	0.00	12.66

t = 12-13days after fall in rainfall intensity				i_c[m/s]=	i_b[m/s]=	
Slice width[m]	2.11			2.00E-06	1.00E-06	
Slice no.	10	L_D[m]		6.33	12.66	
WSC_c at steady state[m]	0.0961	WSC[m]		0.0961	0.0937	
WSC_b at steady state[m]	0.0937	Q_{max}[m/s]		1.266E-05	1.266E-05	
time	x=18.99m	WS	dQx/dx	qi	dWS/dt	x=21.1m
x10^3 s]	Q_x [x10^{-6}m^2/s]	[m]	[x10^{-6}m/s]	[x10^{-6}m/s]	[x10^{-6}m/s]	Q_x [x10^{-6}m^2/s]
0.00	12.66	0.0961	0.00	2.00	-1.00	12.66
2.44	12.66	0.0937	0.00	1.00	0.00	12.66
8.26	12.66	0.0937	0.00	1.00	0.00	12.66
11.72	12.66	0.0937	0.00	1.00	0.00	12.66
15.05	12.66	0.0937	0.00	1.00	0.00	12.66
16.01	12.66	0.0937	0.00	1.00	0.00	12.66
24.99	12.66	0.0937	0.00	1.00	0.00	12.66
34.54	12.66	0.0937	0.00	1.00	0.00	12.66

t = 12-13days after fall in rainfall intensity				i_c[m/s]=	i_b[m/s]=	
Slice width[m]	2.11			2.00E-06	1.00E-06	
Slice no.	11	L_D[m]		6.33	12.66	
WSC_c at steady state[m]	0.0961	WSC[m]		0.0961	0.0937	
WSC_b at steady state[m]	0.0937	Q_{max}[m/s]		1.266E-05	1.266E-05	
time	x=21.1m	WS	dQx/dx	qi	dWS/dt	x=23.21m
[x10^3 s]	Q_x [x10^{-6}m^2/s]	[m]	[x10^{-6}m/s]	[x10^{-6}m/s]	[x10^{-6}m/s]	Q_x [x10^{-6}m^2/s]
0.00	12.66	0.0961	0.00	2.00	-1.00	12.66
2.44	12.66	0.0937	0.00	1.00	0.00	12.66
8.26	12.66	0.0937	0.00	1.00	0.00	12.66
11.72	12.66	0.0937	0.00	1.00	0.00	12.66
15.05	12.66	0.0937	0.00	1.00	0.00	12.66
16.01	12.66	0.0937	0.00	1.00	0.00	12.66
24.99	12.66	0.0937	0.00	1.00	0.00	12.66
34.54	12.66	0.0937	0.00	1.00	0.00	12.66

t = 12-13days after fall in rainfall intensity				i_c[m/s]=	i_b[m/s]=	
Slice width[m]	2.11			2.00E-06	1.00E-06	
Slice no.	12	L_D[m]		6.33	12.66	
WSC_c at steady state[m]	0.0961	WSC[m]		0.0961	0.0937	
WSC_b at steady state[m]	0.0937	Q_{max}[m/s]		1.266E-05	1.266E-05	
time	x=23.21m	WS	dQx/dx	qi	dWS/dt	x=25.32m
[x10^3 s]	Q_x [x10^{-6}m^2/s]	[m]	[x10^{-6}m/s]	[x10^{-6}m/s]	[x10^{-6}m/s]	Q_x [x10^{-6}m^2/s]
0.00	12.66	0.0961	0.00	2.00	-1.00	12.66
2.44	12.66	0.0937	0.00	1.00	0.00	12.66
8.26	12.66	0.0937	0.00	1.00	0.00	12.66
11.72	12.66	0.0937	0.00	1.00	0.00	12.66
15.05	12.66	0.0937	0.00	1.00	0.00	12.66
16.01	12.66	0.0937	0.00	1.00	0.00	12.66
24.99	12.66	0.0937	0.00	1.00	0.00	12.66
34.54	12.66	0.0937	0.00	1.00	0.00	12.66

Table D- 4 Interface flow rates calculated by simplified method between t = 13days and 14 days (after fall in rainfall intensity)

t = 13-14 days after fall in rainfall intensity			i_b[m/s]=	i_a[m/s]=		t = 13-14 days after fall in rainfall intensity			i_b[m/s]=	i_a[m/s]=		t = 13-14 days after fall in rainfall intensity			i_b[m/s]=	i_a[m/s]=	
Slice width[m] 2.11			1.00E-06	2.00E-07		Slice width[m] 2.11			1.00E-06	2.00E-07		Slice width[m] 2.11			1.00E-06	2.00E-07	
Slice no. 1		L_D[m]	12.66	63.30		Slice no. 2		L_D[m]	12.66	63.30		Slice no. 3		L_D[m]	12.66	63.30	
$WS_{x,b}$ at steady state[m] 0.0625		WSC[m]	0.0937	0.0896		$WS_{x,b}$ at steady state[m] 0.0706		WSC[m]	0.0937	0.0896		$WS_{x,b}$ at steady state[m] 0.0766		WSC[m]	0.0937	0.0896	
$WS_{x,a}$ at steady state[m] 0.0485		Qmax[m^2/s]	1.266E-05	1.266E-05		$WS_{x,a}$ at steady state[m] 0.0527		Qmax[m^2/s]	1.266E-05	1.266E-05		$WS_{x,a}$ at steady state[m] 0.0556		Qmax[m^2/s]	1.266E-05	1.266E-05	
time	x=0m	WS	dQx/dx	qi	dWS/dt	x=2.11m	time	x=2.11m	WS	dQx/dx	qi	dWS/dt	x=4.22m	time	x=4.22m	WS	dQx/dx	qi	dWS/dt	x=6.33m
[x10^3 s]	Q_x [x$10^{-6}$$m^2$/s]	[m]	[x10^{-6}m/s]	[x10^{-6}m/s]	[x10^{-6}m/s]	Q_x [x$10^{-6}$$m^2$/s]	[x10^3 s]	Q_x [x$10^{-6}$$m^2$/s]	[m]	[x10^{-6}m/s]	[x10^{-6}m/s]	[x10^{-6}m/s]	Q_x [x$10^{-6}$$m^2$/s]	[x10^3 s]	Q_x [x$10^{-6}$$m^2$/s]	[m]	[x10^{-6}m/s]	[x10^{-6}m/s]	[x10^{-6}m/s]	Q_x [x$10^{-6}$$m^2$/s]
0	0	0.0625	1.00	0.00	-0.80	2.110	0.00	2.110	0.0706	1.00	0.00	-0.80	4.220	0.00	4.220	0.0766	1.00	0.00	-0.80	6.330
17.42	0	0.0485	0.20	0.00	0.00	0.422	17.42	0.422	0.0567	1.00	0.00	-0.80	2.532	17.42	2.532	0.0627	1.00	0.00	-0.80	4.642
							22.36	0.422	0.0527	0.20	0.00	0.00	0.844	22.36	0.844	0.0587	1.00	0.00	-0.80	2.954
														26.32	0.844	0.0556	0.20	0.00	0.00	1.266

t = 13-14 days after fall in rainfall intensity			i_b[m/s]=	i_a[m/s]=		t = 13-14 days after fall in rainfall intensity			i_b[m/s]=	i_a[m/s]=		t = 13-14 days after fall in rainfall intensity			i_b[m/s]=	i_a[m/s]=	
Slice width[m] 2.11			1.00E-06	2.00E-07		Slice width[m] 2.11			1.00E-06	2.00E-07		Slice width[m] 2.11			1.00E-06	2.00E-07	
Slice no. 4		L_D[m]	12.66	63.30		Slice no. 5		L_D[m]	12.66	63.30		Slice no. 6		L_D[m]	12.66	63.30	
$WS_{x,b}$ at steady state[m] 0.0818		WSC[m]	0.0937	0.0896		$WS_{x,b}$ at steady state[m] 0.0866		WSC[m]	0.0937	0.0896		$WS_{x,b}$ at steady state[m] 0.0913		WSC[m]	0.0937	0.0896	
$WS_{x,a}$ at steady state[m] 0.0578		Qmax[m^2/s]	1.266E-05	1.266E-05		$WS_{x,a}$ at steady state[m] 0.0597		Qmax[m^2/s]	1.266E-05	1.266E-05		$WS_{x,a}$ at steady state[m] 0.0615		Qmax[m^2/s]	1.266E-05	1.266E-05	
time	x=6.33m	WS	dQx/dx	qi	dWS/dt	x=8.44m	time	x=8.44m	WS	dQx/dx	qi	dWS/dt	x=10.55m	time	x=10.55m	WS	dQx/dx	qi	dWS/dt	x=12.66m
[x10^3 s]	Q_x [x$10^{-6}$$m^2$/s]	[m]	[x10^{-6}m/s]	[x10^{-6}m/s]	[x10^{-6}m/s]	Q_x [x$10^{-6}$$m^2$/s]	[x10^3 s]	Q_x [x$10^{-6}$$m^2$/s]	[m]	[x10^{-6}m/s]	[x10^{-6}m/s]	[x10^{-6}m/s]	Q_x [x$10^{-6}$$m^2$/s]	[x10^3 s]	Q_x [x$10^{-6}$$m^2$/s]	[m]	[x10^{-6}m/s]	[x10^{-6}m/s]	[x10^{-6}m/s]	Q_x [x$10^{-6}$$m^2$/s]
0.00	6.330	0.0818	1.00	0.00	-0.80	8.440	0.00	8.44	0.0866	1.00	0.00	-0.80	10.550	0.00	10.55	0.0913	1.00	0.00	-0.80	12.66
17.42	4.642	0.0679	1.00	0.00	-0.80	6.752	17.42	6.75	0.0727	1.00	0.00	-0.80	8.862	17.42	8.86	0.0774	1.00	0.00	-0.80	10.97
22.36	2.954	0.0639	1.00	0.00	-0.80	5.064	22.36	5.06	0.0688	1.00	0.00	-0.80	7.174	22.36	7.17	0.0734	1.00	0.00	-0.80	9.28
26.32	1.266	0.0608	1.00	0.00	-0.80	3.376	26.32	3.38	0.0656	1.00	0.00	-0.80	5.486	26.32	5.49	0.0703	1.00	0.00	-0.80	7.60
30.01	1.266	0.0578	0.20	0.00	0.00	1.688	30.01	1.69	0.0626	1.00	0.00	-0.80	3.798	30.01	3.80	0.0673	1.00	0.00	-0.80	5.91
							33.63	1.69	0.0597	0.20	0.00	0.00	2.110	33.63	2.11	0.0644	1.00	0.00	-0.80	4.22
														37.32	2.11	0.0615	0.20	0.00	0.00	2.53

Table D-4 Interface flow rates calculated by simplified method between t = 13 days and 14 days (after fall in rainfall intensity) (continued)

t = 13-14 days after fall in rainfall intensity				i_b[m/s]=	i_a[m/s]=	
Slice width[m] 2.11				1.00E-06	2.00E-07	
Slice no. 7			L_D[m]	12.66	63.30	
WSC_b at steady state[m] 0.0937			WSC[m]	0.0937	0.0896	
$WS_{x,a}$ at steady state[m] 0.0631			Q_{max}[m/s]	1.266E-05	1.266E-05	
time	x=12.66m	WS	dQx/dx	qi	dWS/dt	x=14.77m
[x10^3 s]	Q_x [x10^{-6}m^2/s]	[m]	[x10^{-6}m/s]	[x10^{-6}m/s]	[x10^{-6}m/s]	Q_x [x10^{-6}m^2/s]
0.00	12.66	0.0937	0.00	0.20	0.00	12.66
17.42	10.97	0.0937	0.80	0.04	-0.64	12.66
22.36	9.28	0.0905	1.00	0.00	-0.80	11.39
26.32	7.60	0.0874	1.00	0.00	-0.80	9.71
30.01	5.91	0.0844	1.00	0.00	-0.80	8.02
33.63	4.22	0.0815	1.00	0.00	-0.80	6.33
37.32	2.53	0.0786	1.00	0.00	-0.80	4.64
56.70	2.53	0.0631	0.20	0.00	0.00	2.95

t = 13-14 days after fall in rainfall intensity				i_b[m/s]=	i_a[m/s]=	
Slice width[m] 2.11				1.00E-06	2.00E-07	
Slice no. 8			L_D[m]	12.66	63.30	
WSC_b at steady state[m] 0.0937			WSC[m]	0.0937	0.0896	
$WS_{x,a}$ at steady state[m] 0.0646			Q_{max}[m/s]	1.266E-05	1.266E-05	
time	x=14.77m	WS	dQx/dx	qi	dWS/dt	x=16.88m
[x10^3 s]	Q_x [x10^{-6}m^2/s]	[m]	[x10^{-6}m/s]	[x10^{-6}m/s]	[x10^{-6}m/s]	Q_x [x10^{-6}m^2/s]
0.00	12.66	0.0937	0.00	0.20	0.00	12.66
17.42	12.66	0.0937	0.00	0.20	0.00	12.66
22.36	11.39	0.0937	0.60	0.08	-0.48	12.66
26.32	9.71	0.0918	1.00	0.00	-0.80	11.82
30.01	8.02	0.0888	1.00	0.00	-0.80	10.13
33.63	6.33	0.0859	1.00	0.00	-0.80	8.44
37.32	4.64	0.0830	1.00	0.00	-0.80	6.75
56.70	2.95	0.0675	1.00	0.00	-0.80	5.06
60.37	2.95	0.0646	0.20	0.00	0.00	3.38

t = 13-14 days after fall in rainfall intensity				i_b[m/s]=	i_a[m/s]=	
Slice width[m] 2.11				1.00E-06	2.00E-07	
Slice no. 9			L_D[m]	12.66	63.30	
WSC_b at steady state[m] 0.0937			WSC[m]	0.0937	0.0896	
$WS_{x,a}$ at steady state[m] 0.0660			Q_{max}[m/s]	1.266E-05	1.266E-05	
time	x=16.88m	WS	dQx/dx	qi	dWS/dt	x=18.99m
[x10^3 s]	Q_x [x10^{-6}m^2/s]	[m]	[x10^{-6}m/s]	[x10^{-6}m/s]	[x10^{-6}m/s]	Q_x [x10^{-6}m^2/s]
0.00	12.66	0.0937	0.00	0.20	0.00	12.66
17.42	12.66	0.0937	0.00	0.20	0.00	12.66
22.36	12.66	0.0937	0.00	0.20	0.00	12.66
26.32	11.82	0.0937	0.40	0.12	-0.32	12.66
30.01	10.13	0.0925	1.00	0.00	-0.80	12.24
33.63	8.44	0.0896	1.00	0.00	-0.80	10.55
37.32	6.75	0.0867	1.00	0.00	-0.80	8.86
56.70	5.06	0.0712	1.00	0.00	-0.80	7.17
60.37	3.38	0.0682	1.00	0.00	-0.80	5.49
63.21	3.38	0.0660	0.20	0.00	0.00	3.80

t = 13-14 days after fall in rainfall intensity				i_b[m/s]=	i_a[m/s]=	
Slice width[m] 2.11				1.00E-06	2.00E-07	
Slice no. 10			L_D[m]	12.66	63.30	
WSC_b at steady state[m] 0.0937			WSC[m]	0.0937	0.0896	
$WS_{x,a}$ at steady state[m] 0.0673			Q_{max}[m/s]	1.266E-05	1.266E-05	
time	x=18.99m	WS	dQx/dx	qi	dWS/dt	x=21.1m
[x10^3 s]	Q_x [x10^{-6}m^2/s]	[m]	[x10^{-6}m/s]	[x10^{-6}m/s]	[x10^{-6}m/s]	Q_x [x10^{-6}m^2/s]
0.00	12.66	0.0937	0.00	0.20	0.00	12.66
17.42	12.66	0.0937	0.00	0.20	0.00	12.66
22.36	12.66	0.0937	0.00	0.20	0.00	12.66
26.32	12.66	0.0937	0.00	0.20	0.00	12.66
30.01	12.24	0.0937	0.20	0.16	-0.16	12.66
33.63	10.55	0.0931	1.00	0.00	-0.80	12.66
37.32	8.86	0.0901	1.00	0.00	-0.80	10.97
56.70	7.17	0.0746	1.00	0.00	-0.80	9.28
60.37	5.49	0.0717	1.00	0.00	-0.80	7.60
63.21	3.80	0.0694	1.00	0.00	-0.80	5.91
65.87	3.80	0.0673	0.20	0.00	0.00	4.22

t = 13-14 days after fall in rainfall intensity				i_b[m/s]=	i_a[m/s]=	
Slice width[m] 2.11				1.00E-06	2.00E-07	
Slice no. 11			L_D[m]	12.66	63.30	
WSC_b at steady state[m] 0.0937			WSC[m]	0.0937	0.0896	
$WS_{x,a}$ at steady state[m] 0.0686			Q_{max}[m/s]	1.266E-05	1.266E-05	
time	x=21.1m	WS	dQx/dx	qi	dWS/dt	x=23.21m
[x10^3 s]	Q_x [x10^{-6}m^2/s]	[m]	[x10^{-6}m/s]	[x10^{-6}m/s]	[x10^{-6}m/s]	Q_x [x10^{-6}m^2/s]
0.00	12.66	0.0937	0.00	0.20	0.00	12.66
17.42	12.66	0.0937	0.00	0.20	0.00	12.66
22.36	12.66	0.0937	0.00	0.20	0.00	12.66
26.32	12.66	0.0937	0.00	0.20	0.00	12.66
30.01	12.66	0.0937	0.00	0.20	0.00	12.66
33.63	12.66	0.0937	0.00	0.20	0.00	12.66
37.32	10.97	0.0937	0.80	0.04	-0.64	12.66
56.70	9.28	0.0813	1.00	0.00	-0.80	11.39
60.37	7.60	0.0783	1.00	0.00	-0.80	9.71
63.21	5.91	0.0761	1.00	0.00	-0.80	8.02
65.87	4.22	0.0739	1.00	0.00	-0.80	6.33
72.55	4.22	0.0686	0.20	0.00	0.00	4.64

t = 13-14 days after fall in rainfall intensity				i_b[m/s]=	i_a[m/s]=	
Slice width[m] 2.11				1.00E-06	2.00E-07	
Slice no. 12			L_D[m]	12.66	63.30	
WSC_b at steady state[m] 0.0937			WSC[m]	0.0937	0.0896	
$WS_{x,a}$ at steady state[m] 0.0698			Q_{max}[m/s]	1.266E-05	1.266E-05	
time	x=23.21m	WS	dQx/dx	qi	dWS/dt	x=25.32m
[x10^3 s]	Q_x [x10^{-6}m^2/s]	[m]	[x10^{-6}m/s]	[x10^{-6}m/s]	[x10^{-6}m/s]	Q_x [x10^{-6}m^2/s]
0.00	12.66	0.0937	0.00	0.20	0.00	12.66
17.42	12.66	0.0937	0.00	0.20	0.00	12.66
22.36	12.66	0.0937	0.00	0.20	0.00	12.66
26.32	12.66	0.0937	0.00	0.20	0.00	12.66
30.01	12.66	0.0937	0.00	0.20	0.00	12.66
33.63	12.66	0.0937	0.00	0.20	0.00	12.66
37.32	12.66	0.0937	0.00	0.20	0.00	12.66
56.70	11.39	0.0937	0.60	0.08	-0.48	12.66
60.37	9.71	0.0919	1.00	0.00	-0.80	11.82
63.21	8.02	0.0896	1.00	0.00	-0.80	10.13
65.87	6.33	0.0875	1.00	0.00	-0.80	8.44
72.55	4.64	0.0822	1.00	0.00	-0.80	6.75
87.97	4.64	0.0698	0.20	0.00	0.00	5.06

Appendix E Additional extreme rainfall events: numerical validation of simplified method of analysis

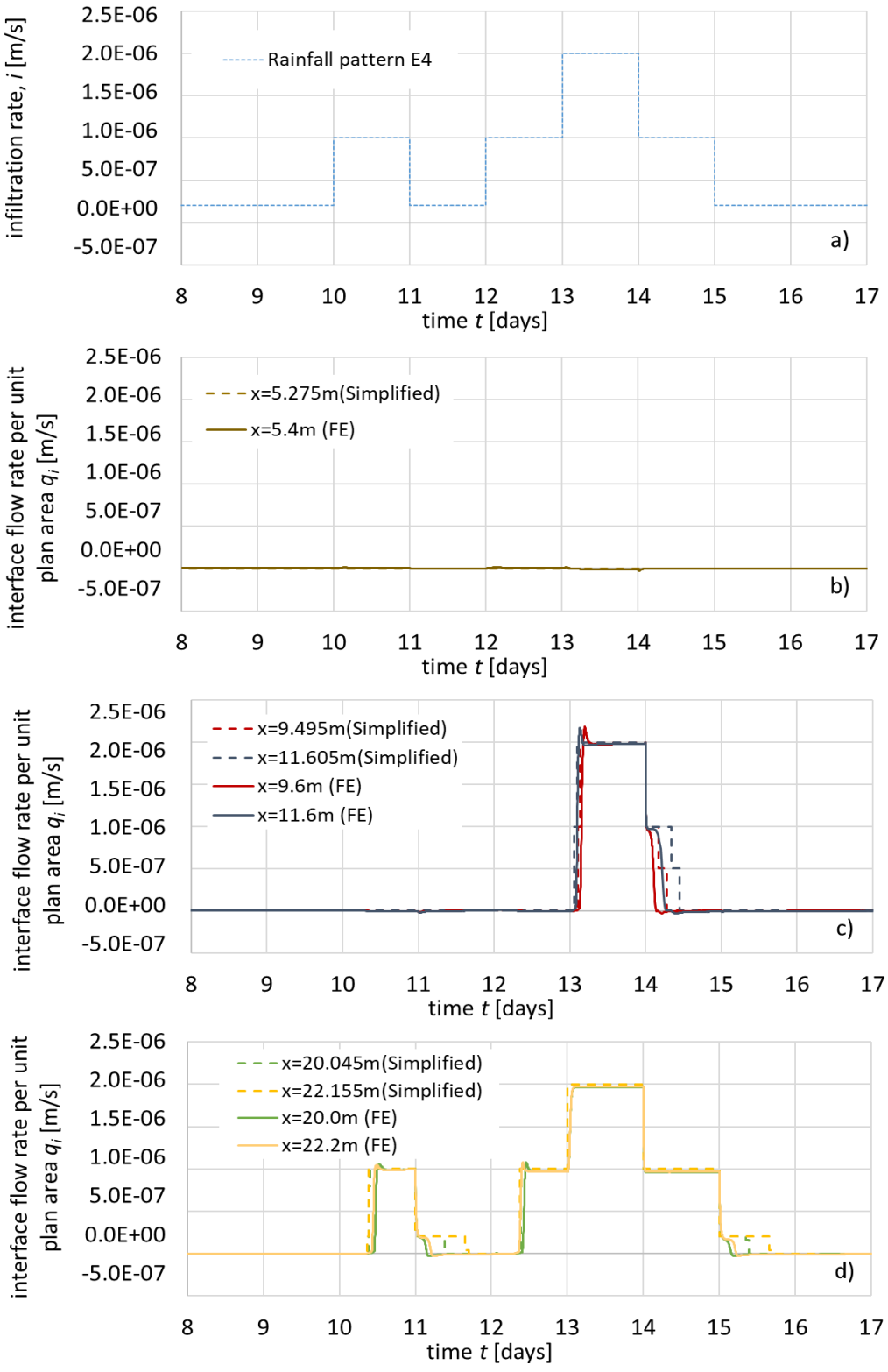

Figure E- 1 Sloping CBS with F.L. made of fine sand subjected to extreme rainfall pattern E4: comparison of FE results and simplified method predictions (β = 35°, FSGV, t_f = 40 cm)

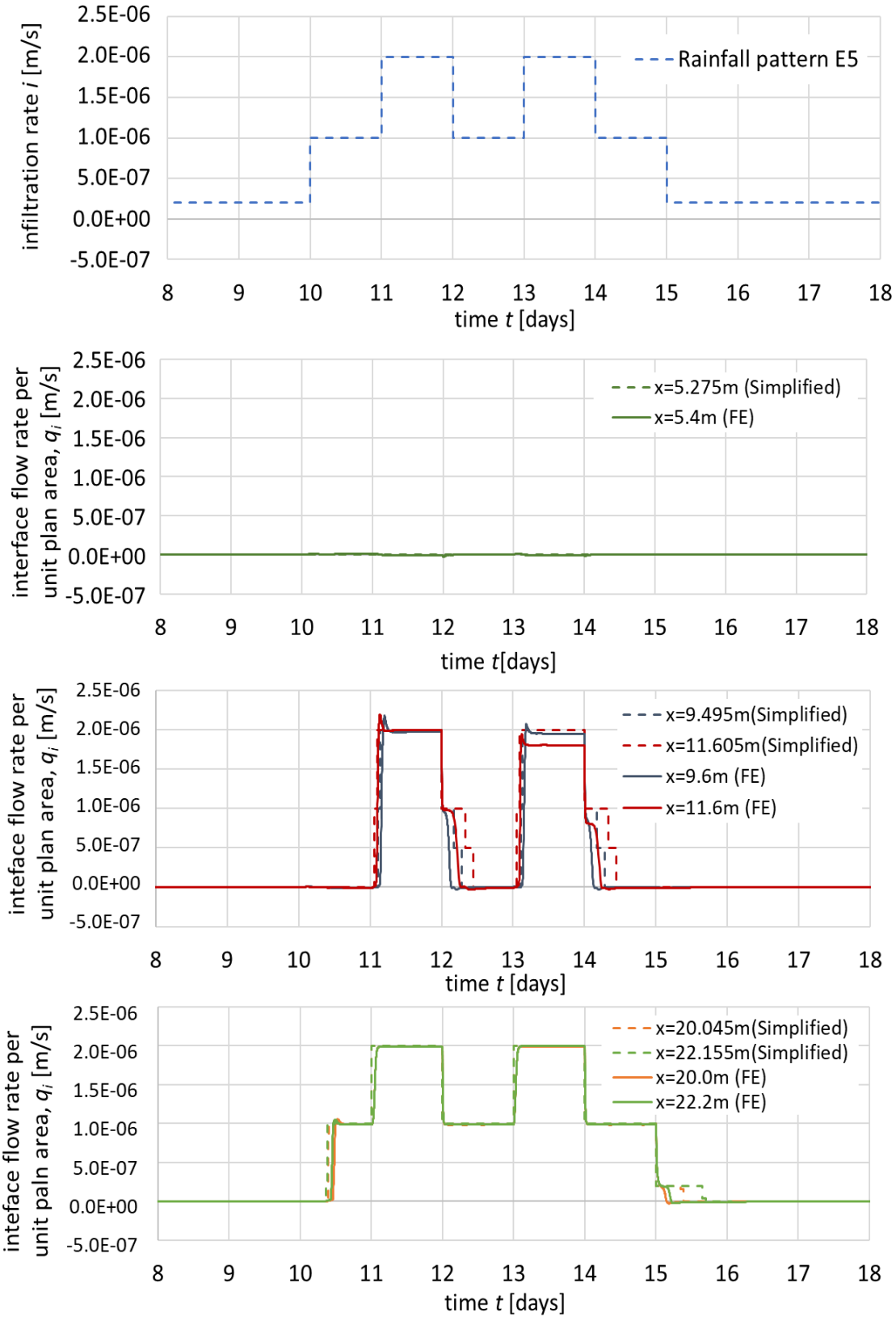

Figure E- 2 Sloping CBS with F.L. made of fine sand subjected to extreme rainfall pattern E5: comparison of FE results and simplified method predictions (β = 35°, FSGV, t_f = 40 cm)

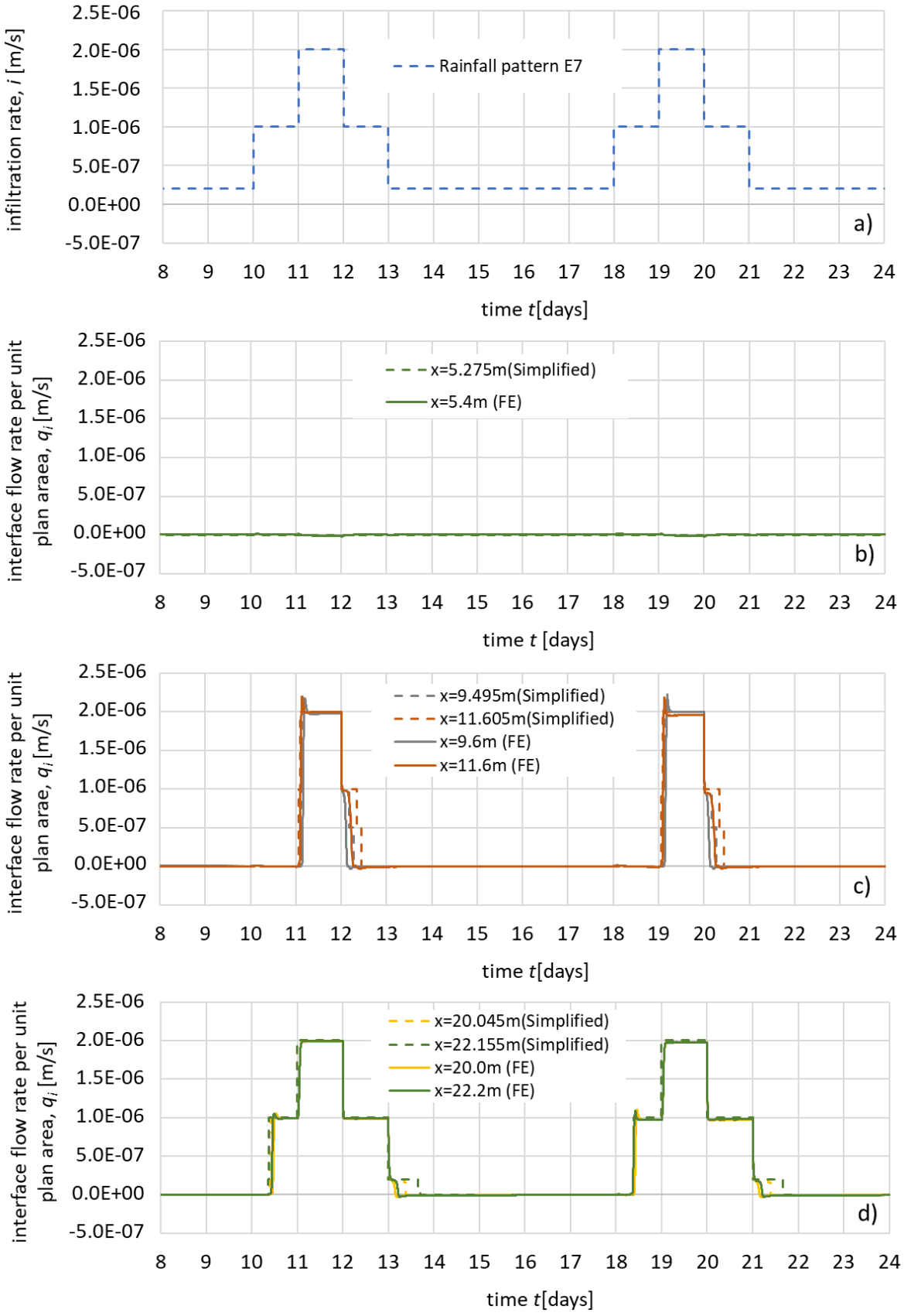

Figure E- 3 Sloping CBS with F.L. made of fine sand subjected to extreme rainfall pattern E7: comparison of FE results and simplified method predictions (β =35°, FSGV, t_f = 40 cm)

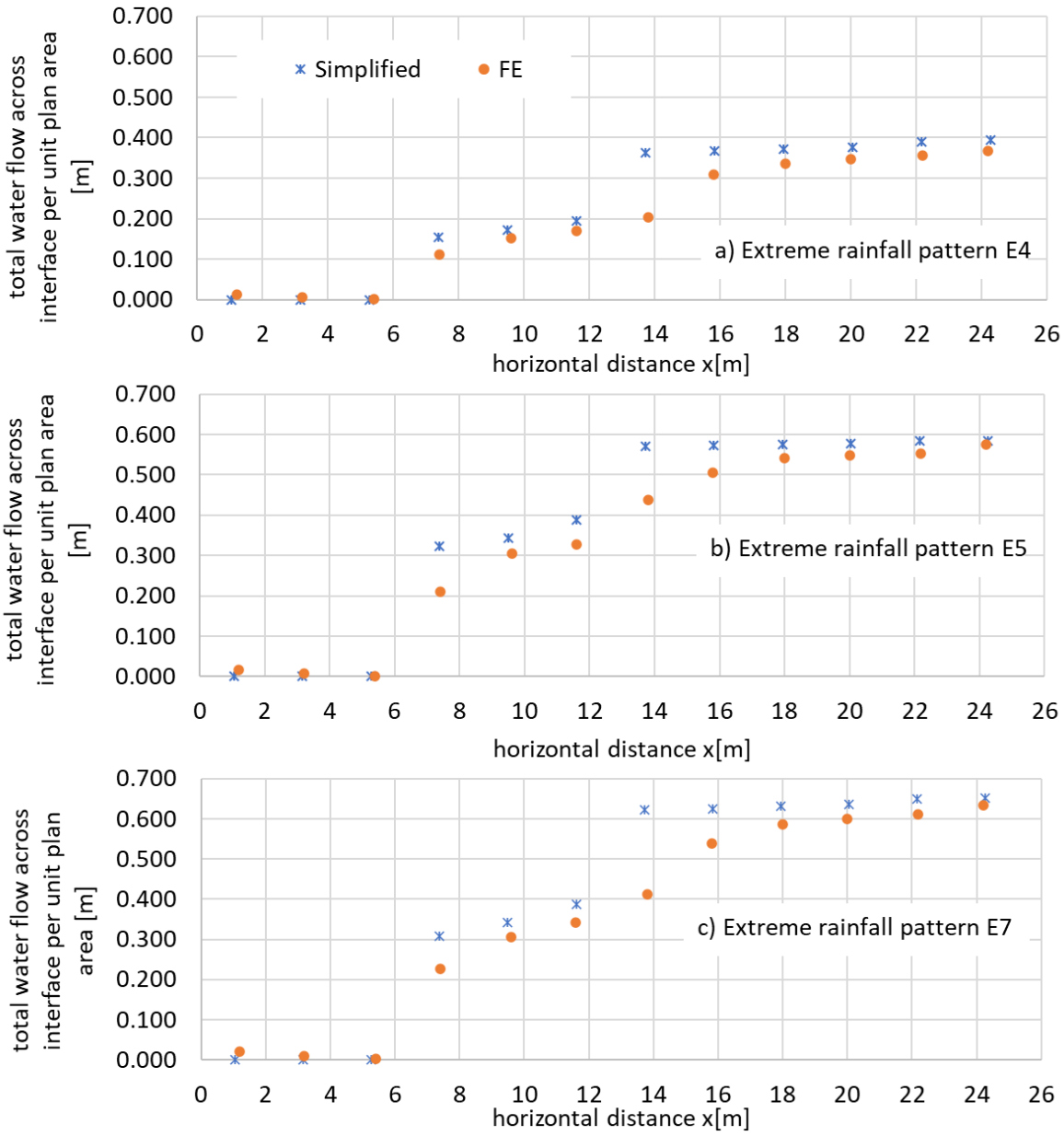

Figure E- 4 Variation of total water flow across interface per unit plan area: comparison of simplified method and FE results; a) rainfall pattern E4; b) rainfall pattern E5; and c) rainfall pattern E7 (β = 35°, FSGV, t_f = 40 cm)

Appendix F Derivation of factor of safety expression from infinite slope analysis

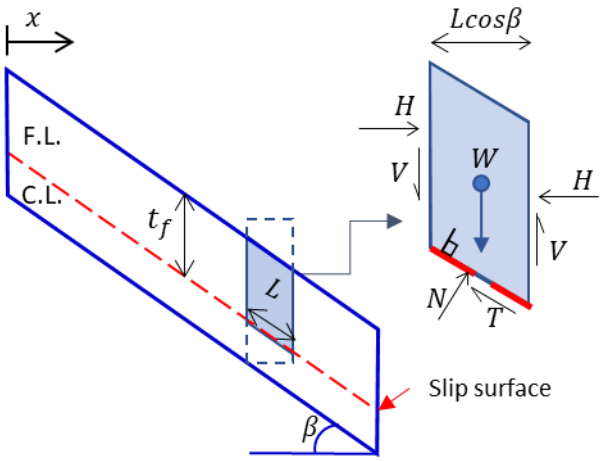

Figure F-1 Schematic of slice within infinite slope

The derivation of Equation 8-3 is described in this appendix. The weight W (per unit length in the out-of-plane direction) of a typical slice of F.L within an infinite slope, shown in Figure B-1, is given by:

$$W = \gamma_f t_f L \cos\beta \qquad \text{F-1}$$

where γ_f is the bulk unit weight of the F.L material, t_f is the vertical thickness of the F.L, L is the inclined length of the slice and β is the slope angle.

Resolving parallel to the interface, the shear force T (per unit length in the out-of-plane direction) on the section of interface forming the bottom of the slice is given by:

$$T = W \sin\beta = \gamma_f t_f L \sin\beta \cos\beta$$

Hence, the shear stress τ on the interface is given by:

$$\tau = T/L = \gamma_f t_f \sin\beta \cos\beta \qquad \text{F-2}$$

Resolving perpendicular to the interface, the normal force N (per unit length in the out-of-plane direction) on the section of interface forming the bottom of the slice is given by:

$$N = W\cos\beta = \gamma_f t_f \cos^2\beta$$

Hence, the normal total stress σ on the interface is given by:

$$\sigma = N/L = \gamma_f t_f \cos^2\beta \quad \text{F-3}$$

But, if the value of pore water pressure on the interface is u_w and the soil at this interface is saturated, the normal effective stress σ' on the interface is given by:

$$\sigma' = \sigma - u_w = \gamma_f t_f \cos^2\beta - u_w \quad \text{F-4}$$

But the shear strength equation for a cohesionless saturated soil (when c'= 0) is:

$$\tau_{failure} = \sigma' \tan\emptyset'$$

Hence,

$$\tau_{failure} = \left(\gamma_f t_f \cos^2\beta - u_w\right)\tan\emptyset' \quad \text{F-5}$$

Therefore, the factor of safety (FoS), for a potential failure surface at the interface is given by:

$$FoS = \frac{\tau_{failure}}{\tau} = \frac{\left(\gamma_f t_f \cos^2\beta - u_w\right)\tan\emptyset'}{\gamma_f t_f \sin\beta\cos\beta}$$

$$FoS = \left(1 - \frac{u_w}{\gamma_f t_f \cos^2\beta}\right)\frac{\tan\emptyset'}{\tan\beta} \quad \text{F-6}$$

References

Abdolahzadeh, A. M., Vachon, B. L.and Cabral, A. R. 2011. Evaluation of the effectiveness of a cover with capillary barrier effect to control percolation into a waste disposal facility. *Canadian Geotechnical Journal,* 48, *7*, 996-1009.

Akin, I. D.and Likos, W. J. 2017. Implications of Surface Hydration and Capillary Condensation for Strength and Stiffness of Compacted Clay. *Journal of Engineering Mechanics,* 143, *8*, 4017054.

Alonso, E. E., Gens, A.and Josa, A. 1990. A constitutive model for partially saturated soils. *Géotechnique,* 40, *3*, 405-430.

Aubertin, M., Cifuentes, E., Apithy, S. A., Bussiere, B., Molson, J.and Chapuis, R. P. 2009. Analyses of water diversion along inclined covers with capillary barrier effects. *Canadian Geotechnical Journal,* 46, *10*, 1146-1164.

Benson, C. H., Barlaz, M. A., Lane, D. T.and Rawe, J. M. 2007. Practice review of five bioreactor/recirculation landfills. *Waste Management,* 27, *1*, 13-29.

Bishop, A. W. 1959. The Principle of Effective Stress. *Teknisk Ukeblad,* 39, 859-863.

Blanco-Canqui, H., Gantzer, C. J., Anderson, S. H., Alberts, E. E.and Ghidey, F. 2002. Saturated Hydraulic Conductivity and Its Impact on Simulated Runoff for Claypan Soils. *Soil Science Society of America Journal,* 66, *5*, 1596-1602.

Blight, G. E. 1997. Interactions between the atmosphere and the earth. *Geotechnique,* 47, *4*, 715-766.

Bond, J.and Willis, W. 1969. Soil water evaporation: surface residue rate and placement effects. *Soil Science Society of America Journal,* 33, *3*, 445-448.

Brennen, C. E. 2014. Cavitation and bubble dynamics. Cambridge: Cambridge University Press.

Brooks, R. H.and Corey, A. T. 1964. Hydraulic properties of porous media. *Hydrology papers,* 24, *Colorado State University (Fort Collins)*, 37.

Brutsaert, W. 1982. *Evaporation into the atmosphere: Theory, history, and applications,* London, D. Reidel.

Burdine, N. T. 1953. Relative permeability calculations from pore size distribution data *Transactions of the American Institute of Mining and Metallurgical Engineers* 198, 71-78.

Bussière, B., Aubertin, M.and Zhan, G. 2007. Design of Inclined Covers with Capillary Barrier Effect by S.-E. Parent and A. Cabral. *Geotechnical and Geological Engineering,* 25, *6*, 673-678.

Bussiere, B., M, A.and R.P, C. 2003. The behavior of inclined covers used as oxygen barriers. *Canadian Geotechnical Journal,* 40, *3*, 512-535.

Campbell, G.and Shiozawa, S. 1992. Prediction of hydraulic properties of soils using particle-size distribution and bulk density data. *Indirect methods for estimating the hydraulic properties of unsaturated soils,* 317-328.

Chen, R., Liu, J., Ng, C. W. W.and Chen, Z. K. 2019. Influence of Slope Angle on Water Flow in a Three-Layer Capillary Barrier Soil Cover under Heavy Rainfall. *Soil Science Society of America Journal,* 83, *6*, 1637-1647.

Cheng, Q., Zhou, C., Ng, C. W. W.and Tang, C. 2019. Thermal effects on water retention behaviour of unsaturated collapsible loess. *Journal of Soils and Sediments,* 20, *2*, 756-762.

Coppin, N. J.and Richards, I. G. 1990. *Use of vegetation in civil engineering*, CIRIA, Butterworths.

De Vries, D. 1958. Simultaneous transfer of heat and moisture in porous media. *Eos, Transactions American Geophysical Union,* 39, *5*, 909-916.

Thailand Meteorological Department [Online]. Available: https://www.tmd.go.th [Accessed 28-10-2020].

Dong, Y., McCartney, J. S.and Lu, N. 2015. Critical Review of Thermal Conductivity Models for Unsaturated Soils. *Geotechnical and Geological Engineering,* 33, *2*, 207-221.

Escario, V.and Saez, J. 1986. The shear strength of partly saturated soils. *Géotechnique,* 36, *3*, 453-456.

Everett, D. H. 1955. A general approach to hysteresis – part 4: an alternative formulation of the domain model. *Transactions of the Faraday Society,* 51, 1551-1557.

Fayer, M. J.and Simmons, C. S. 1995. Modified Soil Water Retention Functions for All Matric Suctions. *Water Resources Research,* 31, *5*, 1233-1238.

Fredlund, D. G. 2006. Unsaturated soil mechanics in engineering practice. *Journal of Geotechnical and Geoenvironmental Engineering,* 132, *3*, 286-321.

Fredlund, D. G., Morgenstern, N. R.and Widger, R. A. 1978. The shear strength of unsaturated soils. *Canadian Geotechnical Journal,* 15, *3*, 313-321.

Fredlund, D. G.and Rahardjo, H. 1993. *Soil mechanics for unsaturated soils*, John Wiley & Sons.

Fredlund, D. G.and Xing, A. 1994. Equations for the soil-water characteristic curve. *Canadian Geotechnical Journal,* 31, *4*, 521-532.

Gallipoli, D. 2012. A hysteretic soil-water retention model accounting for cyclic variations of suction and void ratio. *Géotechnique,* 62, *7*, 605-616.

Gallipoli, D., Bruno, A. W., D'Onza, F.and Mancuso, C. 2015. A bounding surface hysteretic water retention model for deformable soils. *Géotechnique,* 65, *10*, 793-804.

Gallipoli, D., Gens, A., Sharma, R.and Vaunat, J. 2003. An elasto-plastic model for unsaturated soil incorporating the effects of suction and degree of saturation on mechanical behaviour. *Géotechnique,* 53, *1*, 123-135.

Gardner, W. 1958. Some steady-state solutions of the unsaturated moisture flow equation with application to evaporation from a water table. *Soil science,* 85, *4*, 228-232.

Gens, A. 2010. Soil–environment interactions in geotechnical engineering. *Géotechnique,* 60, *1*, 3-74.

Haines, W. B. 1930. Studies in the physical properties of soil. V. The hysteresis effect in capillary properties, and the modes of moisture distribution associated therewith. *The Journal of Agricultural Science,* 20, *1*, 97-116.

Hanks, R. J., Klute, A.and Bresler, E. 1969. A numeric method for estimating infiltration, redistribution, drainage, and evaporation of water from soil. *Water Resources Research,* 5, *5*, 1064-1069.

Harnas, F. R., Rahardjo, H., Leong, E. C.and Wang, J. Y. 2014. Experimental study on dual capillary barrier using recycled asphalt pavement materials. *Canadian Geotechnical Journal,* 51, *10*, 1165-1177.

Henry, W. Experiments on the quantity of gases absorbed by water, at different temperatures, and under different pressures. Abstracts of the Papers Printed in the Philosophical Transactions of the Royal Society of London, 1832. The Royal Society London, 103-104.

Jaynes, D. B. 1984. Comparison of soil-water hysteresis models. *Journal of Hydrology,* 75, *1*, 287-299.

Jennings, J. E. B.and Burland, J. B. 1962. Limitations to the Use of Effective Stresses in Partly Saturated Soils. *Géotechnique,* 12, *2*, 125-144.

Kampf, M.and Montenegro, H. 1997. On the performance of capillary barriers as landfill cover. *Hydrology and Earth System Sciences,* 1, *4*, 925-930.

Kaye, G. W. C.and Laby, T. H. 1926. *Tables of physical and chemical constants and some mathematical functions*, Longmans, Green and Company.

Khalili, N., Habte, M. A.and Zargarbashi, S. 2008. A fully coupled flow deformation model for cyclic analysis of unsaturated soils including hydraulic and mechanical hysteresis. *Computers and Geotechnics,* 35, *6*, 872-889.

Khire, M. V., Benson, C. H.and Bosscher, P. J. 2000. Capillary Barriers: Design Variables and Water Balance. *Journal of Geotechnical and Geoenvironmental Engineering,* 126, *8*, 695-708.

Khlosi, M., Cornelis, W. M., Gabriels, D.and Sin, G. 2006. Simple modification to describe the soil water retention curve between saturation and oven dryness: Technical Note. *Water Resources Research,* 42, *11*, W11501.

Klausner, Y. 2012. *Fundamentals of continuum mechanics of soils*, Springer Science & Business Media.

Kool, J. B.and Parker, J. C. 1987. Development and evaluation of closed-form expressions for hysteretic soil hydraulic properties. *Water Resources Research,* 23, *1*, 105-114.

Kosugi, K. 1996. Lognormal distribution model for unsaturated soil hydraulic properties. *Water Resources Research,* 32, *9*, 2697-2703.

Krynine, D. 1948. Analysis of the latest American tests on soil capillarity. Second International Conference on Soil Mechanics and Foundation Engineering, Rotterdam.

Lacroix Vachon, B., Cabral, A. R.and Abdolahzadeh, A. M. 2015. Predicting the diversion length of capillary barriers using steady state and transient state numerical modeling: case study of the Saint-Tite-des-Caps landfill final cover. *Canadian Geotechnical Journal,* 52, *12*, 2141-2148.

Laloui, L.and Loria, A. F. R. 2019. Analysis and design of energy geostructure:Theoretical Essentials and practical application. *Academic Press*.

Laplace, P. 1806. Supplement to the tenth edition. *Méchanique céleste,* 10, 1985-1990.

Laroussi, C.and De Backer, L. 1979. Relations between geometrical properties of glass beads media and their main ψ (θ) hysteresis loops. *Soil Science Society of America Journal,* 43, *4*, 646-650.

Lebeau, M.and Konrad, J.-M. 2010. A new capillary and thin film flow model for predicting the hydraulic conductivity of unsaturated porous media. *Water Resources Research,* 46, *12*, W12554.

Li, J. H., Du, L., Chen, R.and Zhang, L. M. 2013. Numerical investigation of the performance of covers with capillary barrier effects in South China. *Computers and Geotechnics,* 48, 304-315.

Li, X. S. 2005. Modelling of hysteresis response for arbitrary wetting/drying paths. *Computers and Geotechnics,* 32, *2*, 133-137.

Li, Y., Satyanaga, A.and Rahardjo, H. 2021. Characteristics of unsaturated soil slope covered with capillary barrier system and deep-rooted grass under different rainfall patterns. *International Soil and Water Conservation Research,* 9, *3*, 405-418.

Likos, W. J., Lu, N.and Godt, J. W. 2014. Hysteresis and Uncertainty in Soil Water-Retention Curve Parameters. *Journal of Geotechnical and Geoenvironmental Engineering,* 140, *4*, 4013050.

Liu, C.and Muraleetharan, K. K. 2006. Description of Soil Water Characteristic Curves Using the Bounding Surface Plasticity Theory. 4th Int. Conf. Unsaturated Soils 2006, 2, 2432-2440.

Liu, J., Chen, R.and Ng, C. W. W. 2015. Discussion of "Physical and numerical study of lateral diversion by three-layer inclined capillary barrier covers under humid climatic conditions". *Canadian Geotechnical Journal,* 52, *4*, 530-531.

Lu, N.and Likos, W. J. 2004. *Unsaturated soil mechanics,* Hoboken, NJ, John Wiley & Sons.

Mallants, D., Volckaert, G.and Marivoet, J. 1999. Sensitivity of protective barrier performance to changes in rainfall rate. *Waste Management,* 19, *7*, 467-475.

Miyazaki, T. 1988. Water flow in unsaturated soil in layered slopes. *Journal of Hydrology,* 102, *1-4*, 201-214.

Morel-Seytoux, H. J. 1994. Steady- state effectiveness of capillary barrier system on sloping interface. *Hydrology Days,* 335-346.

Morel-Seytoux, H. J., Meyer, P. D., Nachabe, M., Tourna, J., van Genuchten, M. T.and Lenhard, R. J. 1996. Parameter Equivalence for the Brooks-Corey and Van Genuchten Soil Characteristics: Preserving the Effective Capillary Drive. *Water Resources Research,* 32, *5*, 1251-1258.

Morris, C. E.and Stormont, J. C. 1999. Parametric Study of Unsaturated Drainage Layers in a Capillary Barrier. *Journal of Geotechnical and Geoenvironmental Engineering,* 125, *12*, 1057-1065.

Mualem, Y. 1974. A conceptual model of hysteresis. *Water Resources Research,* 10, *3*, 514-520.

Mualem, Y. 1976. A new model for predicting the hydraulic conductivity of unsaturated porous media. *Water Resources Research,* 12, *2*, 513-522.

Mualem, Y. 1977. Extension of the similarity hypothesis used for modeling the soil water characteristics. *Water Resources Research,* 13, *4*, 773-780.

Mualem, Y. 1984. Prediction of the soil boundary wetting curve. *Soil Science,* 137, *6*, 379-390.

Muneta, Y., Mubarak, M., Alhassani, H.and Arisaka, K. 2005. Formulation of capillary force barriers in moderately oil-wet systems and their application to reservoir simulation. *SPE Reservoir Evaluation & Engineering,* 8, *5*, 388-396.

Néel, L. 1942. Théorie des lois d'aimantation de Lord Rayleigh 1. *Cahiers de Physique,* 12, 1-20.

Néel, L. 1943. Théorie des lois d'aimantation de Lord Rayleigh, 2. *Cahiers de Physique,* 13, 18-30.

Ng, C. W. W., Liu, J., Chen, R.and Coo, J. L. 2015a. Numerical parametric study of an alternative three-layer capillary barrier cover system. *Environmental Earth Sciences,* 74, *5*, 4419-4429.

Ng, C. W. W., Liu, J., Chen, R.and Xu, J. 2015b. Physical and numerical modeling of an inclined three-layer (silt/gravelly sand/clay) capillary barrier cover system under extreme rainfall. *Waste Management,* 38, 210-221.

Nuth, M.and Laloui, L. 2008. Advances in modelling hysteretic water retention curve in deformable soils. *Computers and Geotechnics,* 35, *6*, 835-844.

MET Office [Online]. Available: http://www.metoffice.gov.uk [Accessed 28-09 2020].

Oldenburg, C. M.and Pruess, K. 1993. On numerical modeling of capillary barriers. *Water Resources Research,* 29, *4*, 1045-1056.

Olivella, S., Carrera, J., Gens, A.and Alonso, E. 1994. Nonisothermal multiphase flow of brine and gas through saline media. *Transport in Porous Media,* 15, *3*, 271-293.

Olivella, S., Gens, A., Carrera, J.and Alonso, E. E. 1996. Numerical formulation for a simulator (CODE_BRIGHT) for the coupled analysis of saline media. *Engineering Computations,* 13, *7*, 87-112.

Parent, S.-É.and Cabral, A. 2006. Design of Inclined Covers with Capillary Barrier Effect. *Geotechnical and Geological Engineering,* 24, *3*, 689-710.

Parker, J. C.and Lenhard, R. J. 1987. A model for hysteretic constitutive relations governing multiphase flow: 1. Saturation-pressure relations. *Water Resources Research,* 23, *12*, 2187-2196.

Pedone, G., Tsiampousi, A., Cotecchia, F.and Zdravkovic, L. 2022. Coupled hydro-mechanical modelling of soil–vegetation–atmosphere interaction in natural clay slopes. *Canadian Geotechnical Journal,* 59, *2*, 272-290.

Peters, A. 2013. Simple consistent models for water retention and hydraulic conductivity in the complete moisture range. *Water Resources Research,* 49, *10*, 6765-6780.

Peters, A. 2014. Reply to comment by S. Iden and W. Durner on "Simple consistent models for water retention and hydraulic conductivity in the complete moisture range". *Water Resources Research,* 50, *9*, 7535-7539.

Peters, A.and Durner, W. 2008. A simple model for describing hydraulic conductivity in unsaturated porous media accounting for film and capillary flow. *Water Resources Research,* 44, *11*, W11417.

Pham, H. Q., Fredlund, D. G.and Barbour, S. L. 2005. A study of hysteresis models for soil-water characteristic curves. *Canadian Geotechnical Journal,* 42, *6*, 1548-1568.

Philip, J. R. 1964. Similarity hypothesis for capillary hysteresis in porous materials. *Journal of Geophysical Research,* 69, *8*, 1553-1562.

Poulovassilis, A. 1962. Hysteresis of pore water, an application of the concept of independent domains. *Soil science,* 93, *6*, 405-412.

Qian, T., Huo, L.and Zhao, D. 2010. Laboratory Investigation Into Factors Affecting Performance of Capillary Barrier System in Unsaturated Soil. *Water, Air, and Soil Pollution,* 206, *1*, 295-306.

Rahardjo, H. 2015. Capillary barrier as a slope protection. First Distinguished Lecture, Proceedings of the 6th Asia-Pacific Conference on Unsaturated Soils (AP-UNSAT2015), 2015. 23-26.

Rahardjo, H., Santoso, V. A., Leong, E. C., Ng, Y. S.and Hua, C. J. 2012. Performance of an Instrumented Slope Covered by a Capillary Barrier System. *Journal of Geotechnical and Geoenvironmental Engineering,* 138, *4*, 481-490.

Rahardjo, H., Satyanaga, A., Harnas, F. R.and Leong, E. C. 2016. Use of Dual Capillary Barrier as Cover System for a Sanitary Landfill in Singapore. *Indian Geotechnical Journal,* 46, *3*, 228-238.

Raveendiraraj, A. 2009. *Coupling of mechanical behaviour and water retention behaviour in unsaturated soils.* PhD thesis, University of Glasgow, UK.

Ribo, R., Pasenau, M., Escolano, E., Ronda, J., Gonzalez, L.and Rosa, E. 1999. Gid user manual. Barcelona: CIMNE.

Richards, B. G. 1965. Measurement of free energy of soil moisture by the psychometric technique, using thermistors. *In Moisture Equilibria and Moisture Change in soils Beneath Covered areas,* 35-46.

Ross, B. 1990. The diversion capacity of capillary barriers. *Water Resources Research,* 26, *10,* 2625-2629.

Rossi, C.and Nimmo, J. R. 1994. Modeling of soil water retention from saturation to oven dryness. *Water Resources Research,* 30, *3,* 701-708.

Scarfone, R. 2020. *Modelling the hydraulic behaviour of unsaturated soils and application to the numerical and experimental study of capillary barrier systems.* PhD Thesis, University of Glasgow, UK.

Scarfone, R.and Wheeler, S. J. 2022. Analytical and numerical modelling of air trapping during wetting of unsaturated soils. *Acta Geotechnica,* 17.

Scarfone, R., Wheeler, S. J.and Lloret-Cabot, M. 2020a. Conceptual Hydraulic Conductivity Model for Unsaturated Soils at Low Degree of Saturation and Its Application to the Study of Capillary Barrier Systems. *Journal of Geotechnical and Geoenvironmental Engineering,* 146, *10,* 4020106.

Scarfone, R., Wheeler, S. J.and Lloret-Cabot, M. 2020b. A hysteretic hydraulic constitutive model for unsaturated soils and application to capillary barrier systems. *Geomechanics for Energy and the Environment,* 30, 100224.

Scarfone, R., Wheeler, S. J.and Smith, C. C. 2022. Numerical modelling of the application of capillary barrier systems for prevention of rainfall-induced slope instability. *Acta Geotechnica,* 18, 355-378.

Schubert, H., Herrmann, W.and Rumpf, H. 1975. Deformation behaviour of agglomerates under tensile stress. *Powder Technology,* 11, *2,* 121-131.

Scott, P. S., Farquhar, G. J.and Kouwen, N. 1983. Hysteretic effects on net infiltration. In Advances in Infiltration. *American Society of Agricultural Engineers,* 163-170.

Sherard, J. L.and Dunnigan, L. P. Filters and leakage control in embankment dams. Seepage and leakage from dams and impoundments, 1985. ASCE, 1-30.

Steenhuis, T. S., Parlange, J. Y.and Kung, K. J. S. 1991. Comment on "The Diversion Capacity of Capillary Barriers" by Benjamin Ross. *Water Resources Research,* 27, *8,* 2155-2156.

Stormont, J. C. 1995. The Effect of Constant Anisotropy on Capillary Barrier Performance. *Water Resources Research,* 31, *3,* 783-785.

Stormont, J. C.and Anderson, C. E. 1999. Capillary Barrier Effect from Underlying Coarser Soil Layer. *Journal of Geotechnical and Geoenvironmental Engineering,* 125, *8,* 641-648.

Stormont, J. C.and Morris, C. E. 1998. Method to Estimate Water Storage Capacity of Capillary Barriers. *Journal of Geotechnical and Geoenvironmental Engineering,* 124, *4,* 297-302.

Tami, D., Rahardjo, H., Leong, E.-C.and Fredlund, D. G. 2004. Design and laboratory verification of a physical model of sloping capillary barrier. *Canadian Geotechnical Journal,* 41, *5,* 814-830.

Tang, A. M., Hughes, P. N., Dijkstra, T. A., Askarinejad, A., Brenčič, M., Cui, Y. J., Diez, J., Firgi, T., Gajewska, B.and Gentile, F. 2018. Atmosphere–vegetation–soil interactions in a climate change context; impact of changing conditions on engineered transport infrastructure slopes in Europe. *Quarterly Journal of Engineering Geology and Hydrogeology,* 51, *2,* 156-168.

Tokunaga, T. K. 2009. Hydraulic properties of adsorbed water films in unsaturated porous media. *Water Resources Research,* 45, *6,* W06415-n/a.

Topp, G. C. 1971. Soil-Water Hysteresis: the Domain Theory Extended to Pore Interaction Conditions1. *Soil Science Society of America Journal,* 35, 219-225.

Tsiampousi, A., Zdravkovic, L.and Potts, D. M. 2017. Numerical study of the effect of soil–atmosphere interaction on the stability and serviceability of cut slopes in London clay. *Canadian Geotechnical Journal,* 54, *3,* 405-418.

Tuller, M.and Or, D. 2001. Hydraulic conductivity of variably saturated porous media: Film and corner flow in angular pore space. *Water Resources Research,* 37, *5,* 1257-1276.

UPC. 2019. CODE_BRIGHT User's guide. *In:* DEPARTMENT OF CIVIL AND ENVIRONMENTAL ENGINEERING, U. P. D. C. (ed.).

van Genuchten, M. T. 1980. A closed-form equation for predicting the hydraulic conductivity of unsaturated soils *Soil Science Society of America Journal,* 44, *5,* 892-898.

Wheeler, S. J., Sharma, R. S.and Buisson, M. S. R. 2003. Coupling of hydraulic hysteresis and stress-strain behaviour in unsaturated soils. *Géotechnique,* 53, *1,* 41-54.

Yang, H., Rahardjo, H.and Leong, E. C. 2006. Behavior of Unsaturated Layered Soil Columns during Infiltration. *Journal of Hydrologic Engineering,* 11, *4,* 329-337.

Young, T. 1805. III. An essay on the cohesion of fluids. *Philosophical Transactions of the Royal Society of London,* 95, 65-87.

Zhan, L.-t., Li, G.-y., Jiao, W.-g., Wu, T., Lan, J.-w.and Chen, Y.-m. 2017. Field measurements of water storage capacity in a loess–gravel capillary barrier cover using rainfall simulation tests. *Canadian Geotechnical Journal,* 54, *11*, 1523-1536.

Zhan, T. L. T., Jia, G. W., Chen, Y. M., Fredlund, D. G.and Li, H. 2013. An analytical solution for rainfall infiltration into an unsaturated infinite slope and its application to slope stability analysis. *International Journal for Numerical and Analytical Methods in Geomechanics,* 37, *12*, 1737-1760.

Zhan, T. L. T., Li, H., Jia, G. W., Chen, Y. M.and Fredlund, D. G. 2014. Physical and numerical study of lateral diversion by three-layer inclined capillary barrier covers under humid climatic conditions. *Canadian Geotechnical Journal,* 51, *12*, 1438-1448.

Zhang, Q., Werner, D., Aviyanto, F.and Hutson, L. 2009. Influence of soil moisture hysteresis on the functioning of capillary barriers. *Hydrological Processes,* 23, *9*, 1369-1375.

Zhang, W., Sun, C.and Qiu, Q. 2016. Characterizing of a capillary barrier evapotranspirative cover under high precipitation conditions. *Environmental Earth Sciences,* 75, *6*, 1-11.

Zhang, Z. F. 2011. Soil Water Retention and Relative Permeability for Conditions from Oven-Dry to Full Saturation. *Vadose Zone Journal,* 10, *4*, 1299-1308.

Zhou, A.-N., Sheng, D., Sloan, S. W.and Gens, A. 2012. Interpretation of unsaturated soil behaviour in the stress – Saturation space, I: Volume change and water retention behaviour. *Computers and Geotechnics,* 43, 178-187.